Mission-Oriented Seismic
Research Program

Annual Report

2011

M-OSRP

University of Houston

Sponsors and Advisory Board representatives

May 25, 2012

Corporate Sponsors

Anadarko ..... Roger Reagan
BHP ..... Corey Morgan
BP ..... Jingfeng Zhang
Chevron ..... Debbie Bones
ConocoPhillips ..... Haiyan Zhang, Robert Stolt
Devon Energy ..... Kenneth Beeney, Richard Brietzke
Encana ..... David Mackidd
ENI-Agip ..... Nicola Bienati
ExxonMobil ..... Peter Traynin
GX Technology ..... Nick Bernitsas, Robert Bloor
Hess ..... Scott Morton
IBM ..... Tom McClure
Landmark ..... Dave Diller
Petrobras ..... Neiva Zago
Petrochina Company Limited ..... Jixiang Xu
PGS ..... Nizar Chemingui, Sverre Brandsberg-Dahl
Repsol ..... Gladys Gonzalez, Francisco Ortigosa
Saudi Aramco ..... Yi Luo
Shell ..... Jonathan Sheiman
Statoil ..... Marianne Houbiers, Lasse Amundsen
Total ..... Wafik Beydoun
WesternGeco ..... Richard Coates

Federal Support

DOE Basic Sciences award DE-FG02-05ER15697 ..... Nick Woodward
NSF-CMG award DMS-0327778 ..... Henry A. Warchall

M-OSRP Personnel

Faculty

Hicham Ayadi ..... Research Scholar (Physics)
Lasse Amundsen (Statoil) ..... Adjunct Professor (Physics)
Douglas J. Foster (ConocoPhillips) ..... Adjunct Professor (Physics)
Wilberth Herrera ..... PostDoc Fellow (Physics)
Kristopher A. Innanen (Associate Professor, University of Calgary) .. Adjunct Professor (Physics)
Robert G. Keys (ConocoPhillips) ..... Adjunct Professor (Physics)
Jacques Leveille (Amerada Hess) ..... Adjunct Professor (Physics)
Fang Liu ..... Research Assistant Professor (Physics)
Ken H. Matson (Shell) ..... Adjunct Associate Professor (Physics)
Bogdan Nita (Assistant Professor, Montclair State U.) ..... Adjunct Assistant Professor (Physics)
Partha Routh ..... Adjunct Professor (Physics)
Jon Sheiman (Shell) ..... Adjunct Professor (Physics)
Robert H. Stolt (ConocoPhillips) ..... Adjunct Professor (Physics)
T. Hing Tan (Shell) ..... Adjunct Professor (Physics)
Arthur B. Weglein ..... Cullen Professor (Physics)
Daniel Whitmore (PGS) ..... Adjunct Professor (Physics)

Graduate Students

Di Chang ..... Physics
Hong Liang ..... Physics
Chao Ma ..... Physics
Jim Mayhan ..... Physics
Mozhdeh Niazmand ..... Physics
Lin Tang ..... Physics
Zhiqiang Wang ..... Physics
Jinlong Yang ..... Physics

Recent Alumni

Andre Ferreira[2] ..... Geosciences
Zhiqiang Guo ..... Geosciences
Shih-Ying Hsu ..... Physics
Xu Li ..... Physics
Jose Eduardo Lira[2] ..... Geosciences
Fang Liu ..... Physics
Francisco Miranda ..... Physics
Adriana Citlali Ramirez ..... Physics
Simon A. Shaw ..... Geosciences
Haiyan Zhang ..... Physics
Jingfeng Zhang ..... Physics

Administrative Support

Jennifer Chin-Davis ..... Associate Director, Physics Department
Andrew Fortney ..... Computer/IT Support
Chris Watts ..... Webmaster/NSM IT

[2]Petrobras, Brazil

Table of Contents

M-OSRP 2011 Annual Report: INTRODUCTION AND SUMMARY:

Arthur B. Weglein

May 25, 2012

In this Introduction to the 2011 M-OSRP Annual Report (covering the Summer 2011, Fall 2011-Spring 2012 time period), we provide: (1) the yearly highlights of progress over the past year, and (2) a discussion of how that progress serves our overall goals, and determines our strategy and plans.

The Mission-Oriented Seismic Research Program (M-OSRP) is an academic, educational, and research enterprise that addresses pressing seismic exploration challenges. While the projects within the program focus on certain prioritized processing objectives, M-OSRP takes ownership of, and responsibility for, the entire seismic processing chain. It assures that any needed advances in preprocessing steps are provided often by providing the steps' own intrinsic value, and/or satisfying prerequisites of processing steps that are further along our specific processing chain and methods. No earlier preprocessing step that can affect the efficacy of subsequent processing steps is ever "not our business." The entire processing chain is guided by our efforts to be a consistent and supportive linked activity, in which the success of any step will always improve the success of the next and subsequent steps, and every step is derived under the same exact and consistent set of assumptions and aligned purposes. The latter approach allows the processing methods, for example, for removing multiples, depth imaging, and inverting primaries, to reach their full efficacy and potential and to deliver their added value and impact.

M-OSRP has several research initiatives, which are catalogued into four projects within the program. Each of these four broad projects introduces new concepts and develops and tests algorithms for more effectiveness and efficiency. These new concepts and algorithms allow: (1) achievement of preprocessing goals, for example, for source-signature and radiation-pattern estimation and source and receiver de-ghosting and data reconstruction; (2) removal of free-surface and internal multiples, directly and without subsurface information, for marine and on-shore plays; and (3) provision of added value within conventional concepts and mainstream thinking, for the purpose of high-grading and improving (a) seismic modeling (e.g., P-wave amplitude and phase modeling in an elastic heterogeneous medium), (b) velocity-dependent depth imaging (e.g., Green's theorem RTM, without PML), and (c) non-linear direct inversion capability and inverse scattering series (ISS) delivery.

Project (4) is driven by evidence of serious and persistent outstanding issues and hurdles in leading-edge velocity analysis and imaging capability within current mainstream concepts and algorithms.

Those issues and hurdles are especially evident under complex, daunting, and costly high-risk conditions. Under those circumstances, the cause and magnitude of those imaging challenges can suggest that further investments along the lines of traditional thinking and approaches can, are, and will face diminishing returns. And that motivates and galvanizes the search and call for fundamentally new depth-imaging concepts that, for example, can totally avoid the traditional and mainstream imaging need for an accurate velocity model.

Is there really a need for fundamentally new depth-imaging approaches and capabilities? That need is not generally spoken about or ever evident at the self-congratulatory SEG or EAGE conferences and workshops, or in papers published in our technical journals. However, the fact that, for example, the exploration-drilling success rate (of one in ten) in the deep-water Gulf of Mexico has not noticeably improved over the last few decades, gives credence to a deep and serious outstanding problem and need, and to the demand for fundamentally new and more effective imaging approaches. Also the high cost of drilling in deep-water plays exerts pressure to drill fewer development wells.

In response to the undisputed reality of industry's low exploration-drilling success rate, combined with the ever-higher drilling costs in deep water, M-OSRP pursues and develops fundamentally new seismic-imaging concepts and inversion capabilities. The idea is to provide the same uplift and stand-alone capability we have provided (and still are providing) in the area of multiple removal to other processing challenges. Specifically, we expect to now extend that thinking and capability to primaries and, starting with the same exact unchanged set of equations as was used to derive the multiple-removal algorithms, to mine the capability of those equations for the direct prediction of depth and the delineation of targets, without requiring a velocity model or any other subsurface information. Our multiple-removal methods precisely demonstrate their mettle and stand-alone added value in the most complex and challenging offshore and on-shore exploration plays. And it's in precisely those complex and challenging circumstances that our current, mainstream concepts and methods for the processing of primaries are lagging. Indeed, our methods for processing primaries need to catch up with and match the current effectiveness of our multiple-removal techniques. That's not simple or easy — but that's the plan, and after our first field-data test now we know it's possible.

Each of these four project categories requires new theory, concepts, testing, and development. We just last year demonstrated, with a very early off-shore Norway Kristin field-data test, that category (4), that is, direct depth imaging without a velocity model is possible. Further, we published a paper that explains in step-by-step detail and logic the argument and evidence that underpin that important claim and conclusion. When nearly everyone believes that determining depth directly without a velocity model is fundamentally and innately impossible, and in fact believes that velocity and direct determination of depth are intrinsically related, then the very first (and admittedly simple) off-shore Norway Kristin field-data example that unambiguously speaks another truth is important and newsworthy. With that truth established, we now move ahead to the real goal: To show that it is not only possible but is also useful by showing that it is able to directly predict a more accurate depth image, without using a velocity model, than we can achieve with state-of-the-art imaging methods that require a velocity. We explained in our Dec. 9th 2011 video conference, and in the Annual Report, and will again present at an upcoming meeting, a strategy to take us from "it's possible" to "it's useful." Steps along the way are producing spinoffs, such as P-wave-only elastic-wave-theory modeling, with clear potential advantages for SEAM modeling objectives and RTM. We will basically be "paying the rent" with the first three projects, giving category (4) the time to reach its place in the seismic tool box.

The 2011 Annual Report takes the reader through the projects in the M-OSRP program, in an order that follows the steps that the data themselves take as they move from link to link in the processing chain. The report describes the progress within each link and project, and details how the upgrade in that specific link both provides its own value and also serves later links further along the processing chain.

Mission-oriented seismic research is fundamental, directed research, which begins with the problem that needs to be solved whether or not we know how to solve the problem (more often "not") in contrast to "methods" looking for a problem or solving convenient, cosmetic-tweaking, current-mainstream techniques and initiatives. The latter are definitely useful and worthwhile, but that massaging will never provide a response to a major challenge and high hurdle, nor will it provide a fundamental new capability. We seek direct methods for solving processing problems and providing prerequisites. Direct methods offer many benefits over indirect methods. With a direct method you know that you are solving the problem that you are interested in solving.

Among the great examples of solving convenient rather than priority problems is the long term and significant focus and resource allocation to ever more parameter defining anisotropic homogeneous media, for imaging and inversion, where the real priority and challenge is rapid laterally and vertically varying heterogeneous isotropic media. The former can be important, but the latter is the much more significant and the actual and tougher first priority problem. But trying to stay positive, I guess it's better to solve a lower priority problem than no problem — as long as we recognize and acknowledge it.

A direct method provides a framework for precise data needs and establishes a straight-ahead formula that takes in your data and actually solves and explicitly and directly outputs the solution that you seek.

Direct methods represent "hope," clarity, definition, and determinism, whereas "indirect methods" represent relinquishment of hope, hopelessness, randomness, reliance on statistics, and then a search and computation with a clue or attribute in mind of what a solution might satisfy and might look like. There is a note in the report, titled "Antidote to P-wave "FWI"," that (along with references cited therein) speaks to the general direct and indirect distinction and the conceptual and practical consequences, and addresses the proper, important, and essential role for indirect methods. However, overall progress is measured when the boundary between direct and indirect shifts and more territory sits within the direct realm, where you know what you are doing and what you are pursuing. The unfortunate truth is that the boundary has moved in the opposite direction, and there is little indication that that trend will slow or will cease.

The projects and papers in the Annual Report (and the presentations at the Annual Meeting) follow the steps that the data take in the processing chain.

We cite a few project highlights here, and the titles and authors are easy to locate in the Annual Report Table of Contents and the Meeting Agenda.

1 PREPROCESSING

Source and receiver de-ghosting, wavelet estimation methods, and reference wave-field development based on Green's theorem, all have had successful tests using analytic, synthetic, SEAM data, and

field data, with added value demonstrated for boosting the low frequency and removing source and receiver notches. The positive impact on multiple-removal methods was convincingly demonstrated, as well. These Green's theorem methods do not require a flat horizontal measurement surface, and, for example, can be applied directly to an undulating, dipping, and corrugated water bottom. For towed-streamer data with either over/under or dual measurements, a collection of single-source experiments can effectively remove receiver and source ghosts. With deeper source and receiver ocean-bottom measurements, there could be certain stability advantages to having over/under sources, as well.

2 MULTIPLE REMOVAL

Free-surface and internal-multiple algorithms have been modified to incorporate source and receiver array information. These modifications benefit from the Green's theorem preprocessing step of identifying the reference wave-field and its radiation pattern. Those source and receiver array modifications, along with de-ghosting and inclusion of obliquity factors, provide amplitude and phase uplift and reduce the burden on adaptive subtraction.

The recent August 2011 TLE paper published by the Saudi Aramco multiple-removal group led by Yi Luo concluded that "...the Inverse Scattering Series internal-multiple method demonstrated effectiveness on complex synthetic and field data, and that effectiveness was unmatched by other methods..." Never-the-less, in our "Multiple Attenuation: Recent Advances and Road Ahead (2011)" article in that same TLE issue, we pointed out certain shortcomings in that leading-order ISS internal-multiple attenuator. Those shortcomings have subsequently been addressed by including higher-order terms in the multiple-removal series, and two reports and SEG Abstracts speak to that new inclusiveness and heightened capability. Another major impediment to further progress in removing multiples, which we also pointed out in our "Recent Advances" paper, was the use of energy-minimization adaptive subtraction. There is a note in this Report with a candidate replacement for energy-minimization adaptive subtraction for use with free-surface-multiple removal. In contrast to energy-minimization adaptive subtraction, our replacement candidate is always in line with the method it's meant to serve: the prediction and subtraction of free-surface multiples. Also, (effective) primaries generated from sub-resolution internal multiples have demonstrated ISS effectiveness for removing internal multiples generated by primaries and effective primaries (please see below the two papers submitted to *Geophysics* from collaboration with Yi Luo and the Saudi Aramco Group). Another paper within the Report provides an aperture- and dip-limitation user option for the free-surface and internal-multiple codes to produce significant run-time cost savings. Finally, we have Andre Ferreira's thesis, with spectacular Petrobras offshore Brazil ISS internal-multiple results, where a suite of methods, including vendor methods, were previously tried and were unable to produce satisfactory results in the subsalt target area of interest.

3 IMAGING

A paper was published with the first field-data tests of ISS imaging, and it concluded that the method is viable. The next step is to show that ISS imaging can provide relevant and differential added

value. A strategy to arrange that outcome and delivery involves several components, one of which is a P-wave-only amplitude and phase wave-modeling method for heterogeneous elastic media. A Note in the Report describes the approach. A paper in the Report describes regularization methods for multi-parameter ISS depth imaging with band-limited data. Another report compares the results from applying the Weiner filter, spectral division, and Green's theorem for the wavelet estimation needed for ISS depth imaging, both on synthetic data and in the Kristin-field-data test. The Green's theorem RTM without PML generated interest in finite difference methods, and papers within the Report discuss finite-difference modeling, boundary conditions, and PML. Progress in providing modeling codes for the displacement wave-field for 1D elastic media is presented in a paper in the Report.

Several theoretical advances are needed within the strategy to move ISS imaging from the "is possible" to the "is stand-alone capable and is step-change added-value useful" category. Such advances comprise further inclusion of ISS imaging terms and capability, imaging events that have only P episodes in their history, and recasting the ISS imaging series in terms of spikes moving rather than boxes.

4 SUMMARY

Research within M-OSRP consists of a portfolio of projects that serve the same goal. These projects manage potential benefit, investment, and risk.

Our research portfolio of projects involves every link in the seismic processing chain, with Green's-theorem-based methods for preprocessing (source signature and radiation pattern; reference wave and reflection data separation at all offsets; and de-ghosting) and with the inverse scattering series (ISS) for removing multiples and depth imaging and inverting primaries. All of these preprocessing and processing methods are direct, wave-theory methods that do not assume any subsurface information. We also have projects that high-grade the effectiveness and efficiency of seismic modeling methods and mainstream velocity-dependent (RTM) imaging methods, often with spin-offs from strategic steps in the Green's theorem preprocessing and ISS processing initiatives.

The M-OSRP has developed and delivered algorithms that are based on the inverse-scattering-series methods for the attenuation of free-surface and internal multiples. Those techniques have received much positive attention, regarding their effectiveness both in absolute terms and also in comparison with all other methods from other consortia and vendors, as reported in, e.g., several articles in the August 2011 issue of TLE. While that is positive and welcome news, we point out in our "Recent Advances and Road Ahead (2011)" August TLE article that a careful examination of the synthetic- and field-data examples from the TLE 2011 papers makes it clear that, aside from certain obvious and practical issues resolvable by advances in acquisition and computing power, more than a few significant and fundamental theoretical challenges remain.

The objective of predicting the amplitude and phase of all orders of free-surface and internal multiples, without damaging primaries, is not a closed subject from a conceptual, theoretical, and practical point of view. Several of the open issues pointed out in the August 2011 TLE overview paper have subsequently been addressed or improved upon (and that progress is represented within the submitted SEG Abstracts, submitted papers, and in Annual Reports), but other serious challenges

remain, and the removal of multiples is far from a closed subject. Much as-yet-untapped power for addressing those outstanding issues resides within the ISS, and replacing the minimum-energy adaptive-subtraction concept would also be a big step forward.

5 ISS DEPTH IMAGING

We recognize that pursuing a direct depth-imaging method without a velocity model has been and remains "a bridge too far" for most within the geophysical community, including many of our sponsors. Some might feel that it isn't needed and that keeping on the current mainstream path of improving the velocity, with tomography and CIG and "FWI," and then depth imaging, will provide sufficient progress to make a major dent in the unacceptable and essentially unchanging one-in-ten drilling-success rate in the deep-water Gulf of Mexico. Others might not believe that current mainstream research efforts and initiatives will have that much impact, but they cannot imagine as a realistic alternative a possibility that would totally avoid the need for a velocity model, a velocity model that so many have spent their entire careers believing is necessary and seeking to directly or indirectly determine. All of those attitudes are reasonable, understandable, and anticipated.

However, we come from a different place and from a history in which, when we started out with multiple-removal research, we were told by our academic and industry colleagues that: (1) multiple removal was not an open issue and was essentially a closed and solved problem by high-resolution Radon methods, (2) internal multiples were never a significant or priority problem on field data, and (3) removing all multiples directly and without subsurface information was in violation of basic mathematical physics and fundamentally impossible.

Well, things didn't turn out that way regarding any of those three admonitions. In research, if most of your colleagues understand and agree with your approach, then what you are proposing really isn't new and instead fits comfortably within conventional thinking and concepts and is limited by where that thinking can bring us. Fundamental, directed research begins with a view that the scale of the challenge is beyond where current concepts and thinking can reach. Such research, in fact, springs from awareness that the outstanding and pressing challenge is the actual "bridge too far," in terms of where conventional thinking and perspectives can take us.

When the ISS internal-multiple-removal method was tested and compared using complex and daunting off-shore and on-shore field data, and when it demonstrated stand-alone added-value, then support and understanding were universal and took no vision or courage. In our past, when first proposed it was considered absolutely and completely absurd, and now it's mainstream and "pays our rent".

This perspective is presented here to express our gratitude and appreciation for allowing us to pursue a portfolio of projects with a balance of risk, investment, and potential benefit.

If all of our projects and proposals within M-OSRP were clear to us and to our sponsors and understandable and reasonable and made everyone comfortable, M-OSRP would be failing, failing absolutely, failing ourselves, failing our students, failing our college and university, and failing our petroleum sponsors. We would not be doing research and would not be "solving the right problem". In research, we have to welcome and be comfortable with being uncomfortable and steady when

the path forward is unclear and we are facing skepticism or worse. But today's uncomfortable and unbelievable thought and concept will invariably be tomorrow's mainstream and conventional thinking and methodology, and that process assures a pipeline that will address current major league and daunting challenges and will pay tomorrow's rent.

We are enormously fortunate to have your confidence and support to pursue and progress a portfolio of projects, some of which "pay today's rent" and some that will "pay tomorrow's rent".

6 Abstracts/Papers submitted or that appeared in the Summer 2011, Fall 2011- Spring 2012

Please see the References (below) for M-OSRP papers that appeared or were submitted in the Spring 2011–Fall 2012 time period. Copies of these papers are included in this Annual Report as Attachments.

This was another successful and productive year, and we look forward to another good year ahead. We are grateful for your encouragement and support.

Best regards,

Art

Arthur B. Weglein

References

Liang, Hong, Yi Luo, Panos G. Kelamis, and Arthur B. Weglein. "Prediction of Distinguishable Internal Multiples." Submitted. *Geophysics* 77 (2012).

Liang, Hong, Yi Luo, Panos G. Kelamis, and Arthur B. Weglein. "Reflector Spectrum for Relating Seismic Arrivals to Reflectors." Submitted. *Geophysics* 77 (2012).

Liang, Hong, Chao Ma, and Arthur B. Weglein. "A new ISS internal multiple attenuation algorithm addressing a shortcoming of the current leading-order ISS algorithm for removing first order internal multiples: derivation and testing of the algorithm for arbitrary number of reflectors." *82nd Annual International Meeting, SEG, Expanded Abstracts*. . Submitted. Society of Exploration Geophysicists, 2012.

Luo, Yi, Panos G. Kelamis, Qiang Fu, Shoudong Huo, Ghada Sindi, Shih-Ying Hsu, and Arthur B. Weglein. "Elimination of land internal multiples based on the inverse scattering series." *The Leading Edge* 30 (2011): 884–889.

Luo, Yi, Hong Liang, Panos G. Kelamis, and Arthur B. Weglein. "Unraveling internal multiples via the reflector spectrum concept." *82nd Annual International Meeting, SEG, Expanded Abstracts*. . Submitted. Society of Exploration Geophysicists, 2012.

Ma, Chao, Hong Liang, and Arthur B. Weglein. "A new higher order Inverse Scattering Series (ISS) internal multiple attenuation algorithm addresses a limitation in the current leading order algorithm: derivation for a three-reflector model and a test with analytic data." *82nd Annual International Meeting, SEG, Expanded Abstracts*. . Submitted. Society of Exploration Geophysicists, 2012.

Mayhan, James D., Arthur B. Weglein, and Paolo Terenghi. "First application of Green's theorem derived source and receiver deghosting on deep water Gulf of Mexico synthetic (SEAM) and field data." *82nd Annual International Meeting, SEG, Expanded Abstracts*. . Submitted. Society of Exploration Geophysicists, 2012.

Terenghi, Paolo, Shih-Ying Hsu, Arthur B. Weglein, and Xu Li. "Exemplifying the specific properties of the inverse scattering series internal-multiple attenuation method that reside behind its capability for complex onshore and marine multiples." *The Leading Edge* 30 (2011): 876–882.

Wang, Zhiqiang, Arthur B. Weglein, James D. Mayhan, Paolo Terenghi, and Christian Rivera. "Green's theorem derived deghosting: fundamental analysis, numerical test results, and impact on ISS free-surface multiple elimination." *82nd Annual International Meeting, SEG, Expanded Abstracts*. . Submitted. Society of Exploration Geophysicists, 2012.

Weglein, Arthur B., Shih-Ying Hsu, Paolo Terenghi, Xu Li, and Robert H. Stolt. "Multiple attenuation: Recent advances and the road ahead (2011)." *The Leading Edge* 30 (2011): 864–875.

Weglein, Arthur B., Fang Liu, Xu Li, Paolo Terenghi, Ed Kragh, James D. Mayhan, Zhiqiang Wang, Joachim Mispel, Lasse Amundsen, Hong Liang, Lin Tang, and Shih-Ying Hsu. "First field data examples of inverse scattering series direct depth imaging without the velocity model." *82nd Annual Internat. Mtg., SEG, Expanded Abstracts*. . Submitted. Society of Exploration Geophysicists, 2012.

Weglein, Arthur B., Fang Liu, Xu Li, Paolo Terenghi, Ed Kragh, James D. Mayhan, Zhiqiang Wang, Joachim Mispel, Lasse Amundsen, Hong Liang, Lin Tang, and Shih-Ying Hsu. "Inverse scattering series direct depth imaging without the velocity model: first field data examples." *Journal of Seismic Exploration* 21 (2012): 1–28.

Green's theorem-derived preprocessing of marine seismic data

James D. Mayhan, Arthur B. Weglein, and Paolo Terenghi

May 25, 2012

Abstract

We report Green's theorem-derived preprocessing of marine seismic data, i.e., deghosting and wavefield separation, including the first use of Green's theorem-derived source and receiver deghosting on deep water Gulf of Mexico synthetic (SEG Advanced Modeling Corp., or SEAM) and field data. Green's theorem-derived preprocessing is put into context in the complete M-OSRP processing chain, Green's theorem-derived theory is presented, and an algorithm implementing the theory is discussed. The algorithm has been tested on field data and several kinds of synthetic data with positive and encouraging results. This algorithm is the first of a set of deliverables based on Green's theorem in 3D. Release 1 (deghosting) has been delivered to the sponsors (via the sponsors-only section at mosrp.uh.edu). Green's theorem-derived deghosting has several qualities that separate it from previous deghosting methods: it works in a multi-dimensional earth, it doesn't require a Fourier transform over space coordinates, it works in every depth of water, it allows for any shape of measurement surface (e.g., a corrugated water bottom), and it is consistent with wave theory methods. We also discuss Green's theorem based reverse time migration (RTM).

1 Introduction

Because it allows the freedom of choosing a convenient reference medium, Green's theorem offers a flexible framework for defining a number of useful algorithms — ghost removal, wavefield separation (into reference P_0 and scattered P_s), source-wavelet estimation, and two-way wavefield continuation (RTM) (Weglein and Secrest, 1990; Weglein et al., 2002; Zhang and Weglein, 2005, 2006; Zhang, 2007; Ramírez and Weglein, 2009). Green's theorem methods are multidimensional, work in the $(\mathbf{r}, \omega)$ data space (and hence are simple to extend to irregularly spaced data), work in every depth of water, exact (fully consistent with the wave equation), and make no assumptions about the earth. Therefore, Green's theorem-derived preprocessing methods are fully consistent with inverse scattering series isolated-task subseries. For a discussion of the inverse scattering series (ISS), see Weglein et al. (2003).

Deghosting is important for two reasons. (1) It is a prerequisite for many processing algorithms, including (a) data-driven-multiple elimination (inverse scattering series free-surface-multiple elimination and internal-multiple removal and conventional surface-related-multiple elimination (SRME)), and (b) imaging (wavefield continuation often assumes one-way waves). (2) Removing the downward

component of the field enhances seismic resolution and boosts low frequencies. Hence, deghosting benefits traditional seismic processing and also fulfills an important role in all inverse scattering series-based isolated-task processing.

Deghosting is a prerequisite for the inverse scattering series. The inverse scattering series can perform certain tasks (e.g., elimination of free-surface multiples) without a priori estimates of the spatial distribution of velocity. To accomplish certain seismic data-processing goals, the Mission-Oriented Seismic Research Program (M-OSRP) has generated algorithms that are based on the inverse scattering series (free-surface-multiple elimination, internal-multiple removal, depth imaging, nonlinear direct amplitude variation with offset (AVO), and Q compensation) and Green's theorem (deghosting, source signature estimation, and data reconstruction). While the inverse scattering series is independent of subsurface velocity (and in fact of all subsurface properties), it is data dependent and makes certain assumptions about its input data. Weglein et al. (2003) describe how every inverse scattering series isolated-task subseries requires (1) the removal of the reference wavefield, (2) an estimate of the source signature and radiation pattern, and (3) source and receiver deghosting. Weglein et al. (2003) also describe how the inverse scattering series has a nonlinear, cascaded dependence on these preprocessing steps. Therefore, the Green's theorem deghosting methods are critically important to the success of the inverse series methods since they may be used to bring seismic data in line with the assumptions of inverse scattering. The fact that the inverse scattering series is nonlinear places a higher bar on preprocessing. An error in the input to a linear process creates a linear error in its output, but the same error in inverse scattering series input creates linear, quadratic, cubic, and higher-order errors in its output.

The industry uses adaptive methods, which keep changing a model until some measure of the difference between the model and actual data is small. However, there are times when adaptive methods are injurious to data, and adaptive methods can fail when we have interfering or nearby events. Wang et al. (2012) and Mayhan et al. (2011, 2012b) provide something that doesn't injure multiple removal, thereby reducing the burden on adaptive methods.

1.1 Terminology

A brief aside on our terminology. (1) The total wavefield P measured by the hydrophones consists of the reference wavefield P_0 (which doesn't experience the earth) and the scattered wavefield P_s (which does experience the earth). (2) Ghosts begin their propagation moving upward from the source (source ghosts), end their propagation moving downward to the receiver (receiver ghosts), or both (source/receiver ghosts) and have at least one upward reflection from the earth. (3) Free-surface multiples have at least one downward reflection from the free surface (air-water interface) and at least one upward reflection from the earth. (An nth order free-surface multiple has n downward reflections from the free surface.) (4) Internal multiples have no downward reflections from the free surface, more than one upward reflection from the earth, and at least one downward reflection from inside the earth. (An nth order internal multiple has n downward reflections from inside the earth.) (5) Primaries have only one upward reflection from the earth. These marine events are summarized in Figure 1.

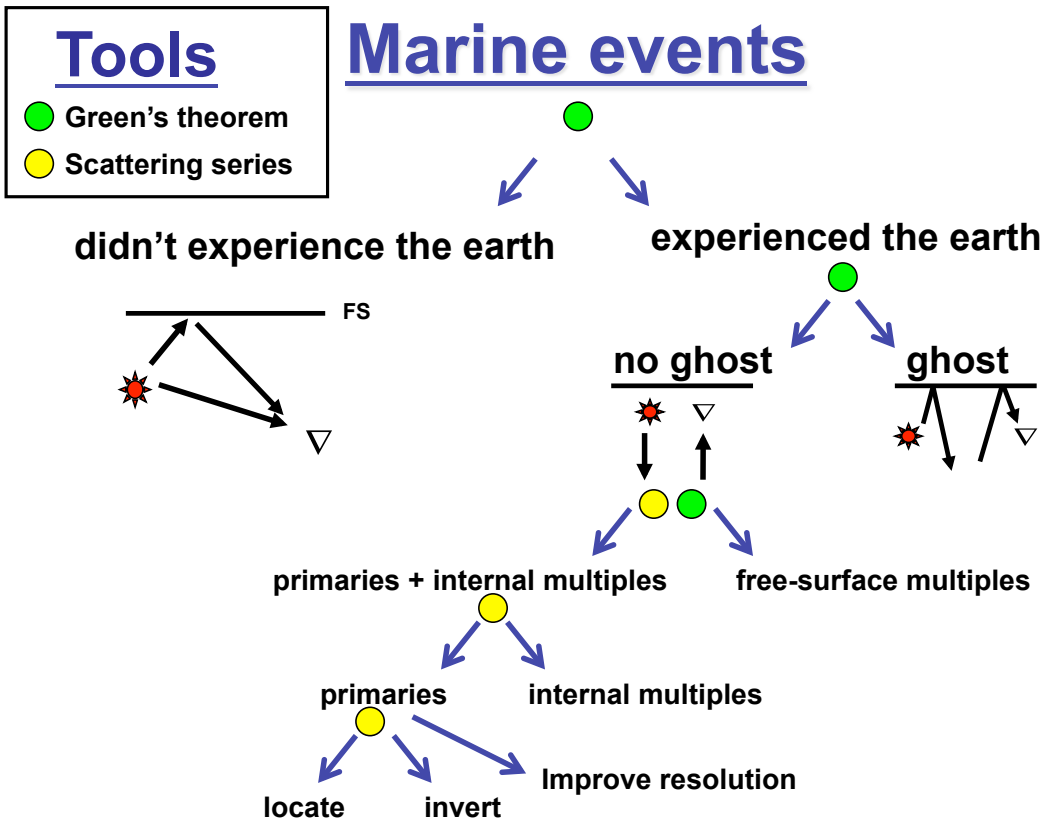

Figure 1: *Classification of marine events and how they are processed.*

2 Receiver deghosting

2.1 Tutorial

Several processing algorithms for eliminating multiples (including the inverse scattering series) assume that deghosting has been performed on the data and that an accurate estimate of the source wavelet is available. (The latter can be computed from P_0.) Green's theorem derived preprocessing, like the inverse scattering series, is based on perturbation theory. A reference medium (and its associated Green's function) is chosen to facilitate solving the problem at hand, and the perturbation is the difference between the real world medium and the selected reference medium. Within that framework, Green's theorem derived preprocessing is remarkably wide ranging. For example, Figure 2 shows the configuration chosen for Green's theorem derived deghosting. Choosing a reference medium that consists of a whole space of water, a hemispherical surface of integration bounded below by the measurement surface, and the prediction/observation point inside the surface of integration, gives deghosted data P'. A different choice of a reference medium (a half space of air and a half space of water, separated by a free surface), with the prediction/observation point outside

or inside the surface of integration, gives wavefield separation, in which the total wavefield P is separated into the reference wavefield P_0 (outside) and the scattered wavefield P_s (inside).

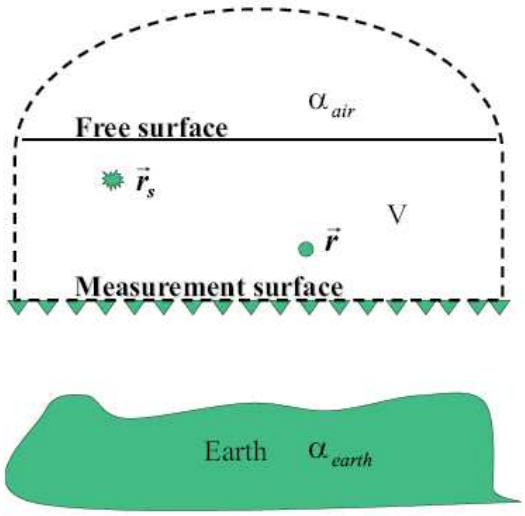

Figure 2: *Configuration for Green's theorem derived deghosting (Zhang, 2007, Fig. 2.10). α_{air} and α_{earth} are perturbations, the differences between the actual medium (half space of air, water, half space of earth) and the reference medium (whole space of water). The closed surface S of integration is the measurement surface plus the dashed line.*

Green's theorem-derived deghosting (both receiver and source) is based on Weglein et al. (2002), Zhang and Weglein (2005), Zhang and Weglein (2006), and Zhang (2007). The theory assumes measurement of the pressure wavefield P and its normal derivative $\partial P/\partial n \equiv \nabla P(\mathbf{r}, \mathbf{r}_s, \omega) \cdot \hat{n}$ where $\mathbf{r}$ is the receiver location, $\mathbf{r}_s$ is the source location, and $\hat{n}$ is the unit normal to the measurement surface (pointing away from the enclosed volume V). The reference medium is chosen to be a whole space of water (where a causal, analytic solution exists for the acoustic wave equation). The whole-space Green's function is

$$G_0(\mathbf{r}, \mathbf{r}'_g, \omega) = G_0^d = \begin{cases} -(1/4\pi)\exp(ikR_+)/R_+ & \text{in 3D} \\ -(i/4)H_0^{(1)}(kR_+) & \text{in 2D} \end{cases}$$

where $\mathbf{r}'_g$ is the observation/prediction location, $k = \omega/c_0$, c_0 is the wave speed in the reference medium, and $R_+ = |\mathbf{r} - \mathbf{r}'_g|$. $H_0^{(1)}$ is the zeroth-order Hankel function of the first kind (Morse and Feshbach, 1953, § 7.2). The observation/prediction point is chosen between the free surface and the measurement surface, i.e., inside the volume V bounded by the closed surface of integration consisting of the measurement surface and the dashed line in Figure 2.

The configuration in Figure 2, Green's theorem, and the acoustic wave equations for P and G_0^d combine to give the key equation,

$$P'_R(\mathbf{r}_g, \mathbf{r}_s, \omega) = \oint_S dS\, \hat{n} \cdot [P(\mathbf{r}, \mathbf{r}_s, \omega)\nabla G_0^d(\mathbf{r}, \mathbf{r}'_g, \omega) - G_0^d(\mathbf{r}, \mathbf{r}'_g, \omega)\nabla P(\mathbf{r}, \mathbf{r}_s, \omega)], \tag{2.1}$$

where S is the closed surface consisting of the measurement surface and the dashed line in Figure 2, and $\hat{n}$ is the unit normal to S (pointing away from the enclosed volume V). Extending the radius of the hemisphere to infinity, invoking the Sommerfeld radiation condition, and assuming a horizontal measurement surface, the integral over the closed surface becomes an integral over the measurement surface (Weglein et al., 2002, equation 5),

$$P'_R(\mathbf{r}_g, \mathbf{r}_s, \omega) = \int_{m.s.} dS \left[P(\mathbf{r}, \mathbf{r}_s, \omega) \frac{\partial}{\partial z} G_0^d(\mathbf{r}, \mathbf{r}'_g, \omega) - G_0^d(\mathbf{r}, \mathbf{r}'_g, \omega) \frac{\partial}{\partial z} P(\mathbf{r}, \mathbf{r}_s, \omega) \right]. \tag{2.2}$$

The algorithm in equation 2.2 lends itself to application in a marine single-shot experiment. More details on the above derivation are given in Appendix B. Portions of the material in this section were published in Mayhan et al. (2011).

2.2 Code

The implementation of the above theory is done in a straightforward manner. The Green's theorem algorithm computes the surface integral in equation 2.2. The method requires as input two wavefields, the pressure measurements P and their normal derivatives $\partial P/\partial z'$. Measuring the latter requires a dual-sensor cable or over/under cables.

This code is the first of a set of deliverables that are based on Green's theorem in 3D. The new programs use data in the Seismic Unix (SU) format and integrate with all native SU programs. Release 1 consists of the following components: (1) Code (sujim.c), which calculates the surface integral in equation 2.2 (deghosting), reduced to the contribution from the measurement surface, as explained previously; (2) Code (sugreen.c), which computes the Green's function for a homogeneous half space or whole space, and optionally convolves with a Ricker wavelet. The input and output are in the $\mathbf{r}, t$ domain, while calculations are performed in the $\mathbf{r}, \omega$ domain; (3) Synthetic data created from flat-layer model I and used to create Figure 3; (4) Files required to compile sujim.c and sugreen.c; a PBS script that can be used to submit the two programs, and code documentation, are also included. These items are in directory Jim_Greens.tar in the sponsors-only section of mosrp.uh.edu.

A brief history of the code is given in Appendix H.

2.3 Example: Flat-layer model I

The left panel of Figure 3 shows synthetic data (produced using reflectivity code and flat-layer model I) that are designed so that deghosting is easy to demonstrate. (More detail about input data is given in Appendix A.) The depth of the receivers is chosen such that primaries and ghosts appear as distinct seismic events. The right panel of Figure 3 shows Green's theorem output using equation 2.2; note that the primary's receiver ghost at 0.45s and the free-surface multiple's receiver ghost at 0.85s are attenuated. Figure 4 shows the spectra of the input data (blue) and receiver deghosted output (red). As expected, the receiver deghosted data fill in notches related to receiver ghosts (at intervals of 5.4 Hz).

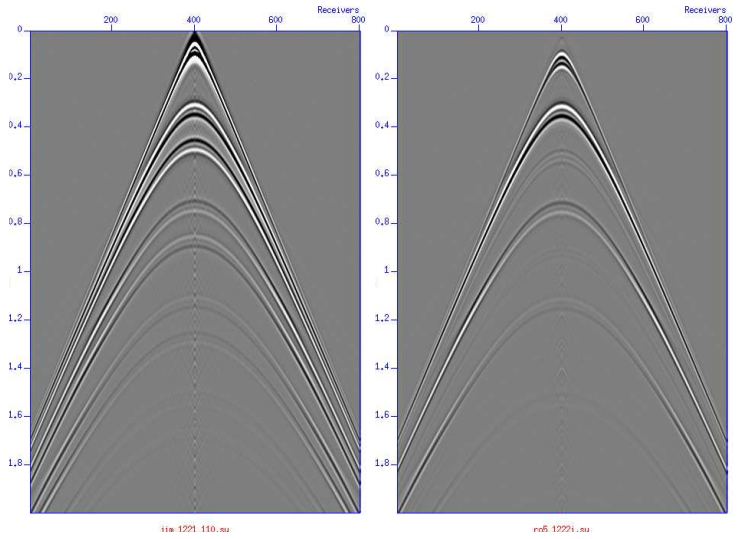

Figure 3: *Flat-layer model I (source at 30m, cable at 140m, water bottom at 300m): input data at 110m (left), receiver deghosted input data at 100m (right). The primary's receiver ghost at 0.45s and the free-surface multiple's receiver ghost at 0.85s are attenuated.*

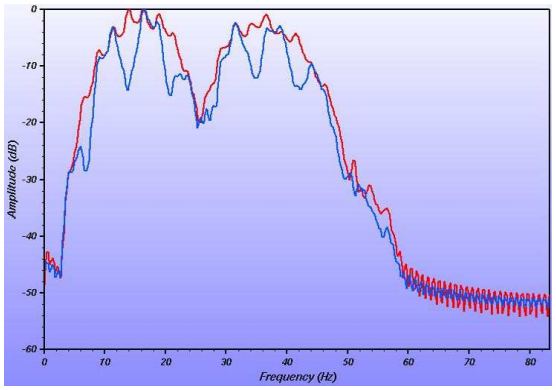

Figure 4: *Flat-layer model I: muted input data (blue), receiver deghosted input data (red). The receiver notches (at intervals of 5.4Hz) have been filled in; the notch at 25Hz is a source notch.*

2.4 Example: SEAM application

Green's theorem was applied to the SEAM data set generated on the basis of a deepwater Gulf of Mexico earth model (Figure 5) (SEG Advanced Modeling Corporation (SEAM), 2011). We used the special SEAM classic data set modeled to simulate dual-sensor acquisition by recording the pressure wavefield at two different depths, 15m and 17m respectively. These dual-sensor data consisted of nine sail lines for an equivalent wide-azimuth towed-streamer survey. The source interval is 150m by 150m, while the receiver interval is 30m in both inline and crossline directions. Figure 6 displays a typical shot gather from the SEAM model. Given the low frequency of the data (lower than 30Hz)

and the source and receiver depths of 15m and 17m, the ghost reflections are not as separable as in the previous flat-layer model. In this situation, successful deghosting would correspond to a change in the wavelet shape. Figure 7 shows SEAM input (a window of Figure 6) and receiver deghosted output computed by the Green's theorem approach. In the right panel of Figure 7, note the collapsed wavelet. In Figure 8, note the increased amplitude in lower frequencies and the decreased amplitude in higher frequencies, i.e., the shift of the amplitude spectrum towards low frequencies.

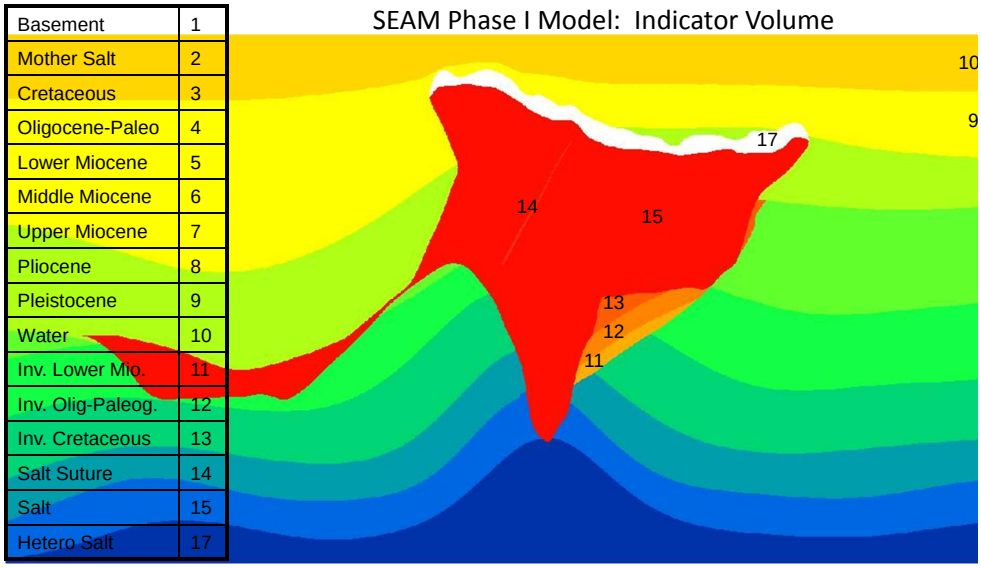

Figure 5: *SEAM deepwater Gulf of Mexico model: inline section from the middle of the model. Figure courtesy of SEAM.*

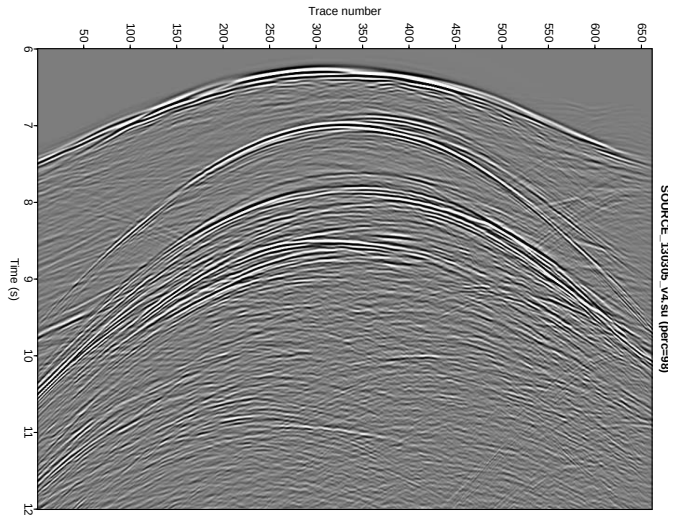

Figure 6: *SEAM data, shot 130305 (located at sx=16,975m, sy=20,000m, sz=15m, i.e., near the center of the shot grid).*

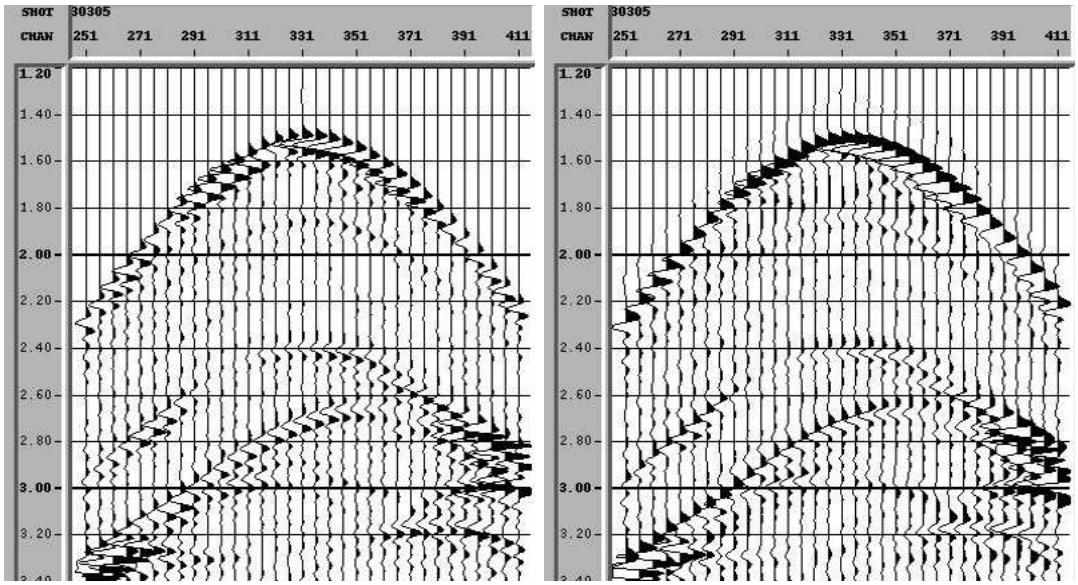

Figure 7: *SEAM data, shot 130305: recorded data at 17m (left), receiver deghosted input data at free surface (right). Note the collapsed wavelet in the right panel.*

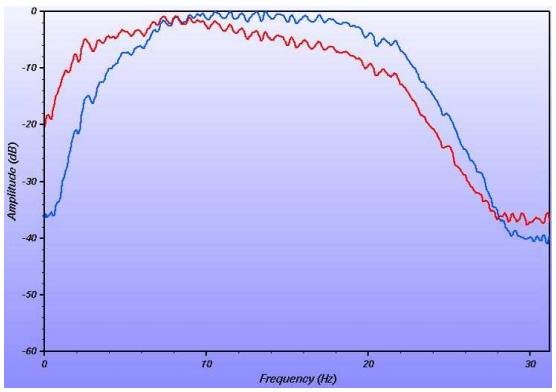

Figure 8: *SEAM data, shot 130305: recorded data at 17m (blue), receiver deghosted input data at the free surface (red). Note the shift of the spectrum towards lower frequencies. The first source notch (50Hz) and first receiver notch (44Hz) are to the right of the highest source energy (30Hz).*

2.5 Example: Field data

We also applied the deghosting approach to a field survey from the deepwater Gulf of Mexico. The data were acquired using dual-sensor streamers comprised of hydrophones and vertical geophones. The left panel in Figure 9 shows a close-up of an input shot record while the right panel displays the same traces after receiver deghosting. Note the collapsed wavelet in the output image. This is also demonstrated in Figure 10 which shows the amplitude spectra before and after receiver deghosting. The receiver depth is about 25m which corresponds to notches in the input spectra around 30Hz, 60Hz, and 90Hz. In the bandwidth from 20Hz to 100Hz, note the removal of the receiver notches by receiver deghosting.

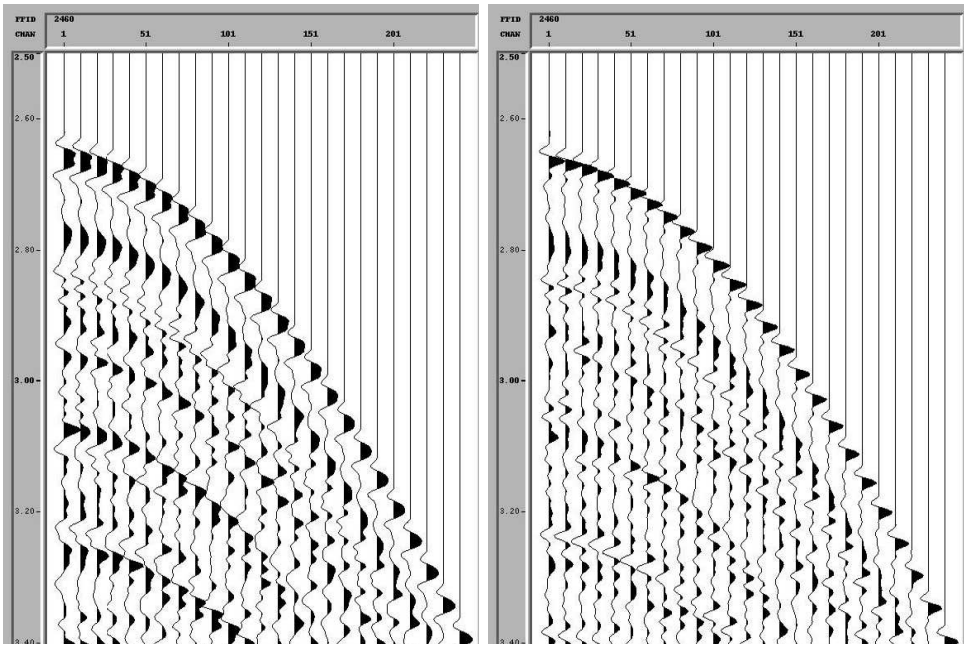

Figure 9: *Field data: hydrophones at 22–25m (left), receiver deghosted input data at the free surface (right). Note the collapsed wavelet in the right panel. Input data courtesy of PGS.*

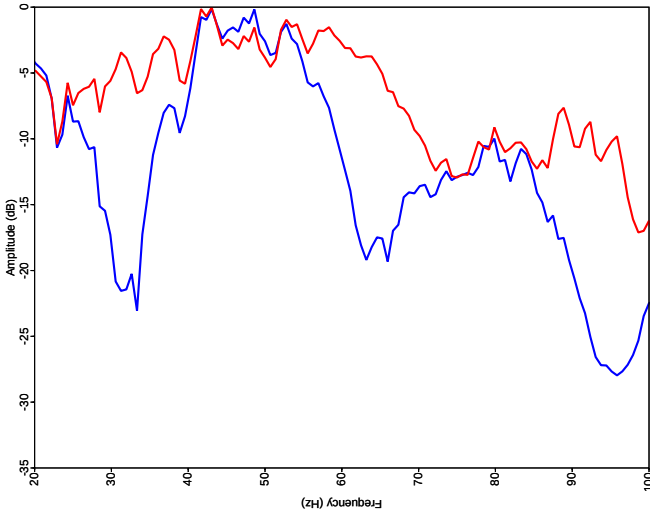

Figure 10: *Field data: hydrophones (blue), receiver deghosted input data (red). The receiver notches around 30Hz, 60Hz, and 90Hz have been filled in. Input data courtesy of PGS.*

3 Source deghosting

3.1 Tutorial

The last section has shown how Green's theorem can be applied to select the portion of the seismic wavefield that is up-going at the receiver. The algorithm uses data from a single shot gather and the receiver coordinate as the integration variable. This section shows how the theory can be similarly applied for source deghosting, where the portion of the wavefield that is down-going at the source is sought. It will be assumed here that the derivative of the wavefield on the source side is available (e.g., through repeating the seismic experiment with sources at two or more depths, or by using the notion that the wavefield is zero at the free surface). The procedure of receiver deghosting produces the up-going wavefield at $\mathbf{r}$. If $\mathbf{r}$ is chosen shallower than the source ($\mathbf{r}_s$), applying the source-receiver reciprocity principle (i.e., swapping the source and receiver x, y, z coordinates) brings the problem back to the same setup as in receiver deghosting, where the total wavefield and its derivative are known on the receiver side and the up-going portion is sought. The analogous integral is

$$P'_{SR}(\mathbf{r}'_g, \mathbf{r}'_s, \omega) = \int_{\text{sources}} dS\, \hat{n} \cdot [P'_R(\mathbf{r}'_g, \mathbf{r}, \omega) \nabla G_0^+(\mathbf{r}, \mathbf{r}'_s, \omega) - G_0^+(\mathbf{r}, \mathbf{r}'_s, \omega) \nabla P'_R(\mathbf{r}'_g, \mathbf{r}, \omega)]. \tag{3.1}$$

In practice the algorithm in equation 2.2 is reused via the steps summarized in Figures 11 and 12. (1) Interpolate shots so that the distance between shots equals the distance between receivers, (2) sort data from CSGs to CRGs, (3) swap shot and receiver coordinates, (4) source deghost the sail line one receiver gather at a time, (5) resort the data from CRGs to CSGs, and (6) unswap the shot and receiver coordinates. Step (1) is required because the distance between shots (which becomes the distance between receivers in the CRGs) may be too large, thus creating artifacts. For example, SEAM data have 30m between receivers but 150m between shots. Source deghosting without interpolation introduced artifacts that were removed by interpolating four shots between each pair of input shots so that the distance between shots equals the distance between receivers (i.e., equals 30m). Steps (2), (3), (5), and (6) are required to allow source deghosting one CRG at a time.

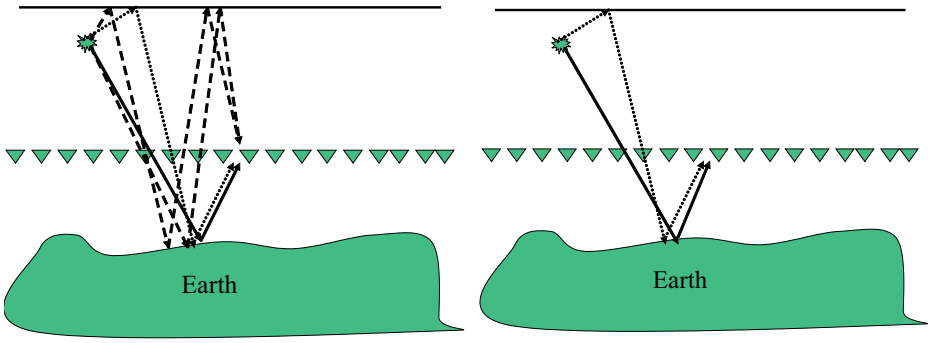

Figure 11: *Receiver deghosting is performed in the CSG domain. In the left panel, the primary is the solid line, the receiver ghost and source-receiver ghost are the dashed lines, and the source ghost is the dotted line. In the right panel, the Green's theorem algorithm removes down-going waves at the receivers, i.e., receiver ghosts and source-receiver ghosts. (Zhang, 2007, Fig. 2.14)*

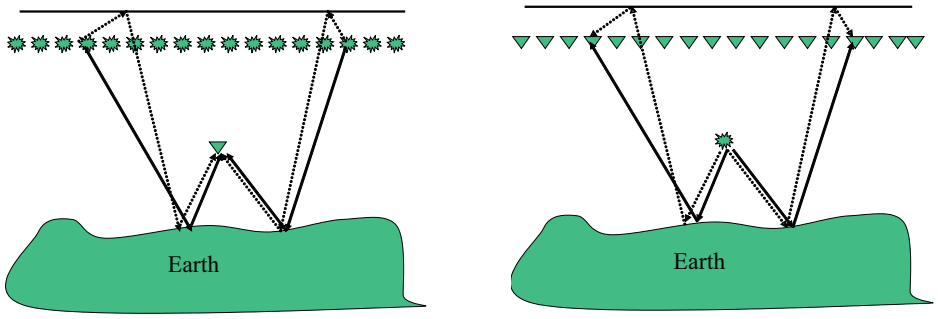

Figure 12: *Source deghosting is performed in the CRG domain. In the left panel, the right panel from Figure 11 has been sorted from CSGs to CRGs. The primary is the solid line and the source ghost is the dotted line. In the right panel, the coordinates of the sources and receivers in the left panel have been swapped , and the Green's theorem algorithm again removes down-going waves at the receivers, but now they are source ghosts. (Zhang, 2007, Figs. 2.15 and 2.16)*

Additional discussion is given in Appendices E and D. 1D analytic examples and numeric tests are shown in Wang et al. (2012). Portions of the material in this section were submitted in Mayhan et al. (2012a).

3.2 Example: Flat-layer model II

This example, suggested by Zhiqiang Wang, uses over/under sources. This does not imply a need for two sources, because (following Zhang, 2007) the second source can be predicted using Green's theorem. (More detail about input data is given in Appendix A.) In Figure 13, the left panel shows the input data, the center panel is receiver deghosted input data, and the right panel is source and receiver deghosted input data. The first author used the following procedure to create Figure 13:
(1) For each source, use the over/under cables to compute dP/dz.
(2) For each source, use the under cable and dP/dz to receiver deghost at 20m.
(3) For each receiver deghosted pseudo-cable, swap the shot and receiver z coordinates. Because the flat-layer model is 1D, it isn't necessary to swap the x and y coordinates.
(4) Use the two pseudo cables to compute receiver deghosted dP/dz.
(5) Use the under pseudo cable and receiver deghosted dP/dz to source deghost at 10m.
(6) Unswap the shot and receiver z coordinates.

Figure 14 shows the spectra of the input data (blue), receiver deghosted input data (red), and source/receiver-deghosted input data (green).

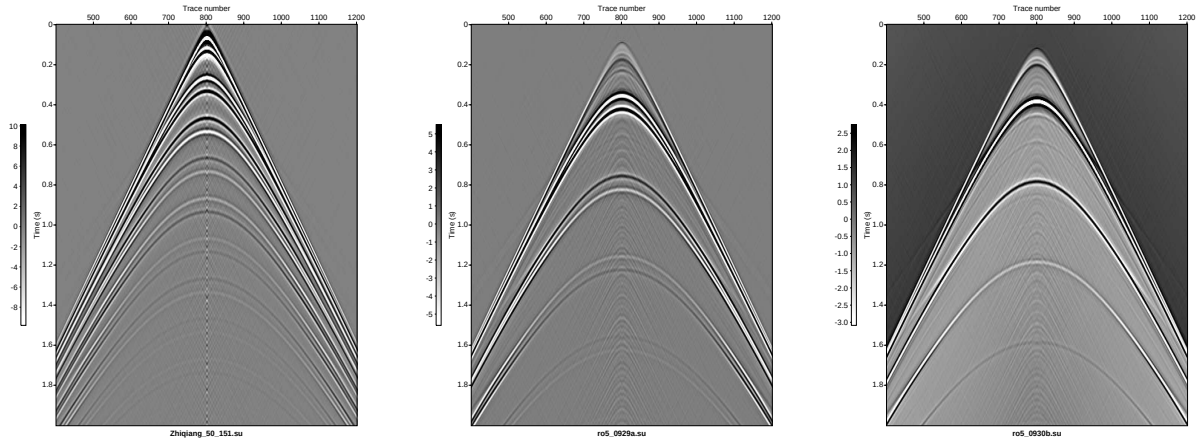

Figure 13: *Flat-layer model II (sources at 50m and 52m, cables at 150m and 151m, water bottom at 300m): input data at 151m (left), receiver deghosted input data at 20m (center), source/receiver deghosted input data at 10m (right).*

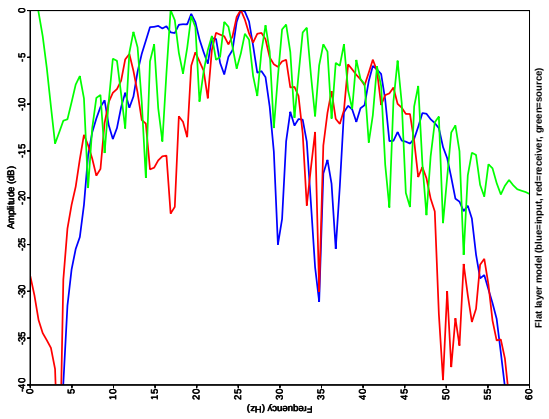

Figure 14: *Flat-layer model II: input data (blue), receiver deghosted input data (red), source and receiver deghosted input data (green). The receiver notches (at intervals of 5Hz) and source notches (at intervals of 15Hz) have been filled in.*

Using the times computed in section C, we see that:
(1) The events in the left panel of Figure 13 are (from the top) the direct wave G_0^d and its FS reflection G_0^{FS}, the WB primary and its source ghost, the WB primary's receiver ghost and source/receiver ghost, the first FSM and its source ghost, and the first FSM's receiver ghost and source/receiver ghost.
(2) In the center panel of Figure 13, all events are attenuated except the WB primary and its source ghost and the first FSM and its source ghost.
(3) In the right panel of Figure 13, all events are attenuated except the WB primary and the first FSM.

More work is needed here. In Figure 13, why is the right panel biased? (The figure uses the quick-fix sugain bias=12.)

3.3 Example: SEAM application

Recalling that SEAM has sources at 15m and receivers at 15m and 17m, the first author used the following procedure to source deghost a sail line consisting of 133 shots: (1) Use $P(15m)$ and $P(17m)$ to compute $dP/dz(16m)$. (2) Use $P(17m)$ and $dP/dz(16m)$ to receiver deghost at 8m and 10m. (3) Use receiver deghosted $P(8m)$ and $P(10m)$ to compute receiver deghosted $dP/dz(9m)$. (4) Sort receiver deghosted $P(10m)$ and $dP/dz(9m)$ from CSGs to CRGs, swap source and receiver coordinates, and use them to source deghost at 2m. (5) Sort source/receiver deghosted $P(2m)$ from CRGs to CSGs and unswap source and receiver coordinates. (6) Again swap the shot and receiver z coordinates.

The result is shown in Figure 15. With regard to receiver deghosting, successful deghosting would correspond to a change in the wavelet shape. In Figure 16 (a window of Figure 15) we see there is

no source notch to fill; the first source notch is at 44Hz which lies above the source frequency range (1–30Hz).

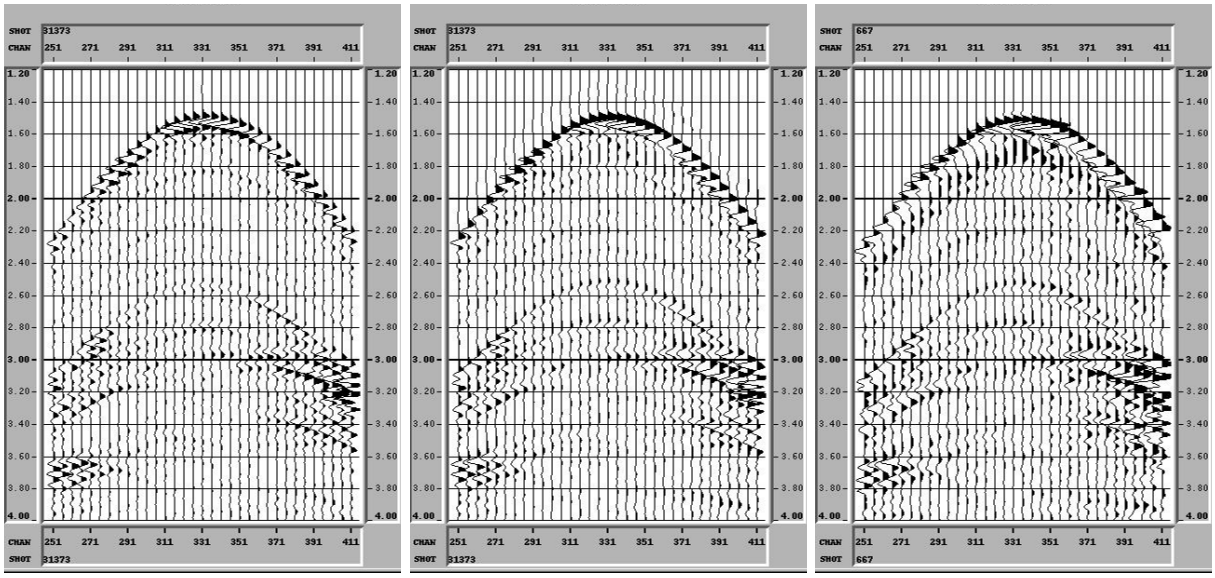

Figure 15: *SEAM data, shot 131373: recorded data at 17m (left panel), receiver deghosted at 10m (middle panel), source and receiver deghosted input data at 10m (right panel). Note the collapsed wavelets in the middle and right panels.*

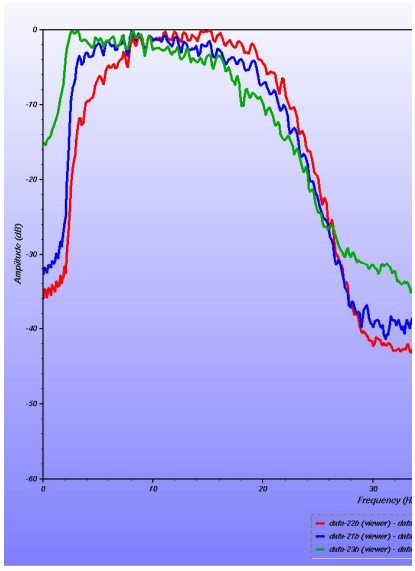

Figure 16: *SEAM data, shot 131373, frequency spectra: red=P at 17m, blue=receiver deghosted input data at 10m, green=source and receiver deghosted input data at 10m. The first source notch is at 44Hz, which lies above the source frequency range (1–30Hz). Note the shift of the spectrum towards lower frequencies (which may be of interest to FWI).*

3.4 Example: Field data

Recalling that the field data have sources at 9m and hydrophones and geophones at 23–25m, the first author used the following procedure to source deghost a sail line consisting of 374 shots: (1) Compute $dP/dz = i\omega\rho V_z$ where ρ is the density of the reference medium (seawater). (2) Use P and dP/dz to receiver deghost at 8m and 10.5m. (3) Use receiver deghosted $P(8m)$ and $P(10.5m)$ to compute receiver deghosted $dP/dz(9.25m)$. (4) Sort receiver deghosted $P(8m)$ and $dP/dz(9.25m)$ from CSGs to CRGs, swap source and receiver coordinates, and use them to source deghost at 2m. (5) Sort source/receiver $P(2m)$ from CRGs to CSGs and unswap source and receiver coordinates.

The result is shown in Figure 17. In Figure 18 (a window of Figure 17), the source notch at 83Hz has been filled in.

In the SEAM data, we have only 17m to work with (the depth of the under cable). Testing showed best results were obtained by "splitting the difference", i.e., by receiver deghosting at 8m and 10m and source deghosting at 2m. Similarly, in the field data, we have only 23–25m to work with so the first author receiver deghosted at 8m and 10.5m and source deghosted at 2m.

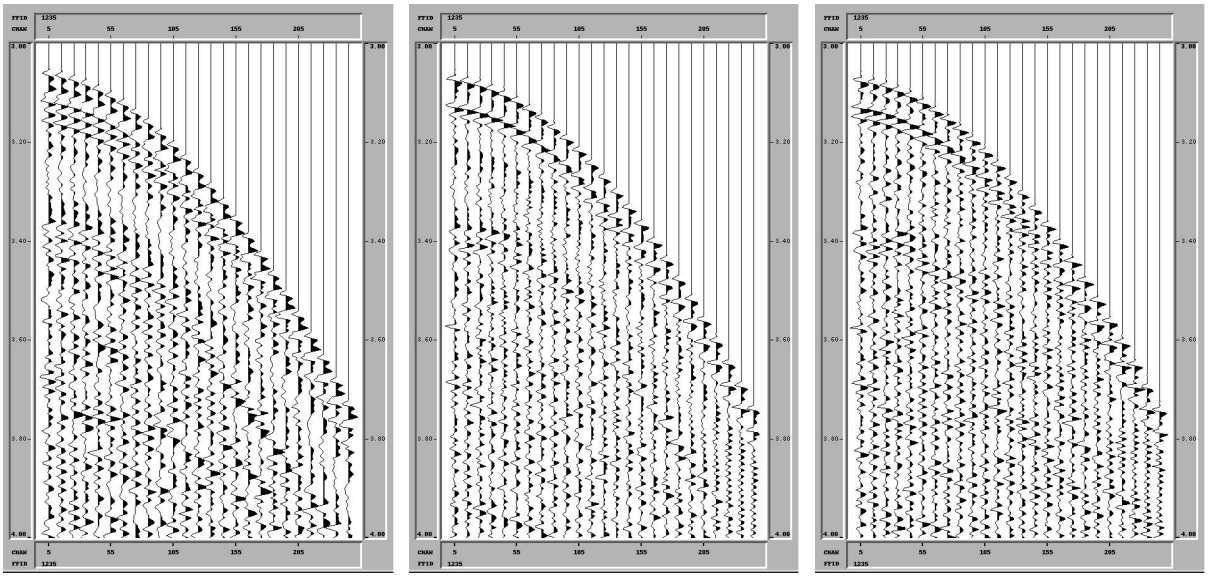

Figure 17: *Field data: hydrophones at 22–25m (left panel), receiver deghosted input data at 10.5m (middle panel), source and receiver deghosted input data at 8m (right panel). Note the collapsed wavelets in the middle and right panels. Input data courtesy of PGS.*

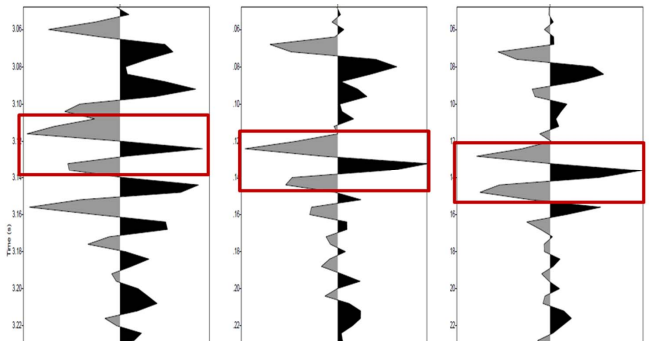

Figure 18: *Field data, zoomed in on trace 5 in each of the panels in Figure 17: Note the gradual recovery of the shape of the wavelet: by receiver deghosting (middle trace) and then by both source and receiver deghosting (right trace). Input data courtesy of PGS.*

4 Wavefield separation and source wavelet estimation

4.1 Tutorial

Green's theorem wavefield separation and source wavelet estimation are based on Weglein and Secrest (1990), who use the geometry shown in Figure 19. The reference medium is chosen to be a half space of water plus a half space of air, separated by a free surface. Recall that wavefield separation is $P = P_0 + P_s$, where P is the total wavefield measured by the hydrophones, P_0 is the reference wavefield (which doesn't experience the earth), and P_s is the scattered wavefield (which does experience the earth).

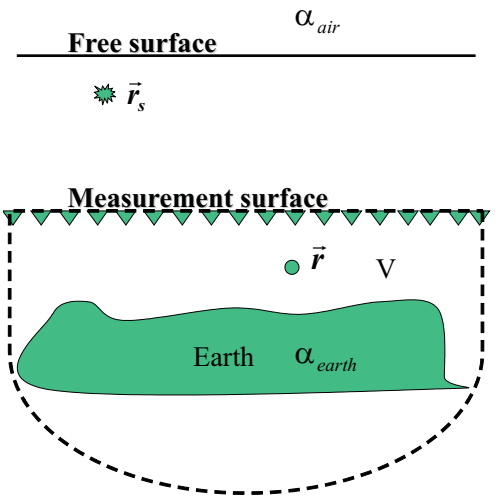

Figure 19: *Configuration for estimating the source wavelet $A(\omega)$ (Zhang, 2007, Fig. 2.1). The closed surface S of integration consists of the measurement surface and the dashed line.*

The key equation is the same as that used for deghosting (equation 2.2) except that a different Green's function is used,

$$\begin{aligned}&\int_{m.s.} dS\,\hat{n}\cdot[P(\mathbf{r},\mathbf{r}_s,\omega)\nabla' G_0^D(\mathbf{r},\mathbf{r}'_g,\omega) - G_0^D(\mathbf{r},\mathbf{r}'_g,\omega)\nabla P(\mathbf{r},\mathbf{r}_s,\omega)],\\ &= \begin{cases} -P_0(\mathbf{r}'_g,\mathbf{r}_s,\omega) & \text{if } z \text{ below cable}\\ P_s(\mathbf{r}'_g,\mathbf{r}_s,\omega) & \text{if } z \text{ above cable}\end{cases}\end{aligned} \tag{4.1}$$

where G_0^D is a Dirichlet Green's function constructed (using the method of images) to vanish on the free surface.

$$\begin{aligned}G_0^D(\mathbf{r},\mathbf{r}'_g,\omega) &= G_0^d + G_0^{FS}\\ &= \begin{cases} -(1/4\pi)(\exp(ikR_+)/R_+ - \exp(ikR_-)/R_-) & \text{in 3D}\\ -(i/4)(H_0^{(1)}(kR_+) - H_0^{(1)}(kR_-)) & \text{in 2D}\end{cases}\end{aligned}$$

where $R_+ = |\mathbf{r} - \mathbf{r}'_g|$, $R_- = |\mathbf{r} - \mathbf{r}_I|$, and $\mathbf{r}_I$ is the mirror image of $\mathbf{r}$ above the free surface (Morse and Feshbach, 1953, § 7.2).

The source wavelet $A(\omega)$ can be estimated by averaging the reference wavefield divided by a Green's function:

$$A(\omega) = \frac{1}{N}\sum_{i=1}^{N}\frac{P_0(\mathbf{r}_i,\mathbf{r}_s,\omega)}{G_0^D(\mathbf{r}_i,\mathbf{r}_s,\omega)}. \tag{4.2}$$

Inside/outside the integration volume is an important concept. The surface of integration S divides all space into two regions — one inside and one outside the integration volume V. The integral over S of $(P\nabla G_0^D - G_0^D\nabla P)\cdot\hat{n}$ gives the field inside (outside) the integration volume due to sources outside (inside) the integration volume, a result called the extinction theorem (Born and Wolf, 1964, pp. 101–102). Selecting the integration volume V between the free surface and the measurement surface (Figure 19) gives the reference wavefield P_0 (if the observation/prediction point is outside V/below the cable) or the scattered wavefield P_s (if the observation point is inside V/above the cable). An electromagnetic analogy is shown in Figure 20. Sources outside (inside) the integration volume induce sources on the measurement surface that then create the field inside (outside) the integration volume (Orfanidis, 2008, pp. 679–681,[pp. 36–37]jackson:1999).

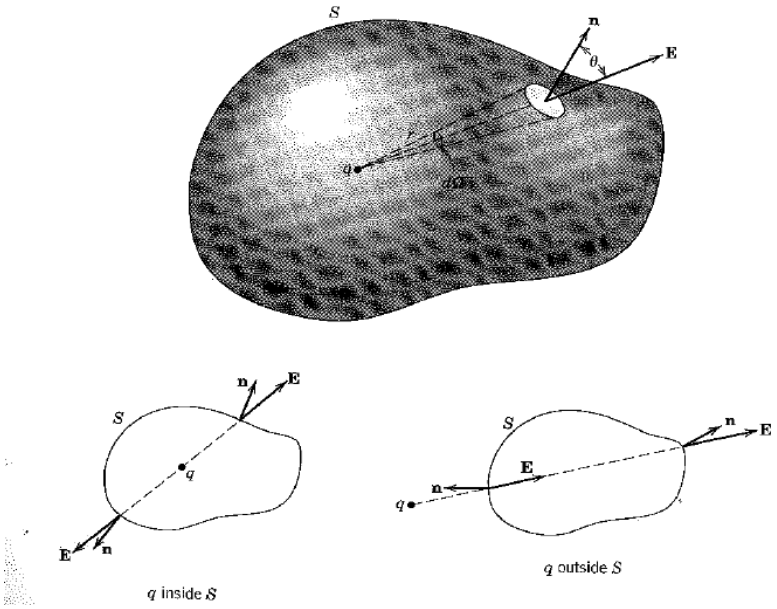

Figure 20: *Gauss's law (Jackson, 1999). The normal component of the electric field* $\mathbf{E}\cdot\hat{n}$ *is integrated over the closed surface* S*. If the charge is inside (outside)* S*, the total solid angle subtended at the charge is* 4π *(zero).*

4.2 Example: Synthetic data[1]

The first author tested his Green's theorem code using synthetic data provided by ExxonMobil. (More detail about input data is given in Appendix A.) The input data are shown in Figure 21 and the output data are shown in Figure 22. Note that the estimated wavelet (blue) is slightly rotated clockwise relative to the analytic wavelet (red). This rotation can be analytically reproduced as shown in Figure 23. What causes rotation in the frequency domain (shift in the time domain)? For a single isotropic source, equation 4.1 says $-P_0 = -A(\omega)G_0^+ = \int_{m.s.}$ or $A(\omega) = -\int_{m.s.}/G_0^+$. If the prediction point falls on a ghost notch, $1/G_0^+$ is truncated by ϵ (in equation 4.2). Truncation at specific frequencies in the frequency domain becomes a phase shift across all times in the time domain.

[1] Courtesy of ExxonMobil.

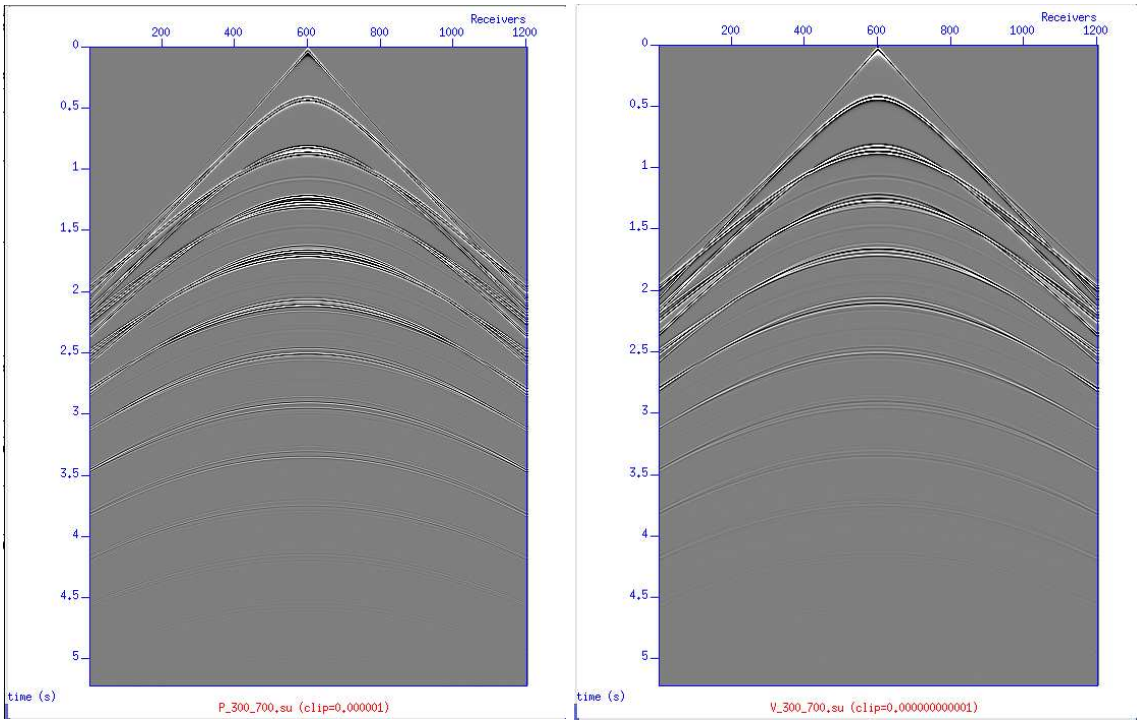

Figure 21: *Pressure wavefield (left), vertical component of particle velocity (right). Data courtesy of ExxonMobil.*

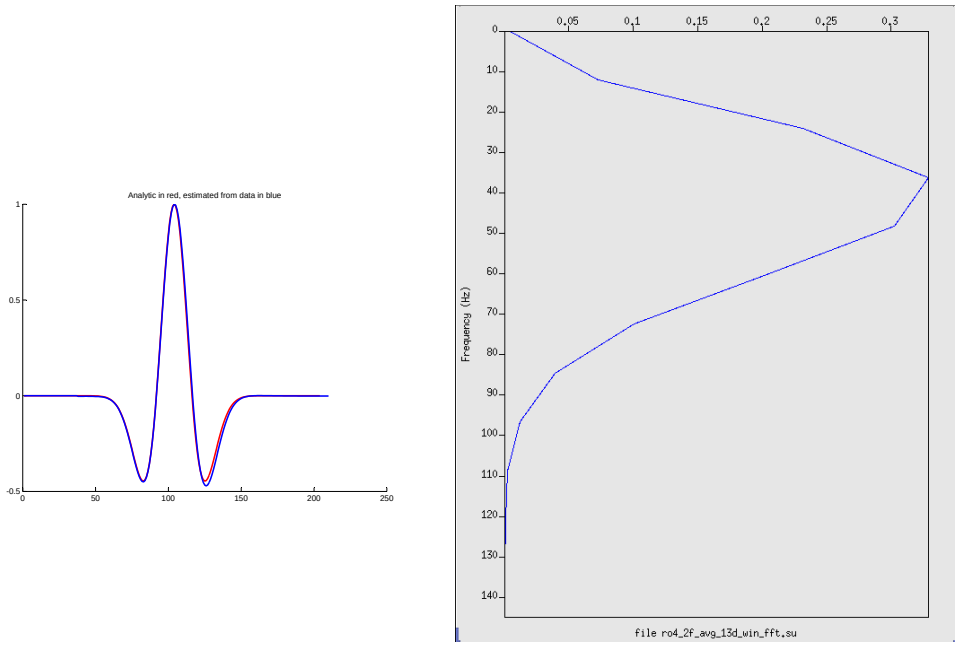

Figure 22: *Analytic wavelet (red), wavelet estimated using Green's theorem (blue), Fourier transform of estimated wavelet. Input data courtesy of ExxonMobil.*

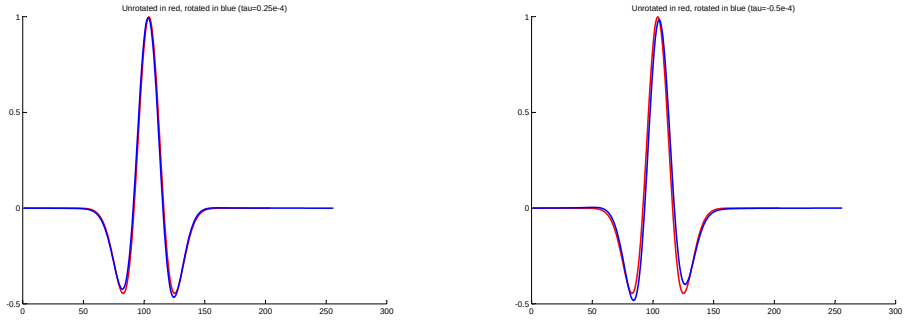

Figure 23: *The shape of the estimated wavelets can be analytically reproduced via rotation in the frequency domain (*$blue = red * \exp(-i\omega\tau)$*).*

4.3 Example: One-sided data

The purpose of Figures 24–27 is to show that the Green's theorem algorithm can work with one-sided data (as well as with split-spread data). This was also shown earlier because deep water Gulf of Mexico synthetic data (SEAM) are split spread, whereas deepwater Gulf of Mexico field data are one sided. Figures 24 and 25 use a 2D Green's function. Comparing the center and right panels of Figure 25 shows that P_0 computed using Green's theorem is close to P_0 computed using Cagniard de Hoop code. For comparison Figures 26 and 27 use a 3D Green's function; we can see no difference relative to the 2D Green's function.

The Green's theorem algorithm (equations 2.2 and 4.1) works with either split-spread or one-sided data because the integrand $(P\nabla G_0 - G_0\nabla P)\cdot\hat{n}$ is local, as shown in Figures 28 and 29. As we approach the source, the integrand becomes more narrow.

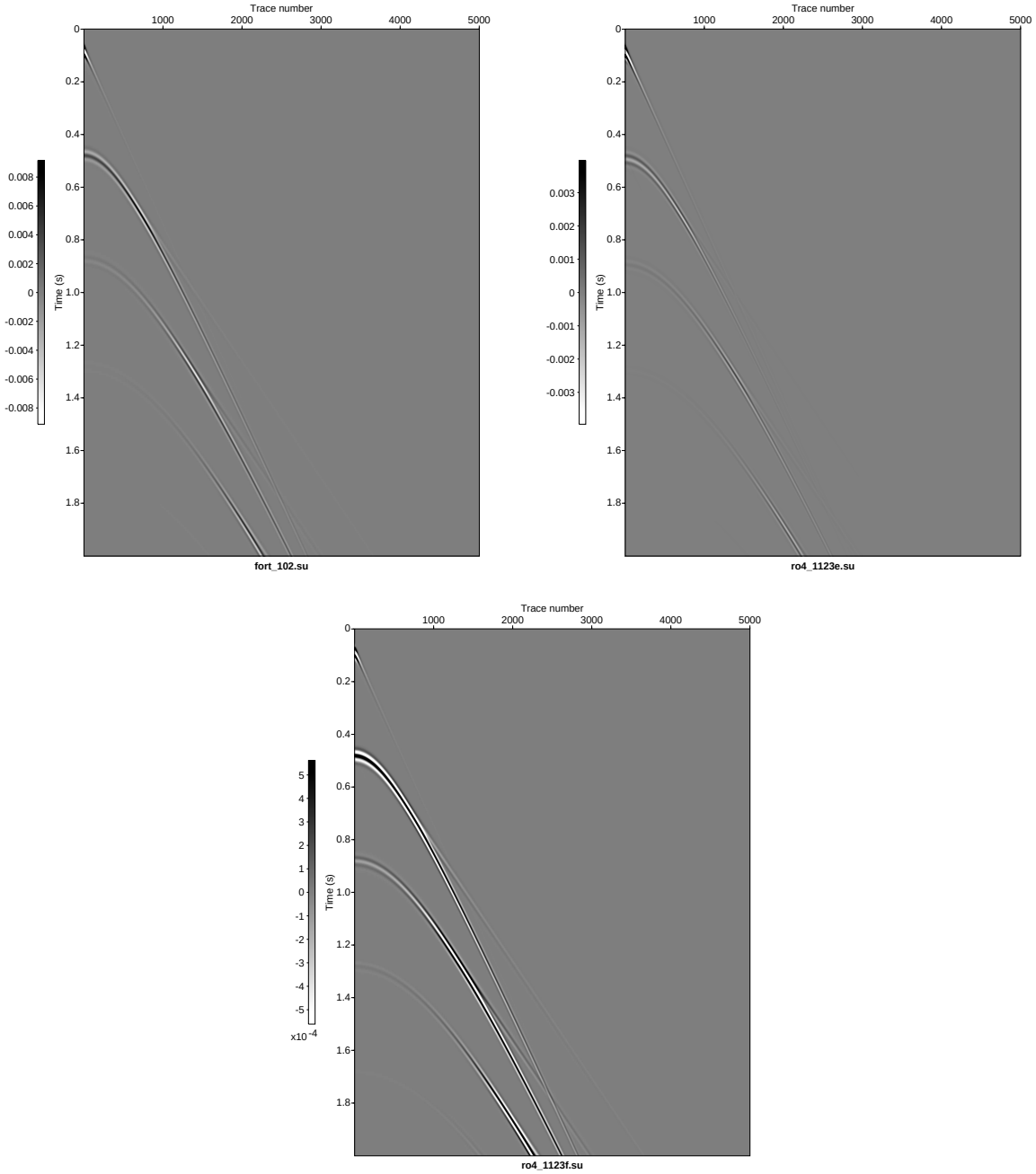

Figure 24: *Flat-layer model IV, 2D source, 2D Green's function: Cagniard de Hoop P at 12m (top left), Green's theorem P_0 10m below cable (top right) and P_s 10m above cable (bottom).*

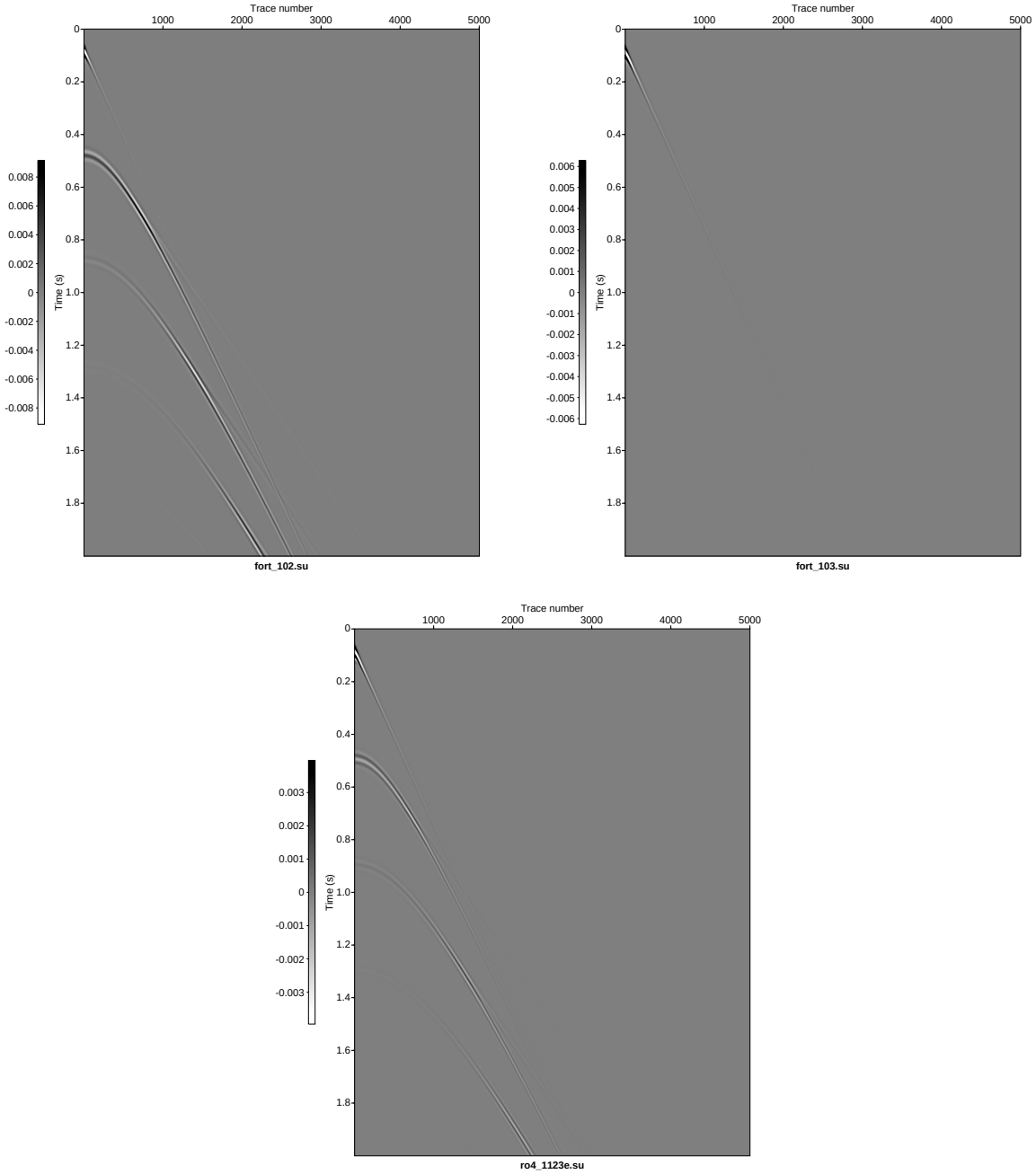

Figure 25: *Flat-layer model IV, 2D source, 2D Green's function: Cagniard de Hoop P at 12m (top left) and P_0 10m below cable (top right), Green's theorem P_0 10m below cable (bottom).*

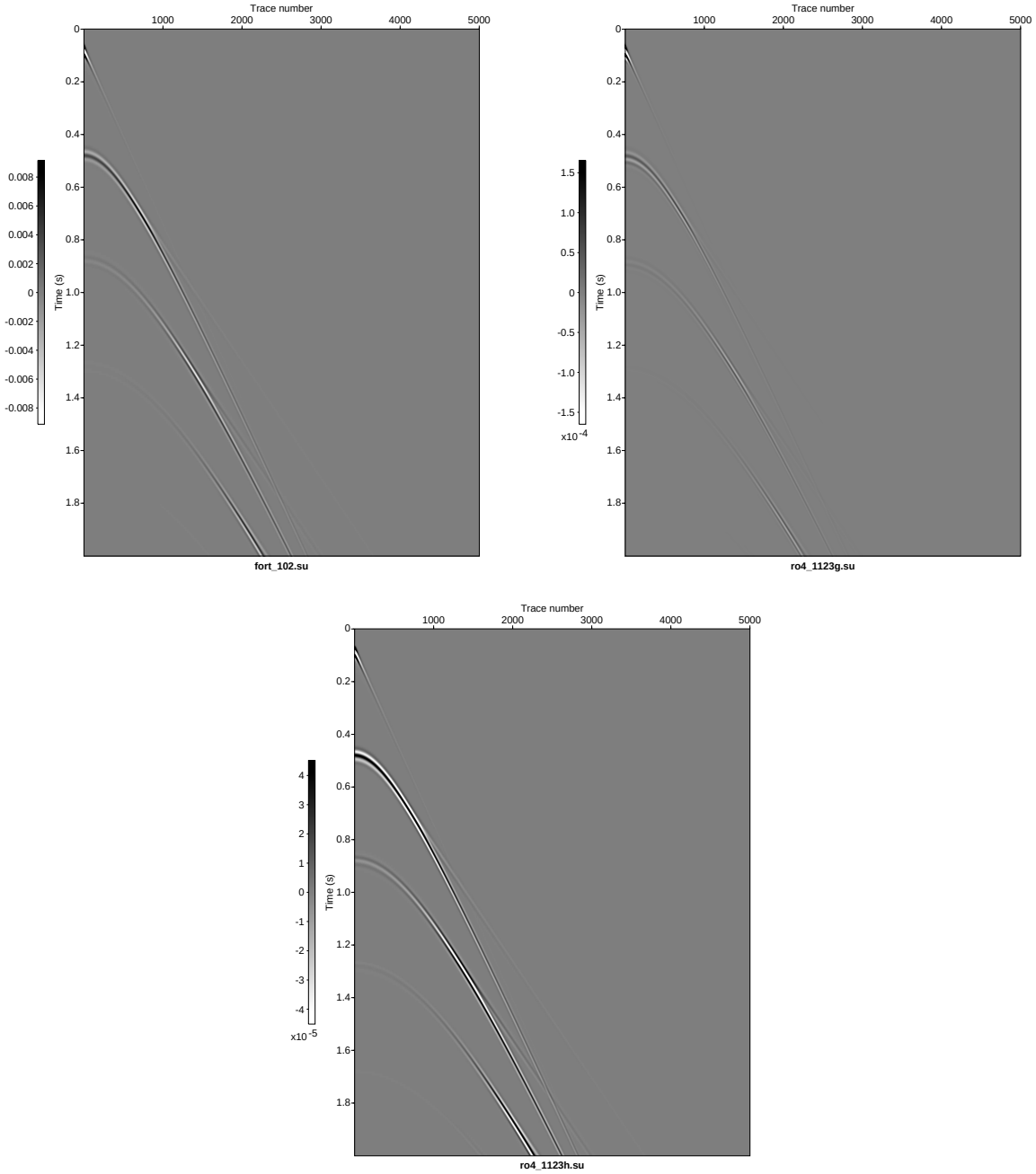

Figure 26: *Flat-layer model IV, 2D source, 3D Green's function: Cagniard de Hoop P at 12m (top left), Green's theorem P_0 10m below cable (top right) and P_s 10m above cable (bottom).*

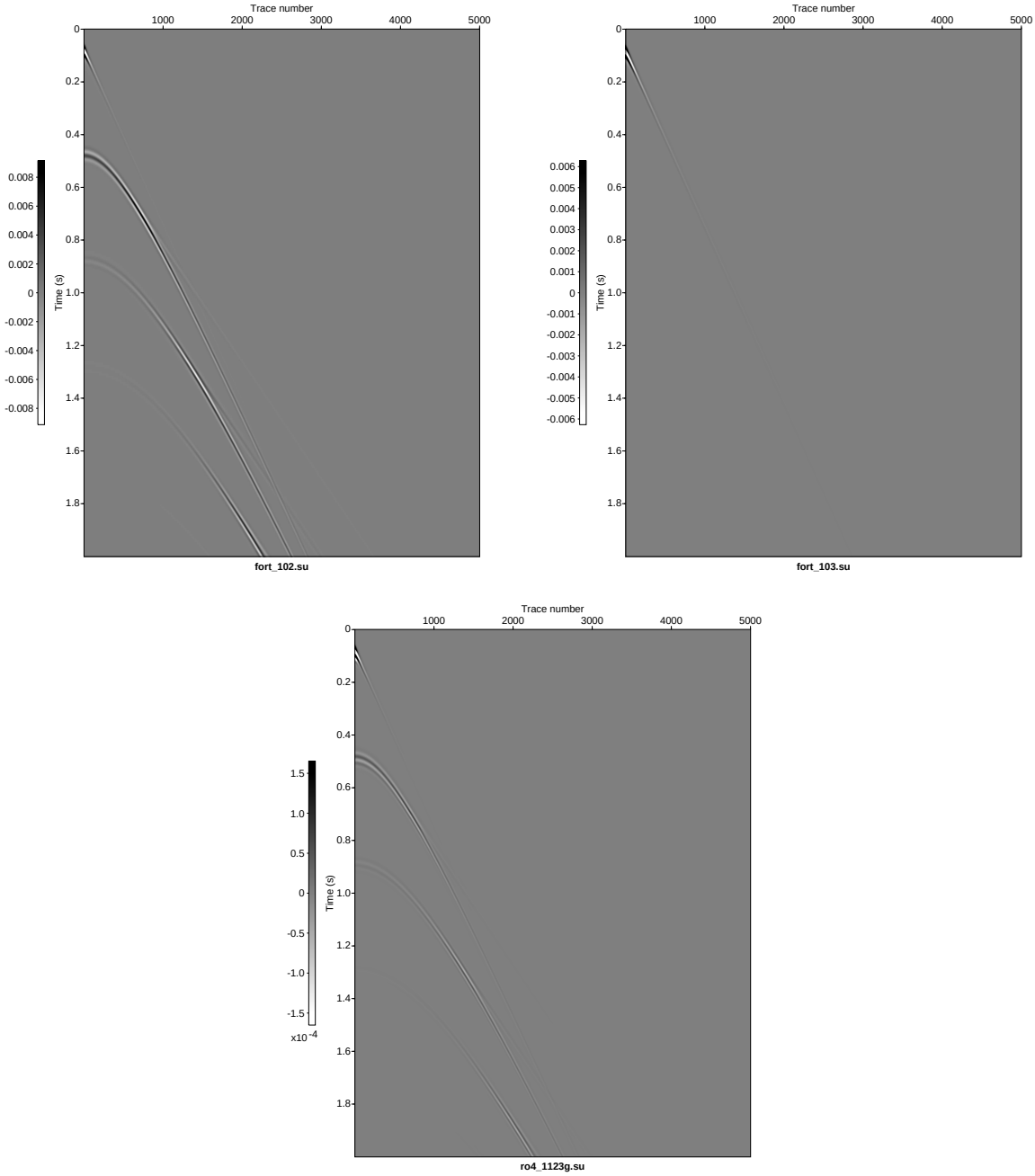

Figure 27: *Flat-layer model IV, 2D source, 3D Green's function: Cagniard de Hoop P at 12m (top left) and P_0 10m below cable (top right), Green's theorem P_0 10m below cable (bottom).*

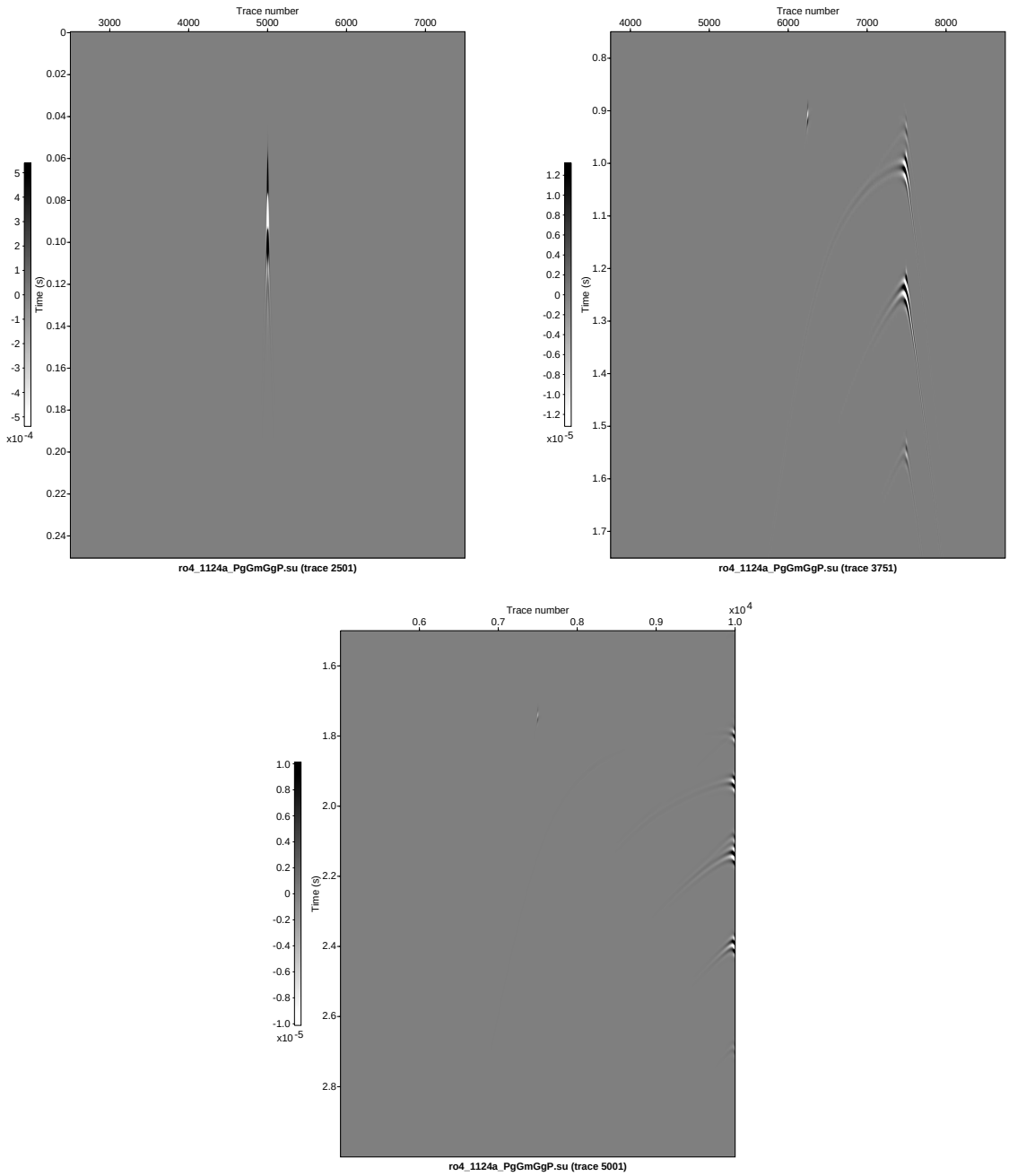

Figure 28: *Flat-layer model IV (Cagniard de Hoop code), split-spread data (source above trace 2501), P_0 10m below cable: trace 2501 (top left), trace 3751 (top right), trace 5001 (bottom).*

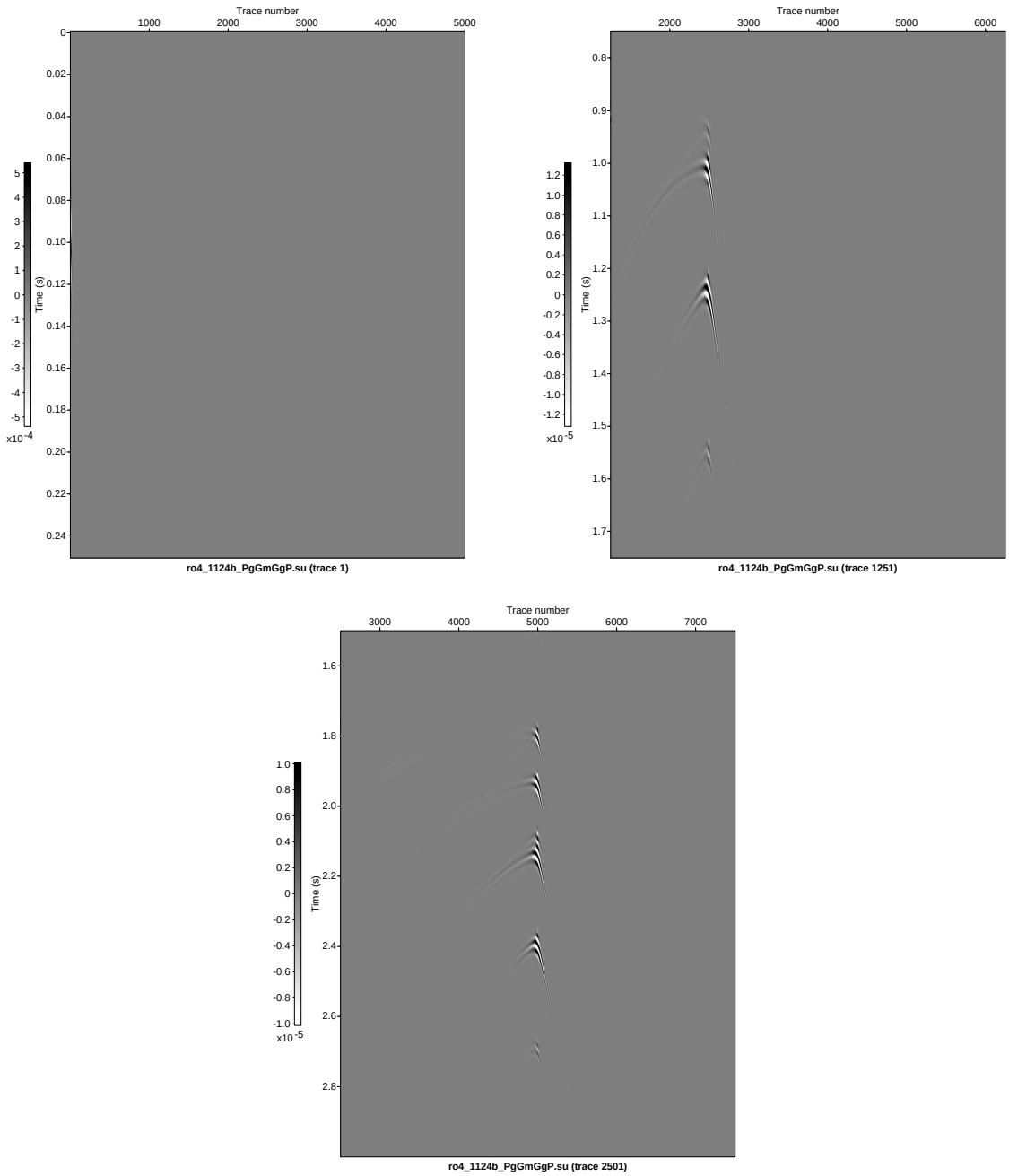

Figure 29: *Flat-layer model IV (Cagniard de Hoop code), one-sided data (source above trace 1), P_0 20m below cable: trace 1 (top left), trace 1251 (top right), trace 2501 (bottom).*

4.4 Example: Jinlong Yang's data (nine point sources)

The purpose of Figure 30 is to show that the Green's theorem algorithm can work with a distributed source (as well as with a point source). This was also shown earlier because deep water Gulf of

Mexico synthetic data (SEAM) uses a point source, whereas deep water Gulf of Mexico field data uses a distributed source (air-gun array).

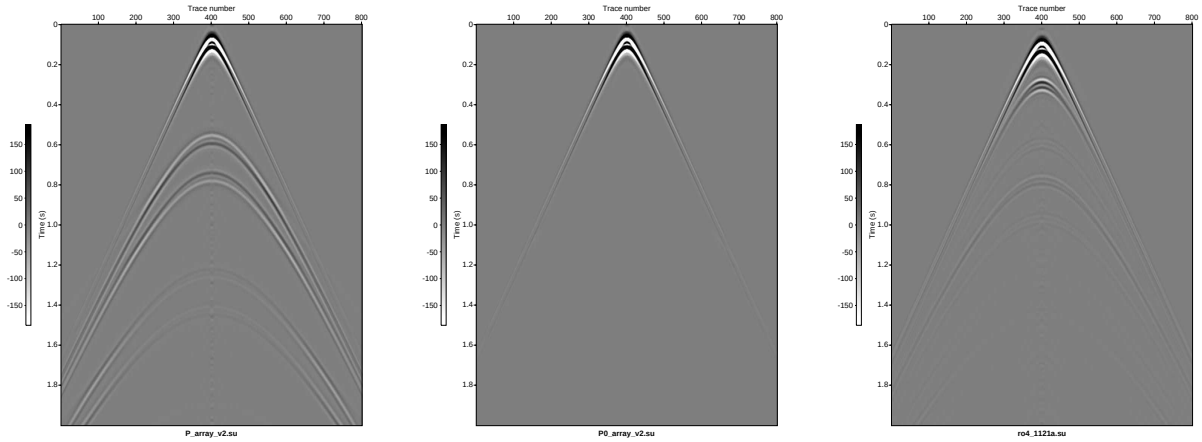

Figure 30: *Flat-layer model, nine collinear 3D point sources, 2D Green's function (clip=170): reflectivity P at 140m (left) and P_0 at 140m (center), Green's theorem P_0 at 170m (right).*

4.5 Fourier-Bessel integral

Per Zhiqiang Wang (from Fang Liu), we can restate the integral from rectangular coordinates to polar coordinates: $\int dy \int dx\, f(x,y,z) = \int \rho\, d\rho \int d\theta\, f(\rho,\theta,z)$. If $f(\rho,\theta,z) = f(\rho,z)$ (azimuthal symmetry) then $\int \rho\, d\rho \int d\theta\, f(\rho,\theta,z) = 2\pi \int \rho\, d\rho\, f(\rho,z)\, (= 2\pi \int x\, dx\, f(x,z))$. The first author tried using this form for wavefield separation (Figures 31 and 32) but more work is needed to understand this integral.

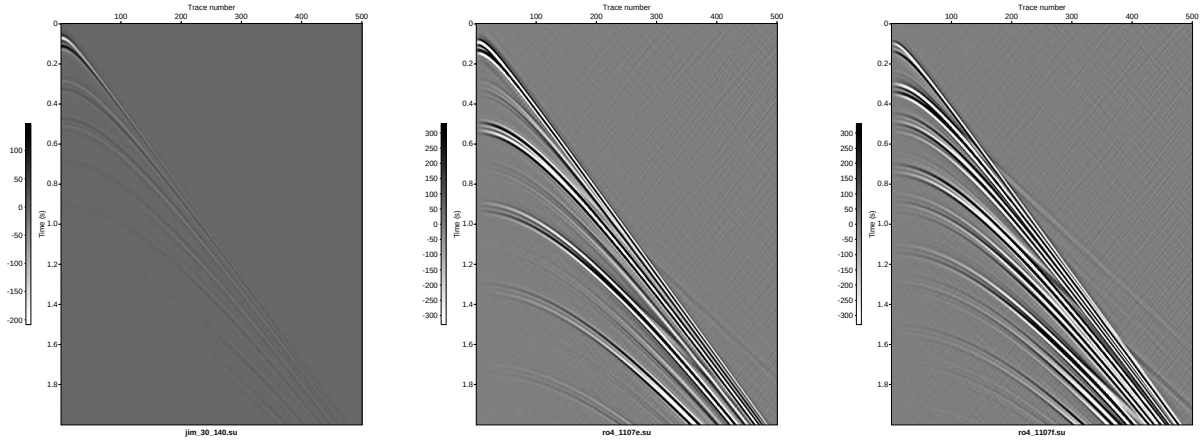

Figure 31: *Flat-layer model I, 3D source, 3D Green's function (clip=300): reflectivity P at 140m (left), Green's theorem P_0 30m below cable (center) and P_s 30m above cable (right).*

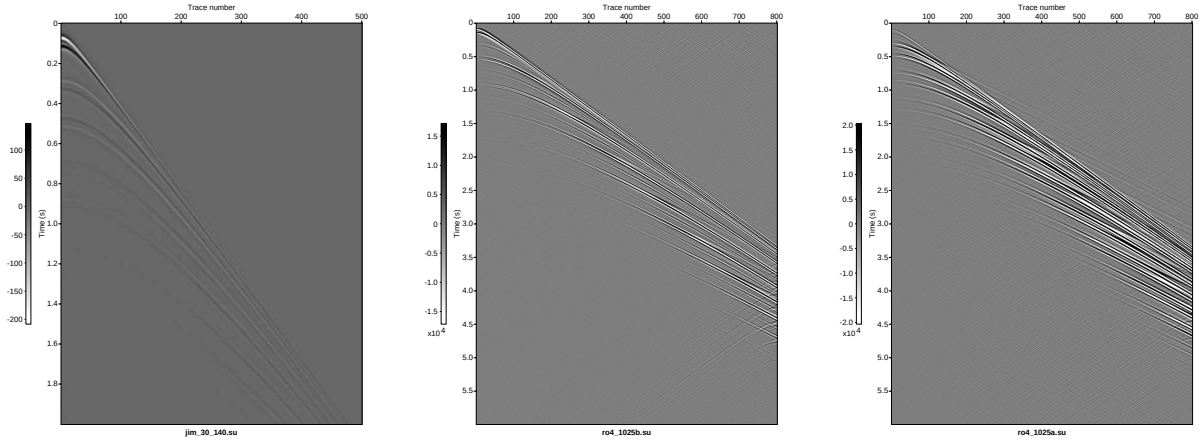

Figure 32: *Flat-layer model I, 3D source, 2D Green's function (clip=18000): reflectivity P at 140m (left), Green's theorem P_0 30m below cable (center) and P_s 30m above cable (right).*

5 Near-offset extrapolation

5.1 Example: Synthetic data[2]

Near-offset extrapolation using Green's theorem is discussed in chapter 4 of Ramírez (2007) and chapter 2 of Zhang (2007). The first author tested his Green's theorem code using synthetic data provided by ExxonMobil. (More detail about input data is given in Appendix A.) The input data are shown in Figure 21 and the output data in Figure 33. Next, the data were presented with a near-offset gap, and the first author tried to interpolate P_s across the gap (Figure 34). How do we explain the lack of interpolation across the gap? Equation 2.1 says there's no support for near-offset extrapolation from measured data; the support in the gap is only from the Green's function. In other words, Green's theorem assumes P and ∇P are known on the measurement surface, but the gap consists of $P = 0$ and $\nabla P = \mathbf{0}$. This was the clue that led to the finding that the integrand in the Green's theorem surface integral (equations 4.1 and 2.2) is local (as shown in Figures 28 and 29).

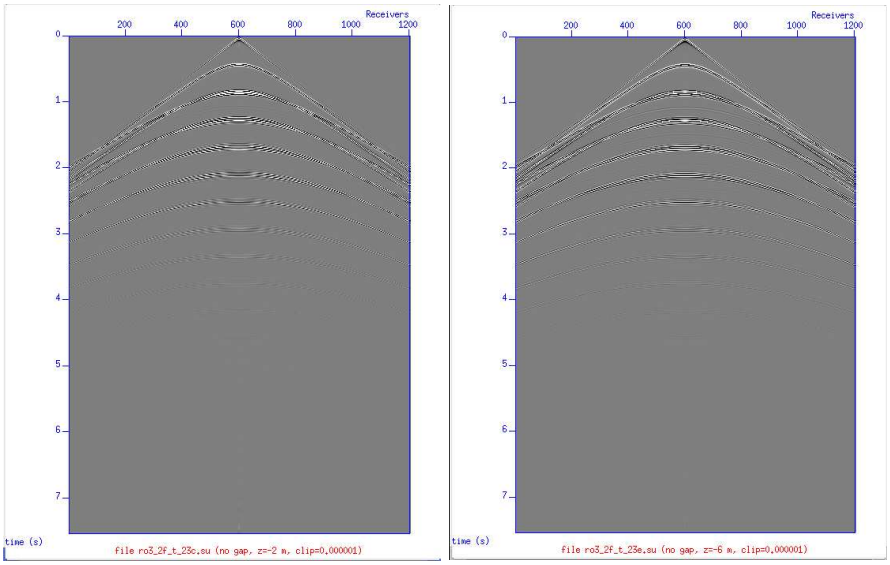

Figure 33: *Reconstructed cables 4m above (left) and at towed cable (right). Input data courtesy of ExxonMobil.*

[2]Courtesy of ExxonMobil.

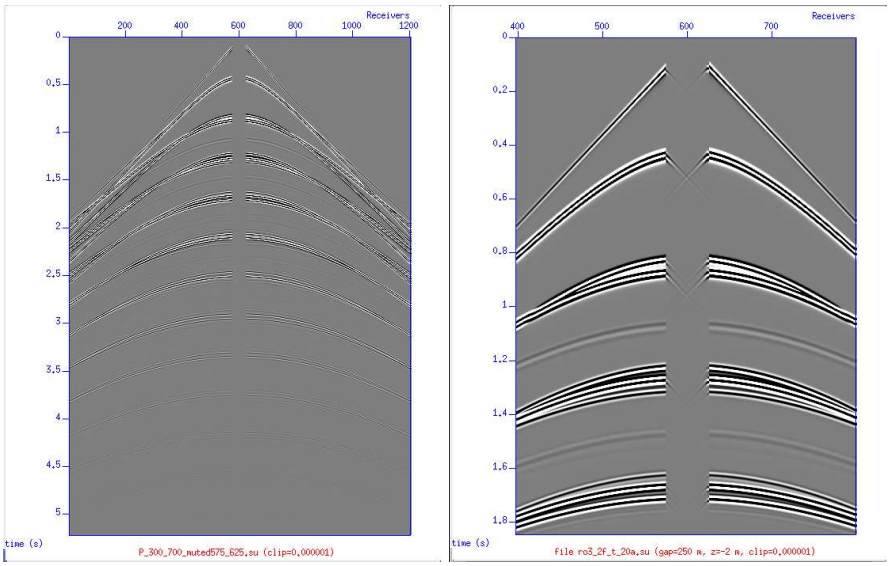

Figure 34: *Pressure wavefield with 250m gap (left); attempt to fill the gap 4m above the towed cable (right). Input data courtesy of ExxonMobil.*

6 FSM elimination with and without Green's theorem preprocessing

M-OSRP's theory of free-surface-multiple elimination (FSME) is derived in Carvalho (1992). This derivation has been included in this Annual Report (in Appendix I) because the first author is in the process of running M-OSRP's 3D FSME code with and without the 3D Green's theorem code (using synthetic and field data) to test the hypothesis that deghosting and source wavelet estimation by the 3D Green's theorem code will enable more competent prediction of free-surface multiples by the 3D FSME code.

6.1 Green's theorem output → FSM removal input

Green's theorem output is in the same configuration as its input (one or more towed streamers). However, the free-surface-multiple prediction algorithm requires coincident sources and receivers as input. Green's theorem output is transformed into FSME input using several Seismic Unix scripts.
(1) Interpolate data so that the distance between shots equals the distance between receivers (the second author's scripts interp.sh and interp_by_channel.sh).
(2) Assign station numbers to sources and receivers (Andre Ferreira's script stationAssign.sh).
(3) Use reciprocity between sources and receivers to compute the opposite side of shots, i.e., convert one-sided data into split-spread data (Andre Ferreira's script reciprocity.sh).
(4) Replace source and receiver x coordinates (sx and gx) by source and receiver stations ($sstat$ and $gstat$) and make $sy = gy = 0$ (Andre Ferreira's script hdr.sh).
(5) Select blocks, i.e., if selected block < offset, we don't need to pad, but if selected block > (longer)

than offset, we need to pad traces (Figure 59) (Andre Ferreira's script selectBlock.sh).
(6) Fill shots with all required offsets, i.e., each shot should be surrounded by zero padding (Andre Ferreira's script force_pad4.sh).
(7) To smooth the transition from the original data to the padded null traces, taper the amplitudes of the last few traces of original data (Andre Ferreira's script tapering.sh).

We wanted to show the results of free-surface-multiple removal with and without Green's theorem preprocessing but found that, in the absence of any preprocessing, free-surface-multiple removal gives nonsensical results. Per Andre Ferreira, as a minimum the direct wave G_0^d must be removed from the data. Thus, we will compare (a) free-surface-multiple removal with the direct wave removed (and using a default estimate of the source wavelet, i.e., a spike) and (b) free-surface-multiple removal with the reference wave $G_0^d + G_0^{FS}$ removed and using the source wavelet $A(t)$. The first author is currently in the process of testing using reflectivity data, OASES data, and Kristin data. (More detail about input data is given in Appendix A.)

6.2 Flat-layer model III without and with preprocessing

We use for input synthetic data created using reflectivity code[3] and flat-layer model III. The details are shown in Appendices J.1 and J.2, and the results are shown in Figures 35, 36, and 37. In Figure 37, more work is needed to interpret the right panel.

[3]Courtesy of BP.

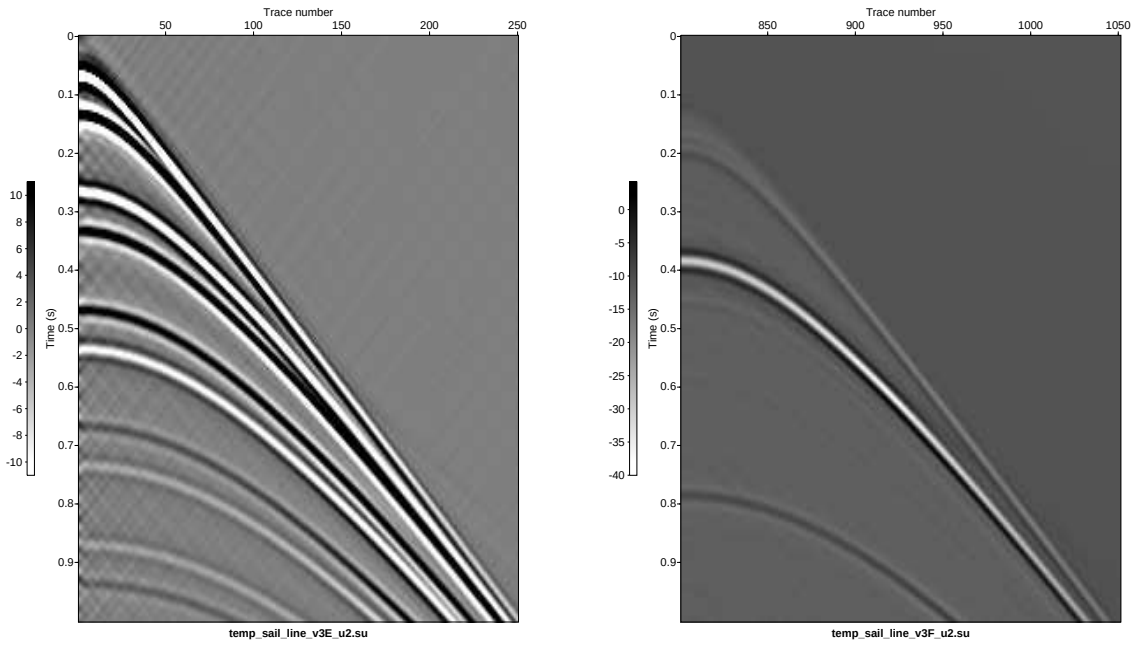

Figure 35: *Flat-layer model III, reflectivity code, P at 151m. The left panel shows the data, and the right panel shows the same data after source and receiver deghosting. The events in the left panel are (for increasing time)* G_0^d *and* G_0^{FS} *(first pair), WB primary and WB primary source ghost (second pair), WB primary receiver ghost and WB primary source/receiver ghost (third pair), 1st FSM and 1st FSM source ghost (fourth pair), and 1st FSM receiver ghost and 1st FSM source/receiver ghost (fifth pair). The events in the right panel are (for increasing time) WB primary (just above 0.4s) and 1st FSM (just above 0.8s). All other events have been attenuated.*

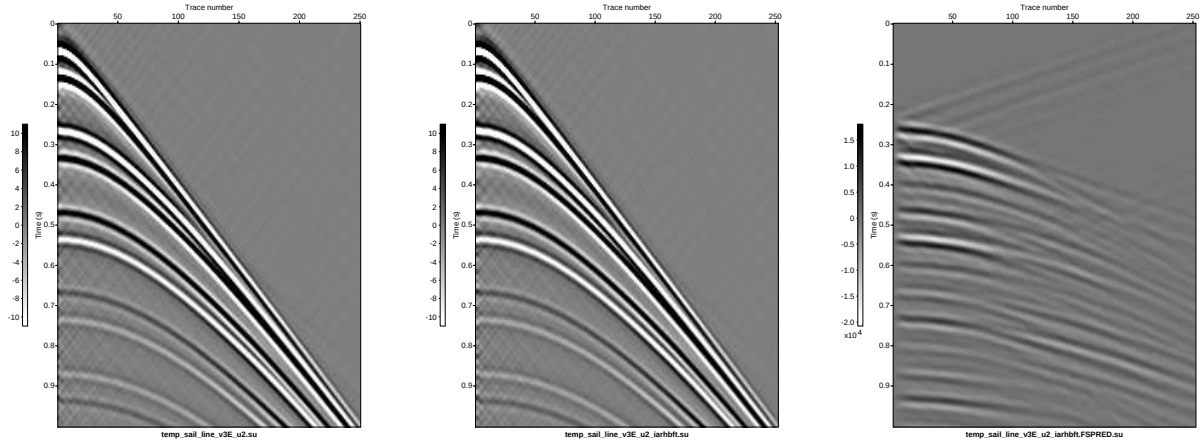

Figure 36: *Flat-layer model III, reflectivity code, P at 151m. The left panel shows the data before configuration transformation (shot 1 of 301). The events are the same as those in the left panel of Figure 35. The middle panel shows the data after configuration transformation (shot station 1 of 901). The right panel shows the output of the free-surface-multiple prediction code (shot station 1 of 901). The prediction code seems to think (without deghosting) that the second through fifth pairs of events are FSMs.*

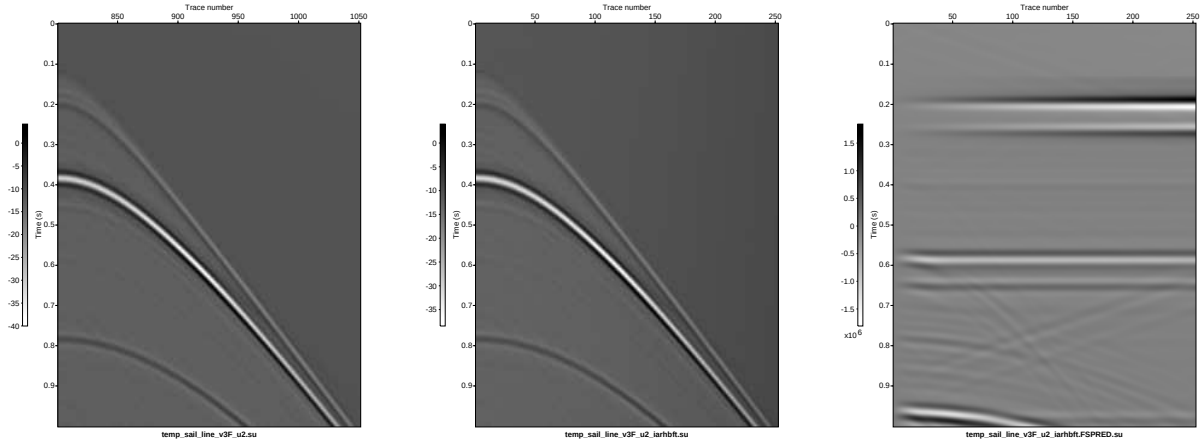

Figure 37: *Flat-layer model III, reflectivity code, P at 151m. The left panel shows the data before configuration transformation (shot 1 of 301). The events are the same as those in the right panel of Figure 35. The middle panel shows the data after configuration transformation (shot station 1 of 901). The right panel shows the output of the free-surface-multiple prediction code (shot station 1 of 901).*

6.3 Elastic model 1 with preprocessing

OASES data (see section A) were modified as follows: (1) traces were time padded to get finer sampling in ω, (2) data were converted from one sided to split spread to avoid truncation at zero

offset, (3) data were receiver deghosted, and (4) data were source deghosted. Then a window (traces 501–801) was taken and replicated to form a sail line with 301 shots x 301 receivers. The result is shown in Figure 38.

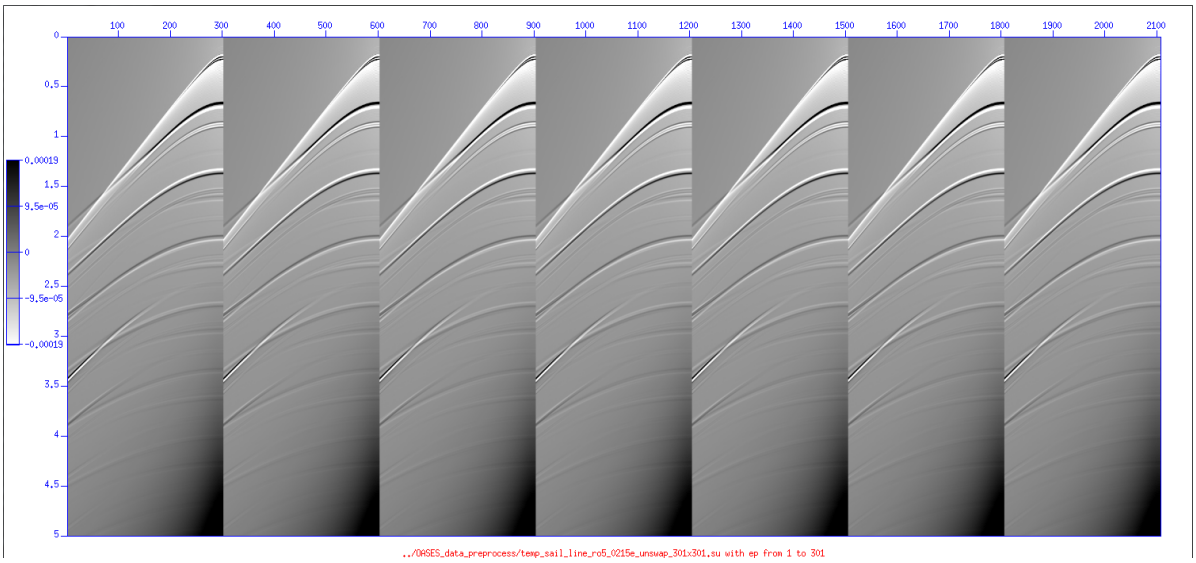

Figure 38: *Source and receiver deghosted P at 25m. Shots 1–301 by 50.*

The processing steps are shown in Appendix J.3.

Running the internal-multiple attenuation code is a work in progress.

6.4 Elastic model 2 with preprocessing

OASES data (see section A) were modified as follows: (1) traces were time padded to get finer sampling in ω, (2) data were converted from one sided to split spread to avoid truncation at zero offset, (3) data were receiver deghosted, and (4) data were source deghosted. Then a window (traces 501–801) was taken and replicated to form a sail line with 301 shots x 301 receivers. The result is shown in Figure 39.

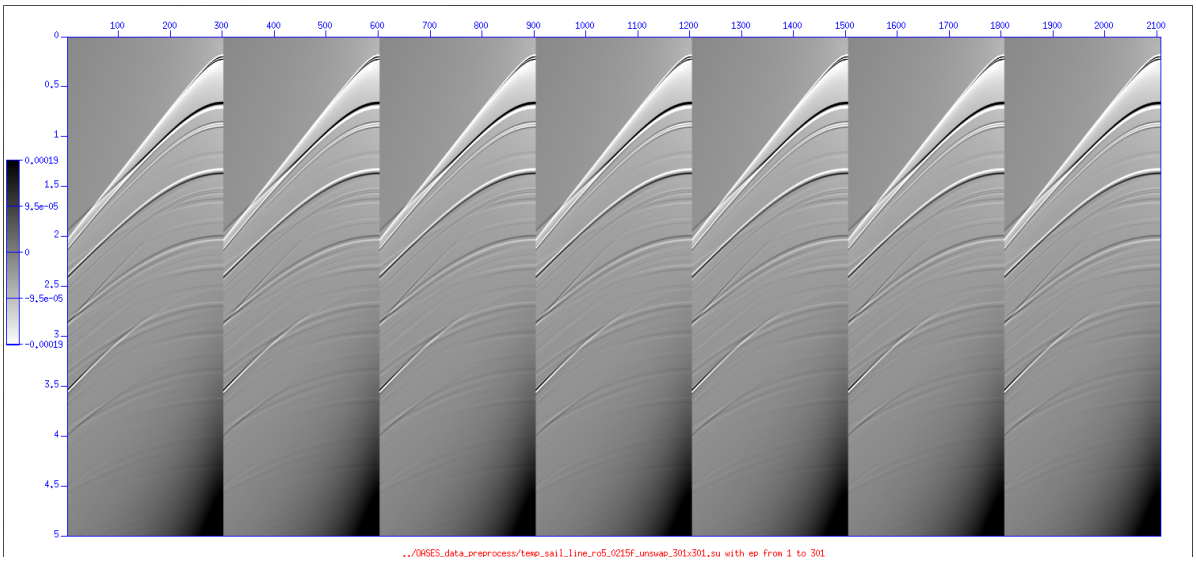

Figure 39: *Source and receiver deghosted P at 25m. Shots 1–301 by 50.*

The processing steps are shown in Appendix J.4.

Running the internal-multiple attenuation code is a work in progress.

6.5 Field data[4] without and with preprocessing

The details are shown in Appendices J.5 and J.6, and the results are shown in Figures 40–42. In Figure 41, more work is needed to debug the left-hand side of the right panel.

[4]Courtesy of Statoil ASA, Petoro, ExxonMobil, Eni, Total, and Schlumberger/WesternGeco.

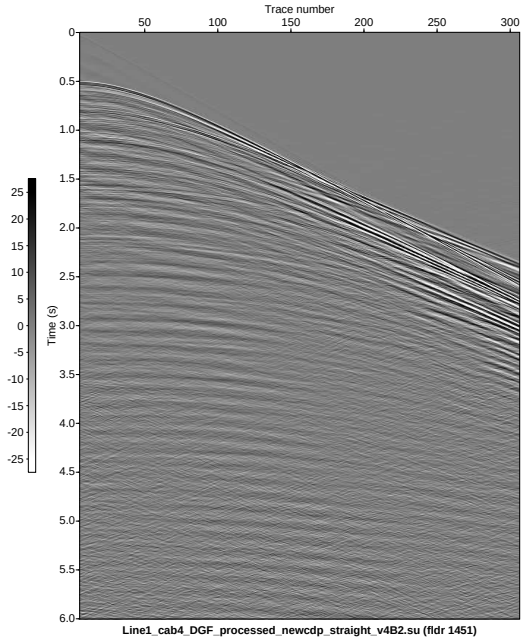

Figure 40: *Field data, P at 25m. Data courtesy of Statoil ASA, Petoro, ExxonMobil, Eni, Total, and Schlumberger/WesternGeco.*

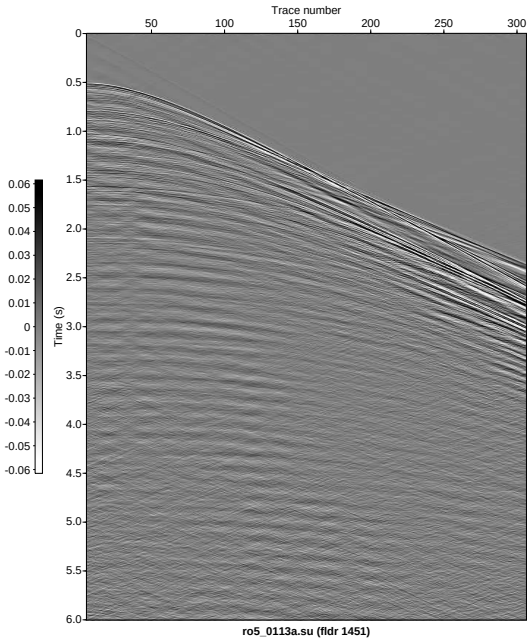

Work in progress

Figure 41: *Field data, receiver deghosted at 15m (left), source and receiver deghosted at 15m (right).*

Figure 42: *Field data, input to FSM prediction code (left), output of FSM prediction code (right).*

7 RTM

7.1 Tutorial

Green's theorem reverse time migration (RTM) is based on Weglein et al. (2011a) and Weglein et al. (2011b). Green's theorem assumes a closed surface S to define inside/outside a volume V. For deghosting and wavefield separation, we assume V is a hemisphere with the flat surface coinciding with the measurement surface (Figures 2 and 19). Taking the radius of the hemisphere to infinity and invoking the Sommerfeld radiation condition means that contributions to the surface integral in equation 2.1 go to zero except on the measurement surface (Zhang, 2007, chapter 2). For 2D RTM we assume that V is a rectangle in the x, z plane with the upper surface coinciding with the measurement surface (Figure 43). We assume we can find a Green's function such that it and its normal derivative vanish on the other three sides of the rectangle.

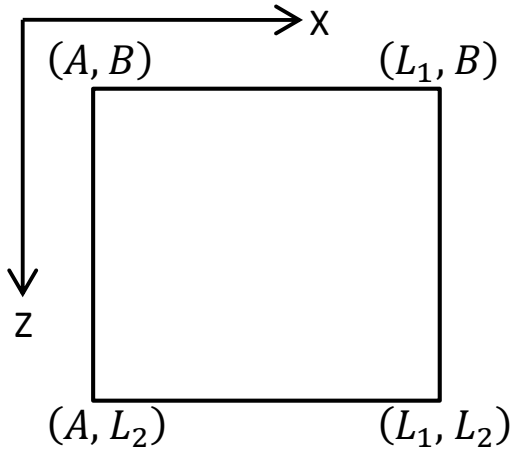

Figure 43: *Two-dimensional finite-volume model.*

RTM modifies Figure 1 (see Figure 44) because RTM assumes we know the actual medium (green), whereas the inverse scattering series does not make this assumption (yellow).

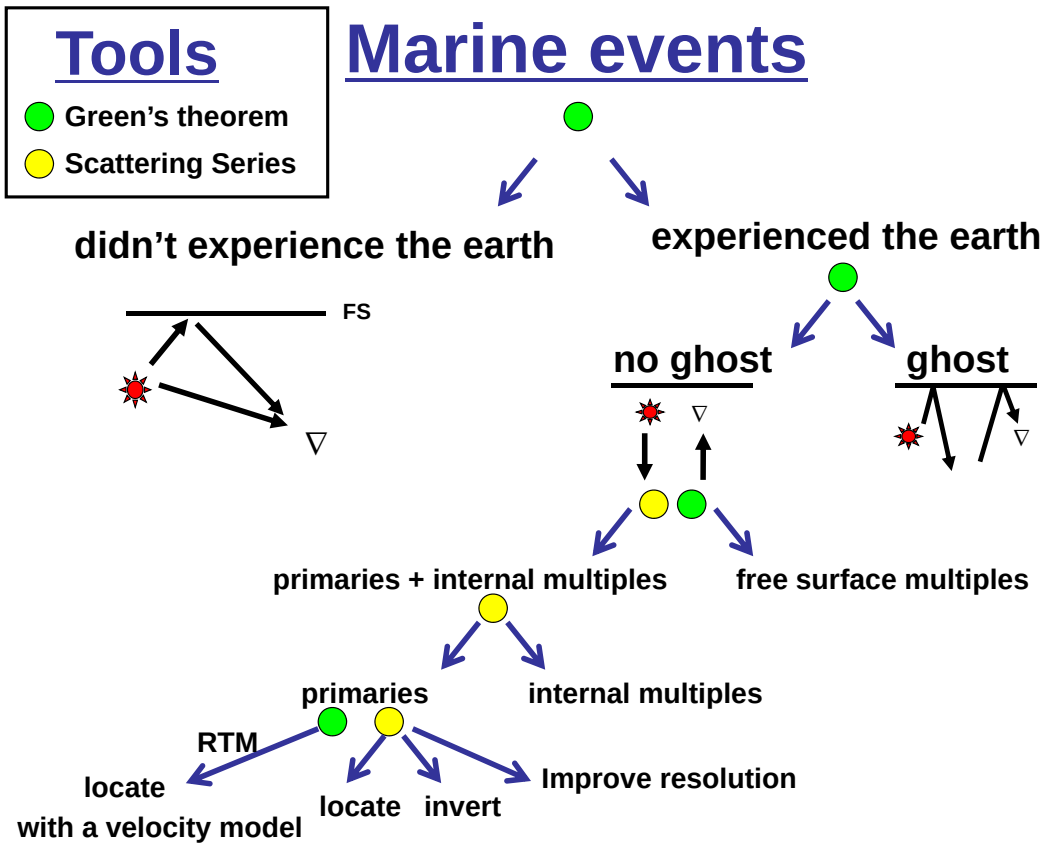

Figure 44: *Classification of marine events and how they are processed.*

Wilberth Herrera and the first author try solutions of the form (note that in this section and in section 7.2, the equation numbers refer to those in Weglein et al. (2011b)):

$$G(\mathbf{r}^{'},\mathbf{r},\omega) = A(\mathbf{r})X(x')Z(z') + G_P(\mathbf{r}^{'},\mathbf{r},\omega), \quad (42)$$

$$G_H(\mathbf{r}^{'},\mathbf{r},\omega) = A(\mathbf{r})X(x')Z(z'), \quad (43)$$

with the boundary conditions that G and $\partial G/\partial n$ vanish at $x' = A$, $z' = L_2$, and $x' = L_1$, i.e.,

$$\text{at } x' = A \; G = 0 \text{ and } -\partial G/\partial x' = 0, \quad (44)$$

$$\text{at } z' = L_2 \; G = 0 \text{ and } \partial G/\partial z' = 0, \text{ and} \quad (45)$$

$$\text{at } x' = L_1 \; G = 0 \text{ and } \partial G/\partial x' = 0. \quad (46)$$

We assume the wavefield is known (measured) at $z' = B$. Substituting (43) into $(\nabla'^{\,2} + k^2)G_H = 0$ gives:

$$0 = \left(\frac{\partial^2}{\partial x'^{\,2}} + \frac{\partial^2}{\partial z'^{\,2}} + k^2\right) X(x')Z(z')$$

$$
\begin{aligned}
&= X''(x')Z(z') + X(x')Z''(z') + k^2X(x')Z(z') \\
&= \frac{X''(x')}{X(x')} + \frac{Z''(z')}{Z(z')} + k^2 \\
\Rightarrow \frac{Z''(z')}{Z(z')} &= -\lambda^2 \\
0 &= Z''(z') + \lambda^2 Z(z') \\
Z(z') &= C_1 e^{i\lambda z'} + C_2 e^{-i\lambda z'} \quad (47) \\
0 &= X''(x') + (\underbrace{k^2 - \lambda^2}_{\equiv \mu^2})X(x') \\
X(x') &= C_3 e^{i\mu x'} + C_4 e^{-i\mu x'}, \quad (48)
\end{aligned}
$$

where $\mu^2 \iff X(x')$ and $\lambda^2 \iff Z(z')$. We assume $k^2 > \lambda^2$, i.e., $\mu^2 > 0$, so as to get oscillating solutions and hence equation 48.

The boundary conditions on the left are $G(A, z') = 0$ and $G_{x'}(x', z')|_{x'=A} = 0$, on the right $G(L_1, z') = 0$ and $G_{x'}(x', z')|_{x'=L_1} = 0$, and on the bottom $G(x', L_2) = 0$ and $G_{z'}(x', z')|_{z'=L_2} = 0$. Substituting these boundary conditions into equation 42 gives:

$$
\begin{aligned}
0 &= G(A, z', x, z) = A(\mathbf{r})X(A)Z(z') + G_P(A, z', x, z), \quad (49) \\
0 &= \frac{\partial G}{\partial x'}(x', z', x, z)|_{x'=A} = A(\mathbf{r})\frac{dX}{dx'}(x')|_{x'=A}Z(z') + \frac{\partial G_P}{\partial x'}(x', z', x, z)|_{x'=A}, \quad (50) \\
0 &= G(L_1, z', x, z) = A(\mathbf{r})X(L_1)Z(z') + G_P(L_1, z', x, z), \quad (51) \\
0 &= \frac{\partial G}{\partial x'}(x', z', x, z)|_{x'=L_1} = A(\mathbf{r})\frac{dX}{dx'}(x')|_{x'=L_1}Z(z') + \frac{\partial G_P}{\partial x'}(x', z', x, z)|_{x'=L_1}, \quad (52) \\
0 &= G(x', L_2, x, z) = A(\mathbf{r})X(x')Z(L_2) + G_P(x', L_2, x, z), \quad (53) \\
0 &= \frac{\partial G}{\partial z'}(x', z', x, z)|_{z'=L_2} = A(\mathbf{r})X(x')\frac{dZ}{dz'}(z')|_{z'=L_2} + \frac{\partial G_P}{\partial z'}(x', z', x, z)|_{z'=L_2}. \quad (54)
\end{aligned}
$$

Equations 55–61 are no longer needed. We have six boundary conditions and seven unknowns: C_1, C_2, C_3, C_4, λ, μ, and $A(\mathbf{r})$. The seventh boundary condition is to be determined (perhaps by renormalization).

We substitute equations 47–48 into equations 49–54. We also need expressions for G_P, $\partial G_P/\partial x'$, and $\partial G_P/\partial z'$. In 2D with no free surface, $G_P(\mathbf{r}', \mathbf{r}, \omega) = -(i/4)H_0^{(1)}(kR_+)$, where $R_+ = |\mathbf{r} - \mathbf{r}'|$ and $H_0^{(1)}$ is the zeroth-order Hankel function of the first kind (Morse and Feshbach, 1953, § 7.2). Check: For $R_+ \neq 0$

$$
\begin{aligned}
&(\nabla'^2 + k^2)(G_H + G_P) \\
&= \underbrace{(\nabla'^2 + k^2)G_H}_{=0} + (\nabla'^2 + k^2)G_P \\
&= \left(\frac{\partial^2}{\partial x'^2} + \frac{\partial^2}{\partial z'^2} + k^2\right)\frac{-i}{4}H_0^{(1)}(kR_+)
\end{aligned}
$$

$$
\begin{aligned}
=&\frac{-i}{4}\left(\frac{\partial}{\partial x'}(-H_1^{(1)}(kR_+)k\underbrace{\frac{\partial R_+}{\partial x'}}_{-(x-x')/R_+})+\frac{\partial}{\partial z'}(-H_1^{(1)}(kR_+)k\underbrace{\frac{\partial R_+}{\partial z'}}_{-(z-z')/R_+})+k^2H_0^{(1)}(kR_+)\right)\\
=&\frac{-i}{4}\left(\frac{\partial}{\partial x'}\left(H_1^{(1)}(kR_+)\frac{k(x-x')}{R_+}\right)+\frac{\partial}{\partial z'}\left(H_1^{(1)}(kR_+)\frac{k(z-z')}{R_+}\right)+k^2H_0^{(1)}(kR_+)\right)\\
=&\frac{-i}{4}\left(\frac{1}{2}(H_0^{(1)}(kR_+)-H_2^{(1)}(kR_+))(-1)\left(\frac{k(x-x')}{R_+}\right)^2+H_1^{(1)}(kR_+)\frac{k(R_+(-1)-(x-x')(-(x-x')/R_+))}{R_+^2}\right.\\
&+\frac{1}{2}(H_0^{(1)}(kR_+)-H_2^{(1)}(kR_+))(-1)\left(\frac{k(z-z')}{R_+}\right)^2+H_1^{(1)}(kR_+)\frac{k(R_+(-1)-(z-z')(-(z-z')/R_+))}{R_+^2}\\
&\left.+k^2H_0^{(1)}(kR_+)\right)
\end{aligned}
$$

$$
\begin{aligned}
=&\frac{-i}{4}\left(H_0^{(1)}(kR_+)\frac{1}{2}\left(\underbrace{-\left(\frac{k(x-x')}{R_+}\right)^2-\left(\frac{k(z-z')}{R_+}\right)^2}_{-k^2}+2k^2\right)\right.\\
&+H_1^{(1)}(kR_+)\frac{k}{R_+^3}(-2R_+^2+\underbrace{(x-x')^2+(z-z')^2}_{R_+^2})\\
&\left.-H_2^{(1)}(kR_+)\frac{1}{2}\underbrace{\left(-\left(\frac{k(x-x')}{R_+}\right)^2-\left(\frac{k(z-z')}{R_+}\right)^2\right)}_{-k^2}\right)\\
=&\frac{-i}{4}\left(H_0^{(1)}(kR_+)\frac{1}{2}k^2+H_1^{(1)}(kR_+)\frac{k}{R_+^3}(-R_+^2)-H_2^{(1)}(kR_+)\frac{1}{2}(-k^2)\right)\\
=&\frac{-i}{4}\left(\frac{k^2}{2}H_0^{(1)}(kR_+)-\frac{k}{R_+}H_1^{(1)}(kR_+)+\frac{k^2}{2}H_2^{(1)}(kR_+)\right)\\
=&\frac{-i}{4}\left(-\frac{k}{R_+}H_1^{(1)}(kR_+)+\frac{k^2}{2}(\underbrace{H_2^{(1)}(kR_+)+H_0^{(1)}(kR_+)}_{2/(kR_+)H_1^{(1)}(kR_+)})\right)\\
=&\frac{-i}{4}\left(-\frac{k}{R_+}H_1^{(1)}(kR_+)+\frac{k^2}{2}\frac{2}{kR_+}H_1^{(1)}(kR_+)\right)\\
=&0,
\end{aligned}
$$

where we used $H_\nu^{(1)}(z)=J_\nu(z)+iY_\nu(z)$ (Abramowitz and Stegun, 1965, equation 9.1.3), $J_0'(z)=-J_1(z)$ and $Y_0'(z)=-Y_1(z)$ (Abramowitz and Stegun, 1965, equation 9.1.28), and $J_1'(z)=(1/2)(J_0(z)-J_2(z))$ and $Y_1'(z)=(1/2)(Y_0(z)-Y_2(z))$ (Spiegel, 1968, equation 24.18). Hence $H_0'^{(1)}(z)=-H_1^{(1)}(z)$ and $H_1'^{(1)}(z)=(1/2)(H_0^{(1)}(z)-H_2^{(1)}(z))$. For $R_+\to 0$, $Y_1(kR_+)\to-\infty$; therefore, G_P behaves like a δ function.

Hence we can write

$$G_P = -\frac{i}{4}H_0^{(1)}(kR_+)$$
$$\frac{\partial G_P}{\partial x'} = \frac{k(x-x')}{R_+}H_1^{(1)}(kR_+)$$
$$\frac{\partial G_P}{\partial z'} = \frac{k(z-z')}{R_+}H_1^{(1)}(kR_+)$$

and equations 49–54 become

$$0 = A(\mathbf{r})(C_3e^{i\mu A} + C_4e^{-i\mu A})(C_1e^{i\lambda z'} + C_2e^{-i\lambda z'}) - \frac{i}{4}H_0^{(1)}(kR_+) \quad (49')$$
where $R_+ = \sqrt{(x-A)^2 + (z-z')^2}$,
$$0 = A(\mathbf{r})(C_3e^{i\mu A}i\mu + C_4e^{-i\mu A}(-i\mu))(C_1e^{i\lambda z'} + C_2e^{-i\lambda z'}) + \frac{k(x-A)}{R_+}H_1^{(1)}(kR_+) \quad (50')$$
where $R_+ = \sqrt{(x-A)^2 + (z-z')^2}$,
$$0 = A(\mathbf{r})(C_3e^{i\mu L_1} + C_4e^{-i\mu L_1})(C_1e^{i\lambda z'} + C_2e^{-i\lambda z'}) - \frac{i}{4}H_0^{(1)}(kR_+) \quad (51')$$
where $R_+ = \sqrt{(x-L_1)^2 + (z-z')^2}$,
$$0 = A(\mathbf{r})(C_3e^{i\mu L_1}i\mu + C_4e^{-i\mu L_1}(-i\mu))(C_1e^{i\lambda z'} + C_2e^{-i\lambda z'}) + \frac{k(x-L_1)}{R_+}H_1^{(1)}(kR_+) \quad (52')$$
where $R_+ = \sqrt{(x-L_1)^2 + (z-z')^2}$,
$$0 = A(\mathbf{r})(C_3e^{i\mu x'} + C_4e^{-i\mu x'})(C_1e^{i\lambda L_2} + C_2e^{-i\lambda L_2}) - \frac{i}{4}H_0^{(1)}(kR_+) \quad (53')$$
where $R_+ = \sqrt{(x-x')^2 + (z-L_2)^2}$, and
$$0 = A(\mathbf{r})(C_3e^{i\mu x'} + C_4e^{-i\mu x'})(C_1e^{i\lambda L_2}i\lambda + C_2e^{-i\lambda L_2}(-i\lambda)) + \frac{k(z-L_2)}{R_+}H_1^{(1)}(kR_+), \quad (54')$$
where $R_+ = \sqrt{(x-x')^2 + (z-L_2)^2}$.

7.2 Code

Coding of equations 49′–54′ is a work in progress by Wilberth Herrera and the first author.

7.3 Example: Flat-layer model

This section to be written when the code is ready for use.

8 Conclusions

We have implemented Green's theorem-derived source and receiver deghosting for the first time on deepwater Gulf of Mexico synthetic and field data. Testing to date has shown that the algorithm works with positive and encouraging results. Green's theorem-derived deghosting has several

qualities that separate it from previous deghosting methods. For example, Green's theorem preprocessing for source and receiver deghosting, wavefield separation, etc., and ISS processing for multiples, imaging, etc., comprise a consistent set of methods in which the preprocessing works in cooperation with the methods it is meant to serve.

9 Acknowledgements

We are grateful to the M-OSRP sponsors for their support of this research. The first author is also grateful to ExxonMobil and PGS for internships and to Nizar Chemingui for mentoring.

Appendices

A Input data

A.1 Elastic model 1

This is the model in (Li, 2011, Fig. 3.13) modified here by Jinlong Yang so that the model can be used with OASES code.

Parameter	Value
Number of shots	1
Number of channels per shot	801
Number of samples per trace	1024
Time sampling	5ms
Record length	5.12s
Shot interval	n.a.
Group interval	10m
Shortest offset	0m
Gun depth	30m
Streamer depth	140m and 150m

1 towed over/under streamer
$dP/dz \simeq (P(150m) - P(140m))/10m$

A.2 Elastic model 2

This is the model in (Li, 2011, Fig. 3.16) modified here by Jinlong Yang so that the model can be used with OASES code.

Parameter	Value
Number of shots	1
Number of channels per shot	801
Number of samples per trace	1024
Time sampling	5ms
Record length	5.12s
Shot interval	n.a.
Group interval	10m
Shortest offset	0m
Gun depth	30m
Streamer depth	140m and 150m

1 towed over/under streamer
$dP/dz \simeq (P(150m) - P(140m))/10m$

A.3 Field data: Deep water Gulf of Mexico[5]

Parameter	Value
Number of shots	374
Number of channels per shot	960
Number of samples per trace	3585
Time sampling	4ms
Record length	14.34s
Shot interval	32m
Group interval	12.5m
Shortest offset	112m
Gun depth	9m
Streamer depth	23–25m

1 dual-sensor towed streamer
$dP/dz = i\omega\rho V_z$, where ρ is the density of the reference medium (seawater)

[5]Courtesy of PGS.

A.4 Field data: North Sea[6]

Parameter	Value
Number of shots	694
Number of channels per shot	shallow cable 478 middle cable 542 deep cable 606
Number of samples per trace	2301
Time sampling	4ms
Record length	9.204s
Shot interval	≃18.76m
Group interval	≃12.55m
Shortest offset	59m
Gun depth	7m
Streamer depth	shallow cable 9m middle cable 18m deep cable 25m

1 towed over/under/under streamer
$dP/dz \simeq (P(25m) - P(18m))/7m$ etc.

A.5 Synthetic data[7]

Parameter	Value
Number of shots	1
Number of channels per shot	1201
Number of samples per trace	11340
Time sampling	0.46ms
Record length	5.2164s
Shot interval	n.a.
Group interval	5m
Shortest offset	0m
Gun depth	2m
Streamer depth	6m

1 dual-sensor towed streamer
$dP/dz = i\omega\rho V_z$, where ρ is the density of the reference medium (seawater)

[6]Courtesy of Statoil ASA, Petoro, ExxonMobil, Eni, Total, and Schlumberger/WesternGeco.
[7]Courtesy of ExxonMobil.

A.6 Synthetic data: Flat-layer model IV and Cagniard de Hoop code[8]

Parameter	Value
Number of shots	1
Number of channels per shot	5001
Number of samples per trace	4601
Time sampling	1ms
Record length	4.6s
Shot interval	n.a.
Group interval	1m
Shortest offset	0m
Gun depth	2m
Streamer depth	shallow cable 6m deep cable 12m

Free surface, water bottom at 300m, 1D constant-density acoustic earth ($\rho = 1.667 g/cm^3$, c = 2250m/s)
2D source, Ricker wavelet with peak amplitude at 25Hz
1 over/under towed streamer
$dP/dz \simeq (P(12m) - P(6m))/6m$

A.7 Synthetic data: Flat-layer model I and reflectivity code[9]

Parameter	Value
Number of shots	1
Number of channels per shot	801
Number of samples per trace	1500
Time sampling	4ms
Record length	6s
Shot interval	n.a.
Group interval	6.25m
Shortest offset	0m
Gun depth	30m
Streamer depth	shallow cable 140m deep cable 145m

Free surface, water bottom at 300m, 1D constant-density acoustic earth ($\rho = 1.667 g/cm^3$, c = 2250m/s)
3D source with source wavelet trapezoid 1, 20, 25, 60Hz
1 over/under towed streamer
$dP/dz \simeq (P(145m) - P(140m))/5m$

[8] Written by Jingfeng Zhang.
[9] Courtesy of BP.

A.8 Synthetic data: Flat-layer model II and reflectivity code[8]

Parameter	Value
Number of shots	1
Number of channels per shot	1601
Number of samples per trace	1500
Time sampling	4ms
Record length	6s
Shot interval	n.a.
Group interval	6m
Shortest offset	0m
Gun depth	shallow 50m
	deep 52m
Streamer depth	shallow cable 150m
	deep cable 151m

Free surface, water bottom at 300m, 1D constant-density acoustic earth ($\rho = 1.667 g/cm^3$, c = 2250m/s)
3D source with source wavelet trapezoid 1, 20, 25, 60Hz
1 over/under towed streamer
$dP/dz \simeq P(151m) - P(150m)$

A.9 Synthetic data: Flat-layer model III and reflectivity code[8]

Parameter	Value
Number of shots	301
Number of channels per shot	301
Number of samples per trace	1500
Time sampling	4ms
Record length	6s
Shot interval	18m
Group interval	6m
Shortest offset	0m
Gun depth	30m
Streamer depth	150m

Free surface, water bottom at 300m, 1D constant-density acoustic earth ($\rho = 1.667 g/cm^3$, c = 2250m/s)
3D source with source wavelet trapezoid 1, 20, 25, 60Hz
1 over/under towed streamer

A.10 Synthetic data: SEAM deepwater Gulf of Mexico model

Parameter	Value
Number of shots	133
Number of channels per shot	661
Number of samples per trace	2001
Time sampling	8ms
Record length	16s
Shot interval	150m
Group interval	30m
Shortest offset	0m
Gun depth	15m
Streamer depth	shallow cable 15m
	deep cable 17m

Free surface, variable water depth, 3D variable density acoustic earth
3D source, frequency of source: 1-30 Hz
661 over/under towed streamers each with 661 receivers
Distance between towed streamers: 30m
$dP/dz \simeq (P(17m) - P(15m))/2m$

B Receiver deghosting: Supplemental tutorial

Following chapter 2 of Zhang (2007), to separate upward-moving and downward-moving waves, we define the following (see Figure 2):
(1) a reference medium consisting of a whole space of water,
(2) a perturbation $\alpha_{\text{air}}(\mathbf{r})$ that is the difference between the reference medium (water) and the upper part (air) of the actual medium,
(3) a perturbation $\alpha_{\text{earth}}(\mathbf{r})$ that is the difference between the reference medium (water) and the lower part (earth) of the actual medium,
(4) an integration volume V consisting of a hemisphere bounded from below by the measurement surface,
(5) a free surface (air-water interface) above the measurement surface (*i.e.*, inside V),
(6) a source at $\mathbf{r}_s$ on or above the measurement surface (again inside V),
(7) a causal Green's function $G_0^+(\mathbf{r}, \mathbf{r}'_g, \omega)$ in the reference medium,
(8) $k_0 = \omega/c_0$,
(9) the prediction/observation point $\mathbf{r}'_g \in V$ lying on or below the free surface, and
(10) S as the hemisphere's surface.

Substituting the above and the partial differential equations for the pressure wavefield P and causal Green's function G_0^+ into Green's theorem gives

$$\oint_S \mathbf{n}\, dS \cdot [\widetilde{P}(\mathbf{r}, \mathbf{r}_s, \omega)\nabla G_0^+(\mathbf{r}, \mathbf{r}'_g, \omega) - G_0^+(\mathbf{r}, \mathbf{r}'_g, \omega)\nabla \widetilde{P}(\mathbf{r}, \mathbf{r}_s, \omega)]$$

$$= \int_V d\mathbf{r}[\widetilde{P}(\mathbf{r},\mathbf{r}_s,\omega)\underbrace{\nabla'^2 G_0^+(\mathbf{r},\mathbf{r}'_g,\omega)}_{-k_0^2 G_0^+ + \delta(\mathbf{r}-\mathbf{r}'_g)} - G_0^+(\mathbf{r},\mathbf{r}'_g,\omega)\underbrace{\nabla'^2\widetilde{P}(\mathbf{r},\mathbf{r}_s,\omega)}_{-k_0^2 P + \widetilde{A}(\omega)\delta(\mathbf{r}-\mathbf{r}_s)+k_0^2(\alpha_{air}+\alpha_{earth})P}] \quad \text{(B.1)}$$

$$= \int_V d\mathbf{r}[\underbrace{\widetilde{P}(\mathbf{r},\mathbf{r}_s,\omega)\delta(\mathbf{r}-\mathbf{r}'_g)}_{\widetilde{P}(\mathbf{r}'_g,\mathbf{r}_s,\omega)}\underbrace{-\widetilde{P}(\mathbf{r},\mathbf{r}_s,\omega)k_0^2 G_0^+(\mathbf{r},\mathbf{r}'_g,\omega) + G_0^+(\mathbf{r},\mathbf{r}'_g,\omega)k_0^2\widetilde{P}(\mathbf{r},\mathbf{r}_s,\omega)}_{\text{cancel}}$$
$$-k_0^2(\alpha_{air}(\mathbf{r}) + \underbrace{\alpha_{earth}(\mathbf{r})}_{0})\widetilde{P}(\mathbf{r},\mathbf{r}_s,\omega)G_0^+(\mathbf{r},\mathbf{r}'_g,\omega)$$
$$-\underbrace{\widetilde{A}(\omega)\delta(\mathbf{r}-\mathbf{r}_s)G_0^+(\mathbf{r},\mathbf{r}'_g,\omega)}_{\widetilde{A}(\omega)G_0^+(\mathbf{r}_s,\mathbf{r}'_g,\omega)}]$$

$$= \widetilde{P}(\mathbf{r}'_g,\mathbf{r}_s,\omega) - \int_V d\mathbf{r}\, k_0^2\alpha_{air}(\mathbf{r})\widetilde{P}(\mathbf{r},\mathbf{r}_s,\omega)G_0^+(\mathbf{r},\mathbf{r}'_g,\omega) - \widetilde{A}(\omega)\underbrace{G_0^+(\mathbf{r}_s,\mathbf{r}'_g,\omega)}_{G_0^+(\mathbf{r}'_g,\mathbf{r}_s,\omega)}$$

$$= \widetilde{P}(\mathbf{r}'_g,\mathbf{r}_s,\omega) - \int_V d\mathbf{r}\, G_0^+(\mathbf{r},\mathbf{r}'_g,\omega)k_0^2\alpha_{air}(\mathbf{r})\widetilde{P}(\mathbf{r},\mathbf{r}_s,\omega) - \widetilde{A}(\omega)G_0^+(\mathbf{r}'_g,\mathbf{r}_s,\omega). \quad \text{(B.2)}$$

The physical meaning of equation B.2 is that the total wavefield at $\mathbf{r}'_g$ can be separated into three parts:
(1) the direct wave that travels from the source at $\mathbf{r}_s$ to the prediction/observation point $\mathbf{r}'_g$ (third term on the right-hand side),
(2) the pressure field whose last motion is downward from the free surface (second term on the right-hand side), and
(3) the pressure field whose last motion is upward from the earth (the entire right-hand side).
Hence, equation B.2 is the receiver-deghosting algorithm.

Letting the radius of the hemisphere go to ∞, the Sommerfeld radiation condition gives

$$\int_{m.s.} \mathbf{n}\, dS \cdot [\widetilde{P}(\mathbf{r},\mathbf{r}_s,\omega)\nabla G_0^+(\mathbf{r},\mathbf{r}'_g,\omega) - G_0^+(\mathbf{r},\mathbf{r}'_g,\omega)\nabla\widetilde{P}(\mathbf{r},\mathbf{r}_s,\omega)]$$
$$= \widetilde{P}'_R(\mathbf{r}'_g,\mathbf{r}_s,\omega), \quad \text{(B.3)}$$

where $\widetilde{P}(\mathbf{r},\mathbf{r}_s,\omega)$ and $\nabla\widetilde{P}(\mathbf{r},\mathbf{r}_s,\omega)$ are respectively the hydrophone measurements and their spatial derivatives (in the frequency domain).

B.1 Green's theorem vs. a single receiver

To be written.

B.2 Additional considerations

What if we have an extended (vs. a point) source? We modify equation B.1, in which we assume (as for a point source) the distributed source $\tilde{\rho}(\mathbf{r},\mathbf{r}_s,\omega)$ is in V (above the measurement surface and below the free surface).

$$
\begin{aligned}
&\oint_S \mathbf{n}\, dS \cdot [\widetilde{P}(\mathbf{r},\mathbf{r}_s,\omega)\nabla G_0^+(\mathbf{r},\mathbf{r}'_g,\omega) - G_0^+(\mathbf{r},\mathbf{r}'_g,\omega)\nabla\widetilde{P}(\mathbf{r},\mathbf{r}_s,\omega)] \\
= &\int_V d\mathbf{r}[\widetilde{P}(\mathbf{r},\mathbf{r}_s,\omega)\underbrace{\nabla'^2 G_0^+(\mathbf{r},\mathbf{r}'_g,\omega)}_{-k_0^2 G_0^+ + \delta(\mathbf{r}-\mathbf{r}'_g)} - G_0^+(\mathbf{r},\mathbf{r}'_g,\omega)\underbrace{\nabla'^2\widetilde{P}(\mathbf{r},\mathbf{r}_s,\omega)}_{-k_0^2 P + \tilde{\rho}(\mathbf{r},\mathbf{r}_s,\omega) + k_0^2(\alpha_{air}+\alpha_{earth})P}] \\
= &\int_V d\mathbf{r}[\underbrace{\widetilde{P}(\mathbf{r},\mathbf{r}_s,\omega)\delta(\mathbf{r}-\mathbf{r}'_g)}_{\widetilde{P}(\mathbf{r}'_g,\mathbf{r}_s,\omega)}\underbrace{-\widetilde{P}(\mathbf{r},\mathbf{r}_s,\omega)k_0^2 G_0^+(\mathbf{r},\mathbf{r}'_g,\omega) + G_0^+(\mathbf{r},\mathbf{r}'_g,\omega)k_0^2\widetilde{P}(\mathbf{r},\mathbf{r}_s,\omega)}_{\text{cancel}} \\
&-k_0^2(\alpha_{air}(\mathbf{r}) + \underbrace{\alpha_{earth}(\mathbf{r})}_{0})\widetilde{P}(\mathbf{r},\mathbf{r}_s,\omega)G_0^+(\mathbf{r},\mathbf{r}'_g,\omega) \qquad \text{(B.4)} \\
&-\tilde{\rho}(\mathbf{r},\mathbf{r}_s,\omega)G_0^+(\mathbf{r},\mathbf{r}'_g,\omega)] \\
= &\widetilde{P}(\mathbf{r}'_g,\mathbf{r}_s,\omega) - \int_V d\mathbf{r}\, k_0^2\alpha_{air}(\mathbf{r})\widetilde{P}(\mathbf{r},\mathbf{r}_s,\omega)G_0^+(\mathbf{r},\mathbf{r}'_g,\omega) - \int_V d\mathbf{r}\tilde{\rho}(\mathbf{r},\mathbf{r}_s,\omega)G_0^+(\mathbf{r}_s,\mathbf{r}'_g,\omega). \qquad \text{(B.5)}
\end{aligned}
$$

The interpretation of equation B.5 is the same as that for equation B.2.

We note the following about equations B.3 and B.5.
(i) $\widetilde{P}(\mathbf{r},\mathbf{r}_s,\omega)$ and $\nabla\widetilde{P}(\mathbf{r},\mathbf{r}_s,\omega)$ in the integrand are data. The derivation makes no assumptions about earth properties (elastic or inelastic, absorptive, dispersive, etc.). $G_0^+(\mathbf{r},\mathbf{r}'_g,\omega)$ and $\nabla G_0^+(\mathbf{r},\mathbf{r}'_g,\omega)$ are analytic because we choose a homogeneous reference medium.
(ii) In equation B.4, $\alpha_{earth}(\mathbf{r})$, the perturbation containing earth properties, does not contribute because the integral is over V (by construction the earth is below V).
(iii) We have shown that, for a source in V, the integral is valid for both a point source and an extended source.
(iv) Testing on deepwater Gulf of Mexico data (SEAM and field) demonstrates that the integral works for acoustic and actual earth, and for point and extended sources.

B.3 January 6, 2012 letter from SEG

Society of Exploration Geophysicists
The international society of applied geophysics

President
BOB HARDAGE
c/o Bureau of Economic Geology
University Station, Box X
Austin, TX 78713
United States
bob.hardage@beg.utexas.edu

6 January 2012

James Davis Mayhan Jr.
15622 Four Leaf Dr.
Houston, TX 77084-3665

Dear James Davis Mayhan Jr.:

Congratulations on your excellent technical presentation titled, *Green's theorem derived methods for preprocessing seismic data when the pressure P and its normal derivative are measured,* presented at the 2011 SEG Annual Meeting in San Antonio, Texas. Your research and preparation were also noticed by your fellow SEG members, who judged your paper, ranking it in the top 31 papers presented at the San Antonio meeting.

It is technical presentations such as yours the SEG Executive Committee would like to offer to its international Sections and Associated Societies. Throughout the coming year, you might find you have the opportunity to visit an area where one of these Sections or Associated Societies is located. If so, the SEG Executive Committee strongly encourages you to contact the Section or Associated Society in the local area you are visiting and extend to them an offer to present your paper. Enclosed is a list of Sections and Associated Societies affiliated with the SEG.

As you might surmise, there is no financial assistance being offered to the speakers from either the SEG or the affiliated Section/Associated Society for these technical presentations.

For your information, we have also enclosed a copy of the letter that was sent to SEG Sections and Associated Societies.

Once again, thank you for your excellent contribution to the 2011 Technical Program and for considering participating in the exchange of geophysical technology, in the manner described above. I appreciate the time and consideration you are giving this initiative, and if you have any questions or suggestions, please do not hesitate to contact me.

Sincerely,

Bob Hardage
SEG President 2011-2012

SEG BUSINESS OFFICE / P.O. BOX 702740 / TULSA, OK USA 74170-2740 / PHONE: +1-918-497-5500
STREET ADDRESS: 8801 S. YALE / TULSA, OK USA 74137-3575 / FAX: +1-918-497-5557

C Computing travel times in Figure 13

Computing the event times for the data in the left panel of Figure 13 (source at 50m, cable at 151m, water bottom at 300m) gives the following:

Event	Distance (m)	Time (s)	Event
G_0^d	151-50	.067	1 over
G_0^{FS}	50+151	.134	1 under
WB primary	(300-50)+(300-151)	.266	2 over
Source ghost	50+300+(300-151)	.333	2 under
Receiver ghost	(300-50)+300+151	.467	3 over
Source/receiver ghost	50+300+300+151	.534	3 under
1st FSM	(300-50)+300*2+(300-151)	.666	4 over
Source ghost	50+300*3+(300-151)	.733	4 under
Receiver ghost	(300-50)+300*3+151	.867	5 over
Source/receiver ghost	50+300*4+151	.934	5 under

Computing the event times for the data in the middle panel of Figure 13 (source at 50m, cable at 20m, water bottom at 300m) gives the following:

Event	Distance	Time	Event
G_0^d	50-20	.020	1 over
G_0^{FS}	50+20	.047	1 under
WB primary	(300-50)+(300-20)	.353	2 over
Receiver ghost	(300-50)+300+20	.380	2 under
Source ghost	50+300+(300-20)	.420	3 over
Source/receiver ghost	50+300+300+20	.447	3 under
1st FSM	(300-50)+300*2+(300-20)	.753	4 over
Receiver ghost	(300-50)+300*3+20	.780	4 under
Source ghost	50+300*3+(300-20)	.820	5 over
Source/receiver ghost	50+300*4+20	.847	5 under

Computing the event times for the data in the right panel of Figure 13 (source at 20m, cable at 10m, water bottom at 300m) gives the following:

Event	Distance	Time	Event
G_0^d	20-10	.007	1 over
G_0^{FS}	20+10	.020	1 under
WB primary	(300-20)+(300-10)	.380	2 over
Receiver ghost	(300-20)+300+10	.393	2 under
Source ghost	20+300+(300-10)	.407	3 over
Source/receiver ghost	20+300+300+10	.420	3 under
1st FSM	(300-20)+300*2+(300-10)	.780	4 over
Receiver ghost	(300-20)+300*3+10	.793	4 under
Source ghost	20+300*3+(300-10)	.807	5 over
Source/receiver ghost	20+300*4+10	.820	5 under

D Using reciprocity in source deghosting

D.1 Problem statement

Can we show that, if we have over/under towed streamers, reciprocity requires shots at two different depths (Figure 45)?

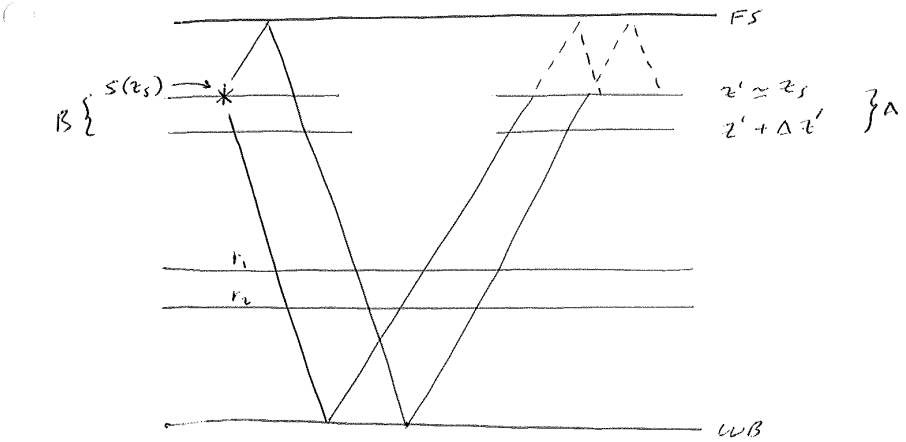

Figure 45: *The problem statement per Dan Whitmore (July 8, 2011).*

D.2 Background

For simplicity assume all upward reflections occur at the water bottom. Then we have the following ghosts in Figure 45:

Ghost	Path
Receiver	$z_s \to WB \to FS \to z'$ $z_s \to WB \to FS \to z' + \Delta z'$ $z_s + \Delta z \to WB \to FS \to z'$ $z_s + \Delta z \to WB \to FS \to z' + \Delta z'$
Source-receiver	$z_s \to FS \to WB \to FS \to z'$ $z_s \to FS \to WB \to FS \to z' + \Delta z'$ $z_s + \Delta z \to FS \to WB \to FS \to z'$ $z_s + \Delta z \to FS \to WB \to FS \to z' + \Delta z'$
Source	$z_s \to FS \to WB \to z'$ $z_s \to FS \to WB \to z' + \Delta z'$ $z_s + \Delta z \to FS \to WB \to z'$ $z_s + \Delta z \to FS \to WB \to z' + \Delta z'$

Receiver deghosting removes waves down-going at the receivers and so removes receiver ghosts and

source-receiver ghosts. Now use the following trick. Sorting from CSGs to CRGs and swapping source and receiver coordinates puts the "sources" above the "receivers", thereby making the source ghosts look like receiver ghosts. Running the Green's theorem code a second time removes these "receiver" ghosts.

D.3 First pass

For simplicity, use SEAM depths on the first pass, i.e., sources at 15m and receivers at 15m and 17m.

Step 1 Use the over/under receivers to compute

$$\frac{dP}{dz}(16m) \simeq \frac{P(17m) - P(15m)}{17m - 15m}.$$

Step 2 Use P(17m) and dP/dz(16m) to compute receiver deghosted "pseudo cables" at 8m and 10m. The Green's theorem code checks that dP/dz has the same number of traces as P has, and then uses source and receiver coordinates in the P trace headers to compute the Green's functions in the integrand. We have only 17m (depth of the deeper towed streamer) to work with. Testing has shown we get best results when we "split the difference", i.e., when we receiver deghost at about halfway between the deeper towed streamer and the free surface (with the caveat that we're above the sources), and then we source deghost at or near the free surface.

Step 3 Use the receiver deghosted pseudo cables to compute receiver deghosted dP_R/dz:

$$\frac{dP_R}{dz}(9m) \simeq \frac{P_R(10m) - P_R(8m)}{10m - 8m}.$$

Step 4 Sort the receiver deghosted $P_R(10m)$ and $dP_R/dz(9m)$ from CSGs to CRGs and swap source and receiver coordinates; this gives "sources" at 10m, "receivers" at 15m, and dP_R/dz at 15m.

Step 5 Use $P_R(15m)$, $dP_R/dz(15m)$, and reciprocity to source deghost at 2m.

Step 6 Sort the source and receiver deghosted $P_{SR}(2m)$ from CRGs to CSGs and again swap source and receiver coordinates; this gives sources at 2m and receivers at 10m.

Whitmore's argument is that point sources and point receivers satisfy reciprocity, but wavefield derivatives don't, i.e.,

$$\frac{dP_R}{dz}(9m) \simeq \frac{P_R(10m) - P_R(8m)}{10m - 8m}$$

is not the same as

$$\frac{dS}{dz}(14m) \simeq \frac{S(15m) - S(13m)}{15m - 13m},$$

assuming that SEAM had sources at 13m as well as at 15m.

D.4 Second pass

Now try a more general notation. Suppose we have sources at depths z_s and $z_s + \Delta z$ and receivers at depths r_1 and r_2 (where $r_1 < r_2$) (Figure 45).

Step 1 Use the over/under towed streamers to compute

$$\frac{dP}{dz}\left(\frac{r_1 + r_2}{2}\right) \simeq \frac{P(r_2) - P(r_1)}{r_2 - r_1}.$$

Step 2 Use $P(r_2)$ and $dP/dz((r_1 + r_2)/2)$ to compute receiver deghosted pseudo cables at depths z' and $z' + \Delta z'$. We have r_2 to work with (depth of the deeper towed streamer). Testing has shown that we get best results when we "split the difference", i.e., when we receiver deghost at about halfway between r_2 and the free surface (with the caveat that we're above the sources), then we source deghost at or near the free surface. Hence we choose $FS < z' < z' + \Delta z' < z_s$.

Step 3 Use the receiver deghosted pseudo cables to compute receiver deghosted dP_R/dz:

$$\frac{dP_R}{dz}\left(z' + \frac{1}{2}\,\Delta z'\right) \simeq \frac{P_R(z' + \Delta z') - P_R(z')}{\Delta z'}.$$

Step 4 Sort the receiver deghosted $P_R(z' + \Delta z')$ and $dP_R/dz(z' + 1/2\,\Delta z')$ from CSGs to CRGs and swap source and receiver coordinates; this gives "sources" at $z' + \Delta z'$, "receivers" at $z_s + \Delta z$, and dP_R/dz at $z_s + \Delta z$.

Step 5 Use $P_R(z_s + \Delta z)$, $dP_R/dz(z_s + \Delta z)$, and reciprocity to source deghost at z'' where z'' is at or near the free surface, i.e., $FS \leq z'' < z'$.

Step 6 Sort the source and receiver deghosted $P_{SR}(z'')$ from CRGs to CSGs and again swap source and receiver coordinates; this gives sources at z'' and receivers at $z_s + \Delta z$.

Whitmore's point is that taking derivatives at A in the receiver coordinates is not the same as taking derivatives at B in the source coordinates (Figure 45).

D.5 Discussion

The integral used in Green's theorem deghosting (equation 2.2) assumes an infinitely long cable with an infinite number of receivers separated by infinitesimal distances. The code approximates this integral with a sum over a finite-length cable with a finite number of receivers separated by finite distances. Consider Figure 45. The integral in equation 2.2 cares about vertical (not horizontal) derivatives so the question is whether the difference in depth between A and B is significant. The difference in taking derivatives at A vs. taking them at B is therefore the vertical path difference $z_s + 1/2\,\Delta z - (z' + 1/2\,\Delta z') = z_s - z' + 1/2\,(\Delta z - \Delta z')$, which is $\mathcal{O}(2\text{m})$ (using field data depths and assuming $\Delta z = 5\text{m}$). This difference is small in deep water but may become non-negligible in shallow water.

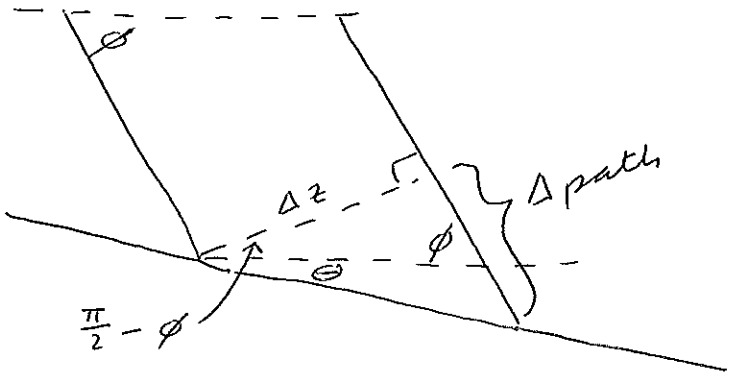

Figure 46: *Reflection of source ghosts at dipping water bottom.*

Can dipping reflectors affect this vertical path difference? The shortest path followed by source ghosts is the second Source Ghost in the above table, and the longest path is the third Source Ghost in the above table. These two paths impinging on a reflector with dip θ will see a relative change of $\tan(\pi/2 - \phi + \theta) = \Delta\text{path}/\Delta z$ or $\Delta\text{path} = \Delta z \tan(\pi/2 - \phi + \theta)$ where ϕ is the dip of the path leaving the source (Figure 46). (Check: For vertical reflection ($\phi = \pi/2$) from a flat water bottom ($\theta = 0$), we have $\Delta\text{path} = \Delta z \tan(\pi/2 - \pi/2 + 0) = 0$ as expected.) For $0 \lesssim \pi/2 - \phi + \theta \lesssim \pi/4$, this is $0m \lesssim \Delta\text{path} \lesssim 16m$ (using Kristin depths). For a water-bottom primary, $\tan(\pi/2 - \phi) = 1/2x_h/(WB - z_s)$ where x_h is the offset. This allows us to substitute $\pi/2 - \phi = \arctan(x_h/2(WB - z_s))$. Thus, the difference between the shortest and longest path lengths is the sum of the above factors: $\Delta\text{path} = z_s - z' + 1/2(\Delta z - \Delta z') + \Delta z \tan(\pi/2 - \phi + \theta)$ where $\pi/2 - \phi = \arctan(x_h/2(WB - z_s))$. Using field data we have $z_s = 9$m, $z' = 8$m, $\Delta z = 5$m (assumed), $\Delta z' = 2.5$m, WB $= \mathcal{O}(1$ mile) and WB-$z_s \simeq$ WB, and $9 \times 12.5m \leq x_h \leq (960-1) \times 12.5m$ or $0.1km \leq x_h \leq 12.0km$. Hence 88degrees $\gtrsim \phi \gtrsim$ 15degrees and (assuming $\theta = 0$) $2.1m \gtrsim \Delta\text{path} \gtrsim -16.5m$, which is small compared with the water depth (in deep water). More work is needed here to interpret the minus sign.

D.5.1 Numerical test

On July 8, 2011, Whitmore suggested the following experiment. Given the configurations in Figures 47 and 48, is there any difference in deghosting? Figure 49 suggests no, which is consistent with the above discussion.

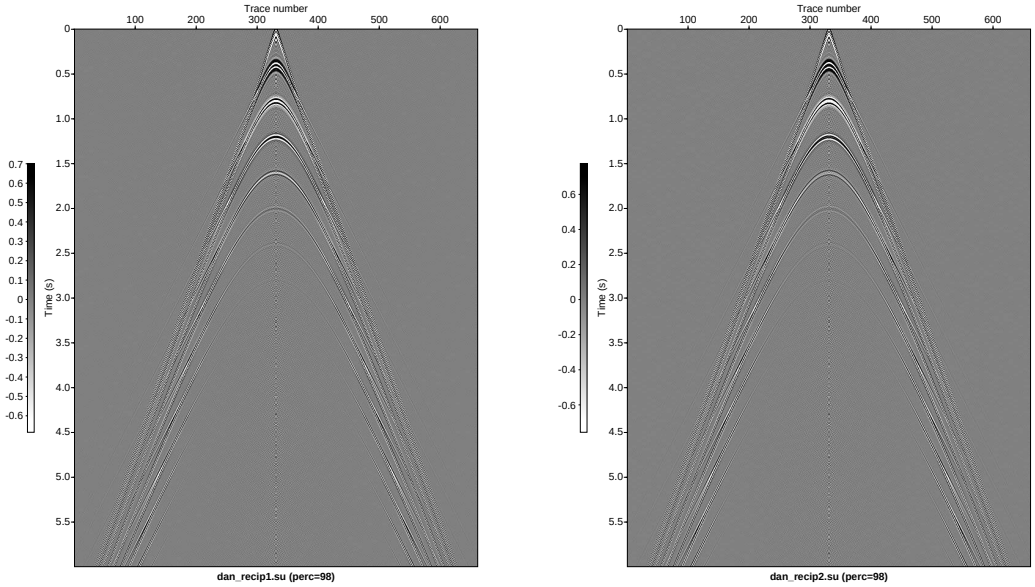

Figure 47: *Source at 10m, cable at 20m (left) and 25m (right).*

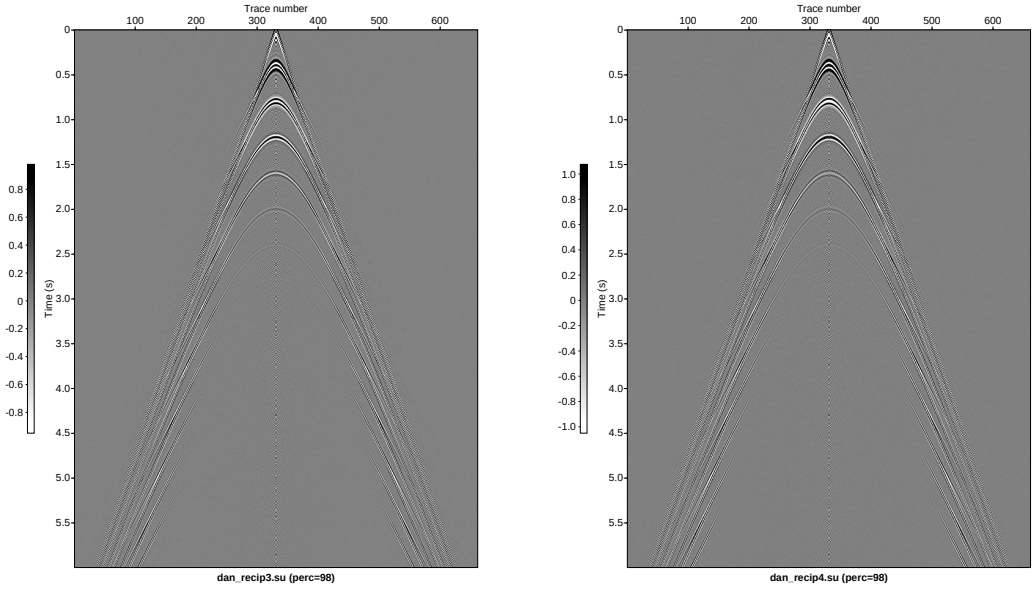

Figure 48: *Source at 15m, cable at 20m (left) and 25m (right).*

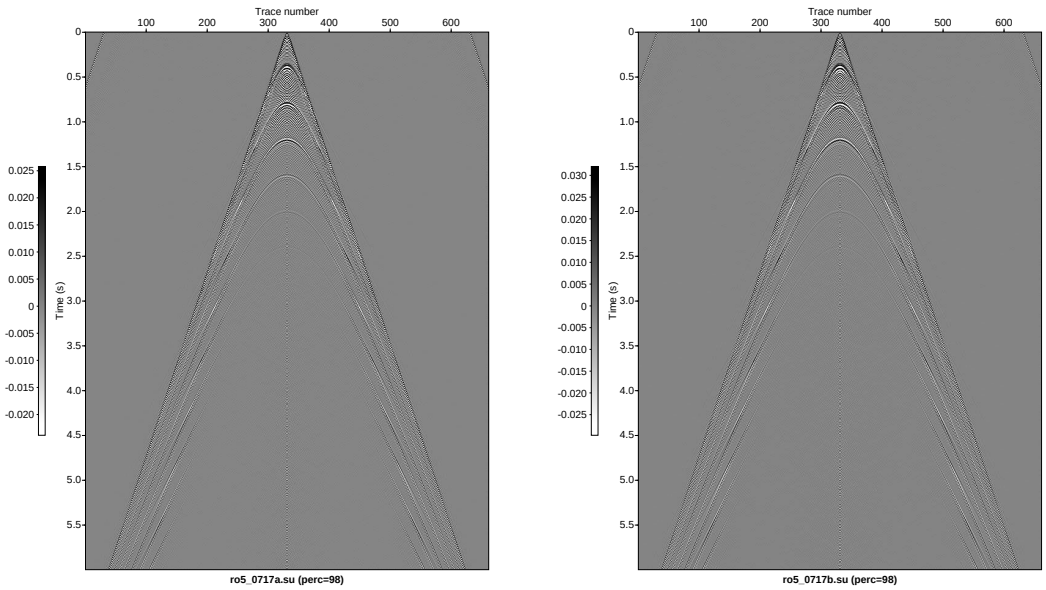

Figure 49: *Receiver deghosted input data using source at 10m (left) and 15m (right).*

E Source deghosting: Some mechanics

Here are the steps used by the first author to source and receiver deghost SEAM data. SEAM has sources at 15m and receivers at 15m and 17m.
(1) Use $P(15m)$ and $P(17m)$ to compute dP/dz. The Seismic Unix command is sudiff $P(17m)$ file name $P(15m)$ file name | sugain > dP/dz file name norm=2.
(2) Use $P(17m)$ and dP/dz to receiver deghost at 8m and 10m. Because these are large files, Seismic Unix script suwind_seam_v2.sh is used to break up each file into six smaller files. Six Green's theorem jobs are run in parallel, and the cat command is used to combine the six outputs into one output file for each depth.
(3) Interpolate four shots between each pair of input shots in receiver deghosted $P(8m)$ and $P(10m)$. This was done by Mikhail Orlovich (PGS) using inhouse software. He corrected for spherical divergence (multiplied by t^1), did interpolation in common-depth-point (CDP) domain, and then undid spherical divergence (multiplied by t^{-1}). This can also be done using the second author's Seismic Unix scripts interp.sh and interp_by_channel.sh.
(4) Use receiver deghosted (and interpolated) $P(8m)$ and $P(10m)$ to compute receiver deghosted (and interpolated) dP_R/dz. The Seismic Unix command is sudiff $P(10m)$ file name $P(8m)$ file name | sugain > dP/dz file name norm=2.
(5) Sort receiver deghosted (and interpolated) $P(10m)$ and dP_R/dz from CSGs to CRGs, swap source and receiver coordinates, and use them to source deghost at 2m. Sort and swap uses Seismic Unix script swap_seam_v3.sh, the resulting files are broken up into six smaller files, and six Green's theorem jobs are run in parallel. The six outputs are combined into one output file.
(6) Sort the source and receiver deghosted $P(2m)$ from CRGs to CSGs and unswap source and receiver coordinates.

F Second author's deghosting suggestion of 9.13.11

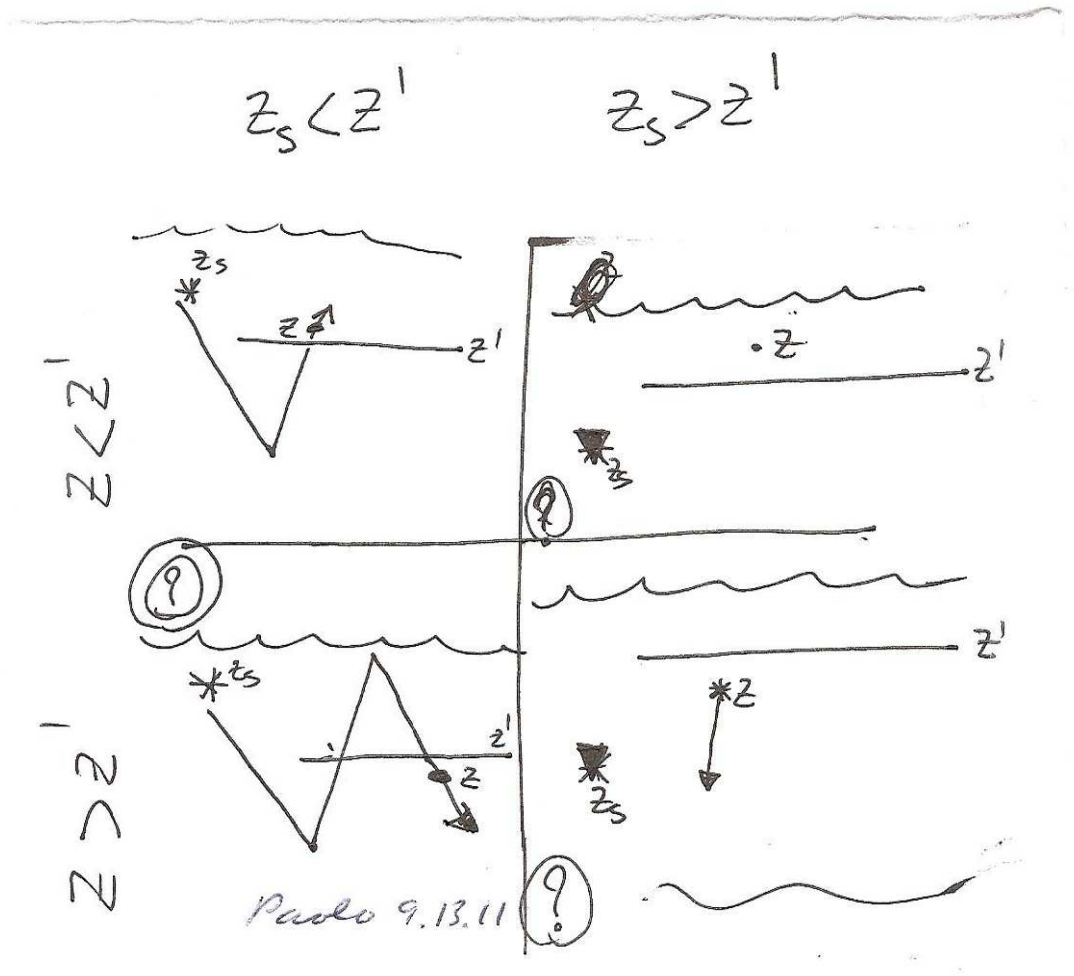

Figure 50: *Second author's deghosting suggestion of 9.13.11.*

F.1 Compute event times

Reflectivity code and flat-layer model I, source at 30m, cable at 140m, water bottom at 300m ($z_s < z'$):

Event	Distance	Time	Event
G_0^d	140-30	.073	1 over
G_0^{FS}	30+140	.113	1 under
WB primary	(300-30)+(300-140)	.287	2 over
Source ghost	30+300+(300-140)	.327	2 under
Receiver ghost	(300-30)+300+140	.473	3 over
Source/receiver ghost	30+300+300+140	.52	3 under
1st FSM	(300-30)+300*2+(300-140)	.687	4 over
Source ghost	30+300*3+(300-140)	.727	4 under
Receiver ghost	(300-30)+300*3+140	.873	5 over
Source/receiver ghost	30+300*4+140	.913	5 under

Receiver deghosted 20m above cable ($z_s < z', z < z'$):

Event	Distance	Time	Event
G_0^d	120-30	.06	1 over
G_0^{FS}	30+120	.1	1 under
WB primary	(300-30)+(300-120)	.3	2 over
Source ghost	30+300+(300-120)	.34	2 under
Receiver ghost	(300-30)+300+120	.46	3 over
Source/receiver ghost	30+300+300+120	.507	3 under
1st FSM	(300-30)+300*2+(300-120)	.7	4 over
Source ghost	30+300*3+(300-120)	.74	4 under
Receiver ghost	(300-30)+300*3+120	.86	5 over
Source/receiver ghost	30+300*4+120	.9	5 under

Receiver deghosted 20m below cable ($z_s < z', z > z'$):

Event	Distance	Time	Event
G_0^d	160-30	.086	1 over
G_0^{FS}	30+160	.126	1 under
WB primary	(300-30)+(300-160)	.274	2 over
Source ghost	30+300+(300-160)	.314	2 under
Receiver ghost	(300-30)+300+160	.486	3 over
Source/receiver ghost	30+300+300+160	.533	3 under
1st FSM	(300-30)+300*2+(300-160)	.674	4 over
Source ghost	30+300*3+(300-160)	.714	4 under
Receiver ghost	(300-30)+300*3+160	.886	5 over
Source/receiver ghost	30+300*4+160	.926	5 under

Reflectivity code and flat layer model, source at 140m, cable at 30m, water bottom at 300m ($z_s > z'$):

Event	Distance	Time	Event
G_0^d	140-30	.073	1 over
G_0^{FS}	30+140	.113	1 under
WB primary	(300-30)+(300-140)	.287	2 over
Receiver ghost	(300-140)+300+30	.327	2 under
Source ghost	140+300+(300-30)	.473	3 over
Source/receiver ghost	30+300+300+140	.513	3 under
1st FSM	(300-30)+300*2+(300-140)	.687	4 over
Receiver ghost	(300-140)+300*3+30	.727	4 under
Source ghost	140+300*3+(300-30)	.873	5 over
Source/receiver ghost	30+300*4+140	.913	5 under

Receiver deghosted 20m above cable ($z_s > z', z < z'$):

Event	Distance	Time	Event
G_0^d	140-10	.087	1 over
G_0^{FS}	10+140	.1	1 under
WB primary	(300-10)+(300-140)	.3	2 over
Receiver ghost	(300-140)+300+10	.313	2 under
Source ghost	140+300+(300-10)	.487	3 over
Source/receiver ghost	10+300+300+140	.5	3 under
1st FSM	(300-10)+300*2+(300-140)	.7	4 over
Receiver ghost	(300-140)+300*3+10	.713	4 under
Source ghost	140+300*3+(300-10)	.887	5 over
Source/receiver ghost	10+300*4+140	.9	5 under

Receiver deghosted 20m below cable ($z_s > z', z > z'$):

Event	Distance	Time	Event
G_0^d	140-50	.06	1 over
G_0^{FS}	50+140	.127	1 under
WB primary	(300-50)+(300-140)	.273	2 over
Receiver ghost	(300-140)+300+50	.34	2 under
Source ghost	140+300+(300-50)	.46	3 over
Source/receiver ghost	50+300+300+140	.527	3 under
1st FSM	(300-50)+300*2+(300-140)	.673	4 over
Receiver ghost	(300-140)+300*3+50	.74	4 under
Source ghost	140+300*3+(300-50)	.86	5 over
Source/receiver ghost	50+300*4+140	.927	5 under

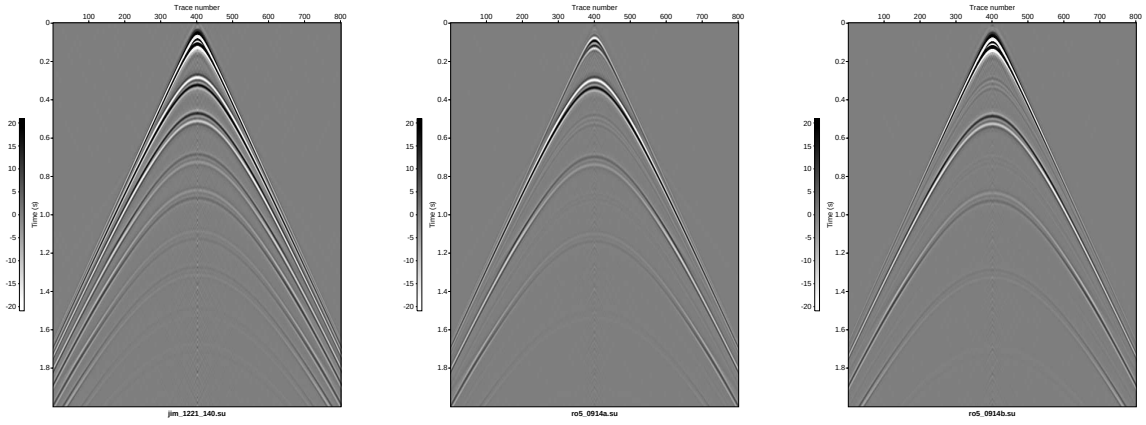

Figure 51: *Reflectivity data, source at 30m, cable at 140m, water bottom at 300m: input data at 140m (left), receiver deghosted input data 20m above cable (center), receiver deghosted input data 20m below cable (right).*

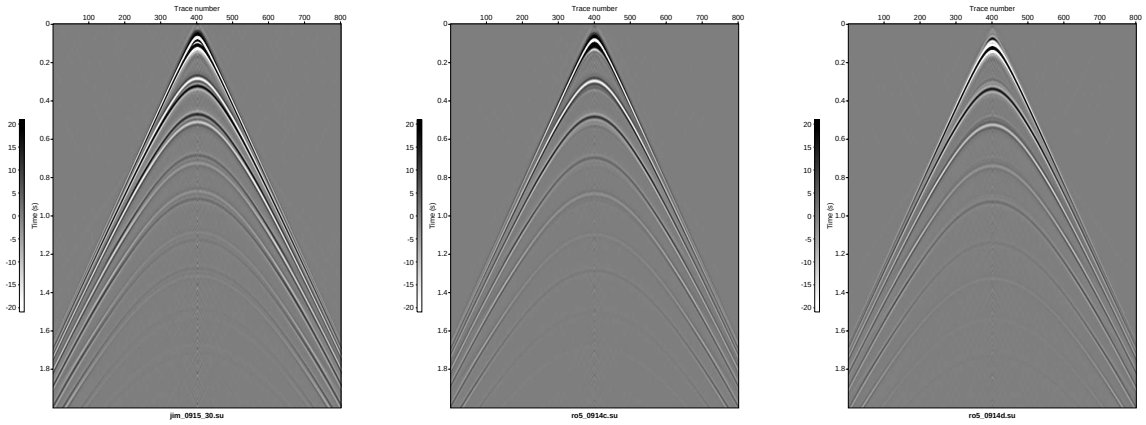

Figure 52: *Reflectivity data, source at 140m, cable at 30m, water bottom at 300m: input data at 30m (left), receiver deghosted input data 20m above cable (center), receiver deghosted input data 20m below cable (right).*

Using the times computed in the above tables, we see that:
(1) The events in the left panel of Figure 51 ($z_s < z'$) are (from the top) the direct wave G_0^d and its FS reflection G_0^{FS}, the WB primary and its source ghost, the WB primary's receiver ghost and source/receiver ghost, the first FSM and its source ghost, and the first FSM's receiver ghost and source/receiver ghost.
(2) In the center panel of Figure 51 ($z_s < z', z < z'$), all events are attenuated except the WB primary and its source ghost and the first FSM and its source ghost.
(3) In the right panel of Figure 51 ($z_s < z', z > z'$), the following events are attenuated: the WB primary and its source ghost and the first FSM and its source ghost. Thus, (3) is the "mirror image" of (2).
(4) The events in the left panel of Figure 52 ($z_s > z'$) are (from the top) the direct wave G_0^d and its FS reflection G_0^{FS}, the WB primary and its receiver ghost, the WB primary's source ghost and source/receiver ghost, the first FSM and its receiver ghost, and the first FSM's source ghost and source/receiver ghost.
(5) In the center panel of Figure 52 ($z_s > z', z < z'$), all events are attenuated except the direct wave G_0^d and its FS reflection G_0^{FS}.
(6) In the right panel of Figure 52 ($z_s > z', z > z'$), the following events are attenuated: the direct wave G_0^d, the WB primary and its source ghost, and the first FSM and its source ghost.

F.2 Compare with theory

Are the above results consistent with theory? Starting with Green's theorem, assuming a whole space reference medium (with three sources), and substituting the acoustic wave equations for the pressure wavefield P and associated causal Green's function G_0^+, we get

$$P(\mathbf{r}, \mathbf{r}_s, \omega) - A(\omega) G_0^+(\mathbf{r}, \mathbf{r}_s, \omega) - \int_V G_0^+(\mathbf{r}', \mathbf{r}, \omega) k_0^2 \alpha_{\text{air}} P(\mathbf{r}', \mathbf{r}_s, \omega) d\mathbf{r}'$$

$$= \oint_S [P(\mathbf{r}', \mathbf{r}_s, \omega)\nabla' G_0^+(\mathbf{r}', \mathbf{r}, \omega) - G_0^+(\mathbf{r}', \mathbf{r}, \omega)\nabla' P(\mathbf{r}', \mathbf{r}_s, \omega)] \cdot d\mathbf{S}' \tag{F.1}$$

(Zhang, 2007, equation 2.22), where $\mathbf{r}_s$ is the location of the air gun array, $\mathbf{r}'$ is a measurement point, and $\mathbf{r}$ is the observation/prediction point. The left-hand side consists of the total wavefield P less the downgoing waves (the direct wave AG_0^+ and the FS reflection $\int_V$), leaving us with the upgoing wavefield $P^{\text{deghosted}}$ at the prediction/observation point. Equation (F.1) is consistent with the extinction theorem (Born and Wolf, 1964): $\oint_S$ with the observation/prediction point inside (outside) V extinguishes the contribution of sources inside (outside) V. The wavefields due to the air guns and FS are down-going at the cable, whereas the wavefield due to the earth is up-going at the cable. We are inside the volume V bounded by the FS and MS, and $\oint_S$ will attenuate the wavefields due to the sources in V (air guns and FS). This is the configuration for the case $z_s < z', z < z'$, and our computed results (attenuated receiver ghosts and source/receiver ghosts) are consistent with theory.

Now consider the case $z_s < z', z > z'$. We are on the opposite side of the cable (relative to the above case) and expect the surface integral in equation (F.1) to extinguish the upgoing wavefield (from the earth) at the prediction/observation point. In fact, $\oint_S$ has attenuated the WB primary, first FSM, and their source ghosts.

Next, consider the case $z_s > z', z < z'$. The configuration is the same as the first case except the source has moved to the opposite side of the cable. We are inside the volume V, and the extinction theorem predicts that the surface integral will extinguish the field from sources inside V (the FS). Our computed results are only partially consistent with prediction because $\oint_S$ attenuated source ghosts and source/receiver ghosts but not receiver ghosts (which are also reflected at the FS). Note: This source deghosting configuration says I should sort from CSGs to CRGs but not swap source and receiver coordinates.

Finally, consider the case $z_s > z', z > z'$ (the reciprocal configuration of the case $z_s < z', z < z'$). We are outside the volume V, and the extinction theorem predicts that the surface integral will extinguish the field from sources outside V (the air guns and the earth), leaving only waves reflected from the FS. Our computed results (attenuated direct wave G_0^d, WB primary, WB primary receiver ghost, first FSM, and first FSM's receiver ghost) are only partially consistent with prediction because the last three are reflected from the FS.

G Theory of source-signature estimation

M-OSRP's theory of source-signature estimation comes from Weglein and Secrest (1990) who derive two equations containing the source signature: the Lippmann-Schwinger equation and a second equation derived from Green's theorem. Comparing the two equations gives an equation for the source signature, which is a function of measured 3D data and a reference-medium Green's function.

G.1 Lippmann-Schwinger approach

The constant-density acoustic wave equation for the pressure field P at $\mathbf{r}$ created by a source $A(t)$ at $\mathbf{r}_s$ is

$$\left(\nabla^2 - \frac{1}{c^2(\mathbf{r})}\frac{\partial^2}{\partial t^2}\right) P(\mathbf{r}, \mathbf{r}_s, t) = A(t)\delta(\mathbf{r} - \mathbf{r}_s). \tag{G.1}$$

Fourier transforming from the time domain to the frequency domain gives

$$\left(\nabla^2 + \frac{\omega^2}{c^2(\mathbf{r})}\right) \widetilde{P}(\mathbf{r}, \mathbf{r}_s, \omega) = \widetilde{A}(\omega)\delta(\mathbf{r} - \mathbf{r}_s). \tag{G.2}$$

Restating wave speed $c(\mathbf{r})$ as a function of reference-medium speed c_0 and a perturbation $\alpha(\mathbf{r})$ gives

$$\frac{1}{c^2(\mathbf{r})} = \frac{1}{c_0^2}(1 - \alpha(\mathbf{r})). \tag{G.3}$$

Substituting equation G.3 into equation G.2 gives

$$\left(\nabla^2 + \frac{\omega^2}{c_0^2}\right) \widetilde{P}(\mathbf{r}, \mathbf{r}_s, \omega) = \widetilde{A}(\omega)\delta(\mathbf{r} - \mathbf{r}_s) + \frac{\omega^2}{c_0^2}\alpha(\mathbf{r})\widetilde{P}(\mathbf{r}, \mathbf{r}_s, \omega). \tag{G.4}$$

Converting equation G.4 from a partial-differential equation into an integral equation (the Lippmann-Schwinger equation) gives

$$\widetilde{P}(\mathbf{r}, \mathbf{r}_s, \omega) = \widetilde{A}(\omega)\widetilde{G}_0(\mathbf{r}, \mathbf{r}_s, \omega) + \int_\infty d\mathbf{r}'\widetilde{G}_0(\mathbf{r}, \mathbf{r}', \omega)\frac{\omega^2}{c_0^2}\alpha(\mathbf{r}')\widetilde{P}(\mathbf{r}', \mathbf{r}_s, \omega). \tag{G.5}$$

Because the Lippmann-Schwinger equation covers all space, there is no boundary condition to impose a causal solution; therefore choose a causal Green's function $\widetilde{G}_0^+$ to get a causal solution $\widetilde{P}(\mathbf{r}, \mathbf{r}_s, \omega)$:

$$\widetilde{P}(\mathbf{r}, \mathbf{r}_s, \omega) = \widetilde{A}(\omega)\widetilde{G}_0^+(\mathbf{r}, \mathbf{r}_s, \omega) + \int_\infty d\mathbf{r}'\widetilde{G}_0^+(\mathbf{r}, \mathbf{r}', \omega)\frac{\omega^2}{c_0^2}\alpha(\mathbf{r}')\widetilde{P}(\mathbf{r}', \mathbf{r}_s, \omega). \tag{G.6}$$

G.2 Green's theorem approach

To isolate the source signature, Weglein and Secrest (1990) define the following:
(1) a reference medium consisting of a half space of air above a half space of water,
(2) a perturbation $\alpha(\mathbf{r})$ that is the difference between the earth and the lower part of the half space of water,
(3) an integration volume V consisting of a hemisphere bounded from above by the measurement surface (the plane $z = 0$),
(4) a free surface (air-water interface) above the measurement surface (i.e., outside V), and
(5) a source $\mathbf{r}_s$ on or above the measurement surface (again outside V).

Substituting $\widetilde{P}$ and $\widetilde{G}_0$ into Green's theorem gives

$$\begin{aligned}
&\int_V d\mathbf{r}'[\widetilde{P}(\mathbf{r}',\mathbf{r}_s,\omega)\nabla'^2\widetilde{G}_0(\mathbf{r}',\mathbf{r},\omega) - \widetilde{G}_0(\mathbf{r}',\mathbf{r},\omega)\nabla'^2\widetilde{P}(\mathbf{r}',\mathbf{r}_s,\omega)] \\
&= \oint_S dS'\,\hat{\mathbf{n}}\cdot[\widetilde{P}(\mathbf{r}',\mathbf{r}_s,\omega)\nabla'\widetilde{G}_0(\mathbf{r}',\mathbf{r},\omega) - \widetilde{G}_0(\mathbf{r}',\mathbf{r},\omega)\nabla'\widetilde{P}(\mathbf{r}',\mathbf{r}_s,\omega)], \qquad \text{(G.7)}
\end{aligned}$$

where V is the hemispheric volume defined above, and S is the hemisphere's surface. Substituting equation G.4 and its corresponding reference-medium Green's function differential equation into equation G.7 gives

$$\begin{aligned}
&\oint_S dS'\,\hat{\mathbf{n}}\cdot[\widetilde{P}(\mathbf{r}',\mathbf{r}_s,\omega)\nabla'\widetilde{G}_0(\mathbf{r}',\mathbf{r},\omega) - \widetilde{G}_0(\mathbf{r}',\mathbf{r},\omega)\nabla'\widetilde{P}(\mathbf{r}',\mathbf{r}_s,\omega)] \\
&= \int_V d\mathbf{r}'[\widetilde{P}(\mathbf{r}',\mathbf{r}_s,\omega) \quad \underbrace{\nabla'^2\widetilde{G}_0(\mathbf{r}',\mathbf{r},\omega)}_{(-\omega^2/c_0^2)\widetilde{G}_0(\mathbf{r}',\mathbf{r},\omega)+\delta(\mathbf{r}'-\mathbf{r})} \\
&\quad - \widetilde{G}_0(\mathbf{r}',\mathbf{r},\omega) \quad \underbrace{\nabla'^2\widetilde{P}(\mathbf{r}',\mathbf{r}_s,\omega)}_{(-\omega^2/c_0^2)\widetilde{P}(\mathbf{r}',\mathbf{r}_s,\omega)+(\omega^2/c_0^2)\alpha(\mathbf{r}')\widetilde{P}(\mathbf{r}',\mathbf{r}_s,\omega)+\widetilde{A}(\omega)\delta(\mathbf{r}'-\mathbf{r}_s)} \;] \qquad \text{(G.8)} \\
&= \int_V d\mathbf{r}'[\underbrace{-\frac{\omega^2}{c_0^2}\widetilde{G}_0(\mathbf{r}',\mathbf{r},\omega)\widetilde{P}(\mathbf{r}',\mathbf{r}_s,\omega)}_{cancels} + \delta(\mathbf{r}'-\mathbf{r})\widetilde{P}(\mathbf{r}',\mathbf{r}_s,\omega) \\
&\quad + \underbrace{\frac{\omega^2}{c_0^2}\widetilde{P}(\mathbf{r}',\mathbf{r}_s,\omega)\widetilde{G}_0(\mathbf{r}',\mathbf{r},\omega)}_{cancels} - \frac{\omega^2}{c_0^2}\alpha(\mathbf{r}')\widetilde{P}(\mathbf{r}',\mathbf{r}_s,\omega)\widetilde{G}_0(\mathbf{r}',\mathbf{r},\omega) \\
&\quad - \widetilde{A}(\omega)\delta(\mathbf{r}'-\mathbf{r}_s)\widetilde{G}_0(\mathbf{r}',\mathbf{r},\omega)] \\
&= \int_V d\mathbf{r}'[\widetilde{P}(\mathbf{r}',\mathbf{r}_s,\omega)\delta(\mathbf{r}'-\mathbf{r}) - \frac{\omega^2}{c_0^2}\alpha(\mathbf{r}')\widetilde{P}(\mathbf{r}',\mathbf{r}_s,\omega)\widetilde{G}_0(\mathbf{r}',\mathbf{r},\omega) \\
&\quad - \widetilde{A}(\omega)\delta(\mathbf{r}'-\mathbf{r}_s)\widetilde{G}_0(\mathbf{r}',\mathbf{r},\omega)]. \qquad \text{(G.9)}
\end{aligned}$$

Choosing $\mathbf{r}$ in V gives

$$\begin{aligned}
&\oint_S dS'\,\hat{\mathbf{n}}\cdot[\widetilde{P}(\mathbf{r}',\mathbf{r}_s,\omega)\nabla'\widetilde{G}_0(\mathbf{r}',\mathbf{r},\omega) - \widetilde{G}_0(\mathbf{r}',\mathbf{r},\omega)\nabla'\widetilde{P}(\mathbf{r}',\mathbf{r}_s,\omega)] \\
&= \int_V d\mathbf{r}'[\underbrace{\widetilde{P}(\mathbf{r}',\mathbf{r}_s,\omega)\delta(\mathbf{r}'-\mathbf{r})}_{\widetilde{P}(\mathbf{r},\mathbf{r}_s,\omega)} - \frac{\omega^2}{c_0^2}\alpha(\mathbf{r}')\widetilde{P}(\mathbf{r}',\mathbf{r}_s,\omega)\widetilde{G}_0(\mathbf{r}',\mathbf{r},\omega) \\
&\quad - \widetilde{A}(\omega)\underbrace{\delta(\mathbf{r}'-\mathbf{r}_s)}_{0}\widetilde{G}_0(\mathbf{r}',\mathbf{r},\omega)] \\
&= \widetilde{P}(\mathbf{r},\mathbf{r}_s,\omega) - \int_V d\mathbf{r}'\frac{\omega^2}{c_0^2}\alpha(\mathbf{r}')\widetilde{P}(\mathbf{r}',\mathbf{r}_s,\omega)\widetilde{G}_0(\mathbf{r}',\mathbf{r},\omega). \qquad \text{(G.10)}
\end{aligned}$$

If the support for α is in V, rearranging equation G.10 gives

$$\widetilde{P}(\mathbf{r},\mathbf{r}_s,\omega)$$

$$
\begin{aligned}
&= \int_{V\to\infty} d\mathbf{r}' \widetilde{G}_0(\mathbf{r}', \mathbf{r}, \omega) \frac{\omega^2}{c_0^2} \alpha(\mathbf{r}') \widetilde{P}(\mathbf{r}', \mathbf{r}_s, \omega) \\
&\quad + \oint_S dS', \hat{\mathbf{n}} \cdot [\widetilde{P}(\mathbf{r}', \mathbf{r}_s, \omega) \nabla' \widetilde{G}_0(\mathbf{r}', \mathbf{r}, \omega) - \widetilde{G}_0(\mathbf{r}', \mathbf{r}, \omega) \nabla' \widetilde{P}(\mathbf{r}', \mathbf{r}_s, \omega)] \\
&= \int_{\infty} d\mathbf{r}' \widetilde{G}_0(\mathbf{r}', \mathbf{r}, \omega) \frac{\omega^2}{c_0^2} \alpha(\mathbf{r}') \widetilde{P}(\mathbf{r}', \mathbf{r}_s, \omega) \\
&\quad + \oint_S dS' \, \hat{\mathbf{n}} \cdot [\widetilde{P}(\mathbf{r}', \mathbf{r}_s, \omega) \nabla' \widetilde{G}_0(\mathbf{r}', \mathbf{r}, \omega) - \widetilde{G}_0(\mathbf{r}', \mathbf{r}, \omega) \nabla' \widetilde{P}(\mathbf{r}', \mathbf{r}_s, \omega)]. \qquad \text{(G.11)}
\end{aligned}
$$

In equation G.11 the surface integral involves actual pressure measurements and their vertical derivatives. Hence, the surface integral will choose a causal solution. For consistency with equation G.6, choose a causal Green's function, which gives

$$
\begin{aligned}
\widetilde{P}(\mathbf{r}, \mathbf{r}_s, \omega) = &\int_{\infty} d\mathbf{r}' \widetilde{G}_0^+(\mathbf{r}', \mathbf{r}, \omega) \frac{\omega^2}{c_0^2} \alpha(\mathbf{r}') \widetilde{P}(\mathbf{r}', \mathbf{r}_s, \omega) \\
&+ \oint_S dS' \, \hat{\mathbf{n}} \cdot [\widetilde{P}(\mathbf{r}', \mathbf{r}_s, \omega) \nabla' \widetilde{G}_0^+(\mathbf{r}', \mathbf{r}, \omega) - \widetilde{G}_0^+(\mathbf{r}', \mathbf{r}, \omega) \nabla' \widetilde{P}(\mathbf{r}', \mathbf{r}_s, \omega)]. \qquad \text{(G.12)}
\end{aligned}
$$

G.3 Comparing approaches

Comparing equations G.6 and G.12 gives an equation for the source signature:

$$
\begin{aligned}
\widetilde{A}(\omega) = &\frac{1}{\widetilde{G}_0^+(\mathbf{r}, \mathbf{r}_s, \omega)} \oint_S dS' \, \hat{\mathbf{n}} \cdot [\widetilde{P}(\mathbf{r}', \mathbf{r}_s, \omega) \nabla' \widetilde{G}_0^+(\mathbf{r}', \mathbf{r}, \omega) \\
&- \widetilde{G}_0^+(\mathbf{r}', \mathbf{r}, \omega) \nabla' \widetilde{P}(\mathbf{r}', \mathbf{r}_s, \omega)] \\
= &\frac{P_0(\mathbf{r}, \mathbf{r}_s, \omega)}{G_0^+(\mathbf{r}, \mathbf{r}_s, \omega)}, \qquad \text{(G.13)}
\end{aligned}
$$

where $\mathbf{r}$ is below the measurement surface (inside V).

A few comments about equation G.13:
(1) Equation G.13 is one form of the "triangle relation" that relates the pressure wavefield $\widetilde{P}(\mathbf{r}', \mathbf{r}_s, \omega)$, its vertical derivative $\nabla' \widetilde{P}(\mathbf{r}', \mathbf{r}_s, \omega)$, and the source signature $\widetilde{A}(\omega)$. In this instance the first two variables are used to calculate the third.
(2) The numerator and denominator in equation G.13 can be evaluated at any $\mathbf{r}$ in V.
(3) The source-signature estimation code uses the 3D form $\widetilde{G}_0^+(\mathbf{r}, \mathbf{r}_s, \omega) = \exp(ikR)/R$, where $k = \omega/c_0$ and $R = |\mathbf{r} - \mathbf{r}_s|$ (Morse and Feshbach, 1953, p. 810).
(4) We can get a better estimate of the source by averaging the computed points as follows:

$$
\begin{aligned}
A(\omega) &= \frac{1}{N} \sum_{i=1}^{N} \frac{P_0(\mathbf{r}_i, \mathbf{r}_s, \omega)}{G_0^+(\mathbf{r}_i, \mathbf{r}_s, \omega)} \\
&= \frac{1}{N} \sum_{i=1}^{N} \frac{A_i(\omega) G_0^+(\mathbf{r}_i, \mathbf{r}_s, \omega)}{G_0^+(\mathbf{r}_i, \mathbf{r}_s, \omega)} = \frac{1}{N} \sum_{i=1}^{N} A_i(\omega) \qquad \text{(G.14)}
\end{aligned}
$$

Equation G.14 can be unstable near $\mathbf{r}_s$ because $1/G_0^+$ can "blow up", so the algorithm uses $1/(G_0^+ + \epsilon)$.

G.4 Additional considerations

What if we have an extended (vs. a point) source? Modify equation G.1 and assume (as for a point source) that the distributed source $\rho(\mathbf{r}, \mathbf{r}_s, t)$ is in V_s (above the measurement surface and below the free surface):

$$\left(\nabla^2 - \frac{1}{c^2(\mathbf{r})}\frac{\partial^2}{\partial t^2}\right) P(\mathbf{r}, \mathbf{r}_s, t) = \rho(\mathbf{r}, \mathbf{r}_s, t). \tag{G.15}$$

Equation G.6 then becomes

$$\widetilde{P}(\mathbf{r}, \mathbf{r}_s, \omega) = \int_{V_s} d\mathbf{r}'' \widetilde{\rho}(\mathbf{r}'', \mathbf{r}_s, \omega) \widetilde{G}_0^+(\mathbf{r}'', \mathbf{r}_s, \omega) + \int_{\infty} d\mathbf{r}' \widetilde{G}_0^+(\mathbf{r}, \mathbf{r}', \omega) \frac{\omega^2}{c_0^2} \alpha(\mathbf{r}') \widetilde{P}(\mathbf{r}', \mathbf{r}_s, \omega). \tag{G.16}$$

Equation G.10 is unchanged because we're integrating over V but the source is assumed to be outside V. Comparing equations G.16 and G.12 gives:

$$\begin{aligned} &\int_{V_s} d\mathbf{r}'' \widetilde{\rho}(\mathbf{r}'', \mathbf{r}_s, \omega) \widetilde{G}_0^+(\mathbf{r}'', \mathbf{r}_s, \omega) \\ =&\oint_S dS' \, \hat{\mathbf{n}} \cdot [\widetilde{P}(\mathbf{r}', \mathbf{r}_s, \omega) \nabla' \widetilde{G}_0^+(\mathbf{r}', \mathbf{r}, \omega) - \widetilde{G}_0^+(\mathbf{r}', \mathbf{r}, \omega) \nabla' \widetilde{P}(\mathbf{r}', \mathbf{r}_s, \omega)] \\ =&\widetilde{P}_0(\mathbf{r}, \mathbf{r}_s, \omega) \end{aligned} \tag{G.17}$$

($\mathbf{r}$ being below the measurement surface). Dividing by the Green's function gives the desired result:

$$\frac{\int_{V_s} d\mathbf{r}'' \widetilde{\rho}(\mathbf{r}'', \mathbf{r}_s, \omega) \widetilde{G}_0^+(\mathbf{r}'', \mathbf{r}_s, \omega)}{G_0^+(\mathbf{r}, \mathbf{r}_s, \omega)} = \frac{\widetilde{P}_0(\mathbf{r}, \mathbf{r}_s, \omega)}{G_0^+(\mathbf{r}, \mathbf{r}_s, \omega)} = \widetilde{A}(\mathbf{r}, \mathbf{r}_s, \omega).$$

H A brief history of the Green's theorem code

The Green's theorem code was written by the first author at UH during the summer of 2009 with technical assistance provided by Fang Liu. A C front end was used to read input data in Seismic Unix format. Fortran was used to write the engine that evaluated equations 2.2 and 4.1. In brief, the user specified the input data files (P and dP/dz), whether to use a 2D or 3D Green's function, and whether to perform deghosting, wavefield separation, source-wavelet estimation, or near-offset extrapolation. The code was tested during the first author's internship at ExxonMobil (September-December '09) using synthetic data furnished by the first author's mentor (Mamadou Diallo). Key results are summarized in sections 4.2 and 5.1 of this Annual Report. A historical note: Fang Liu's advice was to write the code in C, but the first author had a window of about three months in which to write the code, no prior experience with C, and prior experience with Fortran.

In August 2010 the second author suggested the code be rewritten in C (to enable integration with Seismic Unix) before its planned release to the M-OSRP sponsors. The first author did that with technical assistance provided by the second author, and the Release 1 code was released to the sponsors in April 2011. Release 1 was tested during the first author's internship at PGS (February-July '11) using SEAM synthetic data and field data furnished by the fourth author (the first author's

supervisor). Key results are summarized in sections 2.4, 2.5, 3.3, and 3.4 of Mayhan et al. (2012b). Release 1 was also tested by an employee at BP and a M-OSRP intern at Total.

In April 2011 the second author suggested the code be rewritten to make it more like M-OSRP's demultiple code (which should also decrease run time and correct a bug uncovered in testing at PGS). The second author furnished his new demultiple shell and the first author added the Green's theorem engine (fall '11). Testing with a flat-layer model shows that the new code runs $> 6\times$ faster than Release 1 did (by precomputing the Green's functions). The first author has continued to test the new code (some key results are summarized in section 6), and this new code will be released to the sponsors (as Release 2).

I Free-surface-multiple removal: Tutorial

We follow the logic in Carvalho (1992). If a given term in the forward scattering series creates a certain type of data, that term in the inverse scattering series removes that type of data. For example, if there is no free surface, there are no ghosts and free-surface multiples in the data. Hence, G_0^{FS} creates and removes ghosts and free-surface multiples (free-surface multiples in deghosted data).
(1) Choose the reference medium to be a half space of air and a half space of water separated by a free surface: $G_0 = G_0^d + G_0^{FS}$.
(2) Remove the reference wave: $D = P - P_0$.
(3) Deghost (source and receivers): $D = G_0 V_1 G_0$. Multiply from the left and right by G_0^{-1}, and then by G_0^d, to get $D' = G_0^d V_1 G_0^d$, where the prime indicates deghosted data. (Note: In practice this method is unstable so we use Green's theorem to deghost.)

Carvalho shows that

$$D'(k_g, k_s, \omega) = \sum_{n=1}^{\infty} D'_n(k_g, k_s, \omega), \tag{I.1}$$

$$\text{where } D'_n(k_g, k_s, \omega) = \frac{1}{i\pi\rho_r B(\omega)} \int_{-\infty}^{\infty} dk\, q \exp\left(iq(\epsilon_g + \epsilon_s)\right) \times D'_1(k_g, k, \omega) D'_{n-1}(k, k_s, \omega) \tag{I.2}$$

for $n = 2, 3, 4, \ldots$. Now the prime indicates deghosted and free-surface-demultipled data. Equations I.1 and I.2 are used in M-OSRP's 2D free-surface-multiple elimination code. The terms k_g, k_s, k_x, and k_z are the Fourier conjugates of x_g, x_s, x, and z, respectively, ρ_r is the density of the reference medium (water), $B(\omega)$ is the source signature, $k = \omega/c_0$, c_0 is the speed of sound in the reference medium (water), $q = sgn(\omega)\sqrt{k^2 - k_x^2}$, (x_g, ϵ_g) is the receiver location, and (x_s, ϵ_s) is the (2D) source location.

I.1 Derivation of equation I.2

Carvalho arrives at equation I.2 by substituting equation I.3 into equation I.4.

$$V_n(k_g, k_s, \omega) = -\frac{\rho_r}{4i\pi} \int_{-\infty}^{\infty} \frac{dk}{q} V_1(k_g, k, \omega) V_{n-1}(k, k_s, \omega) \tag{I.3}$$

$$D_n'(k_g,k_s,\omega) = -\frac{B(\omega)}{4}\frac{\rho_r^2}{q_g q_s}\exp\left(-iq_g\epsilon_g\right)\exp\left(-iq_s\epsilon_s\right)V_n(k_g,k_s,\omega) \tag{I.4}$$

for $n = 2, 3, 4, \ldots$.

I.2 Derivation of equation I.4

The derivation of equation I.4 was outlined in the third author's November 3, 2011 lecture. The linear equation in the inverse scattering series can be written

$$D(x_g,\epsilon_g,x_s,\epsilon_s,\omega) = \int d\mathbf{r}_1 \int d\mathbf{r}_2\, G_0(\mathbf{r}_g,\mathbf{r}_1,\omega)V_1(\mathbf{r}_1,\mathbf{r}_2,\omega)G_0(\mathbf{r}_2,\mathbf{r}_s,\omega) \tag{I.5}$$

where V_1 is a nonlocal perturbation. Use the bilinear form of G_0 and Fourier transform to find

$$\begin{aligned}
&D(x_g,\epsilon_g,x_s,\epsilon_s,\omega)\\
&= \int d\mathbf{r}_1 \int d\mathbf{r}_2 \int d\mathbf{k}_1 \frac{\exp\left(i\mathbf{k}'\cdot(\mathbf{r}_g-\mathbf{r}_1)\right)}{-\mathbf{k}'^2+k^2} V_1(\mathbf{r}_1,\mathbf{r}_2,\omega)G_0(\mathbf{r}_2,\mathbf{r}_s,\omega), \qquad \text{(I.6)}\\
&= \int d\mathbf{r}_1 \int d\mathbf{r}_2 \int dk_x' \int dk_z' \frac{\exp\left(ik_x'(x_g-x_1)\right)\exp\left(ik_z'(\epsilon_g-z_1)\right)}{-k_x'^2-k_z'^2+k^2} V_1(\mathbf{r}_1,\mathbf{r}_2,\omega)G_0(\mathbf{r}_2,\mathbf{r}_s,\omega).
\end{aligned}$$

Fourier transform over x_g

$$\begin{aligned}
&\int dx_g \exp\left(-ik_g x_g\right)D(x_g,\epsilon_g,x_s,\epsilon_s,\omega)\\
&= \int dx_g \exp\left(-ik_g x_g\right)\int dx_1\int dz_1\int dx_2\int dz_2\int dk_x'\int dk_z' \frac{\exp\left(ik_x'(x_g-x_1)\right)\exp\left(ik_z'(\epsilon_g-z_1)\right)}{-k_x'^2-k_z'^2+k^2}\\
&\quad\times V_1(x_1,z_1,x_2,z_2,\omega)G_0(\mathbf{r}_2,\mathbf{r}_s,\omega)\\
\text{LHS} &= D(k_g,\epsilon_g,x_s,\epsilon_s,\omega)\\
\text{RHS} &= \int dx_1\int dz_1\int dx_2\int dz_2\int dk_x'\int dk_z' \underbrace{\int dx_g \exp\left(-i(k_g-k_x')x_g\right)}_{2\pi\delta(k_g-k_x')} \frac{\exp\left(-ik_x'x_1\right)\exp\left(ik_z'(\epsilon_g-z_1)\right)}{-k_x'^2-k_z'^2+k^2}\\
&\quad\times V_1(x_1,z_1,x_2,z_2,\omega)G_0(\mathbf{r}_2,\mathbf{r}_s,\omega)\\
&= 2\pi\int dx_1\int dz_1\int dx_2\int dz_2\int dk_z'\int dk_x'\,\delta(k_g-k_x')\frac{\exp\left(-ik_x'x_1\right)\exp\left(ik_z'(\epsilon_g-z_1)\right)}{-k_x'^2-k_z'^2+k^2}\\
&\quad\times V_1(x_1,z_1,x_2,z_2,\omega)G_0(\mathbf{r}_2,\mathbf{r}_s,\omega)\\
&= 2\pi\int dx_1\int dz_1\int dx_2\int dz_2\int dk_z'\frac{\exp\left(-ik_g x_1\right)\exp\left(ik_z'(\epsilon_g-z_1)\right)}{-k_g^2-k_z'^2+k^2}V_1(x_1,z_1,x_2,z_2,\omega)G_0(\mathbf{r}_2,\mathbf{r}_s,\omega)\\
&= 2\pi\int dx_1\int dz_1\int dx_2\int dz_2 \underbrace{\int dk_z'\frac{\exp\left(ik_z'(\epsilon_g-z_1)\right)}{-k_g^2-k_z'^2+k^2}}_{\text{1D Green's function}}\exp\left(-ik_g x_1\right)V_1(x_1,z_1,x_2,z_2,\omega)G_0(\mathbf{r}_2,\mathbf{r}_s,\omega)\\
&= 2\pi\int dx_1\int dz_1\int dx_2\int dz_2\frac{\exp\left(iq_g|\epsilon_g-z_1|\right)}{2iq_g}\exp\left(-ik_g x_1\right)V_1(x_1,z_1,x_2,z_2,\omega)G_0(\mathbf{r}_2,\mathbf{r}_s,\omega)
\end{aligned}$$

$$=2\pi \int dx_1 \int dz_1 \int dx_2 \int dz_2 \frac{\exp\left(iq_g(z_1-\epsilon_g)\right)}{2iq_g} \exp\left(-ik_g x_1\right) V_1(x_1,z_1,x_2,z_2,\omega) G_0(\mathbf{r}_2,\mathbf{r}_s,\omega)$$

where $q_g \equiv \sqrt{(\omega/c_0)^2 - k_g^2}$ and $|\epsilon_g - z_1|$ became $z_1 - \epsilon_g$ because $z_1 > \epsilon_g$ (the perturbation is below the geophones). Recognizing the Fourier transforms over x_1 and z_1 gives

$$\begin{aligned}\text{RHS} &= \int dx_2 \int dz_2 \frac{\exp\left(-iq_g\epsilon_g\right)}{2iq_g} \underbrace{\int dx_1 \exp\left(-ik_g x_1\right) 2\pi \int dz_1 \exp\left(iq_g z_1\right) V_1(x_1,z_1,x_2,z_2,\omega)}_{V_1(k_g,q_g,x_2,z_2,\omega)} G_0(\mathbf{r}_2,\mathbf{r}_s,\omega) \\ &= \int dx_2 \int dz_2 \exp\left(-iq_g\epsilon_g\right) \frac{V_1(k_g,q_g,x_2,z_2,\omega)}{2iq_g} G_0(\mathbf{r}_2,\mathbf{r}_s,\omega).\end{aligned}$$

On the right we do exactly the same thing, which produces

$$D(k_g,\epsilon_g,k_s,\epsilon_s,\omega) = \exp\left(-iq_g\epsilon_g\right) \frac{V_1(k_g,q_g,k_s,q_s,\omega)}{-4q_g q_s} \exp\left(-iq_s\epsilon_s\right). \tag{I.7}$$

which is the same form as equation I.4.

I.3 Derivation of equation I.3

Equation I.3 comes from substituting equation I.8 into equation I.9.

$$G_0(x_1,z_1;x_2,z_2;\omega) = \frac{1}{2\pi}\rho_r \int_{-\infty}^{\infty} dk \frac{\exp\left(ik(x_1-x_2)\right)}{-2iq} \left(\exp\left(iq|z_1-z_2|\right) - \exp\left(iq|z_1+z_2|\right)\right). \tag{I.8}$$

$$\begin{aligned}V_2(k_g,k_s,\omega) = &-\int_{-\infty}^{\infty}\int_{-\infty}^{\infty} dx_1 dz_1 \int_{-\infty}^{\infty}\int_{-\infty}^{\infty} dx_2 dz_2 \exp\left(-ik_g x_1\right) \exp\left(iq_g z_1\right) V_1(x_1,z_1,\omega) \\ &\times G_0(x_1,z_1;x_2,z_2;\omega) V_1(x_2,z_2,\omega) \exp\left(ik_s x_2\right) \exp\left(iq_s z_2\right).\end{aligned} \tag{I.9}$$

Equation I.8 is the bilinear form of the Green's function for the chosen reference medium, and equation I.9 is the quadratic equation in the inverse scattering series. The derivation of equation I.3 was also outlined in the third author's November 3, 2011 lecture. Fourier transform both sides to get

$$\begin{aligned}V_2 &= -V_1 G_0 V_1 \\ \frac{V_2(k_g,k_s,\omega)}{q_g q_s} &= \int d\mathbf{r}_2 \int d\mathbf{r}_3 V_1(\mathbf{k}_g,\mathbf{r}_2,\omega) G_0(\mathbf{r}_2,\mathbf{r}_3,\omega) V_1(\mathbf{r}_3,\mathbf{k}_s,\omega)\end{aligned}$$

Use the bilinear form of G_0

$$\begin{aligned}&\frac{V_2(k_g,k_s,\omega)}{q_g q_s} \\ &= \int dx_2 \int dz_2 \int dx_3 \int dz_3 V_1(k_g,q_g,x_2,z_2,\omega) \int dk_x' \int dk_z' \\ &\times \frac{\exp\left(ik_x'(x_2-x_3)\right) \exp\left(ik_z'(z_2+z_3)\right)}{-k_x'^2 - k_z'^2 + k^2} V_1(x_3,z_3,k_s,q_s,\omega)\end{aligned}$$

$$= \int dk'_x \int dz_2 \int dx_3 \int dz_3 \underbrace{\int dx_2 V_1(k_g, q_g, x_2, z_2, \omega) \exp(ik'_x x_2)}_{V_1(k_g, q_g, k'_x, z_2, \omega)}$$
$$\times \underbrace{\int dk'_z \frac{\exp(ik'_z(z_2+z_3))}{-k'^2_x - k'^2_z + k^2}}_{\text{1D Green's function}} \exp(-ik'_x x_3) V_1(x_3, z_3, k_s, q_s, \omega)$$
$$= \int dk'_x \int dz_2 \int dx_3 \int dz_3 V_1(k_g, q_g, k'_x, z_2, \omega) \frac{\exp(iq|z_2+z_3|)}{2iq} \exp(-ik'_x x_3) V_1(x_3, z_3, k_s, q_s, \omega)$$
$$= \int dk'_x \int dz_2 \int dx_3 \int dz_3 V_1(k_g, q_g, k'_x, z_2, \omega) \frac{\exp(iq(z_2+z_3))}{2iq} \exp(-ik'_x x_3) V_1(x_3, z_3, k_s, q_s, \omega)$$
$$= \int dk'_x \int dx_3 \int dz_3 \underbrace{\int dz_2 V_1(k_g, q_g, k'_x, z_2, \omega) \exp(iqz_2)}_{V_1(k_g, q_g, k'_x, q, \omega)} \frac{\exp(iqz_3)}{2iq} \exp(-ik'_x x_3) V_1(x_3, z_3, k_s, q_s, \omega)$$
$$= \int dk'_x \int dx_3 \int dz_3 V_1(k_g, q_g, k'_x, q, \omega) \frac{\exp(iqz_3)}{2iq} \exp(-ik'_x x_3) V_1(x_3, z_3, k_s, q_s, \omega)$$

where $q \equiv \sqrt{(\omega/c_0)^2 - k'^2_x}$, and the absolute value gets lifted because $z_2 + z_3$ is positive. Now operate on the right-hand V_1

$$RHS = \int dk'_x \int dz_3 V_1(k_g, q_g, k'_x, q, \omega) \frac{\exp(iqz_3)}{2iq} \underbrace{\int dx_3 \exp(-ik'_x x_3) V_1(x_3, z_3, k_s, q_s, \omega)}_{V_1(k'_x, z_3, k_s, q_s, \omega)}$$
$$= \int dk'_x V_1(k_g, q_g, k'_x, q, \omega) \frac{1}{2iq} \underbrace{\int dz_3 \exp(iqz_3) V_1(k'_x, z_3, k_s, q_s, \omega)}_{V_1(k'_x, q, k_s, q_s, \omega)}$$
$$= \frac{1}{2i} \int dk'_x V_1(k_g, q_g, k'_x, q, \omega) \frac{1}{q} V_1(k'_x, q, k_s, q_s, \omega) \tag{I.10}$$

where q is defined in terms of k'_x and ω. The data were originally

$$D(k_g, k_s, \omega) = \frac{V_1(k_g, q_g, k_s, q_s, \omega)}{q_g q_s}.$$

Now substitute V_1 in terms of D in equation I.10

$$RHS = \int dk'_x D(k_g, q_g, k'_x, q, \omega) q_g q \frac{1}{q} q D(k'_x, q, k_s, q_s, \omega) q_s.$$

The form data $\times q \times$ data is the same form as that used by Carvalho (1992), where q is the obliquity factor. This worked because we had a plus sign, which allowed the absolute value to lift and be Fourier transformed.

J FSM elimination with and without Green's theorem preprocessing

J.1 Flat-layer model III without preprocessing

(1) Figure 53 shows the input to the process. These data consist of a subset of the left panel of Figure 13 replicated here to make a sail line. The subset consists of receivers 801–1101 of 1601 and samples 1–301 of 1500 replicated 300 times (to make a sail line with 301 shots).
(2) Figure 54 shows the input data after interpolation. The distance between receivers is 6m and the distance between shots is 18m, so two shots are interpolated between each pair of input shots giving a total of 301+2×300=901 shots.
(3) Figure 55 shows the input data after assignment of station numbers to sources and receivers. We imagine a square fixed in space; the survey ship tows the cable inside the square, and we assign station numbers relative to the fixed square.
(4) Figure 56 shows the input data after use of reciprocity between sources and receivers to compute the opposite side of each shot, i.e., conversion of one-sided data into split-spread data. We could have created split-spread synthetic data but, because many field surveys record one-sided data, we choose to begin with one-sided synthetic data. Because we start with one-sided data, as we move from left to right, we see an increasing number of traces to the left of each shot station, complete hyperbolas, and then a decreasing number of traces to the right of each shot station.
(5) Figure 57 shows the input data after some data "housekeeping"; we replace source and receiver x coordinates (sx and gx) by source and receiver stations ($sstat$ and $gstat$) and make $sy = gy = 0$, which in effect aligns the data with a N-S/E-W coordinate system.
(6) Figure 58 shows the input data after block selection. Our block has 901 shots 6m apart; each shot is centered in a cable with 601 receivers 6m apart. Our cables do not fill the block whose diagonal is defined by the shots, so we pad traces to fill that block. See Figure 59 (Ferreira, 2011).
(7) Figure 60 shows the input data after shots have been filled with all required offsets, i.e., each shot should be surrounded by zero padding.
(8) Figure 61 shows the input data after they have been tapered; these are also the input data to the free-surface-multiple prediction algorithm.
(9) Figure 62 is the output of the free-surface-multiple prediction algorithm.

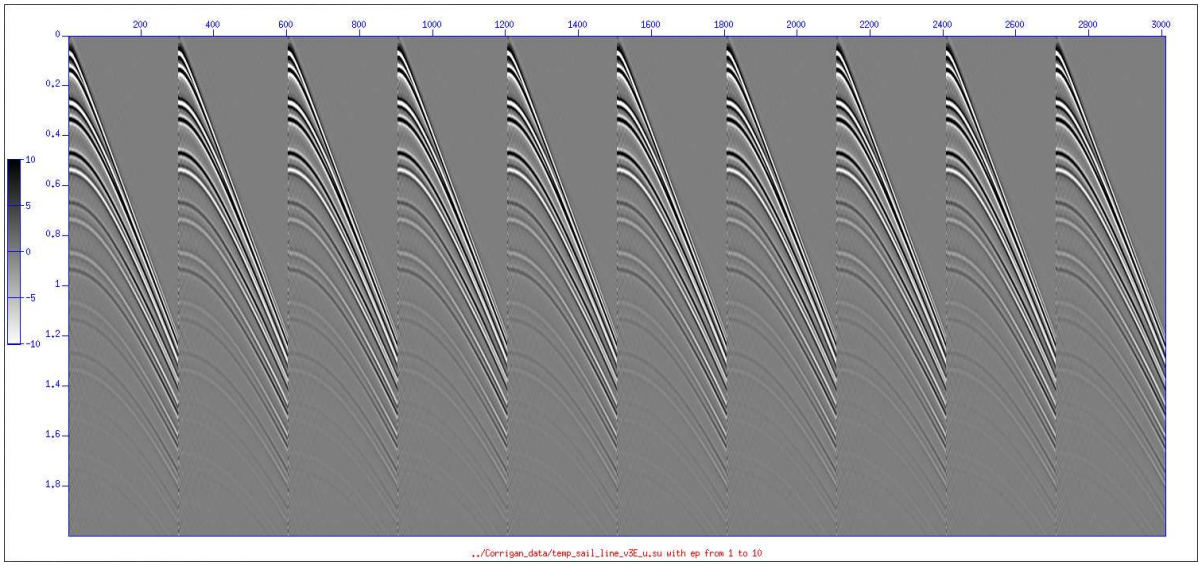

Figure 53: *Flat-layer model III, reflectivity code, P at 151m: Shots 1–10 of 301.*

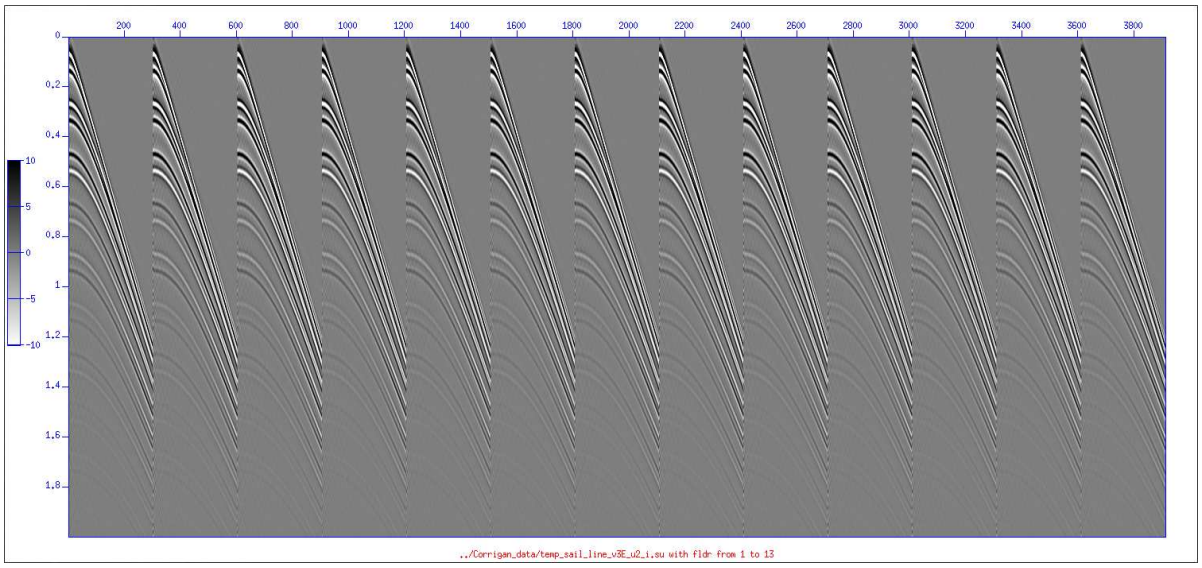

Figure 54: *Flat-layer model III, reflectivity code, P at 151m: Interpolate two shots between each pair of input shots. Shots 1–13 of 901.*

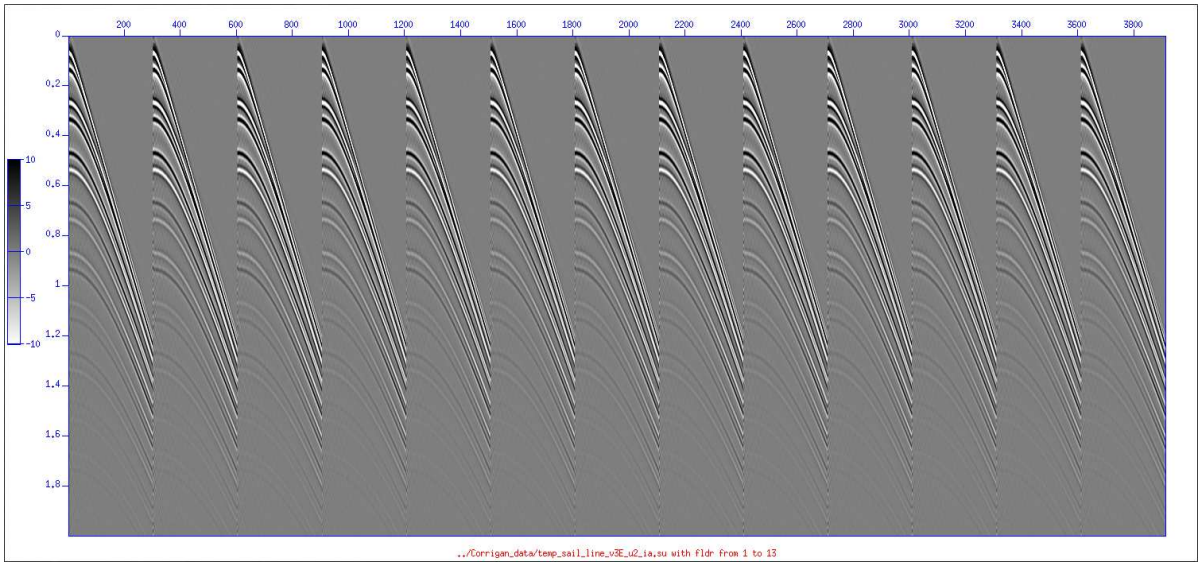

Figure 55: *Flat-layer model III, reflectivity code, P at 151m: Assign station numbers to sources and receivers. Shots 1–13 of 901.*

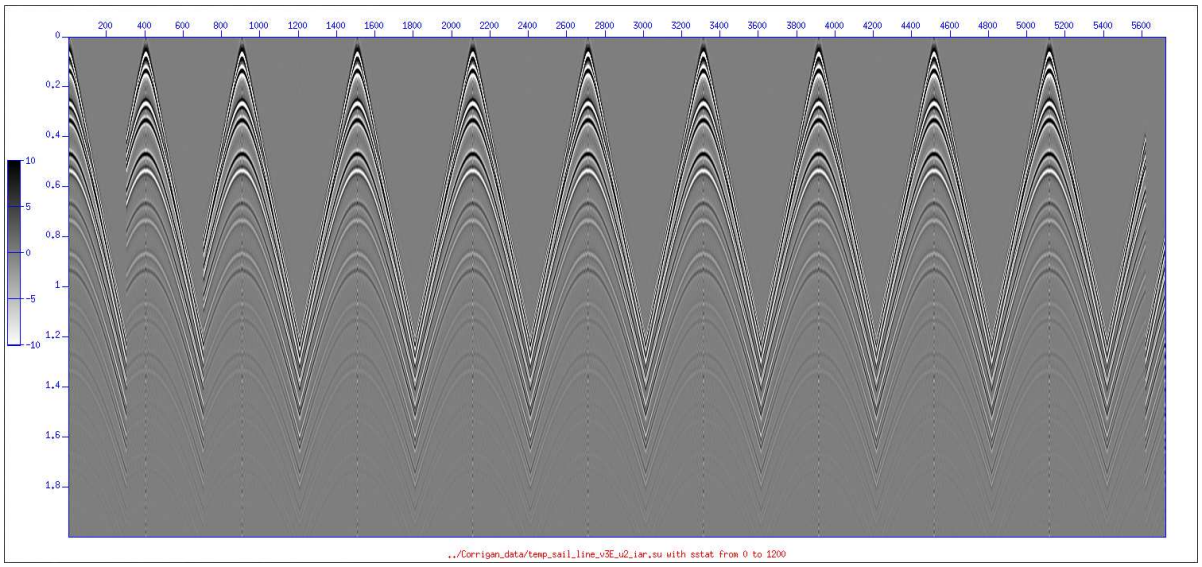

Figure 56: *Flat-layer model III, reflectivity code, P at 151m: Use reciprocity between sources and receivers to compute the opposite side of shots. Shot stations 0–1200 by 100.*

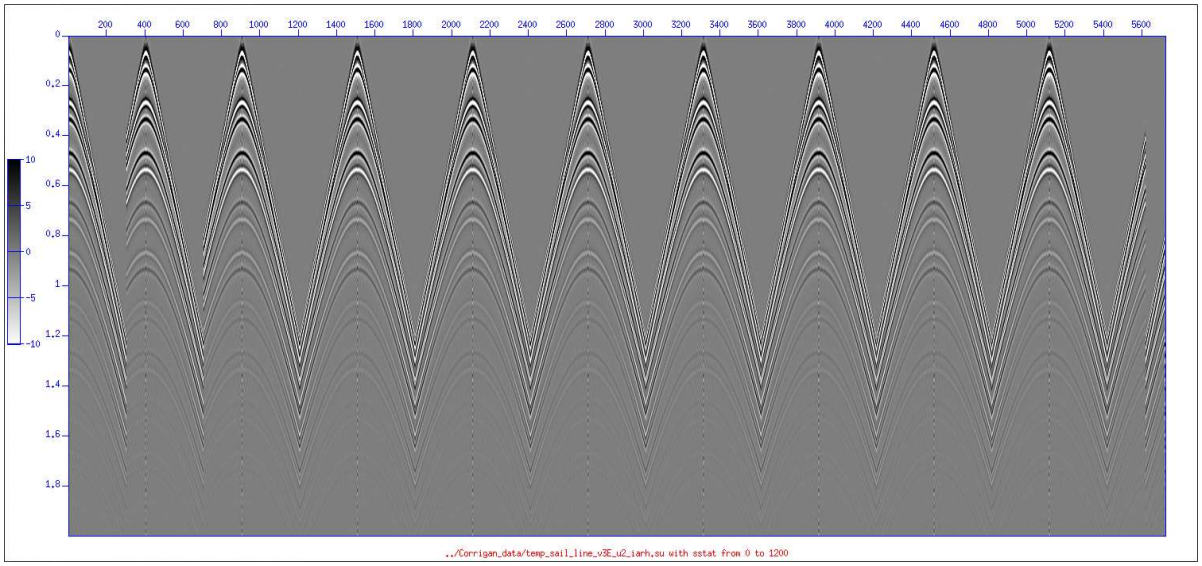

Figure 57: *Flat-layer model III, reflectivity code, P at 151m: Replace source and receiver locations (sx and gx) with source and receiver stations (sstat and gstat) and make sy = gy = 0. Shot stations 0–1200 by 100.*

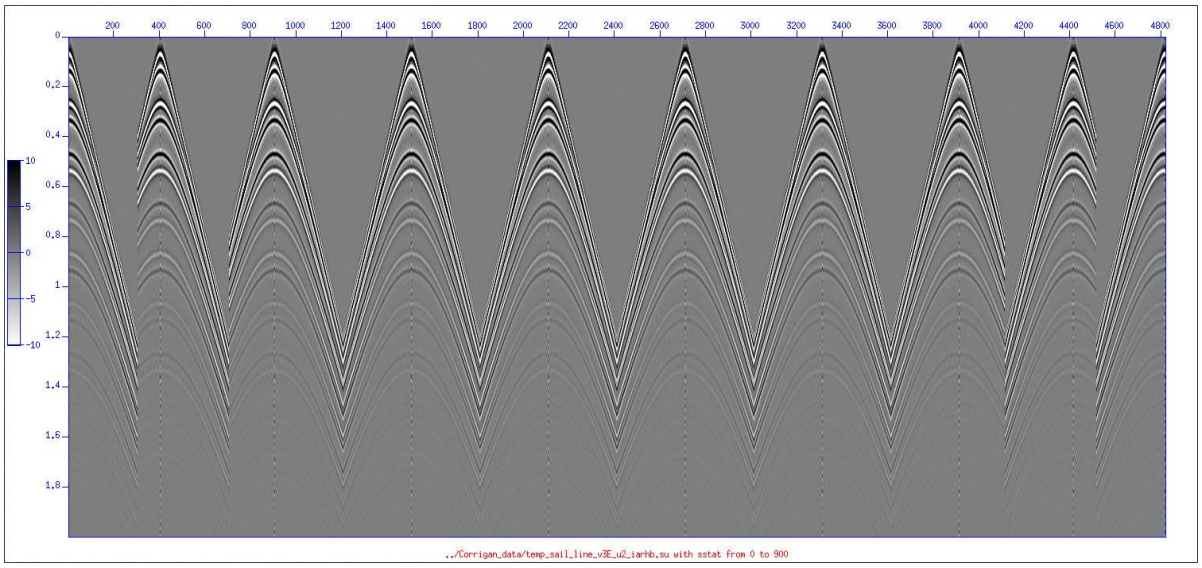

Figure 58: *Flat-layer model III, reflectivity code, P at 151m: Select blocks. Shot stations 0–900 by 100.*

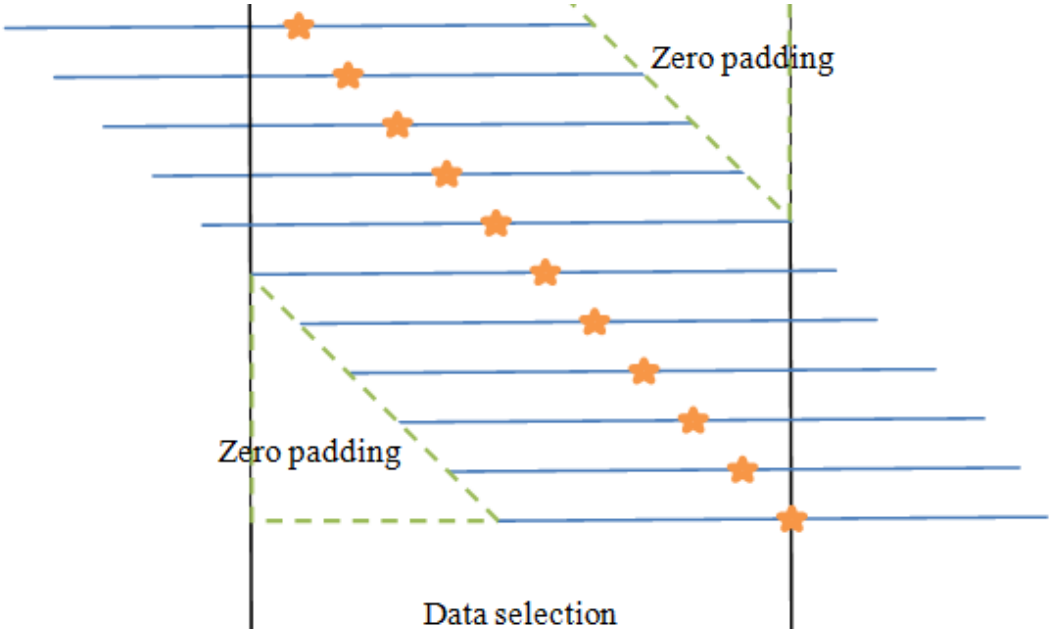

Figure 59: *Shots are represented by stars and the original receiver points are indicated by the solid lines. We need to pad new traces as indicated. (Ferreira, 2011, Figure 6.5)*

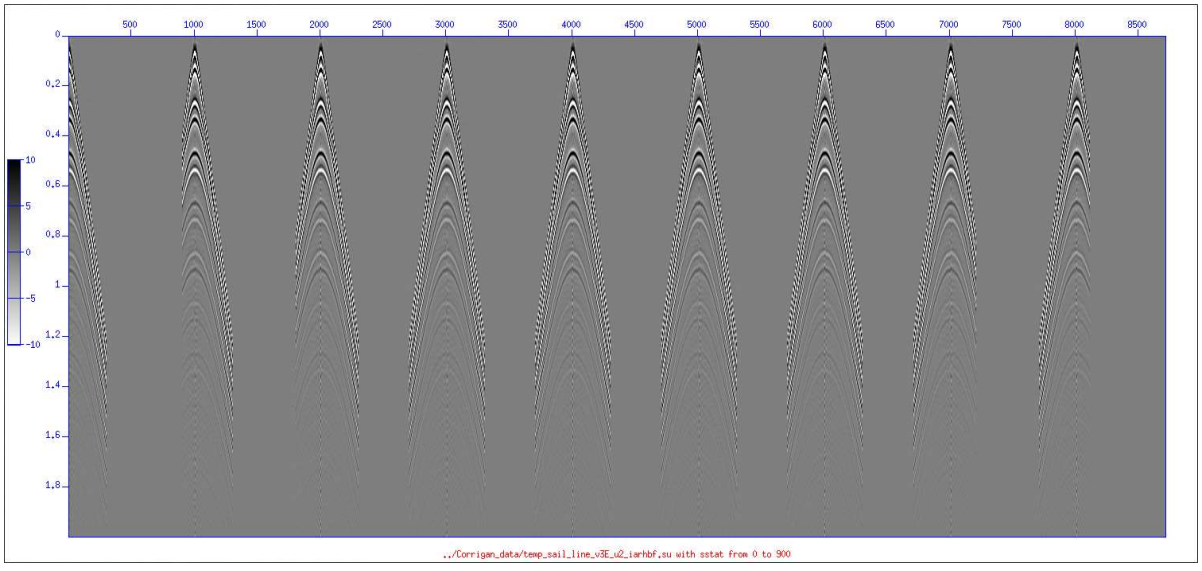

Figure 60: *Flat-layer model III, reflectivity code, P at 151m: Fill shots with all required offsets. Shot stations 0–900 by 100.*

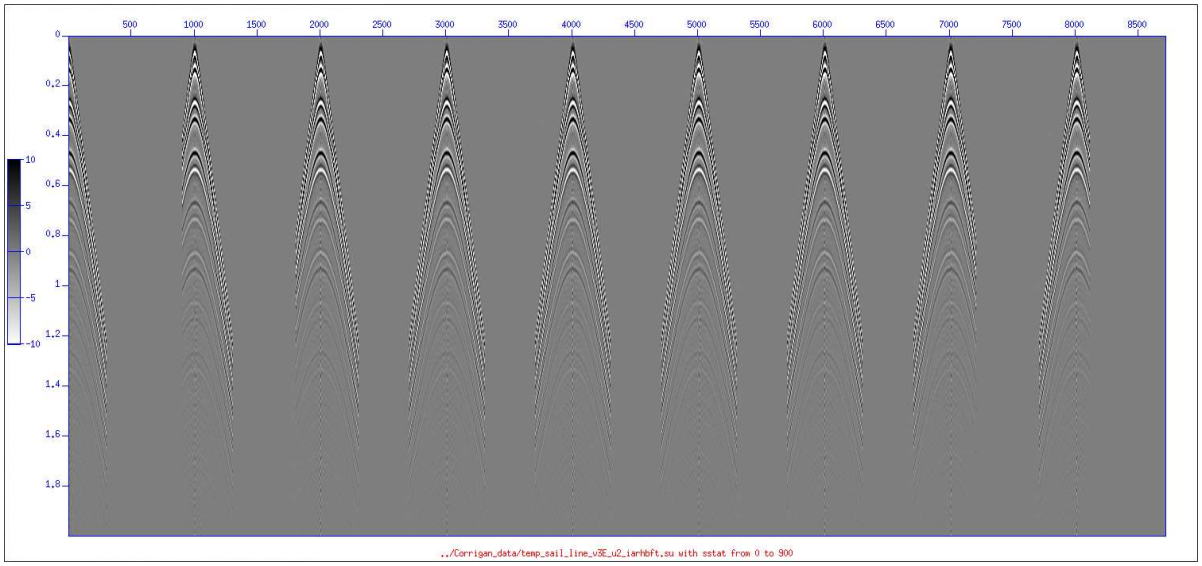

Figure 61: *Flat-layer model III, reflectivity code, P at 151m: After tapering. Shot stations 0–900 by 100.*

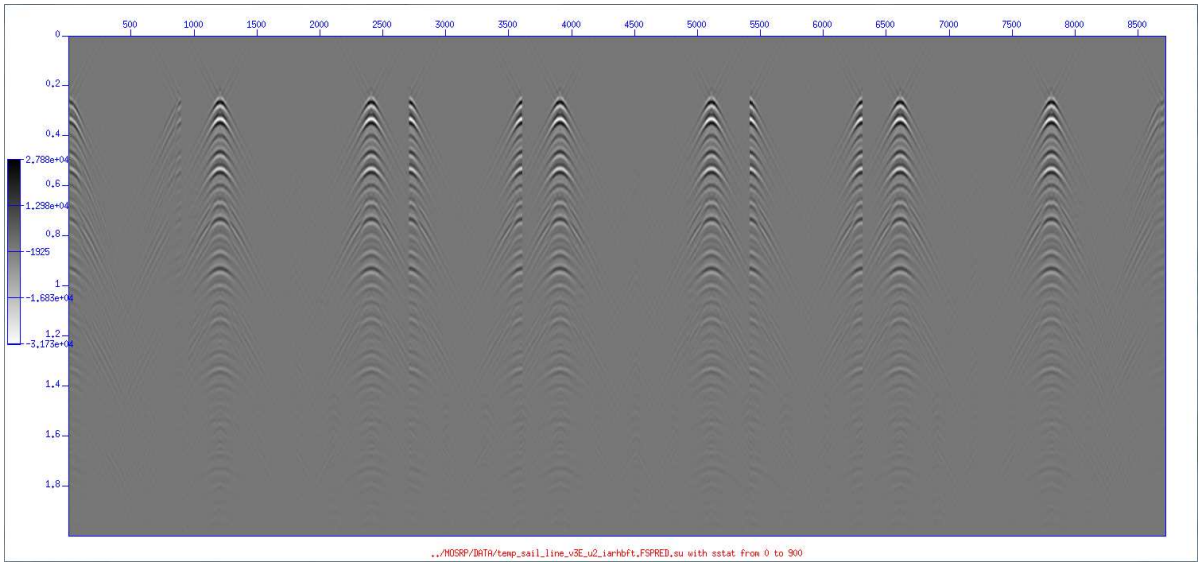

Figure 62: *Flat-layer model III, reflectivity code, P at 151m: Output of free-surface-multiple code. Shot stations 0–900 by 100.*

J.2 Flat-layer model III with preprocessing

(1) Figure 63 shows the input to the process. These data consist of a subset of the right panel of Figure 13 replicated here to make a sail line. The subset and replication are the same as in Figure 53,

i.e., the subset consists of receivers 801–1101 of 1601 and samples 1–301 of 1500, replicated 300 times (to make a sail line with 301 shots).
(2) Figure 64 shows the input data after interpolation,
(3) Figure 65 shows the input data after assignment of station numbers to sources and receivers,
(4) Figure 66 shows the input data after use of reciprocity between sources and receivers to compute the opposite side of each shot,
(5) Figure 67 shows the input data after performance of some data "housekeeping",
(6) Figure 68 shows the input data after block selection,
(7) Figure 69 shows the input data after filling of shots with all required offsets,
(8) Figure 70 shows the input data after tapering, and
(9) Figure 71 is the output of the free-surface-multiple prediction algorithm.

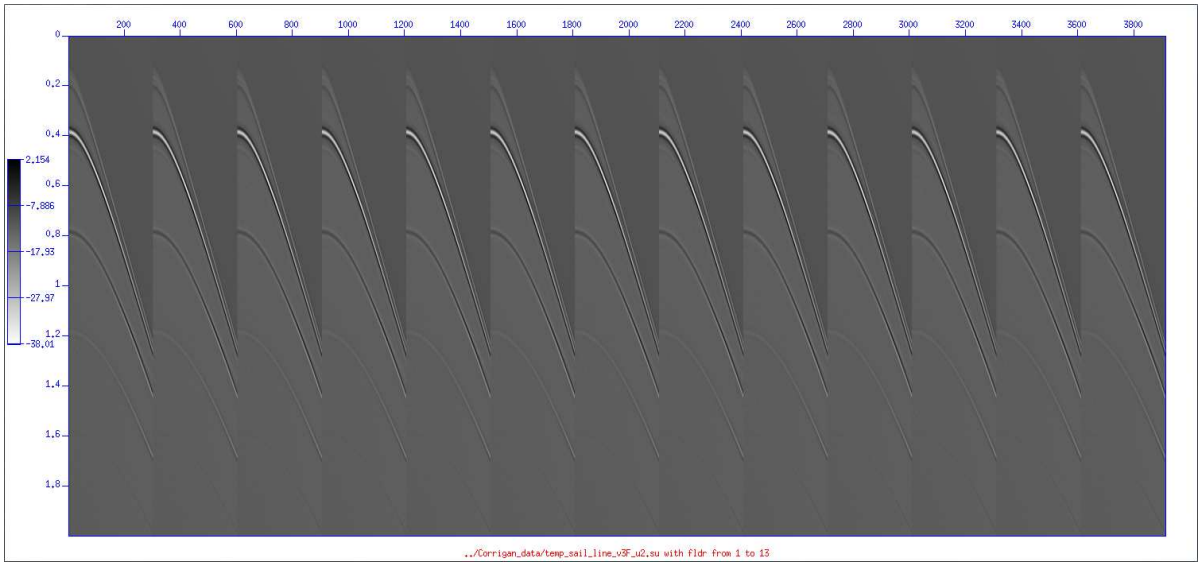

Figure 63: *Flat-layer model III, reflectivity code, deghosted P at 10m: Shots 1–13 of 301.*

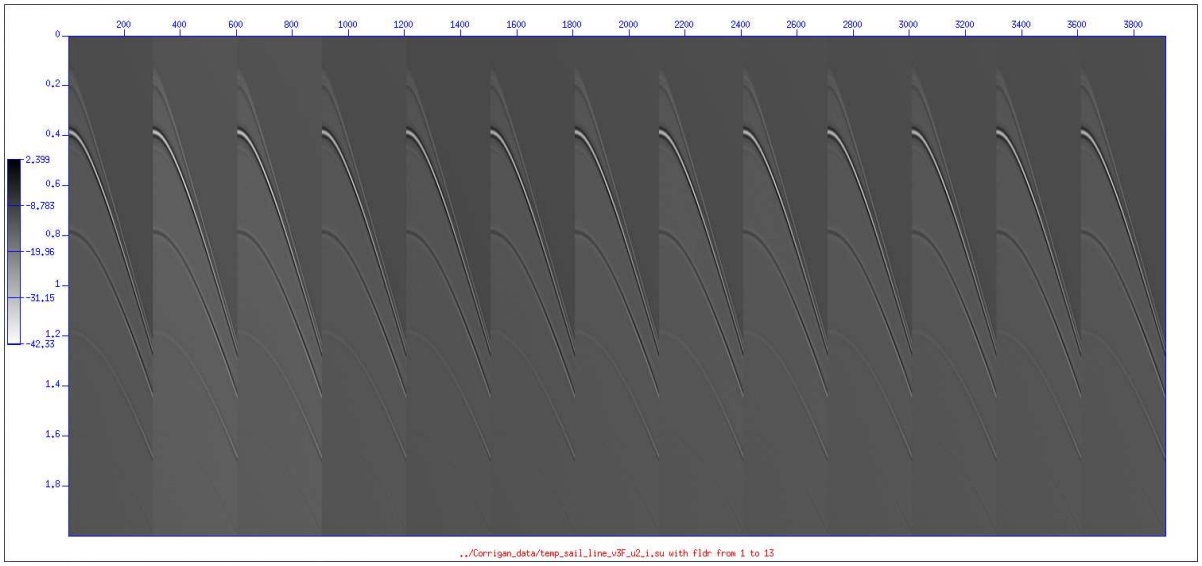

Figure 64: *Flat-layer model III, reflectivity code, deghosted P at 10m: Interpolate two shots between each pair of input shots. Shots 1–13 of 901.*

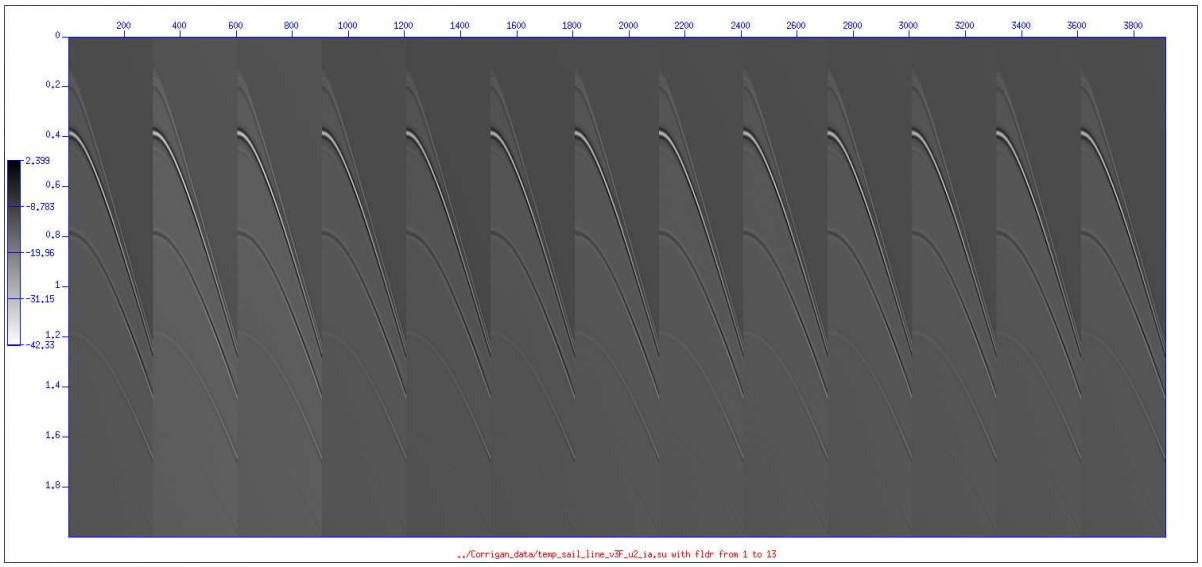

Figure 65: *Flat-layer model III, reflectivity code, deghosted P at 10m: Assign station numbers to sources and receivers. Shots 1–13 of 901.*

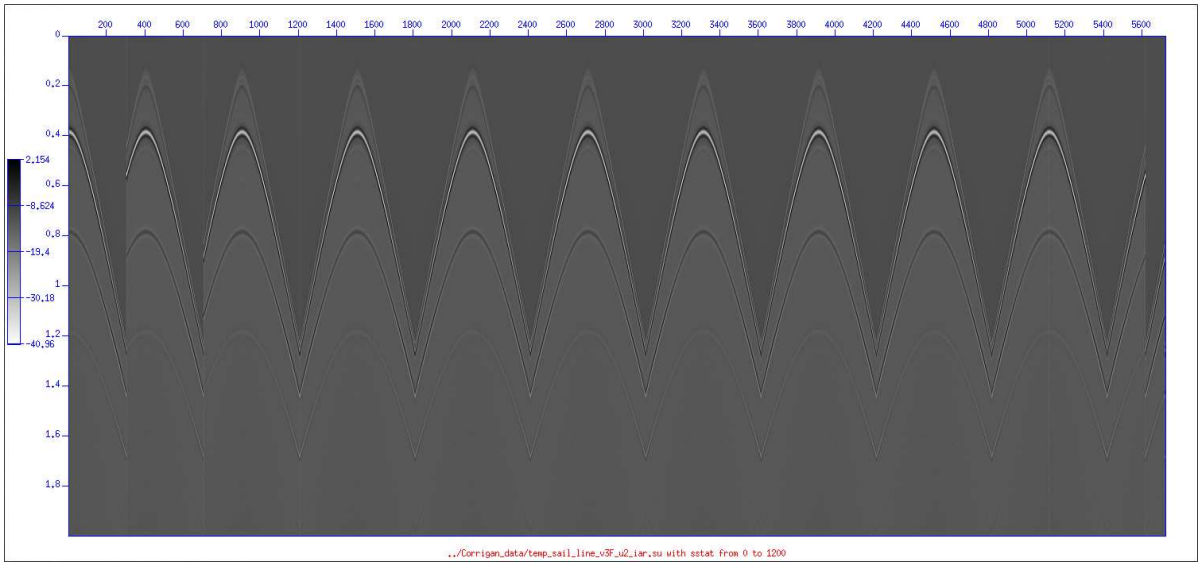

Figure 66: *Flat-layer model III, reflectivity code, deghosted P at 10m: Use reciprocity between sources and receivers to compute the opposite side of shots. Shot stations 0–1200 by 100.*

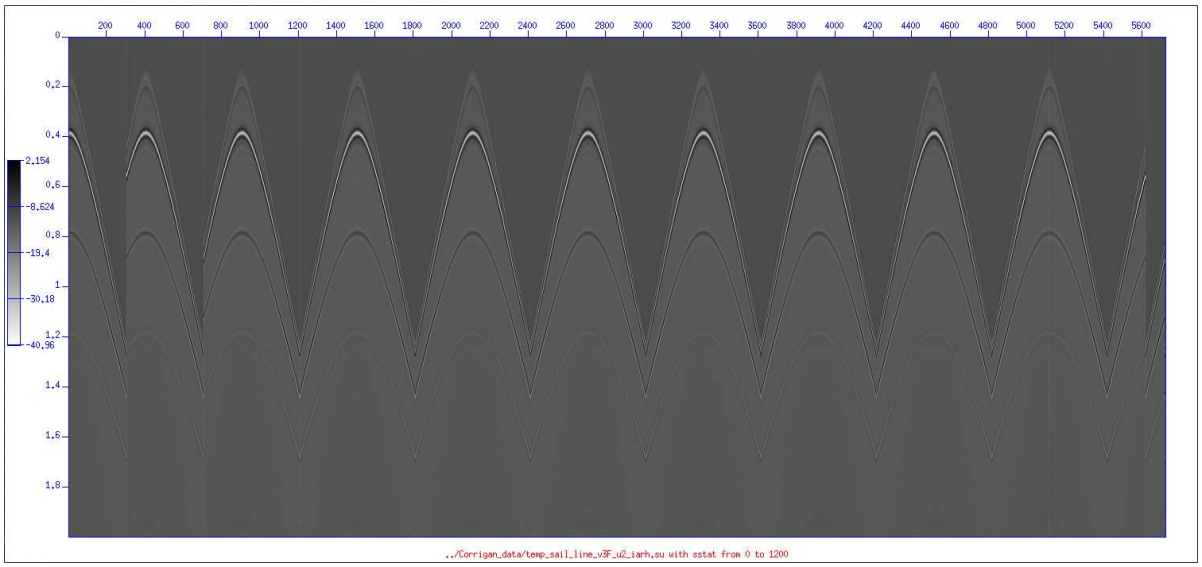

Figure 67: *Flat-layer model III, reflectivity code, deghosted P at 10m: Replace source and receiver locations (sx and gx) with source and receiver stations (sstat and gstat) and make sy = gy = 0. Shot stations 0–1200 by 100.*

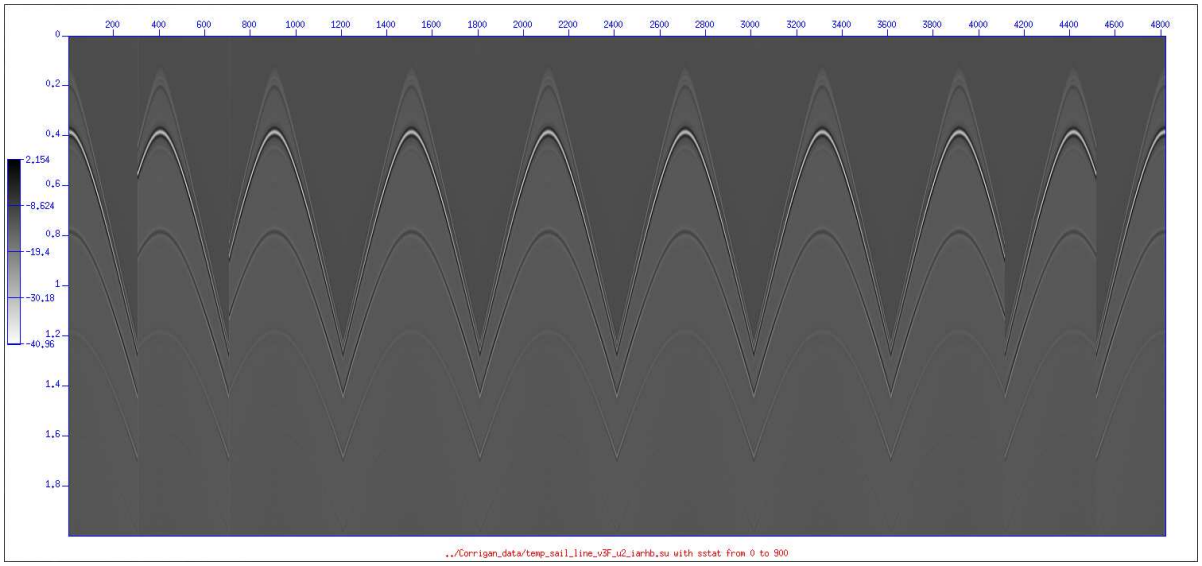

Figure 68: *Flat-layer model III, reflectivity code, deghosted P at 10m: Select blocks. Shot stations 0–900 by 100.*

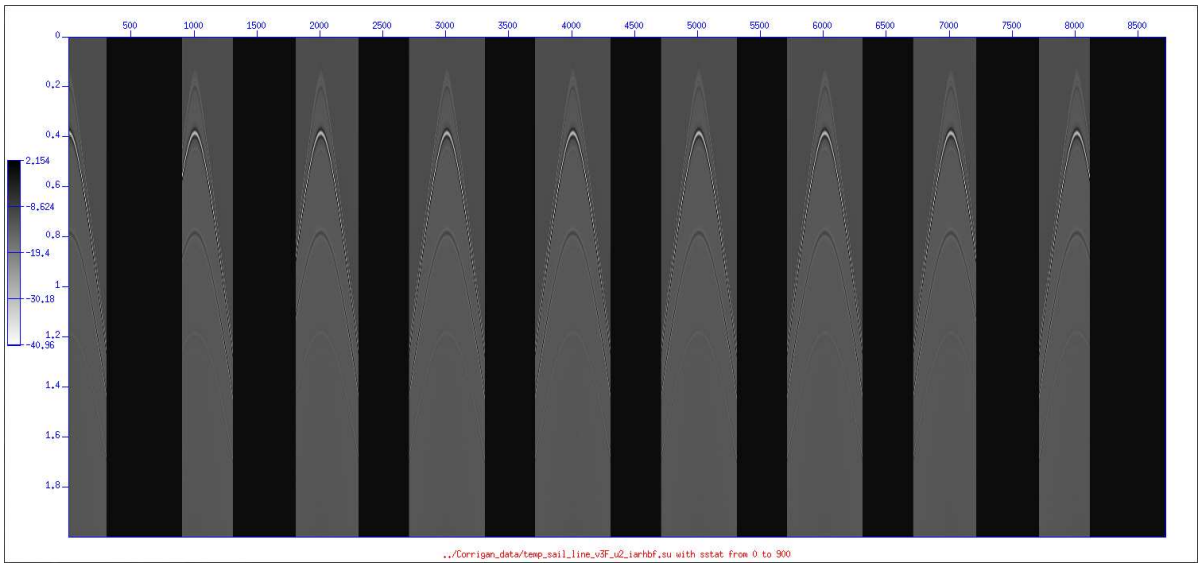

Figure 69: *Flat-layer model III, reflectivity code, deghosted P at 10m: Fill shots with all required offsets. Shot stations 0–900 by 100.*

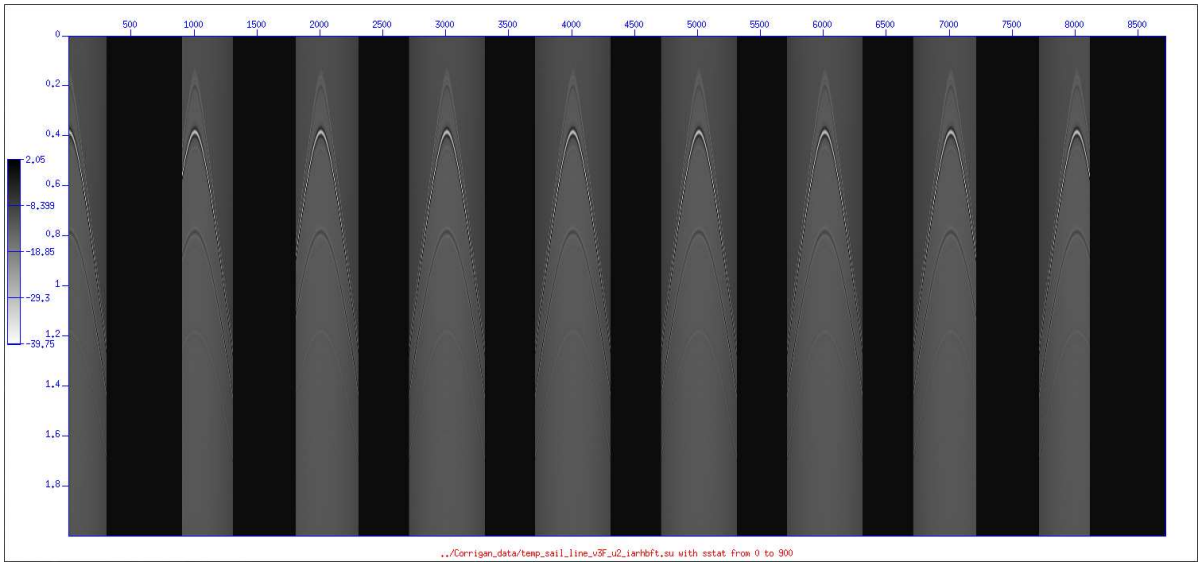

Figure 70: *Flat-layer model III, reflectivity code, deghosted P at 10m: After tapering. Shot stations 0–900 by 100.*

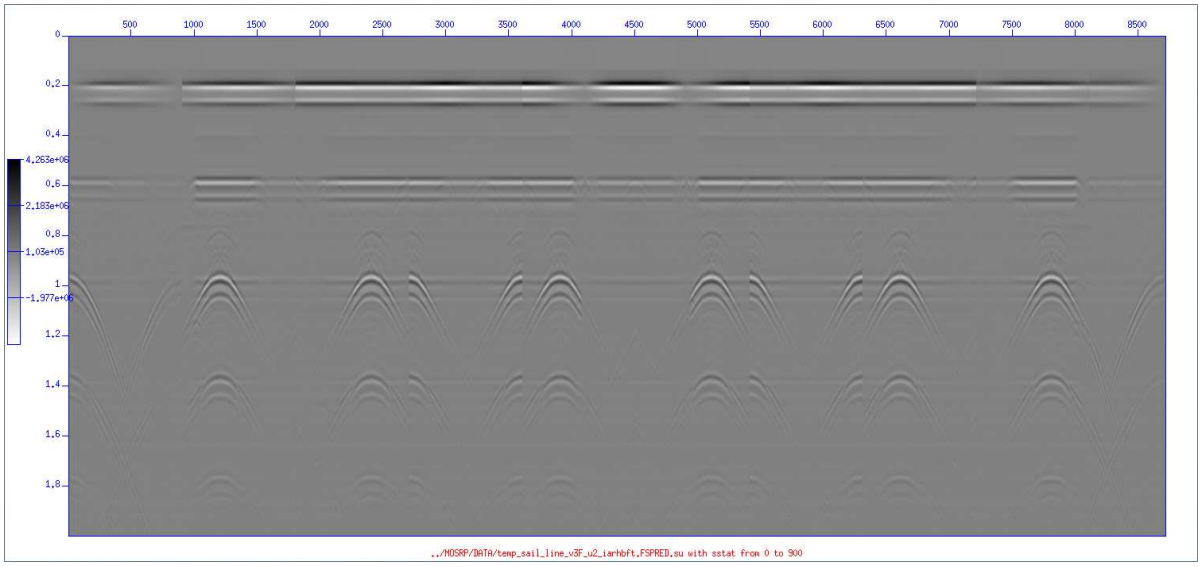

Figure 71: *Flat-layer model III, reflectivity code, deghosted P at 10m: Output of free-surface-multiple code. Shot stations 0–900 by 100.*

J.3 Elastic model 1 with preprocessing

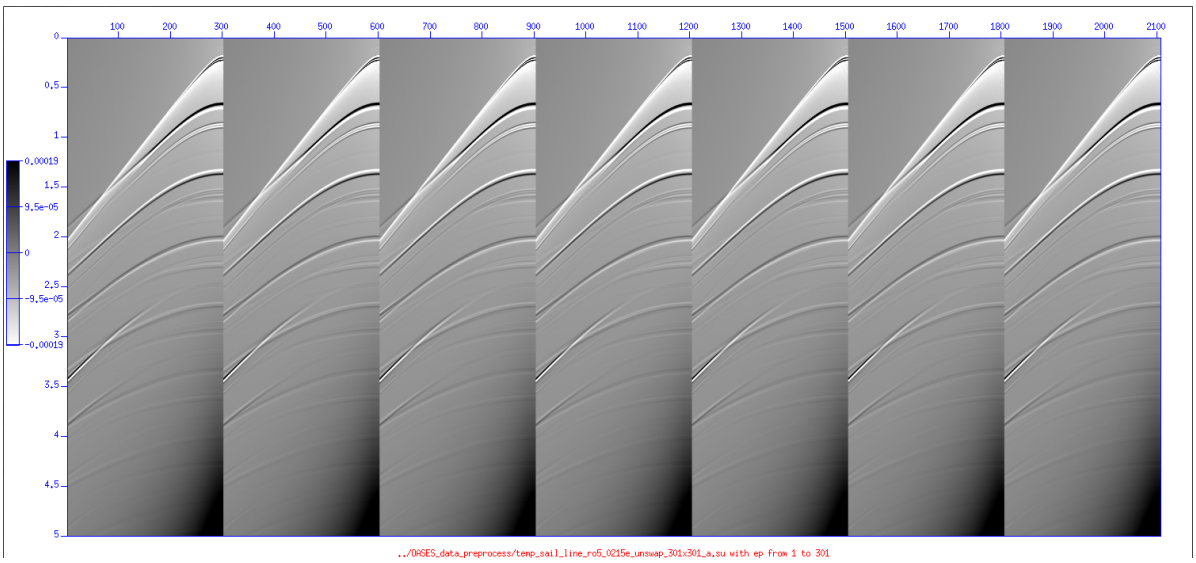

Figure 72: *Elastic model 1: Assign station numbers to source and receiver locations. Shots 1–301 by 50.*

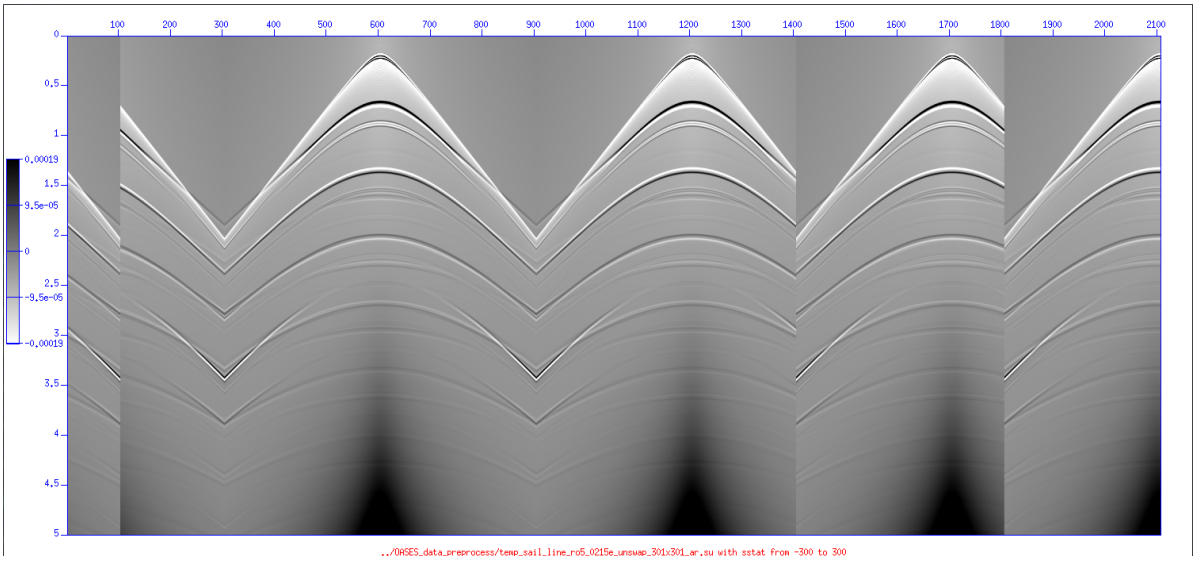

Figure 73: *Elastic model 1: Use reciprocity between sources and receivers to compute the opposite side of each shot, i.e., create split-spread data. Shots 1–301 by 50.*

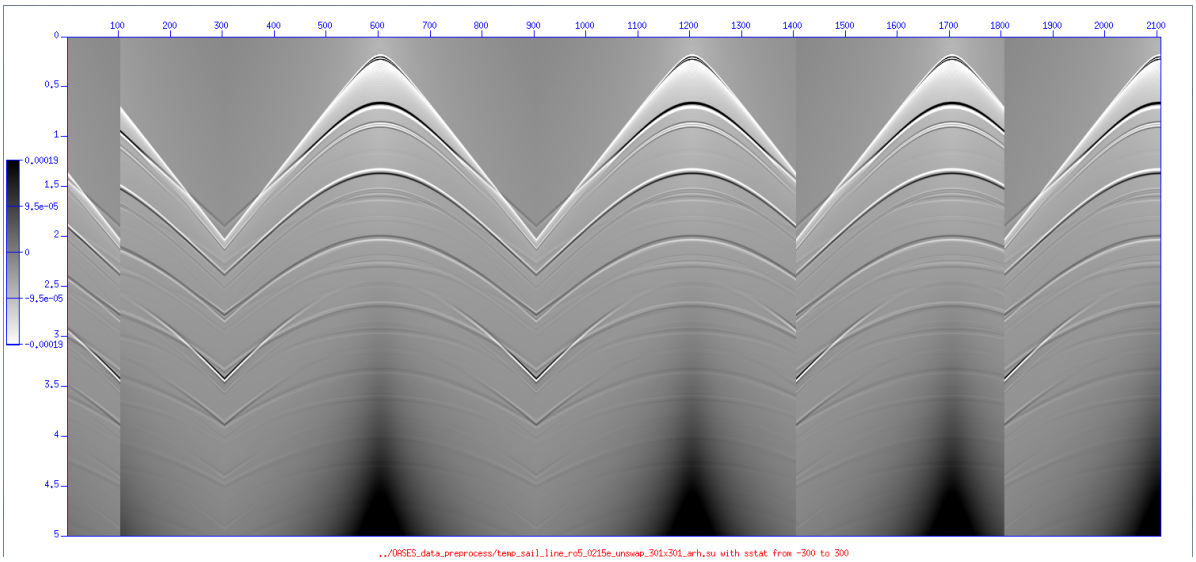

Figure 74: *Elastic model 1: Replace source and receiver locations along inline direction with source and receiver stations, set crossline coordinates=0. Shots 1–301 by 50.*

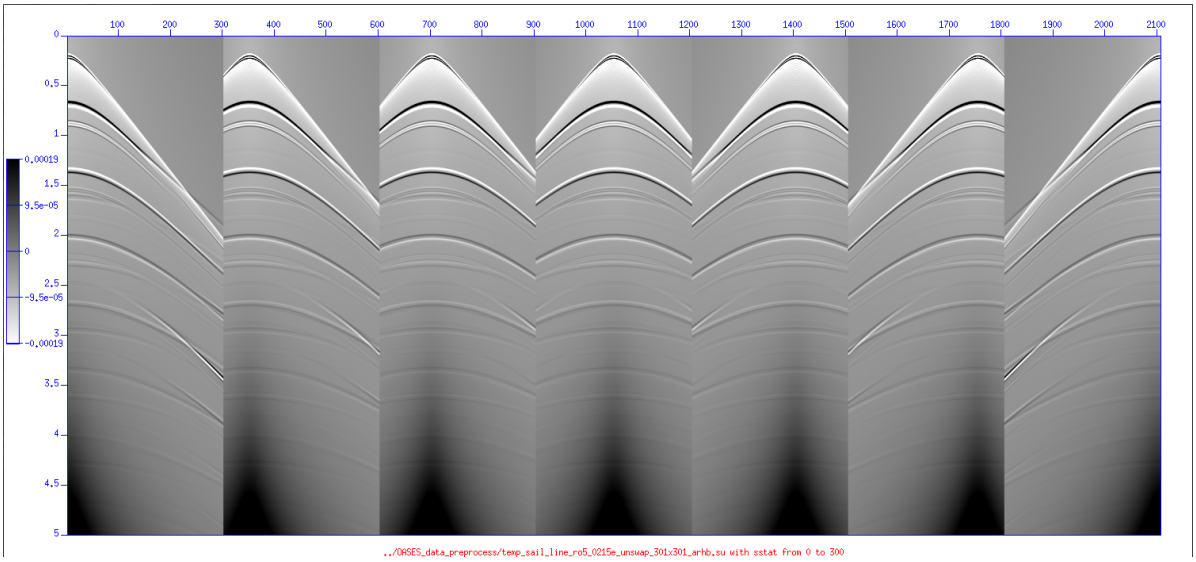

Figure 75: *Elastic model 1: Select blocks (explained in Figure 59. Shots 1–301 by 50.*

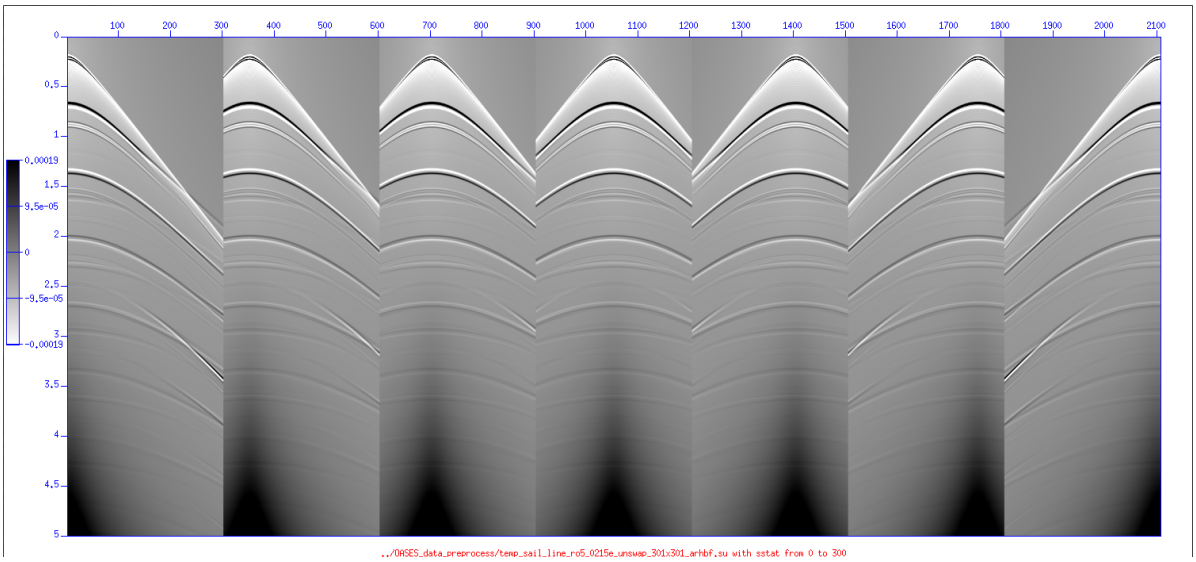

Figure 76: *Elastic model 1: Fill shots with all required offsets. Shots 1–301 by 50.*

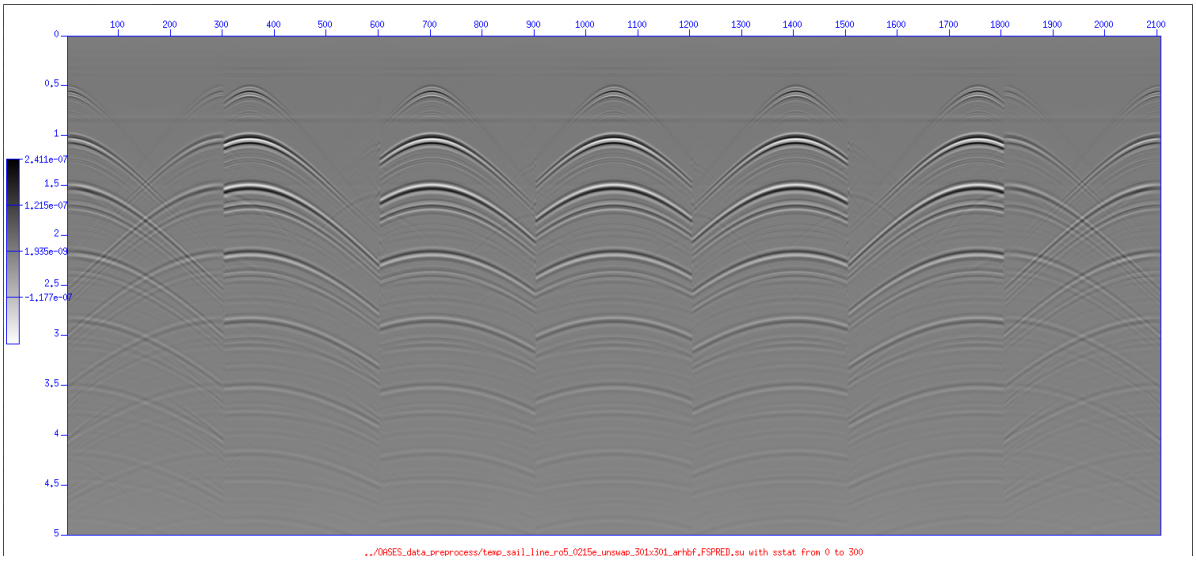

Figure 77: *Elastic model 1: Predict free-surface multiples. Shots 1–301 by 50.*

J.4 Elastic model 2 with preprocessing

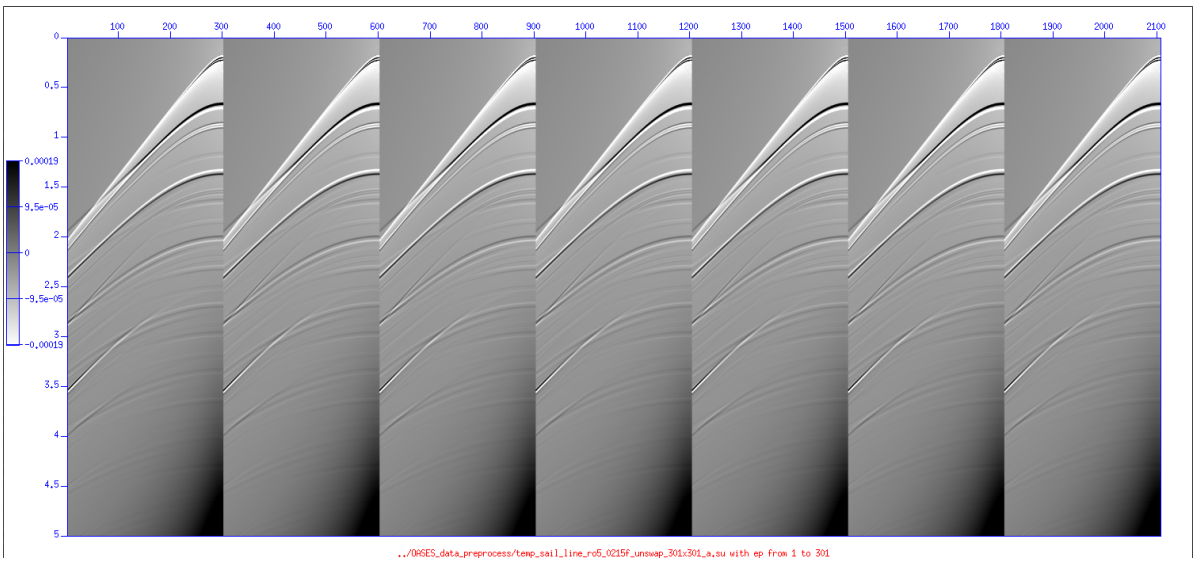

Figure 78: *Elastic model 2: Assign station numbers to source and receiver locations. Shots 1–301 by 50.*

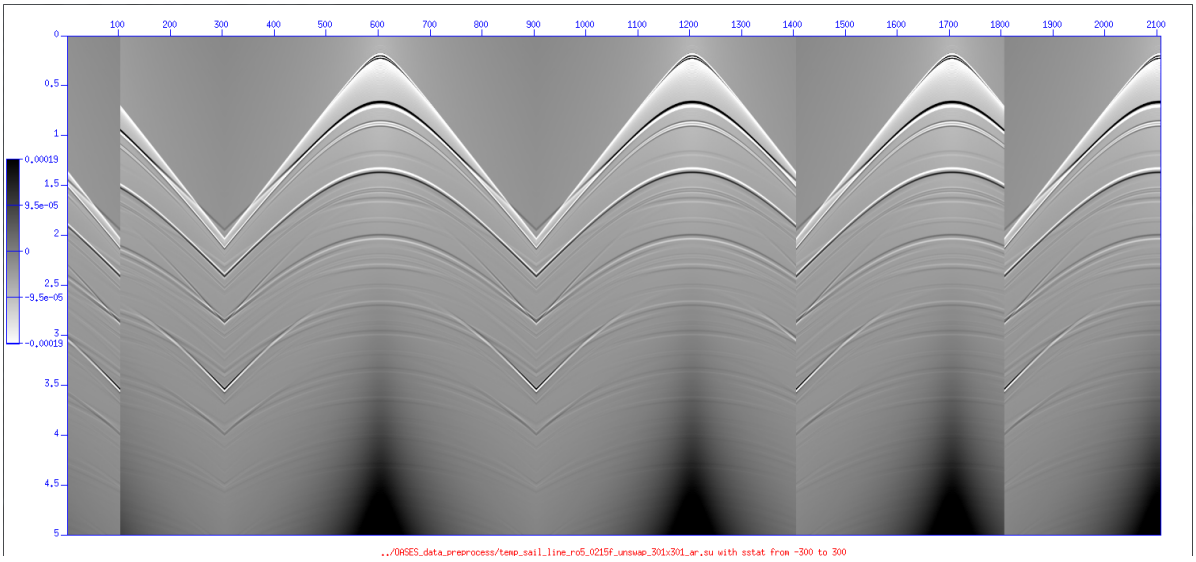

Figure 79: *Elastic model 2: Use reciprocity between sources and receivers to compute the opposite side of each shot, i.e., create split-spread data. Shots 1–301 by 50.*

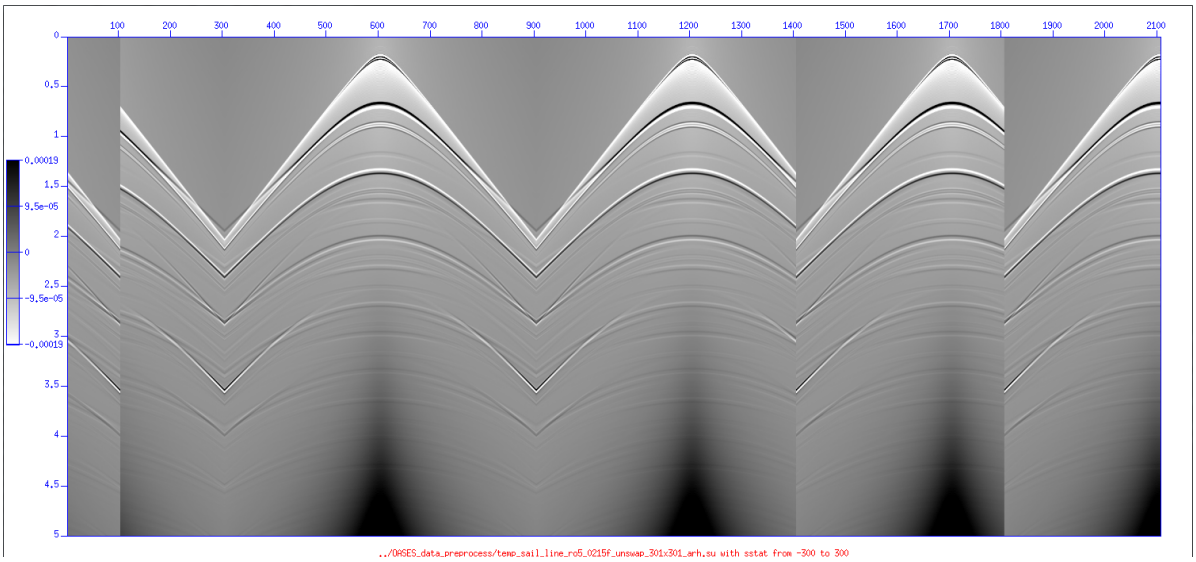

Figure 80: *Elastic model 2: Replace source and receiver locations along inline direction with source and receiver stations, set crossline coordinates=0. Shots 1–301 by 50.*

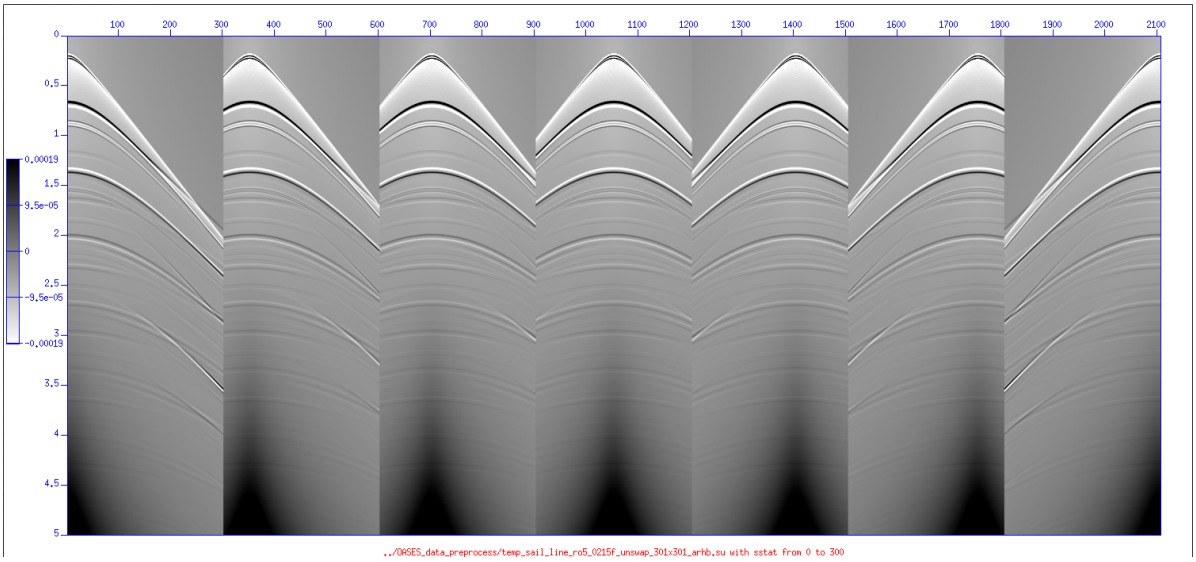

Figure 81: *Elastic model 2: Select blocks (explained in Figure 59). Shots 1–301 by 50.*

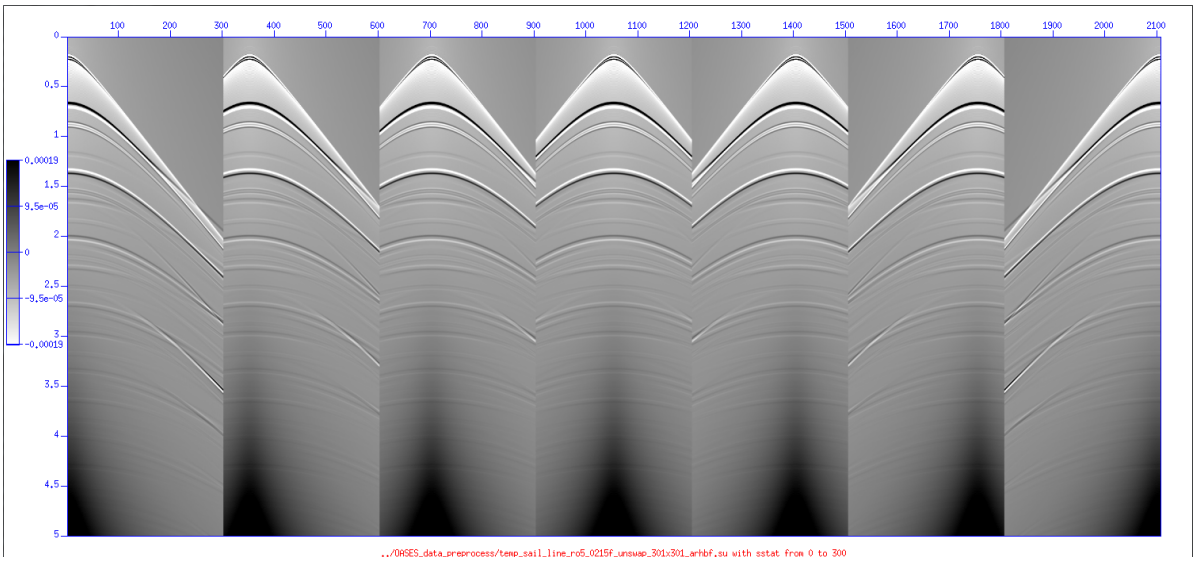

Figure 82: *Elastic model 2: Fill shots with all required offsets. Shots 1–301 by 50.*

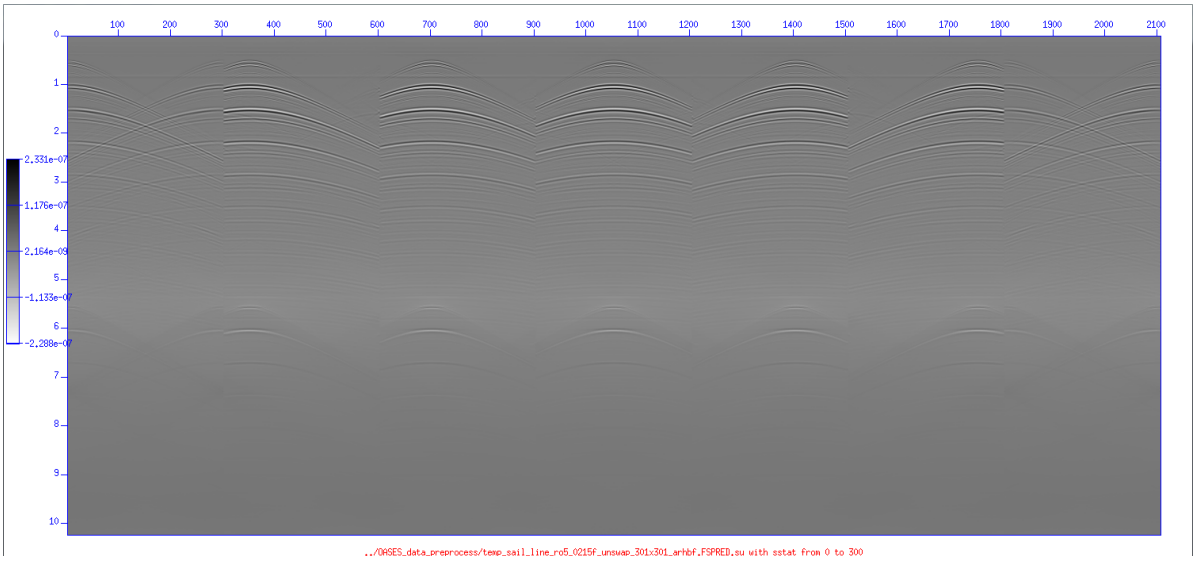

Figure 83: *Elastic model 2: Predict free-surface multiples. Shots 1–301 by 50.*

J.5 Field data without preprocessing

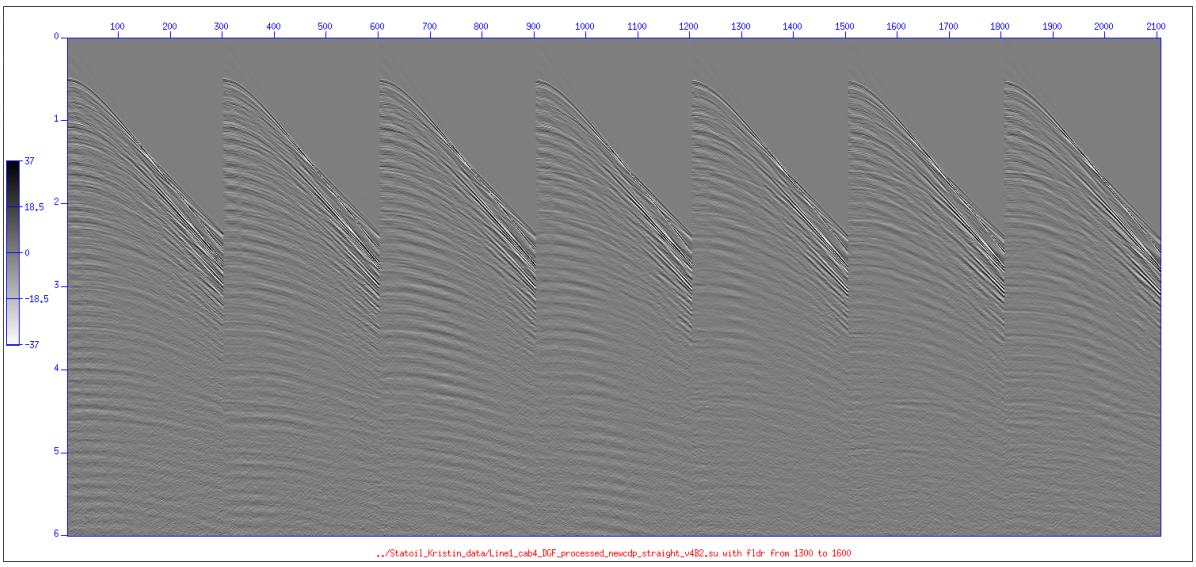

Figure 84: *Kristin P at 25m: Shots 1300–1600 (by 50) of 694.*

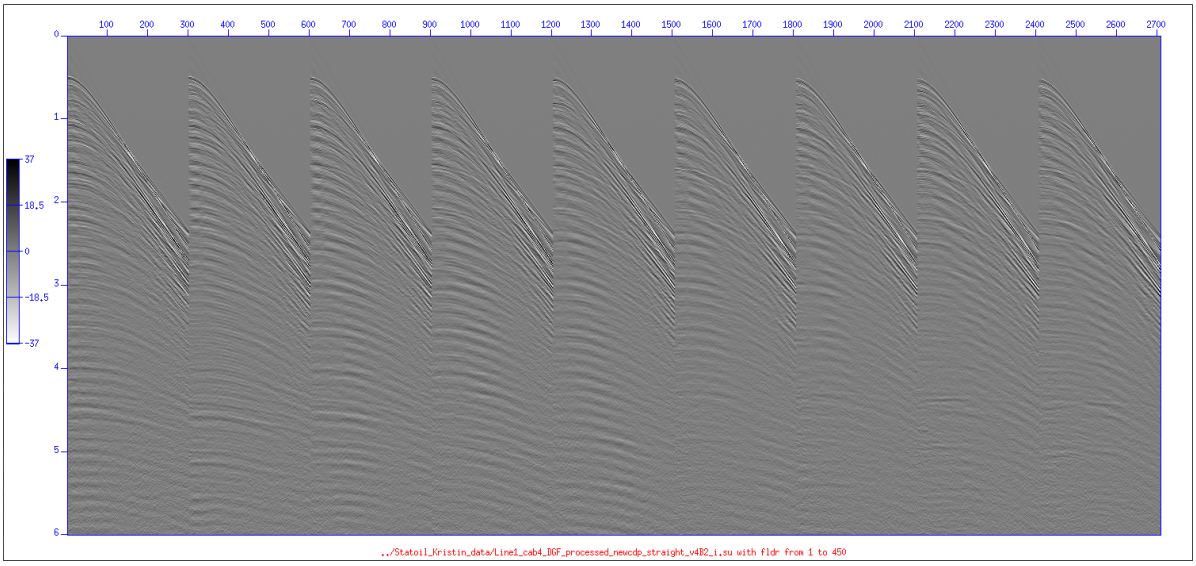

Figure 85: *Kristin P at 25m: Interpolate shots so that distance between shots = distance between receivers. Shots 1–401 (by 50) of 450.*

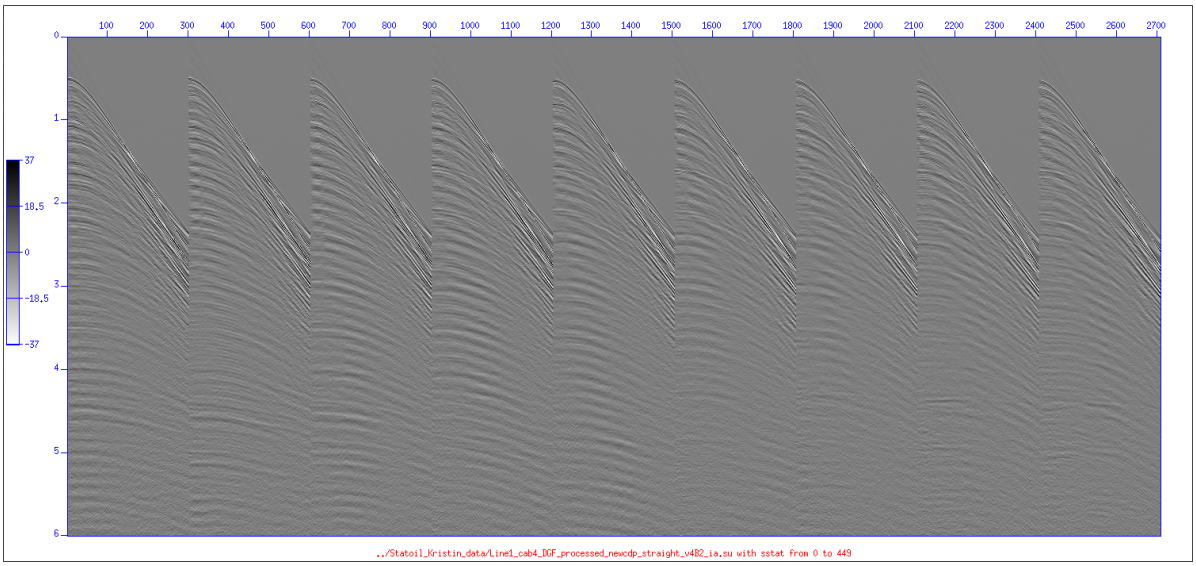

Figure 86: *Kristin P at 25m: Assign station numbers to sources and receivers. Shot stations 0–400 (by 50) of 450.*

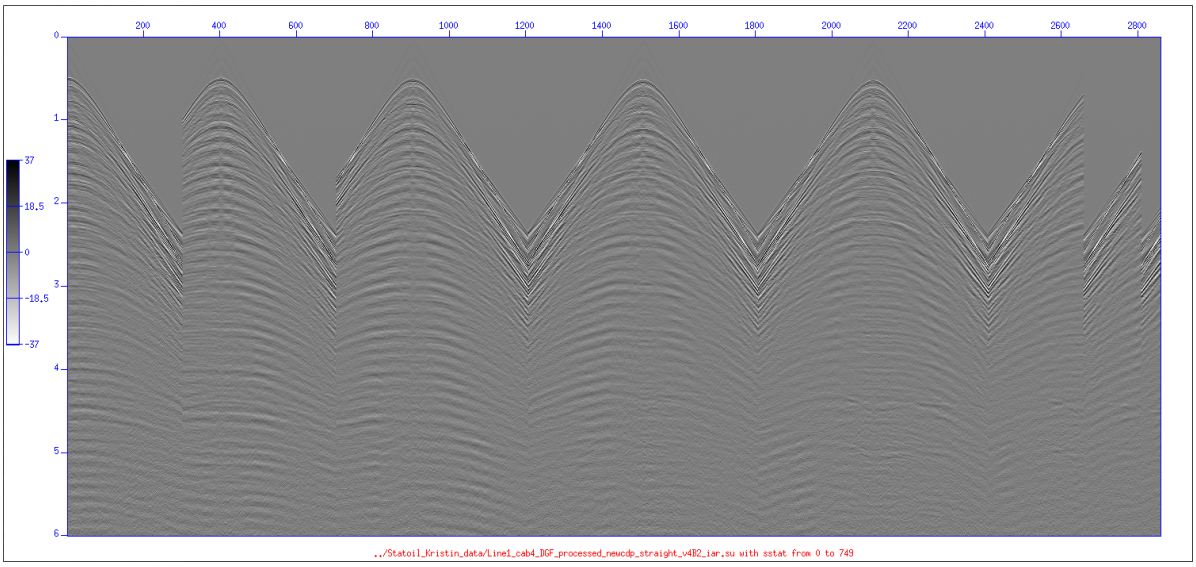

Figure 87: *Kristin P at 25m: Use reciprocity between sources and receivers to compute the opposite side of shots, i.e., convert one-sided data to split-spread data. Shot stations 0–700 (by 100) of 749.*

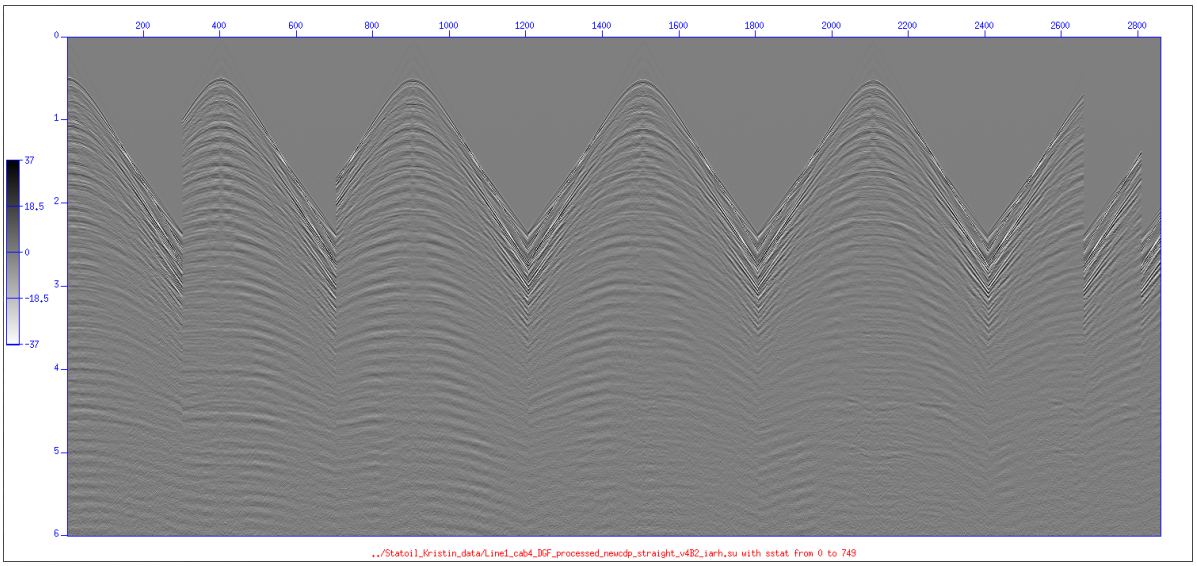

Figure 88: *Kristin P at 25m: Replace source and receiver locations (sx and gx) with source and receiver stations (sstat and gstat) and make sy = gy = 0. Shot stations 0–700 (by 100) of 749.*

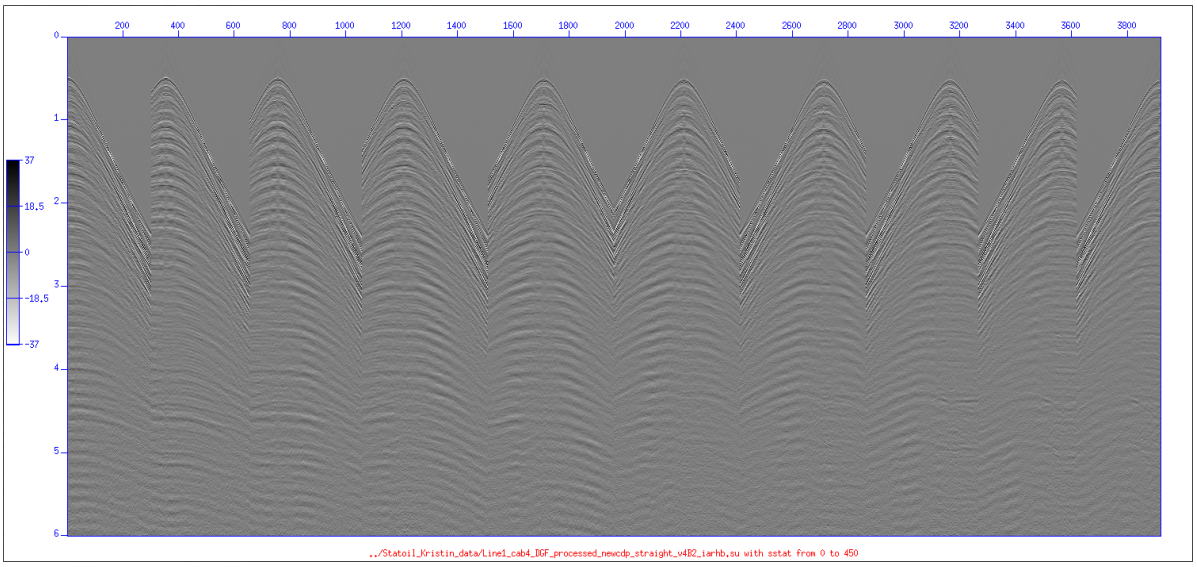

Figure 89: *Kristin P at 25m: Select blocks. Shot stations 0–450 (by 50) of 451.*

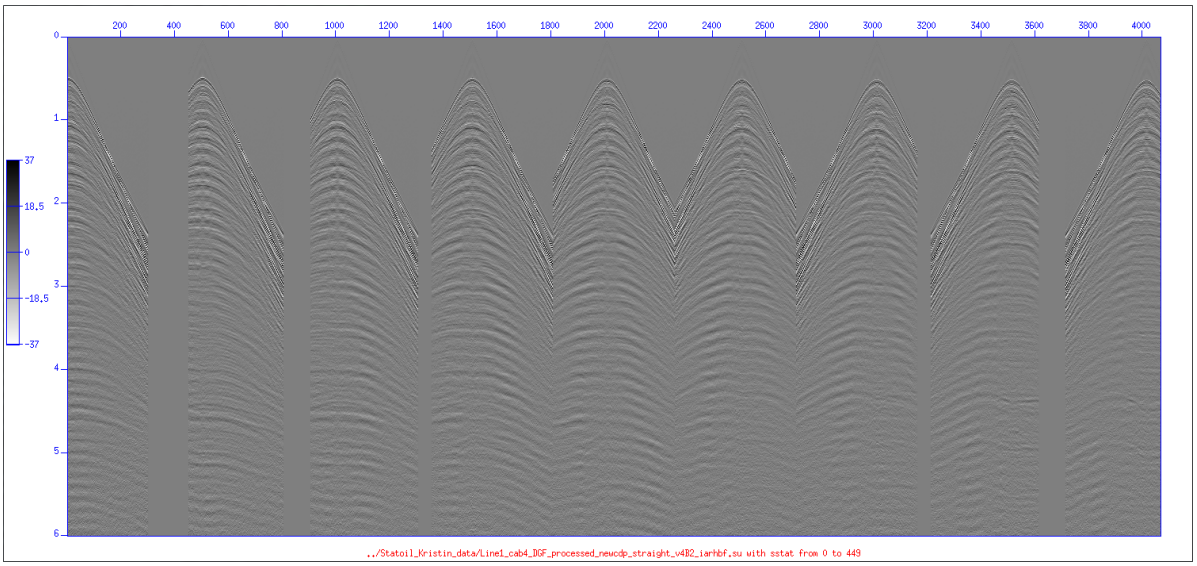

Figure 90: *Kristin P at 25m: Fill shots with all required offsets. Shot stations 0–400 (by 50) of 450.*

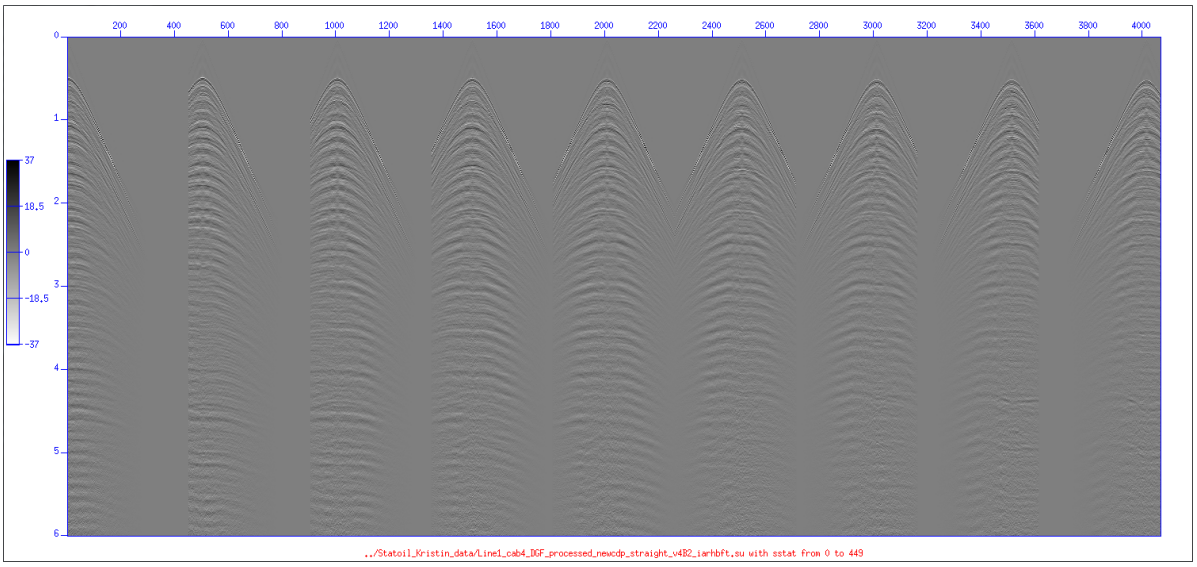

Figure 91: *Kristin P at 25m: Taper to smooth the transition from the original data to the padded null traces. Shot stations 0–400 (by 50) of 450.*

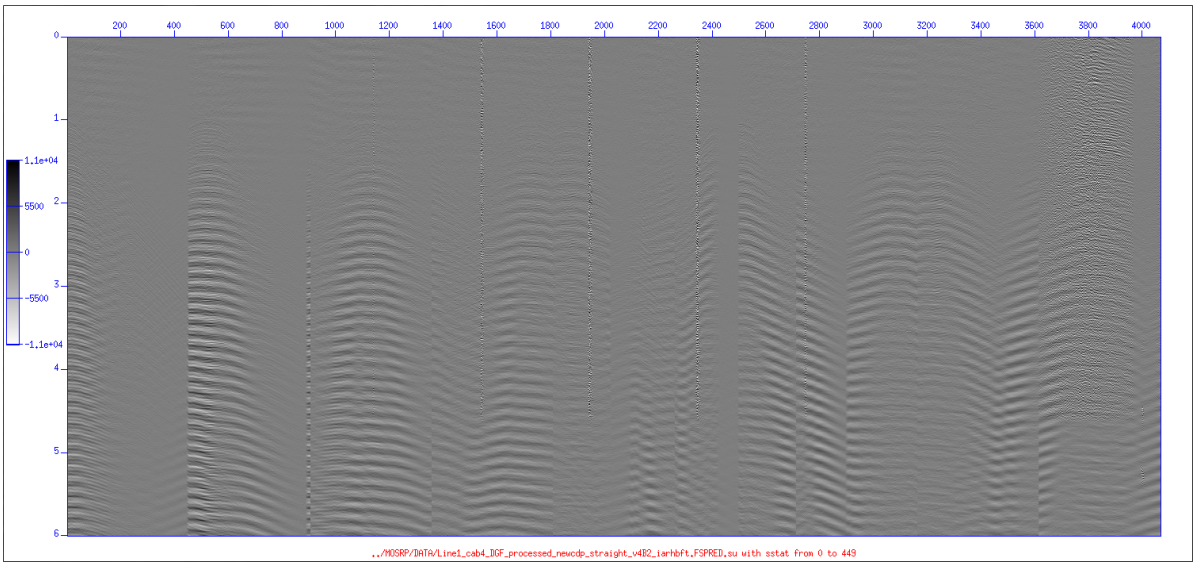

Figure 92: *Kristin P at 25m: Output of the free-surface multiple code. Shot stations 0–400 (by 50) of 450.*

J.6 Field data with preprocessing

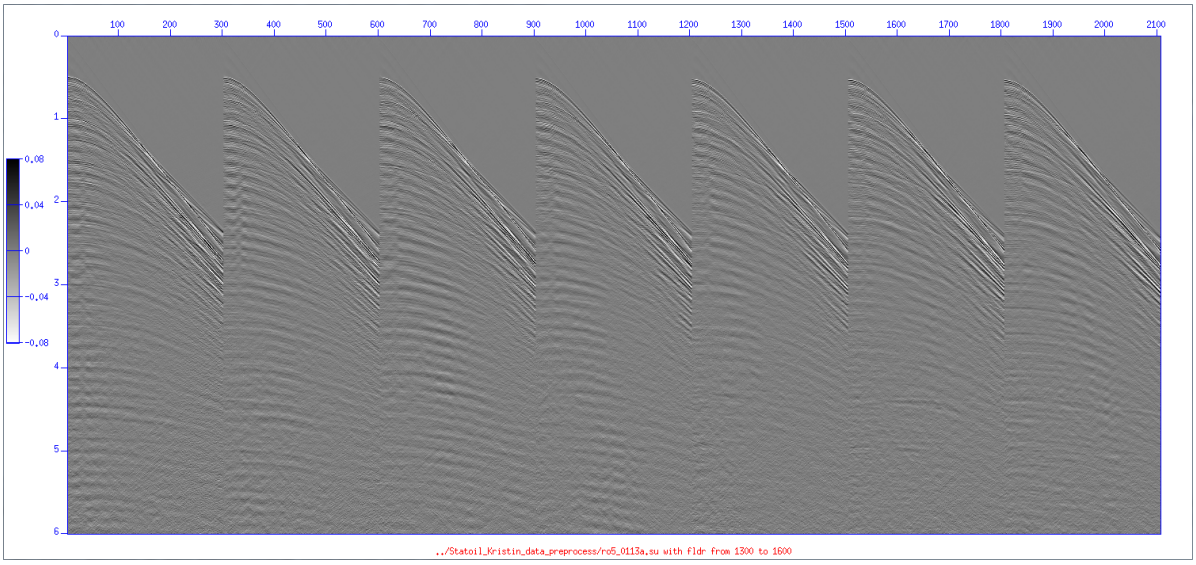

Figure 93: *Receiver deghosted Kristin P at 15m: Shots 1300–1600 (by 50) of 694.*

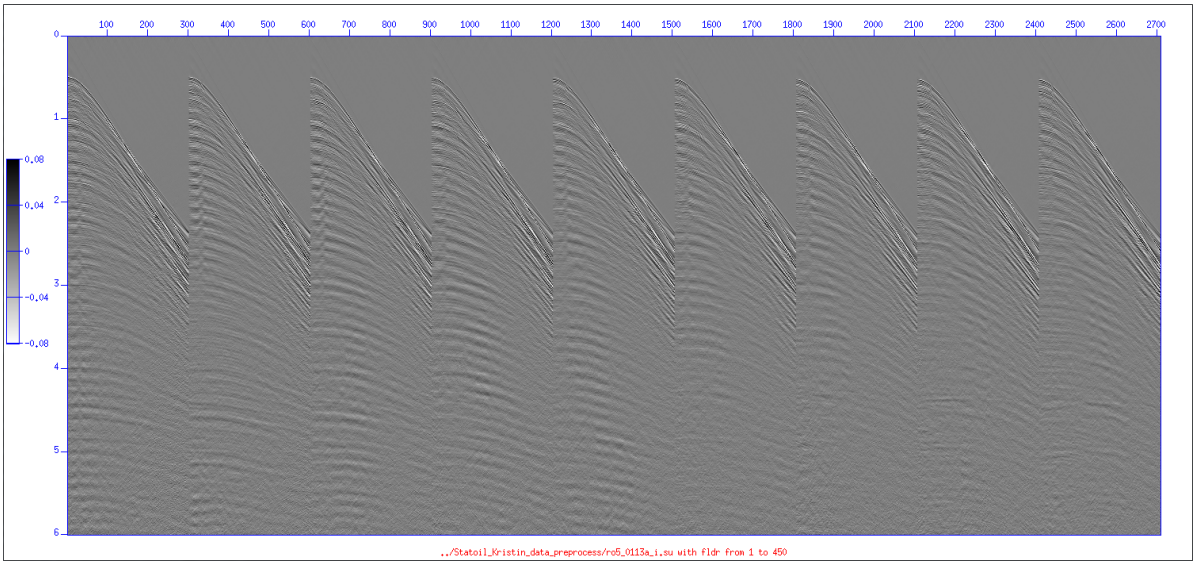

Figure 94: *Receiver deghosted Kristin P at 15m: Interpolate shots so that the distance between shots = distance between receivers. Shots 1–401 (by 50) of 450.*

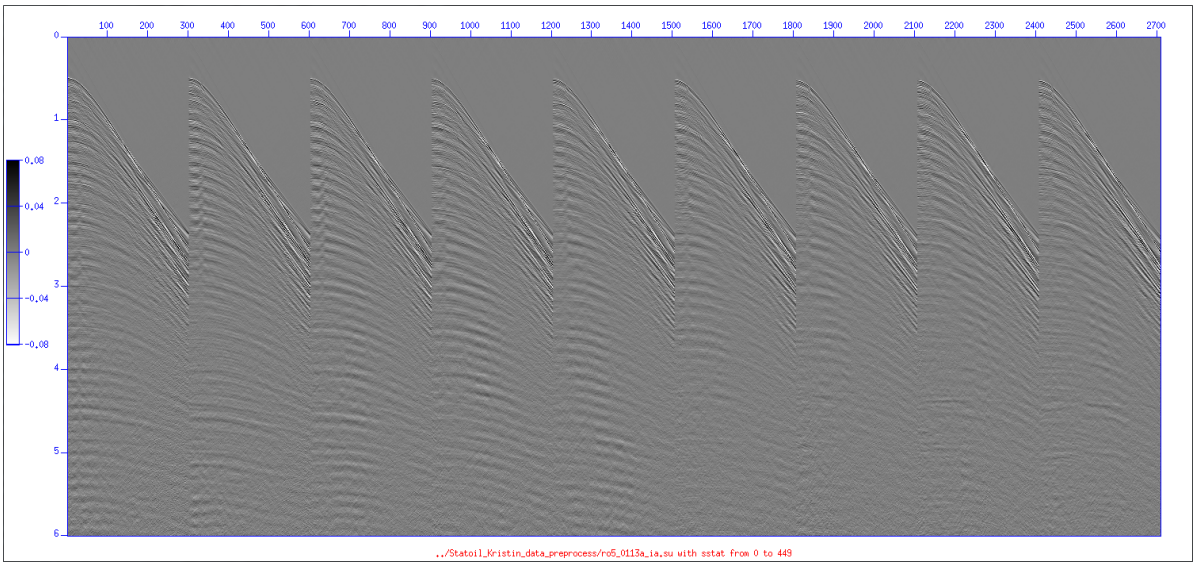

Figure 95: *Receiver deghosted Kristin P at 15m: Assign station numbers to sources and receivers. Shot stations 0–400 (by 50) of 450.*

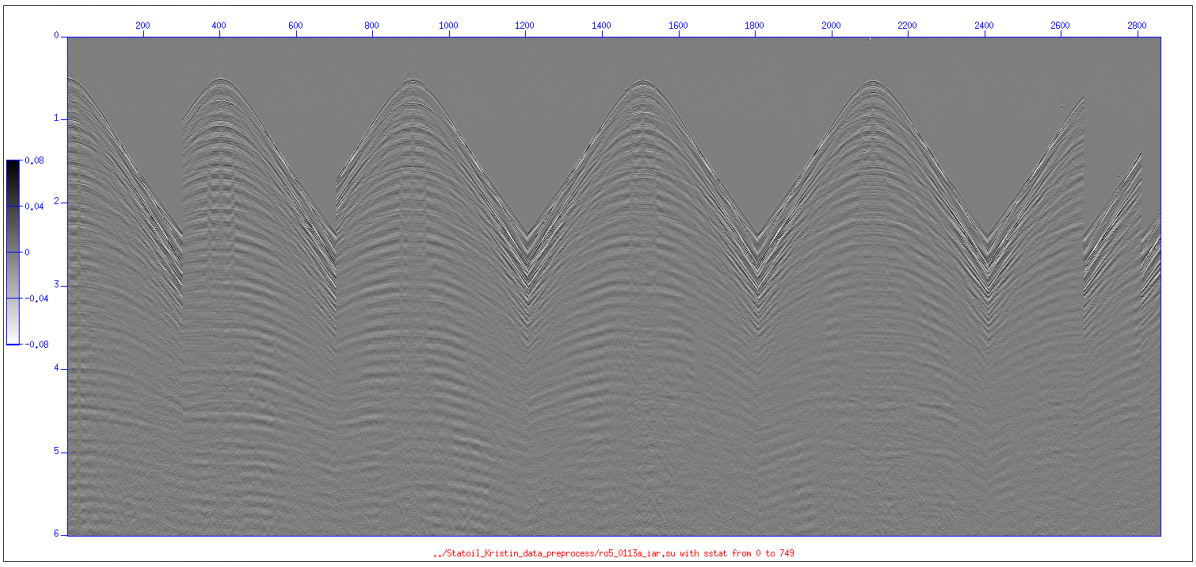

Figure 96: *Receiver deghosted Kristin P at 15m: Use reciprocity between sources and receivers to compute the opposite side of shots, i.e., convert one-sided data to split-spread data. Shot stations 0–700 (by 100) of 749.*

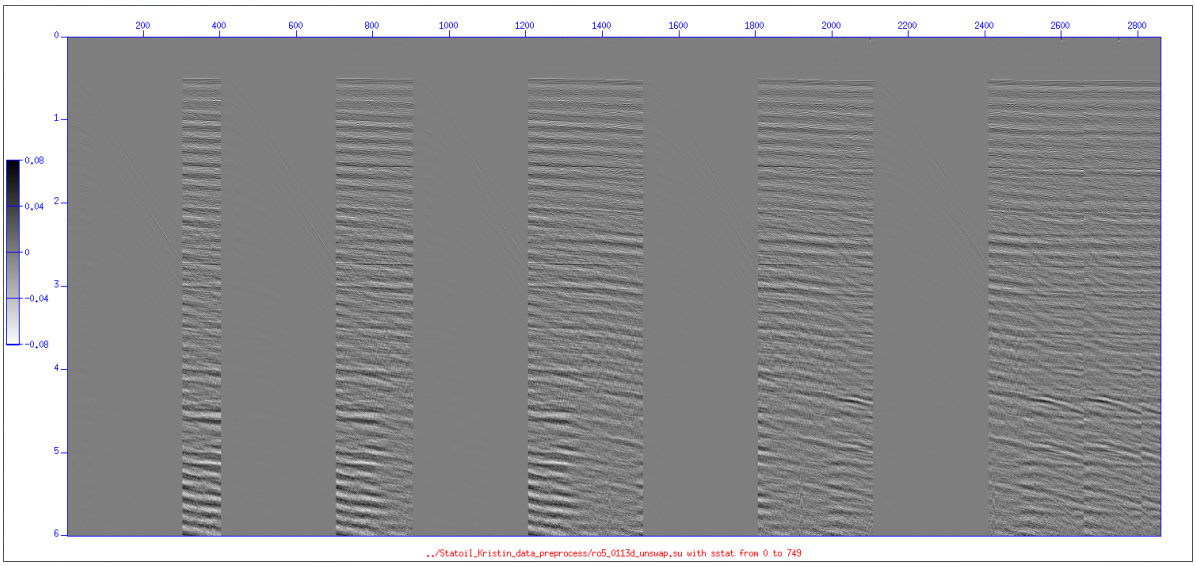

Figure 97: *Source and receiver deghosted Kristin P at 15m: Shot stations 0–700 (by 100) of 749.*

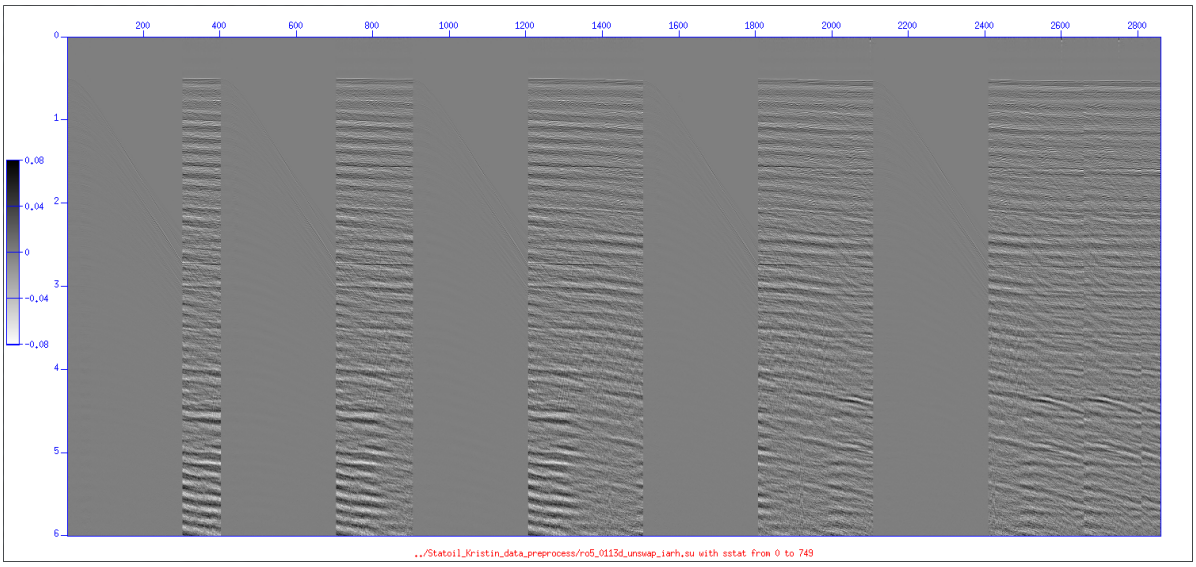

Figure 98: *Source and receiver deghosted Kristin P at 15m: Replace source and receiver locations (sx and gx) with source and receiver stations (sstat and gstat) and make sy = gy = 0. Shot stations 0–700 (by 100) of 749.*

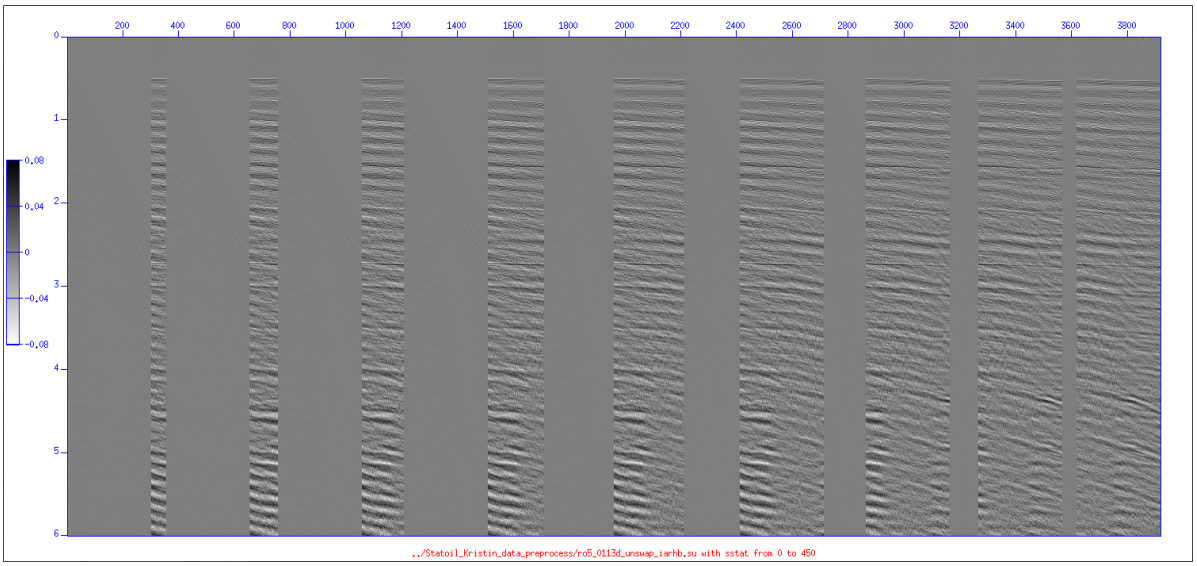

Figure 99: *Source and receiver deghosted Kristin P at 15m: Select blocks. Shot stations 0–450 (by 50) of 451.*

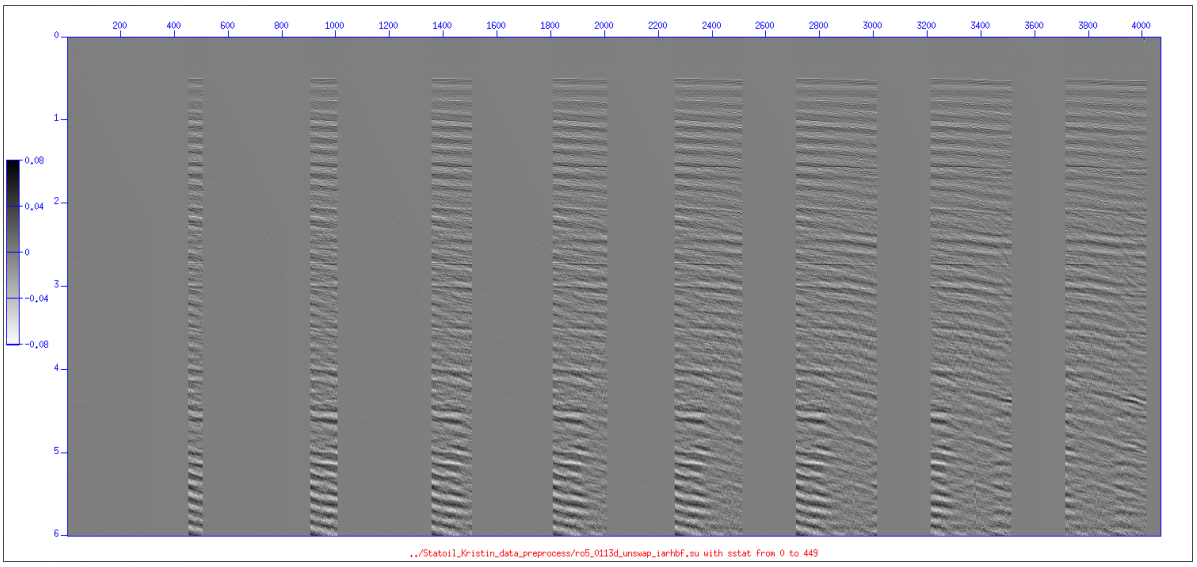

Figure 100: *Source and receiver deghosted Kristin P at 15m: Fill shots with all required offsets. Shot stations 0–400 (by 50) of 450.*

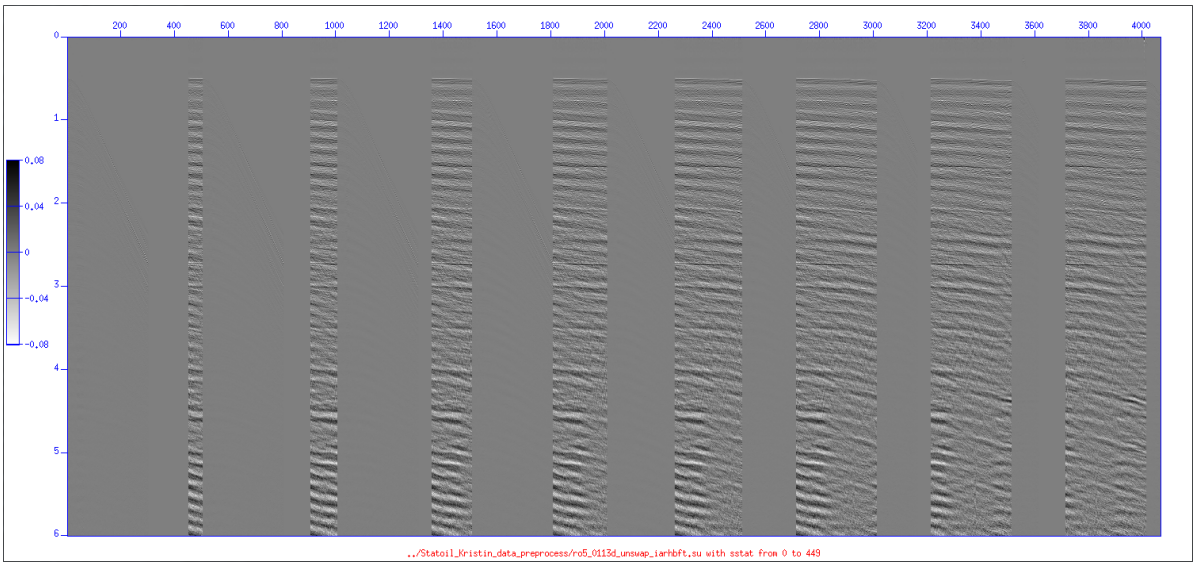

Figure 101: *Source and receiver deghosted Kristin P at 15m: Taper to smooth the transition from the original data to the padded null traces. Shot stations 0–400 (by 50) of 450.*

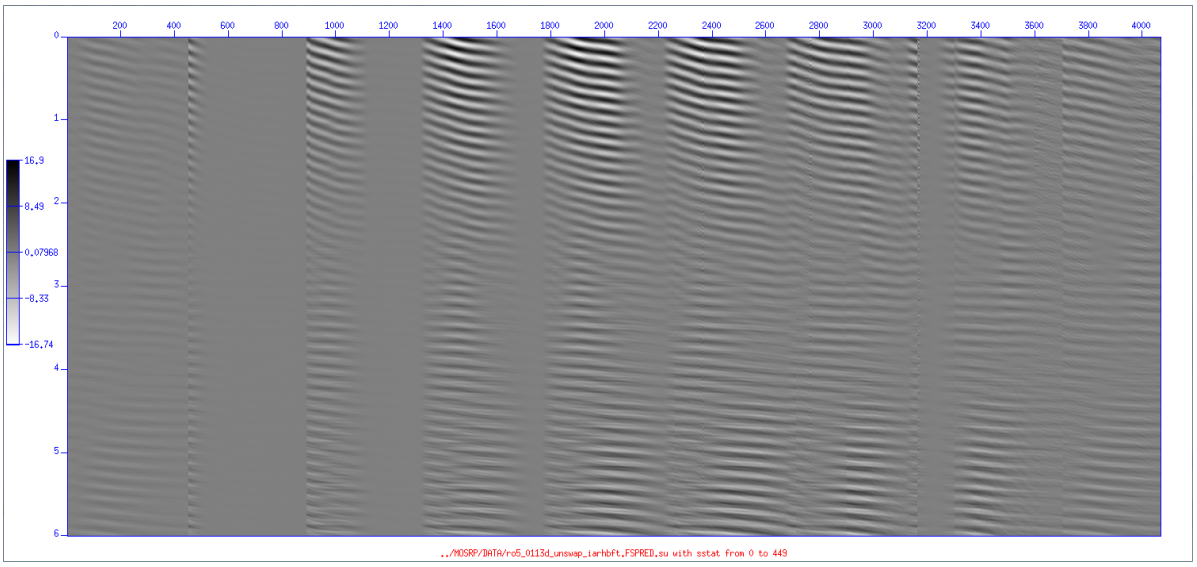

Figure 102: *Source and receiver deghosted Kristin P at 15m: Output of free-surface-multiple code. Shot stations 0–400 (by 50) of 450.*

More work is needed here because of the problem mentioned in section 6.5.

K Isis compute cluster

- 13 AMD Opteron nodes each with 2 dual-core processors and 4 GB of shared memory
- 9 $\frac{1}{2}$ Intel Xeon nodes each with 2 single core processors and 2.5 GB of shared memory
- 14 TB of disk space (expanded from 2 TB)

References

Abramowitz, Milton and Irene A. Stegun, editors. *Handbook of Mathematical Functions with Formulas, Graphs, and Mathematical Tables*. Available online at http://www.math.sfu.ca/~cbm/aands/frameindex.htm. New York: Dover, 1965.

Born, Max and Emil Wolf. *Principles of Optics: Electromagnetic Theory of Propagation, Interference, and Diffraction of Light*. 2nd (revised) edition. New York: The MacMillan Company, 1964.

Carvalho, P. M. *Free-surface multiple reflection elimination method based on nonlinear inversion of seismic data*. PhD thesis, Universidade Federal da Bahia, 1992. In Portuguese.

Ferreira, Andre. Internal multiple removal in offshore Brazil seismic data using the inverse scattering series. Master's thesis, University of Houston, 2011.

Jackson, J. D. *Classical Electrodynamics*. Third edition. New York: John Wiley & Sons, Inc., 1999.

Li, Xu. *I.- MULTI-PARAMETER DEPTH IMAGING USING THE INVERSE SCATTERING SERIES; II.- MULTI-COMPONENT DIRECT NON-LINEAR INVERSION FOR ELASTIC EARTH PROPERTIES USING THE INVERSE SCATTERING SERIES;*. PhD thesis, University of Houston, 2011.

Mayhan, James D., Paolo Terenghi, Arthur B. Weglein, and Nizar Chemingui. "Green's theorem derived methods for preprocessing seismic data when the pressure P and its normal derivative are measured." *81st Annual International Meeting, SEG, Expanded Abstracts*. Ranked by SEG "in the top 31 papers presented at the San Antonio meeting", Society of Exploration Geophysicists, 2011, 2722–2726.

Mayhan, James D., Arthur B. Weglein, and Paolo Terenghi. "First application of Green's theorem derived source and receiver deghosting on deep water Gulf of Mexico synthetic (SEAM) and field data." *82nd Annual International Meeting, SEG, Expanded Abstracts*. . Submitted. Society of Exploration Geophysicists, 2012.

Mayhan, James D., Arthur B. Weglein, and Paolo Terenghi. "Preprocessing marine seismic data with Green's theorem." *M-OSRP 2011 Annual Meeting*. In press, 2012.

Morse, P. M. and H. Feshbach. *Methods of theoretical physics*. New York: McGraw-Hill Book Co., 1953.

Orfanidis, S. J. *Electromagnetic Waves and Antennas*. http://www.ece.rutgers.edu/~orfanidi/ewa/. Distributed via url, 2008.

Ramírez, A. C. *I. - Inverse scattering subseries for removal of internal multiples and depth imaging primaries; II. - Green's theorem as the foundation of interferometry and guiding new practical methods and applications*. PhD thesis, University of Houston, 2007.

Ramírez, Adriana Citlali and Arthur B. Weglein. "Green's theorem as a comprehensive framework for data reconstruction, regularization, wavefield separation, seismic interferometry, and wavelet estimation: a tutorial." *Geophysics* 74 (November-December 2009): W35–W62.

SEG Advanced Modeling Corporation (SEAM), The. The SEG Advanced Model. Technical report, Society of Exploration Geophysicists, 2011. http://www.seg.org/resources/research/seam.

Spiegel, Murray R. *Mathematical Handbook of Formulas and Tables*. New York: McGraw-Hill Book Co., 1968.

Wang, Zhiqiang, Arthur B. Weglein, James D. Mayhan, Paolo Terenghi, and Christian Rivera. "Green's theorem derived deghosting: fundamental analysis, numerical test results, and impact on ISS free-surface multiple elimination." *82nd Annual International Meeting, SEG, Expanded Abstracts*. . Submitted. Society of Exploration Geophysicists, 2012.

Weglein, A. B., F. V. Araújo, P. M. Carvalho, R. H. Stolt, K. H. Matson, R. T. Coates, D. Corrigan, D. J. Foster, S. A. Shaw, and H. Zhang. "Inverse Scattering Series and Seismic Exploration." *Inverse Problems* 19 (2003): R27–R83.

Weglein, A. B., R. H. Stolt, and J. D. Mayhan. "Reverse-time migration and Green's theorem: Part I — The evolution of concepts, and setting the stage for the new RTM method." *Journal of Seismic Exploration* 20 (February 2011): 73–90.

Weglein, A. B., R. H. Stolt, and J. D. Mayhan. "Reverse time migration and Green's theorem: Part II — A new and consistent theory that progresses and corrects current RTM concepts and methods." *Journal of Seismic Exploration* 20 (May 2011): 135–159.

Weglein, Arthur B. and Bruce G. Secrest. "Wavelet estimation for a multidimensional acoustic earth model." *Geophysics* 55 (July 1990): 902–913.

Weglein, Arthur B., S. .A. Shaw, K. H. Matson, J. L. Sheiman, R. H. Stolt, T. H. Tan, A. Osen, G. P. Correa, K. A. Innanen, Z. Guo, and J. Zhang. "New approaches to deghosting towed-streamer and ocean-bottom pressure measurements." *72nd Annual International Meeting, SEG, Expanded Abstracts*. . Society of Exploration Geophysicists, 2002. 1016–1019.

Zhang, Jingfeng. *Wave theory based data preparation for inverse scattering multiple removal, depth imaging and parameter estimation: analysis and numerical tests of Green's theorem deghosting theory*. PhD thesis, University of Houston, 2007.

Zhang, Jingfeng and Arthur B. Weglein. "Extinction theorem deghosting method using towed streamer pressure data: analysis of the receiver array effect on deghosting and subsequent free surface multiple removal." *75th Annual International Meeting, SEG, Expanded Abstracts*. . Volume 24 . Society of Exploration Geophysicists, 2005. 2095–2098.

Zhang, Jingfeng and Arthur B. Weglein. "Application of extinction theorem deghosting method on ocean bottom data." *76th Annual International Meeting, SEG, Expanded Abstracts*. . Volume 25 . Society of Exploration Geophysicists, 2006. 2674–2678.

Incorporating source and receiver arrays in the Inverse Scattering Series free-surface multiple elimination algorithm: theory and examples that demonstrate impact

J. Yang and A. B. Weglein

May 25, 2012

Abstract

In towed marine acquisition, the source arrays that are commonly used exhibit directivity in take-off angle. Directivity is an issue when we are removing or attenuating multiples. In seismic processing, it is essential that we characterize the source array's effect on any seismic processing method. Removing free-surface multiples is a crucial step before internal multiple attenuation/elimination, imaging and inversion. The effectiveness of the free-surface multiple elimination method directly affects the performance of later operations. A new method is proposed for dealing with source array data and is intended to improve the accuracy of predicted multiples. It modifies and extends the current inverse scattering series (ISS) free-surface multiple elimination (FSME) algorithm (Carvalho, 1992; Weglein et al., 1997, 2003) from an isotropic point source to a source array by incorporating an angle-dependent source signature. The modified FSME method is tested on simple 1D acoustic models with a 1D source arrays, and the results indicate that the new method predicts more accurate and encouraging results than does the current FSME algorithm.

1 Introduction

In seismic exploration, a common sequence of data processing is source wavelet estimation, deghosting, free-surface multiple elimination, internal multiple attenuation/removal, imaging, and inversion. The order of these processing steps is important because the performance of the later operations could be affected by the former ones. As one of the crucial steps for imaging and inversion, multiple removal is a classic long-standing problem in marine exploration seismology.

Various methods (e.g., Verschuur et al., 1992; Weglein et al., 1997; Berkhout and Verschuur, 1999; Dragoset et al., 2008) have been developed to either attenuate or eliminate free-surface multiples, which are dominant in the marine cases, especially for the case in which the water bottom has a high velocity contrast. In spite of great efforts in this area, removing multiples continues to be a challenging task in seismic data processing. As we know, if the multiples are not removed, they can be misinterpreted as primaries or can interfere with them.

Frequently there are noticeable residual multiples remaining in the final migration image. There are numerous causes for these residual multiples. First, the predicted multiples are not accurate enough because of insufficient data acquisition, or the directivity of the source array. Second, subsequent subtraction techniques are too conservative to preserve weak primary reflections. Third, the prediction and removal of internal multiples have not yet become routine. These types of residual multiples are commonly found in shallow marine or land data. The residual multiples presented in the final migration images can make the subsequent seismic interpretation work harder, and in some cases may lead to incorrect interpretation. For example, in the Gulf of Mexico, these residual multiples can be mistakenly interpreted as subsalt primary reflections and can also lead to inaccurate salt-body definition.

Hence, effective demultiple algorithms are required in marine seismic data processing. The inverse scattering series (ISS) free-surface multiple elimination method is an important multidimensional free-surface demultiple method. It does not require any subsurface information and most importantly it preserves primary energy (e.g., Carvalho, 1992; Araújo, 1994; Weglein et al., 1997). A crucial assumption in this method, however, is that the source is an isotropic point source, i.e., there is no variation of amplitude or phase with take-off angle. In practice, the source array is widely employed in marine seismic exploration to increase the power of the source, broaden the bandwidth and cancel the random noise. The source array is usually designed to make its signature short and sharp in the vertical-downward direction and to render its spectrum smooth and broad over the frequency band of interest (Giles and Johnston, 1973; Nooteboom, 1978; Brandsaeter et al., 1979). The large marine air-gun arrays exhibit directivity and produce significant variations of the source signature (Loveridge et al., 1984). The directivity and the variation of the source array have significant effects on the ISS FSME algorithm. Therefore, to improve the accuracy of the predicted multiples, in this report, the FSME algorithm is extended in this report from an isotropic point source to a source array with a radiation pattern.

The report is organized as follows: First, the scattering series is discussed for a general source ρ. Second, the modified ISS FSME algorithm (Yang and Weglein, 2011) is derived. Third, we give some analysis on the modified FSME method. Finally, the testing results are provided and discussed.

2 Scattering theory

The scattering series theory can be derived from two basic differential equations (Weglein et al., 2003), which govern wave propagation in actual medium and reference medium, respectively,

$$LP = \rho \tag{2.1}$$

$$L_0 G_0 = \delta \tag{2.2}$$

where L, L_0 are respectively the differential operators in the actual and reference media. The perturbation V can be defined as $L_0 - L$. G_0 is the Green's function in the reference medium and P is the total wavefield in the actual medium; that wavefield is generated by an arbitrary source distribution ρ.

If we know the reference medium, the reference wavefield, and the perturbation operator, the actual wavefield can be obtained using the forward scattering series; on the other hand, if the reference

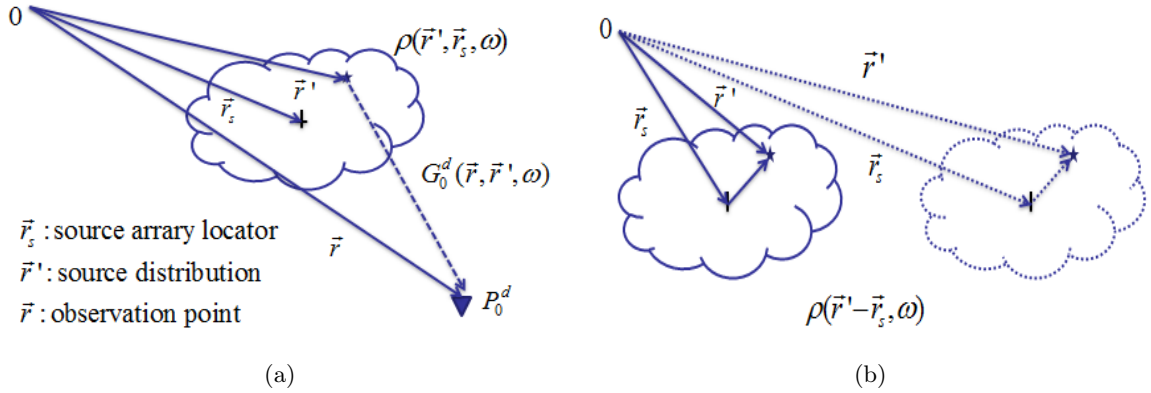

Figure 1: The source array (a) can be described as a function $\rho(\vec{r}', \vec{r}_s, \omega)$, which cares only about the difference between the source array locator $\vec{r}_s$ and the specific air-gun point $\vec{r}'$ when the source is moving (b).

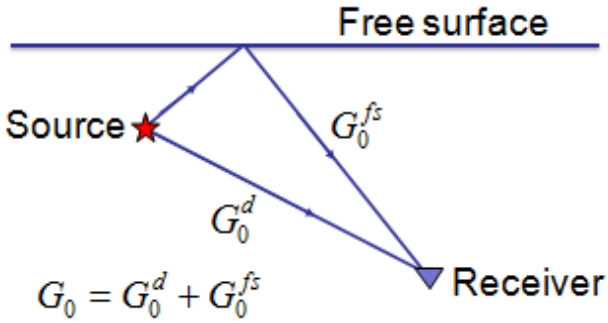

Figure 2: The reference Green's function G_0 consists of two parts: $G_0 = G_0^d + G_0^{fs}$. G_0^d is the direct Green's function and G_0^{fs} is the additional part of the Green's function caused by the presence of the free surface.

medium, the reference wavefield and the actual wavefield are known, the perturbation operator or the earth property can be solved using the inverse scattering series.

On the basis of equations 2.1 and 2.2, the reference wavefield P_0 can be solved as the integral of the causal reference Green's function G_0 over V_s, the whole range occupied by the general source ρ (Morse and Feshbach, 1953), i.e.,

$$P_0(\vec{r}, \vec{r}_s, \omega) = \int_{V_s} d\vec{r}' \rho(\vec{r}', \vec{r}_s, \omega) G_0(\vec{r}, \vec{r}', \omega), \tag{2.3}$$

where $\vec{r}$, $\vec{r}'$ and $\vec{r}_s$ represent, respectively, the observation position, the source distribution and the source array locater, as shown in figure 1(a). Note: P_0 is the response of the reference medium to a general source, which is a superposition of impulsive point sources, while G_0 is an impulse response.

Green's function G_0 consists of two parts: the direct arrival G_0^d and its free-surface reflection G_0^{fs}, shown in figure 2. The reference wavefield also consists of two contributions: the direct reference wavefield P_0^d, and its ghost P_0^{fs}, which propagates from the source up to the free-surface and reflects

down to the receivers:

$$P_0 = P_0^d + P_0^{fs}. \tag{2.4}$$

Thus, the direct reference wavefield P_0^d is expressed as

$$P_0^d(\vec{r}, \vec{r}_s, \omega) = \int_{V_s} d\vec{r}' \rho(\vec{r}', \vec{r}_s, \omega) G_0^d(\vec{r}, \vec{r}', \omega). \tag{2.5}$$

Due to the translational symmetry of the source array, its geometry is invariant with respect to the source array locator $\vec{r}_s$, and the source distribution ρ cares only about the difference between the source array locator $\vec{r}_s$ and the specific air-gun $\vec{r}'$, as shown in figure 1(b), which means that the source distribution ρ doesn't depend on a specific $\vec{r}'$ and $\vec{r}_s$. In other words, for a given source array, the source distribution is the same about the source array locator $\vec{r}_s$. Thus, the source array is only a function of the relative distance to the source array position as $\rho(\vec{r}', \vec{r}_s, \omega) = \rho(\vec{r}' - \vec{r}_s, \omega)$. The direct reference wavefield P_0^d becomes

$$P_0^d(\vec{r}, \vec{r}_s, \omega) = \int d\vec{r}' \rho(\vec{r}' - \vec{r}_s, \omega) G_0^d(\vec{r}, \vec{r}', \omega). \tag{2.6}$$

Note: If the source array reduces to an isotropic point source, the source distribution $\rho(\vec{r}' - \vec{r}_s, \omega)$ becomes $A(\omega)\delta(\vec{r}' - \vec{r}_s)$, where $A(\omega)$ is the point source signature.

When we change the coordinate, $\vec{r}'' = \vec{r}' - \vec{r}_s$, and P_0^d can be rewritten as

$$P_0^d(\vec{r}, \vec{r}_s, \omega) = \int_{V_s} d\vec{r}'' \rho(\vec{r}'', \omega) G_0^d(\vec{r}, \vec{r}'' + \vec{r}_s, \omega).$$

Recalling $\vec{r}''$ as $\vec{r}'$, the direct reference wavefield P_0^d becomes

$$P_0^d(\vec{r}, \vec{r}_s, \omega) = \int_{V_s} d\vec{r}' \rho(\vec{r}', \omega) G_0^d(\vec{r}, \vec{r}' + \vec{r}_s, \omega), \tag{2.7}$$

where $\vec{r}'$ describes the source distribution with respect to $\vec{r}_s$, and $\vec{r}'$ is invariant while the source is moving.

On the other hand, on the basis of Green's theorem, the reference wavefield P_0 can also be obtained by measuring the total wavefield P and its normal derivative (Appendix A) as

$$P_0(\vec{r}, \vec{r}_s, \omega) = \int_{m.s.} dS' \, \hat{n} \cdot [P(\vec{r}', \vec{r}_s, \omega) \nabla' G_0(\vec{r}', \vec{r}, \omega) - G_0(\vec{r}', \vec{r}, \omega) \nabla' P(\vec{r}', \vec{r}_s, \omega)]. \tag{2.8}$$

Here we choose that (1) the reference medium is a half space of air over a half space of water, (2) the source distribution is located between the measurement surface and the free surface (i.e., outside V), and (3) the observation position $\vec{r}$ is in the volume V. Using the deghosting algorithm (Zhang, 2007) that is based on Green's theorem, the reference wavefield P_0 can be deghosted to the direct reference wavefield P_0^d. Jim Mayhan, a fellow graduate student in our group, can provide the numerical P_0 and P_0^d for the FSME algorithm.

3 ISS FSME algorithm for the source array

We assume that the source array is invariable from one shot to the next and only varies along the horizontal axis. The source array locates at the same depth ϵ_s below the free surface. The direct reference wavefield P_0^d for a 2D case can be expressed as

$$P_0^d(x, z, x_s, \epsilon_s, \omega) = \int dx' \rho(x', \epsilon_s, \omega) G_0^d(x, z, x' + x_s, \epsilon_s, \omega), \tag{3.1}$$

where (x, z) and (x_s, ϵ_s) are the observation point and source point, respectively. The term x' is the lateral variation of the source with respect to x_s.

Using the bilinear form of Green's function and Fourier transforming over x_s, we obtain the relationship between ρ and P_0^d (Appendix B) as

$$P_0^d(x, z, k_s, \epsilon_s, \omega) \quad = \quad \rho(k_s, \omega) \frac{e^{iq_s|z-\epsilon_s|}}{2iq_s} e^{ik_s x}, \tag{3.2}$$

where $k_s^2 + q_s^2 = \omega^2/c_0^2$ and $z > \epsilon_s$. Equation 3.2 is also equivalent to

$$P_0^d(k, z, x_s, \epsilon_s, \omega) \quad = \quad \rho(k, \omega) \frac{e^{iq|z-\epsilon_s|}}{2iq} e^{ikx_s} \tag{3.3}$$

after Fourier transforming over x. Therefore, the general source signature, in other words, the angle-dependent source signature $\rho(k, \omega)$, can be calculated theoretically from the direct reference wavefield P_0^d in the f-k domain, where the variable k represents the amplitude variations of the general source signature with angles. To incorporate the source angle dependence, Ikelle et al. (1997) also proposed a similar quantity $A(k, \omega)$, which is the inverse source wavelet and can be solved by the energy minimization criterion.

The FSME algorithm for a source array with a radiation pattern (Yang and Weglein, 2011) is derived by following the procedure of the FSME algorithm (Carvalho, 1992; Weglein et al., 1997, 2003).

The final expression is a series for deghosted and free-surface demultipled data D' in terms of deghosted data D_1' and the angle-dependent source signature $\rho(k, \omega)$, as follows:

$$D_n'(k_g, k_s, \omega) = \frac{1}{i\pi} \int \frac{dk}{\rho(k, \omega)} D_1'(k_g, k, \omega) q e^{iq(\epsilon_g + \epsilon_s)} D_{n-1}'(k, k_s, \omega) \tag{3.4}$$

and

$$D'(k_g, k_s, \omega) = \sum_{n=1}^{\infty} D_n'(k_g, k_s, \omega), \tag{3.5}$$

where k_g, k_s and ω represent the wavenumbers along the source, receiver and temporal frequency axes, respectively. $\rho(k, \omega)$ is the angle-dependent source signature, which is represented as a function of wavenumber k and temporal frequency ω in the f-k domain. The terms ϵ_g and ϵ_s are the depth of the receiver and the source below the free surface, respectively, and q is the obliquity factor given by:

$$q = sgn(\omega) \sqrt{\frac{\omega^2}{c_0^2} - k^2}. \tag{3.6}$$

Using the free-surface multiple removal subseries, the FSME algorithm is extended and derived by incorporating the angle-dependent source signature $\rho(k,\omega)$, which includes the effects of the source directivity. The extended FSME method requires the deghosted data D_1' and the angle-dependent source signature $\rho(k,\omega)$ but does not need any subsurface information.

The details of the derivation for equation 3.4 can be found in Appendix C.

4 Analysis

First, the extended FSME algorithm should be consistent with the current FSME algorithm (Carvalho, 1992; Weglein et al., 1997, 2003) during the time that the source array reduces to a point source. When the source array reduces to an isotropic point source $A(\omega)$, the source distribution $\rho(\vec{r}' - \vec{r}_s, \omega)$ becomes $A(\omega)\delta(\vec{r}' - \vec{r}_s)$ and the direct reference wavefield P_0^d becomes $A(\omega)G_0^d$. Thus, the recursive expression equation 3.4 reduces to

$$D_n'(k_g, k_s, \omega) = \frac{1}{i\pi A(\omega)} \int dk D_1'(k_g, k, \omega) q e^{iq(\epsilon_g + \epsilon_s)} D_{n-1}'(k, k_s, \omega), \tag{4.1}$$

which is exactly the current FSME algorithm.

Second, if all the air guns are at the same depth and are identical, meaning that they have the identical source signature $A(\omega)$, the general source signature $\rho(k,\omega)$ in equation 3.3 becomes

$$\rho(k,\omega) = A(\omega) \sum_{x'=-a}^{a} e^{-ikx'}, \tag{4.2}$$

where we assume that the range of the source array is from $-a$ to a. For example, $\rho(k,\omega)$ can be expressed analytically for 3 point sources as,

$$\rho(k,\omega) = A(\omega) \sum_{x'=-a}^{a} e^{-ikx'} = A(\omega)(1 + 2\cos(ka)). \tag{4.3}$$

5 Numerical tests for synthetic data

For a source array that varies laterally with identical source signatures, the modified FSME algorithm is tested on basis of equation 3.4. The model has only one reflector, i.e., the water bottom, which is shown in figure 3(a).

5.1 Numerical tests for source array data

Using two different source arrays, one with 5 point sources and the other with 9 point sources, as shown in figure 3(b), the data sets are generated by the Cagniard-de Hoop method. Only the primary and free-surface multiples are generated, so we don't need removing the ghosts. The advantage of the Cagniard-de Hoop method is that we can accurately calculate any specific event we

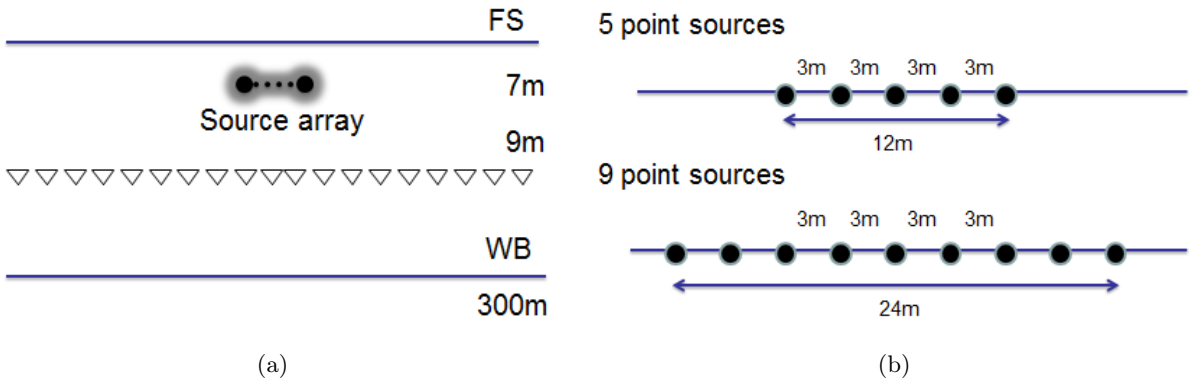

(a) (b)

Figure 3: (a) One-dimensional acoustic constant-density medium. The depths of source, receiver, and water bottom are 7m, 9m and 300m, respectively. The trace interval is 3m. (b) Two source arrays are applied in the model, one with 5 point sources and another with 9 point sources. The ranges of the two source arrays are 12m and 24m, respectively.

are interested in, so that we can compare it with the results predicted by our current and modified FSME algorithms.

Next the free-surface multiples are predicted by the current FSME algorithm and the modified FSME algorithm, respectively, for both data sets. After the predicted free-surface multiples have been subtracted from the data sets, it can be seen that there are still some residual multiples when we use the current FSME algorithm. However, for the modified FSME algorithm, the multiples are removed completely, as shown in figure 4. Comparing figures 4(b) and 4(e), we conclude that the larger the range of the source array is, the more residual multiples there are.

For details, we pick four traces from the source array data with 9 point sources and the predicted free-surface multiples due to both the current and modified FSME algorithms. Here, only the first-order free-surface multiples are compared with the exact calculated multiples. In figure 5(a), at zero offset, both the amplitude and phase of the predicted first-order free-surface multiple are accurate; at large offsets, the predicted free-surface multiple's phase is correct, while its amplitude has some errors. In figure 5(b), the amplitude and phase of the predicted first-order free-surface multiple are very accurate at both zero and large offsets.

5.2 Numerical tests for receiver array data

Up until now, all the tests have been based on point receiver data. A receiver array is a set of receivers whose records are summed together so that the signal can be enhanced and the random noise suppressed. Since this summation will inevitably damage the actual wavefield, it is important to characterize its effect on any wave-theory method. We use the same model as in figure 3(a), and an isotropic point source is used to generate the data. Every 5 receivers are summed together with equal weights to produce a new receiver, as shown in figure 6.

For the receiver array data, both the current and modified FSME algorithms are applied to predict the free-surface multiples. After removing the free-surface multiple, there are residual multiples

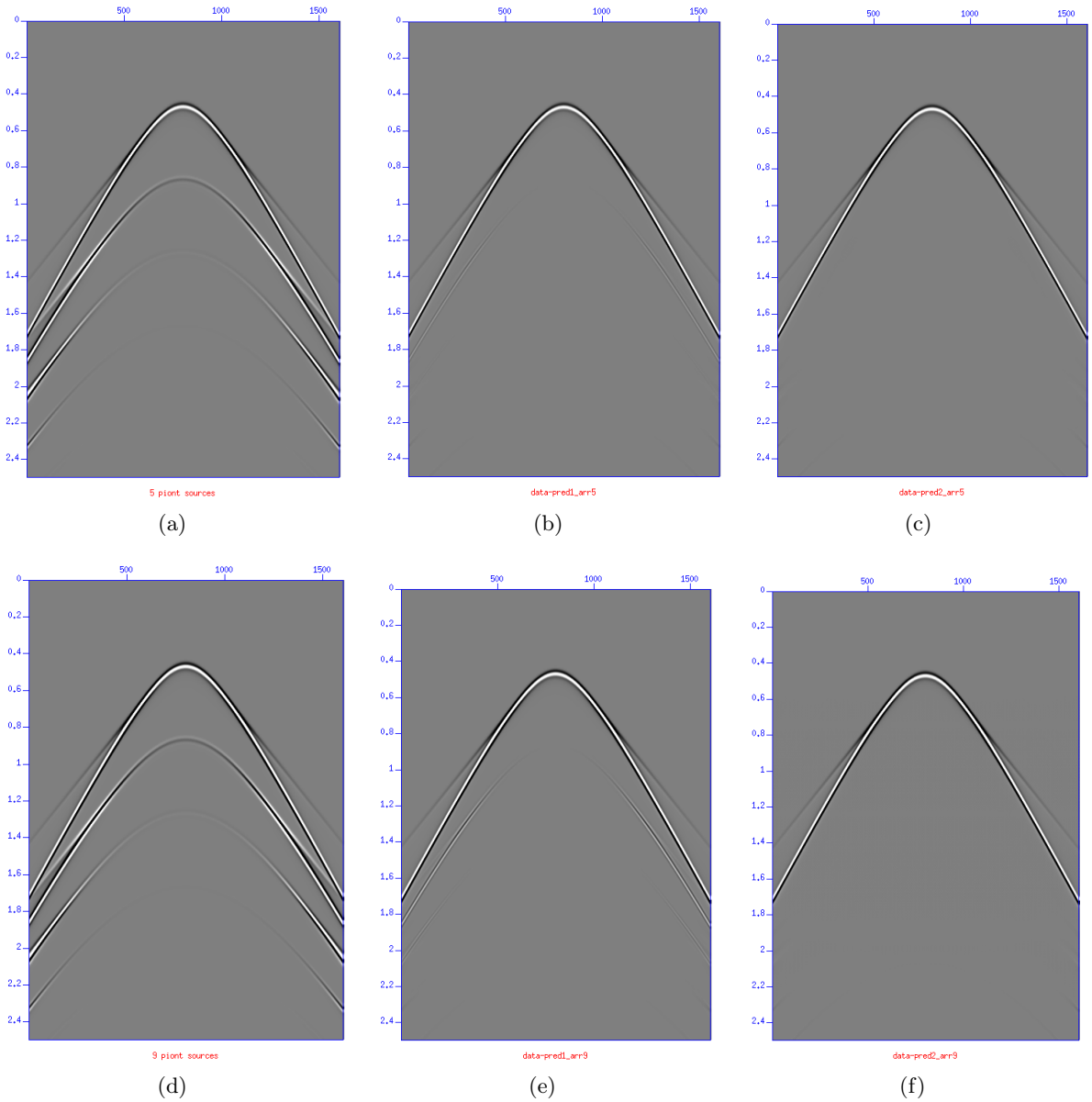

(a) (b) (c)

(d) (e) (f)

Figure 4: For source arrays with 5 and 9 point sources: (a)&(d) the data sets; (b)&(e) following free-surface multiple removal using the current FSME algorithm, there are some residual multiples; (c)&(f) following free-surface multiple removal using the modified FSME algorithm, all the multiples are completely eliminated.

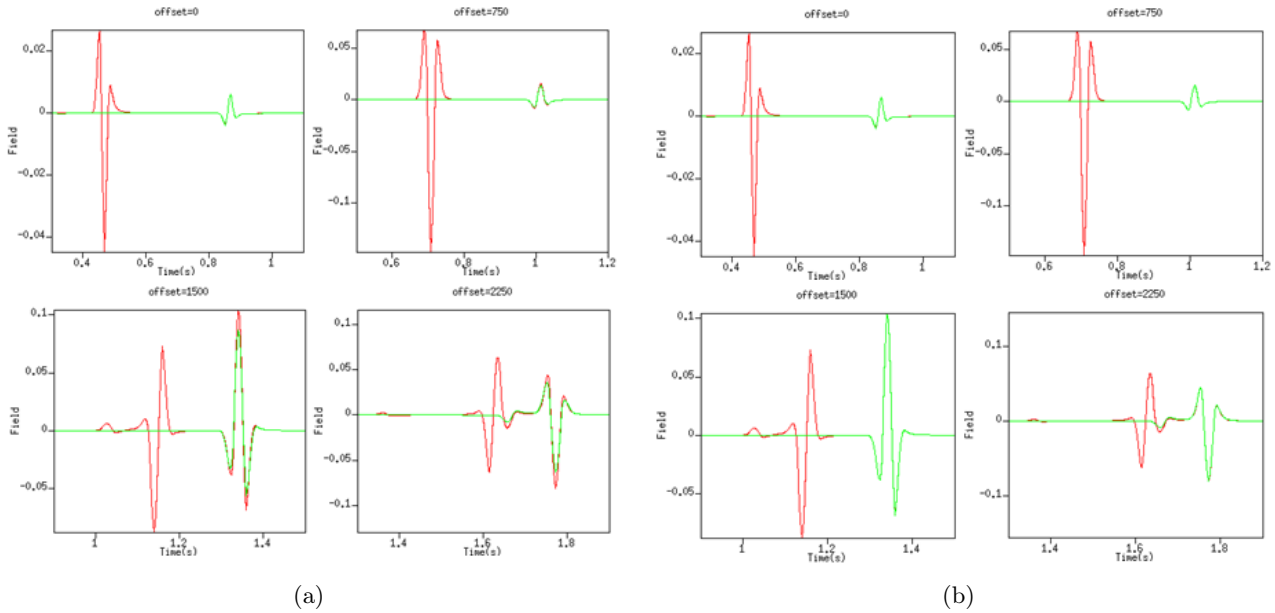

(a) (b)

Figure 5: Red line: The exact calculated first-order free-surface multiple; Green line: (a) first-order free-surface multiple predicted by the current FSME algorithm and (b) first-order free-surface multiple predicted by the modified FSME algorithm.

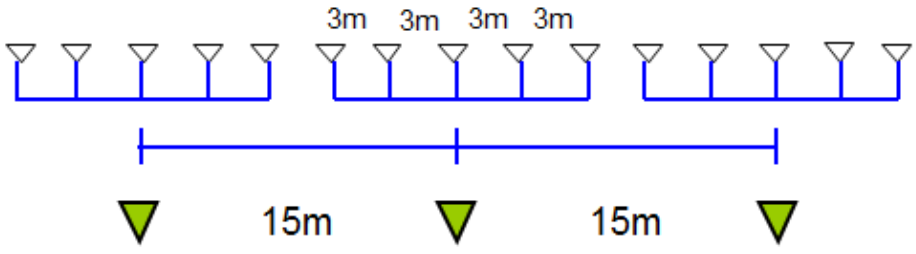

Figure 6: Every 5 receivers are summed together with equal weights to produce one record at the center of the array. The new record interval is 15m.

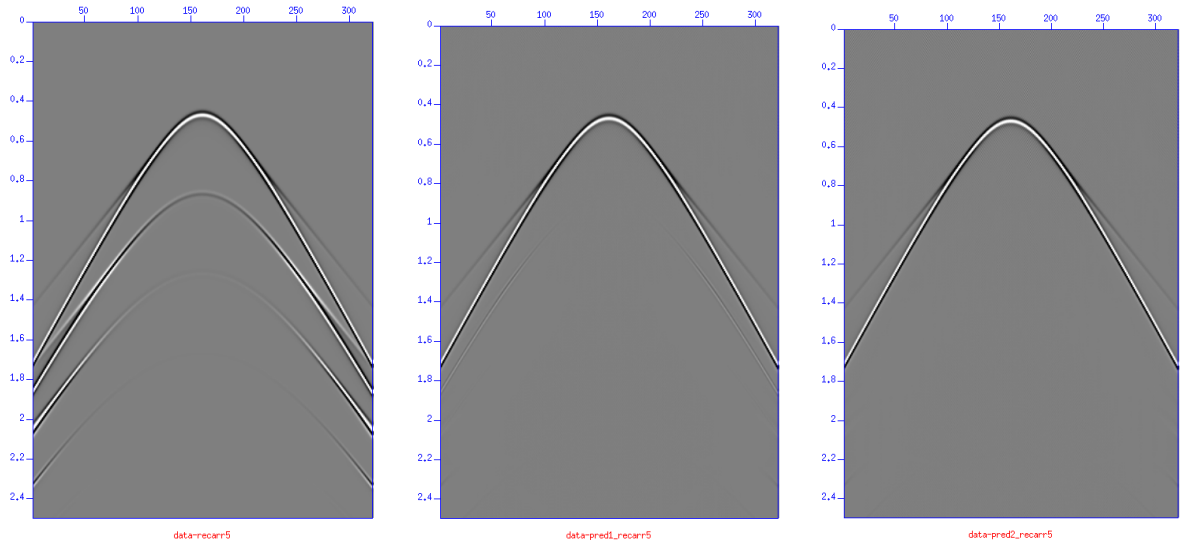

(a) (b) (c)

Figure 7: For a receiver array: (a) the data sets; (b) following free-surface multiple removal using the current FSME algorithm, there are some residual multiples; (c) following free-surface multiple removal using the modified FSME algorithm, all the multiples are completely eliminated.

when we use the current FSME algorithm, while all the multiples are removed completely using the modified FSME algorithm. The testing results are plotted in figure 7. The reason that the modified FSME alogrithm can work for the receiver array data is that the receiver array data and the source array data have the similar configuration.

5.3 Numerical tests for data with source and receiver arrays

The modified FSME method is also tested for data with both source and receiver arrays. Here, we choose the source array data with 9 point sources, and sum every 5 receivers to produce the source-receiver-array data. The data are processed using (a) the current FSME algorithm, and also using the modified FSME algorithms: (b) considering only the source array, (c) considering only the receiver array, and (d) considering both source and receiver arrays. In figure 8, there are some residual multiples in (b), (c) and (d); but all the multiples are removed completely in (e). If we only consider partial array information in the modified algorithm, the results in (c) and (d) are better than in (b), which was processed by the current algorithm. If both source and receiver arrays are considered in the modified algorithm, the result in (e) is better than all other results.

These numerical tests have demonstrated the effectiveness and benefit of the modified FSME algorithm. Use of the current FSME algorithm to remove free-surface multiples leads to many residual multiples, which can make the subsequent seismic interpretation work difficult and in some cases may lead to incorrect interpretation. On the other hand, use of the modified FSME algorithm leads to very accurate results.

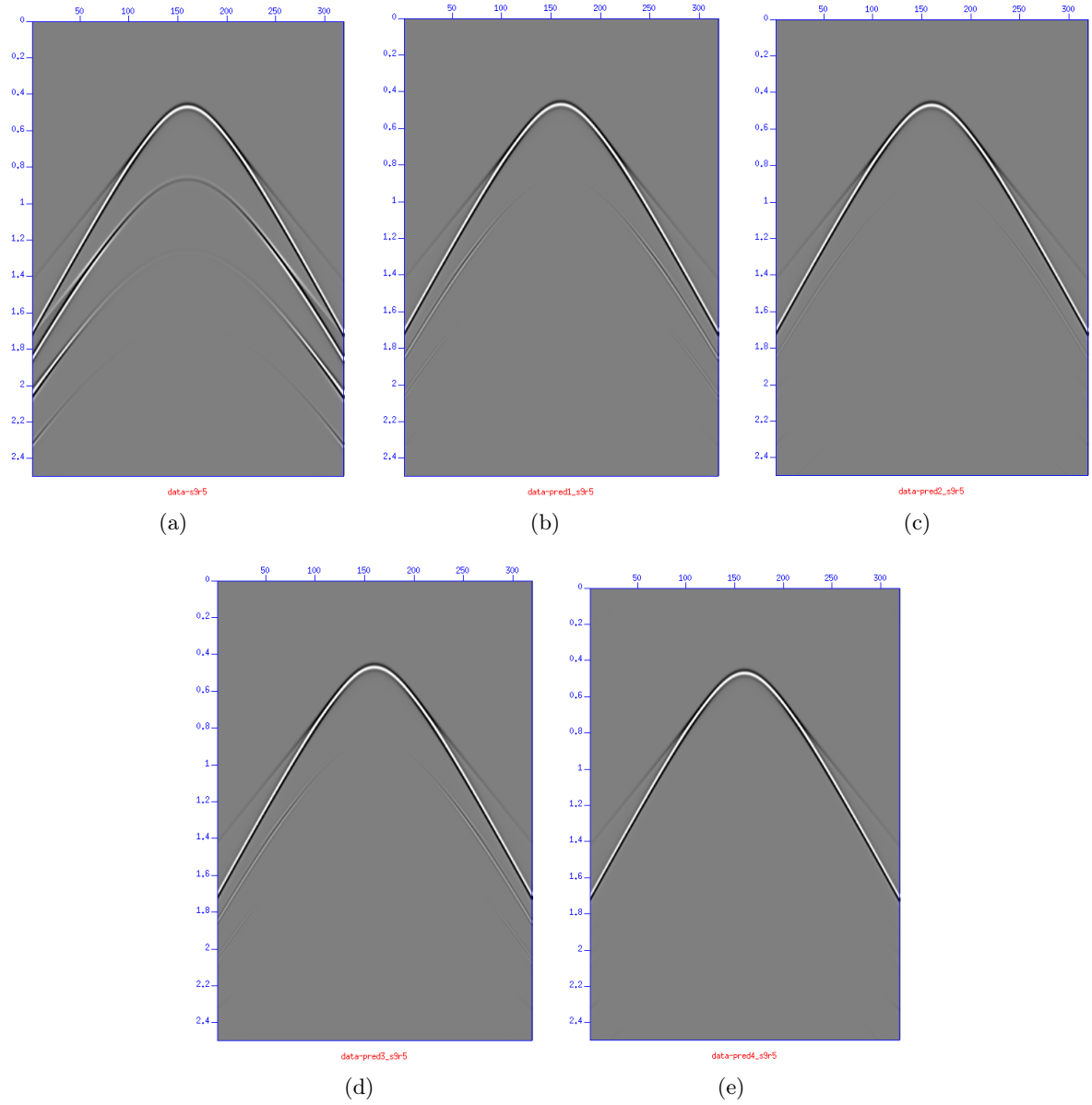

(a) (b) (c)

(d) (e)

Figure 8: Source-receiver array: (a) data sets; following free-surface multiple removal (b) using the current FSME algorithm; and using the modified FSME algorithms (c) considering only the source array, (d) considering only the receiver array, and (e) considering both source and receiver arrays. There are some residual multiples in (b), (c) and (d); but all the multiples are completely eliminated in (e).

6 Conclusions

The modified FSME algorithm is derived by incorporating an angle-dependent source signature $\rho(k,\omega)$, which includes the effects of the source directivity. The wavenumber k describes the amplitude variations with angle in the f-k domain. The modified FSME method requires only the deghosted data and the angle-dependent source signature $\rho(k,\omega)$, without any subsurface information. The modified FSME algorithm is consistent with the current FSME algorithm when the source array reduces to an isotropic point source. The numerical tests for the synthetic data show that the modified FSME algorithm predicts more accurate and encouraging results than the current FSME algorithm produces. The modified FSME algorithm is a multidimensional algorithm, which can be directly extended from 2D to 3D. Therefore, the modified FSME algorithm is a more general and effective multidimensional free-surface multiple elimination method that can deal with a source whether that source is with or without a radiation pattern.

7 Acknowledgements

The first author is grateful to all M-OSRP sponsors for their support of this research and to Di Chang, Jim Mayhan and Lin Tang for their helpful and valuable discussions regarding this research. My special appreciation goes to my advisor, Dr. Arthur Weglein, for his teaching, guidance and patience.

Appendices

A Estimation of reference wavefield P_0

The effective source signature or reference wavefield P_0 is derived in Weglein and Secrest (1990), in which the authors derive two equations: the Lippmann-Schwinger equation and Green's second identity. Comparing the two equations gives an equation for the reference wavefield P_0 as a function of measured data and a reference-medium Green's function.

The acoustic wave equation with constant density for the total field P created by a general source $\rho(\vec{r},\vec{r}_s,t)$ at the effective position $\vec{r}_s$ in frequency domain is

$$\left(\nabla^2+\frac{\omega^2}{c^2(\vec{r})}\right)P(\vec{r},\vec{r}_s,\omega)=\rho(\vec{r},\vec{r}_s,\omega). \tag{A.1}$$

Characterizing $c(\vec{r})$ in terms of c_0 and the variation index of refraction $\alpha(\vec{r})$ gives

$$\frac{1}{c^2(\vec{r})}=\frac{1}{c_0^2}(1-\alpha(\vec{r})). \tag{A.2}$$

Substituting equation A.2 into equation A.1 gives

$$\left(\nabla^2+\frac{\omega^2}{c_0^2}\right)P(\vec{r},\vec{r}_s,\omega)=\rho(\vec{r},\vec{r}_s,\omega)+\frac{\omega^2}{c_0^2}\alpha(\vec{r})P(\vec{r},\vec{r}_s,\omega). \tag{A.3}$$

Converting equation A.3 from a partial differential equation into an integral equation (the Lippmann-Schwinger equation) gives

$$P(\vec{r},\vec{r}_s,\omega)=\int d\vec{r}\,'\rho(\vec{r}\,',\vec{r}_s,\omega)G_0(\vec{r},\vec{r}\,',\omega)+\int_\infty d\vec{r}\,'G_0(\vec{r},\vec{r}\,',\omega)\frac{\omega^2}{c_0^2}\alpha(\vec{r}\,')P(\vec{r}\,',\vec{r}_s,\omega). \tag{A.4}$$

Choosing a causal Green's function G_0^+ in the Lippmann-Schwinger equation gives a causal solution $P(\vec{r},\vec{r}_s,\omega)$:

$$P(\vec{r},\vec{r}_s,\omega)=\int d\vec{r}\,'\rho(\vec{r}\,',\vec{r}_s,\omega)G_0^+(\vec{r},\vec{r}\,',\omega)+\int_\infty d\vec{r}\,'G_0^+(\vec{r},\vec{r}\,',\omega)\frac{\omega^2}{c_0^2}\alpha(\vec{r}\,')P(\vec{r}\,',\vec{r}_s,\omega). \tag{A.5}$$

Substituting P and G_0 into Green's theorem gives

$$\begin{aligned}&\int_V d\vec{r}\,'[P(\vec{r}\,',\vec{r}_s,\omega)\nabla'^2G_0(\vec{r}\,',\vec{r},\omega)-G_0(\vec{r}\,',\vec{r},\omega)\nabla'^2P(\vec{r}\,',\vec{r}_s,\omega)]=\\&\oint_S dS'\,\hat{n}\cdot[P(\vec{r}\,',\vec{r}_s,\omega)\nabla' G_0(\vec{r}\,',\vec{r},\omega)-G_0(\vec{r}\,',\vec{r},\omega)\nabla' P(\vec{r}\,',\vec{r}_s,\omega)],\end{aligned} \tag{A.6}$$

where V is the hemispheric volume below the measurement surface, and S is the hemisphere's surface. Substituting equation A.3 and its corresponding reference-medium Green's function differential equation into equation A.6 gives

$$\oint_S dS'\,\hat{n}\cdot[P(\vec{r}\,',\vec{r}_s,\omega)\nabla' G_0(\vec{r}\,',\vec{r},\omega)-G_0(\vec{r}\,',\vec{r},\omega)\nabla' P(\vec{r}\,',\vec{r}_s,\omega)]$$

$$
\begin{aligned}
&= \int_V d\vec{r}'[P(\vec{r}',\vec{r}_s,\omega) \underbrace{\nabla'^2 G_0(\vec{r}',\vec{r},\omega)}_{(-\omega^2/c_0^2)G_0(\vec{r}',\vec{r},\omega)+\delta(\vec{r}'-\vec{r})} \\
&\quad -G_0(\vec{r}',\vec{r},\omega) \underbrace{\nabla'^2 P(\vec{r}',\vec{r}_s,\omega)}_{(-\omega^2/c_0^2)P(\vec{r}',\vec{r}_s,\omega)+\frac{\omega^2}{c_0^2}\alpha(\vec{r}')P(\vec{r}',\vec{r}_s,\omega)+\rho(\vec{r}',\vec{r}_s,\omega)}] \\
&= \int_V d\vec{r}'[\underbrace{-\frac{\omega^2}{c_0^2}G_0(\vec{r}',\vec{r},\omega)P(\vec{r}',\vec{r}_s,\omega)}_{cancels} + \delta(\vec{r}'-\vec{r})P(\vec{r}',\vec{r}_s,\omega) \\
&\quad + \underbrace{\frac{\omega^2}{c_0^2}P(\vec{r}',\vec{r}_s,\omega)G_0(\vec{r}',\vec{r},\omega)}_{cancels} - \frac{\omega^2}{c_0^2}\alpha(\vec{r}')P(\vec{r}',\vec{r}_s,\omega)G_0(\vec{r}',\vec{r},\omega) \\
&\quad -\rho(\vec{r}',\vec{r}_s,\omega)G_0(\vec{r}',\vec{r},\omega)] \\
&= \int_V d\vec{r}'[P(\vec{r}',\vec{r}_s,\omega)\delta(\vec{r}'-\vec{r}) - \frac{\omega^2}{c_0^2}\alpha(\vec{r}')P(\vec{r}',\vec{r}_s,\omega)G_0(\vec{r}',\vec{r},\omega) \\
&\quad -\rho(\vec{r}',\vec{r}_s,\omega)G_0(\vec{r}',\vec{r},\omega)]. \qquad \text{(A.7)}
\end{aligned}
$$

If we choose $\vec{r} \in V$, the general source ρ is zero because it is outside of the volume, and the equation A.7 will be

$$
\begin{aligned}
&\oint_S dS'\,\hat{n}\cdot[P(\vec{r}',\vec{r}_s,\omega)\nabla' G_0(\vec{r}',\vec{r},\omega) - G_0(\vec{r}',\vec{r},\omega)\nabla' P(\vec{r}',\vec{r}_s,\omega)] \\
&= \int_V d\vec{r}'[\underbrace{P(\vec{r}',\vec{r}_s,\omega)\delta(\vec{r}'-\vec{r})}_{P(\vec{r},\vec{r}_s,\omega)} - \frac{\omega^2}{c_0^2}\alpha(\vec{r}')P(\vec{r}',\vec{r}_s,\omega)G_0(\vec{r}',\vec{r},\omega) \\
&\quad - \underbrace{\rho(\vec{r}',\vec{r}_s,\omega)}_{0} G_0(\vec{r}',\vec{r},\omega)] \\
&= P(\vec{r},\vec{r}_s,\omega) - \int_V d\vec{r}'\frac{\omega^2}{c_0^2}\alpha(\vec{r}')P(\vec{r}',\vec{r}_s,\omega)G_0(\vec{r}',\vec{r},\omega). \qquad \text{(A.8)}
\end{aligned}
$$

If the support for $\alpha \in V$, rearranging equation A.8 gives

$$
\begin{aligned}
P(\vec{r},\vec{r}_s,\omega) &= \int_V d\vec{r}' G_0(\vec{r}',\vec{r},\omega)\frac{\omega^2}{c_0^2}\alpha(\vec{r}')P(\vec{r}',\vec{r}_s,\omega) \\
&\quad + \oint_S dS', \hat{n}\cdot[P(\vec{r}',\vec{r}_s,\omega)\nabla' G_0(\vec{r}',\vec{r},\omega) - G_0(\vec{r}',\vec{r},\omega)\nabla' P(\vec{r}',\vec{r}_s,\omega)] \\
&= \int_\infty d\vec{r}' G_0(\vec{r}',\vec{r},\omega)\frac{\omega^2}{c_0^2}\alpha(\vec{r}')P(\vec{r}',\vec{r}_s,\omega) \\
&\quad + \oint_S dS'\,\hat{n}\cdot[P(\vec{r}',\vec{r}_s,\omega)\nabla' G_0(\vec{r}',\vec{r},\omega) - G_0(\vec{r}',\vec{r},\omega)\nabla' P(\vec{r}',\vec{r}_s,\omega)]. \qquad \text{(A.9)}
\end{aligned}
$$

In equation A.9 the surface integral involves actual pressure measurements and their vertical derivatives. For consistency with equation A.5 choose a causal Green's function, which gives

$$
P(\vec{r},\vec{r}_s,\omega) = \int_\infty d\vec{r}' G_0^+(\vec{r}',\vec{r},\omega)\frac{\omega^2}{c_0^2}\alpha(\vec{r}')P(\vec{r}',\vec{r}_s,\omega)
$$

$$+ \oint_S dS'\, \hat{n} \cdot [P(\vec{r}', \vec{r}_s, \omega) \nabla' G_0^+(\vec{r}', \vec{r}, \omega) - G_0^+(\vec{r}', \vec{r}, \omega) \nabla' P(\vec{r}', \vec{r}_s, \omega)] \quad \text{(A.10)}$$

Comparing the Lippmann-Schwinger equation (A.5) and Green's theroem (A.10) gives an equation for the effective source signature or reference wavefield P_0:

$$\begin{aligned} P_0(\vec{r}\,\vec{r}_s, \omega) &= \int_V d\vec{r}' \rho(\vec{r}', \vec{r}_s, \omega) G_0(\vec{r}', \vec{r}, \omega) \\ &= \oint_S dS'\, \hat{n} \cdot [P(\vec{r}', \vec{r}_s, \omega) \nabla' G_0^+(\vec{r}', \vec{r}, \omega) \\ &\quad - G_0^+(\vec{r}', \vec{r}, \omega) \nabla' P(\vec{r}', \vec{r}_s, \omega)]. \end{aligned} \quad \text{(A.11)}$$

Equation A.11 is one form of the "triangle relation" relating the pressure wavefield $P(\vec{r}', \vec{r}_s, \omega)$, its vertical derivative $\nabla' P(\vec{r}', \vec{r}_s, \omega)$, and the effective source signature or reference wavefield $P_0(\vec{r}\,\vec{r}_s, \omega)$.

B Derivation of Equation 3.2

Here, the general source signature $\rho(k, \omega)$ is solved from the reference wavefield P_0. We assume that (1) the distribution of the general source is the same for each experiment, which means that the source distribution doesn't depend on the effective source position r_s, and (2) the general source only varies along the horizontal variable x'. Thus, P_0^d can be rewritten as

$$P_0^d(x, z, x_s, \epsilon_s, \omega) = \int dx' \rho(x' + x_s, \epsilon_s, \omega) G_0^d(x, z, x' + x_s, \epsilon_s, \omega), \quad \text{(B.1)}$$

where x' is the source distribution with respect to the effective horizontal source position x_s. Since the source distribution doesn't depend on the effective source position x_s, we can express $\rho(x' + x_s, \epsilon_s, \omega)$ as $\rho(x', \omega)$ in this integral. The integral becomes

$$P_0^d(x, z, x_s, \epsilon_s, \omega) = \int dx' \rho(x', \omega) G_0^d(x, z, x' + x_s, \epsilon_s, \omega). \quad \text{(B.2)}$$

Using the bilinear form of Green's function, it becomes

$$P_0^d(x, z, x_s, \epsilon_s, \omega) = \int dx' \rho(x', \omega) \int dk_x dk_z \frac{e^{ik_x(x - x' - x_s)} e^{ik_z(z - \epsilon_s)}}{-k_x^2 - k_z^2 + \frac{\omega^2}{c_0^2}}. \quad \text{(B.3)}$$

Fourier transforming with respect to x_s gives

$$\begin{aligned} P_0^d(x, z, k_s, \epsilon_s, \omega) &= \int dx' \rho(x', \omega) \int dk_x dk_z \frac{e^{ik_x(x - x' - x_s)} e^{ik_z(z - \epsilon_s)}}{-k_x^2 - k_z^2 + \frac{\omega^2}{c_0^2}} e^{ik_s x_s} dx_s \\ &= \int dx' \rho(x', \omega) \int dk_x dk_z \frac{e^{ik_x(x - x')} e^{ik_z(z - \epsilon_s)}}{-k_x^2 - k_z^2 + \frac{\omega^2}{c_0^2}} \delta(k_s - k_x) \\ &= \int dx' \rho(x', \omega) e^{ik_s(x - x')} \int dk_z \frac{e^{ik_z(z - \epsilon_s)}}{\underbrace{-k_z^2 - k_s^2 + \frac{\omega^2}{c_0^2}}_{+q_s^2}} \end{aligned}$$

$$
\begin{aligned}
&= \int dx' \rho(x',\omega) e^{ik_s(x-x')} \int dk_z \frac{e^{ik_z(z-\epsilon_s)}}{-k_z^2+q_s^2} \\
&= \int dx' \rho(x',\omega) e^{ik_s(x-x')} \frac{e^{iq_s|z-\epsilon_s|}}{2iq_s} \\
&= \rho(k_s,\omega) e^{ik_s x} \frac{e^{iq_s|z-\epsilon_s|}}{2iq_s} \\
&= \rho(k_s,\omega) \frac{e^{-iq_s\epsilon_s}}{2iq_s} e^{ik_s x} e^{iq_s z}. \qquad \text{(B.4)}
\end{aligned}
$$

Here $z > \epsilon_s$ is used. Similarly, we can obtain

$$
\begin{aligned}
P_0(x,z,k_s,\epsilon_s,\omega) \qquad &= \rho(k_s,\omega) \frac{e^{iq_s|z-\epsilon_s|} - e^{iq_s|z+\epsilon_s|}}{2iq_s} \\
&= \rho(k_s,\omega) \frac{e^{-iq_s\epsilon_s}(1-e^{2iq_s\epsilon_s})}{2iq_s} e^{iq_s z} \\
&= P_0^d(x,z,k_s,\epsilon_s,\omega)(1-e^{2iq_s\epsilon_s}). \qquad \text{(B.5)}
\end{aligned}
$$

C Derivation of Equation 3.4

The n^{th} order free-surface demultipled data

$$
\begin{aligned}
&D_n'(x_g,\epsilon_g,x_s,\epsilon_s,\omega) = -\int dx_1 dz_1 dx_2 dz_2 G_0^d(x_g,\epsilon_g,x_1,z_1,\omega) V_1(x_1,z_1,x_2,z_2,\omega) \\
&*G_0^{fs}(x_2,z_2,x_3,z_3,\omega) V_{n-1}(x_3,z_3,x_4,z_4,\omega) P_0^d(x_4,z_4,x_s,\epsilon_s,\omega) dx_3 dz_3 dx_4 dz_4. \qquad \text{(C.1)}
\end{aligned}
$$

Substituting the bilinear form of the Green's function

$$
G_0^d(x,z,x',z',\omega) = \int dk_x dk_z \frac{e^{ik_x(x-x')} e^{ik_z(z-z')}}{-k_x^2-k_z^2+\frac{\omega^2}{c_0^2}} \qquad \text{(C.2)}
$$

into equation C.1 gives

$$
\begin{aligned}
&D_n'(x_g,\epsilon_g,x_s,\epsilon_s,\omega) = -\int dx_1 dz_1 dx_2 dz_2 \int dk_x' dk_z' \frac{e^{ik_x'(x_g-x_1)} e^{ik_z'(\epsilon_g-z_1)}}{-k_x'^2-k_z'^2+\frac{\omega^2}{c_0^2}} V_1(x_1,z_1,x_2,z_2,\omega) \\
&* \int dk dk_z \frac{e^{ik(x_2-x_3)} e^{ik_z(z_2+z_3)}}{-k^2-k_z^2+\frac{\omega^2}{c_0^2}} V_{n-1}(x_3,z_3,x_4,z_4,\omega) P_0^d(x_4,z_4,x_s,\epsilon_s,\omega) dx_3 dz_3 dx_4 dz_4. \qquad \text{(C.3)}
\end{aligned}
$$

Fourier transforming with respect to x_g and x_s gives

$$
D_n'(k_g,\epsilon_g,k_s,\epsilon_s,\omega) = -\int dx_1 dz_1 dx_2 dz_2 \int dk_x' dk_z' \frac{e^{ik_x'(x_g-x_1)} e^{ik_z'(\epsilon_g-z_1)}}{-k_x'^2-k_z'^2+\frac{\omega^2}{c_0^2}} e^{-ik_g x_g} dx_g
$$

$$
\begin{aligned}
&*V_1(x_1,z_1,x_2,z_2,\omega)\int dkdk_z\frac{e^{ik(x_2-x_3)}e^{ik_z(z_2+z_3)}}{-k^2-k_z^2+\frac{\omega^2}{c_0^2}}V_{n-1}(x_3,z_3,x_4,z_4,\omega)\\
&*P_0^d(x_4,z_4,x_s,\epsilon_s,\omega)e^{ik_sx_s}dx_sdx_3dz_3dx_4dz_4\\
&=-\int dx_1dz_1dx_2dz_2\int dk_x'dk_z'\frac{e^{-ik_x'x_1}e^{ik_z'(\epsilon_g-z_1)}}{-k_x'^2-k_z'^2+\frac{\omega^2}{c_0^2}}2\pi\delta(k_x'-k_g)V_1(x_1,z_1,x_2,z_2,\omega)\\
&*\int dkdk_z\frac{e^{ik(x_2-x_3)}e^{ik_z(z_2+z_3)}}{-k^2-k_z^2+\frac{\omega^2}{c_0^2}}V_{n-1}(x_3,z_3,x_4,z_4,\omega)P_0^d(x_4,z_4,k_s,\epsilon_s,\omega)dx_3dz_3dx_4dz_4. \qquad \text{(C.4)}
\end{aligned}
$$

Integrating over k_x' gives

$$
\begin{aligned}
&D_n'(k_g,\epsilon_g,k_s,\epsilon_s,\omega)=-\int dx_1dz_1dx_2dz_2dz_2 2\pi\int dk_z'\frac{e^{-ik_gx_1}e^{ik_z'(\epsilon_g-z_1)}}{-k_z'^2\underbrace{-k_g^2+\frac{\omega^2}{c_0^2}}_{+q_g^2}}V_1(x_1,z_1,x_2,z_2,\omega)\\
&*\int dkdk_z\frac{e^{ik(x_2-x_3)}e^{ik_z(z_2+z_3)}}{-k_z^2\underbrace{-k^2+\frac{\omega^2}{c_0^2}}_{+q^2}}V_{n-1}(x_3,z_3,x_4,z_4,\omega)P_0^d(x_4,z_4,k_s,\epsilon_s,\omega)dx_3dz_3dx_4dz_4\\
&=-\int dx_1dz_1dx_2dz_2e^{-ik_gx_1}2\pi\int dk_z'\frac{e^{ik_z'(\epsilon_g-z_1)}}{-k_z'^2+q_g^2}V_1(x_1,z_1,x_2,z_2,\omega)\\
&*\int dkdk_z\frac{e^{ik(x_2-x_3)}e^{ik_z(z_2+z_3)}}{-k_z^2+q^2}V_{n-1}(x_3,z_3,x_4,z_4,\omega)P_0^d(x_4,z_4,k_s,\epsilon_s,\omega)dx_3dz_3dx_4dz_4\\
&=-\int dx_1dz_1dx_2dz_2e^{-ik_gx_1}\frac{e^{iq_g|\epsilon_g-z_1|}}{2iq_g}V_1(x_1,z_1,x_2,z_2,\omega)\frac{1}{2\pi}\int dke^{ik(x_2-x_3)}\frac{e^{iq|z_2+z_3|}}{2iq}\\
&*V_{n-1}(x_3,z_3,x_4,z_4,\omega)P_0^d(x_4,z_4,k_s,\epsilon_s,\omega)dx_3dz_3dx_4dz_4. \qquad \text{(C.5)}
\end{aligned}
$$

Since $\epsilon_g < z_1$ and $z_2, z_3 > 0$, equation C.5 becomes

$$
\begin{aligned}
&D_n'(k_g,\epsilon_g,k_s,\epsilon_s,\omega)=-\int dx_1dz_1dx_2dz_2dz_2e^{-ik_gx_1}\frac{e^{iq_g(\epsilon_g-z_1)}}{2iq_g}V_1(x_1,z_1,x_2,z_2,\omega)\\
&*\frac{1}{2\pi}\int dke^{ik(x_2-x_3)}\frac{e^{iq(z_2+z_3)}}{2iq}V_{n-1}(x_3,z_3,x_4,z_4,\omega)P_0^d(x_4,z_4,k_s,\epsilon_s,\omega)dx_3dz_3dx_4dz_4\\
&=-\frac{1}{2\pi}\int dk\frac{e^{-iq_g\epsilon_g}}{2iq_g}\int dx_1dz_1dx_2dz_2dz_2e^{-ik_gx_1}e^{iq_gx_1}V_1(x_1,z_1,x_2,z_2,\omega)e^{ikx_2}e^{iqz_2}\frac{1}{2iq}\\
&*e^{-ikx_3}e^{iqz_3}V_{n-1}(x_3,z_3,x_4,z_4,\omega)P_0^d(x_4,z_4,k_s,\epsilon_s,\omega)dx_3dz_3dx_4dz_4\\
&=-\frac{1}{2\pi}\int dk\frac{e^{-iq_g\epsilon_g}}{2iq_g}V_1(k_g,-q_g,-k,-q,\omega)\frac{1}{2iq}V_{n-1}(k,-q,x_4,z_4,\omega)\\
&*P_0^d(x_4,z_4,k_s,\epsilon_s,\omega)dx_4dz_4. \qquad \text{(C.6)}
\end{aligned}
$$

Inserting two identities into equation C.6 gives

$$D'_n(k_g,\epsilon_g,k_s,\epsilon_s,\omega) = -\frac{1}{2\pi}\int dk \frac{e^{-iq_g\epsilon_g}}{2iq_g} V_1(k_g,-q_g,-k,-q,\omega) \underbrace{\frac{e^{-iq\epsilon_s}}{2iq}\frac{2iq}{e^{-iq\epsilon_s}}}_{1}\frac{1}{2iq}$$

$$* \underbrace{\frac{2iq}{e^{-iq\epsilon_g}}\frac{e^{-iq\epsilon_g}}{2iq}}_{1} V_{n-1}(k,-q,x_4,z_4,\omega)P_0^d(x_4,z_4,k_s,\epsilon_s,\omega)dx_4dz_4$$

$$= -\frac{1}{2\pi}\int dk \underbrace{\frac{e^{-iq_g\epsilon_g}}{2iq_g}V_1(k_g,-q_g,-k,-q,\omega)\frac{e^{-iq\epsilon_s}}{2iq}}_{\frac{D'_1(k_g,\epsilon_g,k,\epsilon_s,\omega)}{\rho(k,\omega)}} \underbrace{\frac{2iq}{e^{-iq\epsilon_s}}\frac{1}{2iq}\frac{2iq}{e^{-iq\epsilon_g}}}_{2iqe^{iq(\epsilon_s+\epsilon_g)}}$$

$$* \underbrace{\frac{e^{-iq\epsilon_g}}{2iq}V_{n-1}(k,-q,x_4,z_4,\omega)P_0^d(x_4,z_4,k_s,\epsilon_s,\omega)dx_4dz_4}_{D'_{n-1}(k,\epsilon_g,k_s,\epsilon_s,\omega)}$$

$$= \frac{1}{i\pi}\int \frac{dk}{\rho(k,\omega)} D'_1(k_g,\epsilon_g,k,\epsilon_s,\omega)qe^{iq(\epsilon_s+\epsilon_g)}D'_{n-1}(k,\epsilon_g,k_s,\epsilon_s,\omega). \quad \text{(C.7)}$$

References

Araújo, F. V. *Linear and non-linear methods derived from scattering theory: backscattered tomography and internal multiple attenuation.* PhD thesis, Universidade Federal da Bahia, 1994.

Berkhout, A. J. and D. J. Verschuur. "Removal of internal multiples." *69th SEG Annual International Meeting* (1999): 1334–1337.

Brandsaeter, H., A. Farestveit, and B. Ursin. "A new high-resolution or deep penetration air gun array." *Geophysics* 44 (1979): 865–879.

Carvalho, P. M. *Free-surface multiple reflection elimination method based on nonlinear inversion of seismic data.* PhD thesis, Universidade Federal da Bahia, 1992.

Dragoset, B., I. Moore, M. Yu, and W. Zhao. "Removal of internal multiples." *78th SEG Annual International Meeting* (2008): 2426–2430.

Giles, B. F. and R. C. Johnston. "System approach to air gun array design." *Geophys. Prosp.* 21 (1973): 77–101.

Ikelle, Luc T., Graham Roberts, and Arthur B. Weglein. "Source signature estimation based on the removal of the first-order multiples." *Geophysics* 62 (1997): 1904–1920.

Loveridge, M. M., G. E. Parkes, L. Hatton, and M. H. Worthington. "Effects of marine source array directivity on seismic data and source signature deconvolution." *First Break* 2 (1984): 16–22.

Morse, P. M. and H. Feshbach. *Methods of theoretical physics.* McGraw-Hill Book Co., 1953.

Nooteboom, J. J. "Signature and amplitude of linear air gun arrays." *Geophys. Prosp.* 26 (1978): 194–201.

Verschuur, D. J., A. J. Berkhout, and C. P. A. Wapenaar. "Adaptive surface-related multiple elimination." *Geophysics* 57 (1992): 1166–1177.

Weglein, A. B., F. V. Araújo, P. M. Carvalho, R. H. Stolt, K. H. Matson, R. T. Coates, D. Corrigan, D. J. Foster, S. A. Shaw, and H. Zhang. "Inverse Scattering Series and Seismic Exploration." *Inverse Problems* (2003): R27–R83.

Weglein, A. B., F. A. Gasparotto, P. M. Carvalho, and R. H. Stolt. "An Inverse-Scattering Series Method for Attenuating Multiples in Seismic Reflection Data." *Geophysics* 62 (November-December 1997): 1975–1989.

Weglein, Arthur B. and Bruce G. Secrest. "Wavelet estimation for a multidimensional acoustic earth model." *Geophysics* 55 (July 1990): 902–913.

Yang, J. and A. B. Weglein. "Incorporating an angle dependent source signature into an Inverse Scattering Series free surface multiple elimination algorithm: Initial analysis and formulation." *MOSRP Annual Report* 1 (2011): 157–165.

Zhang, Jingfeng. *Wave theory based data preparation for inverse scattering multiple removal, depth imaging and parameter estimation: analysis and numerical tests of Green's theorem deghosting theory.* PhD thesis, University of Houston, 2007.

Modifying the leading order ISS attenuator of first-order internal multiples to accommodate primaries and internal multiples: fundamental concept and theory, development, and examples exemplified when three reflectors generate the data

Chao Ma, Hong Liang and Arthur B.Weglein, M-OSRP University of Houston

May 25, 2012

Abstract

The Inverse Scattering Series (ISS) is a comprehensive framework for achieving seismic data processing goals without requiring subsurface information. Distinct isolated task-specific subseries can accomplish free-surface-multiple removal, internal-multiple attenuation, depth imaging, and inversion of primaries. The ISS can predict and eliminate internal multiples without a priori information. Although the leading-order ISS internal multiple attenuation algorithm for the first-order internal multiples has shown unmatched capability on complex synthetic and onshore data compared with other methods (e.g., Fu et al. (2010); Luo et al. (2011)), there are open issues to be addressed (e.g., Weglein et al. (2011)). For example, spurious events can be predicted in the first-order attenuator (leading-order prediction of the first-order internal multiples) when there are both primaries and internal multiples in the input data. This report proposes a new algorithm to directly address the most significant spurious events observed in Fu et al. (2010) and Luo et al. (2011). It also provides a template for identifying ISS terms addressing these more general spurious events, which can arise from using a leading-order internal multiple attenuation algorithm with complex media and complex data.

1 Introduction

In seismic exploration, primaries are events that have experienced only one upward reflection, while multiples are events that have experienced multiple upward reflections. Multiples are further classified by the location of their downward reflections. Multiples that have at least one downward reflection at the free surface (air-water or air-land) are free-surface multiples. Multiples that have experienced all their downward reflections below the free surface are internal multiples. The number of downward reflections determines the order of an internal multiple. For example, the first-order internal multiples have only one downward reflection below the free surface (dashed line in Figure 2). Although both primaries and internal multiples contain subsurface information, the primaries-only assumption in seismic data analysis requires removal of multiples. The methods for removing multiples were classified as separation and wavefield prediction in Weglein (1999). The separation methods sought a characteristic to distinguish primaries from multiples, while the early wavefield

prediction methods first modeled and then subtracted multiples. Both of these approaches have earned well-deserved places in the seismic toolbox. However, as seismic exploration moves toward more complex areas, such methods have limitations resulting from their assumptions and the requirements for subsurface information. The ISS free surface multiple removal algorithm (Carvalho, 1992; Weglein et al., 1997) and internal multiple attenuation algorithm (Araújo, 1994; Weglein et al., 1997) start by avoiding the assumptions of the earlier methods, e.g., they are completely multi-dimensional and have no requirements for subsurface information. There are both separation and wavefield prediction ingredients in the ISS multiple-removal methods and they can be viewed as a next step in the development of separation and wavefield prediction methods (Weglein et al., 2011). For example, the ISS free-surface-multiple separation distinguishes the free-surface multiples from other events by the downward reflection at the free surface. In contrast, the ISS internal-multiple separation is realized without any a priori information, by understanding the difference in the construction of primaries and internal multiples in the forward series. As an example, the ISS leading-order prediction for the removal of the first-order internal multiple provides a "lower-higher-lower"relationship in the pseudo-depth domain and uses only primaries as subevents to predict the first-order internal multiples from all reflectors, at all depths at once, and without any subsurface information.

Previous work focused on predicting internal multiples using only primaries in the input data. When there are internal multiples in the input data, the ISS leading-order prediction of internal multiples can produce spurious events. This limitation results from using a single *leading-order* term to predict internal multiples with complex data. The term *leading-order* means it can by itself effectively attenuate, but not completely eliminate, internal multiples. While we recognize the shortcomings of the current leading-order ISS internal-multiple-attenuation algorithm, we also recognize that addressing them resides in the ISS (Weglein et al., 2011). Each term in the subseries achieves what the order of that term enables it to achieve. There are certain issues that a term of a given order can address, and other issues that require aid from higher-order terms. The more difficult the task, the more complicated and more inclusive the subseries is. For example, it requires an infinite series (in a closed form) to completely eliminate all first-order internal multiples generated at the shallowest layer when the properties at and above that reflector are unknown (Ramírez and Weglein, 2005). Similarly, the internal-multiple-attenuation task is more difficult when the input data contains internal multiples as well as primaries than it is when the input data contain only primaries. Thus the ISS internal-multiple-attenuation algorithm needs to capture terms in order to address the spurious events. In this report, we provide an understanding of the issue of the leading-order prediction of the first-order internal multiples when the input data consist of both primaries and internal multiples. We also provide a new higher-order ISS internal-multiple-attenuation algorithm to address a particular type of spurious event that is predicted when the middle subevent in the first-order attenuator is an internal multiple.

2 An overview of inverse scattering theory

Scattering theory is a form of perturbation analysis. It describes how the scattered wavefield (the difference between the actual wavefield and the reference wavefield) relates to the perturbation (the difference between the actual medium and the reference medium). A forward scattering series

constructs the scattered wavefield from the perturbation, while an inverse scattering series provides the perturbation from a scattered wavefield.

We start the mathematical description of scattering theory with the differential equations governing wave propagation in the media:

$$LG = \delta(r - r_s) \tag{2.1}$$

$$L_0 G_0 = \delta(r - r_s), \tag{2.2}$$

where L, L_0 are differential operators in the actual and reference medium, respectively. G, G_0 are the actual and reference wavefield, respectively. Define the perturbation as $V \equiv L_0 - L$. Then the Lippmann-Schwinger equation is

$$G = G_0 + G_0 V G. \tag{2.3}$$

Iteratively substituting equation 2.3 into itself gives the forward scattering series

$$\begin{aligned} \psi_s &= G_0 V G_0 + G_0 V G_0 V G_0 + G_0 V G_0 V G_0 V G_0 + \cdots \\ &= (\psi_s)_1 + (\psi_s)_2 + (\psi_s)_3 +, \cdots \end{aligned} \tag{2.4}$$

where $\psi_s = G - G_0$ is the scattered wavefield, and $(\psi_s)_n$ is the portion of ψ_s that is the nth order in V. The data D are the scattered wavefield evaluated on the measurement surface $D = (\psi_s)_{ms}$.

We expand the perturbation V as a series,

$$V = V_1 + V_2 + V_3 + \cdots, \tag{2.5}$$

where V_n is the portion of V that is the nth order in the data, D. Substituting equation 2.5 into equation 2.4 and evaluating both sides on the measurement surface, and then making terms of equal order in the data equal gives the following set of equations

$$(\Psi_s)_m = (G_0 V_1 G_0)_m, \tag{2.6}$$

$$0 = (G_0 V_2 G_0)_m + (G_0 V_1 G_0 V_1 G_0)_m, \tag{2.7}$$

$$0 = (G_0 V_3 G_0)_m + (G_0 V_2 G_0 V_1 G_0)_m + (G_0 V_1 G_0 V_2 G_0)_m + (G_0 V_1 G_0 V_1 G_0 V_1 G_0)_m, \tag{2.8}$$

$$0 = (G_0 V_n G_0)_m + (G_0 V_1 G_0 V_{n-1} G_0)_m + \cdots + (G_0 V_1 G_0 V_1 G_0 V_1 \cdots G_0 V_1 G_0)_m. \tag{2.9}$$

V_1 can be solved in equation 2.6 by using the measured scattered wavefield $(\psi_s)_m$ and the reference wavefield G_0. Then one can substitute the value of V_1 into equation 2.7, and solve for V_2 the same as done for V_1 in equation 2.6. In this manner, we can compute any V_n, and hence $V = \sum_{n=1}^{\infty} V_n$ is an explicit direct inversion framework.

3 An overview of ISS internal-multiple-attenuation algorithm

The *leading-order* contribution to constructing a class of multiples in the forward series suggests the *leading-order* contribution for their removal in the inverse series (Weglein et al., 2003). For example, the mathematical realization of figure 1 is the leading-order contribution to the generation of first-order internal multiples; it suggests the corresponding mathematical expression for the leading-order attenuation of those multiples.

A subseries that focuses on internal-multiple removal can be isolated from the inverse series. The ISS internal-multiple-attenuation subseries, described here, chooses only the leading-order contribution from the removal series of each order of multiple and uses it to form a subseries that attenuates all the internal multiples effectively. The ISS internal-multiple-attenuation algorithm starts with the input data, $D(k_g, k_s, \omega)$, in $2D$, which is the Fourier transform of the prestack data that are deghosted, wavelet deconvolved and that have free-surface multiples removed. The leading-order prediction of the first-order internal multiples makes the leading-order contribution to their removal. In a $2D$ earth, the leading-order prediction of the first-order internal multiples is

$$\begin{aligned} b_3(k_g, k_s, \omega) = \frac{1}{(2\pi)^2} \int_{-\infty}^{\infty} dk_1 \int_{-\infty}^{\infty} dk_2 e^{-iq_1(z_g - z_s)} e^{iq_2(z_g - z_s)} \\ \times \int_{-\infty}^{\infty} dz_1 b_1(k_g, k_1, z_1) e^{i(q_g + q_1)z_1} \\ \times \int_{-\infty}^{z_1 - \epsilon} dz_2 b_1(k_1, k_2, z_2) e^{-i(q_1 + q_2)z_2} \\ \times \int_{z_2 + \epsilon}^{\infty} dz_3 b_1(k_2, k_s, z_3) e^{i(q_2 + q_s)z_3}, \end{aligned} \tag{3.1}$$

where ω is temporal frequency, k_s and k_g are the horizontal wavenumbers for the source and receiver coordinates, respectively; q_g and q_s are the vertical source and receiver wavenumbers defined by $q_i = sgn(\omega)\sqrt{\frac{\omega^2}{c_0^2} - k_i^2}$ for $i \in \{g, s\}$; z_s and z_g are source and receiver depths; and z_j ($i \in \{1, 2, 3\}$) represents pseudo-depth using reference velocity migration. The quantity $b_1(k_g, k_s, z)$ corresponds to an uncollapsed migration (Weglein et al., 1997) of effective plane-wave incident data, and $b_1(k_g, k_s, q_g + q_s) = -2iq_s D(k_g, k_s, \omega)$.

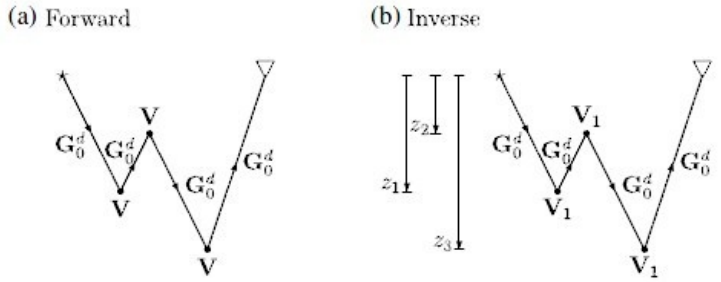

Figure 1: The leading-order contribution to the generation of first-order internal multiples in the forward series is represented in (a) and suggests the leading-order contribution to the removal of first-order internal multiples in the inverse series in (b). Figure adapted from Weglein et al. (2003).

With the input data and the leading-order prediction of the first-order internal multiples, we can obtain the data with the first-order internal multiples attenuated,

$$D(k_g, k_s, \omega) + D_3(k_g, k_s, \omega), \tag{3.2}$$

where $D_3(k_g, k_s, \omega) = (-2iq_s)^{-1} b_3(k_g, k_s, q_g + q_s)$.

The data with both the first-order and higher-order internal multiples attenuated are,

$$D(k_g, k_s, \omega) + D_3(k_g, k_s, \omega) + D_5(k_g, k_s, \omega) + D_7(k_g, k_s, \omega) + \cdots , \tag{3.3}$$

where $D_{2n+1}(k_g, k_s, \omega) = (-2iq_s)^{-1} b_{2n+1}(k_g, k_s, q_g + q_s)$. A recursive relationship that provides b_{2n+1} in terms of b_{2n-1} is given in Araújo (1994) and Weglein et al. (2003).

For a $1D$ earth and a normal incident plane wave, equation 3.1 reduces to

$$b_3(k) = \int_{-\infty}^{\infty} dz_1 e^{ikz_1} b_1(z_1) \int_{-\infty}^{z_1-\epsilon} dz_2 e^{-ikz_2} b_1(z_2) \int_{z_2+\epsilon}^{\infty} dz_3 e^{ikz_3} b_1(z_3). \tag{3.4}$$

The leading-order ISS internal-multiple-attenuation algorithm for the first-order internal multiples of a $1D$ earth and an impulsive incident plane wave is

$$b_1 + b_3. \tag{3.5}$$

Note that the $(-2iq_s)$ factor is not needed here because the incident wave is an impulsive plane wave. However, in general, the output of the ISS leading-order removal of the first-order internal multiples needs the $(-2iq_s)$ factor to take b to D, as in equation 3.2.

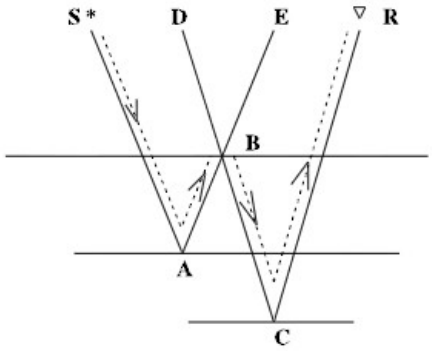

Figure 2: Combination of subevents for the first-order internal multiple (dashed line), $(SABE)_{time} + (DBCR)_{time} - (DBE)_{time} = (SABCR)_{time}$. The capitalized letters indicate a primary or an internal multiple. Figure adapted from Weglein et al. (2003).

The portion of the third-order term of the ISS that predicts the first-order internal multiple is isolated by requiring the "lower(A)-higher(B)-lower(C)"relationship in the pseudo-depth domain, as shown here in Figure 2. The assumption behind the first-order internal-multiple prediction in Figure 2 is that all of the subevents have to be primaries for the prediction to be an internal multiple. There are circumstances, shown in the next section, where the "lower-higher-lower"template would produce spurious events when one of the subevents is an internal multiple. However, these spurious events are fully anticipated and can be attenuated by other terms in the inverse series.

4 A new ISS internal-multiple-attenuation algorithm to attenuate the spurious event arising in a three-reflector model

Now we consider a three-reflector analytic example. We first examine the prediction of the first-order internal multiple attenuator using only primaries. We have

$$D(t) = R_1\delta(t-t_1) + R_2'\delta(t-t_2) + R_3'\delta(t-t_3), \tag{4.1}$$

where $R_2' = T_{01}R_2T_{10}$; $R_3' = T_{01}T_{12}R_3T_{21}T_{10}$, and t_i, R_i are two-way times and reflection coefficients from the ith reflectors, respectively. T_{ij} is the transmission coefficient between the ith and jth reflectors.

Given these data, we find from equation 3.4 that

$$\begin{aligned} b_3(t) =& R_1(R_2')^2\delta(t-(2t_2-t_1)) + 2R_1R_2'R_3'\delta(t-(t_2+t_3-t_1)) \\ &+R_1(R_3')^2\delta(t-(2t_3-t_1)) + R_2(R_3')^2\delta(t-(2t_3-t_2)). \end{aligned} \tag{4.2}$$

The four events are predictions of the first-order internal multiples associated with these three primaries. When added to the data, the predictions can effectively attenuate the first-order internal multiples.

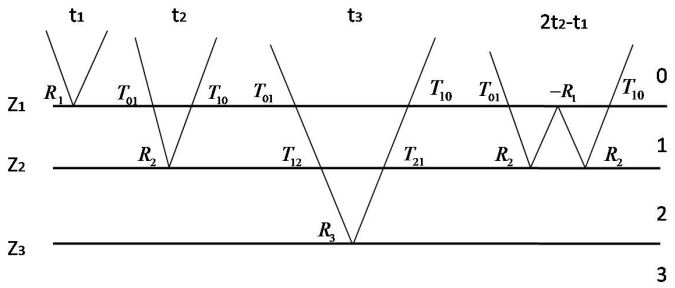

Figure 3: Three primaries and one internal multiple in a three-reflector model.

Next, we examine the prediction when there are three primaries and one specific internal multiple associated with the first two reflectors in the input data. In this case,

$$D(t) = R_1\delta(t-t_1) + R_2'\delta(t-t_2) + R_3'\delta(t-t_3) + R_4'\delta(t-(2t_2-t_1)), \tag{4.3}$$

where $R_4' = T_{01}R_2(-R_1)R_2T_{10}$.

Given these data, we find from equation 3.4 that

$$\begin{aligned} b_3(t) =& R_1(R_2')^2\delta(t-(2t_2-t_1)) + 2R_1R_2'R_3'\delta(t-(t_2+t_3-t_1)) \\ &+R_1(R_3')^2\delta(t-(2t_3-t_1)) + R_2(R_3')^2\delta(t-(2t_3-t_2)) \\ &+2R_1R_2'R_4'\delta(t-(3t_3-2t_1)) + R_2'(R_4')^2\delta(t-(3t_3-2t_2)) \\ &+2R_1R_3'R_4'\delta(t-(t_3+2t_2-2t_1)) + R_1(R_4')^2\delta(t-(4t_2-3t_1)) \\ &+2R_2'R_3'R_4'\delta(t-(t_3+t_2-t_1)) + (R_3')^2R_4'\delta(t-(2t_3-(2t_2-t_1))). \end{aligned} \tag{4.4}$$

We have assumed that $t_3 > 2t_2 - t_1$ in deriving equation 4.4.

In addition to the four first-order internal multiples (first two rows in equation 4.4), the first-order attenuator, b_3, predicts some additional events because of the specific internal multiple in the input. Analysis of the traveltimes of these additional events shows that each of them corresponds to one specific internal multiple of higher order with the exception of the last event $(R_3')^2 R_4' \delta(t - (2t_3 - (2t_2 - t_1)))$, which is a spurious event prediction.

4.1 Properties of the first-order attenuator when both primaries and internal multiples are input as subevents

When there are internal multiples in the data, there will be many other possible subevent combinations in the first-order internal-multiple attenuator, b_3. Because when $b_1 = P + I$, it follows from equation 3.4 that,

$$\begin{aligned} b_3 &= b_1 * b_1 * b_1 \\ &= (P + I)(P + I)(P + I) \\ &= PPP + PPI + PIP + IPP + PII + IPI + IIP + III, \end{aligned}$$

where $*$ stands for the nonlinear interaction between the data. P stands for primaries, and I stands for internal multiples. Besides the primaries-only subevent combination, PPP, there are subevent combinations involved with the internal multiple that produce the spurious event. A more detailed analysis shows that the spurious event $(R_3')^2 R_4' \delta(t - (2t_3 - (2t_2 - t_1)))$ in equation 4.4 comes from PIP as shown in Figure 4 .

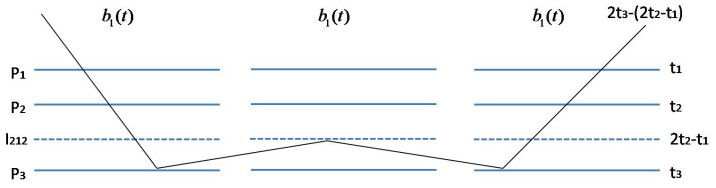

Figure 4: An analogous *W-like* configuration to produce the spurious event using the internal multiple as a subevent.

We use a diagram to illustrate the generation of the spurious event by the PIP subevent combination. The diagram for PIP is shown in the left panel in Figure 5, which satisfies the "lower-higher-lower"relationship, as required by the algorithm.

Following the logic of predicting internal multiples by the "lower-higher-lower"pattern of three primary subevents, the PIP diagram will split into a "lower–higher–much higher–lower–much lower"configuration as shown in the right panel of Figure 5. The resultant configuration does not agree with the double *W-like* configuration, which constructs a second-order internal multiple using five primary subevents.

The pseudo-depth of the two outermost primaries, P, should be deeper than the effective pseudo-depth of the middle internal multiple, I, to allow the PIP spurious events to happen, as shown in

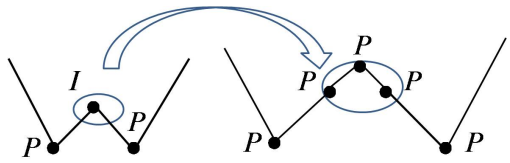

Figure 5: Separation for PIP into a *W-like* configuration.

Figure 4. In other words, the PIP spurious events can exist in a medium that has three or more reflectors. That explains the fact that there are no spurious events produced in the two-reflector example in the work of Zhang and Shaw (2010), even though an internal multiple is included in their data.

When the internal multiple in PPI or IPP is separated into three "lower-higher-lower"primary subevents, it leads to a double *W-like* configuration restricted by our three-reflector example. The double *W-like* configuration will predict the second-order internal multiple, as shown in Figure 6, and explains the additional higher-order internal-multiple predictions in b_3 from our analytic example. It can be shown that there are circumstances where PPI produces spurious events in a medium that has more than three reflectors (Liang et al., 2012).

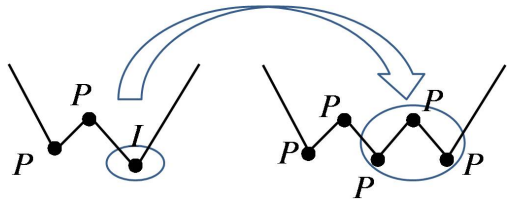

Figure 6: One possible separation for PPI into a double *W-like* configuration.

Terms like IIP or III may also produce spurious events. However when compared with the effects of terms like PIP, these terms can often be ignored in practice. The removal of the latter spurious events also resides in the higher-order ISS terms, and beyond those considered and included in this report.

4.2 A new term to attenuate the PIP spurious event

To remove the spurious events produced by the first-order attenuator when using an internal multiple as the middle subevent, a new and higher-order ISS term, which has that capability, is included in the current algorithm.

Guided by Figure 5, a portion of the fifth-order term from the ISS ($G_0V_1G_0V_3G_0V_1G_0$) can be employed to predict the PIP spurious events in $1D$ given by

$$b_5^{PIP} = \int_{-\infty}^{\infty} dz_1 e^{ikz_1} b_1(z_1) \int_{-\infty}^{z_1-\epsilon} dz_2 e^{-ikz_2} b_3(z_2) \int_{z_2+\epsilon}^{\infty} dz_3 e^{ikz_3} b_1(z_3), \tag{4.5}$$

where $b_1(z)$ is an uncollapsed migration and $b_3(z)$ is the first-order attenuator.

Compared with equation 3.4, this equation also requires the "lower-higher-lower"relationship, but the middle b_1 becomes b_3 to obtain a prediction of the spurious event using the predicted internal multiple.

Then, adding equation 4.5 and equation 3.4 leads to our new algorithm for a $1D$ earth and an impulsive incident plane wave,

$$\begin{aligned} & b_1 + b_3^{PPP} + b_5^{PIP} \\ =& b_1 + \int_{-\infty}^{\infty} dz_1 e^{ikz_1} b_1(z_1) \int_{-\infty}^{z_1-\epsilon} dz_2 e^{-ikz_2} (b_1(z_2) + b_3(z_2)) \int_{z_2+\epsilon}^{\infty} dz_3 e^{ikz_3} b_1(z_3), \end{aligned} \tag{4.6}$$

where $b_3^{PPP} = b_3$. The superscript indicates the subevent combination that the algorithm can accommodate.

Compared with the original algorithm (equation 3.5), the new algorithm includes a portion of a higher-order term (b_5^{PIP}) to attenuate the PIP spurious events predicted by b_3^{PPP} when internal multiples are in the data.

We use the same analytic example to test the new algorithm. Substituting $D(t)$ in equation 4.3 and b_3 in equation 4.4 into equation 4.5 produces

$$\begin{aligned} b_5^{PIP} =& R_1(R_2')^2(R_3')^2\delta(t-(2t_3-(2t_2-t_1))) \\ &+ (2R_1R_2'R_4'(R_3')^2 + R_2'(R_4')^2(R_3')^2)\delta(t-(2t_3-(3t_2-2t_1))) \\ &+ R_1(R_4')^2(R_3')^2\delta(t-(2t_3-(4t_2-3t_1))). \end{aligned} \tag{4.7}$$

The first term is the prediction of the spurious event. Substitution of $R_2' = T_{01}R_2T_{10}$ leads to

$$(T_{01}T_{10})^2R_1(R_2)^2(R_3')^2\delta(t-(2t_3-(2t_2-t_1))).$$

The last term $(R_3')^2R_4'\delta(t-(2t_3-(2t_2-t_1)))$ in equation 4.4 is the spurious event. Substitution of $R_4' = T_{01}R_2(-R_1)R_2T_{10}$ leads to

$$(-T_{01}T_{10})R_1(R_2)^2(R_3')^2\delta(t-(2t_3-(2t_2-t_1))).$$

When added to b_3, the first term in equation 4.7 will effectively attenuate the spurious event. The $T_{01}T_{10}$ error is because b_5^{PIP} uses the predicted internal multiple as the middle subevent to predict the spurious event, whereas b_3 uses the actual internal multiple as the middle subevent (middle b_1), as shown in Figure 4 and Figure 7.

It is the geometric similarity (single *W-like* configuration) between b_5^{PIP} and b_3 (Figure 5) that enables b_5^{PIP} to contribute to removing the spurious events produced in b_3. We note that each term in the inverse series does what the order of that term is capable of performing. Different portions of a given order term in the ISS can contribute to different tasks. For example, in our case, although both the leading-order prediction of the second-order internal multiples b_5 (right side in Figure 6) and b_5^{PIP} (right side in Figure 5) come from the fifth-order term in the inverse series, they have different tasks determined by their different geometries. Indeed, b_5^{PIP} has a single *W-like* geometry that is capable of attenuating the spurious events, whereas b_5 has a double *W-like* geometry that is capable of predicting second-order internal multiples using primaries. Both are contained in the fifth-order term in the ISS.

Therefore, by incorporating a higher-order ISS term into the attenuator, equation 4.6 can effectively attenuate the PIP spurious events predicted by b_3.

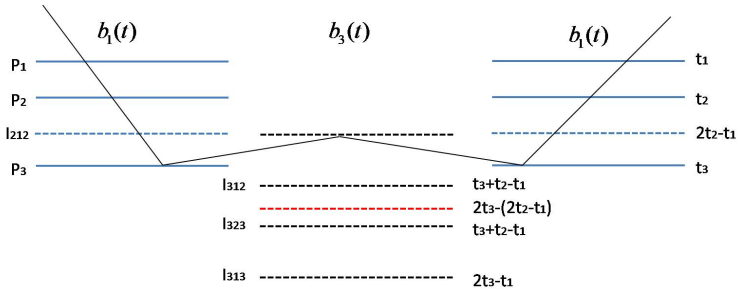

Figure 7: Illustration of the spurious event prediction in b_5^{PIP}. Notice the middle b_3 produces predicted internal multiples that have the opposite sign of the actual internal multiples. Only the first-order predicted internal multiples (black dashed line) and spurious event (red dashed line) are shown.

5 Discussion

In a medium that has more than three reflectors, (1) PPI or IPP can also predict spurious events. Other portions of the fifth-order terms can be identified to address those spurious events (Liang et al., 2012). (2) In equation 4.5, in addition to the prediction using the "primary–predicted internal multiple–primary"subevent combination, there are possible "primary–spurious event–primary"subevent combinations. However, at this point we can often reasonably disregard this kind of newly created event in practice since the amplitude of these events is small. (3) Although b_5^{PIP} is designed to address PIP spurious events, it can also address PII or IIP spurious events using "primary–predicted internal multiple–internal multiple"or "internal multiple–predicted internal multiple–primary"subevent combinations, respectively. The difference between b_5^{PIP} and b_3 is in the middle diagram, one has primaries and *real* internal multiples (middle diagram in Figure 4); one has predicted spurious events and *predicted* internal multiples (middle diagram in Figure 7), and the coefficients of *real* and *predicted* internal multiples are opposite.

6 Conclusions

In this report, we provide both (1) an algorithm to address the most significant spurious events observed in Fu et al. (2010) and Luo et al. (2011) and (2) a template for locating ISS terms addressing these more general spurious events that can arise from using a leading-order internal multiple attenuation algorithm on complex media and complex data. The ISS can remove all internal multiples without subsurface information and can also remove spurious events that arise from using complex data in a leading-order algorithm. We exemplify that capability in this report.

To conclude, the new algorithm in this paper retains the strength of the original algorithm while also addressing a limitation in the current algorithm, and it provides an extension to accommodate data consisting of both primaries and internal multiples.

7 Acknowledgements

We thank all of our sponsors for their support of this research. The authors would like to thank Mason Biamonte, Wilberth Herrera, Jim Mayhan for reviewing and Paolo Terenghi for useful discussions.

Appendix

A Derivation of b_5^{PIP} from the fifth-order term from the ISS

One portion of the fifth-order term in the ISS is capable of predicting the artifacts we want to remove. Start from the fifth-order equation,

$$\begin{aligned} V_5 = &- V_1G_0V_1G_0V_1G_0V_1G_0V_1 - V_2G_0V_1G_0V_1G_0V_1 - V_1G_0V_2G_0V_1G_0V_1 \\ &- V_1G_0V_1G_0V_2G_0V_1 - V_1G_0V_1G_0V_1G_0V_2 - V_3G_0V_1G_0V_1 \\ &- V_1G_0V_3G_0V_1 - V_1G_0V_1G_0V_3 - V_4G_0V_1 - V_1G_0V_4. \end{aligned}$$

Inspired by the analog between the forward and inverse series and the logic of constructing internal multiples using primaries, $V_{57} = V_1G_0V_3G_0V_1$ is chosen for further study. Using effective data in the pseudo-depth domain to express it as (Ramirez, 2007)

$$\begin{aligned} B_{57}(k) = &\int_{-\infty}^{\infty} dz b_1(z) \int_{-\infty}^{\infty} dz' \hat{b_3}(z') \int_{-\infty}^{\infty} dz'' e^{ikz''} b_1(z'') \\ &+ \int_{-\infty}^{\infty} dz b_1(z) \int_{-\infty}^{\infty} dz' e^{-ikz'} \hat{b_3}(z') \int_{-\infty}^{\infty} dz'' b_1(z'') \\ &+ \int_{-\infty}^{\infty} dz e^{ikz} b_1(z) \int_{-\infty}^{\infty} dz' e^{-ikz'} \hat{b_3}(z') \int_{-\infty}^{\infty} dz'' e^{ikz''} b_1(z'') \\ &+ \int_{-\infty}^{\infty} dz e^{ikz} b_1(z) \int_{-\infty}^{\infty} dz' \hat{b_3}(z') \int_{-\infty}^{\infty} dz'' b_1(z''), \end{aligned}$$

where $\hat{b_3}(z')$ is the data representation of one portion of third-order terms such that $\hat{b_3}(z')$ can be employed to predict the artifacts.

To make sure the prediction is of the correct time, the third term is chosen, and in order to satisfy the "lower-higher-lower" requirement in the pseudo-depth domain, the rightmost and middle integral limits are further separated as follows,

$$\begin{aligned} B_{573}(k) = &\int_{-\infty}^{\infty} dz e^{ikz} b_1(z) \int_{-\infty}^{\infty} dz' e^{-ikz'} \hat{b_3}(z') \int_{-\infty}^{\infty} dz'' e^{ikz''} b_1(z'') \\ = &\int_{-\infty}^{\infty} dz e^{ikz} b_1(z) (\int_{-\infty}^{z-\epsilon} + \int_{z-\epsilon}^{z+\epsilon} + \int_{z+\epsilon}^{\infty}) dz' e^{-ikz'} \hat{b_3}(z') \\ &\times (\int_{-\infty}^{z'-\epsilon} + \int_{z'-\epsilon}^{z'+\epsilon} + \int_{z'+\epsilon}^{\infty}) dz'' e^{ikz''} b_1(z'') \\ = &\int_{-\infty}^{\infty} dz e^{ikz} b_1(z) \int_{-\infty}^{z-\epsilon} dz' e^{-ikz'} \hat{b_3}(z') \int_{-\infty}^{z'-\epsilon} dz'' e^{ikz''} b_1(z'') \\ &+ \int_{-\infty}^{\infty} dz e^{ikz} b_1(z) \int_{-\infty}^{z-\epsilon} dz' e^{-ikz'} \hat{b_3}(z') \int_{z'-\epsilon}^{z'+\epsilon} dz'' e^{ikz''} b_1(z'') \\ &+ \int_{-\infty}^{\infty} dz e^{ikz} b_1(z) \int_{-\infty}^{z-\epsilon} dz' e^{-ikz'} \hat{b_3}(z') \int_{z'+\epsilon}^{\infty} dz'' e^{ikz''} b_1(z'') \end{aligned}$$

$$
\begin{aligned}
&+\int_{-\infty}^{\infty} dz e^{ikz} b_1(z) \int_{z-\epsilon}^{z+\epsilon} dz' e^{-ikz'} \hat{b_3}(z') \int_{-\infty}^{z'-\epsilon} dz'' e^{ikz''} b_1(z'') \\
&+\int_{-\infty}^{\infty} dz e^{ikz} b_1(z) \int_{z-\epsilon}^{z+\epsilon} dz' e^{-ikz'} \hat{b_3}(z') \int_{z'-\epsilon}^{z'+\epsilon} dz'' e^{ikz''} b_1(z'') \\
&+\int_{-\infty}^{\infty} dz e^{ikz} b_1(z) \int_{z-\epsilon}^{z+\epsilon} dz' e^{-ikz'} \hat{b_3}(z') \int_{z'+\epsilon}^{\infty} dz'' e^{ikz''} b_1(z'') \\
&+\int_{-\infty}^{\infty} dz e^{ikz} b_1(z) \int_{z+\epsilon}^{\infty} dz' e^{-ikz'} \hat{b_3}(z') \int_{-\infty}^{z'-\epsilon} dz'' e^{ikz''} b_1(z'') \\
&+\int_{-\infty}^{\infty} dz e^{ikz} b_1(z) \int_{z+\epsilon}^{\infty} dz' e^{-ikz'} \hat{b_3}(z') \int_{z'-\epsilon}^{z'+\epsilon} dz'' e^{ikz''} b_1(z'') \\
&+\int_{-\infty}^{\infty} dz e^{ikz} b_1(z) \int_{z+\epsilon}^{\infty} dz' e^{-ikz'} \hat{b_3}(z') \int_{z'+\epsilon}^{\infty} dz'' e^{ikz''} b_1(z'').
\end{aligned}
$$

From the above separation, we choose the third term because it satisfies the requirement in the pseudo-depth domain. Then we examine the third-order term to determine $\hat{b_3}(z')$:

$$V_3 = -V_1 G_1 V_1 G_0 V_1 - V_2 G_0 V_1 - V_1 G_0 V_2.$$

For the same reason, $V_1 G_1 V_1 G_0 V_1$ is chosen for further study. Expressing this term using effective data and doing the separation,

$$
\begin{aligned}
B_3(k) &= \int_{-\infty}^{\infty} dz e^{ikz} b_1(z) \int_{-\infty}^{\infty} dz' e^{-ikz'} b_1(z') \int_{-\infty}^{\infty} dz'' e^{ikz''} b_1(z'') \\
&= \int_{-\infty}^{\infty} dz e^{ikz} b_1(z) (\int_{-\infty}^{z-\epsilon} + \int_{z-\epsilon}^{z+\epsilon} + \int_{z+\epsilon}^{\infty}) dz' e^{-ikz'} b_1(z') \\
&\quad \times (\int_{-\infty}^{z'-\epsilon} + \int_{z'-\epsilon}^{z'+\epsilon} + \int_{z'+\epsilon}^{\infty}) dz'' e^{ikz''} b_1(z'') \\
&= \int_{-\infty}^{\infty} dz e^{ikz} b_1(z) \int_{-\infty}^{z-\epsilon} dz' e^{-ikz'} b_1(z') \int_{-\infty}^{z'-\epsilon} dz'' e^{ikz''} b_1(z'') \\
&\quad + \int_{-\infty}^{\infty} dz e^{ikz} b_1(z) \int_{-\infty}^{z-\epsilon} dz' e^{-ikz'} b_1(z') \int_{z'-\epsilon}^{z'+\epsilon} dz'' e^{ikz''} b_1(z'') \\
&\quad + \int_{-\infty}^{\infty} dz e^{ikz} b_1(z) \int_{-\infty}^{z-\epsilon} dz' e^{-ikz'} b_1(z') \int_{z'+\epsilon}^{\infty} dz'' e^{ikz''} b_1(z'') \\
&\quad + \int_{-\infty}^{\infty} dz e^{ikz} b_1(z) \int_{z-\epsilon}^{z+\epsilon} dz' e^{-ikz'} b_1(z') \int_{-\infty}^{z'-\epsilon} dz'' e^{ikz''} b_1(z'') \\
&\quad + \int_{-\infty}^{\infty} dz e^{ikz} b_1(z) \int_{z-\epsilon}^{z+\epsilon} dz' e^{-ikz'} b_1(z') \int_{z'-\epsilon}^{z'+\epsilon} dz'' e^{ikz''} b_1(z'') \\
&\quad + \int_{-\infty}^{\infty} dz e^{ikz} b_1(z) \int_{z-\epsilon}^{z+\epsilon} dz' e^{-ikz'} b_1(z') \int_{z'+\epsilon}^{\infty} dz'' e^{ikz''} b_1(z'') \\
&\quad + \int_{-\infty}^{\infty} dz e^{ikz} b_1(z) \int_{z+\epsilon}^{\infty} dz' e^{-ikz'} b_1(z') \int_{-\infty}^{z'-\epsilon} dz'' e^{ikz''} b_1(z'')
\end{aligned}
$$

$$+\int_{-\infty}^{\infty} dz e^{ikz} b_1(z) \int_{z+\epsilon}^{\infty} dz' e^{-ikz'} b_1(z') \int_{z'-\epsilon}^{z'+\epsilon} dz'' e^{ikz''} b_1(z'')$$
$$+\int_{-\infty}^{\infty} dz e^{ikz} b_1(z) \int_{z+\epsilon}^{\infty} dz' e^{-ikz'} b_1(z') \int_{z'+\epsilon}^{\infty} dz'' e^{ikz''} b_1(z'').$$

The term we need from the above result is essentially the attenuator, since what we need in $\hat{b_3}(z')$ is the predicted internal multiple. Notice that here the work is almost the same as the work deriving the leading-order internal-multiple eliminator (Ramirez, 2007), the difference being the work in Ramirez (2007) needs data self-interaction whereas our solution needs *W-like* interaction. To summarize, we have,

$$b_5^{PIP} = B_{5733}(k) = \int_{-\infty}^{\infty} dz e^{ikz} b_1(z) \int_{-\infty}^{z-\epsilon} dz' e^{-ikz'} \hat{b_3}(z') \int_{z'+\epsilon}^{\infty} dz'' e^{ikz''} b_1(z''),$$

where

$$\hat{b_3}(k) = \int_{-\infty}^{\infty} dz e^{ikz} b_1(z) \int_{-\infty}^{z-\epsilon} dz' e^{-ikz'} b_1(z') \int_{z+\epsilon}^{\infty} dz'' e^{ikz''} b_1(z'').$$

References

Araújo, F. V. *Linear and non-linear methods derived from scattering theory: backscattered tomography and internal multiple attenuation.* PhD thesis, Universidade Federal da Bahia, 1994.

Carvalho, P. M. *Free-surface multiple reflection elimination method based on nonlinear inversion of seismic data.* PhD thesis, Universidade Federal da Bahia, 1992. In Portuguese.

Fu, Q., Y. Luo, Panos.G. Kelamix, ShouDong Huo, Ghada Sindi, Shih-Ying Hsu, and Arthur. B. Weglein. "The inverse scattering series approach towards the elimination of land internal multiples." *SEG Expanded Abstracts* (2010): 3456–3461.

Liang, H., C. Ma, and A.B. Weglein. "A new ISS internal multiple attenuation algorithm addressing a shortcoming of the current leading-order ISS algorithm for removing first order internal multiples: derivation and testing of the algorithm for arbitrary number of reflectors." *To be submitted to the SEG Expanded Abstracts* (2012).

Luo, Y., Panos G. Kelamis, Q. Fu, ShouDong Huo, Ghada Sindi, Shih-Ying Hsu, and Arthur. B. Weglein. "Elimination of land internal multiples based on the inverse scattering series." *The Leading Edge* (2011): 884–889.

Ramírez, A. C. and A.B. Weglein. "An inverse scattering internal multiple elimination method: Beyond attenuation, a new algorithm and initial tests." *SEG Expanded Abstracts.* (2005): 2115–2118.

Ramirez, A.R. *I-Inverse scattering subseries for removol of internal multiples and depth imaging prinaries;II-Green's theorem as the foundation of interferometry and guiding new practical methods and applications.* PhD thesis, University of Houston, 2007.

Weglein, A. B., F. V. Araújo, P. M. Carvalho, R. H. Stolt, K. H. Matson, R. T. Coates, D. Corrigan, D. J. Foster, S. A. Shaw, and H. Zhang. "Inverse Scattering Series and Seismic Exploration." *Inverse Problems* (2003): R27–R83.

Weglein, A. B., F. A. Gasparotto, P. M. Carvalho, and R. H. Stolt. "An Inverse-Scattering Series Method for Attenuating Multiples in Seismic Reflection Data." *Geophysics* 62 (November-December 1997): 1975–1989.

Weglein, A. B., Shih-Ying Hsu, Paolo Terenghi, Xu Li, and Robert. H. Stolt. "Multiple attenuation: Recent advances and the road ahead (2011)." *The Leading Edge* (2011): 864–875.

Weglein, A.B. "Multiple attenuation: an overview of recent advances and the road ahead (1999)." *The Leading Edge* (1999): 40–44.

Zhang, H. and S. Shaw. "analytic analysis of higher order internal multiples predicted via the inverse scattering series based algorithe." *SEG Expanded Abstracts* 29 (2010): 3493–3498.

A further general modification of the leading order ISS attenuator of first order internal multiples to accommodate primaries and internal multiples when an arbitrary number of reflectors generate the data: theory, development, and examples

H. Liang, C. Ma and A. B. Weglein, M-OSRP, University of Houston

May 25, 2012

Abstract

Multiple removal is a prerequisite for depth imaging and target identification. The inverse scattering series (ISS) predicts and removes internal multiples directly and without any subsurface information. This is achieved through a task-specific subseries within the overall ISS. The ISS leading-order attenuator is the leading-order term of the subseries contributing to the removal of first-order internal multiples. The idea behind the leading-order attenuator is that the time of the first-order internal multiples can be predicted from primaries in the data that act as subevents of the first-order internal multiples. However, the entire data, consisting of primaries and internal multiples, enter the algorithm. When internal multiples in the data themselves act as subevents, the leading-order attenuator produces not only first-order internal multiples, but also higher-order internal multiples and spurious events, which have been observed in the tests of Fu et al. (2010) and Luo et al. (2011). Weglein et al. (2011) also pointed this out and suggested that the resolution of the problem would reside in other terms of the ISS. Within the framework of ISS, each term of a task-specific subseries only performs a certain specific task. The ISS leading-order attenuator has shown stand-alone capabilities for removing internal multiples. This report shows that the removal of the spurious events arising from the leading-order attenuation algorithm is performed by other higher-order terms. Hence, a shortcoming of the current leading-order internal-multiple algorithm is anticipated and addressed in later terms in the ISS. The resulting new ISS internal-multiple algorithm presented in this report retains the strengths of the current algorithm while avoiding a serious shortcoming.

1 Introduction

Seismic processing methods that extract subsurface information from seismic data typically assume that the data consist only of primaries. Thus, multiple removal is a prerequisite to those methods. Depending on the location of downward reflections, multiples can be divided into free-surface multiples or internal multiples. Multiples that have at least one downward reflection at the air-water or air-land surface (free surface) are called free-surface multiples. Multiples that have all their downward reflections below the free surface are called internal multiples. For the purpose of this report, we will focus on the analysis of internal multiples.

The inverse scattering series can achieve all processing objectives directly and without subsurface information. With the ISS free-surface-multiple-removal method, the location and properties of the free surface (the shallowest reflector) responsible for free-surface multiples are well defined. In contrast, with the ISS internal-multiple-removal method, the shallowest reflector at which an internal multiple experience a downward reflection could be anywhere in the subsurface, and its properties are unknown. Thus, the internal-multiple-removal algorithm performs without a priori information; it is data-driven and predicts internal multiples at all depths at once.

The ISS internal-multiple-attenuation algorithm was first proposed by Araújo et al. (1994) and Weglein et al. (1997). It is data-driven, and it can precisely predict the time and can well approximate the amplitude for internal multiples at all depths at once. This algorithm does not depend on the earth model type (Weglein et al., 2003) and is applicable for towed-streamer field data, land data, and ocean bottom data (Matson and Weglein, 1996b; Matson, 1997) and even for internal multiples with converted phase (Coates and Weglein, 1996). Ramírez and Weglein (2005) extended the attenuation algorithm to the elimination method. The ISS internal-multiple algorithm has shown encouraging results; it is distinctive and promises significant value for application (Fu et al., 2010; Hsu et al., 2011; Terenghi et al., 2011; Weglein et al., 2011; Luo et al., 2011).

The ISS internal-multiple method operates without a priori information, and its tasks are more complex than those of the ISS free-surface multiple method. Early analysis of the ISS leading-order attenuator focused on using only primary subevents to predict internal multiples. However, the input data contain both primaries and internal multiples, and all events in the data will be treated as subevents. Under some circumstances treating internal multiples as subevents in the leading-order internal-multiple algorithm can lead to spurious events. We define the conditions when that can occur, and how terms further in the ISS address and remove those spurious events. Following the suggestion of Weglein et al. (2011), Ma et al. (2012) derived the new ISS internal-multiple algorithm, which addresses the shortcomings arising from the second of the three integrals of the ISS leading-order attenuator in a three-reflector medium. This report evaluates that algorithm using numerical examples, and also extends the algorithm to the medium with an arbitrary number of reflectors.

In Section 2, we review the current ISS internal-multiple-attenuation algorithm. In Section 3 we diagrammatically show the output of the leading-order internal-multiple attenuator when both primaries and internal multiples are included in the input, then we analyze the cause of the generation of the false event, and finally we present the newly identified terms in the inverse scattering series that address the false events. In Section 4 we use two numerical examples to evaluate the performance of the new terms. We follow with discussion and conclusions at the end of this report.

2 The leading-order ISS internal-multiple-attenuation algorithm

The development of the ISS internal-multiple attenuation concept was based on the analogy between the forward series and the inverse series (Weglein et al., 2003, 1997). Matson and Weglein (1996a) showed that the forward series could generate primaries and internal multiples through the action of G_0^d on V, where G_0^d is a whole-space Green's function and V is the perturbation operator. The inverse series can achieve a full inversion of V by using G_0^d and the measured data (Weglein et al., 2003). Thus, the way that G_0^d acts on V to construct internal multiples also suggests the way

to remove them. In the forward series the first-order internal multiples have their leading-order contribution from the third term (Figure 1(a)), which suggests that we can find the leading-order attenuator of internal multiples from the third term in the inverse series. Following this logic path, a subseries that attenuates internal multiples has been identified and separated from the entire inverse scattering series (Weglein et al., 1997). Figure 1(b) shows the portion of the third term in the inverse series that contributes to the first-order internal multiple attenuation, where V_1 is the first-order approximation of V, $z_1 > z_2$ and $z_3 > z_2$.

The ISS internal-multiple-attenuation algorithm is a subseries of the inverse scattering series. The algorithm starts with the deghosted input data with the reference wavefield and free-surface multiples removed, $D(k_g, k_s, \omega)$, where k_g and k_s are the horizontal wavenumbers corresponding to receiver and source coordinates x_g and x_s, respectively, and ω is the temporal frequency.

$$D(k_g, k_s, \omega) = (-2iq_s)^{-1} b_1(k_g, k_s, \omega). \tag{2.1}$$

$b_1(k_g, k_s, \omega)$ corresponds to an uncollapsed FK migration of effective incident plane-wave data (Weglein et al., 2003; Hsu et al., 2011). The second term in the algorithm is the leading-order attenuator, which attenuates first-order internal multiples (the order of an internal multiple is defined by the total number of downward reflections). The leading-order attenuator in a 2D earth is given by Araújo et al. (1994) and Weglein et al. (1997)

$$\begin{aligned} b_3(k_g, k_s, q_g + q_s) = \frac{1}{(2\pi)^2} \int_{-\infty}^{\infty} \int_{-\infty}^{\infty} dk_1 e^{iq_1(\epsilon_s - \epsilon_g)} dk_2 e^{iq_2(\epsilon_g - \epsilon_s)} \\ \times \int_{-\infty}^{\infty} dz_1 e^{i(q_g + q_1)z_1} b_1(k_g, -k_1, z_1) \\ \times \int_{-\infty}^{z_1 - \epsilon} dz_2 e^{i(-q_1 - q_2)z_2} b_1(k_1, -k_2, z_2) \\ \times \int_{z_2 + \epsilon}^{\infty} dz_3 e^{i(q_2 + q_s)z_3} b_1(k_2, -k_s, z_3), \end{aligned} \tag{2.2}$$

where c_0 is the reference velocity, $q_g = sgn(\omega)\sqrt{(\frac{\omega}{c_0})^2 - k_g^2}$ and $q_s = sgn(\omega)\sqrt{(\frac{\omega}{c_0})^2 - k_s^2}$ are the vertical wavenumbers, ϵ_i, $i = 1, 2$ is a small positive parameter chosen to insure that the relations between pseudo-depths $z_1 > z_2$ and $z_3 > z_2$ are satisfied, and z_g and z_s are source and receiver depths, respectively.

For a 1D earth and a normal incidence, wave equation 2.2 reduces to

$$b_3^{PPP} = b_3(k) = \int_{-\infty}^{\infty} dz_1 e^{ikz_1} b_1(z_1) \int_{-\infty}^{z_1 - \epsilon} dz_2 e^{-ikz_2} b_1(z_2) \int_{z_2 + \epsilon}^{\infty} dz_3 e^{ikz_3} b_1(z_3) \tag{2.3}$$

where the deghosted data , $D(t)$, for an incident spike wave, satisfy $D(\omega) = b_1(2\omega/c_0)$, $b_1(z) = \int_{-\infty}^{\infty} e^{-ikz} b(k) dk$, and $k = 2\omega/c_0$ is the vertical wavenumber . Here, we introduce a new notation, b_3^{PPP}, in which the superscript ("p" represents primary) indicates specific events in the data that are input into each of the three integrals. The events indicated in this notation are the ones that

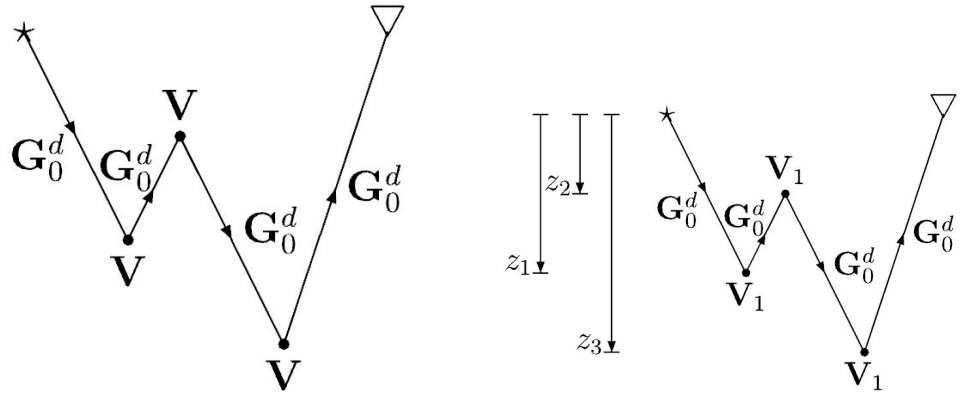

Figure 1: (a) The leading-term contribution to the generation of first-order internal multiples in the forward scattering series. (b) The leading-term contribution to the removal of first-order internal multiples in the inverse scattering series. G_0^d, V, and V_1 are the whole-space Green's function, the perturbation operator, and the first-order approximation to V, respectively. Figure adapted from Weglein et al. (2003).

the algorithm can accommodate in its goal of removing first-order internal multiples. The data with first-order internal multiples attenuated are

$$D(t) + D_3(t), \tag{2.4}$$

where $D_3(t)$ is the inverse Fourier transform of $D_3(\omega)$ and $D_3(\omega) = b_3(k)$ for an incident spike wave. Weglein and Matson (1998) showed that this algorithm can be interpreted as the subevents construction of internal multiples. Figure 2 illustrates the construction of a first-order internal multiple using three primary subevents. The predicted time of the internal multiple is exact and the predicted amplitude approximates the true amplitude (Weglein et al., 2003).

3 The general output of the leading-order internal multiple attenuator when an internal multiple is treated as a subevent

Early analysis focused exclusively on predicting the internal multiples by using primary subevents. However, seismic data contains not only primary events but also internal multiples. Zhang and Shaw (2010) have shown that the leading-order attenuator can predict higher-order internal multiples by using internal multiples as subevents in a two-interface example. However, the situation is considerably more complicated when the data from three or more reflectors are considered. In the latter case, spurious events can be predicted whose traveltimes do not correspond to an event in the data. In this section, we illustrate the specific conditions under which the spurious events are produced by the leading-order attenuator by using one internal multiple subevent in a 1D earth.

In the rest of this section, we will focus on the analysis of the ISS leading-order internal-multiple attenuator for a 1D medium and a normal incident wave. In such a case, a first-order internal

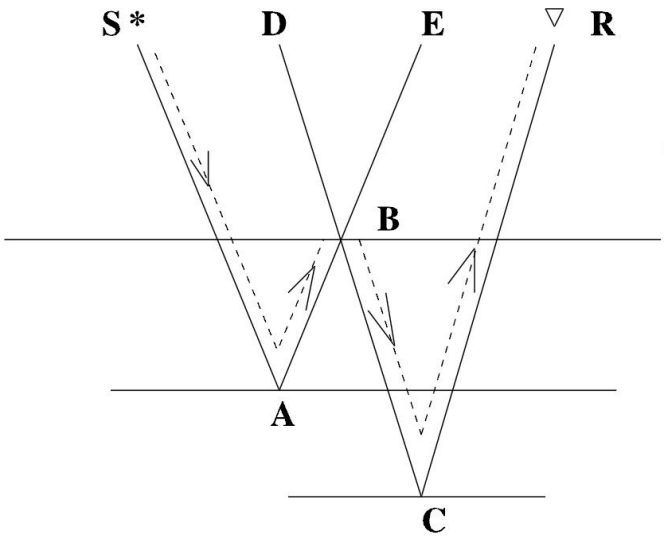

Figure 2: Subevents construction of an internal multiple. The phase relationship between the internal multiple (dashed line) SABCR, and primaries (solid line) SABE, DBCR, DBE, is: $(\text{SABE})_{\text{time}} + (\text{DBCR})_{\text{time}} - (\text{DBE})_{\text{time}} = (\text{SABCR})_{\text{time}}$. Figure adapted from Weglein et al. (2003).

multiple (see Figure 3(a)) can be represented by the diagram in Figure 3(b), where the "-" sign in a red circle means a downward reflection and the "+" sign in a blue circle denotes an upward reflection. If we only consider the pseudo-depths (vertical traveltime) of the events, Figure 3(b) can also be used to illustrate the prediction of internal multiples with three primary subevents, with each circle representing a subevent and the sign "+" or "-" in the circle meaning the addition or subtraction of the pseudo-depth of the subevent. The pseudo-depths of the three primary subevents, z_2, z_1 and z_2, satisfy the "lower–higher–lower" pattern with $z_2 > z_1$. The pseudo-depth of the event predicted by the leading-order attenuator is $2z_2 - z_1$, which is exactly equal to that of the first-order internal multiple in Figure 3(a). Next we will examine the cases in which one of the subevents is an internal multiple.

3.1 An internal-multiple subevent in the second integral

Ma et al. (2012) have shown that in a medium with three reflectors, when an internal multiple acts as a subevent in the second of the three integrals (see equation 2.3), a spurious event can be produced. In this section, we interpret this diagrammatically using Figure 4 (pseudo-depth is determined by the water speed image, $b_1(z)$). An internal multiple has each of its downward reflections between two upward reflections. Then, in the diagrammatic representation of an internal multiple (e.g., Figure 4(a)), a higher red circle with a "-" sign should have lower blue circles with "+" signs on both sides. However, in Figure 4(c) each of the two red circles has only one lower blue circle on one side, and one higher blue circle on the other side. Thus, this predicted event is neither an internal multiple nor a primary. Figure 5 shows the construction of such a false event using the subevent concept.

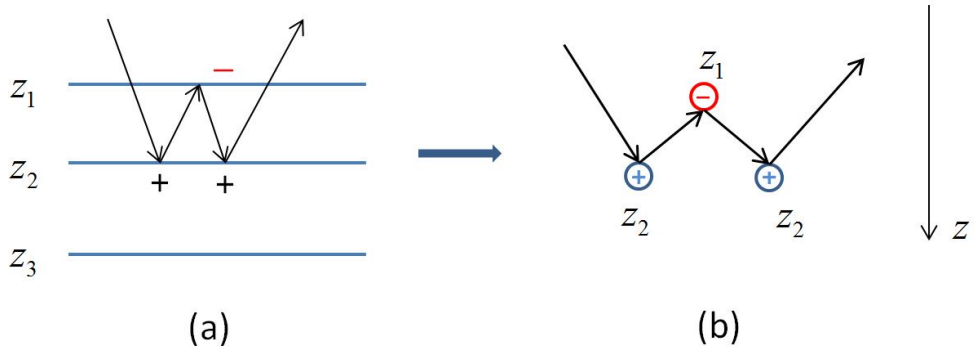

Figure 3: Diagrammatic illustration of a first-order internal multiple: the "-" sign represents a downward reflection and the "+" sign represents an upward reflection.

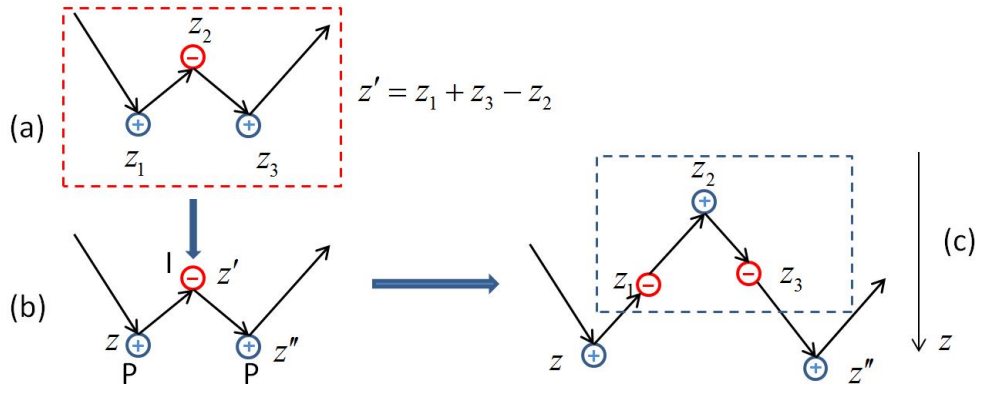

Figure 4: Diagrammatic illustration of the generation of a spurious event. (a) The diagram of a first-order internal multiple. The sign "+" ("-") means an upward (downward) reflection or the pseudo-depth is added (subtracted). (b) Three subevents used by the leading-order attenuator: a primary ("P") with pseudo-depth z, an internal multiple ("I") with pseudo-depth z', and a primary with pseudo-depth z'', with $z' < z, z''$. (c) The spurious event generated with pseudo-depth $(z + z'' - (z_1 + z_3 - z_2))$.

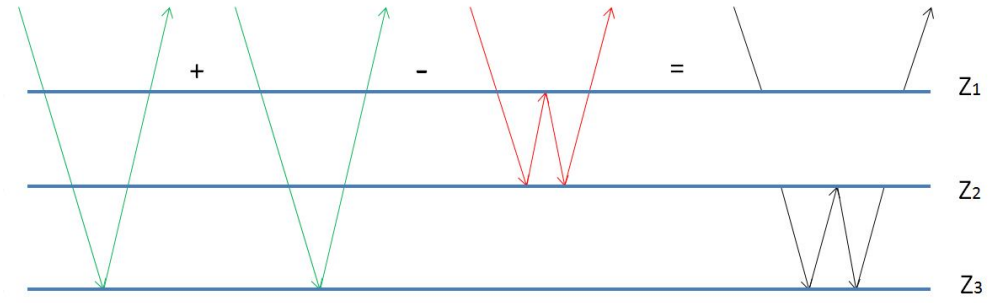

Figure 5: Generation of a false event using an internal multiple as the middle subevent, $2z_2 - z_1 < z_3$.

The spurious event described here is generated by the leading-order attenuator by using an internal-multiple subevent in the second integral. The way the spurious event is generated suggests the way that it can be removed. For the removal of this type of spurious events, substituting b_3 for the second b_1 in equation 2.3 leads to equation 3.1. The subevent combination of "primary–predicted internal multiple–primary" in equation 3.1 can be used to attenuate the spurious event. In this paper, we examine one of the fifth-order terms in the ISS ($G_0V_1G_0V_3G_0V_1G_0$) that satisfies the required Figure 4(c) geometry. The derivation of this term and analytical examples are shown in Ma et al. (2012).

$$b_5^{PIP}(k) = \int_{-\infty}^{\infty} dz_1 e^{ikz_1} b_1(z_1) \int_{-\infty}^{z_1-\epsilon} dz_2 e^{-ikz_2} b_3(z_2) \int_{z_2+\epsilon}^{\infty} dz_3 e^{ikz_3} b_1(z_3) \tag{3.1}$$

The output of the new ISS internal-multiple algorithm for this three reflectors case is

$$D(t) + D_3(t) + D_5^{PIP}(t), \tag{3.2}$$

where $D_5^{PIP}(t)$ is the inverse Fourier transform of $D_5^{PIP}(\omega)$ and $D_5^{PIP}(\omega) = b_5^{PIP}(k)$ for spike data. The original algorithm (see equation 2.4) attenuates the first-order internal multiples and preserves primaries but can also output spurious events. The new algorithm in equation 3.2 provides the benefit of the original algorithm while addressing issues that are due to spurious events.

3.2 An internal-multiple subevent in the outer integral

The problem is yet more complicated when a first-order internal-multiple subevent is in either of the outer integrals. As shown in the left panel of Figure 6, when an internal multiple with pseudo-depth z'' is in the rightmost integral ($z, z'' > z'$), and since $z'' = (z_1 + z_3 - z_2) > z'$, there are several possible relations among z_1, z_2, z_3 and z', which are as follows:

- As shown by the first arrow in Figure 6, when $z_1 > z'$, $z_2 \neq z$ and $z_3 \neq z'$, the predicted event has the same pseudo-depth as dose a second-order internal multiple. Its subevent construction is shown in Figure 7, and this occurs in a medium with the number of reflectors $N \geq 2$.

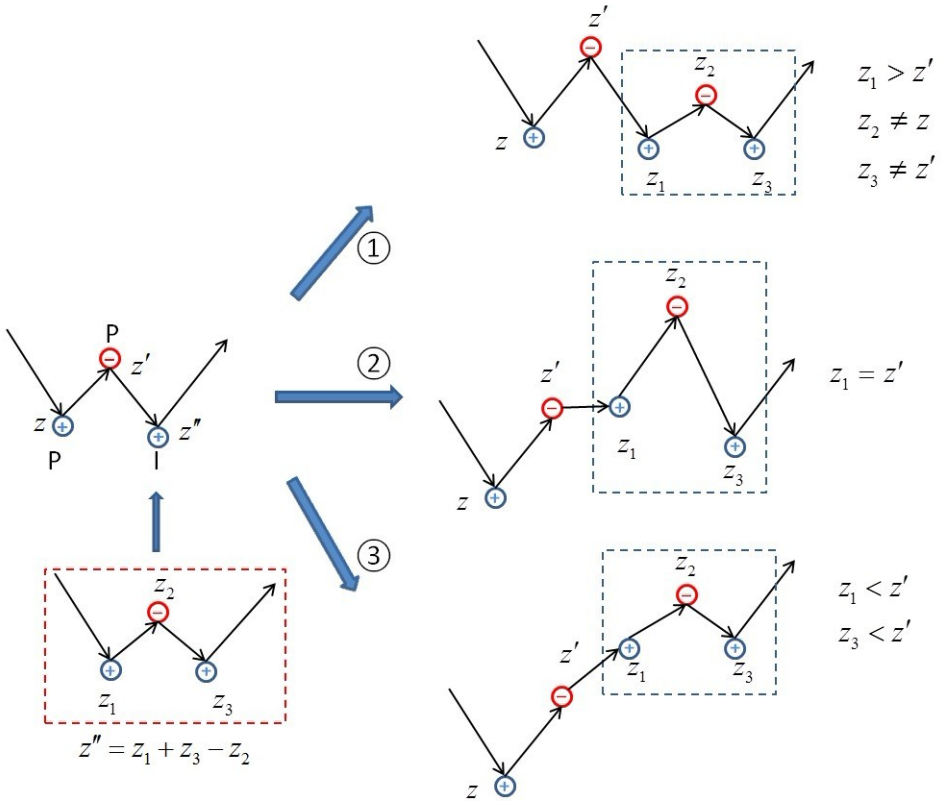

Figure 6: Diagrammatic illustration of predicted events when an internal-multiple subevent is in the outer integral.

- The second arrow in Figure 6 shows that when $z_1 = z'$, the predicted event has the same pseudo-depth as dose a first-order internal multiple. Figure 8 describes its subevent construction, which only happens in a medium with $N \geq 3$.
- The third arrow in Figure 6 shows that a spurious event is produced with $z_1 < z'$ and $z_3 < z'$ (the red circle at z' has only one lower blue circle on one side). Its subevent construction is illustrated by Figure 9. This type of spurious event can only be generated in a medium with $N \geq 4$.

Using the same logic analysis that we used in the previous section, we propose another method to address this type of spurious event, this time by replacing the third b_1 in equation 2.3 with b_3; the new term is shown in equation 3.3. Since this type of spurious event could be produced by the leading-order attenuator using a first-order internal-multiple subevent in either of the outer integrals (these two cases are equivalent), there is a leading coefficient 2 in equation 3.3. This term is also identified from the fifth-order term of the ISS equations (from the term $G_0V_1G_0V_1G_0V_3G_0$).

$$b_5^{PPI}(k) = 2\int_{-\infty}^{\infty} dz_1 e^{ikz_1} b_1(z_1) \int_{-\infty}^{z_1-\epsilon} dz_2 e^{-ikz_2} b_1(z_2) \int_{z_2+\epsilon}^{\infty} dz_3 e^{ikz_3} b_3(z_3) \tag{3.3}$$

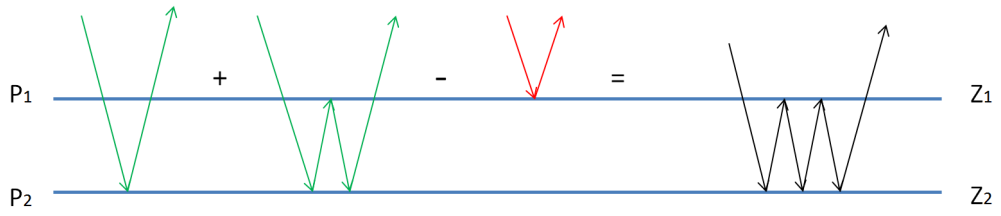

Figure 7: Generation of a second-order internal multiple when an internal-multiple subevent is in the outer integral.

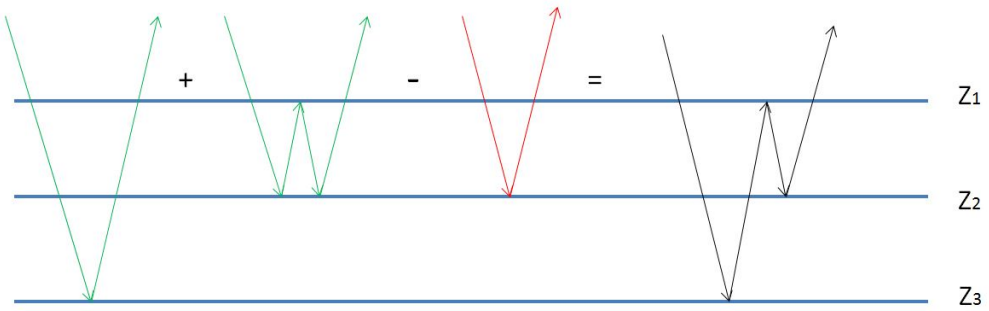

Figure 8: Generation of a first-order internal multiple when an internal-multiple subevent is in the outer integral

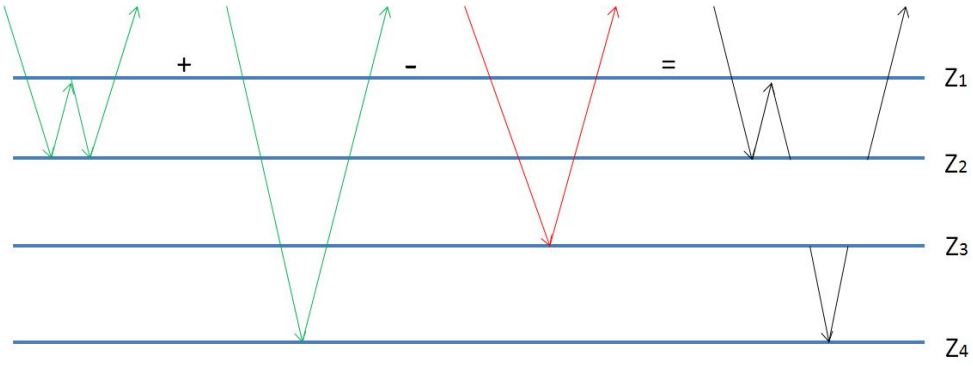

Figure 9: Generation of a false event when an internal-multiple subevent is in the outer integral, $2z_2 - z_1 > z_3$.

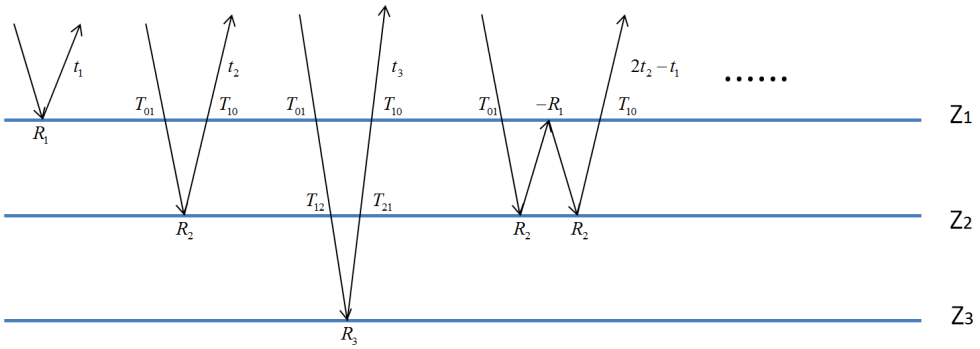

Figure 10: A one-dimensional model with three interfaces.

The new ISS internal-multiple algorithm for this case with more than three reflectors is

$$D_1(t) + D_3(t) + D_5^{PIP}(t) + D_5^{PPI}(t). \tag{3.4}$$

where $D_5^{PPI}(t)$ is the Fourier transform of $D_5^{PPI}(\omega)$, and $D_5^{PPI}(\omega) = b_5^{PIP}(k)$ for an incident spike wave. This new general algorithm in equation 3.4 retains the strengths of the original algorithm while addressing issues that are due to spurious events.

4 Numerical examples

In this section, we will compute and analyze the new terms for one-dimensional, three-interface models. The spurious event would be produced when the internal-multiple subevent is in the second of the three integrals (see the discussions in Sections 3.1 and 3.2). Thus, only the algorithm in Section 3.1 will be tested in this section. Numerical tests are presented using both analytic data and synthetic data.

4.1 Numerical tests using analytic data

The test results obtained by using analytic data are shown in this section. For the model shown in Figure 10 the reflection data that are due to an impulsive incident wave $\delta(t - \frac{z}{c})$ are

$$\begin{aligned} D(t) = {} & R_1\delta(t - t_1) + T_{01}R_2T_{10}\delta(t - t_2) + T_{01}T_{12}R_3T_{21}T_{10}\delta(t - t_3) \\ & - T_{01}R_2^2R_1T_{10}\delta(t - (2t_2 - t_1)) \ldots, \end{aligned} \tag{4.1}$$

where $t_1 = 0.4s$, $t_2 = 0.5s$, and $t_3 = 1.0s$. The velocities in each layer of the model are $c_0 = 1500m/s$, $c_1 = 2500m/s$, $c_2 = 4000m/s$, and $c_3 = 6000m/s$. The densities in the model are constant. Since velocities are increasing with depth, all upward reflections yield positive reflection coefficients. R_i

and T_{ij} are reflection and transmission coefficients, respectively. We choose the temporal data so that they contain only three primaries and all first-order internal multiples. The temporal Fourier transform is given by

$$D(\omega) = R_1 e^{i\omega t_1} + T_{01}R_2T_{10}e^{i\omega t_2} + T_{01}T_{12}R_3T_{21}T_{10}e^{i\omega t_3} - T_{01}R_2^2R_1T_{10}e^{i\omega(2t_2-t_1)}\ldots \tag{4.2}$$

The first term in the internal-multiple-attenuation algorithm is given by Weglein et al. (2003)

$$b_1(k) = D(\omega) = R_1 e^{ikz_1} + T_{01}R_2T_{10}e^{ikz_2} + T_{01}T_{12}R_3T_{21}T_{10}e^{ikz_3} - T_{01}R_2^2R_1T_{10}e^{ik(2z_2-z_1)}\ldots, \tag{4.3}$$

where the pseudo-depths z_1,z_2 and z_3 are defined as $z_1 = c_0t_1/2$, $z_2 = c_0t_2/2$, and $z_3 = c_0t_3/2$, c_0 is a reference velocity, and $k = 2\omega/c_0$ is the vertical wave number. The data in the wavenumber domain (see equation 4.3) are first input into equation 2.3 to calculate b_3. Then both b_1 and b_3 are used by equation 3.1 to calculate b_5^{PIP}.

Figure 11 shows the data consisting of primaries and first-order internal multiples, where P_i represents the primary reflected at the i^{th} reflector, and I_{ijk} denotes the first-order internal multiple with one downward reflection at the j^{th} reflector and two upward reflections at the i^{th} and k^{th} reflectors, respectively. Since the input data consists of both primaries and internal multiples, the leading-order attenuator will produce not only first-order internal multiples, but also higher-order internal multiples (see discussion in 3.2) and false event (see discussion in 3.1). Figure 12(a) shows the calculated D_3, where the false event is at time $1.4s$ and has negative polarity. The false event is produced by the subevents combination of "P_3–I_{212}–P_3", and its amplitude is -3.9331×10^{-4}. Figure 12(b) shows the calculated D_5^{PIP}, where the predicted false event is at time $1.4s$ and has positive polarity. The predicted false event is produced by the subevents combination of "P_3–predicted I_{212}–P_3',' and its amplitude is 3.7832×10^{-4}, which is slightly smaller than amplitude of the produced false event. Figure 13(a) is the result after subtracting primaries from the sum of D and D_3 , while Figure 13(b) is the result after subtracting primaries from the sum of D, D_3 and D_5^{PIP}. From the result, we can see that the false event has been significantly attenuated by the new algorithm (see equation 3.1).

It should be noted that in Figure 12(a) the internal multiple I_{323} predicted by b_3 is composed of three subevent combinations: "P_3–P_2–P_3", "P_3–I_{212}–I_{312}" and "I_{312}–I_{212}–P_3". From Figure 12(b) we can see that D_5^{PIP} can also predict internal multiples since all the events in b_1 are used as subevents in equation 3.1. For example, the event at 1.5s in Figure 12(b) has the same traveltime as dose I_{323}, and it has negative polarity. Further, it can be generated by the following subevent combination: I_{312} in D (negative), predicted I_{212} in D_3 (positive) and P_3 in D (positive). The new algorithm represents progress in the attenuation of first-order internal multiples. Research is ongoing to provide further insight and capability.

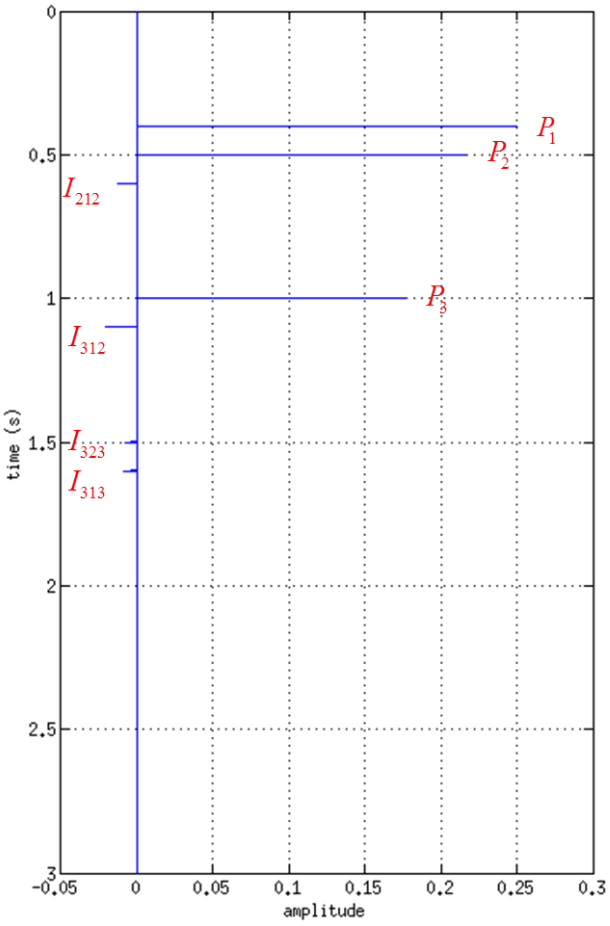

Figure 11: Primaries and first-order internal multiples in the data.

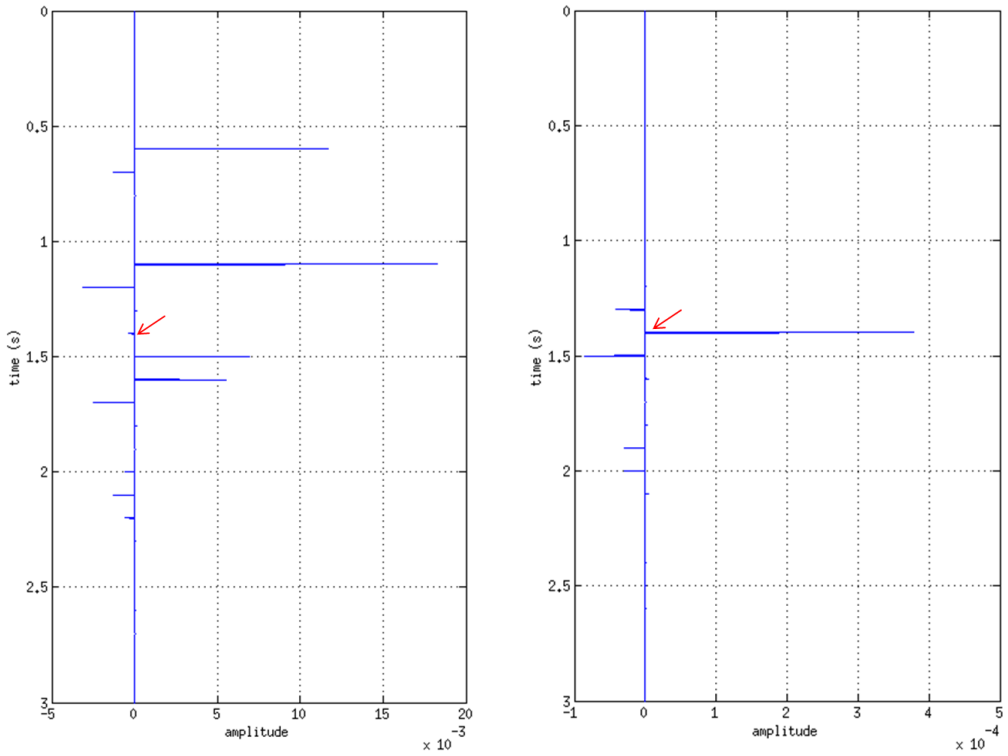

(a) (b)

Figure 12: (a) D_3 consisting of first-order internal multiples, higher-order internal multiples and the false event (pointed to by the red arrow and with an amplitude of -3.9331×10^{-4}). (b) The calculated D_5^{PIP}, containing internal multiples and predicted false event (pointed to by the red arrow and with an amplitude of 3.7832×10^{-4}).

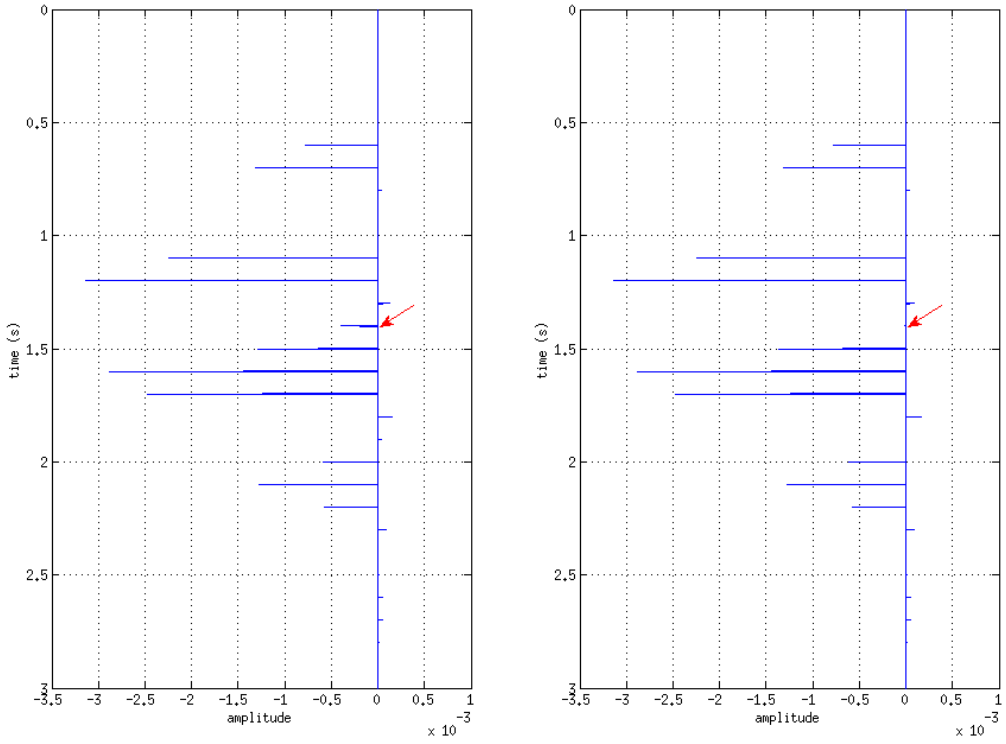

(a) (b)

Figure 13: (a) The result of $D + D_3-$ primaries, containing the remaining multiples and the false event, with a red arrow pointing to the produced false event in D_3. (b) The result of $D+D_3+D_5^{PIP}-$ primaries, containing the remaining multiples and the false event after attenuation, with a red arrow pointing to the attenuated false event.

4.2 Numerical tests using synthetic data

In this section we show the test result obtained by using synthetic data. A one-dimensional two-parameter (with both velocity and density variation) model with three interfaces is used to generate the data. The chosen parameters for the model are:

$c_0 = 1500m/s, c_1 = 2500m/s, c_2 = 3500m/s, c_3 = 4500m/s;$
$\rho_0 = 1.0g/cm^3, \rho_1 = 2.0g/cm^3, \rho_2 = 3.0g/cm^3, \rho_3 = 4.0g/cm^3;$
$z_1 = 500m, z_2 = 1000m, z_3 = 3500m,$

where c_i and ρ_i represent the velocity and density in each layer, respectively, and z_i is the depth of each interface. The model parameters are chosen so that the internal multiples are relatively strong. Figure 14(a) shows the zero-offset data generated using finite-difference modeling. The internal multiples predicted by the leading-order attenuator are shown in Figure 14(b), where the red arrow points to the produced false event. In Figure 15(b) each event predicted by b_3^{IM} is labeled, e.g., "2-1-2" means the first-order internal multiple with two upward reflections at the second reflector and one downward reflection at the first reflector. Figure 15(a) shows the false event predicted by b_5^{PIP}.

Similarly to the case in the previous Section, the b_5^{PIP} term here predicts not only the false event but also internal multiples. For example, the predicted I_{323} in Figure 15(a) is generated by the subevents combination of "I_{312}–predicted I_{212}–P_3" and the predicted I_{312} is generated by the combination of "I_{21212}–predicted I_{212}–P_3".

5 Discussion

In this report, we discussed the general output of the ISS leading-order attenuator when internal multiples are used as subevents and we proposed further new terms to improve that output by avoiding the prediction of spurious events. The logic path that the method uses for removing the spurious event follows the way in which the spurious event is generated. In the analysis of spurious-event generation and removal, we only consider the cases where just one internal multiple is used as a subevent (see discussions in Sections 3.1 and 3.2). When more than one internal multiple is used as subevents, the generated events are weak in amplitude.

As discussed in Section 3.1, the subevents combination of "primary–predicted internal multiple–primary" in the new term b_5^{PIP} is used to attenuate the spurious event produced by the subevents combination of "primary–internal multiple–primary" in b_3. Therefore, if the predicted internal multiples have exactly the same amplitude that the true internal multiples in the data have, the algorithms presented in this report could eliminate the spurious events. For the purpose of spurious-events elimination, further inclusion of the ISS internal-multiple-elimination algorithm could be one possible solution (Ramírez, 2007).

Finally, when spurious events are produced by the leading-order attenuator b_3, they could also be used as subevents in the new terms b_5^{PIP} or b_5^{PPI}, since b_3 is one of their inputs. If this were the case new types of spurious events would be generated. However, the newly generated spurious events have much weaker amplitudes. Furthermore, other types of new terms can be identified to address this issue (Ma et al., 2012).

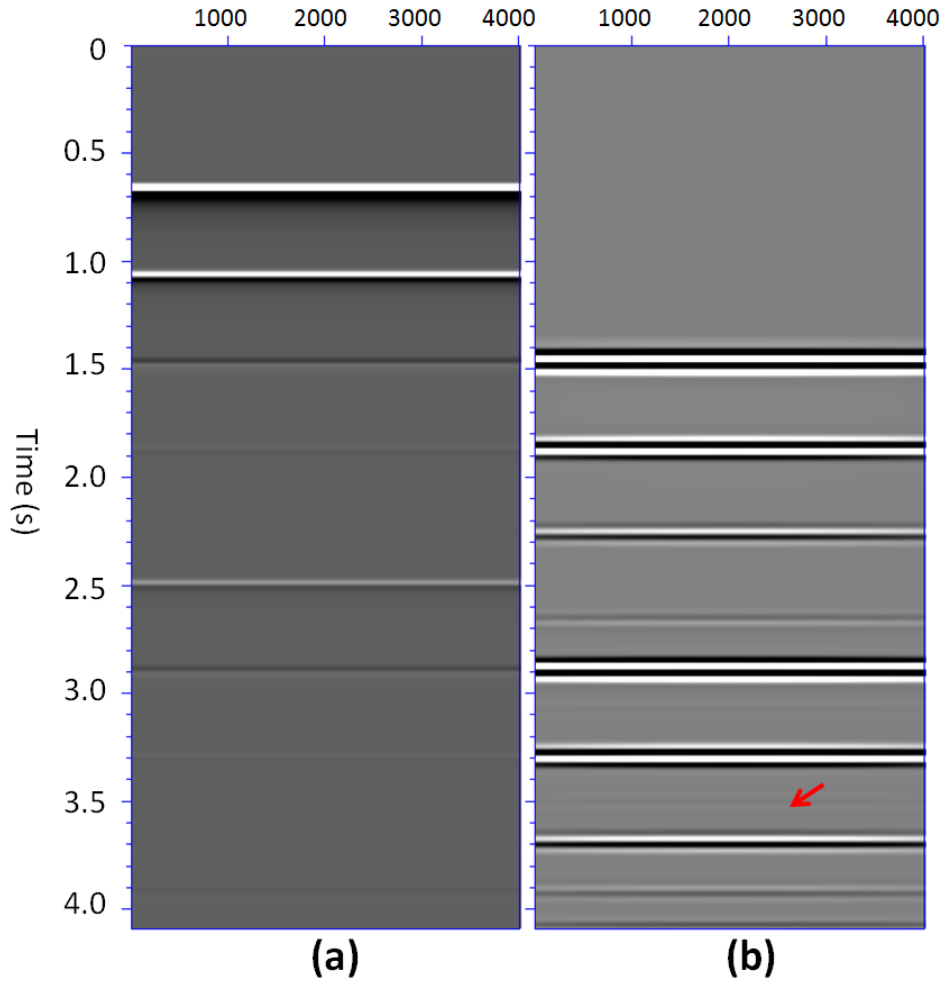

Figure 14: (a) Zero-offset data, where three primaries are at $0.667s$, $1.067s$ and $2.495s$, respectively. (b) Events predicted by b_3, with the red arrow pointing to the spurious event (at $3.524s$).

6 Conclusions

While the ISS leading-order attenuator has demonstrated its capability for internal-multiple removal, it has strengths and limitations as implied by "leading-order" and "attenuator". The algorithm presented in this report and in Ma et al. (2012) addresses a shortcoming of the current leading-order ISS internal-multiple-attenuation algorithm that is observed in the examples of Fu et al. (2010) and Luo et al. (2011). The new ISS internal-multiple-attenuation algorithm retains the benefit of the original algorithm, while addressing one of its shortcomings. The new algorithm now accommodates both primaries and internal multiples in the input data.

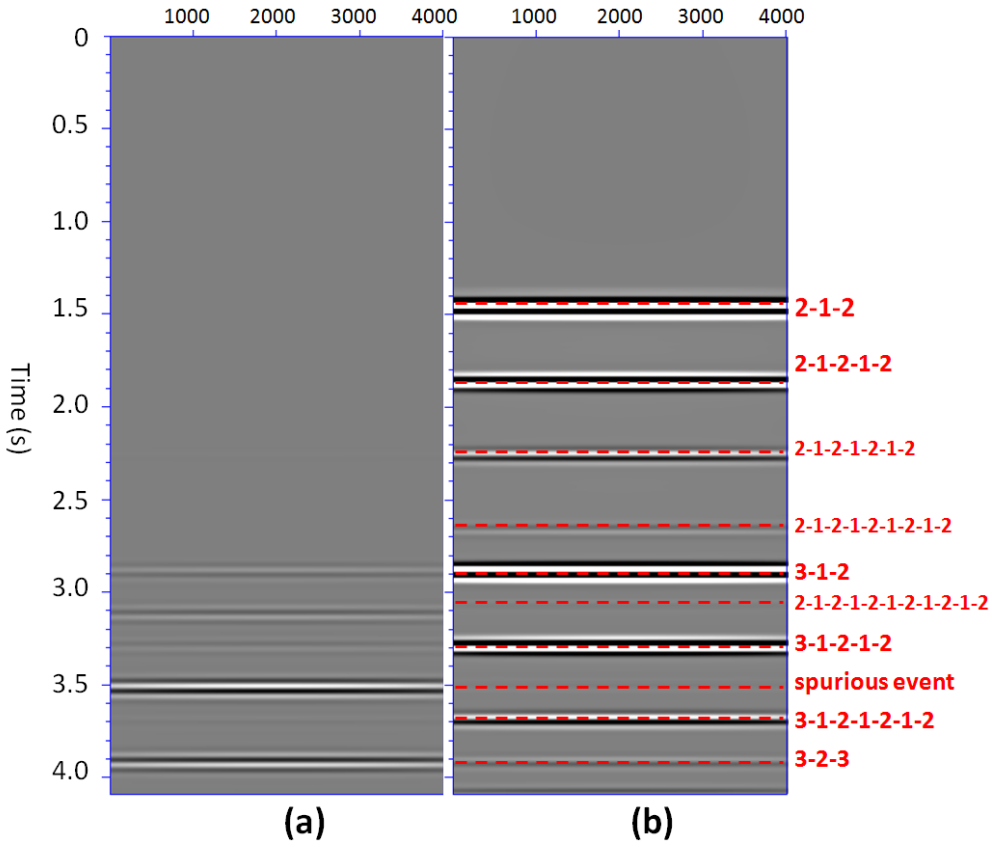

Figure 15: (a) Events produced by b_5^{PIP}, where the negative of the spurious event is at $3.524s$. (b) Events produced by b_3, with labels.

7 Acknowledgements

We are grateful to all M-OSRP sponsors for their support of this research. Special thanks to Paolo Terenghi for assistance, Jim Mayhan for reviewing, Wilberth Herrera for discussions and Adriana Ramírez for useful comments.

References

Araújo, F. V., A. B. Weglein, P. M. Carvalho, and R. H. Stolt. "Inverse scattering series for multiple attenuation: An example with surface and internal multiples." *SEG Technical Program Expanded Abstracts* (1994): 1039–1041.

Coates, R. T. and A. B. Weglein. "Internal multiple attenuation using inverse scattering: Results from prestack 1 & 2D acoustic and elastic synthetics." *SEG Technical Program Expanded Abstracts* (1996): 1522–1525.

Fu, Q., Y. Luo, G. K. Panos, S. Huo, G. Sindi, S. Hsu, and A. B. Weglein. "The inverse scattering

series approach towards the elimination of land internal multiples." *SEG Technical Program Expanded Abstracts* (2010): 3456–3461.

Hsu, S., P. Terenghi, and A. B. Weglein. "The properties of the inverse scattering series internal multiple attenuation algorithm: Analysis and evaluation on synthetic data with lateral variations, choosing reference velocity and examining its sensitivity to near surface properties." *Mission-Oriented Seismic Research Program (M-OSRP), Annual Report* (2011): 16–28.

Luo, Y., P. G. Kelamis, Q. Fu, S. Huo, G. Sindi, S. Hsu, and A. B. Weglein. "Elimination of land internal multiples based on the inverse scattering series." *The Leading Edge* (2011): 884–889.

Ma, C., H. Liang, and A. B. Weglein. "A new Inverse Scattering Series (ISS) internal multiple attenuation algorithm responds to a limitation in the current algorithm: derivation for a three-reflector model and a test with analytic data." *to be submitted to the SEG Technical Program Expanded Abstracts* (2012).

Matson, K. H. *An inverse-scattering series method for attenuating elastic multiples from multi-component land and ocean bottom seismic data.* PhD thesis, University of British Columbia, 1997.

Matson, K. H. and A. B. Weglein. "The relationship between scattering theory and primaries and multiples of reflection seismic data." *Journal of Seismic Exploration* (1996): 63–78.

Matson, K. H. and A. B. Weglein. "Removal of elastic interface multiples from land and ocean bottom data using inverse scattering." *SEG Technical Program Expanded Abstract* (1996): 1526–1530.

Ramírez, A. C. *I.-Inverse scattering subseries for removal of internal multiples and depth imaging primaries; II.-Green's theorem as the foundation of interferometry and guiding new practical methods and applications.* PhD thesis, University of Houston, 2007.

Ramírez, A. C. and A. B. Weglein. "An inverse scattering internal multiple elimination method: Beyond attenuation, a new algorithm and initial test." *SEG Technical Program Expanded Abstracts* (2005): 2115–2118.

Terenghi, P., S. Hsu, A. B. Weglein, and X. Li. "Exemplifying the specific properties of the inverse scattering series internal-multiple attenuation method that reside behind its capability for complex onshore and marine multiples." *The Leading Edge* (2011): 876–882.

Weglein, A. B., F. V. Araújo, P. M. Carvalho, R. H. Stolt, K. H. Matson, R. T. Coates, D. Corrigan, D. J. Foster, S. A. Shaw, and H. Zhang. "Inverse scattering series and seismic exploration." *Inverse Problems* (2003): R27–R83.

Weglein, A. B., F. A. Gasparotto, P. M. Carvalho, and R. H. Stolt. "An inverse-scattering series method for attenuating multiples in seismic reflection data." *Geophysics* (1997): 1975–1989.

Weglein, A. B., S. Hsu, P. Terenghi, X. Li, and R. Stolt. "Multiple attenuation: Recent advances and the road ahead 2011." *The Leading Edge* (2011): 864–875.

Weglein, A. B. and K. H. Matson. "Inverse scattering internal multiple attenuation: an analytic example and subevent interpretation." *Mathematical Methods in Geophysical Imaging V* (1998): 108–117.

Zhang, H. and S. Shaw. "1-D analytical analysis of higher order internal multiples predicted via the inverse scattering series based algorithm." *SEG Technical Program Expanded Abstracts* (2010): 3493–3498.

Progressing amplitude issues for testing 1D analytic data in leading order internal multiple algorithms

Wilberth Herrera*, Chao Ma*, Hong Liang*, Paolo Terenghi*, and Arthur B. Weglein*
M-OSRP/Physics Dept./UH*

May 25, 2012

Abstract

In Ramírez (2007), a subseries of the Inverse Scattering Subseries (ISS) was isolated, whose specific task is to eliminate internal multiples of first order. This subseries naturally splits into two subseries: the Leading-Order Internal-Multiple-Eliminator Subseries (LOIMES) and the Higher-Order Internal-Multiple-Eliminator Subseries (HOIMES).

The purpose of this report is to propose a modification of the LOIMES. The motivation for such a modification is twofold. First, the original formulation carries a limitation for correctly accommodating spike-like data, due to the presence of powers of the data higher than one, which are not well defined mathematically when the data are spike-like. Second, we wish to apply the LOIMES to the Internal-Multiple-Attenuation Subseries (IMAS) obtained in Ma and Weglein (2012). The proposal splits into two cases: spike-like data and non-spike (but continuous) data. For the spike-like case, the proposal correctly overcomes the limitation of the original approach by explicitly avoiding the higher powers of the data, and it also allows for the elimination of the effect described in Ma and Weglein (2012), and originated by the presence of a specific 1st. order internal multiple in the input data of the leading order contribution of the original IMAS. For continuous data the proposal fixes a mathematical issue that is present in the original approach, regarding the behavior of the subseries when ϵ (the parameter introduced to avoid self interactions) goes to zero. At the same time, however, the proposal brings new questions to the subject because it is not general enough to deal with all types of continuous data; it only works for a very restricted class.

1 Introduction

One of the main challenges of exploration seismology is to locate hydrocarbon targets beneath the earth's surface. To achieve this goal, there is a sequence of steps to be performed in the data resulting from seismic experiments: random-noise attenuation, deghosting, source wavelet deconvolution, removal of free-surface multiples, removal of internal multiples, imaging, and inversion. All these steps must be done in the same order in which they are listed. In particular, all current imaging algorithms assume that the data consist exclusively of primaries, which means that any other type of event (i.e., ghosts and multiples) is considered to be noise by the imaging process and therefore needs to be removed from the data before the application of any imaging algorithm.

Today, there are a number of methodologies in the oil industry that are designed to handle the different steps just mentioned. In particular, for the removal of internal multiples, one of the standard methods is the energy-minimization adaptive substraction. This method works by using the internal multiples predicted by a given model, and then systematically substracting this prediction from the actual data, using the minimum energy criteria: the energy after the removal should be minimal. However, this method fails, among other situations, when an internal multiple is interfering with a primary. The reason is that in this situation the minimum energy criterium is no longer valid, and the adaptive substraction affects also the amplitude of the primary.

A new criteria for adaptive subtraction in then necessary, but is not yet available. As such criteria must deal with factors from the system (wavelet, ghosts internal multiples, etc.) and outside the system (such as the irregular shape the free surface), what we can do in the meantime is to lower the burden for the adaptive substraction. This can be done by applying to the system all the preprocessing tools we have at hand. In this way, we help the adaptive subtraction to take care mostly of the factors outside the system, and hence to improve its effectiveness.

Using the ISS and the concept of specific-task subseries, a multidimensional algorithm to remove free-surface multiples was derived in Carvalho (1992), using no information about the earth's subsurface. Later on, this work was extended in Araújo (1994), where a multidimensional algorithm was derived to attenuate internal multiples present in the data. However, to reach the goal of lowering the burden of the adaptive subtraction as much as possible, it is important to move the atenuation of internal multiples to a total elimination.

In response to this necessity, a further subseries was isolated in Ramírez (2007). The specific task of this subseries is to remove, rather than attenuate, internal multiples of first order. However, this subseries is unable to deal with spike-like data, as in this case there is a mathematical inconsistency: the subseries contains powers of the data higher than one and these powers are not well defined when the data are spike-like (analytic). The subseries splits into two subseries: the Leading-Order Internal-Multiple-Eliminator Subseries (LOIMES) and the Higher-Order Internal-Multiple-Eliminator Subseries (HOIMES). The LOIMES eliminates internal multiples that are of first-order and whose downward reflection takes place at the shallowest reflector, while the HOIMES eliminates the first-order internal multiples generated at any reflector other than the shallowest.

Although in practice the field data is never a spike, it is very important to test any new algorithm with analytic data, as in this case the data is error-free and we have total control on them. This means that if we test the algorithm with analytic data, any error in the output is an error in the algorithm. In other words, with analytic data we can isolate and test the concept behind the algorithm. Once the algorithm is successful with analytic data, we can go ahead and test it with synthetic data, and eventually with field data.

In this report, we modify the original derivation of the LOIMES to allow for spike-like data. We focus on the LOIMES because of its immediate application to recent developments in Ma and Weglein (2012) and Liang and Weglein (2012), where the original Internal-Multiple-Attenuator Subseries (IMAS) of Araújo and Weglein is extended to allow the input data to include first-order internal multiples. In particular we show, by specific example, how this modified algorithm for the LOIMES can be used to move the work in Ma and Weglein (2012), from an attenuator to an eliminator of the effect of a particular internal multiple in the input data. Along the way, we also find the need to rederive the LOIMES (and in general the first-order IMES) when the data are not spike-like (but

are continuous). In this case, we find a derivation that is valid only for highly constrained data. This last fact, together with the analysis of Ramírez and Weglein in the original derivation of the first-order IMES, strongly suggests that more research in the subject is necessary, as there is no physical reason for the elimination to take place only within some subset of data.

The organization of this report is as follows: in section 2, we review the original derivation of the IMES proposed by Ramírez and Weglein. In section 3 we point out the limitation of the LOIMES in dealing with spike-like data and explain how to overcome this limitation, by a modification of the algorithm specific for such data. We also apply this modified algorithm to promote (for a specific earth model) the IMAS in Ma and Weglein (2012) to being an eliminator for the effect of the inclusion of a specific internal multiple in the input data. In section 4, we propose a slightly different way to derive the LOIMES for continuous data, and we also make a few comments about the HOIMES. Finally, in section 5 we present final comments and conclusions. There are two appendices, in which we show the details of the calculations needed to follow the main body of this report.

2 Review of the (LO)IMES

In this section, we will provide the line of thought for the original derivation of the LOIMES, and at the same time we will highlight the problem we aim to solve. For simplicity, in this report we will focus on a 1D earth with normal incidence.

The key point in the original approach of Ramírez (2007), in moving from the attenuator to the eliminator, is to take into account certain self interactions of the effective data, denoted $b_1(z)$, that contain the correct amplitude compensation for eliminating the internal multiples rather than just for attenuating them. The resulting Internal-Multiple-Eliminator Subseries (IMES) is

$$b^{IM}(k) = b^{IM}_{LO}(k) + b^{IM}_{HO}(k), \tag{2.1}$$

where

$$b^{IM}_{LO}(k) = \int_{-\infty}^{\infty} dz e^{ikz} b_1(z) \int_{-\infty}^{z-\epsilon} dz' e^{-ikz'} \left(\frac{1}{1-b_1(z')^2} \right) b_1(z') \times \int_{z'+\epsilon}^{\infty} dz'' e^{ikz''} b_1(z''), \tag{2.2}$$

and

$$b^{IM}_{HO}(k) = \int_{-\infty}^{\infty} dz e^{ikz} b_1(z) \int_{-\infty}^{z-\epsilon} dz' e^{-ikz'} \frac{2G(z') \int_{-\infty}^{z'-\epsilon} dz''' J(z''')}{1-\int_{-\infty}^{z'-\epsilon} dz''' J(z''')} \times \int_{z'+\epsilon}^{\infty} dz'' e^{ikz''} b_1(z''), \tag{2.3}$$

where

$$J(z''') = \frac{b_1(z''')^2}{1 - b_1(z''')^2} \qquad G(z') = \frac{b_1(z')}{1 - b_1(z')^2}. \tag{2.4}$$

The task of the leading-order eliminator b_{LO}^{IM} is to eliminate, when it is added to the effective data, the internal multiples of first order generated at the shallowest reflector. The higher-order eliminator b_{HO}^{IM} eliminates the first-order internal multiples created at deeper reflectors, and assumes that b_{LO}^{IM} has been applied to data.

For now, we will focus on the leading-order eliminator b_{LO}^{IM}, whose initial terms are as follows:

$b_{LO}^{IM} = \int_{-\infty}^{\infty} dz e^{ikz} b_1(z) \int_{-\infty}^{z-\epsilon} dz' e^{-ikz'} \left(b_1(z') + b_1(z')^3 + b_1(z')^5 + ... \right) \times$

$$\int_{z'+\epsilon}^{\infty} dz'' e^{ikz''} b_1(z''). \tag{2.5}$$

Expanding (2.5), we notice that the resulting first term is exactly the first term in the IMAS discussed in Araújo (1994), and the following terms contain the self interactions (in the middle integral) mentioned in the second paragraph of the present section. Now, we will briefly describe the origin of these self interactions by analyzing the first self-interacting term-namely, the one containing $b_1(z')^3$:

$$b_5^{IM}(k) = \int_{-\infty}^{\infty} dz e^{ikz} b_1(z) \int_{-\infty}^{z-\epsilon} dz' e^{-ikz'} b_1(z')^3 \int_{z'+\epsilon}^{\infty} dz'' e^{ikz''} b_1(z''). \tag{2.6}$$

The whole term, being of fifth order in the data, must reside somewhere within the fifth inverse scattering equation. The correct term of this equation turns out to be $V_1 G_0 V_3 G_0 V_1$, from which, after selecting the model-type independent contribution, writing it in terms of effective data b_1, picking up the term with the right nonlinear characteristics to predict the internal multiple's time, and finally selecting the *lower-higher-lower* contribution, we are left with

$$\int_{-\infty}^{\infty} dz e^{ikz} b_1(z) \int_{-\infty}^{z-\epsilon} dz' e^{-ikz'} \hat{b}_3(z') \int_{z'+\epsilon}^{\infty} dz'' e^{ikz''} b_1(z''), \tag{2.7}$$

where $\hat{b}_3(z')$ is the data representation of the model-type independent part of the third equation in the inverse scattering series

$$V_3 = -V_1 G_0 V_1 G_0 V_1 - V_1 G_0 V_2 - V_2 G_0 V_1. \tag{2.8}$$

Finally, we still need to focus on $B_3(k)$, the part of $\hat{b}_3(z')$ coming from $V_1 G_0 V_1 G_0 V_1$:

$$B_3(k) = \int_{-\infty}^{\infty} dz e^{ikz} b_1(z) \int_{-\infty}^{\infty} dz' e^{-ikz'} b_1(z') \int_{-\infty}^{\infty} dz'' e^{ikz''} b_1(z''). \tag{2.9}$$

From (2.6) and (2.7), it is clear that the self interactions must arise from (2.9), so we need to split $B_3(k)$ in a way that makes these self interactions evident. The result proposed in Ramírez (2007) is:

$$
\begin{aligned}
&B_3(k) = \textstyle\int_{-\infty}^{\infty} dz e^{ikz} b_1(z) \int_{-\infty}^{z-\epsilon} dz' e^{-ikz'} b_1(z') \int_{z'+\epsilon}^{\infty} dz'' e^{ikz''} b_1(z'') \\
&+ \textstyle\int_{-\infty}^{\infty} dz e^{ikz} b_1(z) \int_{z+\epsilon}^{\infty} dz' e^{-ikz'} b_1(z') \int_{-\infty}^{z'-\epsilon} dz'' e^{ikz''} b_1(z'') \\
&+ \textstyle\int_{-\infty}^{\infty} dz e^{ikz} b_1(z) \int_{z+\epsilon}^{\infty} dz' e^{-ikz'} b_1(z') \int_{z'+\epsilon}^{\infty} dz'' e^{ikz''} b_1(z'') \\
&+ \textstyle\int_{-\infty}^{\infty} dz e^{ikz} b_1(z) \int_{-\infty}^{z-\epsilon} dz' e^{-ikz'} b_1(z') \int_{-\infty}^{z'-\epsilon} dz'' e^{ikz''} b_1(z'') \\
&+ \textstyle\int_{-\infty}^{\infty} dz e^{ikz} b_1(z) \int_{-\infty}^{\infty} dz' e^{-ikz'} b_1(z') \delta(z-z') \int_{-\infty}^{\infty} dz'' e^{ikz''} b_1(z'') \delta(z'-z'') \\
&+ \textstyle\int_{-\infty}^{\infty} dz e^{ikz} b_1(z) \int_{-\infty}^{\infty} dz' e^{-ikz'} b_1(z') \delta(z-z') \int_{z'+\epsilon}^{\infty} dz'' e^{ikz''} b_1(z'') \\
&+ \textstyle\int_{-\infty}^{\infty} dz e^{ikz} b_1(z) \int_{-\infty}^{\infty} dz' e^{-ikz'} b_1(z') \delta(z-z') \int_{-\infty}^{z'-\epsilon} dz'' e^{ikz''} b_1(z'') \\
&+ \textstyle\int_{-\infty}^{\infty} dz e^{ikz} b_1(z) \int_{z+\epsilon}^{\infty} dz' e^{-ikz'} b_1(z') \int_{-\infty}^{\infty} dz'' e^{ikz''} b_1(z'') \delta(z'-z'') \\
&+ \textstyle\int_{-\infty}^{\infty} dz e^{ikz} b_1(z) \int_{-\infty}^{z-\epsilon} dz' e^{-ikz'} b_1(z') \int_{-\infty}^{\infty} dz'' e^{ikz''} b_1(z'') \delta(z'-z'') \\
&= B_{31}(k) + B_{32}(k) + B_{33}(k) + B_{34}(k) \\
&\qquad + B_{35}(k) + B_{36}(k) + B_{37}(k) + B_{38}(k) + B_{39}(k). \qquad (2.10)
\end{aligned}
$$

In the above expression for $B_3(k)$, we can see that the self-interaction terms come from the Delta functions in the last five terms. Performing the integrals with the Delta functions in $B_{35}(k)$, followed by an inverse Fourier transform, we end up with $B_3(z') = b_1(z')^3$. Inserting this portion of $\hat{b}_3(z')$ into (2.7), we find exactly (2.6), the second term of b_{LO}^{IM}.

The next self-interaction contribution to b_{LO}^{IM}, $b_1(z')^5$, is obtained by analogous arguments applied to $V_1 G_0 V_5 G_0 V_1$, to finally get

$$\int_{-\infty}^{\infty} dz e^{ikz} b_1(z) \int_{-\infty}^{z-\epsilon} dz' e^{-ikz'} b_1(z')^5 \int_{z'+\epsilon}^{\infty} dz'' e^{ikz''} b_1(z''). \qquad (2.11)$$

The closed form, eq. (2.2), becomes evident by calculating, following the procedure just described, a few terms beyond $b_1(z')^5$.

3 LOIMES and spike-like data

In this section, we will describe a limitation of the formalism described above to eliminate internal multiples, and we will also explain the solution when the data are spike-like. As a result, the original algorithm for the LOIMES will change and the correct prescription will be provided (at least when the data are spike-like). We will also apply this prescription to illustrate how to promote the IMAS discussed in Ma and Weglein (2012) to an eliminator of certain unwanted events predicted by the IMAS under some circumstances. In the next section we will discuss an approach solving the limitation when the data are not spike-like but instead are continuous.

3.1 Statement of the problem

As we mentioned earlier, we consider a 1D earth with normal incidence and two interfaces at pseudodepths $z_1 \equiv c_0 t_1/2$ and $z_2 \equiv c_0 t_2/2$ with respect to a homogeneous reference medium with constant velocity c_0. The terms t_1 and t_2 are the traveltimes associated with the primaries created at the first (shallowest) and second (deepest) reflector, respectively. Consider also spike-like data, assumed to be built up from primaries and the unique first-order internal multiple allowed by this two-layer example (strictly speaking, for this subsection we do not need any internal multiple in the data, but it is included for further convenience):

$$D(t) = R_1\delta(t-t_1) + T_{01}R_2T_{10}\delta(t-t_2) - T_{01}R_2R_1R_2T_{10}\delta(t-(2t_2-t_1)) \tag{3.1}$$

where $2t_2 - t_1$ is the traveltime associated with the first-order internal multiple and T_{ij} denotes the transmission coefficient when the wave travels from the ith medium to the jth medium. R_k is the reflection coefficient at the kth layer for a downward incident wave. Expressed in depth units the data become

$$b_1(z) = R_1\delta(z-z_1) + T_{01}R_2T_{10}\delta(z-z_2) - T_{01}R_2R_1R_2T_{10}\delta(z-(2z_2-z_1)). \tag{3.2}$$

If we try to compute the second term of b_{LO}^{IM}, eq. (2.6), using the data given by (3.2), we immediately run into serious theoretical issues because $b_1(z')^3$ will involve terms with powers of the Delta functions higher than one, i.e., terms like $\delta^3(z-z_1)$, etc. Unfortunately, the powers of the Delta function are not well-defined mathematical objects and hence the spike-like data do not fit in this formalism.

3.2 Fixing the problem

We will now propose a different way to deal with spike-like data to eliminate internal multiples of first order generated at the shallowest reflector; i.e.; we will explain how to deal with the LOIMES when the data are spike-like.

The starting point is eq. (2.10): it turns out that this expression has a subtle inconsistency. To see this, take the limit $\epsilon \to 0$, and use the following relations, involving definite integrals

$$lim_{\epsilon\to 0}\int_{-\infty}^{z-\epsilon} dz' f(z') = \int_{-\infty}^{z} dz' f(z') \qquad lim_{\epsilon\to 0}\int_{z+\epsilon}^{\infty} dz' f(z') = \int_{z}^{\infty} dz' f(z'). \tag{3.3}$$

The resulting expression is

$$\begin{aligned}
&B_3(k) = B_3(k)\\
&+\textstyle\int_{-\infty}^{\infty} dz e^{ikz} b_1(z) \int_{-\infty}^{\infty} dz' e^{-ikz'} b_1(z')\delta(z-z') \int_{-\infty}^{\infty} dz e^{ikz''} b_1(z'')\delta(z'-z'')\\
&+\textstyle\int_{-\infty}^{\infty} dz e^{ikz} b_1(z) \int_{-\infty}^{\infty} dz' e^{-ikz'} b_1(z')\delta(z-z') \int_{z'}^{\infty} dz e^{ikz''} b_1(z'')\\
&+\textstyle\int_{-\infty}^{\infty} dz e^{ikz} b_1(z) \int_{-\infty}^{\infty} dz' e^{-ikz'} b_1(z')\delta(z-z') \int_{-\infty}^{z'} dz e^{ikz''} b_1(z'')
\end{aligned}$$

$+\int_{-\infty}^{\infty} dz e^{ikz} b_1(z) \int_{z}^{\infty} dz' e^{-ikz'} b_1(z') \int_{-\infty}^{\infty} dz e^{ikz''} b_1(z'') \delta(z'-z'')$

$$+ \int_{-\infty}^{\infty} dz e^{ikz} b_1(z) \int_{-\infty}^{z} dz' e^{-ikz'} b_1(z') \int_{-\infty}^{\infty} dz e^{ikz''} b_1(z'') \delta(z'-z''), \tag{3.4}$$

which is obviously inconsistent, because the contribution of the interaction terms is not zero. To fix this problem, let's go back to eq. (2.9) and split the second and third intervals of integration as follows:

$\int_{-\infty}^{\infty} = \int_{-\infty}^{z-\epsilon} + \int_{z-\epsilon}^{z+\epsilon} + \int_{z+\epsilon}^{\infty}$

$$\int_{-\infty}^{\infty} = \int_{-\infty}^{z'-\epsilon} + \int_{z'-\epsilon}^{z'+\epsilon} + \int_{z'+\epsilon}^{\infty}. \tag{3.5}$$

The resulting expression is

$B_3(k) = \int_{-\infty}^{\infty} dz e^{ikz} b_1(z) \int_{-\infty}^{z-\epsilon} dz' e^{-ikz'} b_1(z') \int_{z'+\epsilon}^{\infty} dz'' e^{ikz''} b_1(z'')$

$+ \int_{-\infty}^{\infty} dz e^{ikz} b_1(z) \int_{z+\epsilon}^{\infty} dz' e^{-ikz'} b_1(z') \int_{-\infty}^{z'-\epsilon} dz'' e^{ikz''} b_1(z'')$

$+ \int_{-\infty}^{\infty} dz e^{ikz} b_1(z) \int_{z+\epsilon}^{\infty} dz' e^{-ikz'} b_1(z') \int_{z'+\epsilon}^{\infty} dz'' e^{ikz''} b_1(z'')$

$+ \int_{-\infty}^{\infty} dz e^{ikz} b_1(z) \int_{-\infty}^{z-\epsilon} dz' e^{-ikz'} b_1(z') \int_{-\infty}^{z'-\epsilon} dz'' e^{ikz''} b_1(z'')$

$\int_{-\infty}^{\infty} dz e^{ikz} b_1(z) \int_{z-\epsilon}^{z+\epsilon} dz' e^{-ikz'} b_1(z') \int_{z'-\epsilon}^{z'+\epsilon} dz'' e^{ikz''} b_1(z'')$

$+ \int_{-\infty}^{\infty} dz e^{ikz} b_1(z) \int_{z-\epsilon}^{z+\epsilon} dz' e^{-ikz'} b_1(z') \int_{z'+\epsilon}^{\infty} dz'' e^{ikz''} b_1(z'')$

$+ \int_{-\infty}^{\infty} dz e^{ikz} b_1(z) \int_{z-\epsilon}^{z+\epsilon} dz' e^{-ikz'} b_1(z') \int_{-\infty}^{z'-\epsilon} dz'' e^{ikz''} b_1(z'')$

$+ \int_{-\infty}^{\infty} dz e^{ikz} b_1(z) \int_{z+\epsilon}^{\infty} dz' e^{-ikz'} b_1(z') \int_{z'-\epsilon}^{z'+\epsilon} dz'' e^{ikz''} b_1(z'')$

$+ \int_{-\infty}^{\infty} dz e^{ikz} b_1(z) \int_{-\infty}^{z-\epsilon} dz' e^{-ikz'} b_1(z') \int_{z'-\epsilon}^{z'+\epsilon} dz'' e^{ikz''} b_1(z'') =$

$B_{31}(k) + B_{32}(k) + B_{33}(k) + B_{34}(k)$

$$+ B'_{35}(k) + B'_{36}(k) + B'_{37}(k) + B'_{38}(k) + B'_{39}(k). \tag{3.6}$$

In the limit $\epsilon \to 0$, (3.6) reduces trivially to $B_3(k) = B_3(k)$, so we will use this expression, instead of (2.10), as the starting point for the derivation of the LOIMES. In our present approach all the arguments in Ramírez (2007) for the derivation of the LOIMES, prior to eq. (2.10), are unchanged. The difference is that instead of $B_{35}(k)$ in eq. (2.10) we now consider the analogous term $B'_{35}(k)$ in eq. (3.6), as both contain two interactions. Thus, the recipe now is that the second term in b_{LO}^{IM} becomes

$$b_5^{IM}(k) = \int_{-\infty}^{\infty} dz e^{ikz} b_1(z) \int_{-\infty}^{z-\epsilon} dz' e^{-ikz'} B'_{35}(z) \int_{z'+\epsilon}^{\infty} dz'' e^{ikz''} b_1(z''). \tag{3.7}$$

3.3 Example: The three-layer earth

In appendix A we work out the details for the above expression for the same earth model as that of section 3.1: a 1D and three-layer (or two-interface) earth with normal incidence. The only difference with respect to section 3.1 is that this time we assume spike-like and primary-only data. The result for $B'_{35}(z)$ is eq. (A.7), which upon its insertion into (3.7), results in

$$b_5^{IM} = R_1^3 R_2'^2 e^{ik(2z_2 - z_1)} = T_{01}T_{10} * R_1^2 * (T_{01}R_2R_1R_2T_{10})e^{ik(2z_2-z_1)}$$

whose explicit calculation is also performed in appendix A, and the result is eq. (A.10). In the above expression, the notation is also as in section 3.1: T_{ij} denotes the transmission coefficient when the wave travels from the ith medium to the jth medium, and R_k is the reflection coefficient at the kth layer for a downward incident wave.

Eq. (A.10) is consistent with the one obtained in Ramírez (2007) for the same earth configuration. However, in that reference it is assumed that $\delta^n(z - z_i) = \delta(z - z_i)$, where $\delta^n(z - z_i)$ means the nth power of $\delta(z - z_i)$. This statement is wrong and is only true for the definition of the Delta function used for numerical simulations:

$$\delta(z - z_i) = \begin{cases} 1 & z = z_i \\ 0 & z \neq z_i \end{cases}.$$

Going back to our approach, we can now perform an analysis similar to the one presented in Ramírez (2007): when the above expression is added to both the data b_1^{IM} and the first term of the eliminator series $b_3^{IM} = T_{01}T_{10} * (T_{01}R_2R_1R_2T_{10})$ (which is also the second term in the IMAS), we have

$$b_1^{IM} + b_3^{IM} + b_5^{IM} = \ primaries + [-1 + T_{01}T_{10} * (1 + R_1^2)] * (T_{01}R_2R_1R_2T_{10}). \tag{3.8}$$

In the above expression the (-1) term comes from the original first-order internal multiple in the data, whose amplitude is $-T_{01}R_2R_1R_2T_{10}$, and the $1 + R_1^2$ term contains the first two terms in the geometric series expansion for 1:

$$1 = T_{01}T_{10}\left(\frac{1}{T_{01}T_{10}}\right) = T_{01}T_{10}\frac{1}{(1 - R_1^2)} = T_{01}T_{10}(1 + R_1^2 + R_1^4 + R_1^6 + R_1^8 + \ldots). \tag{3.9}$$

This means that $b_3^{IM} + b_5^{IM}$ is closer to 1 than is the attenuator b_3^{IM}, and therefore the internal multiple's amplitude is better estimated, which means that $[-1 + T_{01}T_{10} * (1 + R_1^2)]$ is closer to zero and hence this is a first step toward the complete removal of the internal multiple.

As we explained before, in Ramírez (2007) the next term in the eliminator series, b_7^{IM}, whose amplitude is $T_{01}T_{10} * R_1^4 * T_{01}R_2R_1R_2T_{10}$, arises when we are selecting the appropriate part of $V_1V_5V_1$ by a procedure similar to the one applied in the same reference to $V_1V_3V_1$ to get b_5^{IM}. This procedure will bring, when the data are spike-like, the same issue that we had with b_5^{IM}, i.e., an interaction of the form $b_1(z)^5$ implying a fifth power of the Delta function.

3.4 A modified closed form of the LOIMES

The issue explained in the last paragraph of the previous subsection is solved in exactly the same way we solved the analogous problem for b_5^{IM} i.e. by selecting the same term proposed in Ramírez (2007) for b_7^{IM} and performing the resulting integrals with finite intervals of integration. This procedure can be applied to each higher-order term in the original IMES. After computing a few higher-order terms, we can write a closed form for b_{LO}^{IM}:

$b_{LO}^{IM} = \int_{-\infty}^{\infty} dz e^{ikz} b_1(z) \int_{-\infty}^{z-\epsilon} dz' e^{-ikz'} \times$

$$\mathcal{F}^{-1}\left(\int_{-\infty}^{\infty} dz' e^{ikz'} b_1(z') \frac{1}{1-\int\int b_1(z')}\right) \int_{z'+\epsilon}^{\infty} dz'' e^{ikz''} b_1(z'') \tag{3.10}$$

where $\mathcal{F}^{-1}$ means the inverse Fourier transform and

$$\frac{1}{1-\int\int b_1(z')} \equiv 1 + \int\int b_1(z') + \left(\int\int b_1(z')\right)^2 + \left(\int\int b_1(z')\right)^3 + \dots \tag{3.11}$$

and

$\left(\int\int b_1(z')\right)^n \equiv \int_{z'-\epsilon}^{z'+\epsilon} dz_1 e^{-ikz_1} b_1(z_1) \int_{z_1-\epsilon}^{z_1+\epsilon} dz_2 e^{ikz_2} b_1(z_2) \times$

$\int_{z_2-\epsilon}^{z_2+\epsilon} dz_3 e^{-ikz_3} b_1(z_3) \int_{z_3-\epsilon}^{z_3+\epsilon} dz_4 e^{ikz_4} b_1(z_4) \cdots \times$

$$\int_{z_{(2n-2)}-\epsilon}^{z_{(2n-2)}+\epsilon} dz_{(2n-1)} e^{-ikz_{(2n-1)}} b_1(z_{(2n-1)}) \int_{z_{(2n-1)}-\epsilon}^{z_{(2n-1)}+\epsilon} dz_{2n} e^{ikz_{2n}} b_1(z_{2n}), \qquad n > 0. \tag{3.12}$$

$$\left(\int\int b_1(z')\right)^n \equiv 1, \qquad n = 0. \tag{3.13}$$

In this way we have successfully addressed the problem of incorporating the spike-like data in the LOIMES.

3.5 Application to the IMAS: Removal of effects of internal multiples in the input data

We will now explain an application of the modified LOIMES proposed in this report. In particular, we will see how to eliminate the effect, created by the IMAS, when the input data include internal multiples, and we are working with a specific 1D earth model. Speciffically, this effect is a component of the recorded data whose traveltime cannot be related to a set of reflections and transmissions originated in the reflector boundaries at the subsurface. In other words, it is an event that does not exist in the earth.

In the original IMAS algorithm in Araújo (1994), one of the basic assumptions is that the input data were made only of primaries and that the internal multiples' times are constructed via interactions

of these primaries. In other words, the internal multiples are constructed using the primaries as subevents. However, the data collected from the seismic experiment obviously contain internal multiples, and a consequence of their inclusion as part of the input data for the IMAS is that, under certain conditions, the effects mentioned in the paragraph above are created. The presence of such events can potentially decrease the effectiveness of the subsequent imaging algorithm applied to the data. For this reason, it is important to find the way in which the ISS deals with the presence of those events.

The answer to this is provided in Ma and Weglein (2012) and Liang and Weglein (2012), each of which propose an extension of the IMAS. This extended IMAS contains some terms attenuating the amplitude of the unusual events, created by the presence of internal multiples in the input data. We will go a step further and explain how this attenuator subseries can be extended to an eliminator (of effects of internal multiples in the input data) subseries by using the modified LOIMES proposed in this report. For this we will focus on the simplest situation in which such a unusual event is created: a 1D earth with three reflectors and with the traveltime t_3 of the primary associated with the third layer satisfying $t_3 > 2t_2 - t_1$, where t_2 and t_1 are the traveltimes of the primaries associated with the second and first layer, respectively, and $t_2 > t_1$, as before. We also assume normal incidence and include in the input data the first-order internal multiple, associated with the first (shallowest) layer, and with traveltime $2t_2 - t_1$.

With the assumptions of the paragraph above, the second term of this IMAS becomes

$$b_3(k) + \int_{-\infty}^{+\infty} dz_1' e^{ikz_1'} b_1(z_1') \int_{-\infty}^{z_1'-\epsilon} dz_2' e^{-ikz_2'} b_3(z_2') \int_{z_2'+\epsilon}^{\infty} dz_3' e^{ikz_3'} b_1(z_3'), \tag{3.14}$$

where

$$b_3(k) = \int_{-\infty}^{+\infty} dz_1' e^{ikz_1'} b_1(z_1') \int_{-\infty}^{z_1'-\epsilon} dz_2' e^{-ikz_2'} b_1(z_2') \int_{z_2'+\epsilon}^{\infty} dz_3' e^{ikz_3'} b_1(z_3') \tag{3.15}$$

is the leading order contribution in the original IMAS.

The reason for the second term in (3.14) is as follows. The inclusion of the first-order internal multiple $IM_1 = -T_{01}R_2R_1R_2T_{10}e^{ik[2z_2-z_1]}$ in the input data (z_m, T_{ij} and R_k are defined as in section 3.1) results in the presence of the term $SE = (T_{01}T_{12}R_3T_{21}T_{10})^2(-T_{01}R_2R_1R_2T_{10})e^{ik[2z_2-z_1]}$ in (3.15). Now, if the ISS is right, this event should be attenuated at least in some way; in other words, it should be possible to find a term from the ISS predicting the same phase of the SE but with an attenuated amplitude and positive sign. This is exactly what the second term in (3.14) does: it creates the term $(T_{01}T_{10})(T_{01}T_{12}R_3T_{21}T_{10})^2(T_{01}R_2R_1R_2T_{10})e^{ik[2z_2-z_1]}$, which when added to SE event, results in

$$(1 - T_{01}T_{10})(T_{01}T_{12}R_3T_{21}T_{10})^2(-T_{01}R_2R_1R_2T_{10})e^{ik[2z_2-z_1]}. \tag{3.16}$$

The above expression is an attenuator of the amplitude of SE, because $T_{01}T_{10} < 1$. Our claim in this report is that the ISS is able to completely remove SE rather than just to attenuate it.

In the particular earth model we are considering, it is easy to prove our claim: notice in (3.16) that if we can add to (3.14) more terms from the ISS, such that the correction to the amplitude of SE is changed from $T_{01}T_{01}$ to 1, then the amplitude of the SE is canceled. It is clear that the contributions of the extra terms must match exactly those of (3.9), when we explained how to promote the IMAS proposed by Araújo and Weglein to the role of an eliminator. But we know that in (3.9) this contribution comes from the LOIMES, when eliminating the first-order internal multiple generated at the shallowest reflector. Hence, if it is possible to somehow include the modified LOIMES described in this report into (3.14), then we will be able to eliminate the SE. It turns out that the right place to plug in the LOIMES is in the second term of (3.14), because this is the term responsible for the factor $T_{10}T_{01}$ in (3.16). Therefore, at least for this configuration, (3.14) can be promoted to being an eliminator of SE. This subseries takes the form:

$$b_3(k) + \int_{-\infty}^{+\infty} dz_1' e^{ikz_1'} b_1(z_1') \int_{-\infty}^{z_1'-\epsilon} dz_2' e^{-ikz_2'} b_{LO}^{IM}(z_2') \int_{z_2'+\epsilon}^{\infty} dz_3' e^{ikz_3'} b_1(z_3'), \tag{3.17}$$

whose first term is exactly (3.14). To see explicitly how this subseries works, we write the second term in (3.17) in expanded form:

$$\int_{-\infty}^{+\infty} dz_1' e^{ikz_1'} b_1(z_1') \int_{-\infty}^{z_1'-\epsilon} dz_2' e^{-ikz_2'} (b_3(z_2') + b_5^{IM}(z_2') + ...) \int_{z_2'+\epsilon}^{\infty} dz_3' e^{ikz_3'} b_1(z_3'). \tag{3.18}$$

On the other hand, for the particular earth configuration studied in this example, we have

$$b_3(z) = -T_{01}T_{10} * IM_1 + SE + ... \tag{3.19}$$

$$b_3(z) + b_5^{IM}(z) + ... = -T_{01}T_{10}(1 + R_1^2 + ...) * IM_1 + ... \tag{3.20}$$

Inserting (3.20) into (3.18):

$\int_{-\infty}^{+\infty} dz_1' e^{ikz_1'} b_1(z_1') \int_{-\infty}^{z_1'-\epsilon} dz_2' e^{-ikz_2'} (-T_{01}T_{10}(1 + R_1^2 + ...) * IM_1 + ...) \int_{z_2'+\epsilon}^{\infty} dz_3' e^{ikz_3'} b_1(z_3') =$

$$- T_{01}T_{10}(1 + R_1^2 + ...) * \int_{-\infty}^{+\infty} dz_1' e^{ikz_1'} b_1(z_1') \int_{-\infty}^{z_1'-\epsilon} dz_2' e^{-ikz_2'} IM_1 \int_{z_2'+\epsilon}^{\infty} dz_3' e^{ikz_3'} b_1(z_3') + ... \tag{3.21}$$

Among other terms, (3.21) produces, when the middle integral is combined with the two outer integrals containing the primary associated with the third layer, the event SE. Hence, using (3.9), (3.21) reproduces $-SE$ plus other contributions. Therefore, the first term of eq. (3.14), becomes

$$SE - SE + ... = ... \tag{3.22}$$

From the above expression, it becomes evident that the amplitude of SE is completely removed, as desired.

It is not coincidence that the terms added are exactly those of the LOIMES, as we are trying to eliminate the contribution of an event created by the first-order internal multiple generated at the shallowest reflector; this internal multiple is exactly the contribution that the LOIMES takes care of. In more general earth models, in which events similar to SE can be generated by first-order internal multiples generated at reflectors other than the shallowest, we would need the HOIMES.

It is worth mentioning that (3.17) will bring more terms than the ones needed for the elimination of the SE. It would be interesting to do further research into the specific tasks of these terms.

4 LOIMES and continuous data

In section 2, we modified the LOIMES to correctly accomodate spike-like data. The key point was writing the correct splitting of $B_3(k)$, eq. (3.6), as opposed to eq. (2.10), and then selecting $B'_{35}(k)$ instead of $B_{35}(k)$. Analogously, in this section we will propose a derivation for the LOIMES, suitable for nonspike-like but continuous data, starting from eq. (3.6) and $B'_{35}(k)$.

4.1 LOIMES and the mean value theorem

Our goal is to make explicit the interactions contained in the finite-interval integrations in eq. (3.6). For that we will use a sort of "complex mean value theorem" (CMVT) :

$$\int_a^b f(z)dz = (b-a)f(\eta) \quad for\ some\ \eta \in (b,a), \tag{4.1}$$

where $f(z)$ is a complex-valued, real function. Also we assume that the real and imaginary parts of $f(z)$ are continuous on (a,b).

For complex-valued functions, eq. (4.1) is not true in general, but it can be for certain cases. Hence, (4.1) is a restriction for the data in which the present approach to the LOIMES can be applied. To determine whether the CMVT applies to a given data, we need to split $f(z)$ into real and imaginary parts and apply the usual mean value theorem (MVT) to each of them. If η in (4.1) is the same for both integrals, then we can proceed with the application of the LOIMES to these specific data.

Let's now apply the CMVT to $B'_{35}(k)$. From (3.6)

$B'_{35}(k) = \int_{-\infty}^{\infty} dz e^{ikz} b_1(z) \int_{z-\epsilon}^{z+\epsilon} dz' e^{-ikz'} b_1(z') \int_{z'-\epsilon}^{z'+\epsilon} dz e^{ikz''} b_1(z'') =$

$\int_{-\infty}^{\infty} dz e^{ikz} b_1(z) \int_{z-\epsilon}^{z+\epsilon} dz' e^{-ikz'} b_1(z')(2\epsilon) e^{ik(z'+\beta)} b_1(z'+\beta) =$

$\int_{-\infty}^{\infty} dz e^{ikz} b_1(z) e^{ik\beta} b_1(z+\alpha)(2\epsilon)^2 b_1(z+\alpha+\beta) =$

$$e^{ik\beta} \int_{-\infty}^{\infty} (2\epsilon)^2 dz e^{ikz} b_1(z) b_1(z+\alpha) b_1(z+\alpha+\beta), \tag{4.2}$$

where $z+\alpha$ and $z'+\beta$ are the parameter η introduced by the mean value theorem, for the middle and left integrals in $B'_{35}(k)$, respectively. Note that α and β represent the deviation from the center of the interval of integration of the respective integrals, and hence

$\alpha < \epsilon/2 \qquad \beta < \epsilon/2 \qquad \alpha + \beta < \epsilon.$

Notice that the factor $(2\epsilon)^2$ makes the value of $B_{35}^{'}(k)$ go to zero when $\epsilon \to 0$, as is desired. Using the fact that ϵ is small (and also $\epsilon/2$), and with the continuity of $b_1(z)$, we can make the following approximation:

$b_1(z) \approx b_1(z+\alpha) \approx b_1(z+\beta) \approx b_1(z+\alpha+\beta)$.

$$e^{ik\beta} \approx 1, \tag{4.3}$$

Hence we end up with

$$B'_{35}(k) = (2\epsilon)^2 \int_{-\infty}^{\infty} dz e^{ikz} b_1(z)^3, \tag{4.4}$$

which upon a Fourier transform becomes $B'_{35}(z) = (2\epsilon)^2 b_1(z)^3$. We propose eq. (4.4) as the part of $\hat{b}_3$ to be inserted into (3.7) to get b_5^{IM}, the second term in b_{LO}^{IM}. Using the fact that $B'_{35}(z) = (2\epsilon)^2 b_1(z)^3 = (2\epsilon)^2 B_{35}(z)$, the result is the original term (2.6) times a factor $(2\epsilon)^2$:

$$(2\epsilon)^2 \int_{-\infty}^{\infty} dz e^{ikz} b_1(z) \int_{-\infty}^{z-\epsilon} dz' e^{-ikz'} b_1(z')^3 \int_{z'+\epsilon}^{\infty} dz'' e^{ikz''} b_1(z''). \tag{4.5}$$

As we anticipated in the introduction, this CMVT scheme has its own issues. For example, by applying the CMVT to obtain subsequent terms in b_{LO}^{IM}, we predict a subseries whose closed form is, when the data are continuous and hence are not spike-like:

$b_{LO}^{IM} = \int_{-\infty}^{\infty} dz e^{ikz} b_1(z) \int_{-\infty}^{z-\epsilon} dz' e^{-ikz'} \left(\frac{1}{1-(2\epsilon\ b_1(z'))^2} \right) b_1(z') \times$

$$\int_{z'+\epsilon}^{\infty} dz'' e^{ikz''} b_1(z''). \tag{4.6}$$

Notice the 2ϵ factor in the quotient that is present in (4.6) but is not present in the original series (2.2). This means that both subseries agree only if $\epsilon = 1/2$. At first we may think that we have a generalization of (2.2), but this is not true because we should keep in mind that we want a subseries that eliminates multiples and for this we need to predict the right amplitude, which is exactly what (2.2) does. This means that any deviation from the amplitude predicted by (2.2) will result in the failure of the series to eliminate internal multiples. This forces us to interpret the condition $\epsilon = 1/2$ as a restriction to the class of experiments to which the LOIMES can be applied, namely, those for which $\epsilon = 1/2$.

We now discuss some intriguing relations between the approach we have just described for continuous data, and another procedure commonly used in the physics literature to circumvent difficulties similar to the ones encountered in this report.

A common approach used to overcome difficulties such as ill-definiteness of the higher powers of the Delta function is to introduce into $B_{35}(k)$ the two parameters α and β into the arguments of the Delta function, as follows

$B_{35}(\alpha,\beta,k) = \int_{-\infty}^{\infty} dz e^{ikz} b_1(z) \int_{-\infty}^{\infty} dz' e^{-ikz'} b_1(z') \delta(z - z' + \alpha) \int_{-\infty}^{\infty} dz'' e^{ikz''} b_1(z'') \delta(z' - z'' + \beta) =$
$\int_{-\infty}^{\infty} dz e^{ikz} b_1(z) \int_{-\infty}^{\infty} dz' e^{-ikz'} b_1(z') \delta((z+\alpha) - z') e^{ik(z'+\beta)} b_1(z'+\beta)$

$$= e^{ik\beta} \int_{-\infty}^{\infty} dz e^{ikz} b_1(z) b_1(z+\alpha) b_1(z+\alpha+\beta). \tag{4.7}$$

In this way, the self interactions are removed and are, when the data are spike-like, the higher-than-one powers of the Delta function. The next step would be to define

$$B_{35}(k) \equiv lim_{\alpha,\beta\to 0} B_{35}(\alpha,\beta,k), \tag{4.8}$$

where the limit is performed $after$ the integral $B_{35}(\alpha,\beta,k)$ has been calculated. What we have described is analogous to the procedure used in Green's function theory, in which the resulting integral defining the Green's function is not well defined (due to the presence of poles in the path of integration). Hence it is made well defined by deforming the contour of integration, which we accomplished by introducing a small parameter ϵ to avoid the poles of the integrand, followed by the limit $\epsilon \to 0$.

Unfortunately, this solution is not powerful enough for our present issues, and the reason is that if we take (4.8) as the definition for the interactions, then with the spike data $B_{35}(k)$ becomes zero, which is obviously not what we want.

If we assume (1) that the data are continuous and (2) that the operation of taking limits commutes with the integral, then (4.8) reduces to the original integral $B_{35}(k)$ containing interactions. This means that at least for continuous data, we can consider (4.8) to be an equivalent expression for the interaction contribution to the eliminator subseries b_{LO}^{IM}.

At this point it is worth comparing (4.2) with (4.7), the expression obtained using the approach described earlier that was based on the CMVT. We can see that they are similar, with the obvious difference of the factor $(2\epsilon)^2$ in (4.2). In this way, the CMVT approach reproduces the regularization scheme just explained and at the same time fixes the problem with the original splitting of $B_3(k)$, eq. (2.10). It's fair to say that it is not expected for (4.8) to fix the issue related to the limit $\epsilon \to 0$, as it was obtained from the old expression for $B_3(k)$, eq. (2.10), which is not well behaved in this limit. However it is interesting that we partially reproduce the result of the CMVT. This might mean that although not strictly correct, eq. (2.10) may still be useful for studying some properties and obtaining some insight about the LOIMES; after all, in practice ϵ is small but not zero. Another nice feature of the CMVT is that whereas in the regularization scheme both α and β were introduced in a somewhat arbitrary way, here they arise naturally: they are the coordinates of the point whose image is used by the CMVT.

Given the similarities between those two approaches, it would be interesting to perform a more detailed study of the relation between them, in order to better understand the nature of the LOIMES.

As we explained earlier, the LOIMES matches the amplitude of the internal multiple by using interactions in the integrals of certain terms of the ISS. Now, if we just require the filtering (or extraction) of the self interaction contained in the integrals in (3.6) instead of insisting on looking

for a convenient expression for the value of the integrals with a finite interval of integration (i.e., looking for an expression in which are the self interactions become evident), we only need to multiply the integral times a Delta function with the correct argument. In this way we arrive, for the non-spike data, at an expression similar to the right-hand side of (2.10), but we must keep in mind that this expression is not equal to $B_3(k)$ anymore. Now we can proceed by selecting the original $B_{35}(k)$, instead of $B_{35}^{'}(k)$, to be the term associated with the LOIMES. By repeating this filtering process in the appropriate higher-order terms, we arrive at the original form for the LOIMES, eq. (2.2). In general this filtering process can be applied also to the HOIMES, obtaining in this way the original expression for the IMES, as stated in eqs. (2.1)-(2.4).

The advantage of this argument is that, although not mathematically rigorous, it is fairly general and can include all continuous data, as opposed to the scheme proposed in this report. Again, the spike-like are not included, as this would bring the original problem with the powers of the Delta function. However we can now argue, on the basis of of the results of Appendix A, that the filtering process is not necessary for the Delta function. That is because of the function's very particular properties under integration; it automatically selects the self-interaction part of the integral, without the need of any further filtering process. This argument is highly plausible, even though ideally it would be desirable to have a filter working with all kinds of data at once including the Delta function.

Although the central subject of this report is the LOIMES, it is worthwhile to say some words about the HOIMES. As can be seen from the general form, eqs. (2.3) and (2.4), this subseries also contains interaction terms, thereby causing the same problem that the leading-order eliminator subseries has with spike-like data. A detailed analysis of such a case is beyond the objective of this report, but it is easy to provide some evidence that the formalism described here can be also applied to the HOIMES. For this, let's focus on continuous data, so we can apply the CMVT approach.

The first term in the HOIMES is

$$b_{HO}^{IM} = \int_{-\infty}^{\infty} dz e^{ikz} b_1(z) \int_{-\infty}^{z-\epsilon} dz' e^{-ikz'} 2(2\epsilon) b_1(z') \int_{-\infty}^{z'-\epsilon} dz''' b_1^2(z''') \int_{z'+\epsilon}^{\infty} dz'' e^{ikz''} b_1(z''), \qquad (4.9)$$

and it was derived in Ramírez (2007) on the basis of the symmetry $B_{36}(k) = B_{39}(k)$ in (2.10). So, a first hint that the HOIMES can be described by the CMVT approach is that this symmetry is preserved by the corresponding terms in (3.6): $B'_{36}(k) = B'_{39}(k)$. This fact is proved in Appendix B, where we also use this symmetry to show that, in this case, the parameters arising from the application of the CMVT are unambiguously zero. Thus, by using $B'_{36}(k)$ and $B'_{39}(k)$ instead of $B_{36}(k)$ and $B_{39}(k)$, and using the MVT, we get our proposal for the first term of the HOIMES:

$$b_{HO}^{IM} = \int_{-\infty}^{\infty} dz e^{ikz} b_1(z) \int_{-\infty}^{z-\epsilon} dz' e^{-ikz'} 2(2\epsilon) b_1(z') \int_{-\infty}^{z'-\epsilon} dz''' b_1^2(z''') \int_{z'+\epsilon}^{\infty} dz'' e^{ikz''} b_1(z''), \qquad (4.10)$$

which also contains the factor 2ϵ, characteristic of the CMVT approach. Notice that this modified term is, as in the LOIMES, the old term multiplied by a factor of 2ϵ. The rule is that for each time

the CMVT is applied, there is a factor of 2ϵ and also an interaction of the data. More precisely, if the MVT is applied $n$times in a single term of the ISS, we get a factor of $(2\epsilon)^n$ and a factor of $b_1(z)^{n+1}$.

Following these criteria, and provided the corresponding symmetries are preserved, we conjecture that the HOIMES predicted by the MVT is

$$b_{HO}^{IM} = \int_{-\infty}^{\infty} dz e^{ikz} b_1(z) \int_{-\infty}^{z-\epsilon} dz' e^{-ikz'} \frac{2G(z') \int_{-\infty}^{z'-\epsilon} dz''' J(z''')}{1-\int_{-\infty}^{z'-\epsilon} dz''' J(z''')} \times \int_{z'+\epsilon}^{\infty} dz'' e^{ikz''} b_1(z'') \tag{4.11}$$

where

$$J(z''') = \frac{2\epsilon b_1(z''')^2}{1-(2\epsilon b_1(z'''))^2} \qquad G(z') = \frac{b_1(z')}{1-(2\epsilon b_1(z'))^2}. \tag{4.12}$$

By expanding (4.11), we have

$$b_{HO}^{IM} = \int_{-\infty}^{\infty} dz e^{ikz} b_1(z) \int_{-\infty}^{z-\epsilon} dz' e^{-ikz'} (2(2\epsilon) b_1(z') \int_{-\infty}^{z'-\epsilon} b_1^2(z') +$$
$$2(2\epsilon)^3 b_1(z') \int_{-\infty}^{z'-\epsilon} b_1^4(z') + 2(2\epsilon)^3 b_1^3(z') \int_{-\infty}^{z'-\epsilon} b_1^2(z') +$$
$$2(2\epsilon)^2 b_1(z') \int_{-\infty}^{z'-\epsilon} b_1^2(z') \int_{-\infty}^{z'-\epsilon} b_1^2(z')) \int_{z'+\epsilon}^{\infty} dz'' e^{ikz''} b_1(z''). \tag{4.13}$$

Notice that this conjecture also works only for $\epsilon = 1/2$, as in this case it coincides with (2.3), the old version of the HOIMES. Notice also that the factors 2ϵ in each term satisfy the general rule just explained in the paragraph above.

5 Discussion and conclusions

As mentioned in the introduction, the present report is oriented to lower the burden of the adaptive subtraction of internal multiples, by promoting to elimination, the attenuation provided by the leading order contribution of the original attenuator subseries. In particular, we have rederived and modified the LOIMES in order to accommodate spike-like data. As a result we find a modified closed form for the Leading-Order Internal-Multiple-Eliminator Subseries (LOIMES) originally proposed in Ramírez (2007). Such a closed form, eqs. (3.10)-(3.12), is only valid for this kind of data.

The relevance of this work is that now we can test the algorithm itself: as the analytic data is perfect, any problem in the output is caused by the algorithm, which means that it must ve revisited. Also, as we did in this work, this allows the elimination subseries to enhance the effectiveness of other algorithms, which are also being tested with analytic data.

Also, we illustrate how to apply the modified closed form of the LOIMES to promote the IMAS of Ma and Weglein (2012), eq. (3.14), to the role of an eliminator of some effects, caused by the

inclusion of internal multiples in the input data. We do this for the simplest case, in which the contribution of (3.14) differs from that of the original IMAS of Araujo and Weglein: a four-layer $1D$-earth, with normal incidence. The traveltime t_3 represents the primary associated with the third (deepest) layer satisfying $t_3 > 2t_2 - t_1$, where t_2 and t_1 are the traveltimes of the primaries associated with the second and first (shallowest) layer, respectively. We also include in the input data the first-order internal multiple with traveltime $2t_2 - t_1$, associated with the first layer.

As was explained in section 3.1, both the LOIMES and the HOIMES were first derived from (2.10), which is not strictly correct. Hence the need to rederive both suberies, including for continuous data starting from the correct expression, eq. (3.6). We do this for the LOIMES, and we conjecture the answer for the HOIMES. Unfortunately, the derivation we found is not general enough to include all types of continuous data, but only a very restricted class-i.e., continuous data that satisfy the CMVT, eq. (4.1).

A further research topic in this direction is to write the modified closed form, analogous to (3.10), corresponding to the HOIMES. The potential applications are (1) elimination of effects, created by the original IMAS, when the input data includes first-order internal multiples, whose downward reflection is generated at deeper reflectors, and more important, (2) elimination of first-order internal multiples, created at salt deposits beneath the earth's surface.

6 Acknowledgments

We are grateful to the M-OSRP sponsors. The first author wants to knowledge Andre Ferreira and Lujian Peng for useful discussions and suggestions during the realization of this work. We also want to thank Paolo Terenghi and Jim Mayhan for reading a first draft of this report.

A Calculating the modified LOIMES for spike data.

In this appendix we will show explicitly, for 1D and three-layer earth, how to perform the integral (3.7), when the input data are the two spike-like primaries, with normal incidence, associated with the two interfaces.

$$D(t) = R_1\delta(t - t_1) + \underbrace{T_{01}R_2T_{10}}_{R_2'}\delta(t - t_2). \tag{A.1}$$

The notation is the same as in section 3.1: t_1 and t_2 are the traveltimes associated with the primaries created at the first and second reflector, respectively, and $t_2 > t_1$, T_{ij} denotes the transmission coefficient when the wave travels from the ith medium to the jth medium, and R_k is the reflection coefficient at the kth layer for a downward incident wave. We will also need the pseudodepths $z_1 \equiv c_0t_1/2$ and $z_2 \equiv c_0t_2/2$, of the two interfaces, with respect to a homogeneous reference medium with constant velocity c_0.

Inserting (A.1) into the right integral of $B'_{35}(k)$, we get by following eq. (90) in Weglein et al. (2003)

$\int_{z'-\epsilon}^{z'+\epsilon} dz'' e^{ikz''} b_1(z'') = \int_{z'-\epsilon}^{z'+\epsilon} dz'' e^{ikz''} [R_1\delta(z'' - z_1) + R_2'\delta(z'' - z_2)] =$

$R_1 e^{ikz_1} H(z_1 - (z' - \epsilon))H((z' + \epsilon) - z_1) + R_2' e^{ikz_2} H(z_2 - (z' - \epsilon))H((z' + \epsilon) - z_2)$.

Substituting the above result into the second integral in $B_{35}'(k)$, we have

$\int_{z-\epsilon}^{z+\epsilon} dz' e^{-ikz'} b_1(z')[R_1 e^{ikz_1} H(z_1 - (z' - \epsilon))H((z' + \epsilon) - z_1) +$

$R_2' e^{ikz_2} H(z_2 - (z' - \epsilon))H((z' + \epsilon) - z_2)] = \int_{z-\epsilon}^{z+\epsilon} dz' e^{-ikz'} [R_1 \delta(z' - z_1) + R_2' \delta(z' - z_2)] \times$

$[R_1 e^{ikz_1} H(z_1 - (z' - \epsilon))H((z' + \epsilon) - z_1) + R_2' e^{ikz_2} H(z_2 - (z' - \epsilon))H((z' + \epsilon) - z_2)] =$

$\int_{z-\epsilon}^{z+\epsilon} dz' e^{-ikz'} R_1 \delta(z' - z_1) R_1 e^{ikz_1} H(z_1 - (z' - \epsilon))H((z' + \epsilon) - z_1) +$

$\int_{z-\epsilon}^{z+\epsilon} dz' e^{-ikz'} R_1 \delta(z' - z_1) R_2' e^{ikz_2} H(z_2 - (z' - \epsilon))H((z' + \epsilon) - z_2)] +$

$\int_{z-\epsilon}^{z+\epsilon} dz' e^{-ikz'} R_2' \delta(z' - z_2) R_1 e^{ikz_1} H(z_1 - (z' - \epsilon))H((z' + \epsilon) - z_1) +$

$\int_{z-\epsilon}^{z+\epsilon} dz' e^{-ikz'} R_2' \delta(z' - z_2) R_2' e^{ikz_2} H(z_2 - (z' - \epsilon))H((z' + \epsilon) - z_2) =$

$$I_1 + I_2 + I_3 + I_4. \tag{A.2}$$

Performing the four integrations, we arrive at

$I_1 = \int_{z-\epsilon}^{z+\epsilon} dz' e^{-ikz'} R_1 \delta(z' - z_1) R_1 e^{ikz_1} H(z_1 - (z' - \epsilon))H((z' + \epsilon) - z_1) =$

$R_1^2 e^{-ikz_1} e^{ikz_1} H(z_1 - (z - \epsilon))H((z + \epsilon) - z_1) \underbrace{H(z_1 - (z_1 - \epsilon))}_{=1} \underbrace{H((z_1 + \epsilon) - z_1)}_{=1} =$

$R_1^2 H(z_1 - (z - \epsilon))H((z + \epsilon) - z_1)$

$I_2 = \int_{z-\epsilon}^{z+\epsilon} dz' e^{-ikz'} R_1 \delta(z' - z_1) R_2' e^{ikz_2} H(z_2 - (z' - \epsilon))H((z' + \epsilon) - z_2) =$

$R_1 R_2' e^{-ikz_2} e^{ikz_2} H(z_1 - (z - \epsilon))H((z + \epsilon) - z_1) H(z_2 - (z_1 - \epsilon)) \underbrace{H((z_1 + \epsilon) - z_2)}_{=0} = 0$

$I_3 = \int_{z-\epsilon}^{z+\epsilon} dz e^{-ikz'} R_2' \delta(z' - z_2) R_1 e^{ikz_1} H(z_1 - (z' - \epsilon))H((z' + \epsilon) - z_1) =$

$R_1 R_2' e^{-ikz_2} e^{ikz_1} H(z_2 - (z - \epsilon))H((z + \epsilon) - z_2) \underbrace{H(z_1 - (z_2 - \epsilon))}_{=0} H((z_2 + \epsilon) - z_1) = 0$

$I_4 = \int_{z-\epsilon}^{z+\epsilon} dz e^{-ikz'} R_2' \delta(z' - z_2) R_2' e^{ikz_2} H(z_2 - (z' - \epsilon))H((z' + \epsilon) - z_2) =$

$(R_2')^2 e^{-ikz_2} e^{ikz_2} H(z_2 - (z - \epsilon))H((z + \epsilon) - z_2) H(z_2 - (z_2 - \epsilon))H((z_2 + \epsilon) - z_2) =$

$$(R_2')^2 H(z_2 - (z - \epsilon))H((z + \epsilon) - z_2). \tag{A.3}$$

Finally, substituting the value of the integrals in (A.3) into the third integral in $B_{35}'(k)$, we end up with

$B_{35}'(k) = \int_{-\infty}^{\infty} dz e^{ikz} [R_1 \delta(z - z_1) + R_2' \delta(z - z_2)] \times$

$[R_1^2 H(z_1 - (z - \epsilon))H((z + \epsilon) - z_1) + (R_2')^2 H(z_2 - (z - \epsilon))H((z + \epsilon) - z_2)] =$

$\int_{-\infty}^{\infty} dz e^{ikz} R_1 \delta(z-z_1) R_1^2 H(z_1-(z-\epsilon)) H((z+\epsilon)-z_1) +$
$\int_{-\infty}^{\infty} dz e^{ikz} R_1 \delta(z-z_1) (R_2')^2 H(z_2-(z-\epsilon)) H((z+\epsilon)-z_2) +$
$\int_{-\infty}^{\infty} dz e^{ikz} R_2' \delta(z-z_2) R_1^2 H(z_1-(z-\epsilon)) H((z+\epsilon)-z_1)$
$\int_{-\infty}^{\infty} dz e^{ikz} R_2' \delta(z-z_2) (R_2')^2 H(z_2-(z-\epsilon)) H((z+\epsilon)-z_2) =$

$$I_1' + I_2' + I_3' + I_4'. \tag{A.4}$$

Evaluating the integrals above, we have
$I_1' = \int_{-\infty}^{\infty} dz e^{ikz} R_1 \delta(z-z_1) R_1^2 H(z_1-(z-\epsilon)) H((z+\epsilon)-z_1) =$
$R_1^3 e^{ikz_1} H(z_1-(z_1-\epsilon)) H((z_1+\epsilon)-z_1) = R_1^3 e^{ikz_1}$
$I_2' = \int_{-\infty}^{\infty} dz e^{ikz} R_1 \delta(z-z_1) (R_2')^2 H(z_2-(z-\epsilon)) H((z+\epsilon)-z_2) =$
$R_1 (R_2')^2 e^{ikz_1} H(z_2-(z_1-\epsilon)) \underbrace{H((z_1+\epsilon)-z_2)}_{=0} = 0$
$I_3' = \int_{-\infty}^{\infty} dz e^{ikz} R_2' \delta(z-z_2) R_1^2 H(z_1-(z-\epsilon)) H((z+\epsilon)-z_1) =$
$R_1^2 R_2' e^{ikz_2} \underbrace{H(z_1-(z_2-\epsilon))}_{=0} H((z_2+\epsilon)-z_1) = 0$
$I_4' = \int_{-\infty}^{\infty} dz e^{ikz} R_2' \delta(z-z_2) (R_2')^2 H(z_2-(z-\epsilon)) H((z+\epsilon)-z_2) =$

$$(R_2')^3 e^{ikz_2} H(z_2-(z_2-\epsilon)) H((z_2+\epsilon)-z_2) = (R_2')^3 e^{ikz_2}. \tag{A.5}$$

Adding the integrals above, we finally have

$$B_{35}'(k) = R_1^3 e^{ikz_1} + (R_2')^3 e^{ikz_2}. \tag{A.6}$$

When transformed to the space domain, (A.6) becomes

$$B_{35}'(z) = R_1^3 \delta(z-z_1) + (R_2')^3 \delta(z-z_2). \tag{A.7}$$

Now we will evaluate b_5^{IM}, the second term in b_{LO}^{IM}, using (A.7):

$$b_5^{IM}(k) = \int_{-\infty}^{\infty} dz e^{ikz} b_1(z) \int_{-\infty}^{z-\epsilon} dz' e^{-ikz'} B_{35}'(z) \int_{z'+\epsilon}^{\infty} dz'' e^{ikz''} b_1(z). \tag{A.8}$$

The first integral in the above expression is
$\int_{z'+\epsilon}^{\infty} dz'' e^{ikz''} b_1(z) = \int_{z'+\epsilon}^{\infty} dz'' e^{ikz''} [R_1 \delta(z''-z_1) + (R_2')\delta(z''-z_2)] =$
$R_1 e^{ikz_1} H(z_1-(z'+\epsilon)) + R_2' e^{ikz_2} H(z_2-(z'+\epsilon))$.

Substituting the above result into the second integral of (A.8), we get

$\int_{-\infty}^{z-\epsilon} dz' e^{-ikz'}[R_1^3\delta(z'-z_1)+(R_2')^3\delta(z'-z_2)][R_1 e^{ikz_1}H(z_1-(z'+\epsilon))+R_2' e^{ikz_2}H(z_2-(z'+\epsilon))]$

$= \int_{-\infty}^{z-\epsilon} dz' e^{-ikz'} R_1^3\delta(z'-z_1)R_1 e^{ikz_1}H(z_1-(z'+\epsilon))+$

$\int_{-\infty}^{z-\epsilon} dz' e^{-ikz'} R_1^3\delta(z'-z_1)R_2' e^{ikz_2}H(z_2-(z'+\epsilon))$

$\int_{-\infty}^{z-\epsilon} dz' e^{-ikz'} (R_2')^3\delta(z'-z_2)R_1 e^{ikz_1}H(z_1-(z'+\epsilon))+$

$\int_{-\infty}^{z-\epsilon} dz' e^{-ikz'} (R_2')^3\delta(z'-z_2)R_2' e^{ikz_2}H(z_2-(z'+\epsilon)) =$

$$I_1'' + I_2'' + I_3'' + I_4''. \tag{A.9}$$

Evaluating the above integrals, we have

$I_1'' = \int_{-\infty}^{z-\epsilon} dz' e^{-ikz'} R_1^3\delta(z'-z_1)R_1 e^{ikz_1}H(z_1-(z'+\epsilon)) = R_1^4 \underbrace{H(z_1-(z_1+\epsilon))}_{=0} H((z-\epsilon)-z_1) = 0$

$I_2'' = \int_{-\infty}^{z-\epsilon} dz' e^{-ikz'} R_1^3\delta(z'-z_1)R_2' e^{ikz_2}H(z_2-(z'+\epsilon)) =$

$R_1^3 R_2' e^{ik(z_2-z_1)}H(z_2-(z_1+\epsilon))H((z-\epsilon)-z_1)$

$I_3'' = \int_{-\infty}^{z-\epsilon} dz' e^{-ikz'} (R_2')^3\delta(z'-z_2)R_1 e^{ikz_1}H(z_1-(z'+\epsilon)) =$

$R_1(R_2')^3 e^{ik(z_1-z_2)} \underbrace{H(z_1-(z_2+\epsilon))}_{=0} H((z-\epsilon)-z_2) = 0$

$I_4'' = \int_{-\infty}^{z-\epsilon} dz' e^{-ikz'} (R_2')^3\delta(z'-z_2)R_2' e^{ikz_2}H(z_2-(z'+\epsilon)) =$

$(R_2')^4 \underbrace{H(z_2-(z_2+\epsilon))}_{=0} H((z-\epsilon)-z_2) = 0$

Substituting the only nonzero value, I_2'', in the last integral of (A.8), we finally have

$b_5^{IM} = \int_{-\infty}^{\infty} dz e^{ikz}[R_1\delta(z-z_1)+R_2'\delta(z-z_2)]R_1^3 R_2' e^{ik(z_2-z_1)}H(z_2-(z_1+\epsilon))H((z-\epsilon)-z_1) =$

$R_1^4 R_2' e^{ikz_2}H(z_2-(z_1+\epsilon)) \underbrace{H((z_1-\epsilon)-z_1)}_{=0} + R_1^3 R_2'^2 e^{ik(2z_2-z_1)}H(z_2-(z_1+\epsilon))H((z_2-\epsilon)-z_1) =$

$$R_1^3 R_2'^2 e^{ik(2z_2-z_1)}. \tag{A.10}$$

B Calculating α and β for the HOIMES

In this appendix we will show that the ISS requires the parameters α and β to be zero. We begin by showing that the integrals $B_{36}'(k)$ and $B_{39}'(k)$ in (3.6) have the same value.

$B_{39}'(k) = \int_{-\infty}^{\infty} dz e^{ikz} b_1(z) \int_{-\infty}^{z-\epsilon} dz' e^{-ikz'} b_1(z') \int_{z'-\epsilon}^{z'+\epsilon} dz'' e^{ikz''} b_1(z'') =$

$\int_{-\infty}^{\infty} dz e^{ikz} b_1(z) \int_{-\infty}^{\infty} dz' e^{-ikz'} b_1(z') H((z-\epsilon)-z')\times$

$\int_{-\infty}^{\infty} dz'' e^{ikz''} b_1(z'') H((z'+\epsilon)-z'') H(z''-(z'-\epsilon)) =$

$\int_{-\infty}^{\infty} dz'' e^{ikz''} b_1(z'') \int_{-\infty}^{\infty} dz' e^{-ikz'} b_1(z') H((z'+\epsilon)-z'') H(z''-(z'-\epsilon)) \times$

$\int_{-\infty}^{\infty} dz e^{ikz} b_1(z) H((z-\epsilon)-z')$

Making the change of variables $z'' \to z$ and $z \to z''$, we get:

$B'_{39}(k) = \int_{-\infty}^{\infty} dz e^{ikz} b_1(z) \int_{-\infty}^{\infty} dz' e^{-ikz'} b_1(z') H((z'+\epsilon)-z) H(z-(z'-\epsilon)) \times$

$\int_{-\infty}^{\infty} dz'' e^{ikz''} b_1(z'') H((z''-\epsilon)-z') =$

$\int_{-\infty}^{\infty} dz e^{ikz} b_1(z) \int_{-\infty}^{\infty} dz' e^{-ikz'} b_1(z') H(z'-(z-\epsilon)) H((z+\epsilon)-z') \times$

$\int_{-\infty}^{\infty} dz'' e^{ikz''} b_1(z'') H(z''-(z'+\epsilon)) =$

$$\int_{-\infty}^{\infty} dz e^{ikz} b_1(z) \int_{z-\epsilon}^{z+\epsilon} dz' e^{-ikz'} b_1(z') \int_{z'+\epsilon}^{\infty} dz'' e^{ikz''} b_1(z'') = B'_{36}(k). \tag{B.1}$$

The following step is to apply the mean-value theorem to both $B'_{36}(k)$ and $B'_{39}(k)$:

$B'_{36}(k) = \int_{-\infty}^{\infty} dz e^{ikz} b_1(z) \int_{z-\epsilon}^{z+\epsilon} dz' e^{-ikz'} b_1(z') \int_{z'+\epsilon}^{\infty} dz'' e^{ikz''} b_1(z'') =$

$\int_{-\infty}^{\infty} dz e^{ikz} b_1(z) 2\epsilon e^{-ik(z+\alpha)} b_1(z+\alpha) \int_{z+\alpha+\epsilon}^{\infty} dz'' e^{ikz''} b_1(z'') =$

$$(2\epsilon) e^{-ik\alpha} \int_{-\infty}^{\infty} dz b_1(z) b_1(z+\alpha) \int_{-\infty}^{\infty} dz'' e^{ikz''} b_1(z'') H(z''-(z+\alpha+\epsilon)) \tag{B.2}$$

$B'_{39}(k) = \int_{-\infty}^{\infty} dz e^{ikz} b_1(z) \int_{-\infty}^{z-\epsilon} dz' e^{-ikz'} b_1(z') \int_{z'-\epsilon}^{z'+\epsilon} dz'' e^{ikz''} b_1(z'')$

$= \int_{-\infty}^{\infty} dz e^{ikz} b_1(z) \int_{-\infty}^{\infty} dz' e^{-ikz'} b_1(z') H((z-\epsilon)-z') 2\epsilon e^{ik(z'+\beta)} b_1(z'+\beta)$

$= (2\epsilon) e^{ik\beta} \int_{-\infty}^{\infty} dz e^{ikz} b_1(z) \int_{-\infty}^{\infty} dz' b_1(z') b_1(z'+\beta) H((z-\epsilon)-z')$

$= (2\epsilon) e^{ik\beta} \int_{-\infty}^{\infty} dz' b_1(z') b_1(z'+\beta) \int_{-\infty}^{\infty} dz e^{ikz} b_1(z) H((z-\epsilon)-z')$

$$= (2\epsilon) e^{ik\beta} \int_{-\infty}^{\infty} dz b_1(z) b_1(z+\beta) \int_{-\infty}^{\infty} dz'' e^{ikz''} b_1(z'') H((z''-(z+\epsilon)). \tag{B.3}$$

We have just proved that $B'_{36}(k) = B'_{39}(k)$. Hence, (B.2) and (B.3) must be equal-i.e.,

$(2\epsilon) e^{-ik\alpha} \int_{-\infty}^{\infty} dz'' b_1(z) b_1(z+\alpha) \int_{-\infty}^{\infty} dz e^{ikz''} b_1(z'') H(z''-(z+\alpha+\epsilon))$

$$= (2\epsilon) e^{ik\beta} \int_{-\infty}^{\infty} dz b_1(z) b_1(z+\beta) \int_{-\infty}^{\infty} dz'' e^{ikz''} b_1(z'') H(z''-(z+\epsilon)). \tag{B.4}$$

From the phase outside the integral, the argument of the data and the argument of the step function respectively, in the expression above, we get the following over constrained, but consistent set of equations:

$$\alpha = -\beta, \qquad \alpha = \beta, \qquad \alpha = 0. \tag{B.5}$$

whose only solution is $\alpha = \beta = 0$. This shows that the parameters introduced by the CMVT are zero. Notice that those α and β are not the same as the α and β of section 4.

References

Araújo, F. V. *Linear and non-linear methods derived from scattering theory: backscattering tomography and internal-multiple attenuation.* PhD thesis, Universidade Federal da Bahía, Brazil, 1994. In Portuguese.

Carvalho, P. M. *Free-surface multiple reflection elimination method based on nonlinear inversion of seismic data.* PhD thesis, Universidade Federal da Bahia, 1992. In Portuguese.

Liang, Hong and A. B. Weglein. "Addressing the limitations of the Inverse Scattering Series internal multiple attenuation algorithm when both primaries and multiples are included as subevents.." *M-OSRP 2012 Annual Meeting.* 2012, 2.

Ma, Chao and A. B. Weglein. "Addressing issues arising from using the internal multiple itself as subevents in inverse scattering series internal multiple attenuator.." *M-OSRP 2012 Annual Meeting.* 2012, 1.

Ramírez, A. C. *I. - Inverse scattering subseries for removal of internal multiples and depth imaging primaries; II. - Green's theorem as the foundation of interferometry and guiding new practical methods and applications.* PhD thesis, University of Houston, 2007.

Weglein, A. B., F. V. Araújo, P. M. Carvalho, R. H. Stolt, K. H. Matson, R. T. Coates, D. Corrigan, D. J. Foster, S. A. Shaw, and H. Zhang. "Inverse Scattering Series and Seismic Exploration." *Inverse Problems* 19 (2003): R27–R83.

A BACKGROUND REVIEW OF THE THEORY OF THE PERFECTLY MATCHED LAYER (PML) METHOD: THE ACOUSTIC WAVE EQUATION

Wilberth Herrera*, James Mayhan* and Arthur Weglein*, M-OSRP/Physics Dept./UH*

May 25, 2012

Abstract

In this report we provide, in preparation for seismic applications, a review of the theory behind the Perfectly Matched Layer (PML) technique, which aims to minimize the noise in numerical simulations. That noise is caused by reflections of the wavefield at the boundary of the Finite-Difference (FD) domain, where hard-wall (either Dirichlet or Neumann) boundary conditions (BCs) are imposed. We will explain the *split-field* and the *complex-coordinate-stretching* approaches to the subject, focusing on the 2D situation. Although the original formulation (*split-field*) of the PML technique was set for electromagnetic applications, we restrict our attention to the acoustic wave equation as this is of immediate interest for seismic applications. Emphasis is made on the calculation of the reflection coefficient at the interface between two PML media, and on the conditions for rendering this reflection coefficient identically zero. In particular we consider the situation in which one of the PML media is the acoustic host medium.

1 Introduction

The present report aims to provide, in preparation for the seismic applications mentioned later in this section, a background review of the theoretical foundations of the PML technique in 2D. In particular we will explain both the original *split-field* formulation of Bérenger and the *complex-coordinate-stretching* approach. We will follow that by an explanation of the existing relation between them.

One of the most common migration methods used in the oil industry nowadays is Reverse Time Migration (RTM), which allows the imaging of two-way waves, e.g., waves that move down and up from the source to a reflector, and down and up from a reflector to the geophones (Weglein et al. 2011a, Weglein et al. 2011b). This method is computationally implemented by extrapolation of the source wave field forward in time and of continuation of reflection data backwards in time, using the full two-way wave equation. This is followed by an imaging condition to find the reflectivity function. The numerical technique commonly used in the continuation (either of source wave field or reflection data) stages of RTM is the time-domain finite-difference algorithm. The main advantage of FD methods is their ability to produce the full wavefield (reflections, refractions, prismatic waves, etc.) with correct amplitudes and phases.

On the other hand, finite-difference methods intrinsically require the truncation of the computational domain in which the wave equation is being solved. Hence, it is necessary to feed the computer with the values of the wave field at the boundary of the so-called Finite-Difference (FD) domain. This boundary is adjacent to the computational domain and extends a few computational cells beyond, i.e., the FD domain by definition includes the computational domain plus its own boundary, which is a layer surrounding the computational domain (Figure 1). The BCs imposed in the FD domain boundary are usually either Dirichlet or Neumann conditions. Unfortunately, while some problems are naturally truncated, those involving wave equations are not, as they have oscillating solutions. This means that the magnitude of these solutions cannot be neglected at the boundary of the FD domain. Therefore, the truncation of the FD domain with either of the boundary conditions just mentioned, will introduce artifacts in the form of reflections of waves striking the domain's boundary. This is why both, Dirichlet and Neumann boundary conditions, are called hard-wall boundary conditions (Johnson 007a). These reflections are artifacts because they are not present in the original unbounded problem, and their presence in the computational simulation will clearly introduce noise.

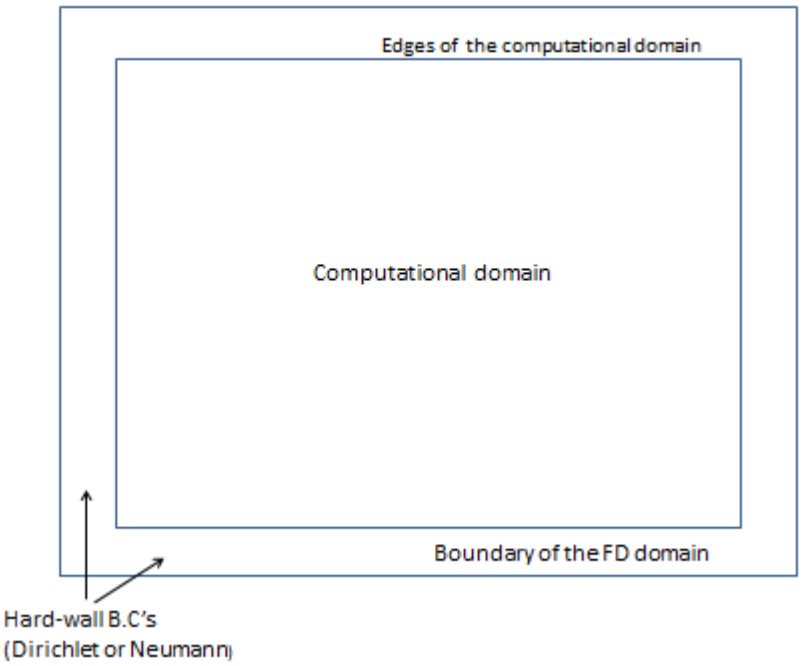

Figure 1: Array of a typical FD simulation in $2D$: The computational domain is the region in which the relevant wave equation is solved. Surrounding this computational domain it is the boundary of the FD domain, with a thickness of a few cells. Altogether, the computational domain and the boundary of the FD domain, constitute the whole FD domain. At the boundary of the FD domain is usually imposed a hard-wall B.C. (either Dirichlet or Neumann).

Over the years, several techniques have been developed in order to deal with the artifacts just mentioned. Although we will not provide a detailed evolution of these techniques, we can mention

some of the most relevant examples. First, we have the *silent-boundary* method for the elastic wave equation described in Lysmer and Kuhlemeyer (1969). This approach works well for the source applied within the grid, but should not be used when the source in applied at the top or bottom boundaries of the computational domain. There is also a family of approaches, based on convenient factorizations of the wave equation (Lindman 1975, Engquist and Majda 1977, Reynolds 1978, etc.), into incoming and outgoing factors. We can also mention Smith (1974), where the wave equation is solved twice for each boundary: once with Dirichlet BCs and once with Neumann BC's; with the final wavefield being defined as the addition of both of them. A further approach to deal with these reflections at the boundary was provided in Keys (1985), where perfect transmission is allowed for two arbitrary directions.

A major development is presented in Bérenger (1994) towards the solution of this puzzle concerning the reflection artifacts produced by truncation of the FD grid. Bérenguer's solution consisted of placing an *absorbing boundary layer* adjacent to the edges of the computational domain. The material filling this layer was designed to absorb incident waves without reflection (for all frequencies and any angle of incidence) at the interface between the propagation medium filling the computational domain and itself. Such an absorbing boundary layer is called, because of its reflectionless properties, a *perfectly matched layer,* or **PML**. This may sound unfamiliar, as a wave is usually reflected when it goes through an interface. However, Bérenger was able to show that a material with such reflectionless properties can be constructed, at least theoretically. It is worth to mention that originally the PML was formulated for the Maxwell's equations of electromagnetism, but it was soon adapted for the acoustic wave equation (Qi and Geers 1998).

The original formulation of the PML method in Bérenger (1994) is called the *split-field* PML. There is also a second formulation called the *uniaxial* PML or UPML. However, those formulations are hard to implement in coordinates systems other than Cartesian; they also hide the important fact that the PML also works for inhomogeneous media. Remarkably, there is a third approach to the PML, called *complex-coordinate-stretching*, from which it is possible to rederive both the *split-field* and the UPML formulations. This approach is based on the analytic continuation of the wave equation into the complex plane.

Our interest in the PML technique arises from the recent papers of Weglein et al. (2011a) and Weglein et al. (2011b). In these references a novel approach to RTM, using Green's theorem, is addressed. This new RTM has the potential to improve the results of the PML technique in RTM, by placing the BC's on a Green's function rather than in the wave-field. This report is part of a broader research project, whose objective is to compare the effectiveness of this new Green's theorem approach with respect to the PML-based RTM.

The organization is as follows: in section 2 we will give a general overview of the PML method, appealing to a typical seismic experiment. In section 3 we briefly state some properties of the general acoustic wave equation, that are needed in later sections. In section 4 we will provide a detailed study of the *split-field* formulation of the PML technique. Section 5 is devoted to the *complex-coordinate-stretching* approach formulation of the PML. Section 6 illustrates the relation between the two formulations studied in earlier sections. Section 7 contains the final conclusions and discussions.

2 PML and finite-difference modeling: A general overview

In this section we will explain in general terms what the PML technique is about. First of all, it is a computational technique developed for the simulation of unbounded wave phenomena, using the Finite-Difference method in the time domain. We will assume a single line of geophones i.e. we will rely on a 2D seismic experiment to explain the technique.

It is useful, for the implementation of the PML technique, to split the space of a seismic experiment into two different zones or regions. First we have the interest region, which is where all the seismic experiment is performed, and of course that is also where we want to see the results of the RTM. In this region we have the sources, the geophones, the reflectors and a portion of the radiation pattern which includes of course the waves scattered towards the geophones i.e. the data. Second, we have the radiation region, consisting of all the space not included in the interest region. This region is the place where the waves produced in the seismic experiment propagates at late times. Being the space in a seismic experiment that is unbounded, this region is infinite and therefore it is also called the infinite region (Figure 2).

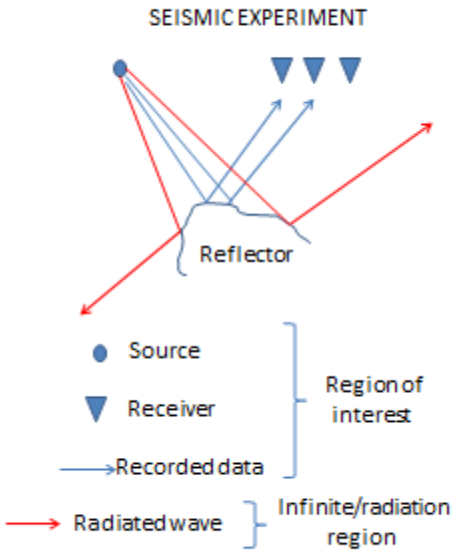

Figure 2: Array of a typical seismic experiment in $2D$: The blue-colored components (including the source, geophones, reflectors and recorded waves) constitute the region of interest for the computational implementation of the PML technique. The red-colored components (the scattered waves not recorded by the geophones) are part of the radiation pattern that eventually propagates to the radiation zone.

To ensure that all interesting phenomena in the seismic experiment are included in the computational implementation of RTM, we place the edges of the computational domain outside the region of interest. The objective is to at least attenuate the reflections created by either of the first two steps in the RTM technique (extrapolation of the source wave field and continuation of the reflection

data) due to the hard-wall B.C's imposed at the boundary of the FD domain. As was mentioned in the introduction, the PML technique is designed for this task, and the idea is to cover the edges of the computational domain with a layer made of a very special material called PML media. This layer extends in the direction opposite to the FD boundary i.e., it is positioned in the interior of the computational domain.

The PML media are engineered to absorb, without reflection, any radiating wave escaping from the region of interest of the seismic experiment, and incident at the interface between the computational domain and the PML layer [1]. Once in the PML media, such an incident wave is attenuated until it strikes the boundary of the FD domain, where it is reflected due to the hard-wall boundary conditions (BCs). The reflected wave keeps being attenuated as long as it remains in the interior of the PML media; but this attenuation stops when the reflected wave returns to the region of the computational domain filled with the original propagation media. However, at this stage, the amplitude of the wave is so attenuated by the PML media, that even if it travels inside the region of interest, its effects can be neglected (Figure 3).

[1]The definition of a PML medium only involves a set of equations governing the propagation of waves in its interior, and it is allowed to have an arbitrary shape. When the shape of the PML medium is a layer, then it is usually called, by abuse of language, just PML instead of PML layer.

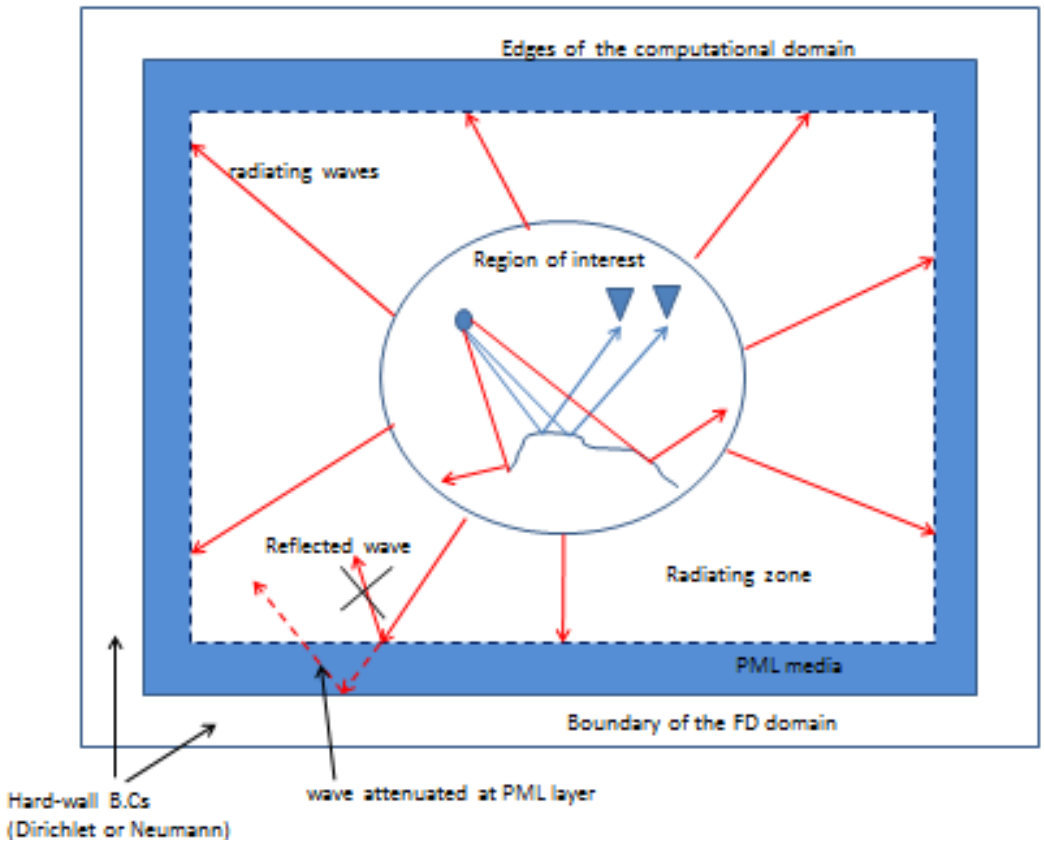

Figure 3: Finite-difference implementation of the PML technique in $2D$: The scattered waves escaping from the interest zone (red colored) eventually strike the radiation zone-PML interface and are transmitted without reflection. Once in the PML media, the transmitted waves keep being attenuated, before and after they are reflected at the boundary of the FD domain, as long as they remain in the interior of the PML zone. In this way, once the waves have left behind the PML zone, they are so well attenuated that their effects in the region of interest can be neglected.

As mentioned in the introduction, in section 4 we will discuss with detail the original *split-field* formulation for the acoustic wave equation. In particular we will provide the mathematical definition of a PML medium and we will also explain how to obtain a zero reflection coefficient, at the interface between the propagation (acoustic) media and the PML media. In section 5 we will explain the *complex-coordinate-stretching* approach to PML. This last approach is used, along with some of its variants, in seismic physics and in particular in RTM.

Strictly speaking, as suggested by Figure 3, we will focus on the forward modeling step of RTM i.e., on the extrapolation of the source wave field. This assumption is implicit in the fact that we will be dealing with waves propagating forward in time. However, the same discussion is valid for the continuation of data backwards in time, as in this step a wave field is also created with the FD technique, starting at a later time t' and ending at the time at which the source was fired, which is usually $t = 0$ (Stolt and Weglein (2011)). This wave field eventually strikes the boundary of the

FD domain where the hard-wall BCs are imposed.

3 The acoustic wave equation

It can be seen in Johnson (007b), that all the familiar wave equations appearing in physics (acoustic, Maxwell, Lamé-Navier equations for elastic waves in solids, etc.) can be written as:

$$\frac{\partial \mathbf{w}}{\partial t} = \hat{D}\mathbf{w}, \tag{3.1}$$

for an anti-Hermitian operator $\hat{D}$. It is this anti-Hermitian property of $\hat{D}$ that makes them "wave equations" i.e., that allows oscillating solutions, conservation of energy, and other properties characteristic of wave phenomena (Johnson 007b). It turns out that the PML ideas apply equally well in all those cases. However, for further applications to seismic physics, in this report we will focus on the implementation of the PML technique for the acoustic case.

The acoustic (source-free) wave equation is:

$$\nabla \cdot (a \nabla P) = \frac{1}{b} \frac{\partial^2 P}{\partial t^2}, \tag{3.2}$$

where $P(\mathbf{x}, t)$ is the wavefield and $c = \sqrt{ab}$ is the phase (or propagation) velocity of the wave, for parameters $a(\mathbf{x})$ and $b(\mathbf{x})$ of the (possibly inhomogeneous) medium. For seismic applications, $a(\mathbf{x})$ is the inverse of the density:

$$a(\mathbf{x}) = \frac{1}{\rho(\mathbf{x})}. \tag{3.3}$$

It is convenient, for its PML implementation, to write eq. (3.2) as an equivalent system of two coupled first-order differential equations:

$$\frac{\partial \mathbf{v}}{\partial t} = -a \nabla P \qquad\qquad \frac{\partial P}{\partial t} = -b \nabla \cdot \mathbf{v}, \tag{3.4}$$

where $\mathbf{v}(\mathbf{x}, t)$ is a new auxiliary vector field.

It is easy to show the equivalence of eq. (3.2) with eqs. (3.4): upon multiplication by b^{-1} and differentiation with time of the second of eqs. (3.4) we have

$$\frac{1}{b} \frac{\partial^2 P}{\partial t^2} = -\nabla \cdot \left(\frac{\partial \mathbf{v}}{\partial t} \right) = \nabla \cdot (a \nabla P). \tag{3.5}$$

For completeness, we will use eqs. (3.4) to show that the acoustic wave equation, eq. (3.2), can be written as (3.1):

$$\frac{\partial \mathbf{w}}{\partial t} = \frac{\partial}{\partial t} \begin{pmatrix} P \\ \mathbf{v} \end{pmatrix} = \begin{pmatrix} & b\nabla\cdot \\ a\nabla & \end{pmatrix} \begin{pmatrix} P \\ \mathbf{v} \end{pmatrix} \equiv \hat{D}\mathbf{w}. \tag{3.6}$$

4 Split-field formulation of the PML technique.

In this section we will explain the *split-field* formulation of the PML technique. As was mentioned in the introduction this is the original formulation and was introduced in Bérenger (1994) for Maxwell's equation of Electromagnetism. We will follow Qi and Geers (1998) in which this formalism is incorporated into the acoustic wave equation.

4.1 Definition of the 2D acoustic PML medium.

For simplicity we will focus on the $2D$ version of the acoustic wave equation, as written in eqs. (3.4). Making explicit the derivatives and the components of the vector field $\mathbf{v}$, eqs. (3.4) are equivalent to the following set of equations:

$$\frac{\partial \mathbf{v}_x}{\partial t} = -a\frac{\partial P}{\partial x} \qquad\qquad \frac{\partial \mathbf{v}_y}{\partial t} = -a\frac{\partial P}{\partial y}$$

$$\frac{\partial P}{\partial t} = -b\left(\frac{\partial \mathbf{v}_x}{\partial x} + \frac{\partial \mathbf{v}_y}{\partial y}\right). \tag{4.1}$$

Now we are ready to provide the definition of a general heterogeneous acoustic-PML medium. Assuming an artificial splitting of the pressure field into two nonphysical subcomponents

$$P = P_x + P_y, \tag{4.2}$$

and the introduction of four positive, nonphysical parameters (q_x, q_x^*, q_y, q_y^*), the definition of the $2D$ acoustic PML medium is given by the following set of equations:

$$\frac{\partial \mathbf{v}_x}{\partial t} + q_x \mathbf{v}_x = -a\frac{\partial}{\partial x}(P_x + P_y), \tag{4.3}$$

$$\frac{\partial \mathbf{v}_y}{\partial t} + q_y \mathbf{v}_y = -a\frac{\partial}{\partial y}(P_x + P_y), \tag{4.4}$$

$$\frac{\partial P_x}{\partial t} + q_x^* P_x = -b\frac{\partial \mathbf{v}_x}{\partial x}, \tag{4.5}$$

$$\frac{\partial P_y}{\partial t} + q_y^* P_y = -b\frac{\partial \mathbf{v}_y}{\partial y}. \tag{4.6}$$

Notice that if

$$q_x = q_x^* = q_y = q_y^* = 0, \tag{4.7}$$

the acoustic PML medium reduces to the original acoustic medium of eqs. (4.1). For this reason the medium defined by eqs. (4.1) is called the *acoustic host medium*.

Notice from eqs. (4.3)-(4.6) that this formalism is defined in the time domain. This is in contrast to the *complex-coordinate-stretching* approach to be explained in the next section, which is formulated in the frequency domain.

4.2 Solutions of the PML equations.

In this subsection we will study solutions of the PML equations, eqs. (4.3)-(4.6). In particular we will search for plane-wave solutions of the form

$$\mathbf{v}_x = \mathbf{v}_{0x} e^{-i\omega t + ik_x x + ik_y y}, \tag{4.8}$$

$$\mathbf{v}_y = \mathbf{v}_{0y} e^{-i\omega t + ik_x x + ik_y y}, \tag{4.9}$$

$$P_x = P_{0x} e^{-i\omega t + ik_x x + ik_y y}, \tag{4.10}$$

$$P_y = P_{0y} e^{-i\omega t + ik_x x + ik_y y}. \tag{4.11}$$

Any other solution can be expressed as a linear superposition of plane-waves. By substitution of eqs. (4.8)-(4.11) into eqs. (4.3)-(4.6) we get the following set of relations:

$$-i\omega \mathbf{v}_{0x} + q_x \mathbf{v}_{0x} = -aik_x \underbrace{(P_{ox} + P_{oy})}_{P_0} \Rightarrow -i\omega \underbrace{\left(1 + \frac{i}{\omega} q_x\right)}_{s_x} \mathbf{v}_{0x} = -aik_x P_0 \Rightarrow$$

$$\omega \mathbf{v}_{0x} = a \frac{k_x}{s_x} P_0, \tag{4.12}$$

$$-i\omega \mathbf{v}_{0y} + q_y \mathbf{v}_{0y} = -aik_y \underbrace{(P_{ox} + P_{oy})}_{P_0} \Rightarrow -i\omega \underbrace{\left(1 + \frac{i}{\omega} q_y\right)}_{s_y} \mathbf{v}_{0y} = -aik_y P_0 \Rightarrow$$

$$\omega \mathbf{v}_{0y} = a \frac{k_y}{s_y} P_0, \tag{4.13}$$

$$-i\omega P_{0x} + q_x^* P_{0x} = -bik_x \mathbf{v}_{0x} \Rightarrow -i\omega \underbrace{\left(1 + \frac{i}{\omega} q_x^*\right)}_{s_x^*} P_{0x} = -bik_x \mathbf{v}_{0x} \Rightarrow$$

$$\omega P_{0x} = b\frac{k_x}{s_x^*}\mathbf{v}_{0x}, \tag{4.14}$$

$$-i\omega P_{0y} + q_x^* P_{0y} = -bik_y\mathbf{v}_{0y} \Rightarrow -i\omega \underbrace{\left(1 + \frac{i}{\omega}q_y^*\right)}_{s_y^*} P_{0y} = -bik_y\mathbf{v}_{0y} \Rightarrow$$

$$\omega P_{0y} = b\frac{k_y}{s_y^*}\mathbf{v}_{0y}. \tag{4.15}$$

In the above equations, s_x, s_y s_x^*, s_y^* are called *stretching factors.*

Adding eqs. (4.14) and (4.15), we have:

$$\omega P_0 = b\left(\frac{k_x}{s_x^*}\mathbf{v}_{0x} + \frac{k_y}{s_y^*}\mathbf{v}_{0y}\right) \tag{4.16}$$

Substituting eqs. (4.12) and (4.13) into eqs. (4.16), we get

$$\omega P_0 = b\left(\frac{k_x}{s_x^*}\frac{a}{\omega}\frac{k_x}{s_x}P_0 + \frac{k_y}{s_y^*}\frac{a}{\omega}\frac{k_y}{s_y}P_0\right) = \frac{ba}{\omega}P_0\left(\frac{k_x^2}{s_x s_x^*} + \frac{k_y^2}{s_y s_y^*}\right), \tag{4.17}$$

which can be expressed as

$$\frac{\omega^2}{ab} = \frac{k_x^2}{s_x s_x^*} + \frac{k_y^2}{s_y s_y^*}. \tag{4.18}$$

Using the relation $c = \sqrt{ab}$, eq. (4.18) can be written as

$$\frac{\omega^2}{c^2} = \frac{k_x^2}{s_x s_x^*} + \frac{k_y^2}{s_y s_y^*}. \tag{4.19}$$

Eq. (4.19) is the dispersion relation for the acoustic PML media and is a necessary condition for the existence of plane-wave solutions, eqs. (4.8)-(4.11).

The following step is to find explicit solutions for eq. (4.19). A particular family of solutions is given by

$$k_x = \frac{\omega}{c}\sqrt{s_x s_x^*}cos\ \phi \qquad\qquad k_y = \frac{\omega}{c}\sqrt{s_y s_y^*}cos\ \phi, \tag{4.20}$$

where ϕ is a free parameter whose interpretation will be explained later in this subsection. It is easy to see that eq. (4.20) is a solution of eq. (4.19):

$$\frac{k_x^2}{s_x s_x^*} + \frac{k_y^2}{s_y s_y^*} = \frac{1}{s_x s_x^*}\left(\frac{\omega}{c}\sqrt{s_x s_x^*} cos\ \phi\right)^2 + \frac{1}{s_y s_y^*}\left(\frac{\omega}{c}\sqrt{s_y s_y^*} sin\ \phi\right)^2 = \frac{\omega^2}{c^2}(cos^2\ \phi + sin^2\ \phi) = \frac{\omega^2}{c^2}. \tag{4.21}$$

It is worthwhile to mention that eq. (4.20) is not unique and there exist more general solutions involving two free parameters. These two-parameters solutions are relevant for the modeling of evanescent waves, and the interested reader can refer to Bérenger (2007) for more details about this application. In this report we will restrict our discussion to solutions of the form eq. (4.20) and to plane-wave solutions of the acoustic wave equation.

Using eq. (4.20), we can now write a generic plane-wave solution for the PML equations:

$$\psi = \psi_0\ e^{-i\omega t}\ e^{i\frac{\omega}{c}\left[\sqrt{s_x s_x^*} cos\phi\ x + \sqrt{s_y s_y^*} sin\phi\ y\right]}, \tag{4.22}$$

where ψ_0 is either $\mathbf{v}_x, \mathbf{v}_y, P_x$, or P_y.

In order to understand the meaning of the free parameter ϕ in eq. (4.20), we need to impose the so-called *matching condition* in the two pairs of stretching factors (s_x, s_x^*) and (s_y, s_y^*) :

$$s_x = s_x^* \qquad and \qquad s_y = s_y^*. \tag{4.23}$$

For the specific case of the acoustic wave equation, the condition in eq. (4.23) can be reformulated in terms of the parameters as

$$q_x = q_x^* \qquad and \qquad q_y = q_y^*, \tag{4.24}$$

respectively. After imposing the condition in eq. (4.23), eq. (4.22) reduces to

$$\psi = \psi_0\ e^{-i\omega t}\ e^{i\frac{\omega}{c}[cos\phi\ x + sin\phi\ y]}\ e^{-\frac{q_x}{c} cos\phi\ x}\ e^{-\frac{q_y}{c} sin\phi\ y}. \tag{4.25}$$

From eq. (4.25) it is evident that if we identify ϕ with the angle between the positive x-direction and a vector $\mathbf{k}'$ with components

$$k'_x = \frac{\omega}{c}\ cos\ \phi \qquad\qquad k'_y = \frac{\omega}{c}\ sin\ \phi, \tag{4.26}$$

then the first two exponentials in eq. (4.25) describe a plane-wave solution propagating in the direction of $\mathbf{k}'$ and velocity c in the acoustic host medium. Also the third and fourth factors in eq. (4.25) are attenuation factors in the x and y directions respectively. In this way, when the matching condition holds for (s_x, s_x^*) and (s_y, s_y^*), the plane-wave solutions for the PML medium represent decaying solutions for the ordinary acoustic host medium. Additionally the matching condition in terms of the parameters, i.e., eq. (4.24), together with $q_x = q_y = 0$, imply that eq. (4.25) reduces to a plane wave for the acoustic host medium, as expected.

4.3 Reflection and transmission of plane waves at a PML-PML interface

The purpose of the present subsection is to study the physics of the propagation of a PML plane wave that is incident at an interface between two PML media built from the same acoustic host medium. For this, let's consider two semi-infinite PML media, adjacent to each other and with the interface between them placed at $x = 0$, and parallel to the y axis. The two PML media are defined by two sets of parameters $(q_{x1}, q^*_{x1}, q_{y1}, q^*_{y1})$ and $(q_{x2}, q^*_{x2}, q_{y2}, q^*_{y2})$ for $x < 0$ and $x > 0$ respectively. Assume also that an incident wave P_1 is striking the PML-PML interface from the left— i.e., the wave is propagating in the medium $(q_{x1}, q^*_{x1}, q_{y1}, q^*_{y1})$ with incident angle ϕ_1. From experience we know that there is a transmitted wave P_2 with refraction angle ϕ_2 and a reflected wave P_r with reflection angle ϕ_r, where all angles are measured relative to the positive x direction (Figure 4). Our goal is to calculate the reflection coefficient at the PML-PML interface of this configuration.

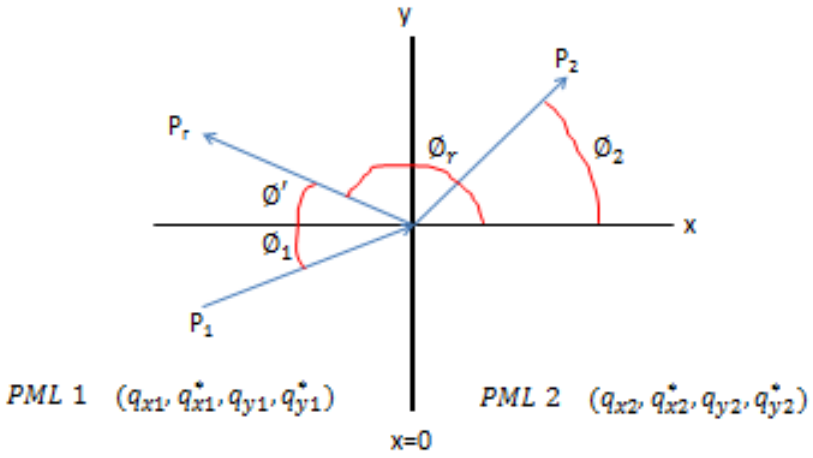

Figure 4: Two semi-infinite PML media defined by two set of parameters $(q_{x1}, q^*_{x1}, q_{y1}, q^*_{y1})$ and $(q_{x2}, q^*_{x2}, q_{y2}, q^*_{y2})$ for $x < 0$ and $x > 0$, respectively, are placed adjacent to each other with the interface at $x = 0$. An incident wave P_1 is striking the interface at an angle ϕ_1, resulting in a transmitted wave P_2 with a refraction angle ϕ_2 and a reflected wave P_r with a reflection angle ϕ_r.

The general solutions for the incident, reflected and refracted waves are

$$P_1 = P_{01}\ e^{-i\omega t} e^{ik_{x1}x + ik_{y1}y} = P_{01}\ e^{-i\omega t}\ e^{i\frac{\omega}{c}\left[\sqrt{s_{x1}s^*_{x1}}cos\phi_1\ x + \sqrt{s_{y1}s^*_{y1}}sin\phi_1\ y\right]}, \tag{4.27}$$

$$P_r = P_{0r}\ e^{-i\omega t} e^{ik_{xr}x + ik_{yr}y} = P_{0r}\ e^{-i\omega t}\ e^{i\frac{\omega}{c}\left[\sqrt{s_{x1}s^*_{x1}}cos\phi_1\ x + \sqrt{s_{y1}s^*_{y1}}sin\phi_1\ y\right]}, \tag{4.28}$$

$$P_2 = P_{02}\ e^{-i\omega t} e^{ik_{x2}x + ik_{y2}y} = P_{02}\ e^{-i\omega t}\ e^{i\frac{\omega}{c}\left[\sqrt{s_{x2}s^*_{x2}}cos\phi_2\ x + \sqrt{s_{y2}s^*_{y2}}sin\phi_2\ y\right]}. \tag{4.29}$$

The presence of $\partial P/\partial x$ in eq. (4.3) means that it must be defined everywhere and in particular at the interface. A necessary condition for this to happen is that the *total pressure field* must be continuous at the interface:

$$P_1 + P_r = P_2 \qquad at \qquad x = 0. \tag{4.30}$$

Upon substitution of eqs. (4.27)-(4.29) into eq. (4.30) we get

$$P_{01}\ e^{ik_{y1}y} + P_{0r}e^{ik_{yr}y} = P_{02}e^{ik_{y2}y}. \tag{4.31}$$

It turns out that each term in eq. (4.31) is independent of the other terms as a function of y. Thus, the condition to guarantee the equality at any point of the interface is

$$k_{y1} = k_{yr} = k_{y2}, \tag{4.32}$$

as in this case eq. (4.31) reduces to

$$P_{01} + P_{0r} = P_{02}, \tag{4.33}$$

which is a constant. Using the first equality in eqs. (4.32) and (4.20) we get

$$sin\ \phi_1 = sin\ \phi_r. \tag{4.34}$$

Under the change of variable $\phi_r = \pi - \phi'$ for $\phi' < \pi/2$, we have the following result:

$$sin\ \phi_r = sin\ (\pi - \phi') = sin\ \pi\ cos\ \phi' - cos\ \pi\ sin\ \phi' = sin\ \phi', \tag{4.35}$$

Eq. (4.35) implies $\phi' = \phi_1$, which means

$$\phi_r = \pi - \phi_1. \tag{4.36}$$

A direct consequence of eq. (4.35) is

$$k_{xr} = \frac{\omega}{c}\sqrt{s_{x1}s^*_{x1}}\ cos\ \phi_r = \frac{\omega}{c}\sqrt{s_{x1}s^*_{x1}}\ cos\ (\pi - \phi_1) = -\frac{\omega}{c}\sqrt{s_{x1}s^*_{x1}}\ cos\ \phi_1 = -k_{x1}. \tag{4.37}$$

Using again eq. (4.32), we have the Snell-Descartes law for a PML media:

$$\sqrt{s_{y1}s^*_{y1}}\ sin\ \phi_1 = \sqrt{s_{y2}s^*_{y2}}\ sin\ \phi_2. \tag{4.38}$$

Also, upon division of (4.33) by P_{01}, we obtain

$$1 + r = t, \tag{4.39}$$

where $r \equiv P_{0r}/P_{01}$ is the reflection coefficient and $t \equiv P_{02}/P_{01}$ is the transmission coefficient. Eq. (4.39) is the first equation relating r and t to each other. However, we still need a further relation in order to solve for r. To find such a relation we will use the continuity of the velocity field $\mathbf{v}(x)$ across the interface i.e. at $x = 0$ and eq. (4.3). The continuity condition is sensitive to the total field P_{tot} at each side of the interface, and not to the individual components of the artificial splitting assumed in eq. (4.2).

Let us start with the medium 2, as in this case $P_{tot} = P_2$, and therefore the calculation is easier than in medium 1 where $P_{tot} = P_1 + P_r$. By inserting P_2 into eq. (4.39) we get

$$-i\omega \mathbf{v}_{x2} + q_{x2}\mathbf{v}_{x2} = \frac{\partial P_2}{\partial x} = P_{02} e^{-i\omega t} e^{i\frac{\omega}{c}\left[\sqrt{s_{x2}s_{x2}^*}cos\phi_2\ x + \sqrt{s_{y2}s_{y2}^*}sin\phi_2\ y\right]} \left(i\frac{\omega}{c}\sqrt{s_{x2}s_{x2}^*}cos\phi_2\ x\right), \tag{4.40}$$

which can be arranged as

$$-i\omega s_{x2}\mathbf{v}_{x2} = -i\frac{a\omega}{c} P_{02}\sqrt{s_{x2}s_{x2}^*}\ cos\phi_2\ e^{-i\omega t} e^{i\frac{\omega}{c}\left[\sqrt{s_{x2}s_{x2}^*}\ cos\phi_2\ x + \sqrt{s_{y2}s_{y2}^*}sin\phi_2\ y\right]}. \tag{4.41}$$

Evaluating eq. (4.41) at $x = 0$ and using eq. (4.38) we arrive at

$$\mathbf{v}_{x2} = \sqrt{\frac{s_{x2}^*}{s_{x2}}}\frac{a}{c} P_{02}\ cos\phi_2\ e^{-i\omega t} e^{i\frac{\omega}{c}\sqrt{s_{y1}s_{y1}^*}sin\phi_1\ y}. \tag{4.42}$$

Evaluating now eq. (4.39) in medium 1, we get

$$-i\omega \mathbf{v}_{x1} + q_{x1}\mathbf{v}_{x1} = P_{01} e^{-i\omega t} e^{i\frac{\omega}{c}\left[\sqrt{s_{x1}s_{x1}^*}cos\phi_1\ x + \sqrt{s_{y1}s_{y1}^*}sin\phi_1\ y\right]} \left(i\frac{\omega}{c}\sqrt{s_{x1}s_{x1}^*}cos\phi_1\ x\right)$$

$$+ P_{0r} e^{-i\omega t} e^{i\frac{\omega}{c}\left[\sqrt{s_{x1}s_{x1}^*}cos\phi_r\ x + \sqrt{s_{y1}s_{y1}^*}sin\phi_r\ y\right]} \left(i\frac{\omega}{c}\sqrt{s_{x1}s_{x1}^*}cos\phi_r\ x\right). \tag{4.43}$$

Using eq. (4.34) and $cos\ \phi_r = -cos\phi_1$, the above expression becomes

$$-i\omega s_{x1}\mathbf{v}_{x1} =$$

$$-i\omega\frac{a}{c}\sqrt{s_{x1}s_{x1}^*}e^{i\frac{\omega}{c}\sqrt{s_{y1}s_{y1}^*}sin\phi_1\ y} e^{-i\omega t}\left(P_{01}e^{i\frac{\omega}{c}\sqrt{s_{x1}s_{x1}^*}cos\phi_1\ x} - P_{0r}e^{-i\frac{\omega}{c}\sqrt{s_{x1}s_{x1}^*}cos\phi_1\ x}\right) cos\ \phi_1, \tag{4.44}$$

which upon evaluation at $x = 0$ reduces to

$$\mathbf{v}_{x1} = \frac{a}{c}\sqrt{\frac{s^*_{x1}}{s_{x1}}}\; e^{-i\omega t} e^{i\frac{\omega}{c}\sqrt{s_{y1}s^*_{y1}}sin\phi_1\; y}(P_{01} - P_{0r})cos\phi_1. \tag{4.45}$$

Continuity of $\mathbf{v}$ implies the matching of eq. (4.45) with eq. (4.42):

$$\frac{a}{c}\sqrt{\frac{s^*_{x1}}{s_{x1}}}\; e^{-i\omega t} e^{i\frac{\omega}{c}\sqrt{s_{y1}s^*_{y1}}sin\phi_1\; y}(P_{01} - P_{0r})cos\phi_1 = \frac{a}{c}\sqrt{\frac{s^*_{x2}}{s_{x2}}}P_{02}\; cos\phi_2\; e^{-i\omega t} e^{i\frac{\omega}{c}\sqrt{s_{y1}s^*_{y1}}sin\phi_1\; y}. \tag{4.46}$$

After division by P_{01} eq. (4.46) becomes

$$\sqrt{\frac{s^*_{x1}}{s_{x1}}}\; (1-r)cos\phi_1 = \sqrt{\frac{s^*_{x2}}{s_{x2}}}\; t\; cos\phi_2. \tag{4.47}$$

Eq. (4.47) is the second relation among r and t. Upon insertion of eq. (4.39) into the right-hand side of eq. (4.47), we can solve for r:

$$r = \frac{\sqrt{\frac{s^*_{x1}}{s_{x1}}}\; cos\phi_1 - \sqrt{\frac{s^*_{x2}}{s_{x2}}}\; cos\phi_2}{\sqrt{\frac{s^*_{x1}}{s_{x1}}}\; cos\phi_1 + \sqrt{\frac{s^*_{x2}}{s_{x2}}}\; cos\phi_2}. \tag{4.48}$$

Eq. (4.48) is the reflection coefficient for the configuration of Figure 4. Let's now study under what conditions $r = 0$. Notice first that if the transverse conductivities on both media are the same i.e., if $q_{y1} = q_{y2} \equiv q_y$ and $q^*_{y1} = q^*_{y2} \equiv q^*_y$ then eq. (4.38) immediately implies that $\phi_1 = \phi_2$ and therefore eq. (4.48) reduces to

$$r = \frac{\sqrt{\frac{s^*_{x1}}{s_{x1}}} - \sqrt{\frac{s^*_{x2}}{s_{x2}}}}{\sqrt{\frac{s^*_{x1}}{s_{x1}}} + \sqrt{\frac{s^*_{x2}}{s_{x2}}}}. \tag{4.49}$$

Furthermore, if the matching condition holds for both PML-media in the x-direction, i.e., if $s_{x1} = s^*_{x1}$ ($q_{x1} = q^*_{x1}$) and $s_{x2} = s^*_{x2}$ ($q_{x2} = q^*_{x2}$), then eq. (4.49) gives $r = 0$. For short, in order to the reflection coefficient to be identically zero, the PML-parameters on both sides of Figure 4 must be as follows:

$$PML\ 1 : (q_{x1}, q_{x1}, q_y, q^*_y) \qquad\qquad PML\ 2 : (q_{x2}, q_{x2}, q_y, q^*_y), \tag{4.50}$$

and this is true for all frequencies and all angles of incidence. Two comments about eq. (4.50) are in order:

1. The reflectionless property remains true for a wave going from medium PML 2 to medium PML 1.

2. If the roles of q_{x1} and q_{x2} are interchanged, so that the two PML materials are interchanged in Figure 4, then by repeating the same analysis as before we can conclude that a plane wave, propagating in the direction of negative x, in the medium $PML1$ (now filling the half-space $x > 0$) will also be transmitted to medium $PML2$(now filling the half-space $x < 0$) without reflection.

In the particular situation in which one of the two PML media is the acoustic host medium, eq. (4.50) takes the form

$$PML\ 1 : (0, 0, 0, 0) \qquad PML\ 2 : (q_x, q_x, 0, 0), \tag{4.51}$$

or

$$PML\ 1 : (q_x, q_x, 0, 0) \qquad PML\ 2 : (0, 0, 0, 0). \tag{4.52}$$

The same discussion can be held if the interface between the two PML media is now parallel to the x direction. In this case the reflectionless property arises if the parameters satisfy

$$PML\ 1 : (q_x, q_x^*, q_{y1}, q_{y1}) \qquad PML\ 2 : (q_x, q_x^*, q_{y2}, q_{y2}), \tag{4.53}$$

for $y < 0$ and $y > 0$, respectively. (Analogously to the vertical interface, we can interchange the role q_{y1} and q_{y2} so that $y > 0$ and $y < 0$ for the media $PML1$ and $PML2$ respectively, and the same result still holds). Moreover if $PML\ 1$ is the acoustic host medium (4.53) reduces to

$$PML\ 1 : (0, 0, 0, 0) \qquad PML\ 2 : (0, 0, q_y, q_y), \tag{4.54}$$

and if $PML\ 2$ is the acoustic host medium (4.53) reduces to

$$PML\ 1 : (0, 0, q_y, q_y) \qquad PML\ 2 : (0, 0, 0, 0). \tag{4.55}$$

4.4 Attenuation factor at a PML layer bounded by the acoustic host medium and hard-wall BCs

Assume we have the configuration depicted in Figure 5: an interface between an acoustic host medium $(0, 0, 0, 0)$ and a matched PML-medium with parameters $(q_x, q_x, 0, 0)$ is placed at $x = 0$ and parallel to the y direction. The PML medium is bounded at $x = \delta$ by an interface where Dirichlet B.C's are imposed. In other words the PML medium is a PML layer (or just PML) with thickness δ. Also a wave P_{inc} is propagating within the acoustic host medium ($x < 0$) towards the interface with the PML layer at $x = 0$. As there is no reflection at this interface, there will only be a transmitted wave P_{trans}. However, when this transmitted wave strikes the interface at $x = \delta$, the Dirichlet BCs produce a reflected wave P_{ref2}, which eventually hits the interface at $x = 0$ and is transmitted again without reflection to the acoustic host medium. This transmitted wave is denoted

as P_{ref1} because it is similar to a reflected wave. The ratio of the magnitude P_{01} of P_{inc} and the magnitude P_{0r1} of P_{ref1} is called the *apparent reflection factor* as P_{0r1} is not the reflection of P_{inc}:

$$R(\omega) = \frac{P_{0r1}}{P_{01}}, \tag{4.56}$$

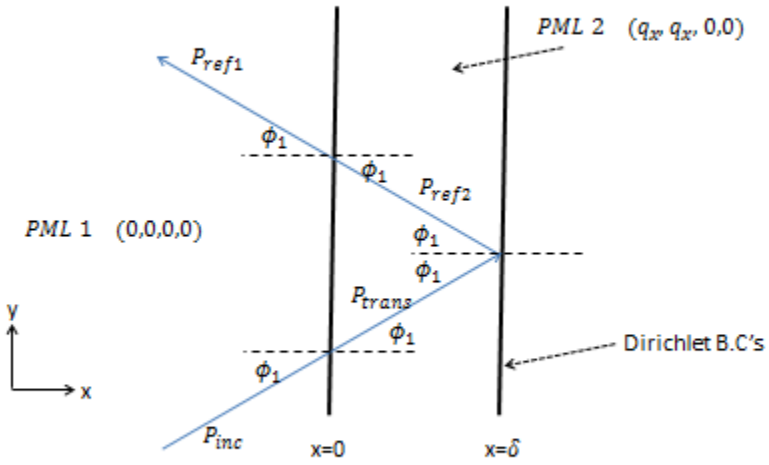

Figure 5: A PML layer with parameters $(q_x, q_x, 0, 0)$ is bounded by the acoustic host medium with parameters $(0, 0, 0, 0)$ at $x = 0$ and by an interface with Dirichlet B.C's at $x = \delta$. Also a wave P_{inc} is propagating in the acoustic host medium and is transmitted without reflection at $x = 0$. The transmitted wave P_{trans} is reflected at $x = \delta$ and this reflected wave, denoted P_{ref1}, is transmitted at $x = 0$, without reflection, back to the acoustic host medium. This last transmitted wave is called P_{ref1} as it resembles a reflection of P_{inc}.

In this subsection we will compute the *apparent reflection factor*, which in general depends on the frequency of the incident wave. For the configuration in Figure 5, we have

$$P_{inc} = P_{01}e^{-i\omega t}\ e^{i\frac{\omega}{c}[cos\phi_1 x + sin\phi_1 y]}, \tag{4.57}$$

$$P_{ref1} = P_{0r1}e^{-i\omega t}\ e^{i\frac{\omega}{c}[-cos\phi_1 x + sin\phi_1 y]}, \tag{4.58}$$

$$P_{trans} = P_{0t}e^{-i\omega t}\ e^{i\frac{\omega}{c}[cos\phi_1 x + sin\phi_1 y]}e^{-\frac{q_x}{c}cos\phi_1 x}, \tag{4.59}$$

$$P_{ref2} = P_{0r2}e^{-i\omega t}\ e^{i\frac{\omega}{c}[-cos\phi_1 x + sin\phi_1 y]}e^{\frac{q_x}{c}cos\phi_1 x}. \tag{4.60}$$

At $x = 0$ eqs. (4.57)-(4.60) reduce to

$$P_{inc} = P_{01}e^{-i\omega t}\ e^{i\frac{\omega}{c}sin\phi_1 y}, \tag{4.61}$$

$$P_{ref1} = P_{0r1}e^{-i\omega t}\ e^{i\frac{\omega}{c}sin\phi_1 y}, \tag{4.62}$$

$$P_{trans} = P_{0t}e^{-i\omega t}\ e^{i\frac{\omega}{c}sin\phi_1 y}, \tag{4.63}$$

$$P_{ref2} = P_{0r2}e^{-i\omega t}\ e^{i\frac{\omega}{c}sin\phi_1 y}. \tag{4.64}$$

On the other hand, continuity of P at $x = 0$ requires $P_{inc} + P_{ref1} = P_{trans} + P_{ref2}$, which upon substitution of eqs. (4.61)-(4.64) gives

$$P_{01} + P_{0r1} = P_{0t} + P_{0r2}. \tag{4.65}$$

Now, using eq. (4.3) at $x = 0$, we have

$$\mathbf{v}_{x1} = (P_{01} - P_{0r1})\frac{a}{c}cos\phi_1\ e^{-i\omega t}\ e^{i\frac{\omega}{c}sin\phi_1 y} \tag{4.66}$$

$$\mathbf{v}_{x2} = (P_{0t} - P_{0r2})\frac{a}{c}cos\phi_1\ e^{-i\omega t}\ e^{i\frac{\omega}{c}sin\phi_1 y}. \tag{4.67}$$

From the above expressions, continuity of $\mathbf{v}_x$ implies

$$P_{01} - P_{0r1} = P_{0t} - P_{0r2}. \tag{4.68}$$

Solving the system (4.65)-(4.68), we have:

$$P_{01} = P_{0t} \qquad\qquad P_{0r1} = P_{0r2}, \tag{4.69}$$

which implies that $R(\omega)$ can be written as

$$R(\omega) = \frac{P_{0r2}}{P_{0t}}. \tag{4.70}$$

At $x = \delta$, the Dirichlet B.C's require

$$P_{trans} + P_{ref2} = P_{0t}e^{-i\omega t}\ e^{i\frac{\omega}{c}[cos\phi_1\delta + sin\phi_1 y]}e^{-\frac{q_x}{c}cos\phi_1\delta} + P_{0r2}e^{-i\omega t}\ e^{i\frac{\omega}{c}[-cos\phi_1\delta + sin\phi_1 y]}e^{\frac{q_x}{c}cos\phi_1\delta} = 0, \tag{4.71}$$

which upon division by P_{0t} and using eq. (4.70) gives

$$e^{-i\omega t}\ e^{i\frac{\omega}{c}[cos\phi_1\delta+sin\phi_1 y]}e^{-\frac{q_x}{c}cos\phi_1\delta} + R(\omega)e^{-i\omega t}\ e^{i\frac{\omega}{c}[-cos\phi_1\delta+sin\phi_1 y]}e^{\frac{q_x}{c}cos\phi_1\delta} = 0. \tag{4.72}$$

Solving eq. (4.72) for $R(\omega)$, we have

$$R(\omega) = e^{\frac{2}{c}i\omega\ cos\phi_1\delta}\ e^{-2\frac{q_x}{c}cos\phi_1\delta}. \tag{4.73}$$

In eq. (4.73) the first exponential factor is a phase that does not affect the amplitude of P_{ref1}; however, the second exponential is an attenuating factor that represents how much P_{inc} is attenuated after its propagation inside the PML layer and back to the acoustic host medium.

Notice also that the attenuation factor in eq. (4.73) is independent of ω. If this were not the case, then in the FD implementation we would need a different PML for each wavelength in the radiation zone, with each PML layer having a different thickness in order to provide good attenuation to the corresponding wavelength. This of course would make impossible the implementation of the FD algorithm.

If the attenuating factor eq. (4.73) is big enough, then the effect of reflections produced by the Dirichlet B.C. at $x = \delta$ is small, i.e., P_{ref1} can be neglected in the FD simulation. At least theoretically we can achieve any attenuation rate by choosing a large enough value of either δ or q_x (or both of them).

In practice however this is not a simple choice: from the point of view of computational cost the thickness δ should be as small as possible; otherwise, the size of the FD domain will be too big and will result in an expensive simulation. On the other hand very large values of q_x produce "numerical reflections" i.e. reflections arising from the discretization of the computational domain. Such numerical reflections can be attenuated by either increasing the resolution of the grid (with the subsequent increased slowness of the algorithm, increased memory requirement and thus increased computational cost again) or by a slow turn-on of q_x (i.e. a slowly varying PML medium[2]). Therefore, the choice of the right q_x is a fundamental issue and it is one of the most important aspects to take into account in the implementation of PML technique (Bérenger (2007)).

It has become a common practice to turn on q_x quadratically (or cubically) from zero (Johnson 007a). This choice results in the numerical reflections becoming tiny and it seems to provide the equilibrium among all the criteria just explained: rate of attenuation, thickness of the PML region, computational cost and numerical reflections.

Finally, if the interface between the acoustic host medium and the PML layer is parallel to the x direction, and if the thickness of the PML layer is also δ, a similar analysis shows that the *apparent attenuation factor* is now

$$R(\omega) = e^{\frac{2}{c}i\omega\ cos\phi_1\delta}\ e^{-2\frac{q_y}{c}cos\phi_1\delta}. \tag{4.74}$$

The same discussion following eq. (4.73) applies for the choose of thickness δ of the PML layer and the value of the parameter q_y.

[2]This is actually a particular case of a more general *adiabatic theorem*, valid also for non-PML media. The adiabatic theorem is important because when the PML method fails, it is the closest tool we have at our disposal to substitute for the PML method

4.5 Theoretical implementation of the PML technique to the Finite-Difference method.

We are now in position to describe the configuration resulting from the incorporation of the PML technique into the 2D Finite-Difference algorithm for the acoustic wave equation. The computational domain is assumed to be a square whose edges are surrounded by suitable PML layers of thickness δ. The parameters of the PML materials are chosen according to equations (4.51) and (4.54) (and their counterparts when their relative position with respect the acoustic host medium is changed), so that there is no reflection at any vertical or horizontal acoustic-PML interface respectively. However, the presence of vertical and horizontal PML layers gives rise to PML-PML interfaces at the corners of the computational domain. Therefore, more general configurations must be chosen in order to avoid reflections at these interfaces. It turns out that the same configuration does the job for all corners, and in such a configuration none of the parameters are set to zero but instead are set to the values shown in Figure 6. It is not a surprise that the parameters at the corner regions depend on the parameters of the vertical and horizontal PML layers.

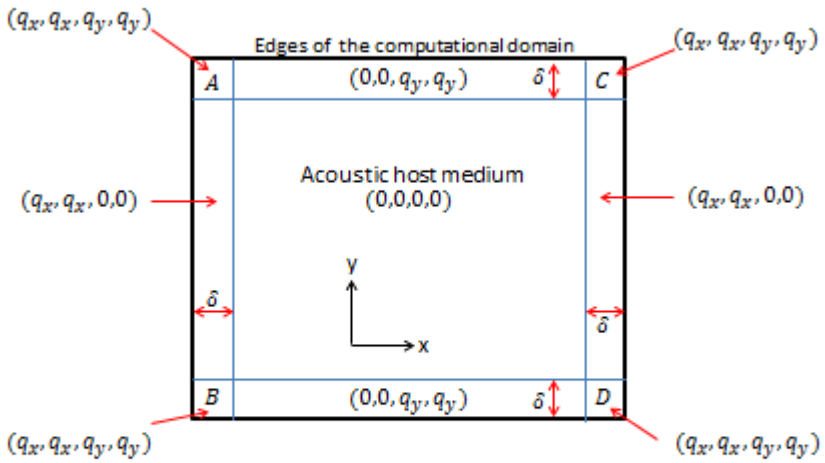

Figure 6: Implementation of the PML technique in the finite-difference array: the boundary of a square-shaped computational domain is surrounded by vertical and horizontal PML layers of thickness δ. The PML parameters are set to $(q_x, q_x, 0, 0)$ for the layers AB and CD, and to $(0, 0, q_y, q_y)$ for the layers AC and BD, in order to avoid any reflection. Also, the same configuration removes reflections at the PML-PML interfaces of all corners: (q_x, q_x, q_y, q_y).

4.6 A limitation of the PML technique.

Notice in eq. (4.73) that the attenuation rate is proportional to $cos\phi_1$, where ϕ_1 is the angle of incidence of the radiating wave, with respect the positive x direction. Hence, as the radiation approaches at grazing incidence the attenuation goes to zero. Therefore for any PML thickness, waves close to grazing incidence will return to the radiation zone (and eventually to the region of interest) with little attenuation.

Fortunately, in practice this is not a problem (Johnson 007a, Bérenger 2007), as in most cases the radiation originates in the region of interest i.e. close to the origin. In this situation, and assuming a cubic computational region, the radiation striking the PML region will be, in the limit as the boundaries move far away, at an angle of incidence $\theta < 55°$. In this case we get a maximum angle of incidence and hence we can make the PML thick enough to absorb all waves within this set of angles. Of course in choosing the thickness of the PML, we should not forget the factors mentioned in subsection 4.4.

This means that for the PML technique to work there cannot be scatterers placed far away (the meaning of small and big is defined relative to the size of the computational region) from the region of interest. If this is the case, then again there exists again the possibility of grazing incidence.

If for some reason grazing incidence occurs, a formalism based in the so-called Convolutional PML (CPML) was developed in Komatitsch and Martin (2007) (for the seismic wave equation) in order to improve the behavior of PML in this situation.

5 Complex-coordinate-stretching

Let's choose a Cartesian coordinate system, with the origin $\mathbf{x} = 0$ near the region of interest. Let also $\mathbf{w}(\mathbf{x}, t)$ be the solution of the equation governing the propagation of the waves in the infinite space/region, which in this case is the acoustic wave equation. As was mentioned in the past section, the present formulation is defined in the frequency domain. Hence, strictly speaking we should consider $\mathbf{w}(\mathbf{x}, w)$, the inverse Fourier transform of $\mathbf{w}(\mathbf{x}, t)$. However, as we will focus our analysis in the spatial dependence of the wave, we will keep the dependence in time so we can continue using concepts that are natural in the time domain and not so clear in the frequency domain such as propagating waves, etc.

For simplicity and for consistency with the previous section we will focus on the truncation along the x-direction. As in the *split-field* formulation, analogous arguments can be applied to other coordinates. The approach consists of three important steps (Johnson 007a):

1. Allow x to take complex values, and perform the *analytic continuation* of the wave equation (and its solutions) in the radiation zone to a convenient complex contour, such that after some point x_0 the oscillating solutions turn into exponentially decaying waves, with no reflections traveling back to the region of interest.

2. Perform a *coordinate transformation* to bring back the now complex coordinate x into a real one. This results in real coordinates and *complex materials*.

3. Truncate this new real coordinate, such that the end point lies inside the complex material region. Since in this region the solution is decaying, after a long enough distance the wave is small enough to impose the usual Dirichlet or Neumann boundary conditions, without bringing significant reflections.

5.1 Analytic continuation.

Consider again a particular plane-wave solution, traveling in the positive x direction:

$$\mathbf{w}(\mathbf{x},t) = \mathbf{W}(y,z)e^{i(kx-\omega t)}. \tag{5.1}$$

The important fact about eq. (6.4) is that it is an analytic function of x, which means that it can be continued analytically to complex values of x, and then evaluated along a convenient contour in the complex plane. Then, a general solution can be constructed by linear superposition of the analytic continuation of each plane-wave component, along such a contour. The original solution will correspond to the contour along the real axis, but consider for example a generic contour in which x has an imaginary part identically zero for $Re\ x \leq x_0$ for some $x_0 \in \mathcal{R}$. Also, $Im\ x > 0$ is a positive and increasing function of $Re\ x$ (i.e $Im\ x = Im\ x(Re\ x)$), for $Re\ x > x_0$. The result of evaluating eq. (5.1) in this contour is an exponentially decaying solution for $Re\ x > x_0$, because the x-dependence becomes

$$e^{ik(Re\ x + i\ Im\ x)} = e^{ikRe\ x}e^{-kIm\ x}, \tag{5.2}$$

which decays exponentially under the conditions just described (and for $k > 0$), as $Re\ x$ increases. Notice that when $Re\ x \leq x_0$, eq. (5.1) is unchanged and hence is still oscillatory (Figure 7).

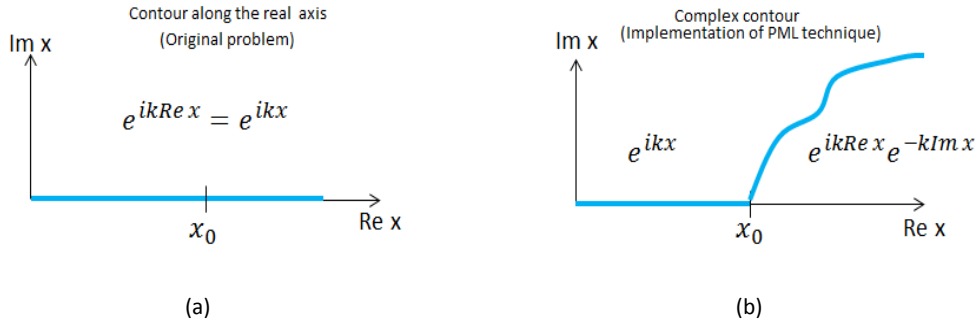

Figure 7: (a) Contour corresponding to the original unbounded problem i.e. the real axis. In this case, we keep the original oscillating solutions of the wave equation. (b) Generic deformed contour corresponding to the "insertion" of a PML layer is shown. In the region where this contour departs from the real axis the oscillating solutions of the original wave equation turn into exponentially decaying ones.

The physical interpretation of the paragraph above is as follows: if we evaluate eq. (5.1), the original solution of the wave equation, in the contour described in Figure 7 (b), then it behaves as a wave propagating in an absorbing material as long as $Re\ x > x_0$. On the other hand when $Re\ x \leq x_0$ it is unchanged; therefore in this region we still have the original solution corresponding to a wave propagating in the radiation zone. Hence, it seems natural to think that in x_0 there is an "interface" between the original non-absorbing media and an absorbing material. However this absorbing material has a very particular property: the fact that the solution is unchanged when

$Re\ x \leq x_0$ can be interpreted as if there are no reflections arising from this "interface" at x_0. This means that we are in the presence of a *reflectionless absorbing material*.

In short, we can think of the "material" filling the region $Re\ x > x_0$ as a *reflectionless absorbing material*, which has the same properties as those of the PML medium defined in the last section. Assuming that we are performing a computational simulation with finite difference, the computational domain is finite and therefore the absorbing material forms a layer called a *perfectly matched layer* (PML).

It is important to remember that the analytically continued solution satisfies the same (analytically continued) differential equation. This will be shown when we explain the relation between this and the *split-field* formulations of PML. In the meantime, to make things simpler it is convenient to rewrite the analytically continued wave equation (and its solutions) in terms of a real variable. This is explained in the next subsection.

5.2 Coordinate transformation back to real x.

Now we use x to denote the real part of the contour $\tilde{x}$, in which we wish to solve the wave equation, i.e.

$$\tilde{x}(x) = x + if(x) \tag{5.3}$$

where $f(x)$ is some function representing the deviation of the complex contour from the real axis. In comparison with the previous subsection, we have the following change in notation:

$$\begin{gathered} Complex\ contour : x \to \tilde{x}, \\ Real\ part\ of\ complex\ contour :\ Re\ x \to x, \\ Imaginary\ part\ of\ complex\ contour : Im\ x \to f, \end{gathered}$$

and hence

$$Im\ x(Re\ x) \to f(x).$$

The natural real variable in this formalism is the real part of the complex contour in which we want to evaluate the solutions. Hence we will change variables to write the relevant equations in terms of x. Notice that this does not mean we are going back to the original wave equation, defined on the real axis, as we already did the analytic continuation and we are solving the wave equation along $\tilde{x}$.

Let $g(x, y)$ be a differentiable function defined in all space, which can be analytically continued to complex values of x and hence evaluated in the contour $\tilde{x}$. Denoting this analytic continuation also as g, we then have a function $g(\tilde{x}(x), y)$. Using the chain rule and eq. (5.3) we have

$$\frac{\partial g}{\partial x} = \frac{\partial \tilde{x}}{\partial x}\frac{\partial g}{\partial \tilde{x}} = \left(1 + i\ \frac{df(x)}{dx}\right)\frac{\partial g}{\partial \tilde{x}} \tag{5.4}$$

Notice that the derivative of $f(x)$ is a total derivative, as it is function exclusively of x. Therefore, from the above expression we have

$$\frac{\partial}{\partial \tilde{x}} = \frac{1}{1 + i\frac{df}{dx}} \frac{\partial}{\partial x}. \tag{5.5}$$

What we have done so far is as follows: we started with a wave equation with partial derivatives with respect to a real coordinate x, and then it was analytically continued. This means substituting the partial derivatives as follows

$$\frac{\partial}{\partial x} \to \frac{\partial}{\partial \tilde{x}}. \tag{5.6}$$

Now we rewrite the analytically continued wave equation as a function of the new real variable x (keep in mind that it is not the initial x we started with) by the substitution

$$\frac{\partial}{\partial \tilde{x}} \to \frac{1}{1 + i\frac{df}{dx}} \frac{\partial}{\partial x}. \tag{5.7}$$

Combining eqs. (5.6) and (5.7), the whole process is equivalent to the following substitution in the initial wave equation:

$$\frac{\partial}{\partial x} \to \frac{1}{1 + i\frac{df}{dx}} \frac{\partial}{\partial x}. \tag{5.8}$$

For convenience we define

$$\frac{df}{dx} = \frac{q_x(x)}{\omega}, \tag{5.9}$$

and eq. (5.5) becomes

$$\frac{\partial}{\partial x} \to \frac{1}{1 + i\frac{q_x(x)}{\omega}} \frac{\partial}{\partial x}. \tag{5.10}$$

Eq. (5.10) is called the PML transformation; regions where $q_x(x) > 0$ are called **PML regions**. It is in the PML regions where oscillating solutions turn into exponentially decaying ones, while in regions where $q_x(x) = 0$ we have $\tilde{x} = x$, meaning that both the wave equation and the solution are unchanged and, as was mentioned before, the interpretation is that there are no reflections.

The reason for the factor $1/\omega$ in eq.(5.9) is to make the attenuation rate in the PML region independent of the wavelength of the propagating wave.

6 Equivalence of the *split-field* and *complex-coordinate-stretching* approaches.

In section 5 we explained the *complex-coordinate-stretching* approach in a simplified way, in order get a clear understanding of this formulation. However, in order to understand the relation between this approach and the *split-field* approach, we need a more rigorous statement of what *complex coordinate stretching* means.

Let's start by writing the acoustic wave equation, expression (3.4), in the frequency domain:

$$-i\omega\mathbf{v} = -a\nabla P \qquad\qquad -i\omega P = -b\nabla\cdot\mathbf{v}. \tag{6.1}$$

By definition, in the *complex-coordinate-stretching* approach the PML equations are obtained by substituting the equations in (6.1) by the following expressions:

$$-i\omega\mathbf{v} = -a\nabla' P \qquad\qquad -i\omega P = -b\nabla^*\cdot\mathbf{v}, \tag{6.2}$$

with

$$\nabla' = \frac{1}{s_x(x)}\frac{\partial}{\partial x}\hat{x} + \frac{1}{s_y(y)}\frac{\partial}{\partial y}\hat{y} \qquad\qquad \nabla^* = \frac{1}{s^*_x(x)}\frac{\partial}{\partial x}\hat{x} + \frac{1}{s^*_y(y)}\frac{\partial}{\partial y}\hat{y}, \tag{6.3}$$

where the *stretching functions* [3], $s_x(x)$, $s_y(y)$, $s^*_x(x)$ and $s^*_y(y)$ are complex-valued analytic functions of their corresponding argument. Notice that if the *stretching functions* are set to 1, then we end with the original acoustic media defined by eq. (6.1); i.e., in this formalism the acoustic host medium is a PML medium with stretching functions set to 1.

Now we introduce the *complex stretched coordinates*

$$dx' = s_x(x)dx \qquad dy' = s_y(y)dy \qquad dx^* = s^*_x(x)dx \qquad dy^* = s^*_y(y)dy. \tag{6.4}$$

From eq. (5.1) we have the following results:

$$\frac{\partial}{\partial x'} = \frac{1}{s_x(x)}\frac{\partial}{\partial x} \qquad \frac{\partial}{\partial y'} = \frac{1}{s_y(y)}\frac{\partial}{\partial y} \qquad \frac{\partial}{\partial x^*} = \frac{1}{s^*_x(x)}\frac{\partial}{\partial x} \qquad \frac{\partial}{\partial y'} = \frac{1}{s^*_y(y)}\frac{\partial}{\partial y}. \tag{6.5}$$

The proofs of the above expressions are all similar and hence we show explicitly the steps leading only to the first relation in eq. (6.5):

$$\frac{\partial g}{\partial x'} = \frac{\partial g}{\partial x}\frac{\partial x}{\partial x'} = \frac{1}{s_x(x)}\frac{\partial g}{\partial x}, \tag{6.6}$$

[3] Usually $s_x(x)$, $s_y(y)$, $s^*_x(x)$ and $s^*_y(y)$ are called stretching factors. We choose to call them stretching functions to highlight their dependence on either x or y, and also to avoid confusion with the constant stretching factors defined in section 4 in the *split-field* formulation.

where the first expression in eq. (5.1) has been used. Then, using eq. (6.5), we can write eq. (6.3) as

$$\nabla' = \frac{\partial}{\partial x'}\hat{x} + \frac{\partial}{\partial y'}\hat{y} \qquad \nabla^* = \frac{\partial}{\partial x^*}\hat{x} + \frac{\partial}{\partial y^*}\hat{y}, \tag{6.7}$$

and hence the name *complex-coordinate stretching*: eq. (6.7) implies that eqs. (6.2) are defined in coordinate systems (x', y') and (x^*, y^*), which are the original coordinate system (x, y) *stretched* by the *complex* stretching functions.

To see the relation with the *split-field* formulation, we write the *split-field* PML eqs. (4.3)-(4.6) in the frequency domain:

$$-i\omega\mathbf{v} + q_x\mathbf{v}_x = -a\frac{\partial}{\partial x}(P_x + P_y) \Rightarrow -i\omega\mathbf{v}_x = -\frac{a}{s_x}\frac{\partial P}{\partial x}, \tag{6.8}$$

$$-i\omega\mathbf{v}_y + q_y\mathbf{v}_y = -a\frac{\partial}{\partial y}(P_x + P_y) \Rightarrow -i\omega\mathbf{v}_y = -\frac{a}{s_y}\frac{\partial P}{\partial y}, \tag{6.9}$$

$$-i\omega P_x + q_x^* P_x = -b\frac{\partial \mathbf{v}_x}{\partial x} \Rightarrow -i\omega P_x = -\frac{b}{s_x^*}\frac{\partial \mathbf{v}_x}{\partial x}, \tag{6.10}$$

$$-i\omega P_y + q_y^* P_y = -b\frac{\partial \mathbf{v}_y}{\partial y} \Rightarrow -i\omega P_y = -\frac{b}{s_y^*}\frac{\partial \mathbf{v}_y}{\partial y}. \tag{6.11}$$

Now, take the special case in which the stretching functions are equal to their analogous stretching factors of the *split-field* formulation i.e.

$$s_x(x) = s_x \qquad s_y(y) = s_y \qquad s_x^*(x) = s_x^* \qquad s_y^*(y) = s_y^*, \tag{6.12}$$

and then using (6.5), eqs. (6.8)-(6.11) can be written in the *stretched coordinate space*:

$$-i\omega\mathbf{v}_x = -a\frac{\partial P}{\partial x'}, \tag{6.13}$$

$$-i\omega\mathbf{v}_y = -a\frac{\partial P}{\partial y'} \tag{6.14}$$

$$-i\omega P_x = -b\frac{\partial \mathbf{v}_x}{\partial x^*} \tag{6.15}$$

$$-i\omega P_y = -b\frac{\partial \mathbf{v}_y}{\partial y^*}. \tag{6.16}$$

By combining eq. (6.13) with eq. (6.14), and eq. (6.15) with eq. (6.16), the *split-field* PML eqs. in the ω domain (and in the *stretched coordinate space*) take the form

$$-i\omega\mathbf{v} = -a\nabla' P \qquad\qquad -i\omega P = -b\nabla^* \cdot \mathbf{v}, \tag{6.17}$$

where

$$\nabla' = \frac{\partial}{\partial x'}\hat{x} + \frac{\partial}{\partial y'}\hat{y} \qquad\qquad \nabla^* = \frac{\partial}{\partial x^*}\hat{x} + \frac{\partial}{\partial y^*}\hat{y}. \tag{6.18}$$

Eqs. (6.17) and (6.18) mean that when (6.12) holds, then the *complex-coordinate-stretching* formulation is equivalent to the *split-field* approach. In other words, the *split-field* is a particular case of the *complex-coordinate-stretching* formulation. Notice that in (6.17) the artificial splitting of the wave-field is not present anymore. For this reason, eq. (6.17) is called an *unsplit* formulation of the PML. In order to avoid confusion, in this section we will refer to eqs. (4.3)-(4.6) (or to their counterparts in the frequency domain, eqs. (6.8)-(6.11)), as *split-field* PML equations. We will refer to eqs. (6.17) simply as PML equations.

Comparing (6.1) with (6.17), and with the help of (6.5), (6.12) and the definition of the stretching factors in terms of the PML parameters (q_x, q_x^*, q_y, q_y^*), we conclude that the PML equations are obtained from the original wave equation by the following substitutions:

$$\frac{\partial}{\partial x} \rightarrow \frac{1}{1+\frac{i}{\omega}q_x}\frac{\partial}{\partial x} \qquad\qquad \frac{\partial}{\partial y} \rightarrow \frac{1}{1+\frac{i}{\omega}q_y}\frac{\partial}{\partial y} \tag{6.19}$$

for the first expression in eq. (6.1) and

$$\frac{\partial}{\partial x} \rightarrow \frac{1}{1+\frac{i}{\omega}q_x^*}\frac{\partial}{\partial x} \qquad\qquad \frac{\partial}{\partial y} \rightarrow \frac{1}{1+\frac{i}{\omega}q_y^*}\frac{\partial}{\partial y} \tag{6.20}$$

for the second one. Eqs. (6.19) and (6.20) are called the PML transformations.

Notice that if we insert eq. (4.7) into eqs. (6.19) and (6.20), then, after the PML transformations we are left with the wave equations governing the original acoustic host medium. On the other hand, (4.7) also implies that

$$s_x = s_y = s_x^* = s_y^* = 1. \tag{6.21}$$

In other words, the conditions for expressing the acoustic host medium as a PML medium in both the *split-field* and the *complex-coordinate-stretching* approaches are consistent.

Notice that when the matching condition holds, i.e., when $s_x = s_x^*$ and $s_y = s_y^*$ we get

$$\nabla' = \nabla^* \tag{6.22}$$

and in this case the PML equations can be obtained by applying the transformations in eq. (6.19) to both equations in (6.17).

The next issue to address is the implementation of the *complex-coordinate-stretching* approach in the configuration shown in Figure 4, when the two media are the acoustic host medium and a PML medium, matched in order for the interface to be reflectionless. That is, the PML parameters are those of eq. (4.51)

$$PML\ 1 : (0, 0, 0, 0) \qquad\qquad PML\ 2 : (q_x, q_x, 0, 0).$$

In this case the implementation of the PML technique reduces to a single transformation in the medium PML 2:

$$\frac{\partial}{\partial x} \rightarrow \frac{1}{1 + \frac{i}{\omega} q_x} \frac{\partial}{\partial x}. \tag{6.23}$$

Notice that if in eq. (5.10) we impose $q_x(x) = q_x$, then we arrive at eq. (6.23), i.e. in Section 6 we focused on a particular *complex coordinate stretching* slightly more general than the original *split-field* formalism.

Strictly speaking we haven't proved the reflectionless property at an acoustic-PML interface for the *complex-coordinate-stretching* formalism: we just transferred this information from the *split-field* formulation. That is, as presented here, the reflectionless property for the *complex-coordinate-stretching* formalism only holds when it is equivalent to the *split-field* formalism. However, in subsection 5.2 we explained in the paragraph following equation (5.10) that this property also holds for more general nonconstant stretching factors such as

$$s_x(x) = 1 + \frac{i}{\omega} q_x(x). \tag{6.24}$$

A proof that the reflectionless property still holds for this variable stretching factor can be found in Chew and Weedon (1994). Actually the proof in this reference is for the electromagnetic case, but it is true also for the acoustic wave equation. Furthermore, this proof remains valid for general $s_x(x)$ and $s_x^*(x)$ in (6.3) as long as the following conditions are satisfied:

1. The general matching condition $s_x(x) = s_x^*(x)$ (for an acoustic-PML interface aligned perpendicularly to the x-direction, i.e., for $s_y(y) = s_y^*(y) = 1$)
2. This matching condition still drives to decaying solutions of the PML equations.

The fact that the reflectionless property holds for any $s_x(x)$ and $s_x^*(x)$ has far-reaching consequences, as this allows us to modify the stretching factors of the *split-field* formulation (as long as we keep the conditions just listed) in order to improve the effectiveness of the PML technique. For example, the CPML proposed in Roden and Gedney (2000) and used in Komatitsch and Martin (2007) to improve the behavior of the PML at grazing incidence, is based on a stretching factor of the form:

$$s_x(x) = \kappa + \frac{i}{\alpha + \omega} q_x(x), \tag{6.25}$$

for positive constants α and κ.

7 Conclusions and Discussion.

As we mentioned in the introduction, our interest in the PML technique is to test its effectiveness in numerical simulations, in comparison with the new RTM that is based on Green's theorem. With this objective in mind, we have reviewed the theoretical principles of the PML technique applied to the acoustic wave equation. We focused on two approaches to the subject: the *split-field* and the *complex-coordinate-stretching* formulations. In particular we explicitly calculated, within the *split-field* approach, the reflection coefficient between two PML media (of which an ordinary acoustic medium is an example) and we set up the conditions to make this coefficient equal to zero for all frequencies and all angles.

The reflectionless property is the heart of the PML method, as can be seen in Figure 3. We have also shown how the reflectionless property is translated to the *complex-coordinate-stretching* formulation, although it can be derived in this formalism without any reference to the *split-field* formulation (see Chew and Weedon 1994 for the electromagnetic case). This last fact should not be a surprise as it was also explained that the *split-field* is a particular case of the *complex-coordinate-stretching* formulation.

It is also important to remember that the *split-field* formulation is naturally implemented in the time domain, while the *complex-coordinate-stretching* is defined in the frequency domain. A further difference is that for the *complex-coordinate-stretching* approach it is not necessary to assume the nonphysical splitting of the field. In this sense it is a *non-split* formulation.

PML has proven to be a strongly robust and highly effective technique for the truncation of FD lattices in the time domain, but there exists a plethora of limitations for this method, of both a theoretical and a numerical nature. Some examples of these limitations were discussed briefly in this report: one of them is the low rate of absorption for waves striking the interfaces (either the acoustic-PML or PML-PML interface) in Figure 3 at close to grazing incidence, resulting in poor effectiveness of the PML technique when these reflections are present. The other limitation discussed is the presence of numerical reflections due to the discretization process naturally involved in the finite-difference sequence. Other problems arise due to late-time low-frequency reflections when one is terminating highly elongated lattices.

To overcome these limitations several improvements have been incorporated to the PML technique, resulting in more efficient PML implementations such as the Complex Frequency Shift PML (CFS-PML) in Kuzuoglu and Mittra (2003), the convolutional PML (CPML) described in Roden and Gedney (2000), etc. A review of all these improvements and their implementations for the acoustic and elastic wave equations is left as part of a continuation of this report.

We want to highlight that we have focused on the theoretical aspect of the PML technique. However, the numerical aspect is equally important, as this method was developed to improve the efficiency of numerical simulations using the Finite-Difference algorithm.

8 Acknowledgements.

We are grateful to the M-OSRP sponsors. We want to acknowledge Di Chang and Zhiqiang Wang for reading a first draft of this report.

References

Bérenger, Jean-Pierre. "A Perfectly Matched Layer for the Absorption of Electromagnetic Waves." *Journal of Computational Physics* 114 (1994): 185–200.

Bérenger, Jean-Pierre. *Perfectly Matched Layer (PML) for Computational Electromagnetics*. Morgan and Claypool Publishers, 2007.

Chew, W. C. and W. H. Weedon. "A 3D Perfectly Matched Medium from Maxwell's equations with stretched coordinates.." *Microwave and Optical Technology Letters* 7 (1994): 599–603.

Engquist, B. and A. Majda. "Absorbing boundary conditions for the numerical simulation of waves.." *Math. Comput.* 31 (1977): 629.

Johnson, Steven G. Notes on Perfectly Matched Layers (PMLs). Technical report, MIT, 2007a. http://math.mit.edu/~stevenj/18.369/pml.pdf.

Johnson, Steven G. Notes on the algebraic structure of wave equations. Technical report, MIT, 2007b. http://math.mit.edu/~stevenj/18.369/wave-equations.pdf.

Keys, R. G. "Absorbing boundary conditions for acoustic media.." *Geophysics.* 50 (1985).

Komatitsch, Dimitri and Roland Martin. "An unsplit convolutional perfectly matched layer improved at grazing incidence for the seismic wave equation." *Geophysics* 72 (2007): SM155–SM167.

Kuzuoglu, M. and R. Mittra. "Frequency dependence of the constitutive parameters of causal perfectly matched absorbers." *IEEE Microw. Guid. Wave Letters* 50 (2003): 348–350.

Lindman, E. L. "Free-space boundary conditions for the time dependent wave equation.." *J. Comput. Phys.* 18 (1975): 66–78.

Lysmer, J. and R. L. Kuhlemeyer. "Finite dynamic model for infinite media.." *J. Eng. Mech. Div., Proc. Am. Soc. Civil Eng.* 95 (1969): 859–877.

Qi, Q. and T. L. Geers. "Evaluation of the perfectly matched layer for computational acoustics." *J. Comput. Phys.* 139 (1998): 166–183.

Reynolds, A. C. "Boundary conditions for the numerical solution of wave propagation problems.." *Geophysics.* 43 (1978): 1099–1110.

Roden, J. A. and S. D. Gedney. "Convolutional PML (CPML): An Efficient FDTD Implementation of the CFS-PML for Arbitrary Media." *Microwave and Optical Technology Letters* 27 (2000): 334–339.

Smith, Warwick D. "A nonreflecting plane boundary for wave propagation problems.." *J. Comput. Phys.* 15 (1974): 492–503.

Stolt, Robert H. and Arthur B. Weglein. *Seismic Imaging and Inversion, Volume 1.* Cambridge University Press, 2011.

Weglein, A. B., R. H. Stolt, and J. D. Mayhan. "Reverse-time migration and Green's theorem: Part I — The evolution of concepts, and setting the stage for the new RTM method." *Journal of Seismic Exploration* 20 (February 2011): 73–90.

Weglein, A. B., R. H. Stolt, and J. D. Mayhan. "Reverse time migration and Green's theorem: Part II — A new and consistent theory that progresses and corrects current RTM concepts and methods." *Journal of Seismic Exploration* 20 (May 2011): 135–159.

An Inverse Scattering Approach to Internal Multiple Removal from Near Surface Quasi-elastic OBC and Land Data

Mozhdeh Niazmand, Paolo Terenghi and Arthur B. Weglein

May 25, 2012

Abstract

We study the inverse scattering series (ISS) method for predicting and eliminating internal multiples from multi-component ocean-bottom and land seismic data. In particular, we focus our analysis on unconsolidated media. This study is inspired by problems associated with sedimented ocean floors(e.g. deep water Gulf of Mexico) or deserts on land where multi-component measurement of seismic data faces technical challenges due to missing or poorly measured shear wave components. A question that we aim to answer is, how adequate single-component data measurement might be when the data collected from such media is subject to the inverse scattering series-based algorithm for internal multiple removal. In this report we closely follow the work of Ken Matson who expanded the marine ISS internal multiple attenuation formulation devised by Fernanda Aurújo, and modified it for an elastic background, thus making it applicable to land and OBC data. This sub-series was tested for attenuating internal multiples for both multi-component and single-component data acquired from fully rigid land and ocean floors. While the elastic ISS internal multiple attenuation proved successful for multi-component land or OBC data taken from fully rigid media, it showed degradations with single-component data (taken from fully rigid media). In order to find out whether such degradation would occur with data acquired form unconsolidated media, we conduct a study to test the tolerance level of the ISS internal multiple attenuation algorithm towards single-component data. For this purpose, we test the algorithm for marine ISS internal multiple attenuation, on some synthetic data generated with a two-interface model in which the rigidity of the middle layer(i.e. ocean-bottom) is gradually reduced to zero to mimic unconsolidation.

1 Motivation and Introduction

Multi-component on-shore and OBC acquisition technologies in general have the potential for providing a more complete map of the subsurface due to the fact that they collect more information than the traditional towed-streamer or single-component on-shore acquisition. The receiver units in both cases have three orthogonally oriented receivers that measure the particle velocity (or acceleration) in three directions (3-components or 3-C); in addition to that, an OBC receiver unit is equipped with a hydrophone for measuring pressure wave components, adding up the the total of its measured data components to four (hence, 4-C). In practice however, it is not always possible

to exploit the information collected in all three or four components for different reasons. One in particular, is poor coupling between the receiver units and the ocean-bottom, in the presence of unconsolidated sediments on the ocean floor. Assuming that problem can be addressed with the advancement in acquisition technology, the next issue to consider is the lack of rigidity that leads to poor measurements in horizontal components of the ground motion in OBC or land data acquisition. A measure of rigidity in a given substance, is *shear modulus* which describes the material's response to shearing strains. The more rigid a substance is, the higher is its shear modulus. For example, the shear modulus of diamond is 478 Gpa. In liquids and gases, on the other hand, the shear modulus is zero. Shear modulus is denoted by μ and is directly related to the shear wave velocity in the substance. It is described mathematically as

$$v_s = \beta = \sqrt{\frac{\mu}{\rho}}, \tag{1.1}$$

where v_s or β is the shear wave velocity and ρ is the density of the substance. Therefore, with μ being identically zero for fluids, it can be seen that they do not support propagation of shear waves. Knowing that, we are motivated to find out how the internal multiple suppression scheme would be affected, if any, for data taken from such unconsolidated media. For this purpose we are taking a close look at the algorithms that are previously developed for internal multiple attenuation using inverse scattering series (ISS). The ISS-based internal multiple attenuation(IMA) sub-series is pioneered by Araújo (1994) and further developed by Weglein et al. (1997), Matson (1997), Weglein et al. (2003) and Ramírez (2007), to name a few. The focus of this report is on the work of Matson (1997) who studied and extended Araújo's (Araújo, 1994) marine ISS-IMA formulation, to an elastic background, making it applicable to land and OBC data. Matson tested the elastic ISS-IMA algorithm on both single-component and multi-component data form fully rigid land and OBC. The results indicated that while the IMA algorithm is effective for multi-component data from fully rigid media, it shows degradations with single-component data from fully rigid media. The question that motivates this research is, are all the four data components also essential to the IMA algorithm if the data is taken form unconsolidated land or ocean-bottom? In other words, we aim to study the adequacy of single-component data for the ISS-IMA algorithm for data form unconsolidated media.

2 Mathematical Background

2.1 An overview of the Inverse Scattering Series (ISS)

Since this report employs ISS for multiple removal, it serves a purpose to give an introduction about inverse scattering series and the mathematical framework through which it's formulated. In physics, a theory that enables us to predict the outcome of some measurements, given a complete description of a system, is referred to as the forward description or forward problem. An inverse problem, therefore, would be to use the actual result of some measurement of an unknown system to infer values of the parameters that characterize that system. Scattering theory is a wave theoretical approach that has been used in many disciplines of physics, engineering, and medical sciences as a tool in studying and investigating the structure of matter. Scattering theory describes the physics of the deviation of any form of radiation (e.g. light, sound or particle beams) from its trajectory

in a medium, by colliding to a localized obstacle or a form of perturbation in that medium. The perturbation can be characterized by a change in the mechanical properties of the medium of propagation(i.e. density and/or velocity) or an inhomogeneity. The deviated wave-field is denoted as the *scattered* wave-field and the change or deviation from the mechanical properties that causes the scattering is known as the *scattering potential*. Forward scattering deals with determining the scattered wave-field from a known scattering potential and a known reference medium.

Inverse scattering theory aims to determine the scattering potential from the measurements of the scattered wave-field that satisfies certain boundary conditions. Inverse scattering-based methods were introduced to geophysical sciences and petroleum exploration industry in the early 1980s (Weglein et al., 1981). Recent developments presented by Weglein et al. (2003) introduces a new framework that utilizes inverse scattering series that consists of several task-specific sub-series for the purposes of multiple removal, imaging and inversion, which does not require any *a priori* information about the subsurface, i.e. it's data-driven.

2.2 The Logic of the ISS

In a perturbative point of view, one can consider any actual medium subject to study, as a reference medium that's known and well-understood, which has somehow been altered by a perturbation. There are an infinite number of ways to split the medium under study into a reference and a perturbation. ISS however, requires that the reference and the actual media agree with each other, at and above the measurement surface. The basis of the ISS formulation is the *Lippmann-Schwinger* equation which describes the relationship between the scattered wave filed and the perturbation.

In operator form, the differential equations that describe wave propagation in these media can be written as

$$\mathbf{LG} = -\delta(\mathbf{r}-\mathbf{r_s}), \tag{2.1}$$

$$\mathbf{L_0G_0} = -\delta(\mathbf{r}-\mathbf{r_s}), \tag{2.2}$$

where $\mathbf{L}$, $\mathbf{L_0}$, $\mathbf{G}$ and $\mathbf{G_0}$ are, respectively, the wave equation differential operators and the Green's function operators of the actual and reference media; $\delta(\mathbf{r}-\mathbf{r_s})$ is a Dirac delta function denoting an impulsive point source located at point $\mathbf{r_s}$ and observed at point $\mathbf{r}$. The scattering potential, denoted by $\mathbf{V}$, indicates the difference between the wave equation operators for the actual and reference media

$$\mathbf{V} = \mathbf{L} - \mathbf{L_0}. \tag{2.3}$$

The data $\mathbf{D}$ is constituted by the difference between the measured wave-field and the reference wave-field at the measurement surface,

$$\mathbf{D} = (\mathbf{G} - \mathbf{G_0})_{\mathbf{m.s.}}, \tag{2.4}$$

where $m.s.$ indicates the measurement surface. The relationship between the data and the perturbation, as mentioned is described by the Lippmann-Schwinger equation, which basically implies

that if a medium is altered by a perturbation, the wave-field that propagates in the altered medium, would hold a non-linear relationship with the perturbation itself.

$$\mathbf{G} - \mathbf{G_0} = \mathbf{G_0 V G}. \tag{2.5}$$

This relationship is considered non-linear since $\mathbf{G}$ appears on both sides of the equation. A way to isolate $\mathbf{G}$ to one side is to keep iterating the equation into itself. That results is an infinite series known as the *Born* (or the forward) series:

$$\mathbf{G} = \mathbf{G_0} + \mathbf{G_0 V G_0} + \mathbf{G_0 V G_0 V G_0} + \dots. \tag{2.6}$$

Using the scattered wavefield in eq. (2.4), we can re-write the Born series as,

$$\mathbf{D} = (\mathbf{G_0 V G_0} + \mathbf{G_0 V G_0 V G_0} + \mathbf{G_0 V G_0 V G_0 V G_0} + \dots)_{\mathbf{m.s.}}, \tag{2.7}$$

At this point, assuming the perturbation $\mathbf{V}$ is itself expandable in a power series ($\mathbf{V} = \mathbf{V_1} + \mathbf{V_2} + ...$), such that the i^{th} order term in $\mathbf{V}$, is the i^{th} order term in the data ($i = 1, 2, 3, ...$), will give rise to the inverse scattering series

$$\begin{aligned} \mathbf{G} - \mathbf{G_0} = \mathbf{G_0}(\mathbf{V_1} + \mathbf{V_2} + \dots)\mathbf{G_0} + \\ \mathbf{G_0}(\mathbf{V_1} + \mathbf{V_2} + \dots)\mathbf{G_0}(\mathbf{V_1} + \mathbf{V_2} + \dots)\mathbf{G_0} + \dots. \end{aligned} \tag{2.8}$$

Evaluating both sides of eq. (2.8) at the measurement surface and equating terms of equal order with each other, we obtain for the first order term

$$\mathbf{D} \quad = (\mathbf{G_0 V_1 G_0})_{\mathbf{m.s.}}, \tag{2.9}$$

for the second order term

$$\mathbf{0} \quad = (\mathbf{G_0 V_2 G_0})_{\mathbf{m}} + (\mathbf{G_0 V_1 G_0 V_1 G_0})_{\mathbf{m.s.}}, \tag{2.10}$$

and for third order term

$$\begin{aligned} \mathbf{0} \qquad &= (\mathbf{G_0 V_3 G_0})_{\mathbf{m}} + (\mathbf{G_0 V_1 G_0 V_2 G_0})_{\mathbf{m}} \\ &+(\mathbf{G_0 V_2 G_0 V_1 G_0})_{\mathbf{m}} + (\mathbf{G_0 V_1 G_0 V_1 G_0 V_1 G_0})_{\mathbf{m.s.}} \end{aligned} \tag{2.11}$$

$$\vdots$$

Equation (2.9) is now an exact equation for $\mathbf{V_1}$ and can be inverted. Once $\mathbf{V_1}$ is obtained we can substitute it in equation (2.10) to determine $\mathbf{V_2}$. Then $\mathbf{V_2}$ itself can be inserted into the third order equation (2.11) to get $\mathbf{V_3}$ and this trend continues to obtain all orders of $\mathbf{V}$. It's important to understand the symmetry between the forward and inverse scattering series. In the forward series, operator $\mathbf{G_0}$ acts on the perturbation $\mathbf{V}$ to create data $\mathbf{D}$; in the inverse series, that same $\mathbf{G_0}$ operator acts on the data $\mathbf{D}$, to create the perturbation $\mathbf{V}$(eq. (2.9)). The significance of this symmetry is that any Green's operator that is in charge of creating a certain type of event in the forward series, is held accountable for removing that same event in the inverse scattering series. This property can be employed to remove free-surface or internal multiples.

3 Internal Multiple Removal from OBC Data

Inversion of seismic data can be viewed as a series of tasks(Weglein et al., 2002):
1. Removal of free-surface multiples,
2. Removal of internal multiples,
3. Locating reflectors in space, and
4. Determining changes in earth mechanical properties.

Once the ghosts and free-surface multiples have been removed, the data is assumed to contain only primaries and internal multiples. The standard practice calls for inversion of data sets that contain only primaries. Therefore, the internal multiples need to be removed next. This section studies the ISS-based IMA sub-series pioneered by Araújo (1994) and Weglein et al. (2003).

For the OBC and land cases, the formulation needs to be adapted for a homogenous elastic background. This adaptation was done by Matson (1997) and proved successful in attenuating internal multiples from OBC data acquired from fully rigid land or ocean-bottom. The goal of this study, as mentioned before, is to test the adequacy of single-component data acquired from not fully rigid media (e.g. sedimented ocean floors or deserts), subject to ISS-IMA.

Once in the internal multiple removal stage, the Green's function can no longer be split into a direct part plus a second part that's in charge of generating internal multiples in the forward series. Here, a different kind of symmetry needs to be drawn between the forward and inverse series that can assist us in constructing a sub series for removing internal multiples. Weglein et al. (1997) postulated that a specific type of wave scattering results in creation of internal multiples in the forward series in which the geometric relationship between the reflections of the scattered wave resembles the letter **W** (Please see figure (1)). The argument is, if this particular shape which is also referred to as the "lower-higher-lower"geometry, creates internal multiples in the forward series, then it can be held accountable for removing those multiples in the inverse series. Therefore, certain terms within the inverse scattering series that match this description will be selected to form the internal multiple attenuation sub-series. Considering the first order internal multiple which has the geometry of the letter **W**, it can be seen that three interactions(reflections)contribute to its construction and therefore, we can start looking for it in the third order scattering series equation. In general, the first contribution to any n^{th} order internal multiple comes from a portion within the $(2n+1)^{th}$ scattering series equation.

3.1 Theory for Elastic Internal Multiple Attenuation

This section closely studies the work of Matson (1997) in which the scheme developed by Araújo (1994) for the marine IMA has been adapted for an elastic background. The ISS equations and the overall procedure are still the same as the marine case. However, since the background medium is assumed to be elastic, both types of body wave propagations, namely P and S-waves need to be taken into consideration. Therefore double-index Green's functions and perturbations are introduced to accommodate for both wave types. For example, the first order ISS equation is written as follows[1]

$$D_{mn} = G_{0_{mk}} V^{(1)}_{kl} G_{0_{ln}}, \tag{3.1}$$

[1]Please note that the order of perturbation is now written as a superscript, for a less messy notation.

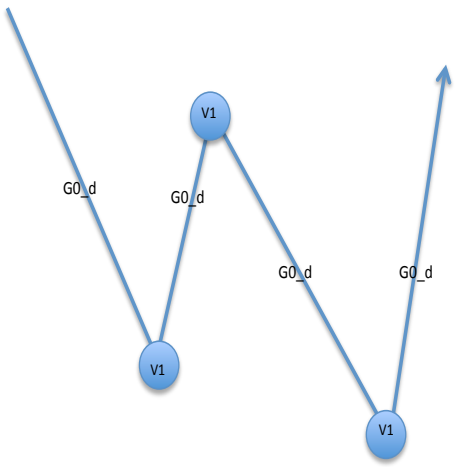

Figure 1: The relative geometry of the reflections within a first order internal multiple

where each subscript can take on values for P, or S-wave propagation and scattering. Thus, each of these Green's functions and perturbations will become 2×2 matrices to describe all possible combinations of wave propagation and conversion modes. If the elastic background medium is assumed to be isotropic and homogeneous, the Green's function in (P,S) potentials will become a diagonal matrix

$$G_{0_m}(x_g, z_g|x_s, z_s; \omega) = \frac{1}{2\pi} \int_{-\infty}^{\infty} \frac{e^{ik(x_g - x_s)}}{2iq_m} e^{iq_m|z_g - z_s|}\, dk, \tag{3.2}$$

where x_g, x_s, z_g and z_s are horizontal and vertical coordinates of the receivers and sources respec-

tivley, ω is the temporal frequency, k is the horizontal wave number and q_m could take on values for P or S-wave vertical wave numbers, ν or η depending on how m is chosen. Recall the definition of the vertical wave numbers

$$q_P = \nu = sgn(\omega)\sqrt{(\frac{\omega}{\alpha})^2 - k^2},$$

$$q_S = \eta = sgn(\omega)\sqrt{(\frac{\omega}{\beta})^2 - k^2},$$

where α and β are respectively P, and S-wave velocities.

By substituting for the Green's function, having in mind that the perturbation is located deeper than the sources and receivers(recall the ISS requirement about the reference and the actual media from section 2.2), the data is obtained as

$$\begin{aligned} D_{mn}(x_g, z_g|x_s, z_s; \omega) = \frac{1}{(2\pi)^2}\int_{-\infty}^{\infty} \frac{1}{2iq_{1m}} e^{ik_1(x_g - x_s)} e^{iq_{1m}(z_1 - z_g)} \\ \times V_{mn}^{(1)}(x_1, x_2, z_1)\, \frac{1}{2iq_{2n}} e^{ik_2(x_2 - x_s)} e^{iq_{2n}(z_1 - z_s)}\, dk_1 dk_2 dx_1 dx_2 dz_1. \end{aligned} \tag{3.3}$$

Taking the Fourier transforms into consideration, will obtain

$$D_{mn}(k_1, z_g|k_2, z_s; \omega) = \frac{1}{2iq_{1m}} e^{-iq_{1m}z_g} V_{mn}^{(1)}(k_1, k_2, q_{1m} + q_{2n}) \frac{1}{2iq_{2n}} e^{-iq_{2n}z_s}. \tag{3.4}$$

Next, in order to identify the first order internal multiple, the third order ISS equation is needed to be considered

$$V_{mn}^{(33)} = V_{ml}^{(1)} G_{0_l} V_{lk}^{(1)} G_{0_k} V_{kn}^{(1)}, \tag{3.5}$$

which, after carrying out some algebraic operations , will yield

$$\begin{aligned} V_{mn}^{(33)}(k_1, k_2|q_{1m} + q_{2n}) = \frac{1}{(2\pi)^2}\int_{-\infty}^{\infty} V_{ml}^{(1)}(k_1, k_3, q_{1m} + q_{3l}) \frac{dk_3}{2iq_{3l}} \\ V_{lk}^{(1)}(k_3, k_4, -q_{3l} - q_{4k}) \int_{-\infty}^{\infty} \frac{dk_4}{2iq_{4k}} V_{kn}^{(1)}(k_4, k_2, q_{4k} + q_{2n}) \\ + \sum \text{Residues due to poles in } V^{(1)}. \end{aligned} \tag{3.6}$$

The part pertaining the residues can not be calculated without specifying a model-type, so it is excluded from the procedure. Selecting only the first term and introducing and substituting for the perturbations with the *"effective data"* [2] defined as

[2]The effective data is basically the original data taken into plane wave format. In Matson (1997), it is denoted with B.

$$b^{(1)}_{mn}(k_1,k_2,q_{1m}+q_{2n}) = \frac{1}{2iq_{1m}} e^{-iq_{1m}z_g}\, V^{(1)}_{mn}(k_1,k_2,q_{1m}+q_{2n}) e^{-iq_{2n}z_s}, \tag{3.7}$$

will yield to $V^{(333)}_{mn}$, which is the not residue-related part of $V^{(33)}_{mn}$. In terms of the effective data, it can be re-written and denoted by $B^{(333)}_{mn}$ such that

$$\begin{aligned} B^{(333)}_{mn}(k_1,k_2,q_{1m}+q_{2n}) = \frac{1}{(2\pi)^2}\int_{-\infty}^{\infty} b^{(1)}_{ml}(k_1,k_3,q_{1m}+q_{3l}) e^{iq_{3l}(z_g+z_s)} \frac{dk_3}{2iq_{3l}} \\ b^{(1)}_{lk}(k_3,k_4,-q_{3l}-q_{4k}) e^{iq_{4k}(z_g+z_s)} \int_{-\infty}^{\infty} \frac{dk_4}{2iq_{4k}} b^{(1)}_{kn}(k_4,k_2,q_{4k}+q_{2n}). \end{aligned} \tag{3.8}$$

To specify the term with the "lower-higher-lower"geometry, the limits of the second and third integrations are each divided into two intervals. But before that, a Fourier transform is needed to take the effective data into the pseudo-depth[3] domain using,

$$b^{(1)}_{mn}(k_1,k_2,q_{1m}+q_{2n}) = \int_{-\infty}^{\infty} b^{(1)}_{mn}(k_1,k_2,z) e^{i(q_{1m}+q_{2n})z}\, dz. \tag{3.9}$$

After the Fourier transform and splitting the integration limits, four terms are obtained out of which only one, qualifies for the "lower-higher-lower"format. Since in the original derivation (Araújo, 1994), it happened to be the third term out of four, It is denoted as $b^{IM}_{3_{(mn)}}$ where IM stands for internal multiple.[4]

$$b^{IM}_{3_{(mn)}}(k_1,k_2,q_{1m}+q_{2n}) = \frac{1}{(2\pi)^2}\int_{-\infty}^{\infty} \frac{dk_3}{2iq_{3l}} \int_{-\infty}^{\infty} b^1_{ml}(k_1,k_3,z_1)\, e^{iz_1(q_{1m}+q_{3l})} dz_1 e^{iq_{3l}(z_g+z_s)} \tag{3.10}$$

$$\times \int_{-\infty}^{\infty} \frac{dk_4}{2iq_{4k}} \int_{-\infty}^{z_1-\epsilon} b^1_{lk}(k_3,k_4,z_2)\, e^{-iz_2(q_{3l}+q_{4k})} dz_2 e^{iq_{4k}(z_g+z_s)} \int_{z_2+\epsilon}^{\infty} b^1_{kn}(k_4,k_2,z_3) e^{z_3(q_{4k}+q_{2n})} dz_3 \tag{3.11}$$

This is in fact the elastic equivalent of the marine equation derived by Araújo (1994),

$$\begin{aligned} b^{IM}_3(k_g,k_s,q_g+q_s) = \frac{1}{(2\pi)^2}\int_{-\infty}^{\infty} dk_1 e^{iq_1(x_s-x_g)} \int_{-\infty}^{\infty} dk_2 e^{iq_2(z_g-z_s)} \\ \times \int_{-\infty}^{\infty} e^{i(q_g+q_1)z_1} b_1(k_g,-k_1,z_1) dz_1 \\ \times \int_{-\infty}^{z_1-\epsilon_1} e^{-i(q_1+q_2)z_2} b_1(k_1,-k_2,z_2) dz_2 \end{aligned} \tag{3.12}$$

[3]Pseudo-depth is the depth to which events would have migrated to, if they were to propagate at the constant reference velocity.

[4]Matson uses k_1 and k_2 in the same way Araujo uses k_g and k_s

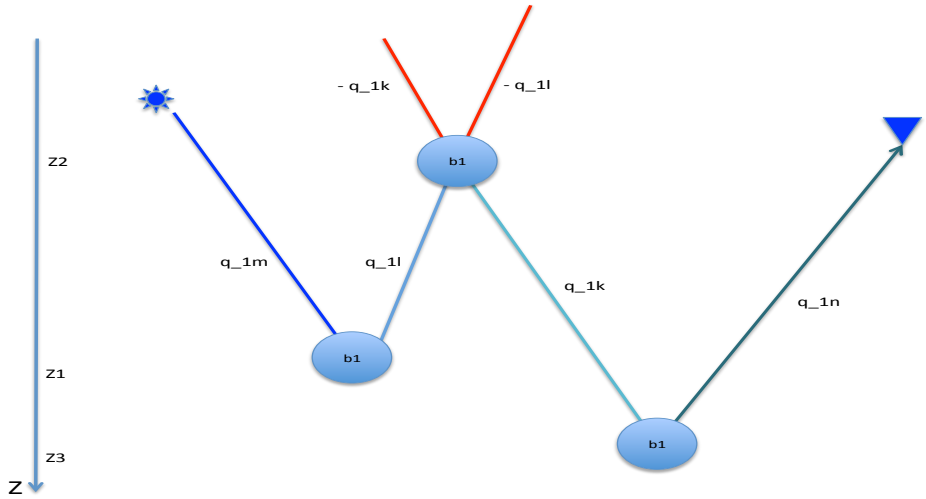

Figure 2: A simple illustration of internal multiple generation in the pseudo depth domain.

$$\times \int_{z_2+\epsilon_2}^{\infty} e^{i(q_2+q_s)z_3} b_1(k_2, -k_s, z_3) dz_3.$$

In both cases, adding the term b_3^{IM} to the original effective data b_1, will attenuate all first order internal multiples. The small and positive parameters ϵ_i, function as an addition to the integration limits in order to avoid self-interaction among the effective data which will affect the primaries.

For the purpose of testing the ISS internal multiple attenuation algorithm on some synthetic data, the one-dimensional version of equation(3.11) is considered. In 1-D earth models, the data varies only with offset and hence the only non-zero values of the data result from setting $k_1 = k_2$. Therefore the first order internal multiple attenuator for a fixed k_1 will become

$$b_{3_{(mn)}}^{IM}(k_1, q_{1m} + q_{1n}) = \frac{1}{(2\pi)^2} \frac{-1}{4q_{1l}q_{1k}} \int_{-\infty}^{\infty} b_{ml}^1(k_1, z_1)\, e^{iz_1(q_{1m}+q_{1l})} dz_1$$
$$\int_{-\infty}^{z_1-\epsilon} b_{lk}^1(k_1, z_2)\, e^{-iz_2(q_{1l}+q_{1k})} dz_2 \int_{z_2+\epsilon}^{\infty} b_{kn}^1(k_1, z_3) e^{z_3(q_{1k}+q_{1n})} dz_3. \tag{3.13}$$

This formula (and of course it 2D version above) describes how the effective data are combined with each other, so that the resulting internal multiple takes on the geometry of a **W**. Figure (2) depicts this process in a simple illustration that can help better understand the formula.

3.2 The Analysis

We aim to study the difference between the full multi-component and single-component source and receiver as a function of the shear modulus(given in terms of shear wave velocity) of the ocean-

Table 1: Models used to generate data

Model	Water-bottom depth(m)	V_p (m/s)	V_s (m/s)
0	330	1600	0
1	330	1600	100
2	330	1600	300
3	330	1600	450
4	330	1600	600
5	330	1600	750

bottom. Prior to that study, we tested the towed streamer ISS-IMA algorithm with some synthetic elastic data.The model used to generate the elastic data is shown in figure(3).(please also see table (1)). The shear modulus of the ocean-bottom (given in terms of shear wave velocity) takes on different values and decreases gradually to zero in six steps, to mimic low/zero rigidity and hence an unconsolidated ocean-bottom.
The data sets are then passed on to two source codes that perform the Stlot migration and the towed streamerISS-IMA algorithms respectively. The modeling and data generation is carried out via OASES [5] . The source codes are written by Paolo Terenghi (Terenghi et al., 2011) of M-OSRP.

3.3 Results and Discussions

Figures 5 through 10 display each data set generated by models described in table(1), along with their corresponding extracted internal multiples. In all the pictures, the data is shown on the left panel. The right panel displays the corresponding internal multiples. In labeling the events, we're borrowing a notation from Matson (1997) where propagations are denoted by upper case letters for the water (top) layer and with lower case letters for the water bottom. For example, PP denotes the water-bottom primary and PspssP indicates a first order internal multiple. Figure(4) provides a guide that helps understand this notation.
As can be seen in the pictures, with the decrease in shear wave velocity, the overall number of internal multiples also decreases. Interestingly enough, the algorithm is effective in attenuating converted internal multiples in addition to reflected ones. It can be seen that the efficiency of the internal multiple attenuation is higher with multiples that contain only P-waves compared to multiples that have some S-waves in their propagation history. This is consistent with the results by Coates and Weglein (1996) where they reported attenuation of all first-order internal multiples with correct time and and approximate amplitude of 80-90 percent for reflected and 20 percent for converted (with one S-wave leg) internal multiples. Another observation is that in addition to first order multiples, second order multiples are also attenuated but with less accuracy in the amplitude. This is expected since in each sub-series, once a certain order term is added to the original data, it eliminates/attenuates the corresponding order multiple and alters the amplitude of the next higher orders(Weglein et al., 2003).

[5]OASES is a general purpose computer code developed by Henrik Schmidt of MIT for modeling seismo-acoustic wave propagation in horizontally stratified media using wave number integration in combination with a method called Direct Global Matrix(DGM) devised by the author.

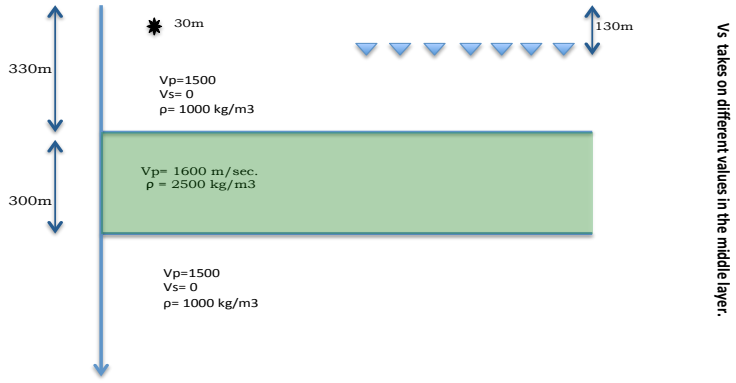

Figure 3: The basic model used to generate synthetic data for the experiments.

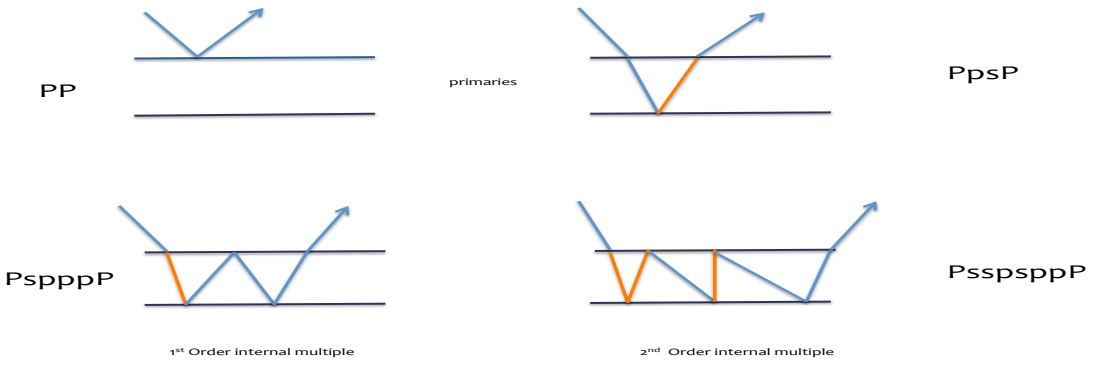

Figure 4: An illustration of the labeling notation.

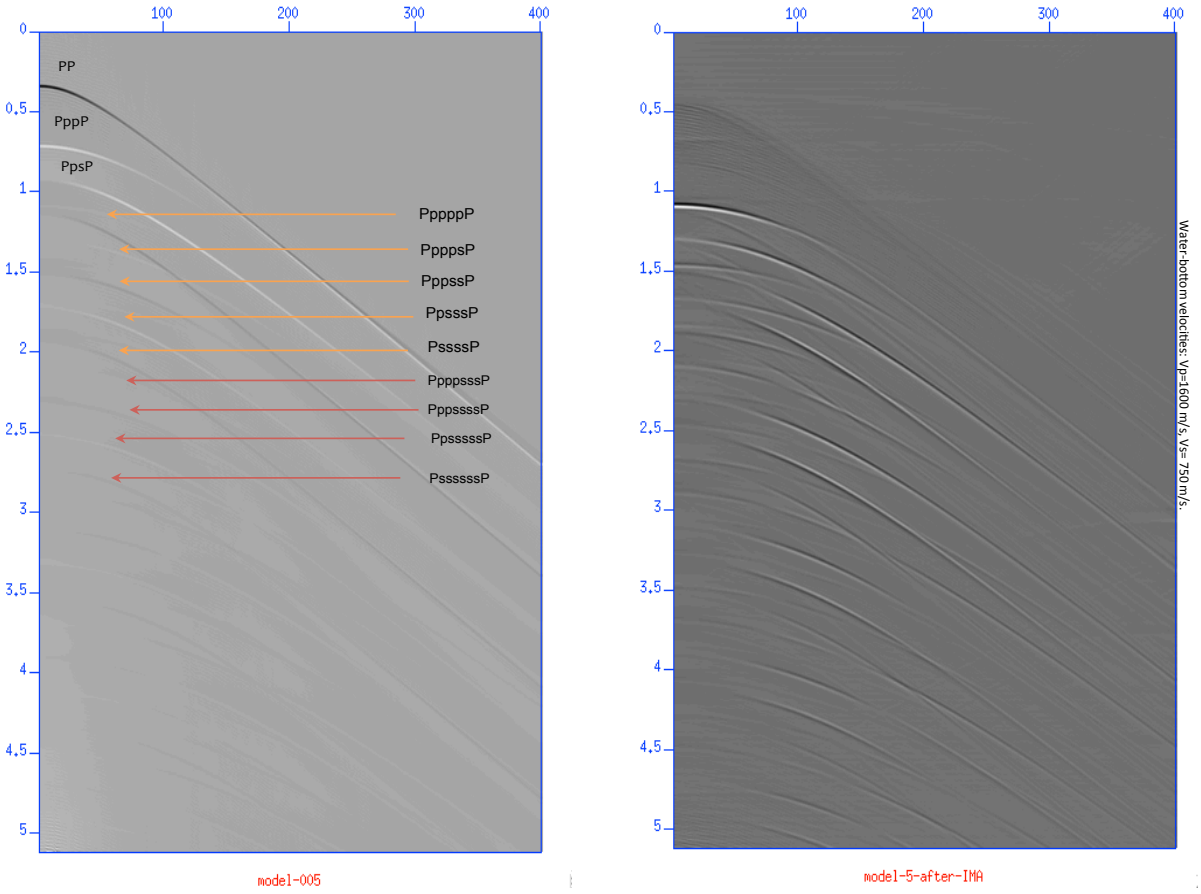

Figure 5: Data set 5(left) and its corresponding extracted internal multiples(right).Water-bottom velocities: (Vp=1600, Vs=750) m/s

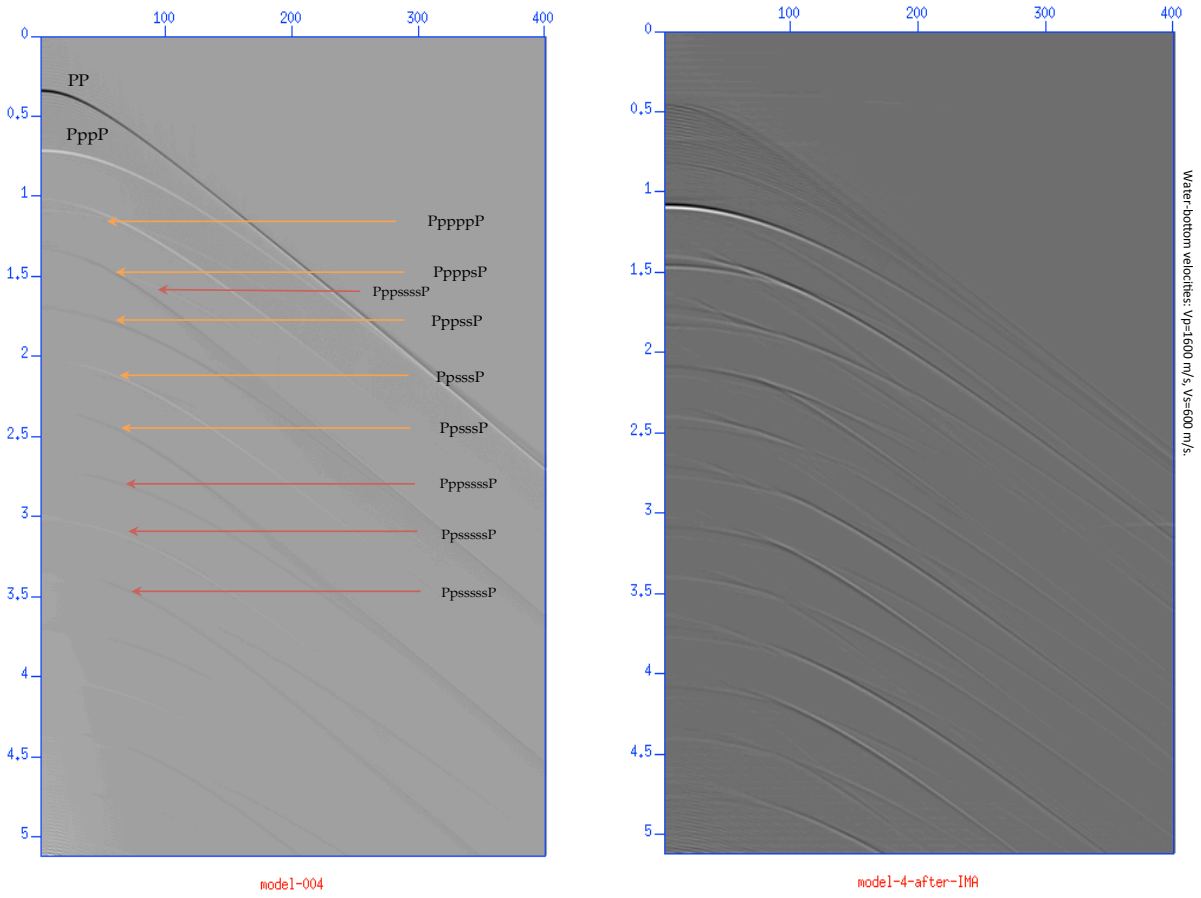

Figure 6: Data set 4 and its corresponding extracted internal multiples.WB velocities: (Vp=1600, Vs=600)m/s

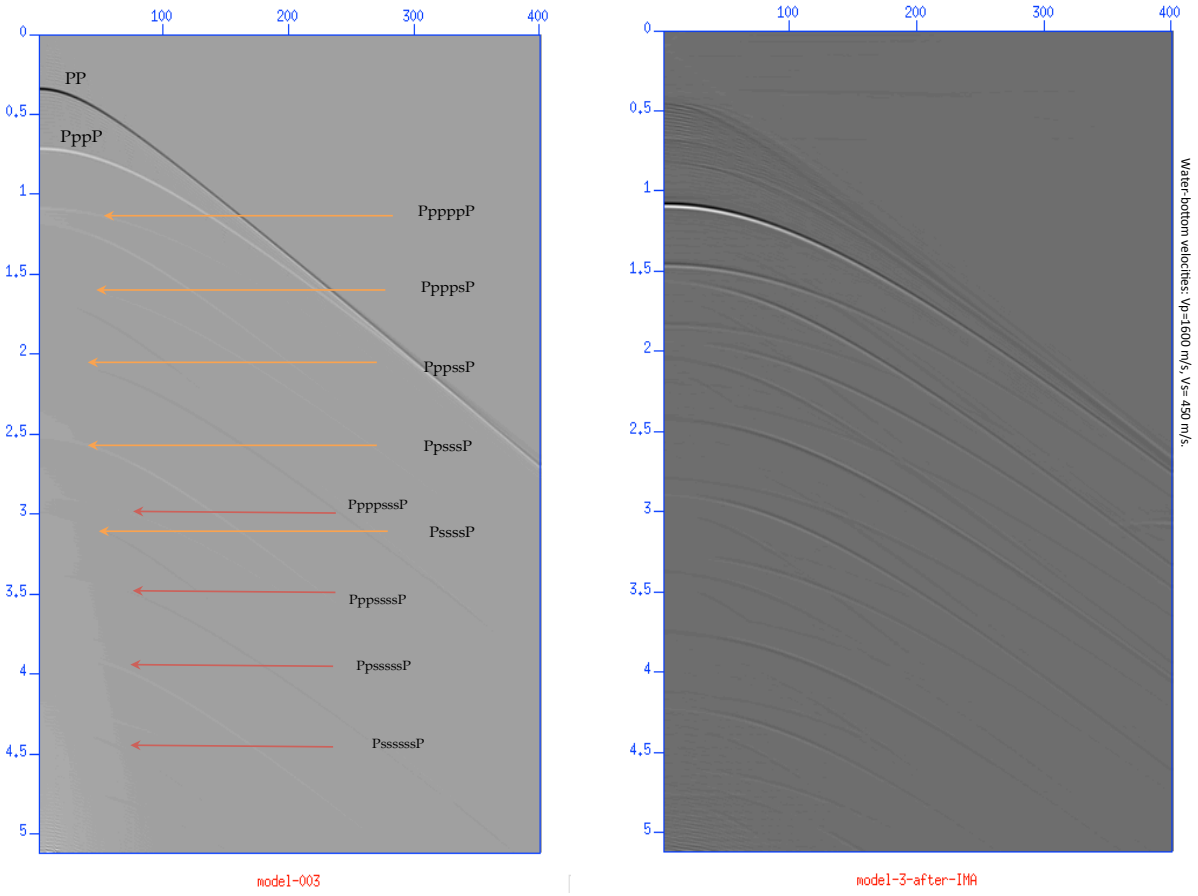

Figure 7: Data set 3 and its corresponding extracted internal multiples.WB velocities:(Vp=1600, Vs=450) m/s

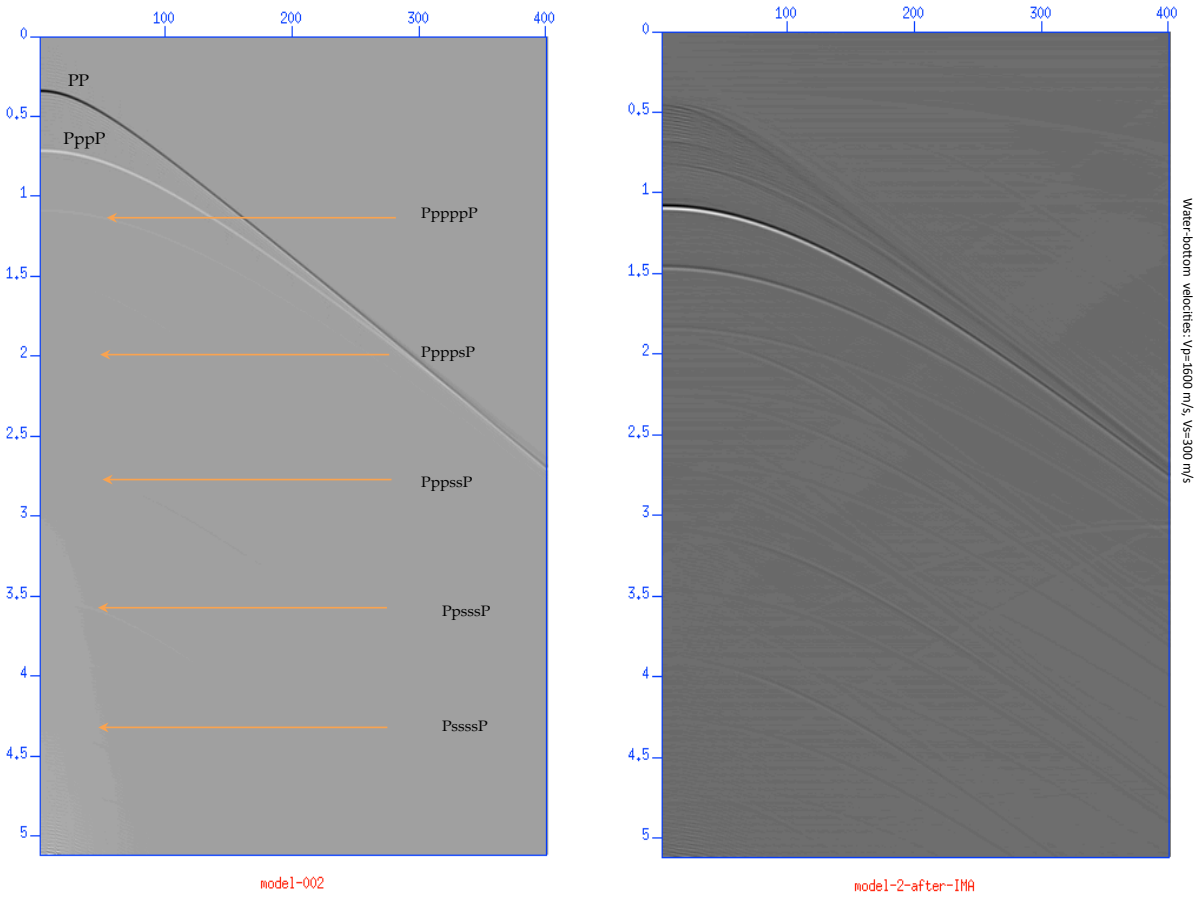

Figure 8: Data set 2 and its corresponding extracted internal multiples.WB velocities:(Vp=1600, Vs=300) m/s

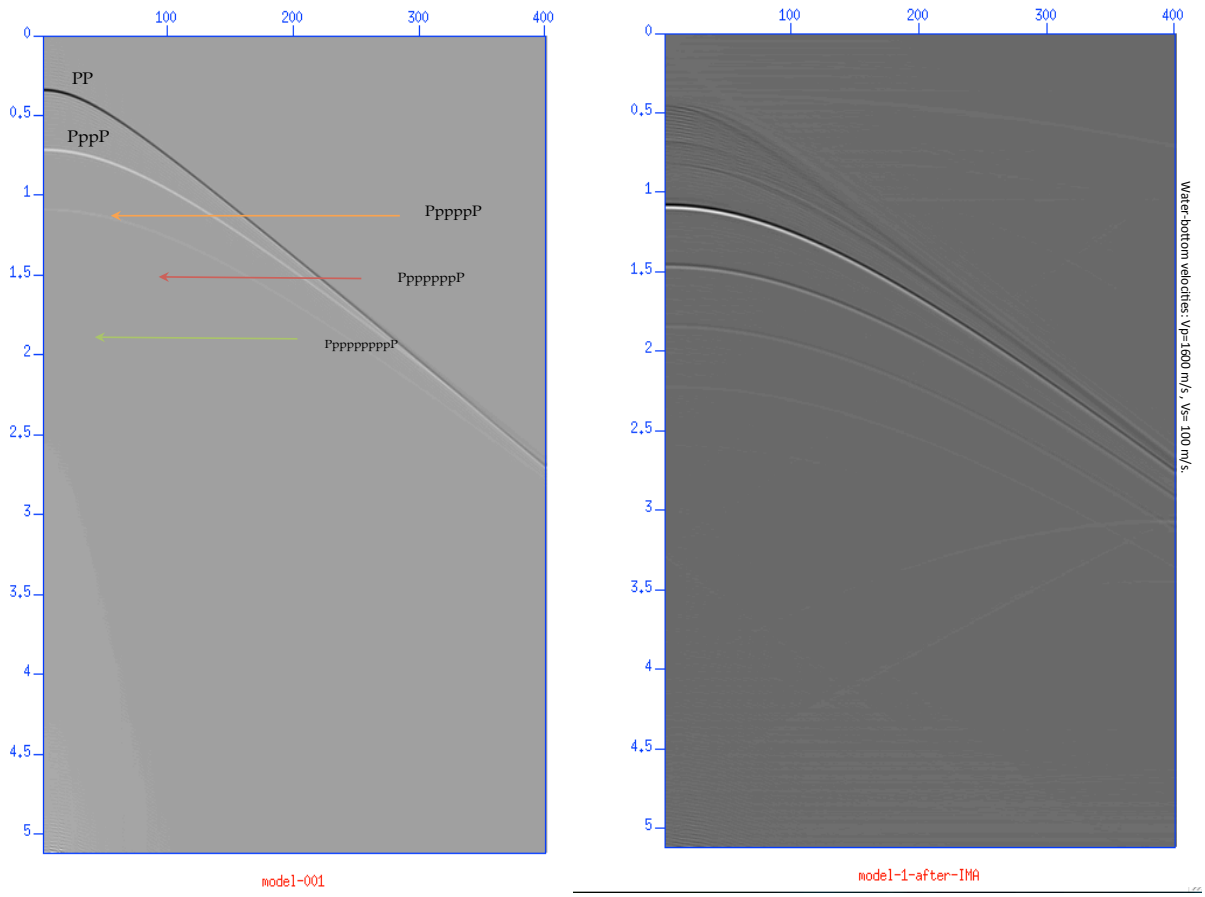

Figure 9: Data set 1 and its corresponding extracted internal multiples.WB velocities:(Vp=1600, Vs=100) m/s.

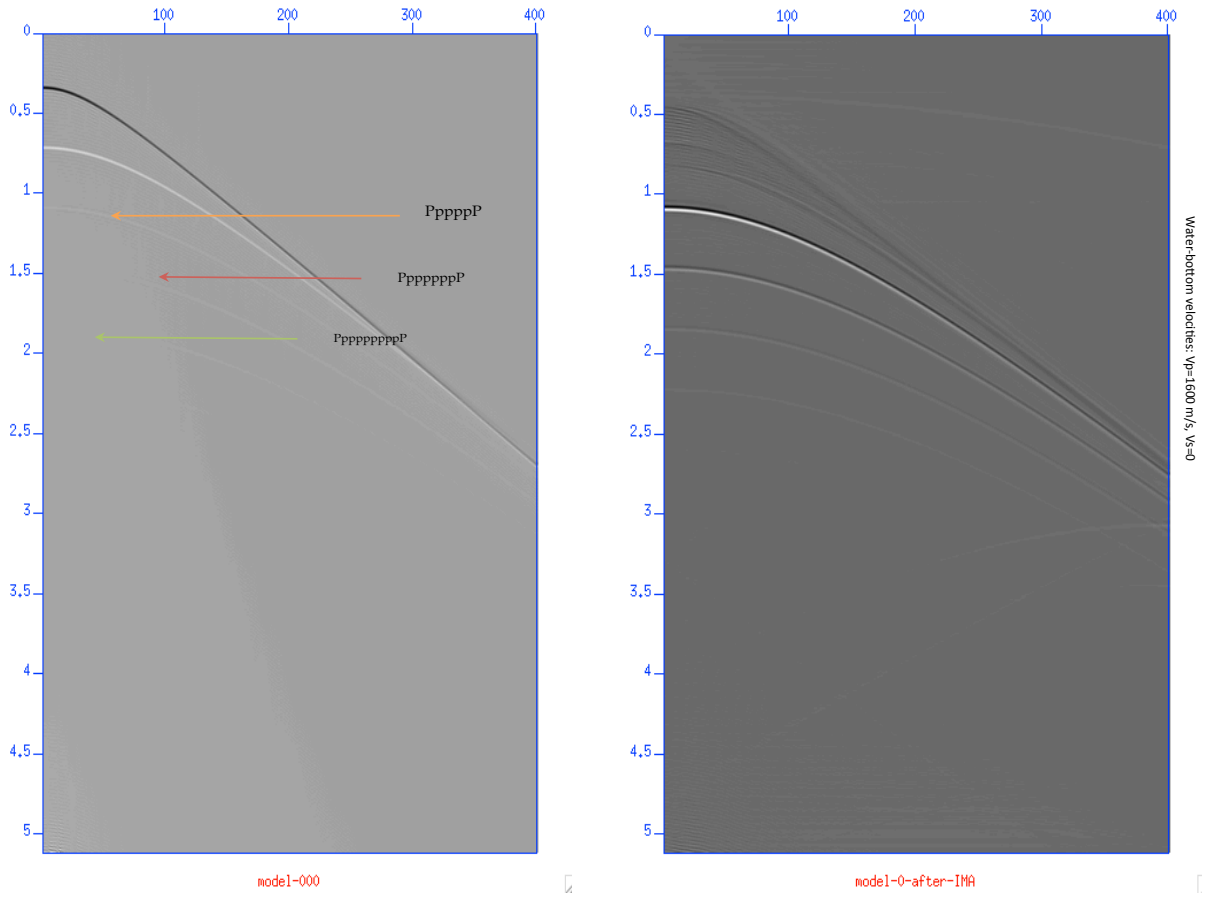

Figure 10: Data set 0 and its corresponding extracted internal multiples.WB velocities:(Vp=1600, Vs=0) m/s.

4 Conclusions and Future Plans

Internal multiple removal can often be the most significant issue with land and OBC single or multi-component data. In many parts of the world, multi-component data acquisition faces some challenges that cause inaccessibility or poor measurement of the whole four components of the data at the same time. One of these challenges is lack of rigidity in land or ocean-bottom which leads to poor shear wave component measurements. The question that motivates this research is, if data is acquired from such unconsolidated media, can the current ISS internal multiple attenuation algorithm suffice to single-component data and still be effective?
In order to answer that question we tested the towed streamer ISS-IMA algorithm with some elastic synthetic data sets that are generated from a two-interface model(figure3). We varied the rigidity of the ocean-bottom in terms of its given shear wave velocity and reduced it to zero in six steps. We then passed each data set on to the towed streamer ISS-IMA algorithm. The results indicate that the algorithm can suppress both reflected and converted internal multiples which is in agreement with the results by Coates and Weglein (1996).

This study is a work in progress as this report is being written.Once complete, it will provide a framework on how adequate single-component data can be when it's subject to the ISS-based internal multiple attenuation algorithm. As a next step, we will take the current acquisition from the water-column to the water-bottom. As a result, all the four elements of the $b^{IM}_{3_{(mn)}}$ will participate in the internal multiple attenuation task. Expanding $b^{IM}_{3_{(mn)}}$ in its matrix form,

$$\begin{aligned}
&\begin{pmatrix} b^{IM}_{3_{(pp)}}(k_1,2\nu_1) & b^{IM}_{3_{(ps)}}(k_1,\nu_1+\eta_1) \\ b^{IM}_{3_{(sp)}}(k_1,\eta_1+\nu_1) & b^{IM}_{3_{(ss)}}(k_1,2\eta_1) \end{pmatrix} \\
&= -(\frac{1}{2\pi})^2 \int_{-\infty}^{\infty} \begin{pmatrix} (\frac{1}{4\nu_1^2})b_{1_{(pp)}}(k_1,z_1)e^{2i\nu_1 z_1} & (\frac{1}{4\nu_1\eta_1})b_{1_{(ps)}}(k_1,z_1)e^{i(\nu_1+\eta_1)z_1} \\ (\frac{1}{4\nu_1\eta_1})b_{1_{(sp)}}(k_1,z_1)e^{i(\eta_1+\nu_1)z_1} & (\frac{1}{4\eta_1^2})b_{1_{(ss)}}(k_1,z_1)e^{2i\eta_1 z_1} \end{pmatrix} dz_1 \\
&\times \int_{-\infty}^{z_1-\epsilon} \begin{pmatrix} b_{1_{(pp)}}(k_1,z_2)e^{2i\nu_1 z_2} & b_{1_{(ps)}}(k_1,z_2)e^{i(\nu_1+\eta_1)z_2} \\ b_{1_{(sp)}}(k_1,z_2)e^{i(\eta_1+\nu_1)z_2} & b_{1_{(ss)}}(k_1,z_2)e^{2i\eta_1 z_2} \end{pmatrix} dz_2 \\
&\times \int_{z_2+\epsilon}^{\infty} \begin{pmatrix} b_{1_{(pp)}}(k_1,z_3)e^{2i\nu_1 z_3} & b_{1_{(ps)}}(k_1,z_3)e^{i(\nu_1+\eta_1)z_3} \\ b_{1_{(sp)}}(k_1,z_3)e^{i(\eta_1+\nu_1)z_3} & b_{1_{(ss)}}(k_1,z_3)e^{2i\eta_1 z_3} \end{pmatrix} dz_3 \qquad (4.1)
\end{aligned}$$

will result in another matrix the elements of which are as follows

$$\begin{aligned}
&b^{IM}_{3_{(pp)}}(k_1,2\nu_1) = \\
&\int_{-\infty}^{\infty} b_{1_{(pp)}}(k_1,z_1)e^{2i\nu_1 z_1}dz_1 \int_{-\infty}^{z_1-\epsilon} b_{1_{(pp)}}(k_1,z_2)e^{-2i\nu_1 z_2}dz_2 \int_{z_2+\epsilon}^{\infty} b_{1_{(pp)}}(k_1,z_3)e^{2i\nu_1 z_3}dz_3 \\
&+\int_{-\infty}^{\infty} b_{1_{(pp)}}(k_1,z_1)e^{2i\nu_1 z_1}dz_1 \int_{-\infty}^{z_1-\epsilon} b_{1_{(ps)}}(k_1,z_2)e^{-i(\eta_1+\nu_1)z_2}dz_2 \int_{z_2+\epsilon}^{\infty} b_{1_{(sp)}}(k_1,z_3)e^{i(\nu_1+\eta_1)z_3}dz_3 \\
&+\int_{-\infty}^{\infty} b_{1_{(ps)}}(k_1,z_1)e^{i(\nu_1+\eta_1)z_1}dz_1 \int_{-\infty}^{z_1-\epsilon} b_{1_{(sp)}}(k_1,z_2)e^{-i(\eta_1+\nu_1)z_2}dz_2 \int_{z_2+\epsilon}^{\infty} b_{1_{(pp)}}(k_1,z_3)e^{2i\nu_1 z_3}dz_3
\end{aligned}$$

$$+\int_{-\infty}^{\infty} b_{1_{(ps)}}(k_1,z_1)e^{i(\nu_1+\eta_1)z_1}dz_1\int_{-\infty}^{z_1-\epsilon} b_{1_{(ss)}}(k_1,z_2)e^{-2i\eta_1 z_2}dz_2\int_{z_2+\epsilon}^{\infty} b_{1_{(sp)}}(k_1,z_3)e^{i(\eta_1+\nu_1)z_3}dz_3, \quad (4.2)$$

$$b^{IM}_{3_{(ps)}}(k_1,\nu_1+\eta_1) =$$
$$\int_{-\infty}^{\infty} b_{1_{(pp)}}(k_1,z_1)e^{2i\nu_1 z_1}dz_1\int_{-\infty}^{z_1-\epsilon} b_{1_{(pp)}}(k_1,z_2)e^{-2i\nu_1 z_2}dz_2\int_{z_2+\epsilon}^{\infty} b_{1_{(ps)}}(k_1,z_3)e^{i(\nu_1+\eta_1)z_3}dz_3$$
$$+\int_{-\infty}^{\infty} b_{1_{(pp)}}(k_1,z_1)e^{2i\nu_1 z_1}dz_1\int_{-\infty}^{z_1-\epsilon} b_{1_{(ps)}}(k_1,z_2)e^{-i(\eta_1+\nu_1)z_2}dz_2\int_{z_2+\epsilon}^{\infty} b_{1_{(ss)}}(k_1,z_3)e^{i(2\eta_1)z_3}dz_3$$
$$+\int_{-\infty}^{\infty} b_{1_{(ps)}}(k_1,z_1)e^{i(\nu_1+\eta_1)z_1}dz_1\int_{-\infty}^{z_1-\epsilon} b_{1_{(sp)}}(k_1,z_2)e^{-i(\eta_1+\nu_1)z_2}dz_2\int_{z_2+\epsilon}^{\infty} b_{1_{(ps)}}(k_1,z_3)e^{i(\nu_1+\eta_1)z_3}dz_3$$
$$+\int_{-\infty}^{\infty} b_{1_{(ps)}}(k_1,z_1)e^{i(\nu_1+\eta_1)z_1}dz_1\int_{-\infty}^{z_1-\epsilon} b_{1_{(ss)}}(k_1,z_2)e^{-2i\eta_1 z_2}dz_2\int_{z_2+\epsilon}^{\infty} b_{1_{(ss)}}(k_1,z_3)e^{i(2\eta_1)z_3}dz_3, \quad (4.3)$$

$$b^{IM}_{3_{(sp)}}(k_1,\eta_1+\nu_1) =$$
$$\int_{-\infty}^{\infty} b_{1_{(sp)}}(k_1,z_1)e^{i(\eta_1+\nu_1)z_1}dz_1\int_{-\infty}^{z_1-\epsilon} b_{1_{(pp)}}(k_1,z_2)e^{-2i\nu_1 z_2}dz_2\int_{z_2+\epsilon}^{\infty} b_{1_{(pp)}}(k_1,z_3)e^{2i\nu_1 z_3}dz_3$$
$$+\int_{-\infty}^{\infty} b_{1_{(sp)}}(k_1,z_1)e^{i(\eta_1+\nu_1)z_1}dz_1\int_{-\infty}^{z_1-\epsilon} b_{1_{(ps)}}(k_1,z_2)e^{-i(\eta_1+\nu_1)z_2}dz_2\int_{z_2+\epsilon}^{\infty} b_{1_{(sp)}}(k_1,z_3)e^{i(\nu_1+\eta_1)z_3}dz_3$$
$$+\int_{-\infty}^{\infty} b_{1_{(ss)}}(k_1,z_1)e^{2i(\eta_1)z_1}dz_1\int_{-\infty}^{z_1-\epsilon} b_{1_{(sp)}}(k_1,z_2)e^{-i(\eta_1+\nu_1)z_2}dz_2\int_{z_2+\epsilon}^{\infty} b_{1_{(pp)}}(k_1,z_3)e^{2i\nu_1 z_3}dz_3$$
$$+\int_{-\infty}^{\infty} b_{1_{(ss)}}(k_1,z_1)e^{2i(\eta_1)z_1}dz_1\int_{-\infty}^{z_1-\epsilon} b_{1_{(ss)}}(k_1,z_2)e^{-2i\eta_1 z_2}dz_2\int_{z_2+\epsilon}^{\infty} b_{1_{(sp)}}(k_1,z_3)e^{i(\eta_1+\nu_1)z_3}dz_3, \quad (4.4)$$

and

$$b^{IM}_{3_{(ss)}}(k_1,2\eta_1) =$$
$$\int_{-\infty}^{\infty} b_{1_{(sp)}}(k_1,z_1)e^{i(\eta_1+\nu_1)z_1}dz_1\int_{-\infty}^{z_1-\epsilon} b_{1_{(pp)}}(k_1,z_2)e^{-2i\nu_1 z_2}dz_2\int_{z_2+\epsilon}^{\infty} b_{1_{(ps)}}(k_1,z_3)e^{i(\nu_1+\eta_1)z_3}dz_3$$
$$+\int_{-\infty}^{\infty} b_{1_{(sp)}}(k_1,z_1)e^{i(\eta_1+\nu_1)z_1}dz_1\int_{-\infty}^{z_1-\epsilon} b_{1_{(ps)}}(k_1,z_2)e^{-(\nu_1+\eta_1)z_2}dz_2\int_{z_2+\epsilon}^{\infty} b_{1_{(ss)}}(k_1,z_3)e^{2i\eta_1 z_3}dz_3$$
$$+\int_{-\infty}^{\infty} b_{1_{(ss)}}(k_1,z_1)e^{2i\eta_1 z_1}dz_1\int_{-\infty}^{z_1-\epsilon} b_{1_{(sp)}}(k_1,z_2)e^{-i(\eta_1+\nu_1)z_2}dz_2\int_{z_2+\epsilon}^{\infty} b_{1_{(ps)}}(k_1,z_3)e^{i(\nu_1+\eta_1)z_3}dz_3$$
$$+\int_{-\infty}^{\infty} b_{1_{(ss)}}(k_1,z_1)e^{2i(\eta_1)z_1}dz_1\int_{-\infty}^{z_1-\epsilon} b_{1_{(ss)}}(k_1,z_2)e^{-2i\eta_1 z_2}dz_2\int_{z_2+\epsilon}^{\infty} b_{1_{(ss)}}(k_1,z_3)e^{2i(\eta_1)z_3}dz_3. \quad (4.5)$$

To enable us to test the algorithm on multi-component data , for the next step we shall expand our current towed streamer IMA source code so that it can accommodate elastic data as well.

Separately, in addition to that, another source code is required to perform up-down separation and P-S decomposition all in one step (please see Wapenaar et al. (1990)). These two items are what we are currently working on.

Acknowledgements

We are grateful for the continuous support and encouragement of M-OSRP sponsors. The first author would like to thank Dr.Weglein for his teachings, support, insightful discussions and questions; Dr. Terenghi for reviewing the manuscript and providing helpful feedback. Chao Ma (M-OSRP) also for reading the manuscript and his helpful suggestions; and Jinlong Yang (M-OSRP) for his helpful comments on elastic modeling with OASES.

References

Morse, Philip M. and Feshbach, Herman, 1953, Methods of theoretical physics: Feshbach publishing, Volume I.

Aki, K. and Richards, P.G., 2002, Quantitative seismology: University Science Books, 2nd edition.

Weglein, A. B., F. V. Araújo Gasparotto, P. M. Carvalho and R. H. Stolt, 1997, An inverse-scattering series method for attenuating multiples in seismic reflection data: Geophysics, **62**, no. 6, 1975–1989.

Weglein, et al., 2003, Inverse scattering series and seismic exploration: Institute of Physics Publishing, Inverse Problems , **19** R27-R83.

Ikelle, L. T. and Amundsen L., 2005, Introduction to petroleum seismology: Investigations in geophysics No.12, Society of Exploration Geophysicist.

Ramírez, A. C.,2007, I.-Inverse scattering sub series for removal of internal multiples and depth imaging primaries; II.-Green's theorem as the foundation of interferometry and guiding new practical methods and applications: Ph.D thesis, University of Houston.

Weglein, A. B., Boyce, W. E., and Anderson, J. E., 1981, Obtaining three-dimensional velocity information directly from reflection seismic data: An inverse scattering formalism: Geophysics, **46**, 1116-1120.

Desanto A. J., 1992, Scalar wave theory;Green's functions and applications: Springer series on wave phenomena, 12th edition.

Matson, K. H., 1997, An inverse scattering series method for attenuating elastic multiples from multicomponent land and ocean bottom seismic data: Ph.D thesis, University of British Columbia.

Carvalho P.M.,1992, Free surface multiple elimination method based on nonlinear inversion of seismic data: Ph.D thesis, Universidade Federal da Bahia, Brazil (in Portuguese).

Carvalho, P. M., Weglein, A. B., and Stolt, R. H., 1992, Nonlinear inverse scattering for multiple suppression: Application to real data. Part i : SEG Technical Program Expanded Abstracts, **11**, 1093-1095.

Keys, Robert G., 1989, Polarity reversals in reflections from layered media: Geophysics, **54**, no. 7, 900-905.

Achenbach, J. D., 1973, Wave propagation in elastic solids: North Holland Publishing Company, Amsterdam-London.

Weglein, A. B., Zhang, H., Ramírez, A. C., Liu, F., and Lira, J. E. M., 2009, Clarifying the underlying and fundamental meaning of the approximate linear inversion of seismic data: Geophysics, **74**, no. 6, P.WCD1-WCD13.

Weglein, A.B., Foster, D. J., Matson, K. H., Shaw, S. A., Carvalho, P. M., and Corrigan, D., 2002, Predicting the correct spatial location of reflectors without knowing or determining the precise medium and wave velocity: Initial concept, algorithm and analytic and numerical example: Journal of seismic exploration, **10**, 367-382.

Araújo, F. V., 1994, Linear and nonlinear methods derived from scattering theory: backscattered tomography and internal multiple attenuation, Ph.D. thesis, Universidade Federal da Bahia, Brazil (in Portuguese).

Coates, R. T., and Weglein, A. B., 1996, Internal multiple attenuation using inverse scattering: Results from pre stack 1 and 2D acoustic and elastic synthetics: 66th Annual Meeting of the Society of Exploration Geophysicist, Expanded Abstracts, 1522-1525.

Razavy, M., 1975, Determination of the wave velocity in an inhomogeneous medium from reflection data, J. Acoust. Soc. Am., **58**, 956-963.

Sheriff, R. E., Geldart L. P., 1995, Exploration Seismology, Cambridge University Press, Second Edition.

Stolt, R. H., and Jacobs, B., 1980, Inversion of seismic data in a laterally heterogeneous medium, SEP Report, **24**, 135-152.

Stolt, R. H., and Weglein, A. B., 1985, Migration and inversion of seismic data, Geophysics, **50**, 2458-2472.

Terenghi, P., Hsu, S., Weglein, A.B., and Li, X., 2011, Exemplifying the specific properties of the inverse scattering series internal-multiple attenuation method that reside behind its capability for complex onshore marine multiples: The Leading Edge, Special edition.

Ferreira A. S., 2011, Internal multiple removal in offshore Brazil seismic data using inverse scattering series: MSc. thesis, University of Houston.

Wapenaar, C. P. A., Herrmann, P., Verschuur, D. J., and Berkhout, A. J., 1990, Decomposition of multicomponent seismic data into primary P- and S-wave responses: Geophysical Prospecting, **38**, 633-661.

ISS internal multiple attenuation with angle constraints

P. Terenghi and A. B. Weglein, University of Houston, M-OSRP

May 25, 2012

Abstract

The algorithms based on the Inverse Scattering Series used in Seismic Exploration for the suppression of multiple reflections are tyipically defined in the source and receiver Fourier-transformed fk domain, where individual fk components can be interpreted as plane waves traveling down from the source into the earth, and then up to the surface. Within that model, two angular quantities (reflector dip and incidence angle) are recognized as playing key roles in establishing a continuous range of intermediate degrees of accuracy between the cost-saving but restrictive 1D assumption and the full multi-dimensional problem and its daunting cost. Limiting the variation of those two angles within a finite range constitutes a powerful control on the computational cost of evaluation for the algorithm, especially in the 3D case. The range of variation may be chosen with the two-fold purpose to scale the computational effort in proportion to the required degree of accuracy and to incorporate a-priori knowledge of the sampled portion of the earth. This approach is placed in firm theoretical context, and then evaluated in its accuracy and performance through examples using 1D and 2D synthetics.

1 Introduction

Internal multiple attenuation through the Inverse Scattering Series (ISS) is among the most intensive computer processes employed in exploration seismology. Several research efforts in the last decade have been dedicated to accellerating the execution of the original algorithm, due to Araújo (1994) and Weglein et al. (1997, 2003), through mathematical analysis, physical insight, and numerical sophistication. The most important contributions along these lines are the decoupling of two of the innermost integrals and the recursive formulation of the integrand function, as found in Kaplan et al. (2004). Other milestones are the recognition that important savings can be realized by preventing non-propagating waves from contributing the integral (Kaplan et al., 2005). The strategy and foundations for the construction of an efficient and scalable 2D parallelization scheme can be found in Kaplan et al. (2005) while Terenghi and Weglein (2009) quantified the resources needed for the evaluation of the series' leading order term for different data sizes and estimated the workload of a hypotetical 3D version. Hsu et al. (2010) applied the Quasi-Monte Carlo technique to evaluate efficiently the spatial integrals in the ISS internal multiple attenuation algorithm.

A further route, also outlined in Kaplan et al. (2004), but not pursued in its entirety, consists in considering the constraints provided by previous knowledge of the earth subject to investigation.

This document expands those initial ideas through a more comprehensive approach based on certain angular quantities, which can be used to control the accuracy and cost of the algorithm. This approach is justified by the fact that reasonable assumptions can often be made regarding the characteristics of each single application. For example, there are geologic scenarios where the structure of the earth can be reasonably approximated as a multi-layer with little or no reflector dip. One possible choice in those cases would be the 1D version of the algorithm, which is remarkably faster and has the considerable advantage of allowing multiple prediction to be performed independently in each gather (shot, receiver, or common-midpoint gather). An example application of the 1D ISS internal multiple attenuation on field and synthetic data generated in a multi-dimensional earth can be found in Terenghi (2010) and Terenghi et al. (2010). However, a seemingly larger number of cases would be better dealt with by an algorithm that accommodates controllably small variations with respect to the horizontal, and whose cost can be proportioned to the problem at hand.

Another interesting use case is the first and speditive evaluation of whether internal multiples constitute an actual issue in the scenario at hand. In that case, a fast evaluation of the ISS internal multiple algorithm, with tight control on cost may provide advice as to whether investing time and computing resources in a lenghtier run with higher accuracy is worthwhile. Ultimately, the approach to ISS internal multiple attenuation described in this document provides a continuous range of intermediate degrees of accuracy between the cost-saving, but often too restrictive, 1D assumption and the full multi-dimensional problem, with its very daunting cost.

In the first portion of this document, largely following ch. 3 in Stolt and Weglein (2012), two angular quantities α and γ are introduced and recognized as the key control parameters for that transition. In a homogeneous medium, α and γ are simply related to the wavefield variables in the fk domain. Physically, α can be identified as the dip of a hypotetic reflector in the subsurface, and γ as the incidence angle between the propagation vector of a wave and the normal to that reflector (figure 3).

The second part of this document seeks to exploit the reciprocal relationship between those two angular quantities and temporal frequency, in order to map a user-defined constraint (e.g. the knowledge that in the sample area reflectors do not exceed a certain dip) into constraints on the field quantities used as integral variables in the ISS internal multiple attenuation algorithm, with the purpose of decresing the cost of its computation.

In the final part, the proposed approach is tested using synthetic data from both a horizontaly layered earth and one with lateral variations.

2 Forward relationship between temporal frequency and angular wavefield quantities

The acoustic scalar wavefield produced by a seismic source located at $\vec{r}_s = \{x_s, y_s, z_s\}$,

$$P(t; \vec{r}|\vec{r}_s),$$

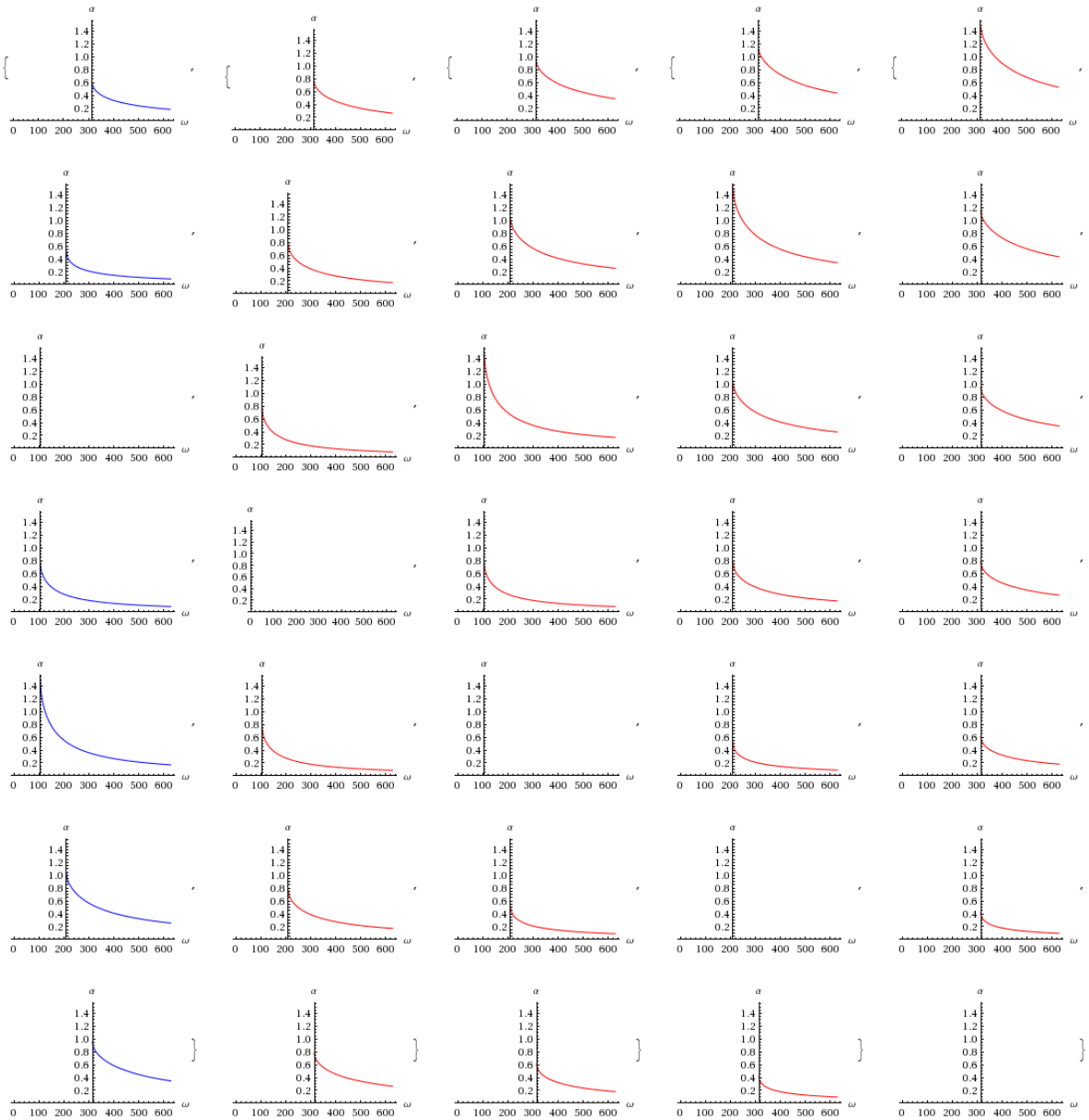

(a) (b) (c) (d) (e)

Figure 1: Dependence of incidence angle α on temporal frequency ω for selected source and receiver wavenumber pairs. The y component of $\vec{\kappa}_g$ and $\vec{\kappa}_s$ is zero. Columns: source wavenumber values $\{-\frac{1}{6},\ 0,\ \frac{1}{6},\ \frac{2}{6},\ \frac{3}{6}\}$ normalized to Nyquist wavenumber. Rows: receiver wavenumber values $\{-\frac{1}{6},\ 0,\ \frac{1}{6},\ \frac{2}{6},\ \frac{3}{6}\}$ normalized to Nyquist wavenumber. All plots are drawn within the non-evenescent portion of the spectrum $\omega^2/c_0^2 \geq \vec{\kappa}_g \cdot \vec{\kappa}_g \wedge \omega^2/c_0^2 \geq \vec{\kappa}_s \cdot \vec{\kappa}_s$. Vertical axes are drawn at minimum propagating frequency $c_0\ max(|\vec{\kappa}_g|, |\vec{\kappa}_s|)$.

is a quantity defined at every generic point in the earth $\vec{r} = \{x, y, z\}$, but known (measured) only at the location of the receiver $\vec{r}_g = \{x_g, y_g, z_g\}$. In seismic exploration, the experiments are normally conducted at fixed sources and receiver depths (z_s and z_g) and the terms *measurement region* or

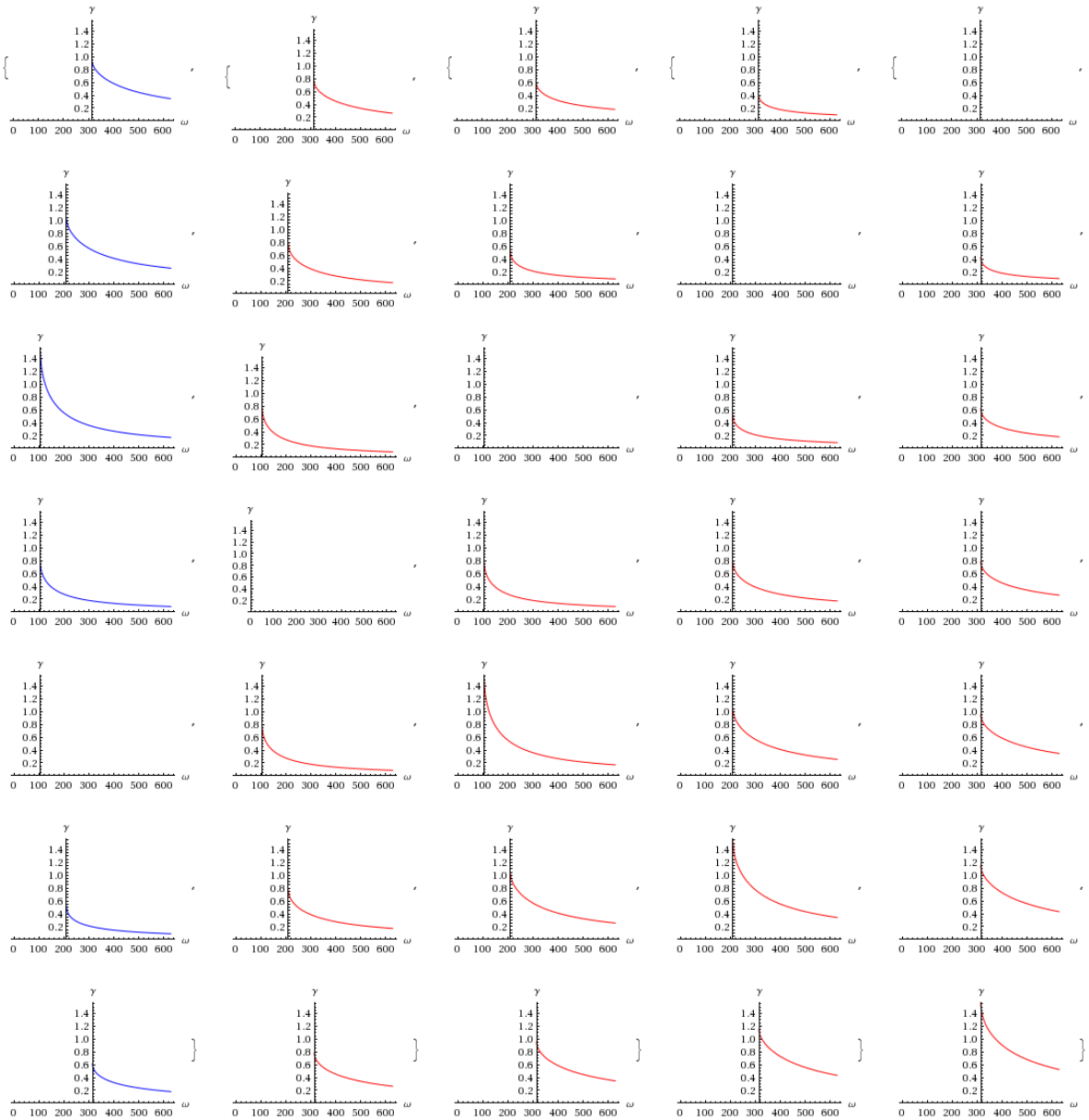

Figure 2: Dependence of incidence angle γ on temporal frequency ω for selected source and receiver wavenumber pairs. The y component of $\vec{\kappa}_g$ and $\vec{\kappa}_s$ is zero. Columns: source wavenumber values $\{-\frac{1}{6},\ 0,\ \frac{1}{6},\ \frac{2}{6},\ \frac{3}{6}\}$ normalized to Nyquist wavenumber. Rows: receiver wavenumber values $\{-\frac{1}{6},\ 0,\ \frac{1}{6},\ \frac{2}{6},\ \frac{3}{6}\}$ normalized to Nyquist wavenumber. All plots are drawn within the non-evenescent portion of the spectrum $\omega^2/c_0^2 \geq \vec{\kappa}_g \cdot \vec{\kappa}_g \wedge \omega^2/c_0^2 \geq \vec{\kappa}_s \cdot \vec{\kappa}_s$. Vertical axes are drawn at minimum propagating frequency $c_0\ max(|\vec{\kappa}_g|, |\vec{\kappa}_s|)$.

measurement surface describe the portion of the earth (approximately a horizontal plane) containing the positions occupied by sources and receivers during the various stages of the experiment. In the case of 3D seismics, the data can be described as a 5-dimensional quantity,

$$D(t;\vec{\chi}_g|\vec{\chi}_s),$$

with $\vec{\chi}_g$ and $\vec{\chi}_s$ defined as the horizontal components of $\vec{r}_g$ and $\vec{r}_s$:

$$\vec{r}_g = \{\vec{\chi}_g, z_g\} = \{x_g, y_g, z_g\}, \qquad \vec{r}_s = \{\vec{\chi}_s, z_s\} = \{x_s, y_s, z_s\},$$

and with the understanding that the wavefield is known only for a single value of z_g and z_s, whereas multiple measurements are carried out for many different values of $\vec{\chi}_g$ and $\vec{\chi}_s$. Similarly, let $\vec{k}_g$ and $\vec{k}_s$ be the Fourier conjugate variables of $\vec{r}_g$ and $\vec{r}_s$ and $\vec{\kappa_g}$ and $\vec{\kappa_s}$ the horizontal components of $\vec{k_g}$ and $\vec{k_s}$.

$$\vec{k}_g = \{\vec{\kappa}_g, q_g\} = \{k_{xg}, k_{yg}, q_g\}, \qquad \vec{k}_s = \{\vec{\kappa}_s, q_s\} = \{k_{xs}, k_{ys}, q_s\},$$

A multi-dimensional Fourier transform of D, applied along time, source, and receiver coordinates,

$$D(\omega;\vec{\kappa}_g|\vec{\kappa}_s) = \int dt d\chi_g d\chi_s D(t;\vec{\chi}_g|\vec{\chi}_s)\ e^{i(\omega t - \vec{\kappa}_g\cdot\vec{\chi}_g + \vec{\kappa}_s\cdot\vec{\chi}_s)}$$

with $d\chi_g = dx_g dy_g$ and $d\chi_s = dx_s dy_s$, corresponds to the portion $P(\omega;\vec{\kappa}_g, q_g|\vec{\kappa}_s, q_s)$ of the fk domain wavefield $P(t;\vec{k}_g|\vec{k}_s)$ which depends on the measured surface data. In particular, the vertical wavenumbers q_g and q_s must not be treated as independent, free-floating variables. On the contrary, they are univoquely defined by the values of ω, $\vec{\kappa}_g$, and $\vec{\kappa}_s$ through the dispersion relationships,

$$q_g = -\frac{\omega}{c_0}\sqrt{1 - \frac{c_0^2}{\omega^2}\vec{\kappa}_g\cdot\vec{\kappa}_g}, \tag{2.1}$$

and

$$q_s = +\frac{\omega}{c_0}\sqrt{1 - \frac{c_0^2}{\omega^2}\vec{\kappa}_s\cdot\vec{\kappa}_s} \tag{2.2}$$

so that wavenumber vectors $\{\vec{\chi}_g, q_g\}$ and $\{\vec{\chi}_s, q_s\}$ yield magnitude $|\omega/c_0|$.

The sign of the square roots in (2.1) and (2.2) are taken positive, hence the sign of q_g is chosen opposite to the sign of ω, to account for upward propagation (towards the negative z direction) from reflector to receiver. Furthermore, the receiver-side and source-side Fourier transform are performed with phases of opposite signs, in agreement with the choice of source and receiver coordinate axes pointing in opposite directions.

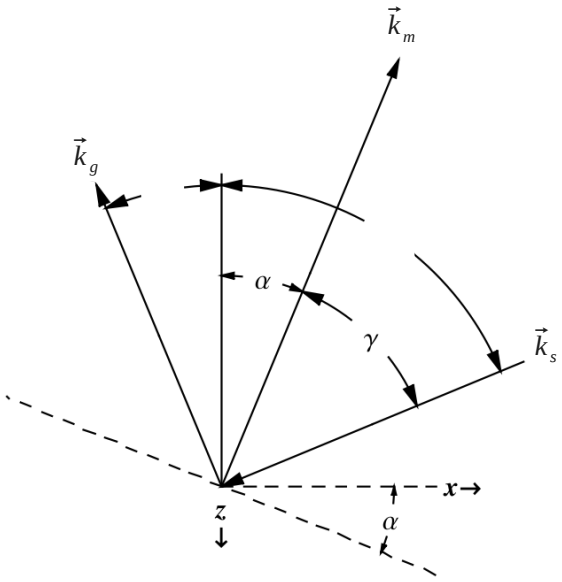

Figure 3: Plane waves at an interface (dashed line) in the subsurface. α is the angle between the *image function wavenumber* $\vec{k}_m$ and the vertical. γ is thre angle between $\vec{k}_m$ and $\vec{k}_g$ or $\vec{k}_s$. After (Stolt and Weglein, 2012, ch 3), modified.

Stolt and Weglein (2012) define the *image function wavenumber* $\vec{k}_m$ as a difference between the receiver and source-side wavenumbers, and the *offset wavenumber* $\vec{k}_h$ as their sum,

$$\vec{k}_m = \vec{k}_g - \vec{k}_s = \{\vec{\kappa}_g - \vec{\kappa}_s, q_g - q_s\}, \qquad \vec{k}_h = \vec{k}_g + \vec{k}_s = \{\vec{\kappa}_g + \vec{\kappa}_s, q_g + q_s\}.$$

These definitions, along with the conventions adopted for the spatial Fourier transforms along $\vec{\chi}_g$ and $\vec{\chi}_s$, imply that $\vec{k}_m$ points upwards and bisects the angle 2γ between $\vec{k}_g$ and $\vec{k}_s$ or, equivalently, the angle between the fronts of an upward and a downward traveling plane wave (figure 3). Those plane waves, when related by Snell's law, probe for the existence of a plane reflector with outgoing normal $\vec{k}_m$, and dip angle α.

Simple trigonometry relates α and γ to the field quantities in the fk domain,

$$|tan(\alpha)| = \frac{\vec{\kappa}_m \cdot \vec{\kappa}_m}{|q_g - q_s|}, \tag{2.3}$$

and

$$cos(2\gamma) = -\frac{c_0^2}{\omega^2}\vec{k}_g \cdot \vec{k}_s = -\frac{c_0^2}{\omega^2}(\vec{\kappa}_g \cdot \vec{\kappa}_s + q_g q_s). \tag{2.4}$$

Hence, (2.3) and (2.4) relate each element in $D(\omega;\vec{\chi}_g|\vec{\chi}_s)$ to specific values of α and γ, and it is worthwhile to emphasize how these relationships hold in general for any wavefield in the source and receiver side Fourier-transformed fk domain, and not only for the particular ISS internal multiple application under consideration.

Further, in (2.3) and (2.4) the dependence of α and γ on temporal frequency is carried by the occurences of the vertical wavenumber q. Since the behavior of those dependencies is difficult to infer by simple inspection, it will be useful to resort to numerical evaluation. A reasonable question to answer is whether the relationships between α and ω, and between γ and ω are monotonic and differentiable within their range of definition, knowing that these properties guarantee that their respective inverses are also monotonic functions.

Figures 1 and 2 display the dependence of reflector dip α and incidence angle γ on temporal frequency ω for source and receiver wavenumber pairs selected within a mostly non-evanescent portion of the $\{\omega,\vec{\kappa}_g,\vec{\kappa}_s\}$ spectrum. Clearly, for fixed $\vec{\kappa}_g$ and $\vec{\kappa}_s$, both α and γ, show a monotonically decreasing dependence with respect to the absolute value of ω.

Studying the sign of the first derivatives of (2.3) and (2.4) with respect to ω, the monotonicity of the relationship tieing ω with α and γ can be proved analytically:

$$\frac{\partial\alpha}{\partial\omega}=\frac{|w|(q_g-q_s)\sqrt{\vec{\kappa}_m.\vec{\kappa}_m}}{2q_gq_s\left(c_0^2(\vec{k}_g.\vec{k}_s)-\omega^2\right)}=\frac{|w|(q_s-q_g)\sqrt{\vec{\kappa}_m.\vec{\kappa}_m}}{2q_gq_s\omega^2\left(\cos(2\gamma)+1\right)} \tag{2.5}$$

and,

$$\frac{\partial\gamma}{\partial\omega}=\frac{q_g^2+q_s^2+2q_gq_s\cos(2\gamma)}{2q_gq_s\omega\sqrt{1-\cos^2(2\gamma)}}. \tag{2.6}$$

The sign of (2.5) depends on q_s-q_g in the numerator, and on q_gq_s in the denominator. Recalling (2.1) and (2.2), the sign of (2.5) can be said negative for a positive value of ω. Again recalling (2.1) and (2.2), the numerator in (2.6) can be written as $q_g^2+q_s^2-2|q_g||q_s|\cos(2\gamma)$, and recognized as positive by comparison with the *law of cosines*. Similarly, for positive temporal frequencies, the sign of the denominator is negative.

In support of the above analysis, figures 4 and 5 display the dependence of the first order derivative of α and γ with respect to temporal frequency ω ($\partial\alpha/\partial\omega$ and $\partial\gamma/\partial\omega$), for source and receiver wavenumber pairs selected within a mostly non-evanescent portion of the $\{\omega,\vec{\kappa}_g,\vec{\kappa}_s\}$ spectrum. As expected, these quantities yield negative sign all along the frequency axis.

3 ISS internal multiple attenuation with angular constraints

The analysis carried out to this point suggests that, at fixed values of $\vec{\kappa}_g$ and $\vec{\kappa}_s$, any given value of ω univocally identifies angles α and γ, and that increasing values of the absolute value of ω map to decreasing values of α and γ. Keeping the final goal in mind, which is to decrease the

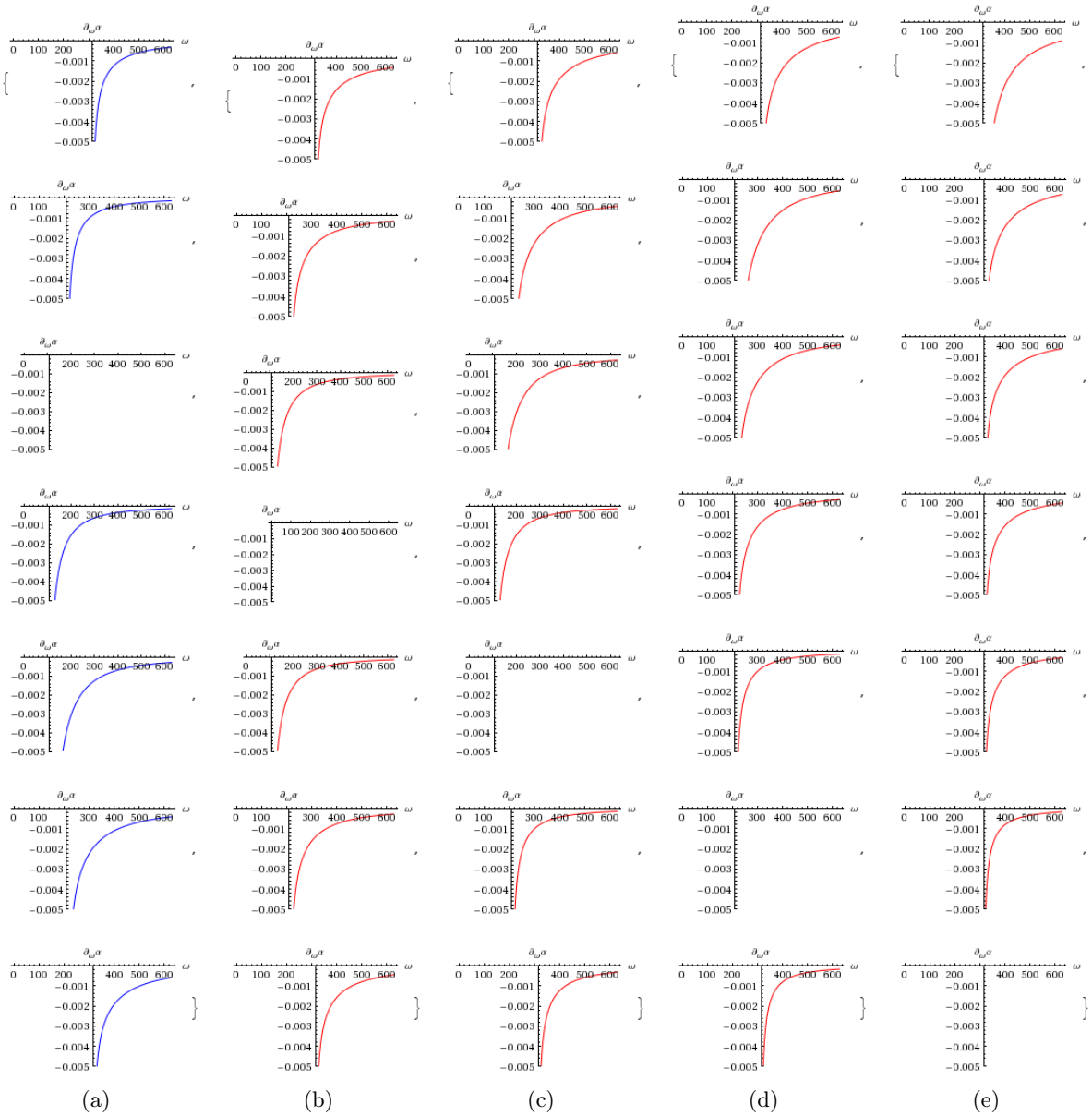

(a) (b) (c) (d) (e)

Figure 4: First derivative with respect to ω of the relatonship between incidence angle α and temporal frequency ω for selected source and receiver wavenumber pairs. The y component of $\vec{\kappa}_g$ and $\vec{\kappa}_s$ is zero. Columns: source wavenumber values $\{-\frac{1}{6},\ 0,\ \frac{1}{6},\ \frac{2}{6},\ \frac{3}{6}\}$ normalized to Nyquist wavenumber. Rows: receiver wavenumber values $\{-\frac{1}{6},\ 0,\ \frac{1}{6},\ \frac{2}{6},\ \frac{3}{6}\}$ normalized to Nyquist wavenumber. All plots are drawn within the non-evenescent portion of the spectrum $\omega^2/c_0^2 \geq \vec{\kappa}_g \cdot \vec{\kappa}_g \wedge \omega^2/c_0^2 \geq \vec{\kappa}_s \cdot \vec{\kappa}_s$. Vertical axes are drawn at minimum propagating frequency $c_0\ max(|\vec{\kappa}_g|, |\vec{\kappa}_s|)$.

computational cost of performing loops on the fk domain field variables, it is useful to pursue a set of inverse relationships, mapping values of α and γ into values of ω. Those relationships may be thought of as *inverse* because they may be used to map a certain range in the wavefield angular quantities back into the fk domain sampling variables $\omega, \vec{\kappa}_g, \vec{\kappa}_s$. In principle, that goal could be achieved by substituting expressions (2.1) and (2.2) into (2.3) and (2.4) and attempting to solve

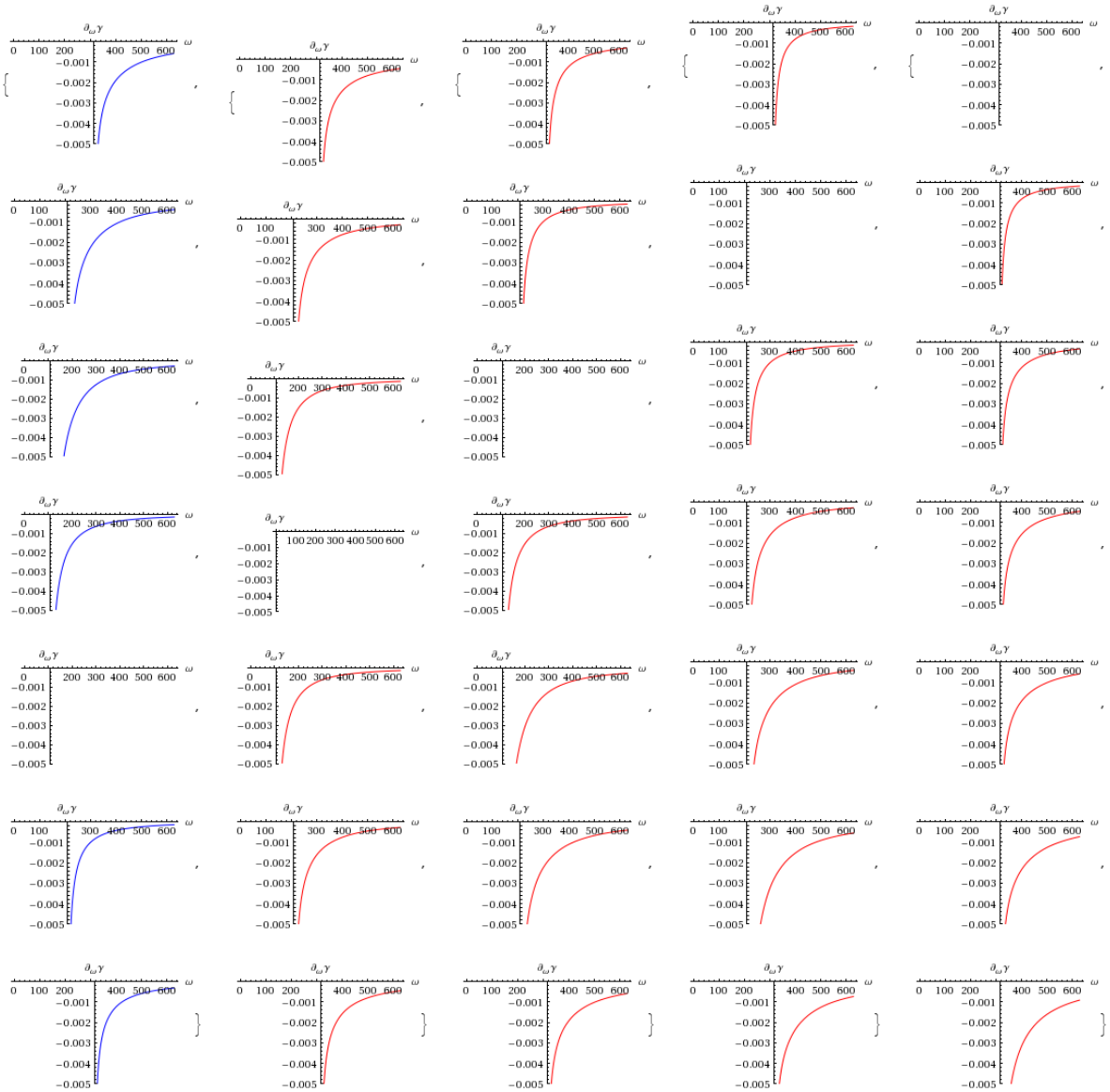

(a) (b) (c) (d) (e)

Figure 5: First derivative with respect to ω of the relatonship between incidence angle γ and temporal frequency ω for selected source and receiver wavenumber pairs. The y component of $\vec{\kappa}_g$ and $\vec{\kappa}_s$ is zero. Columns: source wavenumber values $\{-\frac{1}{6},\ 0,\ \frac{1}{6},\ \frac{2}{6},\ \frac{3}{6}\}$ normalized to Nyquist wavenumber. Rows: receiver wavenumber values $\{-\frac{1}{6},\ 0,\ \frac{1}{6},\ \frac{2}{6},\ \frac{3}{6}\}$ normalized to Nyquist wavenumber. All plots are drawn within the non-evenescent portion of the spectrum $\omega^2/c_0^2 \geq \vec{\kappa}_g \cdot \vec{\kappa}_g \wedge \omega^2/c_0^2 \geq \vec{\kappa}_s \cdot \vec{\kappa}_s$. Vertical axes are drawn at minimum propagating frequency $c_0\ max(|\vec{\kappa}_g|, |\vec{\kappa}_s|)$.

for ω. The algebra implied by this task requires squaring the *forward* relationship several times, until all square roots where ω appears in the argument cancel. However, for the ultimate purpose of this document, which is to devise a strategy to decrease the computational cost of the ISS internal multiple algorithm, studying the properties of the inverse relationships will suffice. In particular, a proof of monotonicity with respect to temporal frequency for the sought for inverse relationships is

given by the theorem of *the derivative of an inverse function*,

$$Df^{-1}(y) = \frac{1}{Df(x)}, \tag{3.1}$$

where $f(x)$ may be identified as the forward relationship between temporal frequency and angles (which has previously been shown to be a monotonically decreasing one), and $f^{-1}(y)$ as the inverse relationship between angles and frequency.

It is now possible to state that increasing temporal frequencies in the data map to decreasing values of reflector dip and aperture angle. As an immediate corollary it is possible to conclude that, for set values of $\vec{\kappa}_g$ and $\vec{\kappa}_s$, any desired finite angle-domain interval maps to a similarly finite frequency domain interval. Therefore, any knowledge or inference about the characteristics of the earth and the wavefield at hand may be employed to decrease the number of loops on temporal frequency required to evaluate the fk algorithm of interest, and hence harvest the computational advantages. Furthermore, ISS internal multiple prediction (as well as any fk domain integral algorithm) can be conveniently decomposed into a set of non overlapping intervals in the angular wavefield quantities, which can be summed to yield a more accurate prediction corresponding to a wider angle range.

The stage is now set to analyze the application of those concepts to the leading order term in the ISS internal multiple elimination algorithm (Araújo, 1994; Weglein et al., 1997, 2003), here written for the 3D data and for sources and receivers located at the surface,

$$\begin{aligned} b_3^{IM}(\omega,\vec{\kappa}_g,\vec{\kappa}_s) \;=\; \int\int_{-\infty}^{\infty} d\kappa_1 d\kappa_2 \int_{-\infty}^{\infty} dz_1 b_1(z_1,\vec{\kappa}_g,\vec{\kappa}_1) e^{i(q_g+q_1)z_1} \\ \int_{-\infty}^{z_1-\epsilon} dz_2 b_1(z_2,\vec{\kappa}_1,\vec{\kappa}_2) e^{-i(q_1+q_2)z_2} \int_{z_2+\epsilon}^{\infty} dz_3 b_1(z_3,\vec{\kappa}_2,\vec{\kappa}_s) e^{i(q_2+q_s)z_3}. \end{aligned} \tag{3.2}$$

with

$$b_1(\omega,\vec{\kappa}_k,\vec{\kappa}_l)) = iq_k\ D(\omega,\vec{\kappa}_k,\vec{\kappa}_l) \qquad for\ \ k,l = g,1,2,s. \tag{3.3}$$

It is worth emphasizing how the dependence on temporal frequency in the right-hand side of (3.2) is carried by the instances of q, where

$$q_k = \frac{\omega}{c_0}\sqrt{1 - \frac{c_0^2}{\omega^2}\vec{\kappa}_k \cdot \vec{\kappa}_k}. \tag{3.4}$$

Consider the field variables $\vec{\kappa}_g$,$\vec{\kappa}_s$, and ω. The condition for the existence of propagating waves is that the argument of the square root in (3.4) be non-negative, so that q be real:

$$\frac{\omega^2}{c_0^2} \;\geq\; \vec{\kappa}_k \cdot \vec{\kappa}_k \qquad with \qquad k = g,1,2,s \tag{3.5}$$

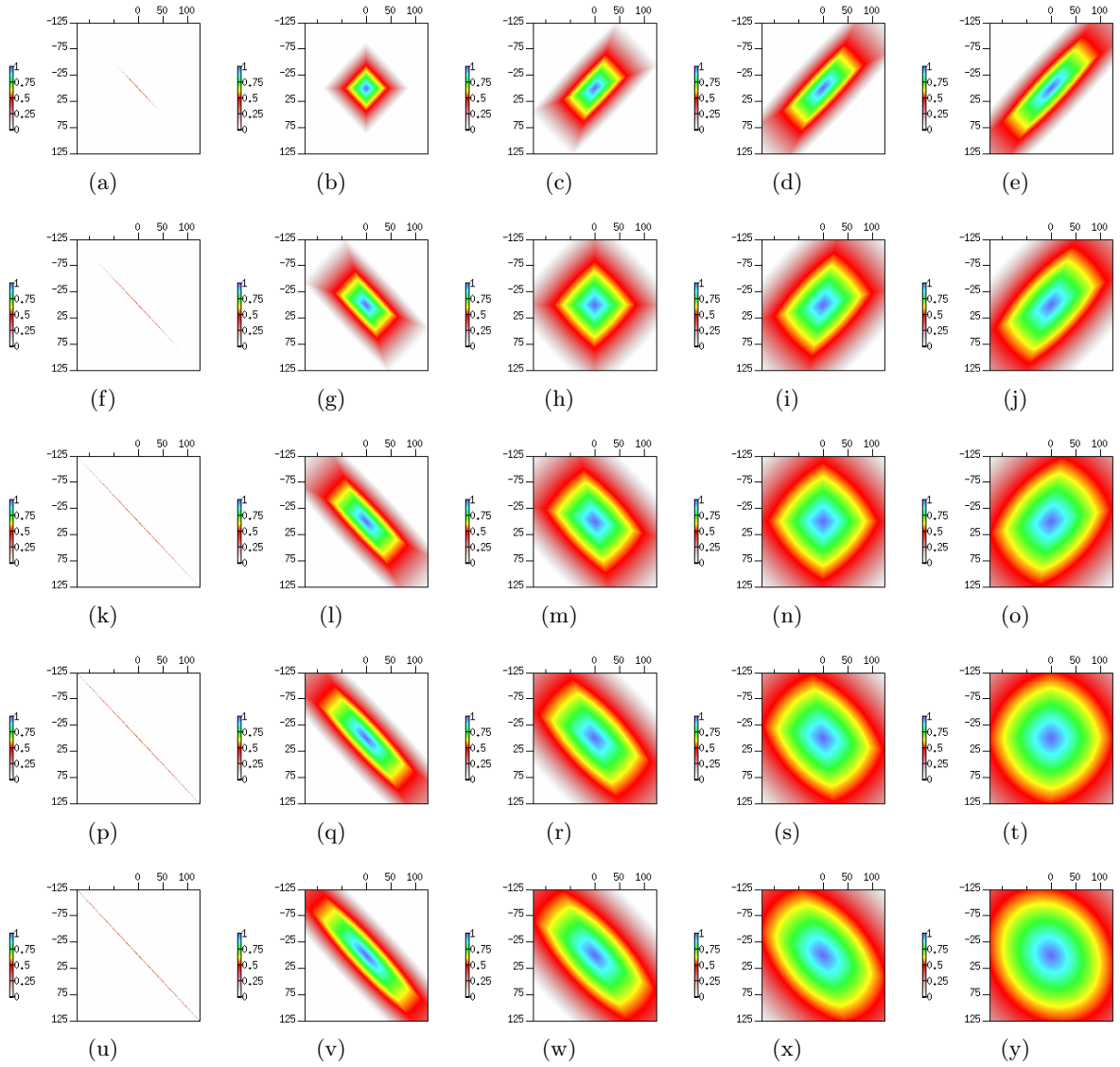

Figure 6: Ratios between the effective frequency ranges and theoretical ones, calculated for $\alpha_{min} = \gamma_{max} = 0$ and several combinations of $\alpha_{max} = \{0, 10, 20, 30, 40\}$ deg, and $\gamma_{max} = \{10, 20, 30, 40, 50\}$ deg. α_{max} varies from row to row, while γ_{max} varies from column to column. Small values of α_{max} confine the contributing region to a narrow nighborhood near the principal diagonal. Similarly, small values of γ_{max} confine the contributing region to a narrow nighborhood near the principal counter-diagonal.

When a priori information on the wavefield or the earth in connection with the problem at hand is available, such that the effective range for α and γ can be inferred or arbitrarily set, a second constraint derives from the relations discussed in section 2. Typically, it may be useful to constrain the algorithm within a range of reflector dips such that $\alpha_{min} <= \alpha <= \alpha_{max}$. Similarly, the incidence angles may be constrained such that $\gamma_{min} <= \gamma <= \gamma_{max}$ ([1]). Denoting with $\omega_{\alpha}^{(min)}$ and

[1] For both α and γ, within this work the choice is made to use unsigned angular values, as dictated by the difficulty in defining reasonable conventions for signed angles in the 3D case. However, the characteristics of modern

$\omega_{\alpha}^{(max)}$ the extremes of the frequency interval implied by the constraints on α, and with $\omega_{\gamma}^{(min)}$ and $\omega_{\gamma}^{(max)}$ those related to the constraints on γ, the total frequency interval of interest is given by

$$\begin{aligned} &max(\omega_{\gamma}^{min}, \omega_{\alpha}^{min}) \leq \omega \ < \ min(\omega_{\gamma}^{max}, \omega_{\alpha}^{max}) && for \quad w > 0, \\ &max(-\omega_{\gamma}^{max}, -\omega_{\alpha}^{max}) < \omega \ \leq \ min(-\omega_{\gamma}^{min}, -\omega_{\alpha}^{min}) && for \quad w < 0, \end{aligned}$$

where the symmetry between positive and negative frequencies has been called upon, based on the assumption that the result is real valued in the tx domain.

All discussed constraints apply independently to all four sets of spatial field variables in expression (3.2): $\{\omega, \vec{\kappa}_g, q_g\}$, $\{\omega, \vec{\kappa}_1, q_1\}$, $\{\omega, \vec{\kappa}_2, q_2\}$, and $\{\omega, \vec{\kappa}_s, q_s\}$. Consequenly, it seems legitimate to expect that the computational saving achieved by incorporating angular limits into the ISS internal multiple attenuation algorithm may follow the same growth law that governs the absolute cost for the complete algorithm, which Terenghi and Weglein (2009) estimate as N^5 for 2D and N^9 for 3D. Since certain portions of the Fourier-transformed input data hyper-volume are excluded from contributing, the effect of the proposed approach can be thought of as decreasing the effective data size, hence lowering the value of N.

The color coded plots in figure 6, for several combinations of α_{max}, and γ_{max}, describe the ratio between the effective frequency range and the theoretical one, thus describing how the angular constraints affect the number of loops required to evaluate the ISS internal multiple algorithm. For small values of α_{max} (with $\alpha_{min} = 0$ and $\gamma_{max} = 0$) the active portion of the spectrum is distributed in the proximity of the principal diagonal $\vec{\kappa}_g = \vec{\kappa}_s$. For $\alpha_{min} = \alpha_{max} = 0$, the active portion of the data is strictly confined to that principal diagonal, in consistency with the notion that reflection upon a horizontal interface leaves the horizontal components of the wavenumber vector unaffected. The larger α_{max}, the wider the active region extends away from the principal diagonal. Similarly, small values of γ_{max} (with $\gamma_{min} = 0$ and $\gamma_{max} = 0$) confine the active region to a narrow neighborhood near the principal counter-diagonal $\vec{\kappa}_g = -\vec{\kappa}_s$. That region widens as γ_{max} increases.

$\alpha_{min} = \gamma_{min} = 0$	$\alpha_{max} = 15$	$\alpha_{max} = 25$	$\alpha_{max} = 35$	$\alpha_{max} = 45$	$\alpha_{max} = 55$
$\gamma_{max} = 20$	11%	15%	17%	19%	20%
$\gamma_{max} = 40$	15%	21%	24%	27%	28%
$\gamma_{max} = 60$	16%	23%	27%	29%	31%
$\gamma_{max} = 80$	17%	23%	N/A	N/A	N/A

Table 1: Percentage ratios of active versus total spectrum for different constraints on incidence angle (half-aperture) γ_{max} and reflector dip α_{max}, with $\gamma_{min} = 0$ and $\alpha_{min} = 0$. Angles in degrees. Calculated for a 2D input dataset with $k_{gz} = k_{sz} = 0$.

acquisition technologies suggest how this may not be the most advantageous choice. In a 3D experiment, in fact, those constraints apply undiscriminately to the inline and crossline directions of a seismic acquisition. A viable alternative would be working on the projections of α and γ onto the inline and crossline directions of the seismic acquisition. In the rest of this document and in the section dedicated to numerical examples, the minimum values for α and γ are both set to zero, unless otherwise indicated.

Table 1 reports the ratios (in %) between number of contributing samples vs total number of samples in the fk domain data hyper-volume. The ratios increase with increasing α_{max} and γ_{max}. However, it is worth to emphasize that even for $\alpha_{max} = \gamma_{max} = 90$ deg, the ratio would not reach 100% due to the exclusion of the evanescence region (non-propagating waves) originally discussed in Kaplan et al. (2005).

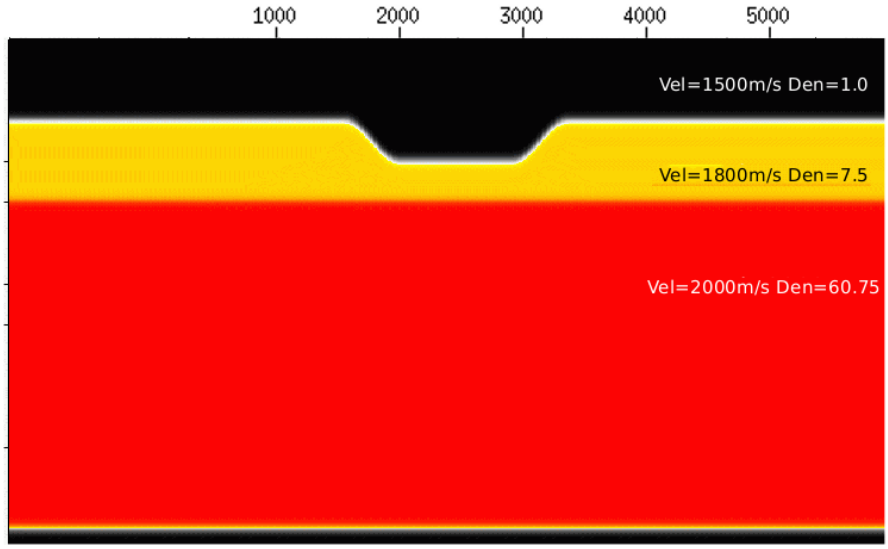

Figure 7: Synthetic velocity and density model used to generate the test data in this section (courtesy of WesternGeco). Note that horizontal and vertical coordinates are not drawn to the same scale. The average dip of the walls of the trench featuring in the center of the model is approximately 20 deg.

4 Numerical examples

The concepts laid out in the previous sections are brought to practice using a new implementation of the ISS internal multiple attenuation algorithm, which allows the user to control the range of the incidence angle γ (aperture) and reflector dip α.

A set of finite difference synthetic data is selected to demonstrate the effect of these constraints in a practical case. The finite difference model is characterized by very large contrasts between different layers, as shown in figure 7. It will be useful to know that the average slope of the shallowest reflector, in correspondence with the walls of the trench, is roughly 20 deg.

The test dataset consists of a single sail line of 251 shots, each of which groups 251 traces of 500 samples. The the sail line convers a total of 6250m, while the duration of the traces is 4s.

Horizontally layered earth - It is worthwhile to observe the behavior of the Fourier domain field quantities $\vec{k}_g$ and $\vec{k}_s$, and angles α and γ for the case of a horizontally layered earth. It is

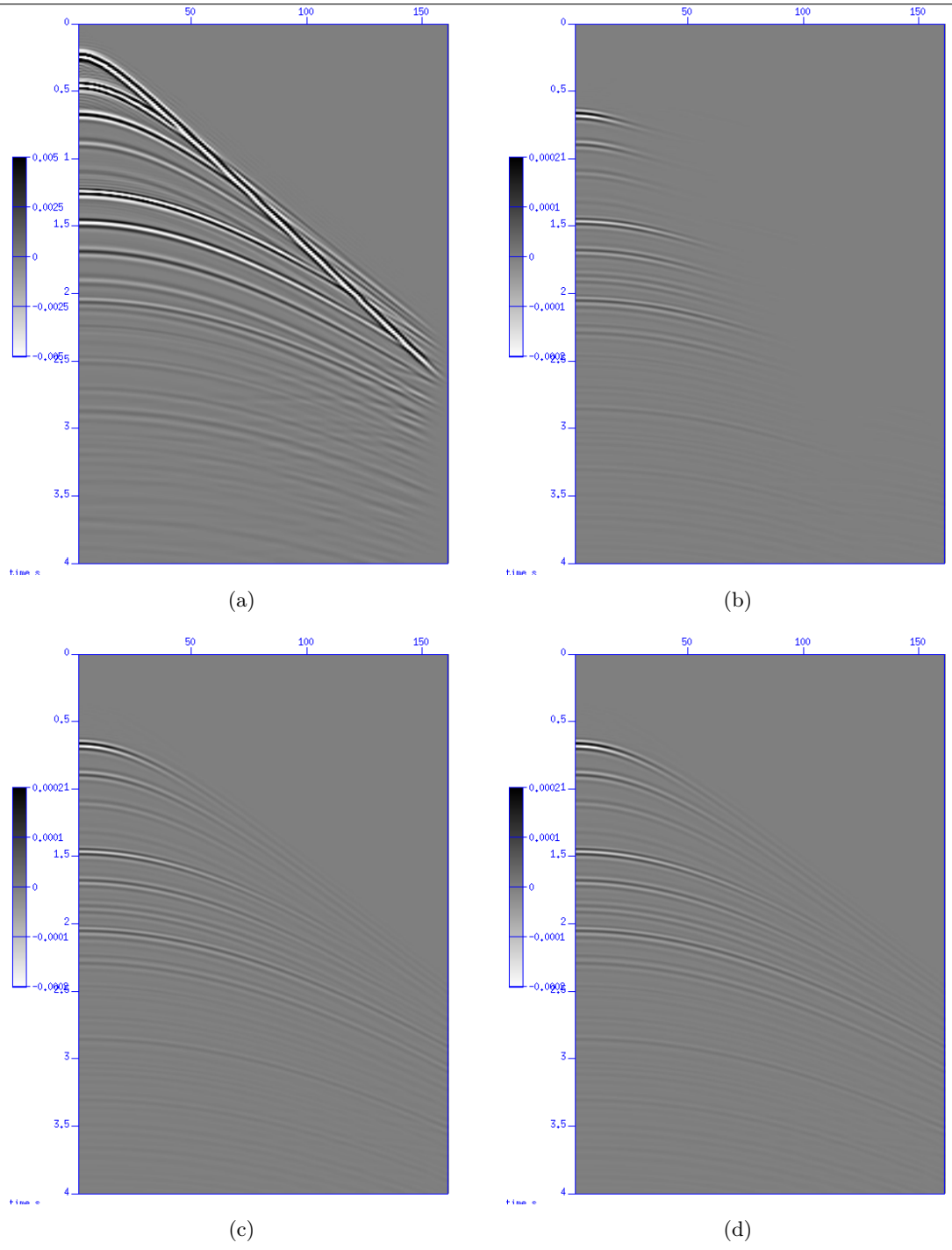

Figure 8: Numerical examples of the ISS internal multiple attenuation algorithm for horizontally layered media using a range of constraints on the incidence angle γ_{max}. (a) input data shot gather; (b) Predicted multiples for $\gamma_{max} = 25$ deg; (c) predicted multiples for $\gamma_{max} = 45$ deg; (d) predicted multiples for $\gamma_{max} = 65$ deg.

known how the reflection of a plane wave on a plane reflector conserves the wavenumber components

parallel to the interface. Hence, if the reflector is horizontal, $\vec{\kappa}_g = \vec{\kappa}_s$.

Consistently, the data acquired in a 1D earth map exclusively to the diagonal of the horizontal wavenumber space:

$$D(\frac{\vec{\kappa}_h}{2}) = D(\vec{\kappa}_g|\vec{\kappa}_s)\ \delta(\vec{\kappa}_g - \vec{\kappa}_s),$$

As expected under these circumstances, α is identially zero, while the expression for γ simplifies to

$$cos(2\gamma) = -\frac{c_0^2}{\omega^2}|\vec{k}_g|^2 = -\frac{c_0^2}{\omega^2}|\frac{\vec{k}_h}{2}|^2. \tag{4.1}$$

Figure 8(a) shows a shot gather computed in a portion of the model (figure 7) away from the trench carved into the second layer, where the medium is safely assumed 1-dimensional. The ISS internal multiple predictions using maximum incidence angles (γ_{max}) of 25, 45, and 65 deg are displayed in figures 8(b-d). The setup characterized by the narrowest aperture calculates an accurate prediction of the internal multiples only for the shortest offsets, while at further distance the amplitude of the result gradually decreases. As expected, predictions characterized by wider apertures provide increasingly better accuracy at the far offsets.

A comparison of the results obtained by the new approach with those from the earlier implementations of both the 1D and multi-D ISS internal multiple prediction algorithm can be found in appendix A

Earth with lateral variations Results from the multi-dimensional version of the algorithm are here proposed using zero-offset sections (figures 9 and 10) and individual shot gathers (figures 11-14), for different algorithm apertures ($\gamma_{max} = 20$ and 60 deg) and reflector dips ($\alpha_{max} = 15, 25, 35$ deg). The zero offset results for $\gamma = 20$ deg (figure 9) and $\gamma = 60$ deg (figure 10) suggest that all setups capture the majority of the internal multiples characterized by near-vertical reflections. However, expectedly, the reverberations recorded below the trench's steep walls (red arrows) are only captured if the chosen upper limit for reflector dip α_{max} exceeds 20 deg (the true dip of the trench walls). Furthermore, internal multiples characterized by complicated wavefield effects (revealed by the bow-ties indicated by yellow arrows) appear more accurately in the predictions characterized by high tresholds for both α_{max} and γ_{max}.

The effect of the constraints applied on dip and aperture angles are best shown using examples in the pre-stack domain. Figures 11-14 show four input shot gathers and the corresponding results selected from the portion of the model in the vicinity of the right slope of the trench characterizing the shallowest reflector. The four shot gathers are chosen with coordinates 2500 (figure 7, centre of trench), 3000 and 3500 (trench wall), and 4000 (outside trench). In figures 11 and 12 the internal multiples are predicted using a narrow aperture ($\gamma_{max} = 20$ deg) and increasing dip values ($\alpha_{max} = 15, 25, 35$ deg), while in figures 13 and 14 the maximum aperture is set to $\gamma_{max} = 60$ deg. In consistency with the observations carried out on the zero-offset sections, comparing the different pre-stack results confirms that the benefit of increasing α_{max} are only realized if supported by sufficient aperture. The value of γ_{max} also seems to control the algorithm's ability to perform accurate predictions at farther offsets.

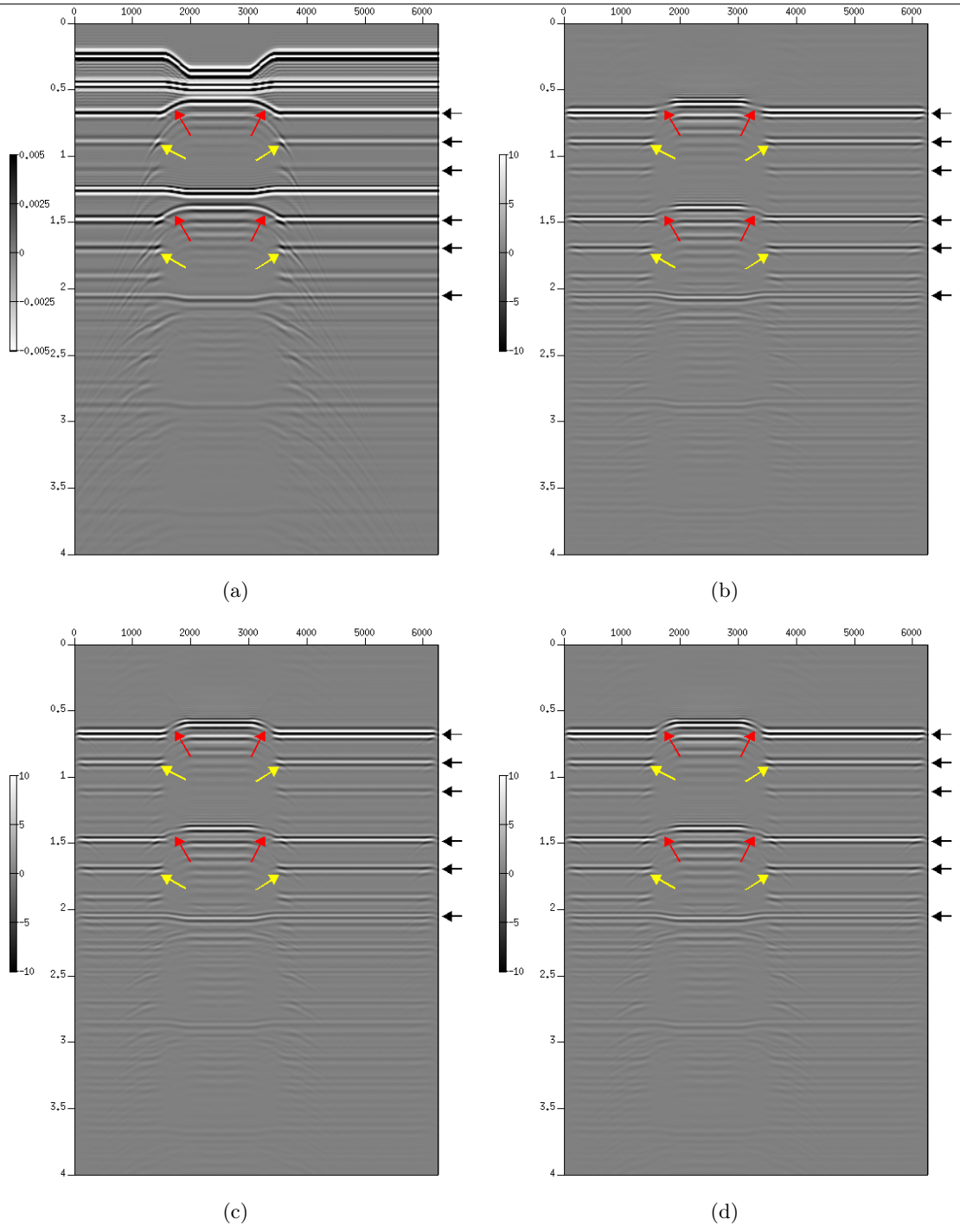

Figure 9: Numerical examples of ISS internal multiple attenuation on 2D data with lateral variations. Zero offset sections of (a) input data, and first order terms in the series, calculated using $\gamma_{max} = 20$ deg and a range of values for α: (b) $\alpha_{max} = 15$ deg; (c) $\alpha_{max} = 25$ deg; (d) $\alpha_{max} = 35$ deg. Some internal multiples are indicated by black and colored arrows.

5 Performance analysis

This section reports the total time required for the evaluation of the algorithm, under different constraints applied to α and γ. The code is evaluated using two different computers. Table 2

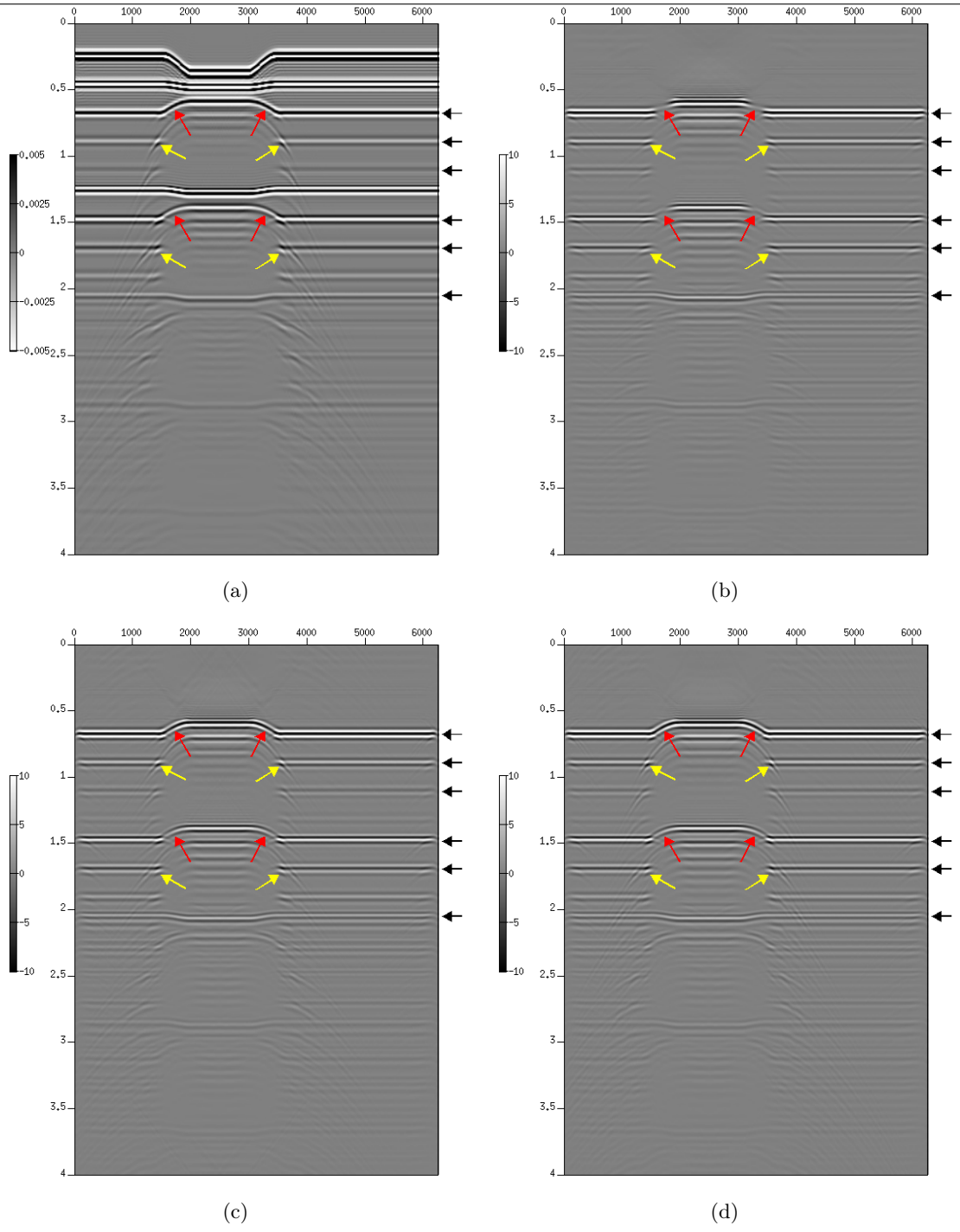

Figure 10: Numerical examples of ISS internal multiple attenuation on 2D data with lateral variations. Zero offset sections of (a) input data, and first order terms in the series, calculated using $\gamma_{max} = 60$ deg and a range of values for α: (b) $\alpha_{max} = 15$ deg; (c) $\alpha_{max} = 25$ deg; (d) $\alpha_{max} = 35$ deg. Some internal multiples are indicated by black and colored arrows.

refers to a single 4 core cluster node purchased in 2002, while table 3 refers to a more recent 8 core

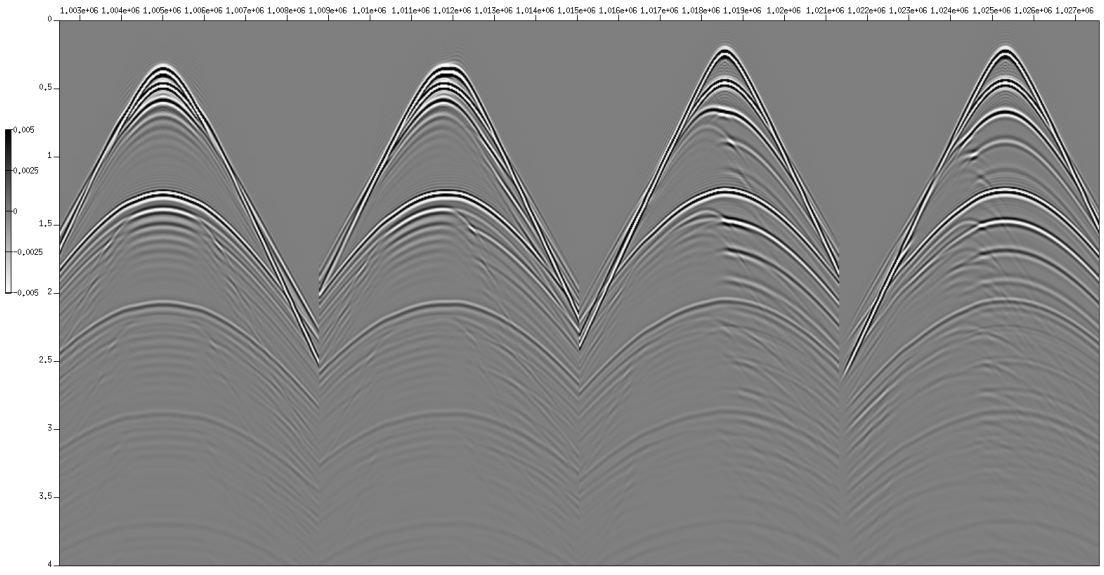

(a)

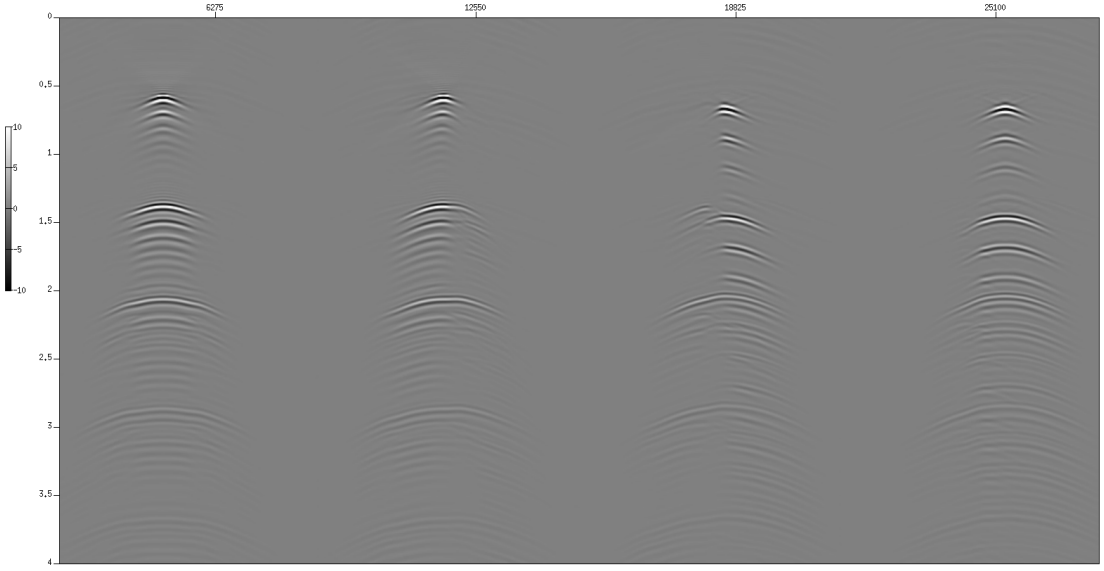

(b)

Figure 11: Numerical examples of ISS internal multiple attenuation on 2D data with lateral variations. (a) selected input shot gathers and (b) first term in the ISS internal multiple elimination series calculated using $\alpha_{max} = 15$ deg and $\gamma_{max} = 20$ deg (continued in figure 12).

machine.

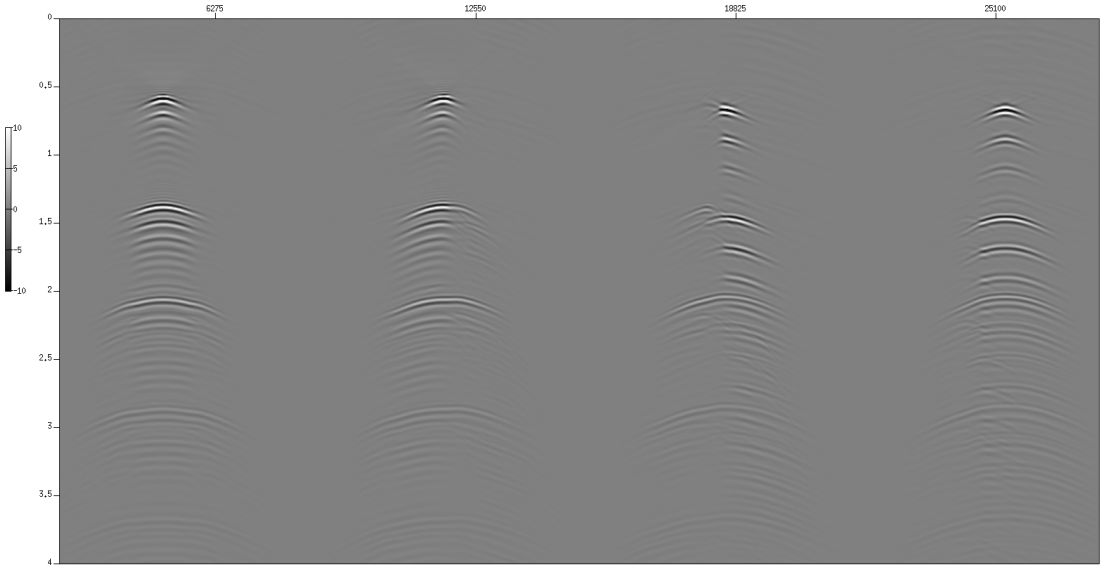

(a)

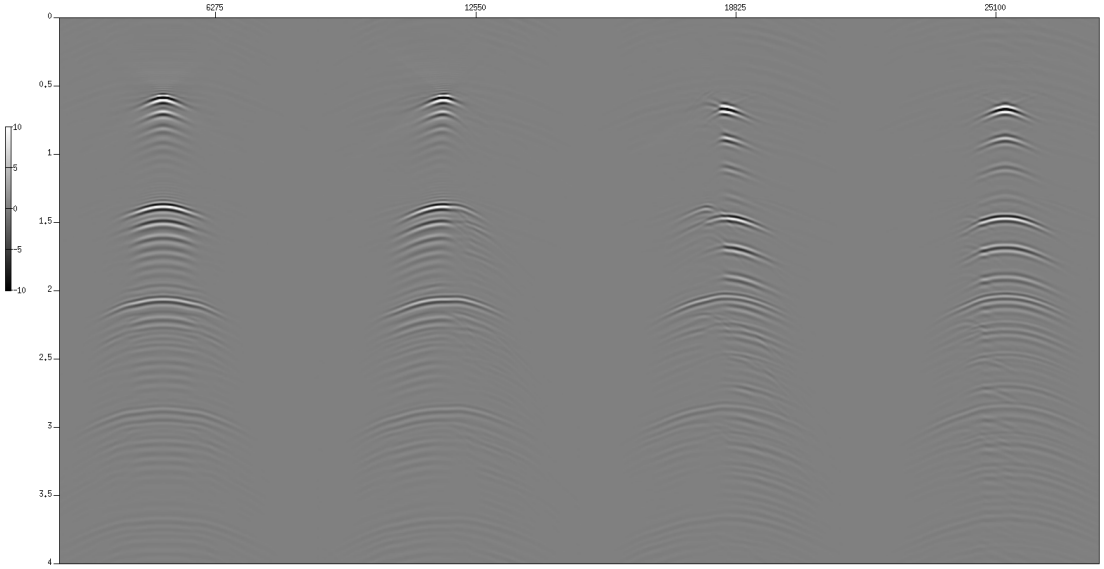

(b)

Figure 12: Numerical examples of ISS internal multiple attenuation on 2D data with lateral variations. Selected shot gathers from the first term in the ISS internal multiple elimination series calculated using (a) $\alpha_{max} = 25$ deg and (b) $\alpha_{max} = 35$ deg. In both (a) and (b) γ_{max} is set to 20 deg (continued from figure 11).

6 Discussion and conclusion

Two angular quantities (reflector dip and incidence angle) have been shown to be of great importance in administering the trade-off between accuracy and cost for the ISS internal multiple attenuation

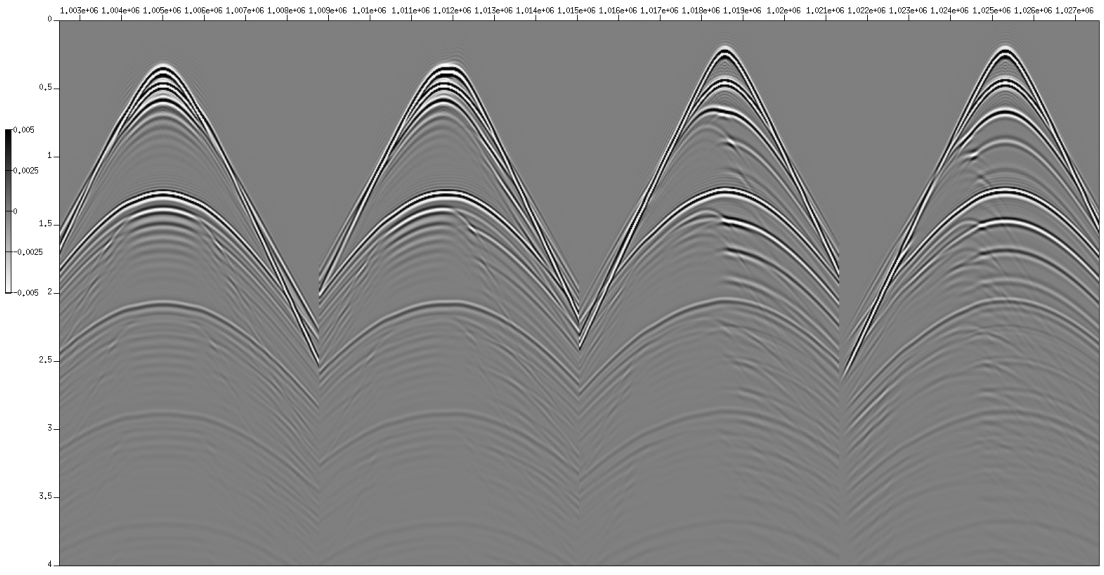

(a)

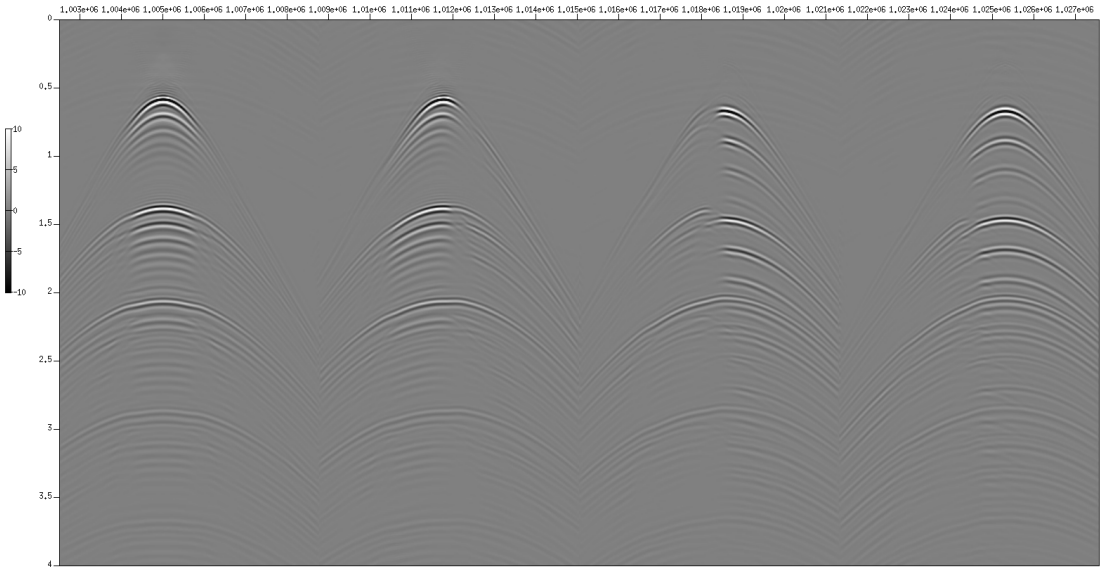

(b)

Figure 13: Numerical examples of ISS internal multiple attenuation on 2D data with lateral variations. (a) selected input shot gathers and (b) first term in the ISS internal multiple elimination series calculated using $\alpha_{max} = 15$ deg and $\gamma_{max} = 60$ deg (continued in figure 14).

algorithm. Whenever the variation range of these angles is known, either through a priori knowledge

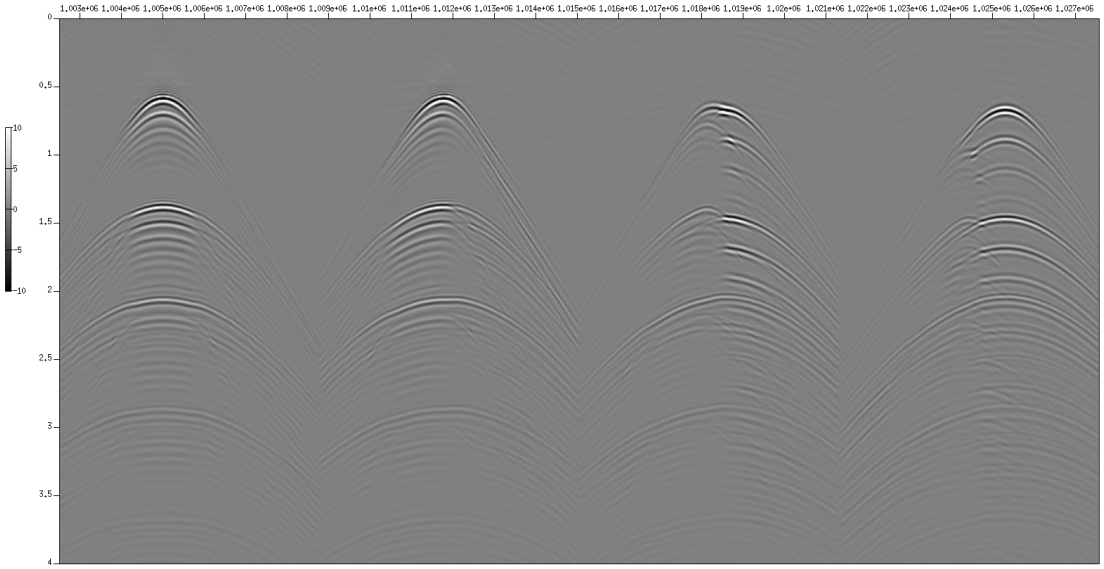

(a)

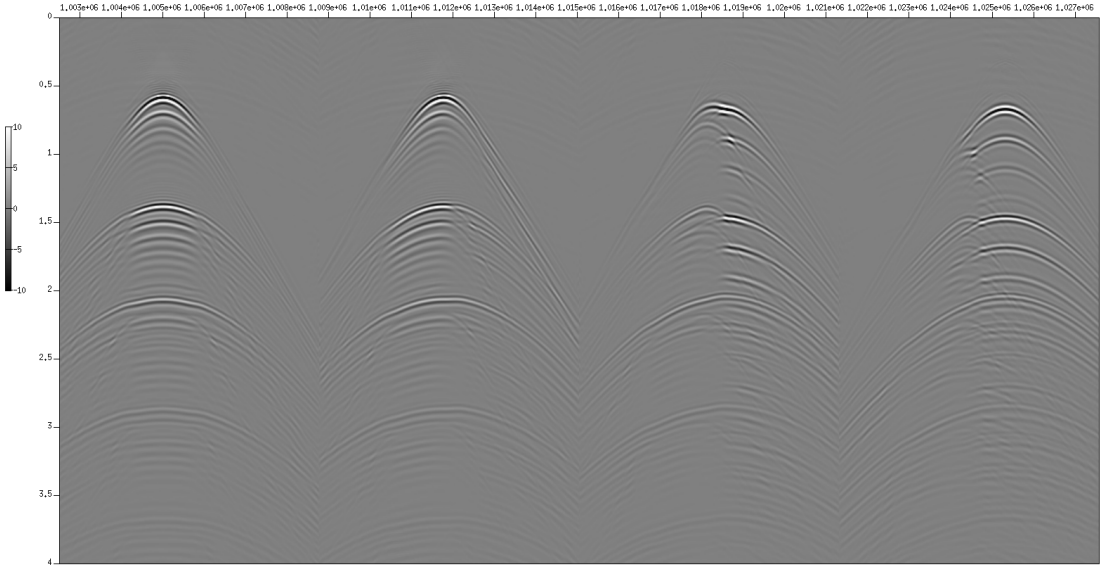

(b)

Figure 14: Numerical examples of ISS internal multiple attenuation on 2D data with lateral variations. (a) selected shot gathers from the first term in the ISS internal multiple elimination series calculated using (a) $\alpha_{max} = 25$ deg and (b) $\alpha_{max} = 35$ deg. In both (a) and (b) γ_{max} is set to 60 deg (continued from figure 13).

of the medium under investigation, or as the result of a deliberate limiting choice, the cost of computing the algorithm can be decreased to a fraction of its theoretical cost. Key to this analysis

	$\alpha_{max} = 15$	$\alpha_{max} = 25$	$\alpha_{max} = 35$	$\alpha_{max} = 45$	$\alpha_{max} = 55$
$\gamma_{max} = 20$	79	163	198	218	227
$\gamma_{max} = 40$	94	331	491	607	665
$\gamma_{max} = 60$	125	346	576	760	864
$\gamma_{max} = 80$	127	374	N/A	N/A	N/A

Table 2: Total execution time (in hours) of algorithm with different constraint of incidence angle (half-aperture) γ and reflector dip α. Slower computer.

	$\alpha_{max} = 15$	$\alpha_{max} = 25$	$\alpha_{max} = 35$	$\alpha_{max} = 45$	$\alpha_{max} = 55$
$\gamma_{max} = 20$	N/A	65	81	90	N/A
$\gamma_{max} = 40$	49	128	N/A	N/A	N/A
$\gamma_{max} = 60$	52	130	236	350	N/A
$\gamma_{max} = 80$	N/A	N/A	N/A	N/A	N/A

Table 3: Total execution time (in hours) of algorithm with different constraint of incidence angle (half-aperture) γ and reflector dip α. Faster computer.

are the properties of the *forward* relationships mapping the wavefield sampling variables of the source and receiver Fourier transfomed domain $(\omega, \vec{\kappa}_g, \vec{\kappa}_s)$ into the angular quantities α and γ. The monotonicity property of the forward relationships guarantees that the cost reduction can be achieved even without formally establishing the *inverse* analytic dependence of temporal frequency upon the angular quantities at any given source and receiver horizontal wavenumber pair.

Furthermore, the ISS internal multiple prediction can be decomposed into a set of non overlapping intervals in the angular wavefield quantities α and γ, and the results can be summed to yield a more accurate prediction at a wider angle range. Hence, the proposed device allows the algorithm to be evaluated incrementally, by gradually widening the range of contributing reflector dips and aperture angles, without repeating calculations already performed. Thus, the high cost of computing the ISS algorithm can be offset through carefully monitoring the benefit achieved by adding incremental terms.

7 Acknowledgments

We wish to thank Andre Ferreira of Petrobras for his contribution in the discussions that resulted in the ideas laid out throughout this paper, and for his patient tutoring with software tools such as Mathematica, which helped those idea take a mathematical shape.

WesternGeco is gratefully acknowledged for permission to use their synthetic data.

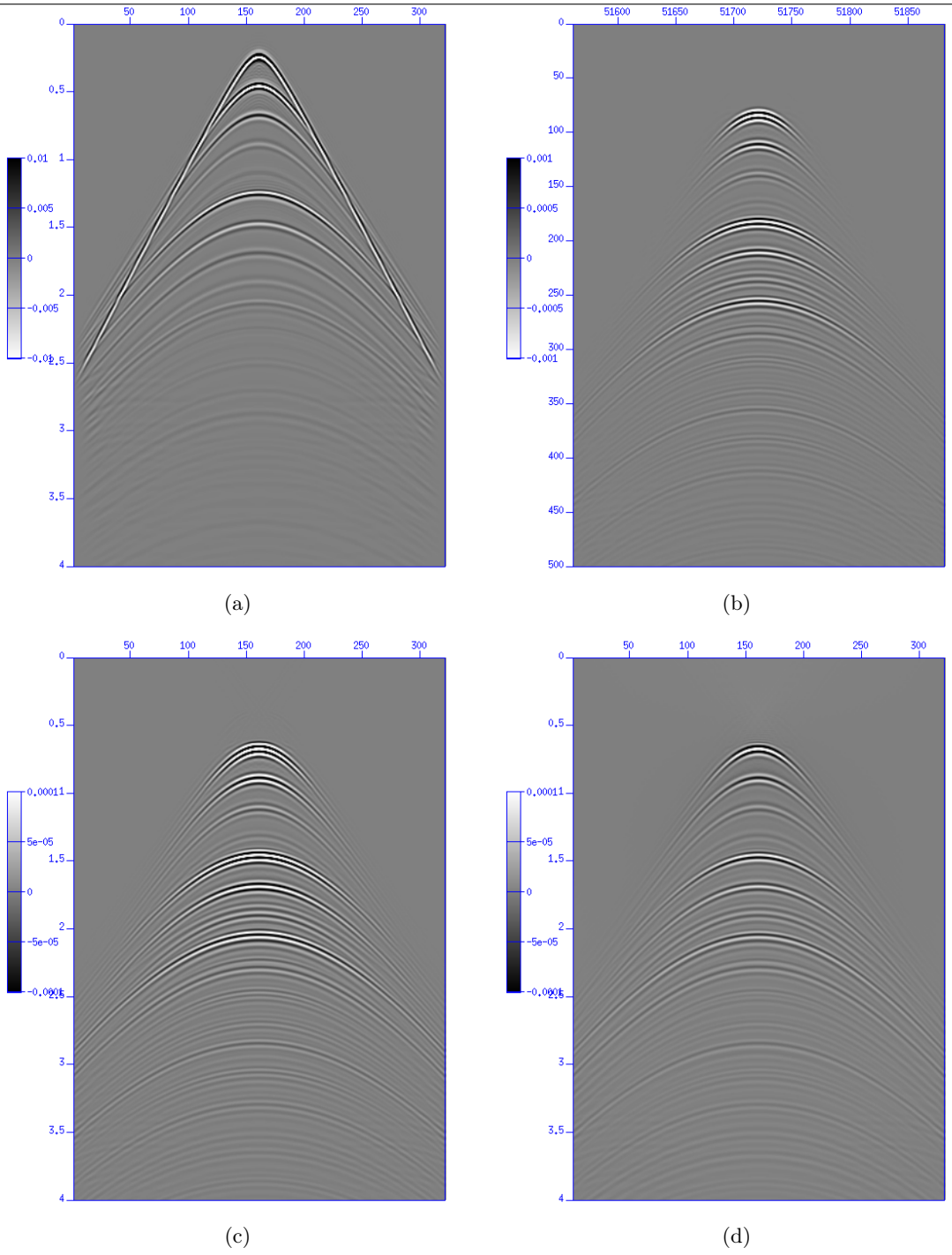

Figure 15: Numerical examples of the ISS internal multiple prediction algorithm for horizontally layered media. (a) input data shot gather; (b) output from a previously released implementation which incorporated an implicit cut-off at a value of γ_{max} smaller than 45 deg; (c) output from new implementation with γ_{max} set to 45 deg; (d) same as (c) except wavelet deconvolution is activated.

A Appendix - Comparison between old and new results

Figure 15(a) shows a shot gather computed in a portion of the model away from the trench carved into the second layer, where the medium is safely assumed to be 1-dimensional. Figure 15(c) shows

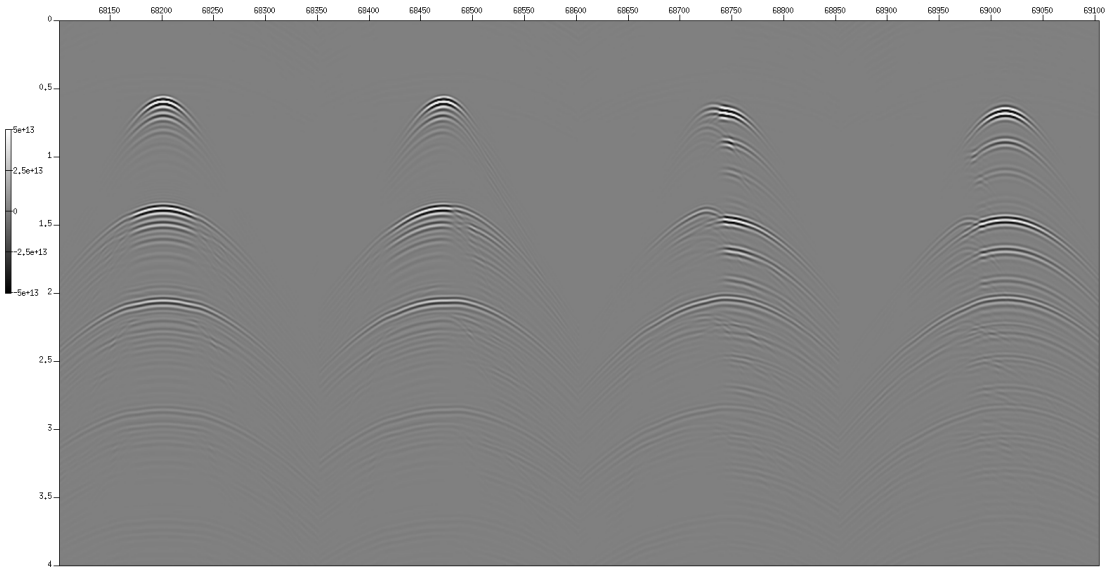

(a)

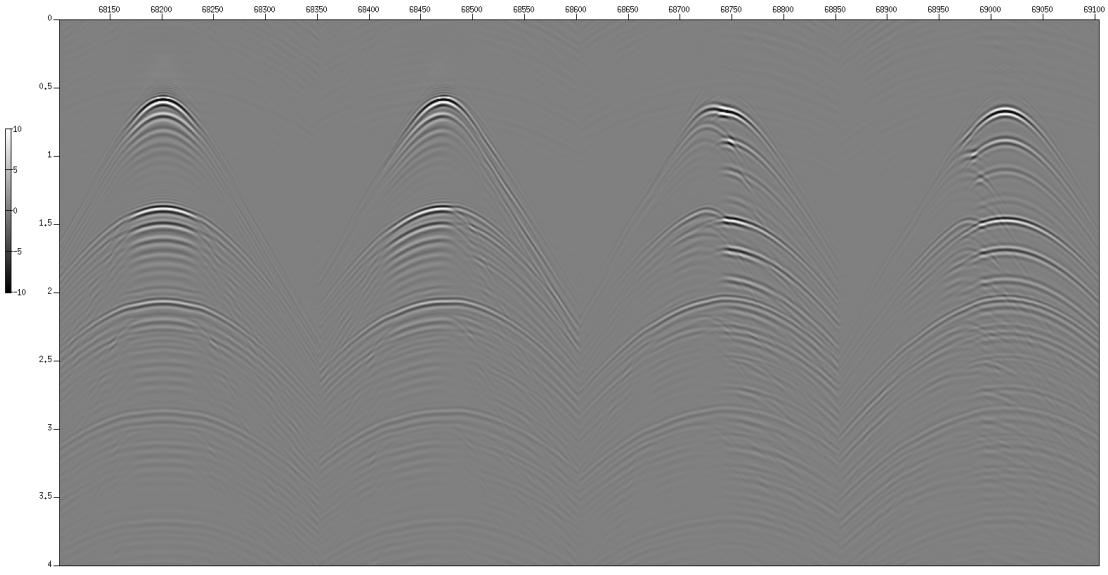

(b)

Figure 16: Numerical examples of the ISS internal multiple prediction algorithm for an earth with lateral variations. (a) internal multiple prediction using a previously released implementation; (b) output of new implementation using a large dip and aperture range ($\alpha_{max} = 55$ deg and $\gamma_{max} = 60$ deg).

the ISS internal multiple prediction computed using the new 1D implementation, parametrized to use a maximum incidence angle of 45 deg. Figure 15(d) shows the result of a setup similar to (c), here with wavelet deconvolution turned on. For comparison, figure 15(b) shows the ISS internal

multiple prediction computed using the earlier version of the 1D code, which incorporated an implicit aperture cut-off at a value of γ smaller than 45 deg.

A pre-stack comparison of the results obtained by the old and new codes for an earth with lateral variation may be seen in figure 16. For both cthe zero-offset ad shot-somain cases, the new code is able to predict multiples more accurately at far offsets and shallow reflector depths.

References

Araújo, Fernanda V. *Linear and non-linear methods derived from scattering theory: backscattered tomography and internal multiple attenuation.* PhD thesis, Universidade Federal da Bahia, 1994.

Hsu, Shih-Ying, Einar Otnes, and Adriana C. Ramìrez. "Quasi-Monte Carlo integration for the inverse scattering internal multiple attenuation algorithm." *SEG Expanded Abstracts.* 2010.

Kaplan, Sam T., K. A. Innanen, and A. B. Weglein. "Updates to M-OSRP internal and free surface multiple coding projects." *Mission-Oriented Seismic Research Program (M-OSRP) Annual Report.* 2005, 139–144.

Kaplan, Sam T., Kristopher A. Innanen, Einar Otnes, and Arthur Weglein. "Internal multiple attenuation code-development and implementation." *Mission-Oriented Seismic Research Program (M-OSRP) Annual Report.* 2004, 83–102.

Kaplan, Sam T., B. Robinson, K. A. Innanen, and A. B. Weglein. "Optimizing internal multiple attenuation algorithms for large distributed computing systems." *Mission-Oriented Seismic Research Program (M-OSRP) Annual Report.* 2005, 145–157.

Stolt, Robert H. and Arthur B. Weglein. *Seismic Imaging and Inversion: Volume 1: Application of Linear Inverse Theory.* Cambridge, United Kingdom: Cambridge University Press, 2012.

Terenghi, Paolo. 2010 "1D internal multiple prediction on the synthetic IM3D dataset.". Slides available on the M-OSRP website http://www.mosrp.uh.edu/secure/mosrp2011/2011%20Agenda%20&%20Presentations.zip.

Terenghi, Paolo, X. Li, Shih-Ying Hsu, and Arthur B. Weglein. "1D preprocessing of the Kristin data." *Mission-Oriented Seismic Research Program (M-OSRP) Annual Report.* 2010, 35–49.

Terenghi, Paolo and Arthur B. Weglein. "3D Internal Multiple Prediction coding project: preliminary notes." *Mission-Oriented Seismic Research Program (M-OSRP) Annual Report.* 2009, 61–71.

Weglein, A. B., F. V. Araújo, P. M. Carvalho, R. H. Stolt, K. H. Matson, R. T. Coates, D. Corrigan, D. J. Foster, S. A. Shaw, and H. Zhang. "Inverse Scattering Series and Seismic Exploration." *Inverse Problems* (2003): R27–R83.

Weglein, A. B., F. A. Gasparotto, P. M. Carvalho, and R. H. Stolt. "An Inverse-Scattering Series Method for Attenuating Multiples in Seismic Reflection Data." *Geophysics* 62 (November-December 1997): 1975–1989.

Application of the Wiener filter in wavelet estimation using Kristin data

L. Tang, P. Terenghi, A.B. Weglein

May 25, 2012

Abstract

The Wiener filter is a very powerful method that can be applied in many fields. During the testing with Kristin data, we employed the Wiener filter to estimate the source signature directly from the information contained in the direct wavefield, using the reference medium's Green's function. In this note we will revisit the principle of the Wiener filter first, and then we will introduce the details of the application of this powerful method in our wavelet estimation test. Finally, we will discuss the unique advantage of this method compared with the spectral division method.

1 Introduction

Source signature estimation is an important step in seismic exploration. The knowledge of the source signature is essential for identifying and removing the contribution of the source from the recorded data. Weglein and Secrest (1990) presented an algorithm for wavelet extraction, based on Green's theorem, that does not require knowledge of the properties of the earth. This algorithm requires the information of the pressure field and its normal derivative on the measurement surface. An alternative method is to extract a wavelet from the direct wave and Green's function of the reference medium. This method has straightforward physical meaning and does not involve complicated numerical calculation. In the field-data test using Kristin data by M-OSRP(Liu et al. (2010)), we use the latter method to estimate the source signature by exploiting the physical separation between the direct wavefield and reflected wavefield (Tang et al. (2010)).

In the marine environment, such as that of Kristin data, we treat the reference medium as a half space of air and a half space of water, or as a whole space of water. On the basis of the convolutional model, the reference wave is the convolution of Green's function with the source signature. In the case of surface marine seismic, the separation between the direct field and the scattered field depends on the depth of the water bottom. If the water is sufficiently deep, the direct and scattered fields do not interfere, and it is possible to estimate the wavelet by deconvolving the direct field by using the Green's function of the reference medium. The method we employed here to perform the deconvolution is the Wiener filter method.

The Wiener filter method, developed by Norbert Wiener (Wiener (1949)), has great practical use for implementation in many fields of signal data processing, such as linear prediction, channel equalization and system identification (Robinson and Treitel (1980),Vaseghi (2008)). It is typically used to estimate the character of the system when one is given the inputs and outputs of that system, or to estimate a signal observed in noise. The objective criterion of the Wiener filter is the least-mean-square error between the filter output and the desired signal. The coefficients of the filter are obtained by minimizing the average squared-error function with respect to the filter coefficients. The solution of the coefficients uses the information of the autocorrelation of the input, and the cross-correlation of the input and the desired signal. In the field-data test using Kristin data, we applied the Wiener filter method to the wavelet estimation process. According to the Wiener filter theory, the wavelet is treated as an estimated filter that shapes the Green's function (the input signal) so that it becomes the recorded data (i.e., the reference wave).

This powerful method provides us an approach for deconvoling robustly in the time domain, thereby avoiding the instability of spectral division. Also, with the length of the filter given as a priori information, the predicted result is very stable. Our test result also shows that compared with the method of spectral division of the reference wave and Green's function, the Wiener filter method can deal with the issue of measurement noise in the reference wave better.

In this note we will introduce the necessary background of the convolutional model first, and then we will present the principle of the Wiener filter method. These sections are extracted from books of Sheriff and Geldart (1995) and Robinson and Treitel (1980), with different signal notations for a better understanding of our specific application of Wiener filter method. Then we will show the specific steps in the application of the Wiener filter in wavelet estimation using Kristin data. The comparison and relation of the Wiener filter method and the spectral division method are discussed next, followed by a general introduction of further possible application of the Wiener filter method in other areas of seismic data processing.

2 Background

When the source signature is an impulsive spike $\delta(t)$ at $\vec{r}_s$, what the receiver at $\vec{r}$ records will be the Green's function, i.e.,

$$P(\vec{r},t) = G(\vec{r},\vec{r}_s,t) \tag{2.1}$$

Assume the source is a point source, $\rho(\vec{r},t) = A(t)\delta(\vec{r}-\vec{r}_s)$. If we also assume that the wavelet $A(t)$ has a finite length of time, we can break it up into a sum of a set of impulsive functions in time, which means

$$A(t) = \int_{-\infty}^{\infty} A(\tau)\delta(t-\tau)d\tau. \tag{2.2}$$

Assuming the linearity and time-invariance of the earth, the response would become

$$P(\vec{r},t) = \int_{-\infty}^{\infty} A(\tau)G(\vec{r},\vec{r}_s,t-\tau)d\tau. \tag{2.3}$$

The contribution to the recorded trace at time t from the portion of wavelet at time τ is $A(\tau)G(t-\tau)$. The total response at t is the sum of all times within the wavelet. The length of the recorded data is the sum of the wavelet and the Green's function.

Equation 2.3 can also be derived in the frequency domain. Assuming source $\rho(\vec{r},\omega)$ and Green's function $G(\vec{r},\vec{r}',\omega)$, the wavefield would be

$$P(\vec{r},\omega) = \int_{-\infty}^{\infty} d\vec{r}' \rho(\vec{r}',\omega) G(\vec{r},\vec{r}',\omega). \tag{2.4}$$

Assuming the source is a point source, $\rho(\vec{r},\omega) = A(\omega)\delta(\vec{r}-\vec{r}_s)$, and we can obtain,

$$P(\vec{r},\omega) = A(\omega) G(\vec{r},\vec{r}_s,\omega). \tag{2.5}$$

Equation 2.3 and Equation 2.5 are the same relation presented in different domains. A Fourier transform over t of Equation 2.3 will give us Equation 2.5.

$$\int_{-\infty}^{\infty} e^{i\omega t} dt \int_{-\infty}^{\infty} A(\tau) G(\vec{r},\vec{r}_s,t-\tau) d\tau \tag{2.6}$$

$$\xrightarrow{t-\tau=s} \int_{-\infty}^{\infty} e^{i\omega s} ds \int_{-\infty}^{\infty} A(\tau) G(\vec{r},\vec{r}_s,s) e^{i\omega t} d\tau \tag{2.7}$$

$$= \int_{-\infty}^{\infty} G(\vec{r},\vec{r}_s,s) e^{i\omega s} ds \int_{-\infty}^{\infty} A(\tau) e^{i\omega t} d\tau \tag{2.8}$$

$$= G(\vec{r},\vec{r}_s,\omega) A(\omega) \tag{2.9}$$

3 The Wiener filter method

In scattering theory, we treat the actual medium as a combination of an unperturbed medium, called the reference medium, plus a perturbation. According to the convolutional model, in the reference-medium world the wavefield P_0 is the convolution of the wavelet A(t) with the reference Green's function G_0, so

$$P_0(t) = \int_{-\infty}^{\infty} A(\tau) G_0(t-\tau) d\tau. \tag{3.1}$$

In the test using Kristin data, we treat the reference medium as a half space of air and a half space of water, so that the reference Green's function G_0 can be calculated from the wave equation easily. Reference wave P_0 can be extracted directly from raw data, where P_0 and the scattered wave P_s do not overlap.

To solve wavelet $A(t)$ from Equation 3.1, one possible solution is to convert this equation to the frequency domain, so that it becomes

$$P_0(\omega) = A(\omega) G_0(\omega), \tag{3.2}$$

Thus, the wavelet in the frequency domain can be solved by a division of $P_0(\omega)$ and $G_0(\omega)$. However, to avoid the problems caused by division, we could use the Wiener filter method to calculate wavelet $A(t)$ in the time domain.

Using the Wiener filter method, we treat the wavelet $A(t)$ as a shaping filter that shapes the input signal (Green's function $G_0(t)$) to be the desired signal (reference wave $P_0(t)$), as shown in Figure 1. In the following section we will explain the mathematical logic of finding the best shaping filter using the correlations of input and desired signals. Then we will offset some thoughts on the connection and relationship of these two methods.

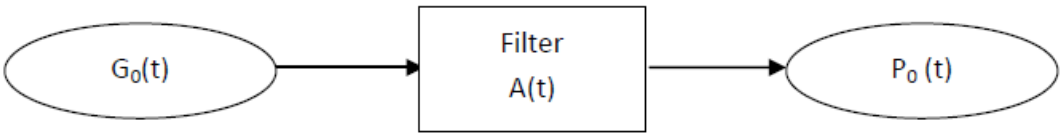

Figure 1: Wavelet A(t) is treated as a filter that shapes the Green's function to be the reference wave.

3.1 Principle

The Wiener filter method uses the least-square criterion to find the "best" filter. Suppose we have an input signal $G_0(t)$ and a filter $A(t)$, which together give an output signal $X(t)$. We need output $P_0(t)$, and the difference between the given output signal $X(t)$ and the needed output is defined as error $E(t)$.

$$X(t) = \int_{-\infty}^{\infty} A(\tau)G_0(t-\tau)d\tau = A(t) * G_0(t), \tag{3.3}$$

$$and \tag{3.4}$$

$$E(t) = P_0(t) - X(t). \tag{3.5}$$

Here $*$ means convolution. In the actual seismic process, functions are discrete number series, so we use the discrete expressions from now on. Assume that filter A is a series $(A_0, A_1, A_2, ..., A_m)$, the input Green's function is $(G_0, G_1, G_2, ..., G_n)$, and the desired P wave is $(P_0, P_1, P_2, ..., P_{m+n})$, so that

$$X_t = \sum_{s=0}^{m} A_s G_{t-s} \qquad t = 0, 1, 2, ..., m+n \tag{3.6}$$

$$and \tag{3.7}$$

$$E_t = P_t - X_t = P_t - \sum_{s=0}^{m} A_s G_{t-s} \qquad t = 0, 1, 2, ..., m+n. \tag{3.8}$$

In order to have the output signal close to the desired function, we need to minimize the energy of error, which is defined as I:

$$I = \sum_{t=0}^{m+n} E_t^2 \tag{3.9}$$

$$= \sum_{t=0}^{m+n} (P_t - \sum_{s=0}^{m} A_s G_{t-s})^2. \tag{3.10}$$

Here we are looking for a least-square error with the choice of filter coefficients A_n, which corresponds to the Wiener filter. Thus, the partial derivative of error energy with each of the coefficients of the filter should be zero, i.e.,

$$\frac{\partial I}{\partial A_i} = 0 \qquad i = 0, 1, 2, ..., m. \tag{3.11}$$

An example of A_0 shows that

$$\begin{aligned}
\frac{\partial I}{\partial A_0} &= \frac{\partial}{\partial A_0}\left[\sum_{t=0}^{m+n}(P_t - \sum_{s=0}^{m} A_s G_{t-s})^2\right] && (3.12)\\
&= \sum_{t=0}^{m+n}\left[\frac{\partial}{\partial A_0}(P_t - \sum_{s=0}^{m} A_s G_{t-s})^2\right] && (3.13)\\
&= \sum_{t=0}^{m+n}\left[2(P_t - \sum_{s=0}^{m} A_s G_{t-s})\right]\left[-\frac{\partial}{\partial A_0}(\sum_{s=0}^{m} A_s G_{t-s})\right] && (3.14)\\
&= 2\sum_{t=0}^{m+n}\left[(P_t - \sum_{s=0}^{m} A_s G_{t-s})(-G_t)\right] && (3.15)\\
&= 2\left[-\sum_{t=0}^{m+n} P_t \cdot G_t + \sum_{s=0}^{m} A_s \cdot (\sum_{t=0}^{m+n} G_{t-s}G_t)\right] && (3.16)\\
&= 0. && (3.17)
\end{aligned}$$

Thus, we have

$$\sum_{s=0}^{m} A_s \cdot (\sum_{t=0}^{m+n} G_{t-s}G_t) = \sum_{t=0}^{m+n} P_t \cdot G_t \quad (3.18)$$

Now we start using the concept of correlation, which measures the similarity of two functions (Sheriff and Geldart (1995) pp.285). It also shows how the similarity varies as we shift one trace with respect to the other. The mathematical definition of cross-correlation $\phi_{xy}(\tau)$ of two functions x_t and y_t is

$$\phi_{xy}(\tau) = \sum_{t=0} x_{t+\tau} y_t. \quad (3.19)$$

The definition implies that we shift the function x past the other by τ, then multiply the corresponding part of the two functions and sum for each value of t. The larger the value of $\phi(\tau)$ is, the more similar the two signals are at lag τ. Likewise, auto-correlation measures how a function correlates with itself shifted in time, and is defined as

$$\phi_{xx}(\tau) = \sum_{t=0} x_{t+\tau} x_t. \quad (3.20)$$

Returning to Equation 3.18, we use the correlation of input G_t and desired signal P_t and the auto-correlation of G_t as

$$\begin{aligned}
\phi_{PG}(0) &= \sum_{t=0}^{m+n} P_t \cdot G_t && (3.21)\\
\phi_{GG}(s) &= \phi_{GG}(-s) = \sum_{t=0}^{m+n} G_{t-s}G_t. && (3.22)
\end{aligned}$$

Notice that auto-correlation is an even function. Equation 3.18 becomes,

$$\sum_{s=0}^{m} A_s \cdot \phi_{GG}(s) = \phi_{PG}(0). \quad (3.23)$$

Equation 3.23 comes from the partial derivative of error energy by the first coefficient A_0 of the filter. Similar results can be obtained from the remaining differential equations of Equation 3.11, which implies

$$\sum_{s=0}^{m} A_s \cdot \phi_{GG}(i-s) = \phi_{PG}(i) \qquad i = 0, 1, 2, ..., m. \tag{3.24}$$

The above equations can be written in a matrix form, which is

$$\begin{bmatrix} \phi_{GG}(0) & \phi_{GG}(1) & ... & \phi_{GG}(m) \\ \phi_{GG}(1) & \phi_{GG}(0) & ... & \phi_{GG}(m-1) \\ \vdots & \vdots & \vdots & \vdots \\ \phi_{GG}(m) & \phi_{GG}(m-1) & ... & \phi_{GG}(0) \end{bmatrix} \begin{bmatrix} A_0 \\ A_1 \\ \vdots \\ A_m \end{bmatrix} = \begin{bmatrix} \phi_{PG}(0) \\ \phi_{PG}(1) \\ \vdots \\ \phi_{PG}(m). \end{bmatrix} \tag{3.25}$$

The above set of equations is the most important relationship in the Wiener filter method. From these equations, filter A_t can be solved by using the Toeplitz recursion (Robinson and Treitel (1980)).

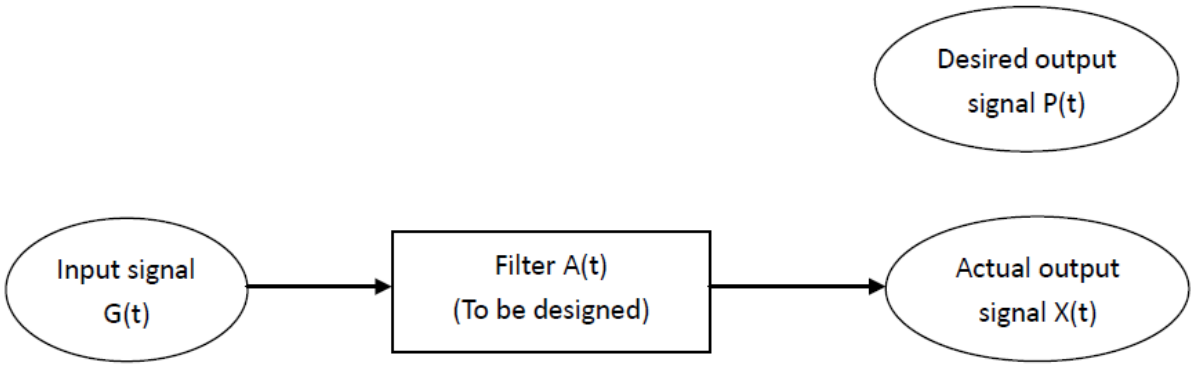

Figure 2: Wiener filter method

3.2 Detailed steps

Now we go back to the beginning. The specific steps of doing wavelet estimation using the Wiener filter method are as follows.

1. Prepare the reference Green's function (input signal) as a discrete series $(G_0, G_1, G_2, ..., G_n)$ with length n+1, and the reference wave (desired signal) as a discrete series $(P_0, P_1, P_2, ..., P_{m+n})$ with length m+n+1. Assume that the length of the filter (the wavelet) is m+1. In the case of Kristin data's case, we assume that the wavelet has 501 discrete points.

2. Calculate the auto-correlation of input signal $(G_0, G_1, G_2, ..., G_n)$ for a lag from 0 to m, i.e.,

$$\phi_{GG}(0) \quad = \quad \sum_{t=0}^{n} G_t \cdot G_t = G_0^2 + G_1^2 + G_2^2 + ... + G_n^2 \tag{3.26}$$

$$\phi_{GG}(1) = \sum_{t=0}^{n-1} G_t \cdot G_{t+1} = G_0G_1 + G_1G_2 + G_2G_3 + ...G_{n-1}G_n \tag{3.27}$$

$$\vdots \tag{3.28}$$

$$\phi_{GG}(m) = \sum_{t=0}^{n-m} G_t \cdot G_{t+1} = G_0G_m + G_1G_{m+1} + ... + G_{n-m}G_n. \tag{3.29}$$

3. Calculate the cross-correlation of the desired signal $(P_0, P_1, P_2, ..., P_{m+n})$ and the input signal $(G_0, G_1, G_2, ..., G_n)$ for a lag from 0 to m, i.e.,

$$\phi_{PG}(0) = \sum_{t=0}^{n} P_t \cdot G_t = P_0G_0 + P_1G_1 + P_2G_2 + ... + P_nG_n \tag{3.30}$$

$$\phi_{PG}(1) = \sum_{t=0}^{n-1} P_t \cdot G_{t+1} = P_0G_1 + P_1G_2 + P_2G_3 + ...P_{n-1}G_n \tag{3.31}$$

$$\vdots \tag{3.32}$$

$$\phi_{PG}(m) = \sum_{t=0}^{n-m} P_t \cdot G_{t+1} = P_0G_m + P_1G_{m+1} + ... + P_{n-m}G_n. \tag{3.33}$$

4. Plug all the ϕ_{GG} and ϕ_{PG} into Equations 3.25. Using the Toeplitz recursion, the coefficients of filter $(A_0, A_1, A_2, ..., A_m)$ can be solved. In this way the wavelet signature is estimated.

4 Relationship with spectral division method

As we introduced in the beginning of this report, the wavelet can also be estimated using spectral division. The equation for this method is

$$A(\omega) = \frac{P_0(\omega)}{G_0(\omega)}. \tag{4.1}$$

It comes from the relationship of recorded data P_0, G_0 and A in the time domain

$$P_0(t) = A(t) * G_0(t), \tag{4.2}$$

where $*$ means convolution. Now we will show that starting from the above convolution and utilizing the definition of correlation, we can get the equations that the Wiener filter method uses. First we correlate the trace $P_0(t)$ with the Green's function, according to the definition of correlation in the integral form,

$$\phi_{PG}(t) = \int_{-\infty}^{\infty} P_0(\tau + t)G_0(\tau)d\tau \tag{4.3}$$

$$= \int_{-\infty}^{\infty} P_0(\tau)G_0(\tau - t)d\tau \tag{4.4}$$

$$= \int_{-\infty}^{\infty} P_0(\tau) G_0[-(t-\tau)] d\tau \tag{4.5}$$

$$= P_0(t) * G_0(-t). \tag{4.6}$$

Next, plug Equation 4.2 into the above equation, and we have

$$\phi_{PG}(t) = (A(t) * G_0(t)) * G_0(-t) \tag{4.7}$$

$$= A(t) * (G_0(t) * G_0(-t)) \tag{4.8}$$

$$= A(t) * \phi_{GG}(t) \tag{4.9}$$

$$= \int_{-\infty}^{\infty} A(\tau) \phi_{GG}(t-\tau) d\tau. \tag{4.10}$$

Compare this with Equation 3.24, which says

$$\sum_{s=0}^{m} A_s \cdot \phi_{GG}(i-s) = \phi_{PG}(i) \qquad i = 0, 1, 2, ..., m \tag{4.11}$$

and we can see that these two equations are actually the same, one in discrete form, the other in continuous form.

The biggest difference between these two methods is that the Wiener filter method involves the statistical characters of the reference wave and Green's function, such as auto-correlation and cross-correlation coefficients. This unique feature makes the estimation result more stable and reliable than that with the spectral division method. In the following test, we generate synthetic data P_0 using a Ricker wavelet, as shown in Figure 3 (a). Then a Gaussian noise with an SNR=20 is applied to the data, as shown in 3 (b). This simulates the background noise in the seismic recording system. Using the noisy data, we predict the wavelet using both the Wiener filter method and the spectral division method. The estimated wavelet is shown in 4. It is clearly seen from the result that the output of the Wiener filter method is better than that of the other method, with much less noise and good stability.

5 Conclusions and future plan

The Wiener filter is a very powerful tool in seismic data processing. In this report we introduce the derivation of the Wiener filter's equations using the least-square method. Also, we present the specific steps of wavelet estimation from Kristin data, using the information of the reference wave and Green's function. To facilitate an understanding of the Wiener filter from another perspective, the relationship between wavelet estimation using the Wiener filter method and estimation by spectral division are presented. Running a preliminary synthetic test, we observe that the Wiener filter method produces a better result than the spectral division does. Thus, the Wiener filter method can deal with the pproblem of background measurement noise in the reference wave better. Further study in the noise-reduction issue is needed in the future.

The Wiener filter can also be used in other areas of seismic processing. If we exchange the position of the wavelet and of Green's function in this report, which means to treat the response of the earth as a shaping filter that shapes the wavelet so that it is the recorded trace, and we still follow the same steps to do the deconvolution, we can actually deconvolve the wavelet from the recorded data. This is also a very common and useful application of the Wiener filter in seismic data processing.

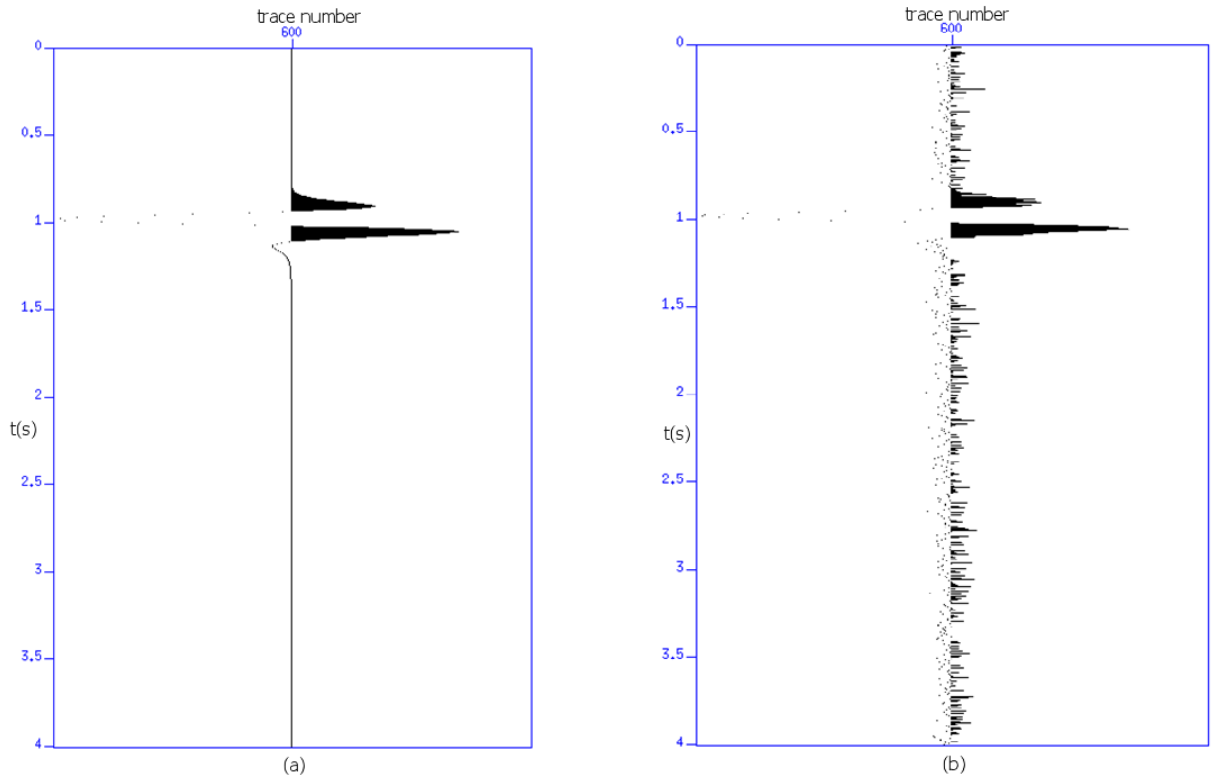

Figure 3: Reference wave P_0 (a) without noise (b) with Gaussian noise, SNR=20

6 Acknowledgments

We are grateful to all M-OSRP sponsors for their long-term encouragement and support in this research. The first author would like to thank Dr. Paolo Terenghi for his helpful advice during the test and for his many suggestions for this report. Di Chang is also appreciated for her helpful feedback on this report. The first author extends her deepest gratitude to Dr. Weglein for his guidance, encouragement and support.

References

Liu, F., X. Li, and A.B. Weglein. "Field data test in Kristin: demonstrating viability." *Mission-Oriented Seismic Research Program Annual Report* (2010): 51–80.

Robinson, Enders A and Sven Treitel. *Geophysical signal analysis.* Englewood Cliffs, N.J.Prentice-Hall, 1980.

Sheriff, R E and L P Geldart. *Exploration Seismology.* 2nd edition. Cambridge University Press, 1995.

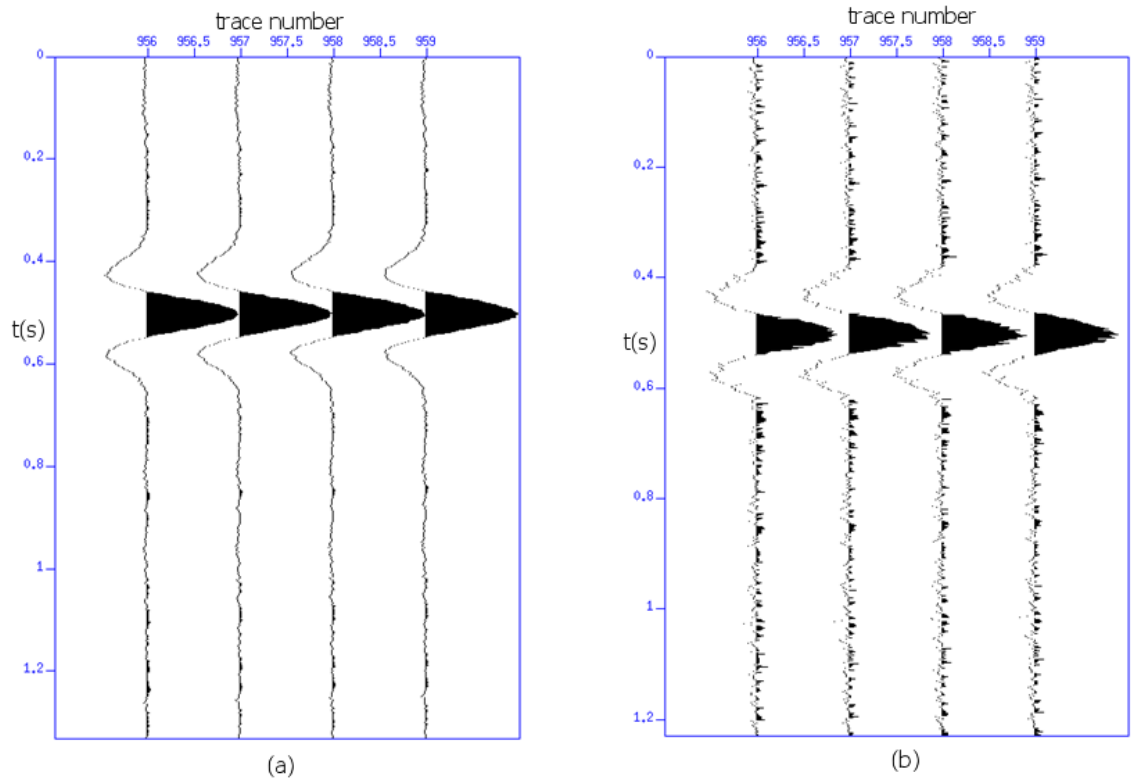

Figure 4: Wavelet estimation result using (a) Wiener filter method (b) spectral division method

Tang, L., A.B. Weglein, P. Terenghi, and J.D. Mayhan. "Wavelet estimation from the reference wave in the Kristin data set." *Mission-Oriented Seismic Research Program Annual Report* (2010): 29–35.

Vaseghi, Saeed V. *Advanced digital signal processing and noise reduction.* 4th edition. Chichester, U.K. : J. Wiley Sons, 2008., 2008.

Weglein, Arthur B. and Bruce G. Secrest. "Wavelet estimation for a multidimensional acoustic earth model." *Geophysics* 55 (July 1990): 902–913.

Wiener, Norbert. *Extrapolation, interpolation, and smoothing of stationary time series : with engineering applications.* Cambridge, MA : Technology Press of the Massachusetts Institute of Technology, 1949.

Part I: Addressing issues of band-limited data in multiparameter ISS imaging; Part II: Advances in finite-difference modeling

Fang Liu and Arthur B. Weglein

May 25, 2012

Abstract

We propose an algorithm that can remove the density contribution from multiparameter acoustic data in the same fashion as is predicted in Weglein (2009). The method uses an $\frac{\partial}{\partial\theta}$ operation that technically involves division by a denominator tending to zero. We apply the technique that benefits from the lesson of Weglein and Secrest (1990) and express the division as an integral over the measurement surface. The quantity we compute is called $\alpha_1 - \beta_1$ in M-OSRP and is very similar to the B parameter (AVO gradient) in AVO analysis. We hope this technique will benefit the current AVO analysis.

A regularization method is derived to cope with the bandlimited nature of the seismic source. The method proposed in this report solves exactly the same issue as that in Liu and Weglein (2010), but for different situations. The current situation can be considered the same as $\Delta\theta \to 0$ in Liu and Weglein (2010). The regularization method requires the wavelet information but is independent of the subsurface information.

The effectiveness of the density separation procedure is demonstrated by finite-difference data in the xt domain. We studied the accuracy of finite difference to give a quantitative measure of the error of our input data. One of the most important conclusions is that extra attention should be paid to the boundary conditions for a discontinuous medium. We hope our result will benefit the reverse time migration (RTM) research in and outside M-OSRP, and also our future elastic finite-difference modeling.

To further extend the aforementioned density separation to the case of an elastic medium, the first step is to implement the elastic P- and S-wave sources. Sections 7 and 8 provide the derivation and numerical examples for this objective.

Velocity-depth ambiguity is a fundamental issue faced by all imaging algorithms. The literature on this topic argues mostly in terms of traveltime in the xt domain, a term that seldom enters into our imaging procedures. We study this issue by testing one of the geological models with large lateral variations in Stork and Clayton (1992) and Ross (1994). Although our result is not perfect, we do not observe any further surprises other than what we had observed with the existing geological models with big lateral variations. One notable observation is that a deeper velocity anomaly is not estimated with reduced accuracy, contrary to the conclusions in other literature.

1 Introduction

The inverse scattering series (ISS) needs the amplitude and phase information to achieve direct non-linear imaging at depth without using the actual velocity model. For a model with only velocity variation, the effectiveness of the ISS in imaging without an actual velocity model has been demonstrated for an acoustic model with large contrast and a large duration of velocity perturbation. But if density variation is introduced, the density contribution to the amplitude has to be removed in order for the imaging structure of the velocity-only ISS imaging formula to remain effective. Consequently, the concept of $\alpha_1 - \beta_1$ (Weglein, 2009) is proposed to isolate the velocity contribution.

Combining the imaging structures from M-OSRP's previous $\alpha_1 - \beta_1$ calculation, and from one-parameter imaging, we proposed a procedure that starts to have the capability of getting rid of the density contribution, thereby making the input ready for the imaging subseries derived for the velocity-only model.

Unlike the ISS multiple-removal procedures from M-OSRP, the current ISS imaging algorithms are not model-type independent. Consequently, there is a model-type assumption (e.g., acoustic, elastic, isotropic, anisotropic) about our existing imaging algorithms. The major objective of this article is to extend the effectiveness achieved by ISS imaging in a velocity-only acoustic medium, to models that have density variations and are of elastic type, in the same fashion as was predicted in Weglein (2009). That is, the density contribution is removed without even ever calculating the density values.

The difficulties in M-OSRP's multiparameter imaging include

1. Although the functions α (the perturbation of bulk modulus) and β (the perturbation of density) expressing the subsurface geology are unique, the first step in their computation, i.e., α_1 (the linear estimation of α) and β_1 (the linear estimation of β), depends on the subset of input data and hence varies with the incident angle θ.

2. To decide the location of a reflector, $\alpha_1 - \beta_1$ calculation seems access the information from deeper layers, as indicated by Figure 1.

Our idea is to mitigate both aforementioned issues by shrinking $\Delta\theta$ (the difference between two angles of data) to zero.

1. The inverse series is neutral to and does not specify the choice of the magnitude of $\Delta\theta$, and $\alpha_1 - \beta_1$ is a function of $\Delta\theta$. We can reduce the arbitrariness of the choice by setting $\Delta\theta$ to zero.

2. From Figure 1, the smaller the value of $\Delta\theta$, the thinner the region is in which the issue of communication with deeper layers will occur. In the limiting case demonstrated in Figure 2 where $\Delta\theta = 0$, this region with a deeper communication issue becomes infinitely thin: exactly at the reflector depth.

M-OSRP's previous research on multiparameter imaging can be grouped into two categories,

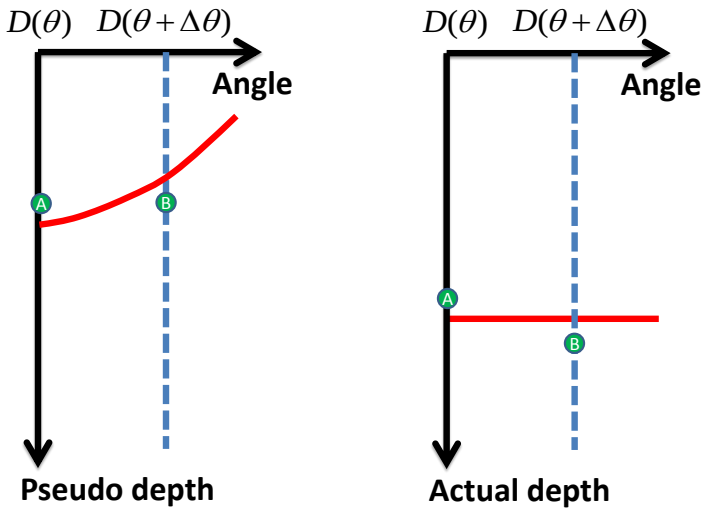

Figure 1: As displayed in the left panel, calculating $\alpha_1 - \beta_1$ at point A involves combining information from the locations indicated by A and B. A comes from $D(\theta)$ and B belongs to $D(\theta + \Delta\theta)$, both of which are located at the same pseudodepth. The red curve is the geological boundary. Note that A is above the boundary but B is below the boundary. Since $\alpha_1 - \beta_1$ at point A will be needed for the decision about the location of this reflector, it seems the information from the deeper layer (in this case from point B) is used to compute the location of this reflector. In the actual depth, the same scenario is shown in the right panel where the reflector is flat as it should be.

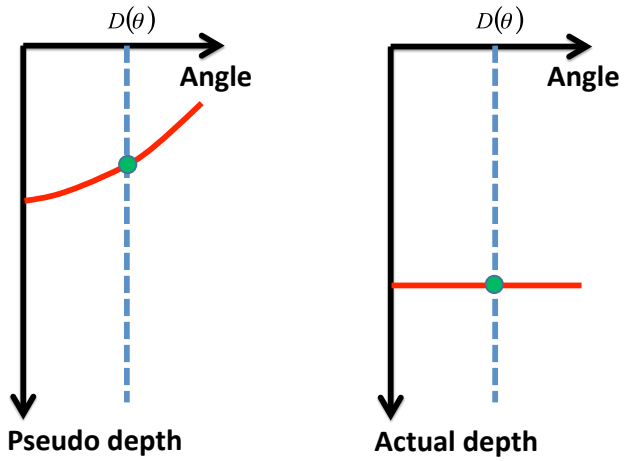

Figure 2: Note that the apparent communication with the deeper layer shown in Figure 1 happens when the points are close to the geological boundary. In this figure we show the worst-case scenario, where the point is exactly on the boundary. If the point is not on the boundary, communicating with deeper layers will not happen in this $\Delta\theta = 0$ scenario. The two points in Figure 1 coincide and are indicated by the single green circle both in the left and right panels. Shrinking $\Delta\theta$ has the effect of reducing the angle where the issue of communicating with deeper layers happens. In this case, $\Delta\theta = 0$, it seems that the only location where communication with deeper layers occurs is at the infinitely thin zone on the geological boundary.

- Li et al. (2008), Jiang et al. (2008), Wang et al. (2009); and Liang et al. (2009), using analytic data in the τp domain[1],
- Chang et al. (2010), who use input data from the xt-domain.

If we have the analytic data in the τp domain, fairly good imaging results can be obtained from very liberal choices of angle θ. Also, the authors generally prefer small $\Delta\theta$ (the difference between the angles of two sets of input data), to minimize communication with deeper layers. But if the data are in the xt domain, the data after a discrete Radon transform give a very unstable result when $\Delta\theta$ is too small. Just like the B parameter in AVO analysis, as is demonstrated in equation 1 of Swan (1997), $\alpha_1 - \beta_1$ which is the AVO gradient, is much harder to compute than the A parameter (intercept) is. When $\Delta\theta$ shrinks to very small values, the stability becomes a big issue since the quantity in the denominator $\tan^2(\theta + \Delta\theta) - \tan^2(\theta)$ is very close to zero.

A similar dilemma can be found in wavelet estimation. In many papers wavelet estimation is a procedure involving division by a quantity that shrinks to zero for some frequencies. A much stabler algorithm, for example that of Weglein and Secrest (1990), applies an integration over the measurement surface to construct a procedure with a very mitigated stability issue. In this article, a similar approach is used to convert the initially unstable division into an integral.

On the Basis of traveltime argument, the velocity-depth ambiguity issue has been studied by many authors. We received expressions of concern from many experts in the geophysics expert about the issue of velocity-depth ambiguities, stating that velocity and depth can be so inextricably tangled with each other that the objective of reaching actual depth is impossible. In order to better understand this issue, we have run one geological model designed for velocity-depth ambiguity with M-OSRP's imaging algorithm. Our result is not perfect, but the issues seem no bigger than those we had observed from previous models. The disruptive impact on some velocity-analysis procedures from this geological model with large lateral variation, is not observed in the imaging subseries of ISS.

It is hard and unfair to make a direct comparison of the final results. We have different objectives: In tomography, the velocity is the output; for ISS imaging, the depth is computed without evaluating the velocity.

The progress we made is based on the acoustic medium, and the extension to the elastic medium will be the focus of the future work.

Since the presence of shear waves will affect the amplitude of the seismic data, the impact of shear waves on the model-type assumption for ISS depth imaging cannot be ignored. Hence, the minimal realism for our imaging algorithm is an isotropic elastic model type (Liang et al., 2011). To study the imaging issues for an elastic medium, we need high-fidelity elastic data to isolate the imaging issues from modeling artifacts. Accurate implementation of the source wavelet is one of the key components in generating a wavefield that is physically consistent with the source signature assumed by the imaging procedure. The technical details can be found in section 7 and 8.

The major technical contributions of this article are:

[1] All these articles work with data with a fixed angle θ, and the τp transform is seldom mentioned. Conceptually, however, they use data in the τp-domain since θ relates to p by a simple formula: $p = \frac{\sin\theta}{c_0}$ where c_0 is the homogeneous reference velocity.

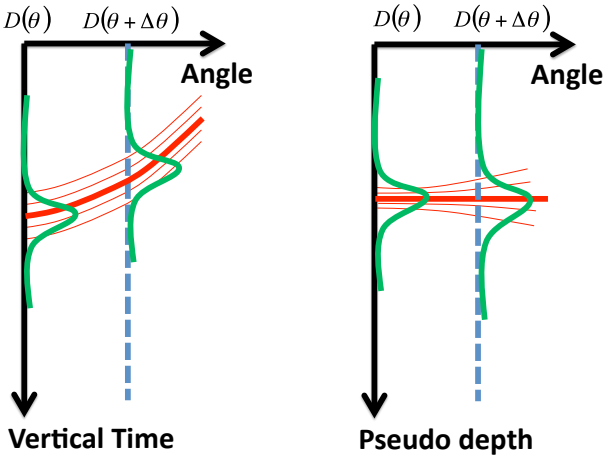

Figure 3: Need for regularization. The green curves show the event packet associated with the geological boundary (its spatial location is indicated by the thick red lines). Note that the event packet is not a perfect step (Heaviside) function; the thin red lines indicate the locations with the same phase in terms of the event packet. In this example, the thick red line in the left panel can be constructed by connecting the locations with maximal amplitude, and the thin red lines are parallel to the thick line and to each connecting location with the same phase as that of the event arrival (for example, half of the maximum amplitude, $\frac{1}{3}$ of the maximum amplitude, etc). In the left panel, the red lines are parallel to each other. But after conversion into the pseudodepth domain, as indicated by the right panel, the red lines are no longer parallel to each other. The tangent of the red lines indicates the direction in which, if the derivative is taken, there will be no regularization issue.

- Separation of density contributions from the amplitude of multiparameter acoustic data,
- Calculation of derivatives over θ from (x,t)-domain data using integration,
- Angle inconsistence regularization to deal with the bandlimited nature of the source wavelet,
- P- and S-wave source implementation for elastic finite-difference modeling, for the future study of elastic imaging,
- Accuracy analysis for finite difference modeling,
- Analysis of the impact of the velocity-depth ambiguity on the ISS imaging algorithms.

2 Notations and terminologies

We place a tilde sign above a function to denote its Fourier transform: for example, $\widetilde{f}$ is the Fourier transform of the function f.

c_0 is the reference velocity, p is the slope used in the Radon (or τp) transform,

$$\mathcal{D}(\tau,\theta) = \int_{-\infty}^{\infty} D\left(x, \tau + \frac{\sin\theta}{c_0}x\right) dx. \tag{2.1}$$

The transform above is just another way of writing the popular slant stacking by defining the angle θ in terms of the slope p as,

$$\theta = \arcsin(c_0 p), \tag{2.2}$$

and the pseudodepth z is defined from the vertical time τ with the help of c_0 (the reference velocity)[2],

$$z = \frac{c_0\tau}{2\cos\theta}. \tag{2.3}$$

The partial derivative of $\mathcal{D}$ with respect to θ can be computed as,

$$\frac{\partial\mathcal{D}(\tau,\theta)}{\partial\theta} = \int_{-\infty}^{\infty} \frac{x\cdot\cos\theta}{c_0} D\left(x, \tau + \frac{\sin\theta}{c_0}x\right) dx. \tag{2.4}$$

[2]The $\frac{1}{\cos\theta}$ is necessary if we require that, in the simplest case, (i.e., a reflector with homogeneous overburden velocity c_0), the reflector be flat in the pseudodepth z domain after undergoing a Radon transform.

In M-OSRP's previous research (for example, Zhang 2006; Li and Weglein 2010), the data are commonly expressed in the z (pseudodepth) domain: the vertical time τ is stretched by a factor $\frac{c_0}{2\cos\theta}$ to become pseudodepth, and the amplitude is modified by the reciprocal of the aforementioned factor to have[3]

$$\mathbb{D}(z,\theta) = \frac{-2\cos\theta}{c_0}\mathcal{D}\left(\frac{2z\cos\theta}{c_0}, \frac{\sin\theta}{c_0}\right). \tag{2.5}$$

In this report $\mathbb{D}$ will be used to denote the Radon-transformed data defined in equation 2.5.

An event in seismic data is a distinct arrival of wave energy. Seismic data consist of many kinds of events with very different types of wave histories, from their creation at the source to their measurement at the receiver. We define an event packet as the wave function associated with a seismic event.

In M-OSRP terminology the wavelet (or source signature) is defined as the temporal function in the source term in the wave equation, i.e., the function $f(t)$ in equation 2.6.

Wavelet is almost the same as an "event packet" in one situation: in 3D the event packet for the direct wave in the homogeneous medium is the same as the wavelet with an additional $\frac{1}{|\vec{r}_g - \vec{r}_s|}$ factor ($|\vec{r}_g - \vec{r}_s|$ is the distance of the receiver from the source).

Let us illustrate the difference between the concept of wavelet and event packet with the simplest types of event: the direct wave, which by definition is the event that corresponds to the wave propagating straight from the source to the receiver. With different definitions of $\vec{x}$ and ∇^2, equation 2.6 can express a wave equation in a homogeneous medium in any dimension. Since the medium is homogeneous, there is only the simplest type of event available: the direct wave.

$$\left(\nabla^2 - \frac{1}{c_0^2}\frac{\partial^2}{\partial t^2}\right) G_0\left(\vec{x}, t\right) = f(t)\delta\left(\vec{x}\right) \tag{2.6}$$

Let the wavelet in equation 2.6 be $f(t) = -\frac{t}{4a\sqrt{\pi}}\exp\left(-\frac{t^2}{4a^2}\right)$ where $a = 20\pi$. The time-domain function $f(t)$ is illustrated in Figure 4, and the corresponding event packets for a direct wave in various dimensions are shown in Figure 5. It is clear that even in the simplest case, the event packets are different from their corresponding wavelet. Extra attention should be paid to this subtle difference in order to maintain a logical and consistent view of phenomena in the development of theory, in the data processing chain, and in technical communications.

3 Issues of accuracy in finite-difference modeling

Multiparameter imaging with data in the xt-domain represents significant progress for M-OSRP and had been first reported in Chang et al. (2010). The major reasons for such significant progress are the following: (1) The data are numerically generated by finite-difference modeling with well-known

[3]This arrangement makes sure that, the total areas of the data calculated by integrating to infinity are the same in the (τ, z) domain. In other words, two definitions are equivalent in the Fourier domain $\widetilde{\mathbb{D}}(k_z = 2\omega/c_0) = \widetilde{\mathcal{D}}(\omega)$.

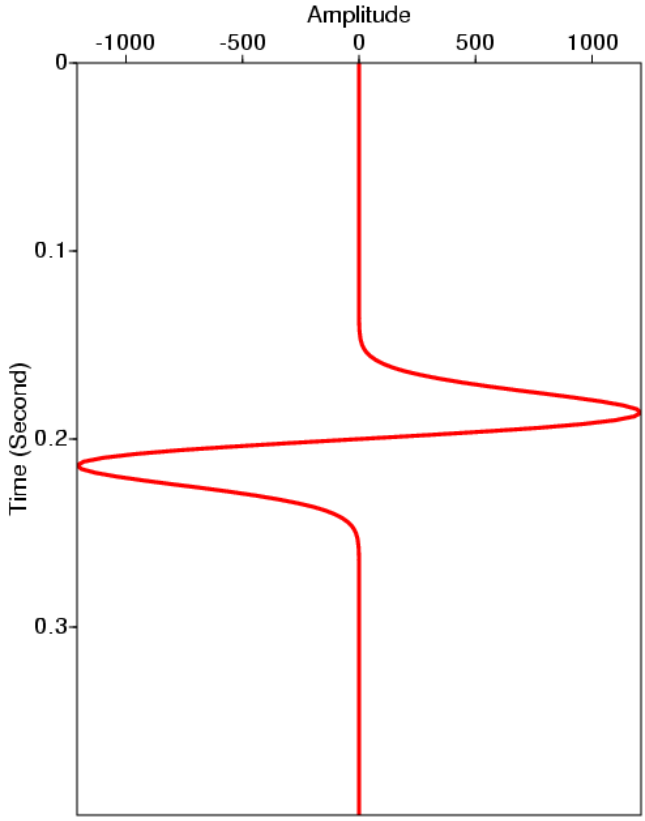

Figure 4: The time-domain wavelet (or source signature) used in all numerical examples in this article is the first-order derivative of a Gaussian function that lacks zero and high-frequency information.

Velocity (m/s)	Density ($\times 10^3$kg/m^3)	Depth Range
1500.0	1.0	$-\infty \sim 697.5$(m)
2000.0	1.0	697.5(m) $\sim \infty$

Table 1: An acoustic model without density variation.

Velocity (m/s)	Density ($\times 10^3$kg/m^3)	Depth Range
1500.0	1.0	$-\infty \sim 697.5$(m)
2000.0	2.0	697.5(m) $\sim \infty$

Table 2: An acoustic model with velocity and density variations. The velocity of this model is identical to that of the model listed in Table 1.

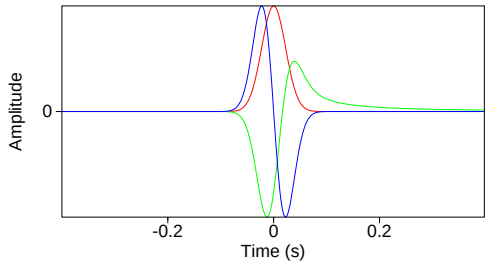

Figure 5: The event packets in three situations: Red, Green, and Blue are curves for 1D, 2D, and 3D respectively. In all three cases, the wavelet (illustrated in Figure 4) is the first derivative of a Gaussian function, which is of the same form as the 3D event packet (in blue). The event packet in 1D (red curve) is a Gaussian function, which is exactly the temporal integral of the wavelet function. The event packet in 2D (in green) has a tail that tapers off slowly. All curves are normalized between -1.0 and 1.0 to expedite visual comparison.

accuracy issues. (2) The numerical Radon transform with an interpolation procedure assumes the Nyquist sampling theorem, and it is well-known that in the x direction the Nyquist sampling theorem is not satisfied even for a wave propagated in the earth without any lateral variations. We have worried whether the accuracy of finite-difference modeling over a long time or insufficient sampling rate may be the issue.

The objective of this accuracy study is to better understand this issue at various stages of the process, for example, where the issue comes from, how we can improve the situation, etc. Another objective of this effort is the potential benefit for M-OSRP's research in reverse time migration (RTM).

- A finite-difference scheme fourth-order in space and second-order in time is used; see equation 8 of Alford et al. (1974) for details.
- The source signature can be found in Figure 4 and is the first-order derivative of a Gaussian function. The formula used to compute the frequency domain's analytic wavefield is equation 7.5 with α_0 set to c_0, and two inverse Fourier transforms at time $t = 89.5(\texttt{ms})$ and $t = 90(\texttt{ms})$ are used to construct the initial conditions for the finite difference scheme.
- The modeling parameters used are: $\Delta x = \Delta z = 5(\texttt{m})$, $\Delta t = 0.5(\texttt{ms})$.

There are many possibilities for the error we observed from the reflection data that were generated by finite-difference modeling:

- Source implementation.
- Propagation in each individual medium.

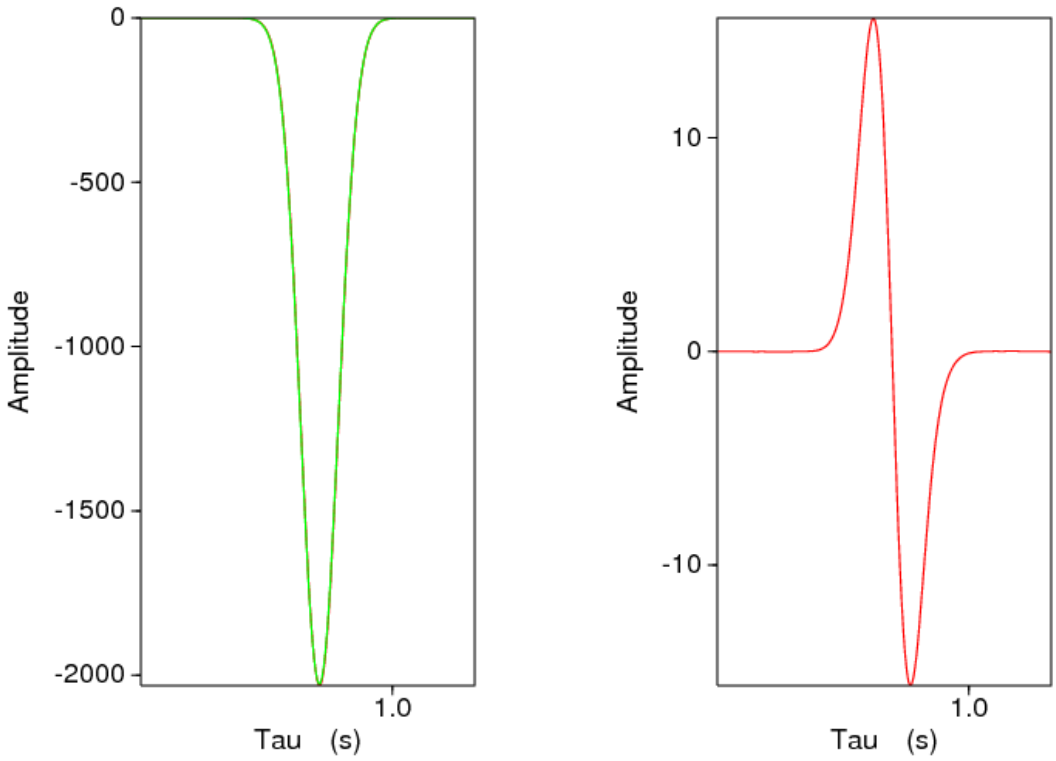

Figure 6: The precision of reflection data after a Radon transform. Left: the analytic result is shown by the green curve, the red curve, obtained through a numerical Radon transform on xt-domain reflection data, is barely visible since it is hidden behind the green curve. Right: the difference between the red and green curves in the left panel. In both panels, the horizontal axis is the vertical time (τ), and the vertical axis is the amplitude. The accuracy after a Radon transform is around 0.7%. The geological model is listed in Table 1 with $z_s = -2.5(\mathtt{m})$, $z_g = 0$, and the source wavelet is the one in Figure 4.

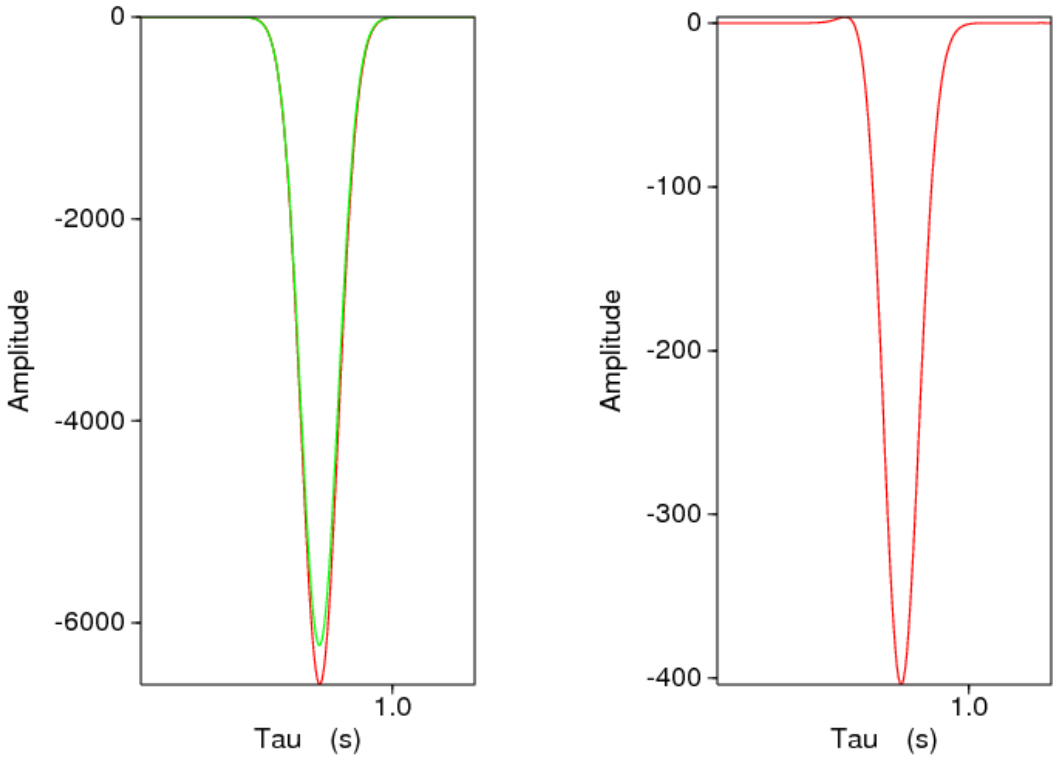

Figure 7: The precision of reflection data after a Radon transform. Left: the analytic result is shown by the green curve; the red curve, obtained through a numerical Radon transform on xt-domain reflection data, is clearly visible since it is no longer hidden behind the green curve. Right: the difference between the red and green curves from the left panel. In both panels, the horizontal axis is the vertical time (τ), and the vertical axis is the amplitude. The accuracy after a Radon transform is around 7%. This geological model has density variation and is listed in Table 2 with $z_s = -2.5(\mathtt{m})$, $z_g = 0$, and the source wavelet is the one in Figure 4.

- Implementation of boundary conditions.
- Sampling rates Δx and Δt may not be fine enough for the Radon transform.

We noticed that although the finite-difference scheme in equation 8 of Alford et al. (1974) is naturally adaptable for an inhomogeneous medium, it is a better approximation to the wave equation if the velocity is homogeneous. It seems that the propagation in the homogeneous medium is very accurate.

We tested a reflection problem without any lateral variations so an easy benchmark after the Radon transform can be easily made. The conclusions for the accuracy issues of finite-difference modeling are,

1. From Figure 8 and Figure 9, it is obvious that the finite-difference propagation in both homogeneous media produces errors much smaller than those that are observed in reflection experiments.
2. We can see the results in Figure 10 for measurement with slow lateral variation, and in Figure 11 for measurement with rapid lateral variation. The Radon transform with sampling interval $\Delta x = 5(\mathtt{m})$ obtains a τp-domain result with very good accuracy. This excludes one of the worst worries: our processing procedure and its associated spatial sampling intervals are not a contributing factor for the error.
3. Since the analytic reflection data in the xt-domain are much harder to obtain, we only compared the results in τp-domain.
4. It seems unlikely that the combination of the three factors: (1) source implementation, (2) the propagation in the first medium, and (3) the propagation in the second medium can generate the error we observed in the reflection data in the τp-domain. The only remaining factor, implementation of the reflection boundaries, must be the major contributor to the error.

4 Separation of the density contribution in a multiparameter acoustic medium

Extensive research in ISS imaging for a single-parameter acoustic medium, for example the work of Weglein et al. (2000, 2002), Shaw et al. (2003), Innanen (2004), Shaw (2005), Liu et al. (2005), and Liu (2006), proposed and identified imaging capabilities that take amplitude and phase information without the density contribution. However, if the density contribution to the amplitude of the reflection data is present, it has to be removed for the current one-parameter algorithms to be effective.

Let us review one concept first proposed in Zhang and Weglein (2003). It has been termed $\alpha_1 - \beta_1$ ever since it was introduced in M-OSRP's multiparameter imaging. The major objective of $\alpha_1 - \beta_1$ is to isolate the velocity contribution. One major characteristic of $\alpha_1 - \beta_1$ is that it vanishes for a 1D medium without velocity variation. Also it is the cornerstone for ISS multiparameter imaging research; see, for example, Jiang and Weglein (2007), Li et al. (2008), Jiang et al. (2008), Li and Weglein (2010), Wang et al. (2009), and Liang et al. (2009).

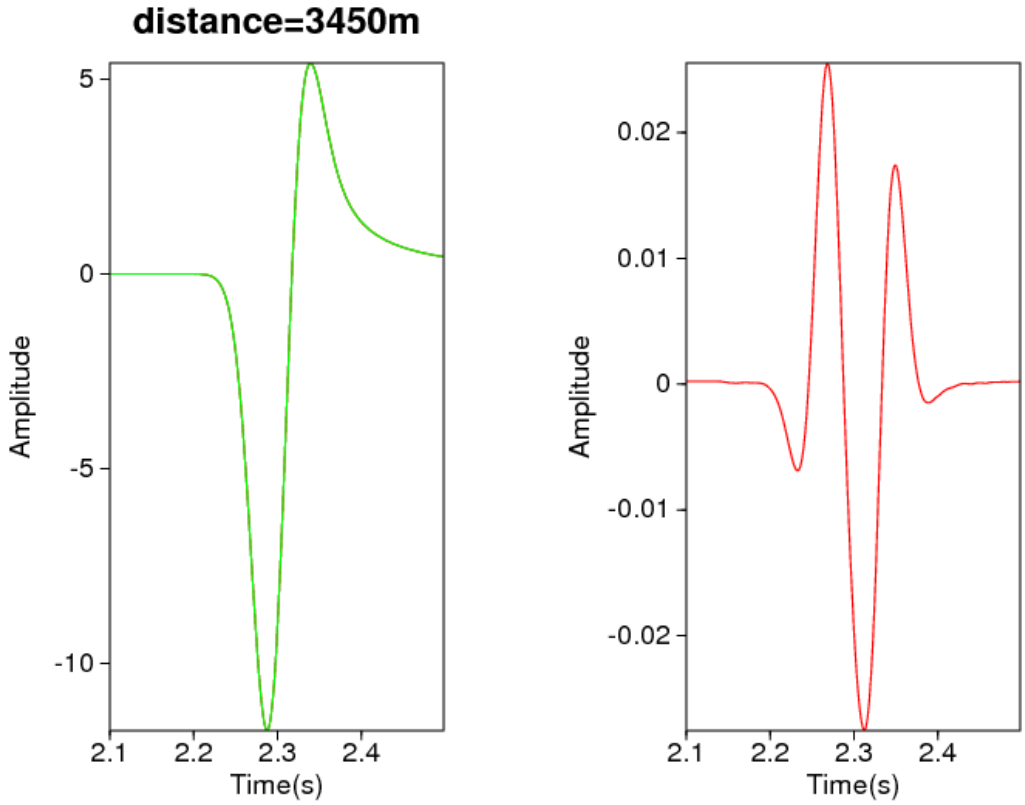

Figure 8: Left: The direct arrival for a wave propagating in a homogeneous medium with $c_0 \equiv 1500\mathtt{m/s}$. Red: analytic result, Green: obtained through finite-difference modeling. The test offset (source-receiver distance) is 3450(m). The accuracy of finite difference is good for this homogeneous medium: the red line is visually hidden behind the almost identical green curve. Right: the difference between the red and green curves to illustrate the error in finite difference modeling. The relative magnitude of the finite-difference error is smaller than 0.2%.

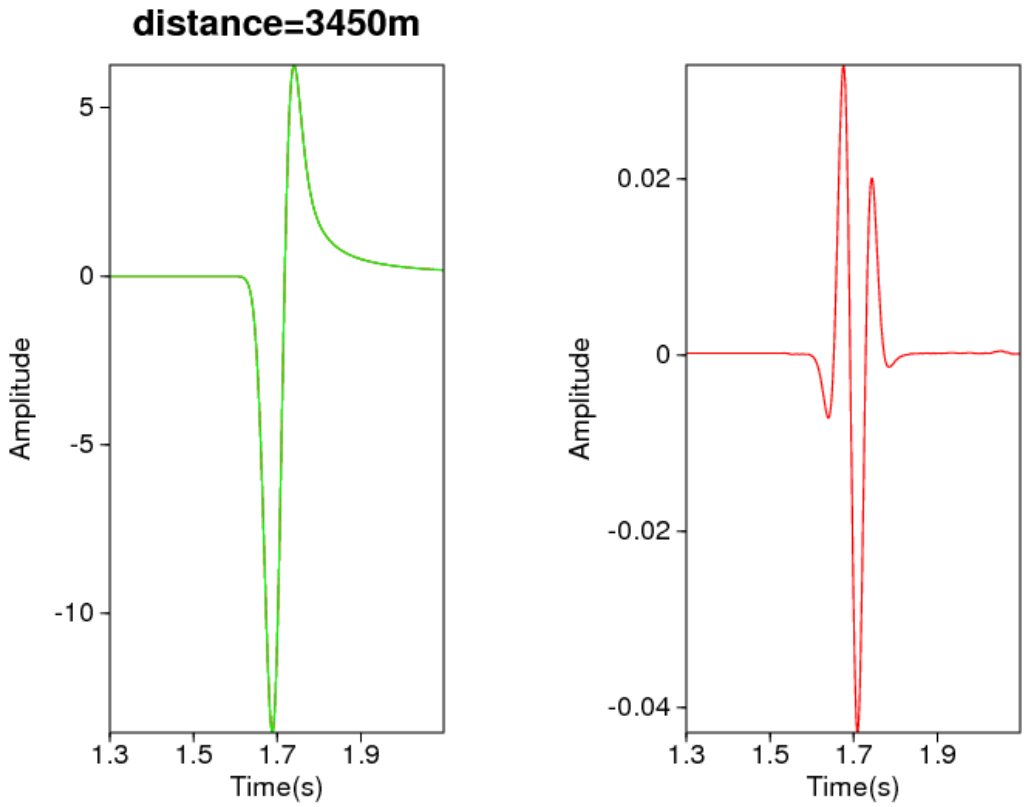

Figure 9: Left: The direct arrival for a wave propagating in a homogeneous medium with $c_0 \equiv 2000\mathtt{m/s}$. Red: analytic result, Green: obtained through finite-difference modeling. The test offset (source-receiver distance) is 3450(m). The accuracy of finite difference in this case is worse than the previous example shown in Figure 8. Right: the difference between the red and green curves to illustrate the error in finite difference modeling. The relative magnitude of the finite-difference error is around 0.4%.

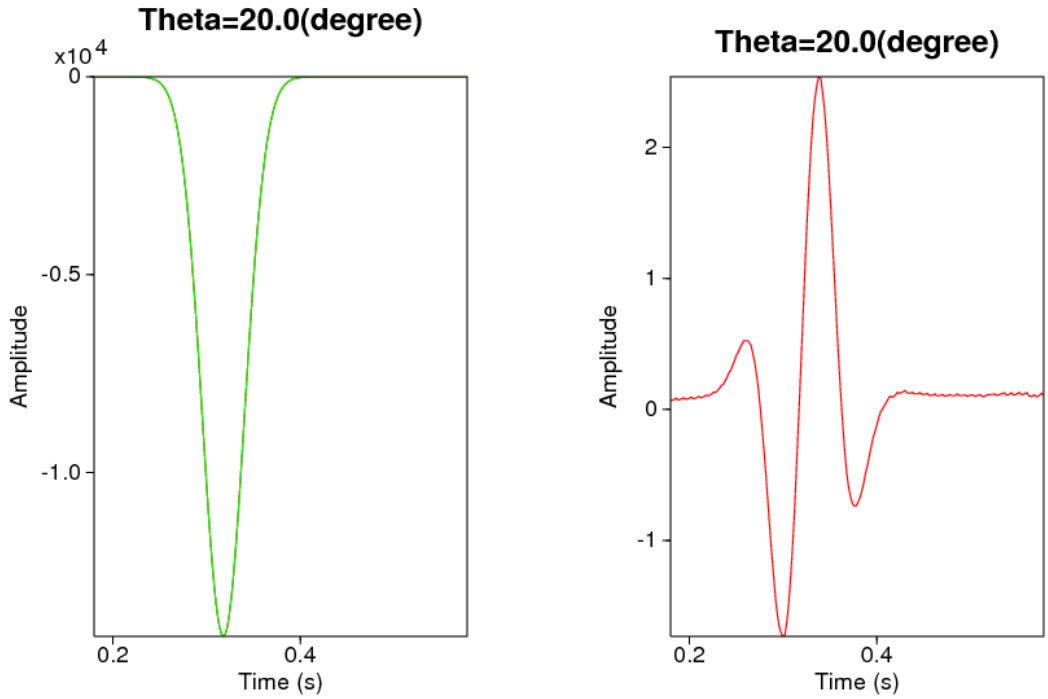

Figure 10: Left: red line is the analytic result, green line is obtained through a digital Radon transform after finite-difference modeling. In this case the measurement surface is deep: $z_g = 507.5(\mathtt{m})$. The red line is completely covered by the green line. Right: the difference between the red and green curves on the left. The relative error is around 0.02%. It demonstrates that the Radon transform with a sampling rate of $\Delta x = 5(\mathtt{m})$ produces very small errors for data (shown in top right panel of Figure 12) with mild lateral changes.

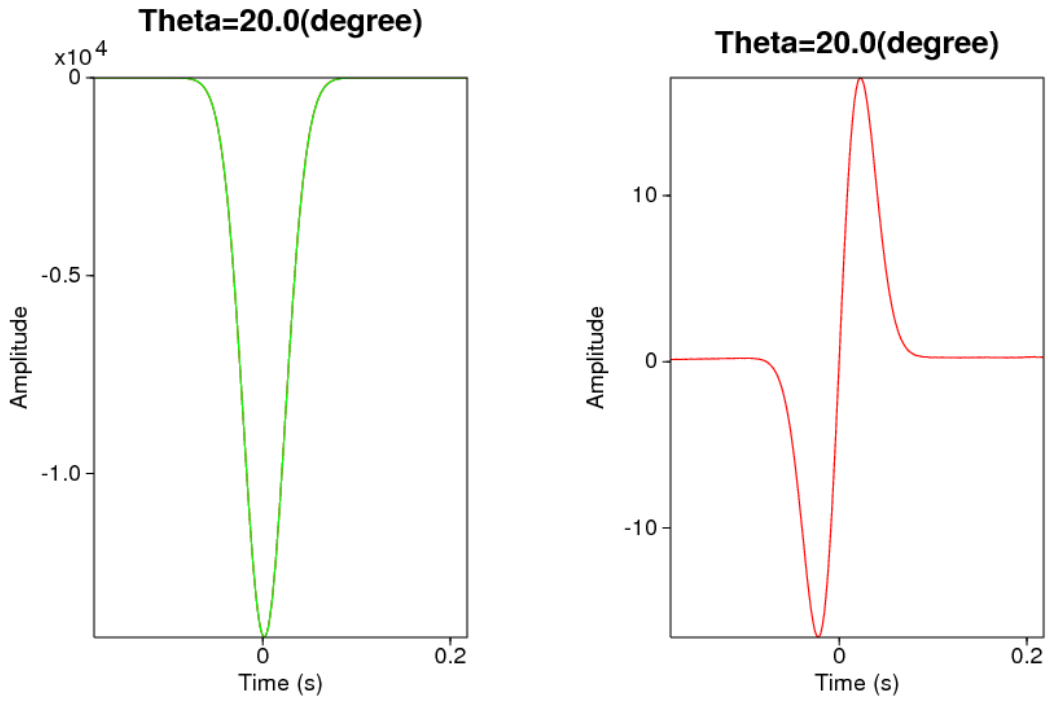

Figure 11: Left: red line is the analytic result, green line is obtained through a digital Radon transform after finite-difference modeling. In this case, the measurement surface is shallow: $z_g = 2.5(\mathtt{m})$. The red line is again completely covered by the green line. Right: the difference between the red and green curves on the left. The relative error is around 0.1%. It demonstrates that a Radon transform with a sampling rate of $\Delta x = 5(\mathtt{m})$ is good enough for shallow z_g where the xt-domain data (shown in the top left panel of Figure 12) have a very fast lateral change especially in the middle (near the source).

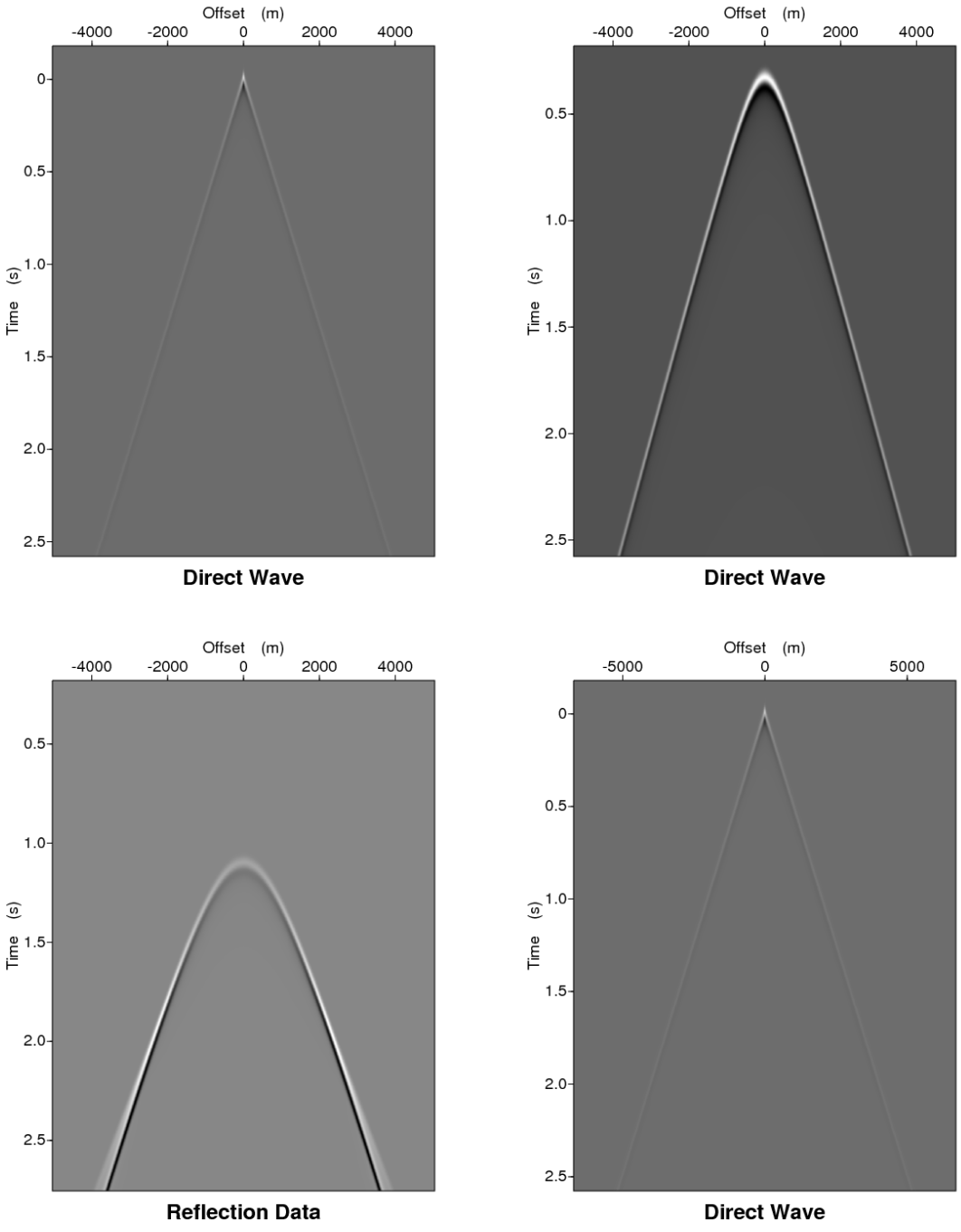

Figure 12: The shot gathers for various geological models and receiver depths, $z_s = 0(\mathtt{m})$ in all four cases. Top left: $c \equiv 1500(\mathtt{m/s})$, $z_g = 2.5(\mathtt{m})$. Top right: $c \equiv 1500(\mathtt{m/s})$, $z_g = 507.5(\mathtt{m})$. Bottom left: reflection data for the model in Table 1 and $z_g = 2.5(\mathtt{m})$. Bottom right: $c \equiv 2000(\mathtt{m/s})$, $z_g = 2.5(\mathtt{m})$.

First let us look at the most basic formula, i.e., equation 3.11 of Zhang (2006). Taking the reference density $\rho_0 = 1$, and with both the source and receiver depth being zero: $z_s = z_g = 0$, we have,

$$\frac{1}{\cos^2\theta}\alpha_1(z) + \left(1 - \tan^2\theta\right)\beta_1(z) = D(z,\theta). \tag{4.1}$$

It can be rewritten as,

$$\left(1 + \tan^2\theta\right)\alpha_1(z) + \left(1 - \tan^2\theta\right)\beta_1(z) = D(z,\theta), \tag{4.2}$$

to expedite the reparameterization process later.

For the objective of imaging, we are interested in $\alpha_1 - \beta_1$, which is the indicator of velocity change, and its conjugate variable $\alpha_1 + \beta_1$ as[4],

$$[\alpha_1(z) + \beta_1(z)] + \tan^2\theta\,[\alpha_1(z) - \beta_1(z)] = D(z,\theta). \tag{4.3}$$

In equation 4.3, there are two unknowns, $\alpha_1(z) + \beta_1(z)$ and $\alpha_1(z) - \beta_1(z)$. They can be solved if this relation is available in another angle $\theta + \Delta\theta$,

$$[\alpha_1(z) + \beta_1(z)] + \tan^2(\theta + \Delta\theta)\,[\alpha_1(z) - \beta_1(z)] = D(z,\theta + \Delta\theta). \tag{4.4}$$

And consequently, the solution of the velocity variation $\alpha_1(z) - \beta_1(z)$ obtained by combining two equations above, is[5],

$$\alpha_1(z) - \beta_1(z) = \frac{D(z,\theta + \Delta\theta) - D(z,\theta)}{\tan^2(\theta + \Delta\theta) - \tan^2(\theta)}. \tag{4.5}$$

Note that the logic above is not perfectly smooth; there are some subtleties worth special attention. Even in ISS with only one parameter, α_1 is also a function of angle θ. In one-parameter imaging, the θ dependency of α_1 is not an issue since the only unknown quantity $\alpha_1(\theta)$ can be sufficiently solved by the corresponding data from that angle $\mathbb{D}(\theta)$.

There are practical difficulties if this θ dependency is added here: there will be four unknowns for equations 4.3 and 4.4, and two equations cannot be combined to obtain a solution. We have to assume that they are not functions of θ, in order to obtain an explicit solution from measured data.

It is very easy to prove that no linear combination of data will get rid of the density contribution since the density contribution to the amplitude of the data is nonlinear[6]. That fact has often been regarded as a headache indicating that our formalism is wrong, and our concept of $\alpha_1 - \beta_1$ is not defined. On the other hand, we should not ignore the positive message it provides. This seemingly

[4] $\alpha_1 - \beta_1$ and $\alpha_1 + \beta_1$ can be viewed as 45°-degree rotations of the original (α_1, β_1) coordinate.

[5] a similar approach can be found in equation 26 of Clayton and Stolt (1981), where α_1 and β_1 are solved by combining data from two or more k_h values. In this article, α_1 is termed a and β_1 is termed b, but conceptually they are exactly the same.

[6] This non-linearity is evident even for the simplest reflection coefficient in equation 5.13.

unfortunate inconsistency is actually our very lucky observation for the incomplete view of the new imaging structure. In equation 4.6, it had already provided us with structures beyond the $\frac{\partial}{\partial\theta}$ operation in the arsenal of the standard differential calculus.

Historically this type of inconsistency often caused skepticism in the beginning. For example, in the old days when all numbers were supposed to be the ratio of any two integers, the existence of $\sqrt{2}$ caused lots of pessimism. Today, however, it constitutes no threat for the human being using it in whatever form of application.

As another example, velocity is defined as the ratio of the distance traveled to the time elapsed (i.e., the traveltime). However, we always obtain a different value when we change the duration of measurement. It seems the concept itself is challenged in the world with acceleration. This is very similar to the issue for multiparameter imaging. The key step to solving the inconsistency problem in the concept of velocity is to shrink the duration to zero to obtain instantaneous velocity, where the free choice of duration is restricted to a quantity approaching zero.

$\alpha_1 - \beta_1$ in the current linear form already contains two categories of information: (1) amplitude variation with respect to angle, and (2) curvature information indicating the inaccuracy of the reference velocity. Currently M-OSRP's existing algorithms focus on the amplitude change, but the curvature information may become the central part of our new imaging algorithms using spike-moving logic.

One solution is to let $\Delta\theta$ shrink to zero, and by doing so, the difference of $\alpha_1 - \beta_1$ caused by angles is minimized.

$$\begin{aligned}\alpha_1(z) - \beta_1(z) &= \lim_{\Delta\theta\to 0} \frac{\mathbb{D}(z,\theta+\Delta\theta) - \mathbb{D}(z,\theta)}{\tan^2(\theta+\Delta\theta) - \tan^2(\theta)} \\ &= \lim_{\Delta\theta\to 0} \frac{\mathbb{D}(z,\theta+\Delta\theta) - \mathbb{D}(z,\theta)}{\Delta\theta} \div \frac{\tan^2(\theta+\Delta\theta) - \tan^2(\theta)}{\Delta\theta} \\ &= \frac{\partial\mathbb{D}(z,\theta)}{\partial\theta} \div \frac{\partial\tan^2\theta}{\partial\theta} = \frac{\cos^3\theta}{2\sin\theta}\frac{\partial\mathbb{D}(z,\theta)}{\partial\theta}\end{aligned} \tag{4.6}$$

Several characteristics of $\alpha_1 - \beta_1$ can be summarized as follows:

- From equation 4.6, it is clear that the derivative of data $\mathbb{D}$ can play a very important role in separating out the density contribution.
- $\alpha_1 - \beta_1$ vanishes if the velocity does not change.
- If the velocity does change, the density contribution remains according to the analytic data in equation 4.22.

According to the definition of the pseudodepth domain data in equation 2.5, the Radon transform to calculate our specifically defined data is,

$$\mathbb{D}(z,\theta) = \frac{-2\cos\theta}{c_0} \int\limits_{-\infty}^{\infty} xD\left(x, \frac{2z\cos\theta + x\sin\theta}{c_0}\right) dx. \tag{4.7}$$

The derivative of $\mathbb{D}$ over the angle is,

$$\begin{aligned}\frac{\partial\mathbb{D}(z,\theta)}{\partial\theta} = &\frac{2\sin\theta}{c_0} \int\limits_{-\infty}^{\infty} D\left(x, \frac{2z\cos\theta + x\sin\theta}{c_0}\right) dx \\ &- \frac{2\cos\theta}{c_0^2} \int\limits_{-\infty}^{\infty} D_t\left(x, \frac{2z\cos\theta + x\sin\theta}{c_0}\right) \cdot [x\cos\theta - 2z\sin\theta]\, dx,\end{aligned} \tag{4.8}$$

where D_t is the partial derivative of the data in the (x,t) domain over t. Expressed in the pseudo-depth domain, the expression above vanishes for models without velocity variation and ideal source with infinite bandwidth. If the source is bandlimited, the expression above does not vanish even for models without velocity variation, as is demonstrated in Figure 3 and 16. In order to compensate for the bandlimited wavelet, a regularization procedure is necessary. For the wavelet listed in Figure 4, the regularized version is,

$$\begin{aligned}\frac{\partial\mathbb{D}(z,\theta)}{\partial\theta} = &\frac{2\sin\theta}{c_0} \int\limits_{-\infty}^{\infty} D\left(x, \frac{2z\cos\theta + x\sin\theta}{c_0}\right) dx \\ &- \frac{2\cos\theta}{c_0^2} \int\limits_{-\infty}^{\infty} D_t\left(x, \frac{2z\cos\theta + x\sin\theta}{c_0}\right) \cdot [x\cos\theta - 2z\sin\theta]\, dx \\ &+ \frac{2\sin\theta}{a^2\cos\theta}\frac{\partial}{\partial z} \int\limits_{-\infty}^{\infty} D_t\left(x, \frac{2z\cos\theta + x\sin\theta}{c_0}\right) dx\end{aligned} \tag{4.9}$$

In equation 4.9, the regularization step is listed in the last line. The objective of this equation is to remove density-only reflections; i.e., for models with only density variation, this equation should vanish. Its effectiveness is demonstrated in Figure 17.

4.1 Proposed new algorithm

Let us define,

$$\psi(\theta) = 1 + \frac{2R}{1-R} = \frac{1+R}{1-R} = \frac{\rho_1 v_1}{\rho_0 v_0}, \tag{4.10}$$

and we have,

$$\frac{1}{\psi(\theta)}\frac{\partial \psi(\theta)}{\partial \theta} = \frac{\partial \log[\psi(\theta)]}{\partial \theta} = \frac{1}{v_1}\frac{\partial v_1(\theta)}{\partial \theta} - \frac{1}{v_0}\frac{\partial v_0(\theta)}{\partial \theta}. \tag{4.11}$$

Please note that in the expression above, the density contribution vanishes. It is just one more step further from our existing $\alpha_1 - \beta_1$ logic, which is of the order of $\frac{\partial \psi(\theta)}{\partial \theta}$. The division by $\psi(\theta)$ can remove the density contribution.

There are several candidate algorithms that can obtain the amplitude profile that is consistent with the one-parameter HOIS algorithm. The algorithm presented below requires only the first-order derivative with respect to θ, which is numerically of the same magnitude as was our previous $\alpha_1 - \beta_1$.

$$\frac{1}{\psi(\theta)}\frac{\partial \psi(\theta)}{\partial \theta} = \frac{1}{v_1}\frac{\partial v_1(\theta)}{\partial \theta} - \frac{1}{v_0}\frac{\partial v_0(\theta)}{\partial \theta} = \left(v_1^2 - v_0^2\right)\frac{\sin\theta\cos\theta}{c_0^2} \tag{4.12}$$

$$\frac{v_1}{v_0} - 1 = \sqrt{\frac{\cos\theta}{\sin\theta}\frac{1}{\psi(\theta)}\frac{\partial \psi(\theta)}{\partial \theta} + 1} - 1. \tag{4.13}$$

Another structure, square-root, is identified.

Since: $\psi(\theta) = 1 + 2R/(1-R) = 1 + 2\mathbb{D}/(1-\mathbb{D})$, $\psi'(\theta) = 2\mathbb{D}'(\theta)/(1-\mathbb{D}(\theta))^2$, we have

$$\frac{1}{\psi(\theta)}\frac{\partial \psi(\theta)}{\partial \theta} = \frac{1-\mathbb{D}(\theta)}{1+\mathbb{D}(\theta)}\frac{2\mathbb{D}'(\theta)}{[1-\mathbb{D}(\theta)]^2} = \frac{2\mathbb{D}'(\theta)}{1-[\mathbb{D}(\theta)]^2},$$

and,

$$\begin{aligned}\frac{v_1}{v_0} - 1 &= \sqrt{\frac{\cos\theta}{\sin\theta}\frac{1}{\psi(\theta)}\frac{\partial \psi(\theta)}{\partial \theta} + 1} - 1 \\ &= \sqrt{\frac{\cos\theta}{\sin\theta}\frac{2\mathbb{D}'(\theta)}{1-[\mathbb{D}(\theta)]^2} + 1} - 1.\end{aligned} \tag{4.14}$$

4.2 Analytic solution of data without internal multiples

Let us assume a geological model consisting of flat layers located at $z_0, z_1, z_2, \cdots, z_N$, with the thickness of each layer being $d_0 = z_0$ $d_n = z_n - z_{n-1}$ $(n = 1, 2, \cdots, N)$. The corresponding reflection data are,

$$\mathcal{D}(\tau, p) = -\frac{c_0}{2\cos\theta} \sum_{n=0}^{N-1} \left(r_n \prod_{m=0}^{n-1} (1 - r_m^2) \right) f(\tau - \tau_n), \tag{4.15}$$

where $p = \frac{\sin\theta}{c_0}$ is the slope of the slant stacking,

$$v_n = \left(c_n^{-2} - p^2 \right)^{-1/2}, \tag{4.16}$$

is the apparent velocity and $a = 20\pi$ determines bandwidth of the source signature.

$$r_n = \frac{\rho_{n+1} v_{n+1} - \rho_n v_n}{\rho_{n+1} v_{n+1} + \rho_n v_n}, \tag{4.17}$$

is the reflection coefficient at the $n^{\texttt{th}}$ reflector. The cumulative transmission loss resulting from the $n-1$ reflectors above can be calculated as,

$$\prod_{m=0}^{n-1} \left(1 - r_m^2\right). \tag{4.18}$$

The product of the transmission coefficient r_n and the cumulative transmission loss resulting from the $n-1$ reflectors above is the amplitude of the reflection event from the $n^{\texttt{th}}$ reflector,

$$r'_n = r_n \prod_{m=0}^{n-1} \left(1 - r_m^2\right). \tag{4.19}$$

We used the prime sign to emphasize its difference from the true reflection coefficient from that reflector. Since the Radon transform has effectively converted the problem into 1D, the wave packet associated with each reflection event is actually the temporal integration of the wavelet: $f(\tau) = \frac{a}{2\sqrt{\pi}} e^{-a^2\tau^2/4}$, a Gaussian function.

If we define a dummy vertical time $\tau_{-1} = 0$, all vertical travel-times in the equation above can be calculated iteratively as:

$$\tau_n = \tau_{n-1} + \frac{2d_n}{v_n} \qquad (n = 0, 1, \cdots). \tag{4.20}$$

We can convert equation 4.20 to the (z, θ) domain as,

$$\begin{aligned}\mathbb{D}(z,\theta) &= -\frac{2\cos\theta}{c_0}\mathcal{D}\left(\frac{2z\cos\theta}{c_0},\frac{\sin\theta}{c_0}\right)\\ &= \sum_{n=0}^{N-1}\left(r_n\prod_{m=0}^{n-1}(1-r_m^2)\right)f\left(\frac{2z\cos\theta}{c_0}-\tau_n\right).\end{aligned} \tag{4.21}$$

Hence, its partial derivative over θ is,

$$\begin{aligned}\frac{\partial\mathbb{D}(z,\theta)}{\partial\theta} &= \sum_{n=0}^{N-1}\frac{\partial}{\partial\theta}\left(r_n\prod_{m=0}^{n-1}(1-r_m^2)\right)f\left(\frac{2z\cos\theta}{c_0}-\tau_n\right)\\ &+\sum_{n=0}^{N-1}\left(r_n\prod_{m=0}^{n-1}(1-r_m^2)\right)f'\left(\frac{2z\cos\theta}{c_0}-\tau_n\right)\left[-\frac{2z\sin\theta}{c_0}-\frac{\partial\tau_n}{\partial\theta}\right].\end{aligned} \tag{4.22}$$

Several characteristics of $\frac{\partial\mathbb{D}(z,\theta)}{\partial\theta}$ can be readily observed: If the velocity does not change, i.e., $c_0=c_1=c_2=\cdots$,

1. Since $v_{n+1}=v_n$, each $r_n=\frac{\rho_{n+1}v_{n+1}-\rho_n v_n}{\rho_{n+1}v_{n+1}-\rho_n v_n}=\frac{\rho_{n+1}-\rho_n}{\rho_{n+1}-\rho_n}$ has no dependency on v_n and v_{n+1} and does not change with respect to angle.

2. The first term of the right-hand side of equation 4.22 vanishes since the amplitude of the reflection event $r_n\prod_{m=0}^{n-1}(1-r_m^2)$ is invariant with respect to θ and $\frac{\partial}{\partial\theta}\left(r_n\prod_{m=0}^{n-1}(1-r_m^2)\right)=0$.

3. The arguments for the function f and f' are the same, $\frac{2z\cos\theta}{c_0}-\tau_n=\frac{2\cos\theta}{c_0}(z-z_n)$. The argument becomes zero when $z=z_n$, i.e., both events are correctly imaged at the actual depth z_n, and there is no imaging issue in this case.

4. The second term, on the other hand, is $\tau_n=2\sum_{m=0}^{n}\frac{d_m\cos\theta}{c_0}$, and $\frac{-2z\sin\theta}{c_0}-\frac{\partial\tau_n}{\partial\theta}=\frac{-2z\sin\theta}{c_0}+2\sum_{m=0}^{n}\frac{d_m\sin\theta}{c_0}=\frac{-2\sin\theta}{c_0}(z-\sum_{m=0}^{n}d_m)$. Note that $z_n=\sum_{m=0}^{n}d_m$ is the actual depth of the $n^{\texttt{th}}$ reflector, and we have: $\tau_n=\frac{2z_n\cos\theta}{c_0}$ and $\frac{2z\cos\theta}{c_0}-\tau_n=\frac{2\cos\theta}{c_0}(z-z_n)$. Consequently each wave packet is of the form

$$(z-z_n)\cdot f'\left(\frac{2\cos\theta}{c_0}(z-z_n)\right),$$

and generally speaking does not vanish for an arbitrary function f. Figure 16 provides an example of non vanishing $\frac{\partial\mathbb{D}}{\partial\theta}$ for models without velocity change.

5. In the ideal case, each event packet is a perfect step jump (Heaviside function), $f(t) = H(t)$. When the wave is produced by the full-bandwidth Green's function, the second term indeed vanishes: $f'(t) = \delta(t)$ and

$$\begin{aligned}&(z - z_n) \cdot f' \left(\frac{2\cos\theta}{c_0} (z - z_n) \right) \\ =&(z - z_n)\, \delta \left(\frac{2\cos\theta}{c_0} (z - z_n) \right) = 0.\end{aligned}$$

6. In the other case, as demonstrated by Figure 17, it will vanish after applying angle-dependency regularization.

But if the velocity field is inhomogeneous,

1. If $f(t) = H(t)$, according to Liu and Weglein (2008), $\sum_{n=0}^{N} r_n \prod_{m=0}^{n-1} (1 - r_m^2) \approx \frac{c_N}{c_0}$

2. If we define the pseudodepth of the $n^{\mathtt{th}}$ reflector as:

$$z'_n = \frac{\tau_n c_0}{2\cos\theta}.$$

   There is an imaging problem $z_n \neq z'_n$ except for the water bottom $n = 0$, where the actual velocity above the reflector agrees with the homogeneous reference velocity.

3. The first term is the amplitude change. The second term is the curvature:

$$-\frac{2z\sin\theta}{c_0} - \frac{\partial \tau_n}{\partial \theta}.$$

5 Relationship in the data after a Radon transform

5.1 The incident wave from a perfect impulsive source

In the frequency domain, the impulse response G_0 for a source located at $x_s = z_s = 0$ in a homogeneous acoustic medium with velocity c_0 and density ρ_0 satisfies:

$$\left(\frac{\partial^2}{\partial x^2} + \frac{\partial^2}{\partial z^2} + \frac{\omega^2}{c_0^2} \right) G_0(x, z, \omega) = \rho_0 \delta(x)\delta(z). \tag{5.1}$$

The formula above can be solved by equation 12.3, applying a Radon transform with constant slope $p = \frac{\sin\theta}{c_0} < \frac{1}{c_0}$. Equivalently, one can apply a forward Fourier transform $\int_{-\infty}^{\infty} dx e^{-ikx}$ on the equation

above, where the wavenumber k is restricted as proportional to the frequency: $k = \omega p$, the original 2D Helmholtz equation is transformed into a 1D Helmholtz equation[7]:

$$\left(\frac{\partial^2}{\partial z^2} + \omega^2 \left[c_0^{-2} - p^2\right]\right) G_0(p, z, \omega) = \rho_0 \delta(z).$$

If the Fourier transform from time to frequency is defined as: $\widetilde{f}(\omega) = \int_{-\infty}^{\infty} f(t) e^{i\omega t} dt$, the physical (causal) solution of the 1D Helmholtz equation above is obviously (Weglein et al., 2003, equation 64)[8]:

$$G_0(p, z, \omega) = \rho_0 \frac{e^{iq|z|}}{2iq} \qquad \texttt{where} \qquad q = \omega\sqrt{c_0^{-2} - p^2}. \tag{5.2}$$

The solution in equation 5.2 can be transformed from the ω-domain into the τ-domain as[9]:

$$\begin{aligned} G_0(p, z, \tau) &= \frac{1}{2\pi} \int_{-\infty}^{\infty} \rho_0 \frac{e^{iq|z|}}{2iq} e^{-i\omega\tau} d\omega = \frac{\rho_0}{2\pi} \int_{-\infty}^{\infty} \frac{e^{i\omega[\sqrt{c_0^{-2}-p^2}|z|-\tau]}}{2i\omega\sqrt{c_0^{-2} - p^2}} d\omega \\ &= \frac{\rho_0}{2\pi\sqrt{c_0^{-2} - p^2}} \int_{-\infty}^{\infty} \frac{e^{-i\omega[\tau-|z|\sqrt{c_0^{-2}-p^2}]}}{2i\omega} d\omega \\ &= -\frac{\rho_0}{2\sqrt{c_0^{-2} - p^2}} H\left(\tau - |z|\sqrt{c_0^{-2} - p^2}\right), \end{aligned} \tag{5.3}$$

where H is the step or the Heaviside function. This solution can also be found in equation 7.3.16 of Morse and Feshbach (1953).

5.2 The incident wave from a bandlimited source

The Green's function is the ideal wave caused by an ideal impulsive source, and it can be regarded as the solution of a more general formula in equation 5.4 where the source signature is $\widetilde{w}(\omega) = 1$ (in the frequency domain) or $w(t) = \delta(t)$ (in the time domain).

[7]The same notation G_0 is used for the Green's function for both before and after the transform. This will not cause much confusion since the domain of G_0 can be identified by the arguments inside the parenthesis immediately after.

[8]It is essentially equation 7.2.19 of Morse and Feshbach (1953).

[9]If p, the ratio between k and ω, is fixed, then the inverse Fourier transform from ω will obtain a result in the vertical time τ domain. The detail can be found in Appendix A, equation 12.4, and the physical interpretation is immediately after.

$$\left(\frac{\partial^2}{\partial x^2}+\frac{\partial^2}{\partial z^2}+\frac{\omega^2}{c_0^2}\right)P_0(x,z,\omega)=\rho_0\delta(x)\delta(z)\widetilde{w}(\omega). \tag{5.4}$$

Obviously, equation 5.4 can be obtained by simply multiplying equation 5.1 by a factor $\widetilde{w}(\omega)$. Hence, in the frequency domain, its solution P_0 is simply G_0 multiplying by the same $\widetilde{w}(\omega)$ factor:

$$P_0(x,z,\omega)=G_0(x,z,\omega)\widetilde{w}(\omega). \tag{5.5}$$

Since a multiplication of $\widetilde{w}(\omega)$ in the frequency domain corresponds to a convolution with $w(\tau)$ in the conjugate vertical-time domain, after a Radon transform with slope $p=\frac{\sin\theta}{c_0}$, the incident wave in the homogeneous medium is the convolution of the source signature $w(t)$ with the Green's function listed in equation 5.3:

$$P_0(p,z,\tau)=\int_{-\infty}^{\infty}G_0(p,z,u)w(\tau-u)du=A\left(\tau-|z|\sqrt{c_0^{-2}-p^2}\right), \tag{5.6}$$

where the function A can be computed as

$$A(t)=-\frac{\rho_0}{2\sqrt{c_0^{-2}-p^2}}\int_{-\infty}^{t}w(u)du=-\frac{c_0\rho_0}{2\cos\theta}\int_{-\infty}^{t}w(u)du. \tag{5.7}$$

We isolate the portion of $A(t)$ that depends only on the wavelet as:

$$W(t)=\int_{-\infty}^{t}w(u)du, \tag{5.8}$$

to expedite the physical interpretation later. Re-writing the amplitude term as $-\frac{\rho_0}{2\sqrt{c_0^{-2}-p^2}}=-\frac{c_0\rho_0}{2\cos\theta}$, the direct arrival is:

$$P_0(p,z,\tau)=A\left(\tau-|z|\sqrt{c_0^{-2}-p^2}\right)=A\left(\tau-\frac{|z|\cos\theta}{c_0}\right). \tag{5.9}$$

The direct wave in equation 5.9 is used to control the quality of the source implementation for the finite-difference modeling and to provide a benchmark for the accuracy of the discretized finite-difference propagation results shown in Figure 10 and Figure 11.

5.3 Solution for an inhomogeneous medium

In a layered inhomogeneous medium where both the velocity field $c(z)$ and density function $\rho(z)$ are piecewise constant functions, the steady wave satisfies the following Helmholtz equation:

$$\left(\frac{\partial^2}{\partial x^2}+\frac{\partial^2}{\partial z^2}+\frac{\omega^2}{c^2(z)}\right)P_0(x,z,\omega)=\rho(z)\delta(x)\delta(z)\widetilde{w}(\omega). \tag{5.10}$$

Applying the Radon transform with fixed p or the Fourier transform over x with the conjugate variable fixed as $k=\omega p$, equation 5.10 becomes:

$$\frac{\partial^2}{\partial z^2}+\omega^2\left[c^{-2}(z)-p^2\right]P_0(p,z,\omega)=\rho(z)\delta(z)\widetilde{w}(\omega). \tag{5.11}$$

We can further transform equation 5.11 into τ by applying the inverse Fourier transform $\frac{1}{2\pi}\int\limits_{-\infty}^{\infty}d\omega e^{-i\omega\tau}$ on both sides to have

$$\frac{\partial^2}{\partial z^2}-\left[c^{-2}(z)-p^2\right]\frac{\partial^2 P_0(\tau,p,z)}{\partial\tau^2}=\rho(z)\delta(z)w(\tau). \tag{5.12}$$

Obviously equation 5.12 is a familiar-looking 1D wave equation with apparent propagation velocity[10] $\left[c^{-2}(z)-p^2\right]^{-1/2}$. It is obvious that in the τ-p domain, the original 2D wave equation is simplified into a 1D wave equation with apparent propagation velocity $\left[c^{-2}(z)-p^2\right]^{-1/2}$, and density ρ is kept the same. The solution for the corresponding 1D wave equation can be easily obtained as follows:

1. After a Radon transform with slope p, the data can be viewed as reflected from a 1D earth with apparent velocity $\left(c^{-2}(z)-p^2\right)^{-1/2}$.
2. The density does not need any modification.
3. The reflector depth does not need to be changed for computation.
4. In 1D, a two-layered acoustic medium with velocity and densities being (c_0,ρ_0) for the first layer and (c_1,ρ_1) for the second layer, and the reflector depth being at $z=h$, the reflection coefficient for the interface is

$$R=\frac{c_1\rho_1-c_0\rho_0}{c_1\rho_1+c_0\rho_0}, \tag{5.13}$$

and its corresponding transmission coefficient through the reflector is

$$T=1+R=\frac{2c_1}{c_1+c_0}. \tag{5.14}$$

[10]The first author of this article felt this logic is the most convenient shortcut in visualizing the multi-D wave problem where the earth has no lateral variation: a simple change to apparent velocity reduces the dimensions of the problem to 1.

Velocity	Density	Depth Range
$1500(\mathtt{m/s})$	$1.0 \times 10^3(\mathrm{kg}/m^3)$	$(-\infty \sim 600(\mathtt{m}))$
$1500(\mathtt{m/s})$	$2.0 \times 10^3(\mathrm{kg}/m^3)$	$600(\mathtt{m}) \sim 800(\mathtt{m})$
$1500(\mathtt{m/s})$	$3.0 \times 10^3(\mathrm{kg}/m^3)$	$800(\mathtt{m}) \sim \infty$

Table 3: The first geological model.

Velocity	Density	Depth Range
$1500(\mathtt{m/s})$	$1.0 \times 10^3(\mathrm{kg}/m^3)$	$(-\infty \sim 600(\mathtt{m}))$
$2000(\mathtt{m/s})$	$1.0 \times 10^3(\mathrm{kg}/m^3)$	$600(\mathtt{m}) \sim 800(\mathtt{m})$
$2500(\mathtt{m/s})$	$1.0 \times 10^3(\mathrm{kg}/m^3)$	$800(\mathtt{m}) \sim \infty$

Table 4: The second geological model.

5. In the situation above, the traveltime to cover a distance h above the reflector is $\frac{h}{c_0}$; the traveltime to traverse a distance h below the reflector is $\frac{h}{c_1}$.

Intensive efforts had been devoted to achieving a better understanding and physical interpretation of various terms in multiparameter imaging, especially for $\mathbb{D}$ (seismic data in the pseudodepth domain). As Dr. Weglein has suggested, it may actually be the FK migration result if the earth has lateral variations. Currently we know that if the earth has no lateral variation, a simple Radon transform[11] will recover all the physics required in the logic since in this case, the migration procedure afterwards[12] will make no difference if the earth has no lateral variation.

6 Numerical examples

The first example we tested is summarized in Table 3.

Observations for $\partial/\partial\theta$ calculated from the integral are

- It is numerically stable.
- It is smooth (except in the truncation area).

[11] For example, equation 2.21 of Liu (2006)

[12] For instance, equation 2.22 of Liu (2006) will make no difference if the earth has no lateral variation.

Velocity	Density	Depth Range
$1500(\mathtt{m/s})$	$1.0 \times 10^3(\mathrm{kg}/m^3)$	$(-\infty \sim 600(\mathtt{m}))$
$2000(\mathtt{m/s})$	$2.0 \times 10^3(\mathrm{kg}/m^3)$	$600(\mathtt{m}) \sim 800(\mathtt{m})$
$2500(\mathtt{m/s})$	$3.0 \times 10^3(\mathrm{kg}/m^3)$	$800(\mathtt{m}) \sim \infty$

Table 5: The third geological model.

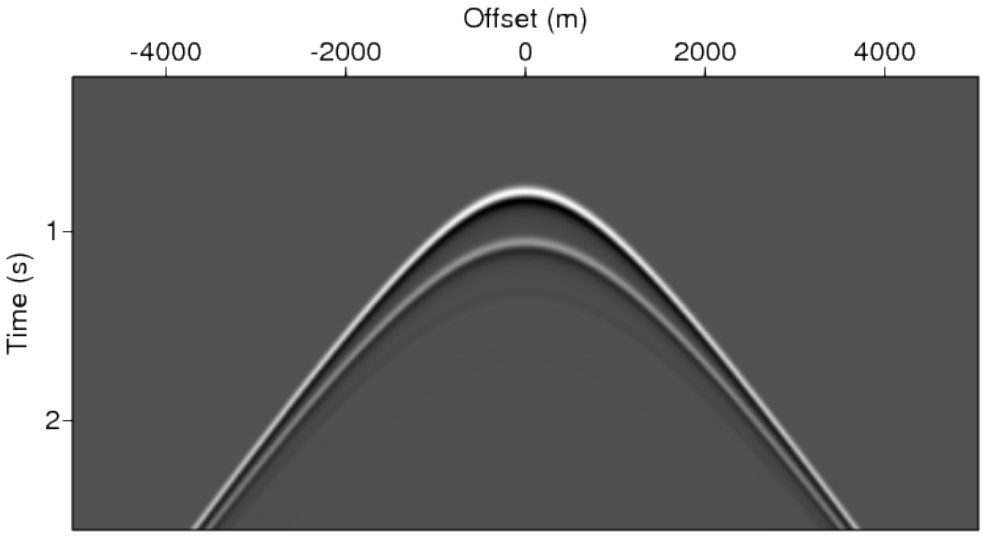

Figure 13: Reflection data from the geological model in Table 3, with the wavelet in Figure 4.

- It is of the same magnitude as was our previous $\alpha_1 - \beta_1$.

7 Implementing the P-wave source for the finite-difference modeling

The progress in section 4 shows promise for removing the density contribution in acoustic data. However, the observations of Liang et al. (2011) suggest that we need an imaging framework capable of handling elastic amplitude. Implementing the P-wave source for elastic finite-difference modeling is a very important component of this effort. The implementation provides high-quality input data for the future imaging algorithms. Also, (1) artifacts (or inaccuracy) in the input data, and/or (2) insufficient processing procedures, can cause a failure in data processing. If we can make sure the first factor does not contribute, we can focus on the second factor. This section follows closely Appendix A of Kelly et al. (1976).

Let us define: $\gamma_0 = \lambda_0 + \mu_0$. The 2D elastic wave equation[13] becomes:

$$\gamma_0 \bigtriangledown (\bigtriangledown \cdot \vec{u}) - \mu_0 \bigtriangledown \times \bigtriangledown \times \vec{u} - \rho_0 \frac{\partial^2 \vec{u}}{\partial t^2} = \bigtriangledown [\delta(\vec{r}) f(t)] \,. \tag{7.1}$$

On the right-hand side of equation 7.1, the source term is the divergence of a scalar field and has no curl, hence it is a P-wave source emitting from the position $\vec{r}_s = \vec{0}$. In the homogeneous medium,

[13]See equations (48) and (49) from Weglein et al. (2003).

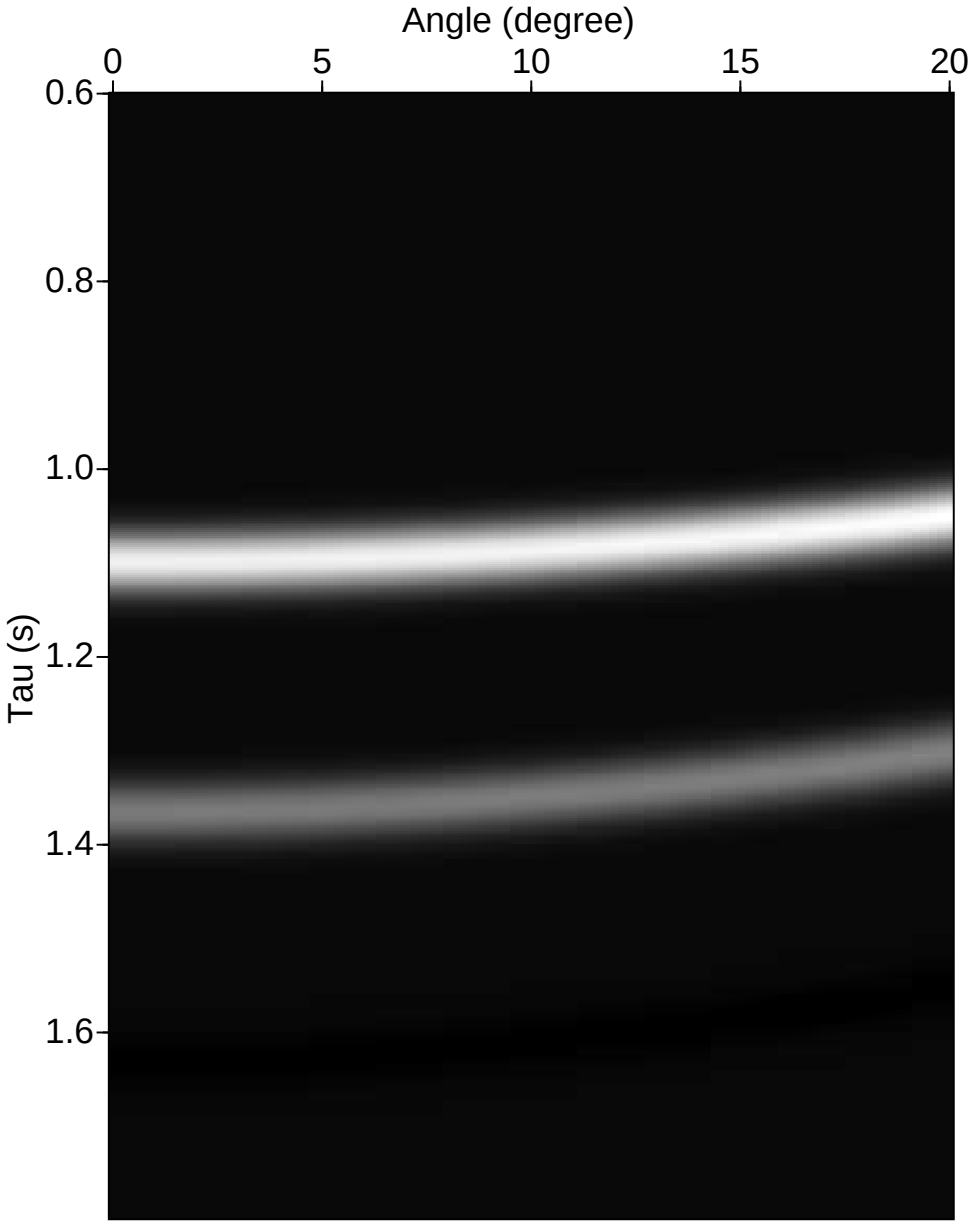

Figure 14: The Radon transform (see equation 2.1) of the reflection data from Figure 13.

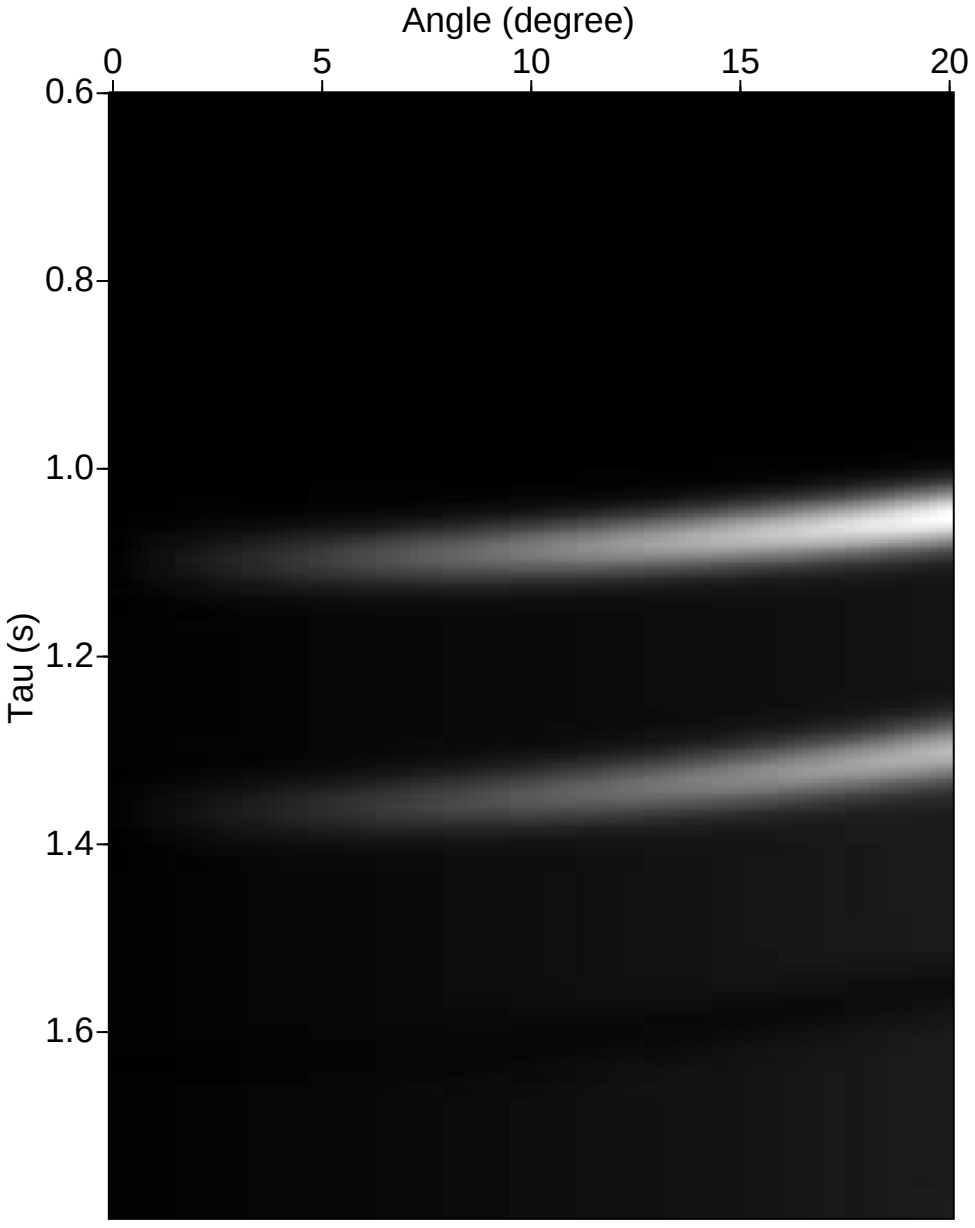

Figure 15: $\frac{\partial \mathcal{D}}{\partial \theta}$ (see equation 2.4 for details) is not flat and does not vanish even for models without velocity change. It has many similarities to the normal Radon transform result (see Figure 14). Most importantly, it is stable and demonstrates the possibilities of converting the unstable operation of division by $\Delta\theta \to 0$ to a much stabler integration.

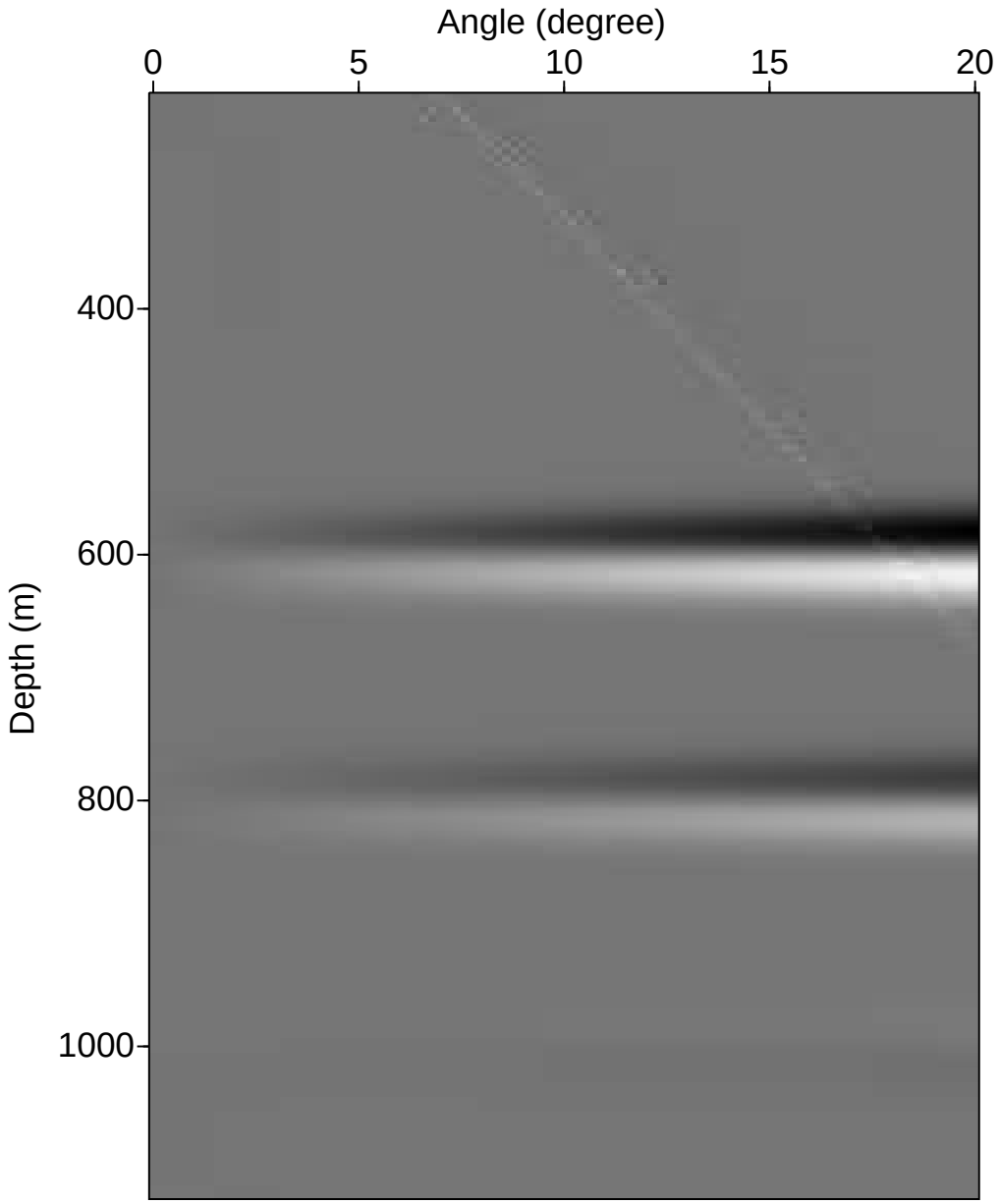

Figure 16: $\frac{\partial \mathbb{D}}{\partial \theta}$ without regularization. Even for the model without velocity change, the bandlimited nature of the wavelet is the only reason.

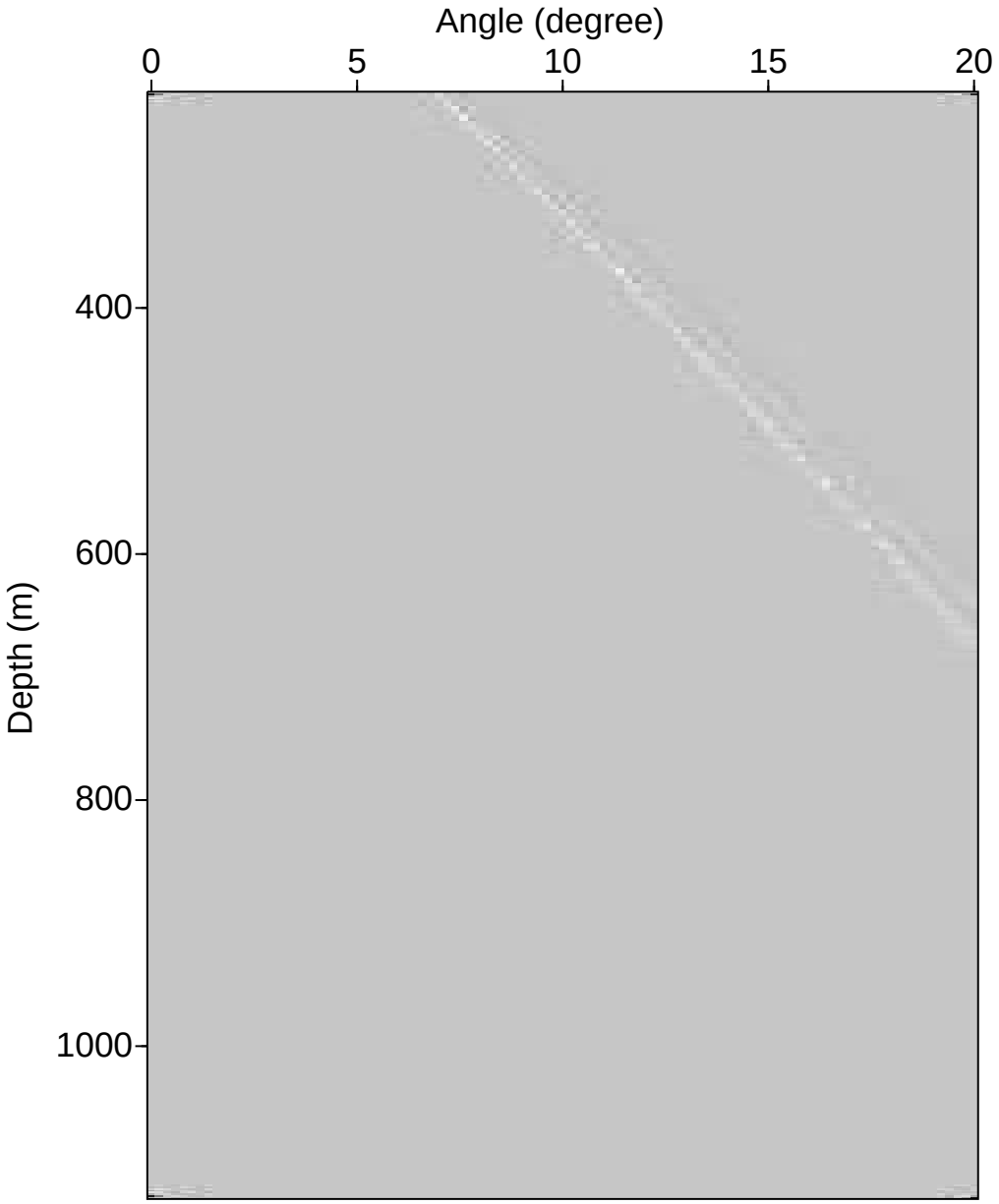

Figure 17: $\frac{\partial \mathbb{D}}{\partial \theta}$ after regularization. The regularization formula can be found in equation 4.9.

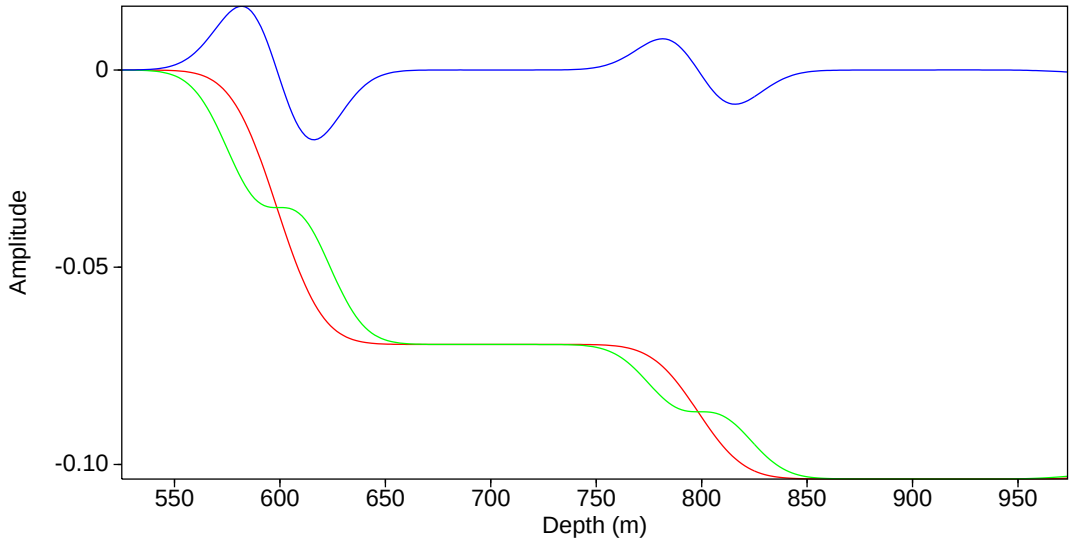

Figure 18: Red: the first term in equation 4.9, Green: the negative of the second term in equation 4.9, Blue: their difference.

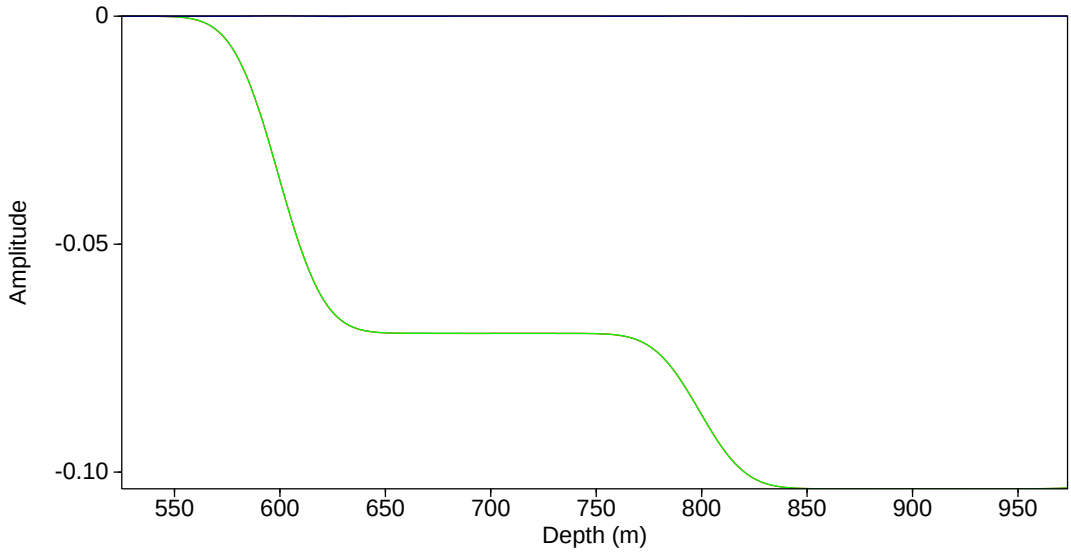

Figure 19: Red: the first term in equation 4.9, Green: the negative of the second term in equation 4.9, Blue: their difference. The red line is so close to the green line that the red is totally hidden by the almost identical green curve.

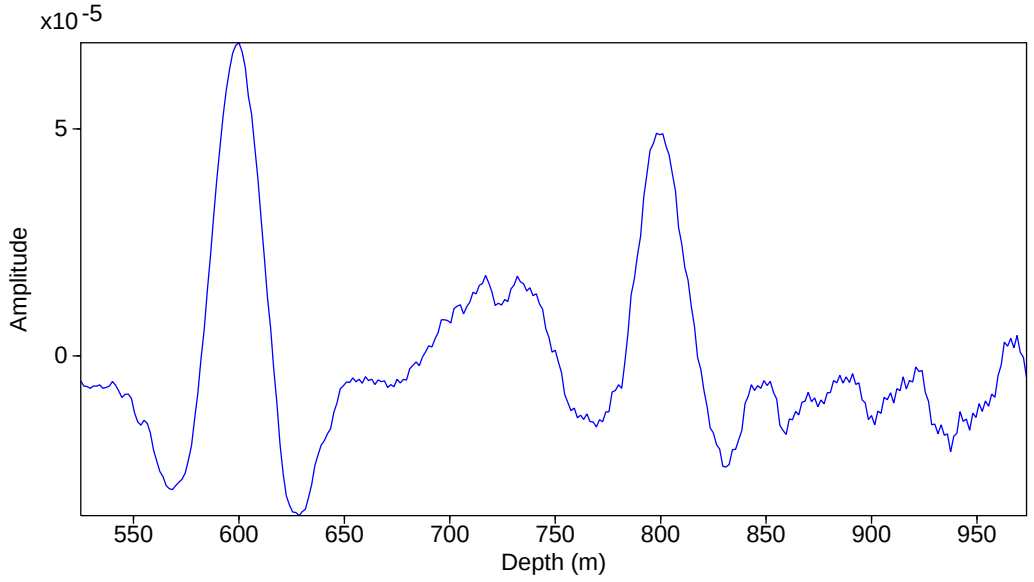

Figure 20: Blue: The difference between the red and green curves in Figure 19

we can assume that the resulting wavefield has no curl and can be expressed as the divergence of a scalar field,

$$\vec{u} = \bigtriangledown\phi \tag{7.2}$$

Substituting equation 7.2 into equation 7.1 and interchanging the order to apply the differential operators, we have,

$$\gamma_0 \bigtriangledown \left[\bigtriangledown^2\phi\right] - \rho_0 \bigtriangledown \left[\frac{\partial^2\phi}{\partial t^2}\right] = \bigtriangledown \left[\delta(\vec{r})f(t)\right]. \tag{7.3}$$

Note that there is a common $\bigtriangledown$ operator in front of every term in the equation above. After removing this common $\bigtriangledown$ operator from the equation above, we have,

$$\gamma_0 \bigtriangledown^2 \phi - \rho_0 \frac{\partial^2\phi}{\partial t^2} = \delta(\vec{r})f(t) \tag{7.4}$$

which has the analytic solution,

$$\phi(r) = \frac{1}{2\pi} \int_{-\infty}^{\infty} \widetilde{F}(\omega) \frac{1}{4} \left[Y_0\left(\frac{\omega}{\alpha_0}r\right) - iJ_0\left(\frac{\omega}{\alpha_0}r\right)\right] e^{-i\omega t} dt, \tag{7.5}$$

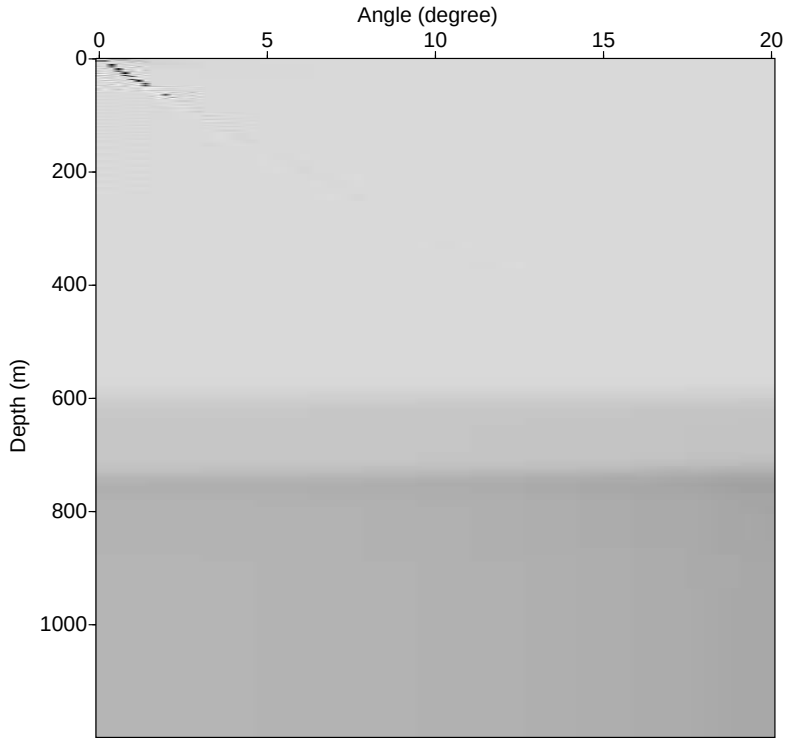

Figure 21: The result from applying the algorithm to separate the density contribution shown in equation 4.14. The geological model, listed in Table 4, is velocity only.

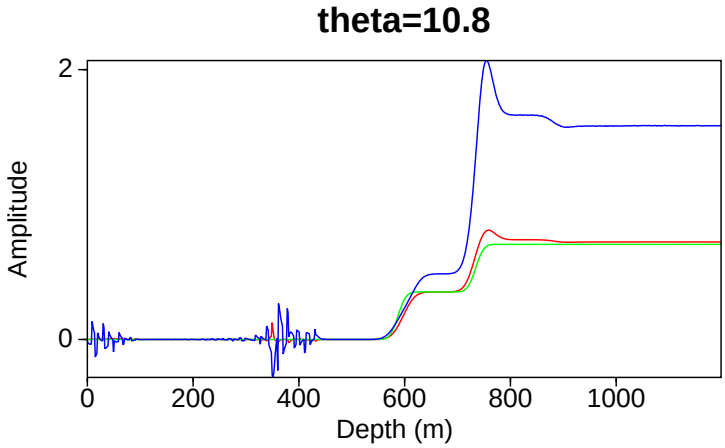

Figure 22: Further details from one trace in the middle of Figure 21. Green: perfect amplitude for the velocity-only HOIS. Red: new algorithm from equation 4.14. Blue: current algorithm from equation 4.5.

and the resulting wave-field is,

$$\begin{aligned}\vec{u} = \bigtriangledown\left[\phi(r)\right] &= \left(\frac{x}{r}\hat{\mathbf{e}}_{\mathbf{x}} + \frac{z}{r}\hat{\mathbf{e}}_{\mathbf{z}}\right)\frac{\partial\phi(r)}{\partial r} \\ &= \left(\frac{x}{r}\hat{\mathbf{e}}_{\mathbf{x}} + \frac{z}{r}\hat{\mathbf{e}}_{\mathbf{z}}\right)\frac{\partial}{\partial r}\frac{1}{2\pi}\int_{-\infty}^{\infty}\widetilde{F}(\omega)\frac{1}{4}\left[Y_0\left(\frac{\omega}{\alpha_0}r\right) - iJ_0\left(\frac{\omega}{\alpha_0}r\right)\right]e^{-i\omega t}dt \\ &= \left(\frac{x}{r}\hat{\mathbf{e}}_{\mathbf{x}} + \frac{z}{r}\hat{\mathbf{e}}_{\mathbf{z}}\right)\frac{1}{2\pi}\int_{-\infty}^{\infty}\frac{\omega}{\alpha_0}\widetilde{F}(\omega)\frac{1}{4}\left[Y_1\left(\frac{\omega}{\alpha_0}r\right) - iJ_1\left(\frac{\omega}{\alpha_0}r\right)\right]e^{-i\omega t}dt\end{aligned} \tag{7.6}$$

8 Implementing the shear-wave source for the finite-difference modeling

Since the source and receiver can both be designed exclusively for a P-wave or an S-wave, the complete set of elastic seismic experiment contains four categories of data, **PP**, **PS**, **SP** and **SS**. Among them, the latter two require a shear-wave source. Consequently, implementing an S-wave source for elastic finite-difference modeling is the first step towards this objective. Our objective is to generate high fidelity input data for the future elastic imaging algorithms - data that are physically consistent with the ISS theory and that release the burden caused by modeling artifacts.

Let us define: $\gamma_0 = \lambda_0 + \mu_0$. According to equations (48) and (49) from Weglein et al. (2003), the 2D elastic wave equation becomes:

$$\gamma_0 \bigtriangledown\left(\bigtriangledown\cdot\vec{u}\right) - \mu_0 \bigtriangledown\times\bigtriangledown\times\vec{u} - \rho_0\frac{\partial^2\vec{u}}{\partial t^2} = \bigtriangledown\times\left[\delta(\vec{r})f(t)\hat{\mathbf{e}}_{\mathbf{y}}\right] \tag{8.1}$$

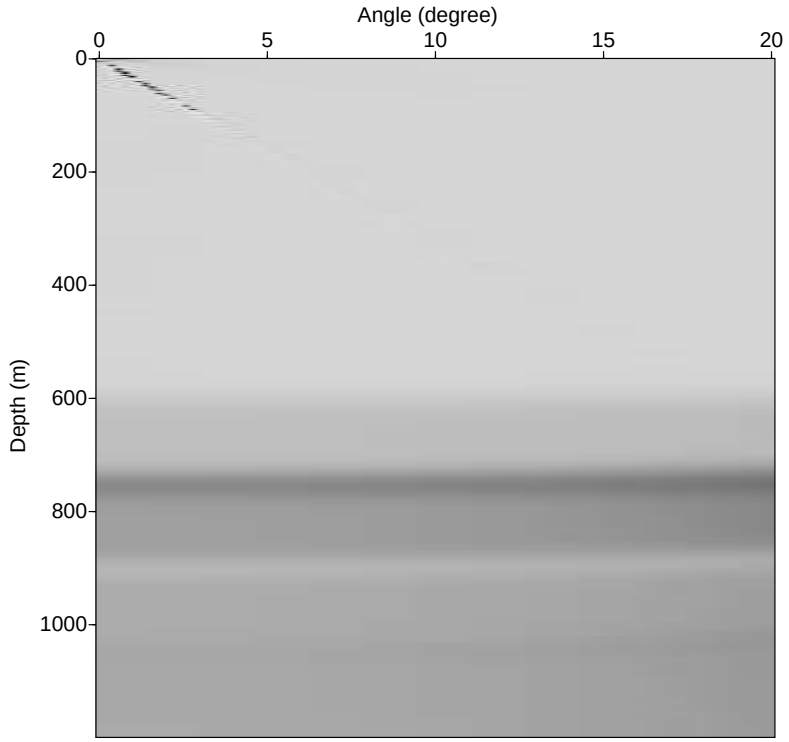

Figure 23: The result from applying the algorithm to separate density the contribution shown in equation 4.14. The geological model, listed in Table 4, has both velocity and density variations.

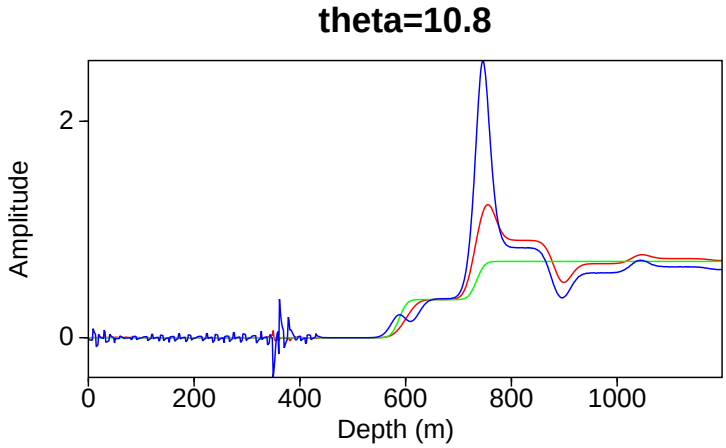

Figure 24: Further details from one trace in the middle of Figure 23. Green: perfect amplitude for the velocity-only HOIS. Red: new algorithm from equation 4.14. Blue: current algorithm from equation 4.5.

where $\hat{\mathbf{e}}_\mathbf{y}$ is the unit vector in the perpendicular y-direction. In this case $\bigtriangledown \times [\delta(\vec{r})\hat{\mathbf{e}}_\mathbf{y}]$ will produce a force in the (x, z) plane.

Since the source has no divergence, we can assume its resulting wavefield is,

$$\vec{u} = \bigtriangledown \times [\phi(r)\hat{\mathbf{e}}_\mathbf{y}] = \begin{vmatrix} \hat{\mathbf{e}}_\mathbf{x} & \hat{\mathbf{e}}_\mathbf{y} & \hat{\mathbf{e}}_\mathbf{z} \\ \partial/\partial x & \partial/\partial y & \partial/\partial z \\ 0 & \phi(r) & 0 \end{vmatrix} = -\frac{\partial \phi(r)}{\partial z}\hat{\mathbf{e}}_\mathbf{x} + \frac{\partial \phi(r)}{\partial x}\hat{\mathbf{e}}_\mathbf{z} = \frac{\phi'(r)}{r}\left(-z\hat{\mathbf{e}}_\mathbf{x} + x\hat{\mathbf{e}}_\mathbf{z}\right). \quad (8.2)$$

In this case we have $\bigtriangledown \cdot \vec{u} = \bigtriangledown \cdot \bigtriangledown \times [\phi(r)\hat{\mathbf{e}}_\mathbf{y}] \equiv 0$, and

$$\bigtriangledown \times \bigtriangledown \times \vec{u} = - \bigtriangledown \bigtriangledown \cdot \vec{u} - \bigtriangledown^2 \vec{u} = - \bigtriangledown^2 \vec{u} \quad (8.3)$$

where in the equation above $\bigtriangledown^2 = \frac{\partial^2}{\partial x^2} + \frac{\partial^2}{\partial z^2}$ is a scalar operator applied on a vector.

Our wave equation then becomes,

$$\mu_0 \bigtriangledown^2 [\bigtriangledown \times (\phi(r)\hat{\mathbf{e}}_\mathbf{y})] - \bigtriangledown \times \left[\rho_0 \frac{\partial^2 \phi(\vec{r})}{\partial t^2}\right] = \bigtriangledown \times [\delta(\vec{r})\hat{\mathbf{e}}_\mathbf{y} f(t)]. \quad (8.4)$$

After removing the common $\bigtriangledown\times$ operator from the equation above, we have,

$$\mu_0 \bigtriangledown^2 \phi(r) - \rho_0 \frac{\partial^2 \phi(r)}{\partial t^2} = \delta(r) f(t), \quad (8.5)$$

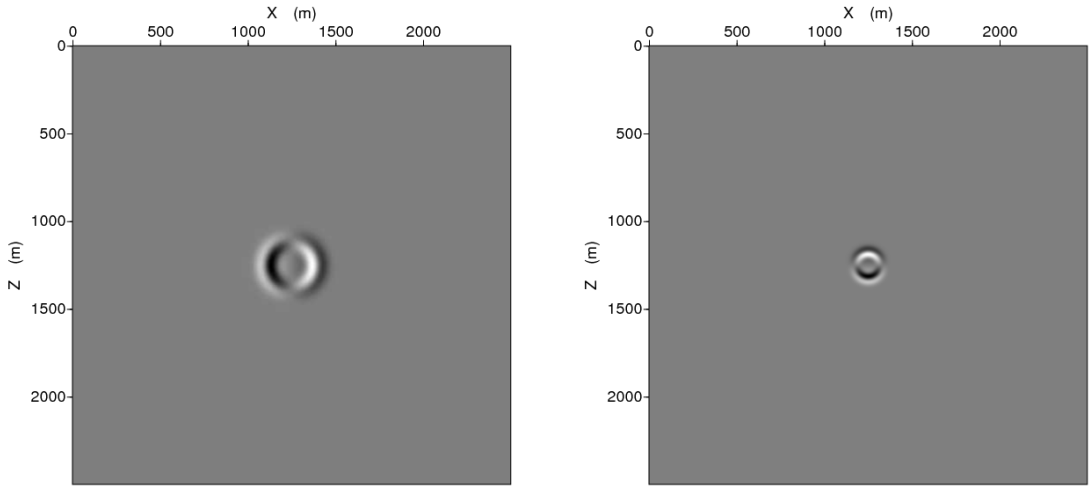

Figure 25: The x-component of the precalculated analytic wavefield at time $t = 0.09(s)$. Left: P-wavefield computed with equation 7.6, Right: S-wavefield calculated with equation 8.7.

which has the analytic solution,

$$\phi(r) = \frac{1}{2\pi} \int_{-\infty}^{\infty} \widetilde{F}(\omega) \frac{1}{4} \left[Y_0 \left(\frac{\omega}{\beta_0} r \right) - i J_0 \left(\frac{\omega}{\beta_0} r \right) \right] e^{-i\omega t} dt, \tag{8.6}$$

and the resulting wave-field is,

$$\vec{u} = \bigtriangledown \times [\phi(r) \hat{\mathbf{e}}_\mathbf{y}] = \left(-\frac{z}{r} \hat{\mathbf{e}}_\mathbf{x} + \frac{x}{r} \hat{\mathbf{e}}_\mathbf{z} \right) \frac{1}{2\pi} \int_{-\infty}^{\infty} \frac{\omega}{\beta_0} \widetilde{F}(\omega) \frac{1}{4} \left[Y_1 \left(\frac{\omega}{\beta_0} r \right) - i J_1 \left(\frac{\omega}{\beta_0} r \right) \right] e^{-i\omega t} dt. \tag{8.7}$$

9 Velocity-depth ambiguity

In the papers that study the issue of velocity-depth ambiguity, for example Bickel (1990), several issues have been observed:

- "Lateral variations in seismic velocity with a spatial wavelength of about 2.7 D, where D is the depth to the reflecting horizon, cannot be unambiguously resolved from traveltime measurements". In other words, the depth of the target has a negative impact on the quality for velocity inversion.

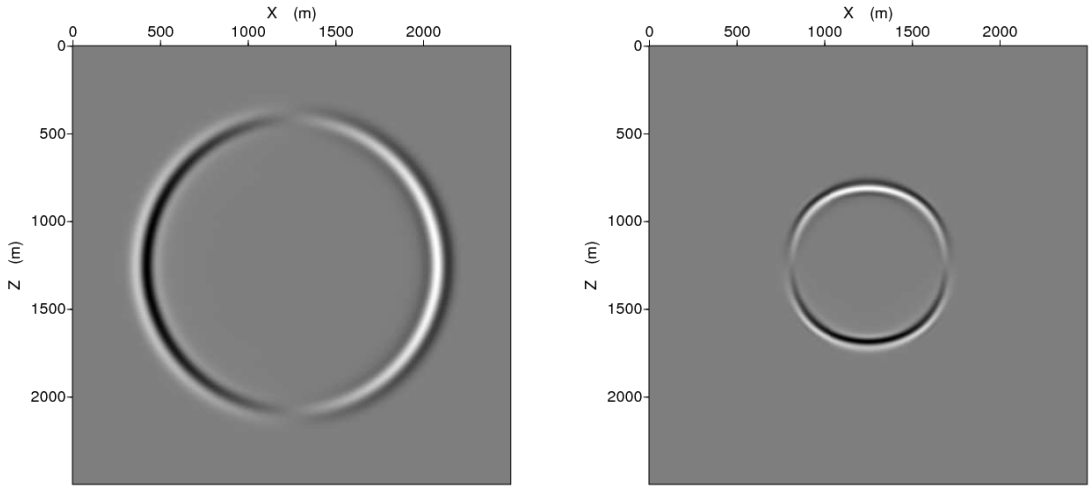

Figure 26: The x-component of the wavefield at time $t = 0.565$ seconds, both panels being computed with equation 2 from Kelly et al. (1976). Left: P-wavefield using the initial condition shown in the left panel of Figure 25, Right: S-wavefield using the initial condition shown in the right panel of Figure 25.

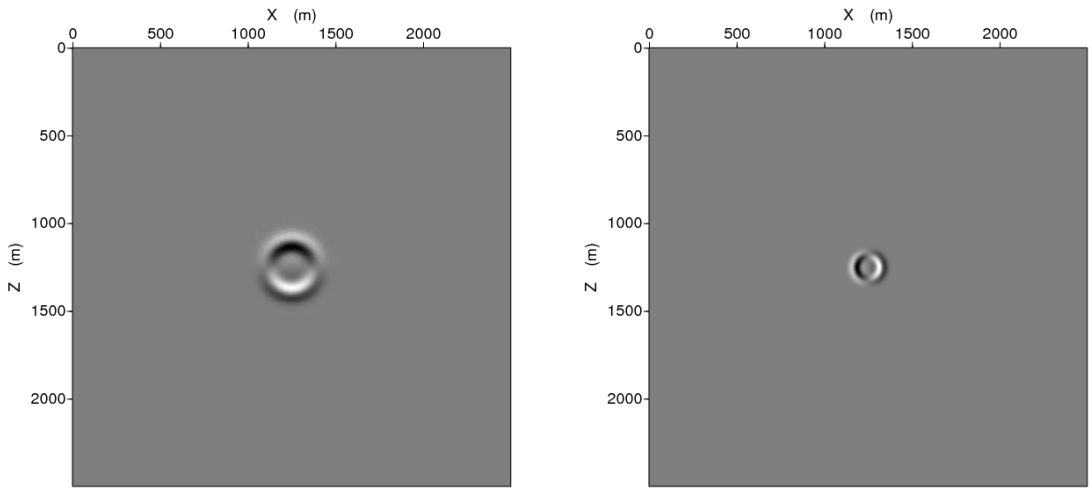

Figure 27: The z-component of the precalculated analytic wavefield at time $t = 0.09(s)$. Left: P-wavefield computed with equation 7.6, Right: S-wavefield calculated with equation 8.7.

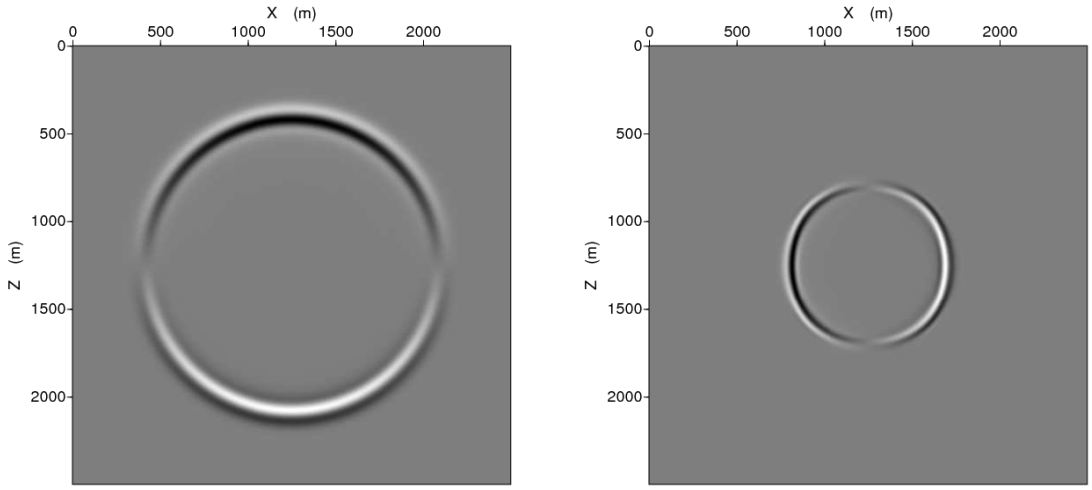

Figure 28: The z-component of the wave field at time $t = 0.565$ seconds, both panels being computed with equation 2 from Kelly et al. (1976). Left: P-wavefield using the initial condition shown in the left panel of Figure 27, Right: S-wavefield using the initial condition shown in the right panel of Figure 27.

- "Figure 10 shows that almost all of the low-frequency information is missing from the estimate of velocity if the filter is designed for 1% ambient noise". In other words, the low-frequency part of the result is very sensitive to the presence of noise.

Let us address one of the fundamental issues in seismic imaging: velocity-depth ambiguity. Since we are not experts in traveltime tomography, we just test one model with ISS imaging to better understand this issue and its impact on ISS imaging algorithms.

Jim Mayhan measured the model from the paper, Fang Liu ran the model with fourth-order finite-difference modeling. The modeling parameters are the following: $\Delta x = \Delta t = 5(\mathtt{m})$, $\Delta t = 0.5(ms)$. Our conclusion is the following: there are no extra surprises compared with the previous models we had tested, i.e., the salt model and the fault model.

- Very big lateral variation and small contrast.
- The lower horizontal reflector is too thin (6 ft) to be faithfully modeled through finite difference. In our experiment, the thickness is increased to 75 m.

10 Conclusions

Towards more realism to accommodate the multiparameter nature of the Earth, a stable and velocity-independent regularization algorithm is developed to harmonize the communication among

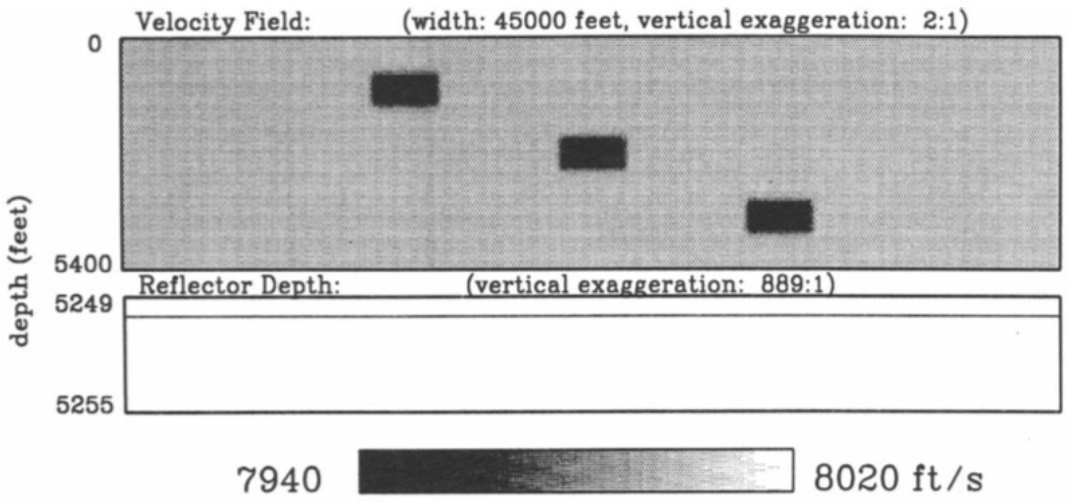

Figure 29: The geological model

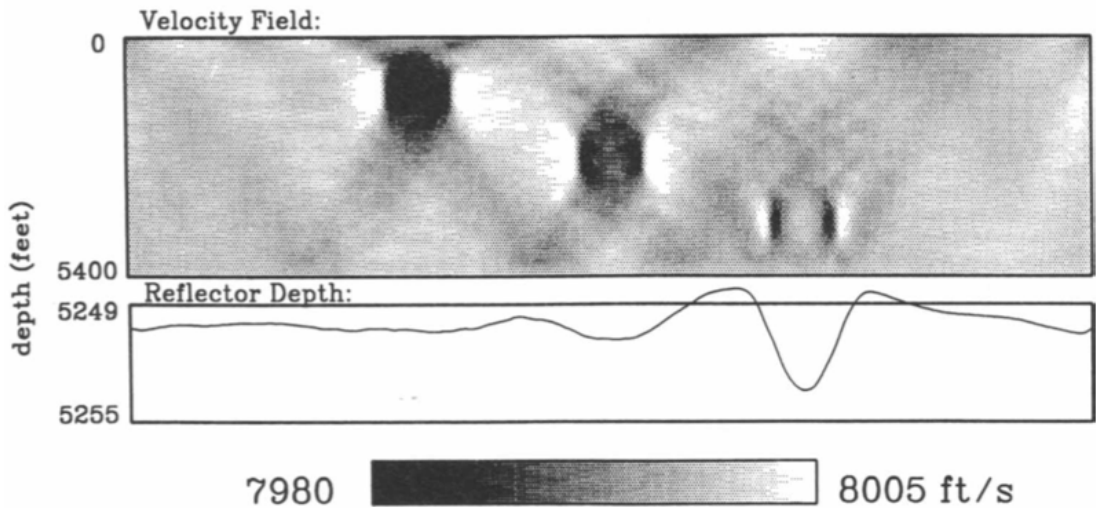

Figure 30: The result from traveltime tomography.

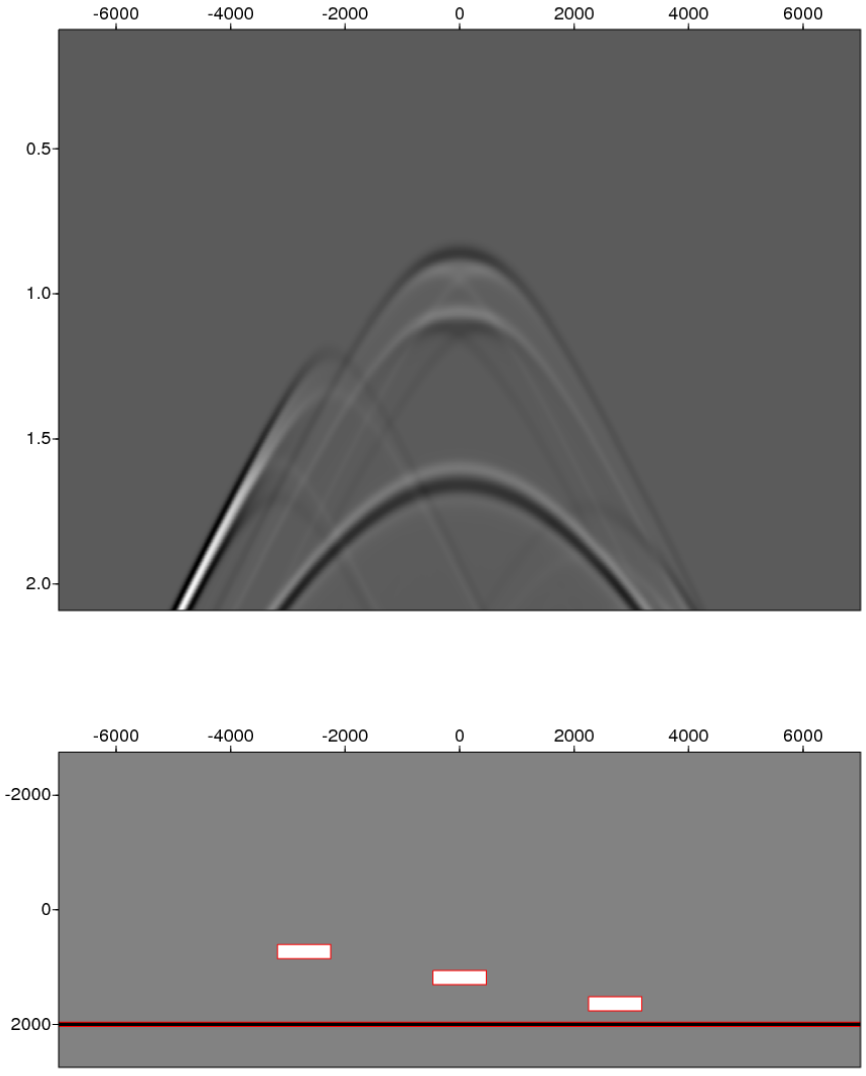

Figure 31: Reflection data (top) and the corresponding geological model (bottom) with $x_s = 0(\mathtt{m})$.

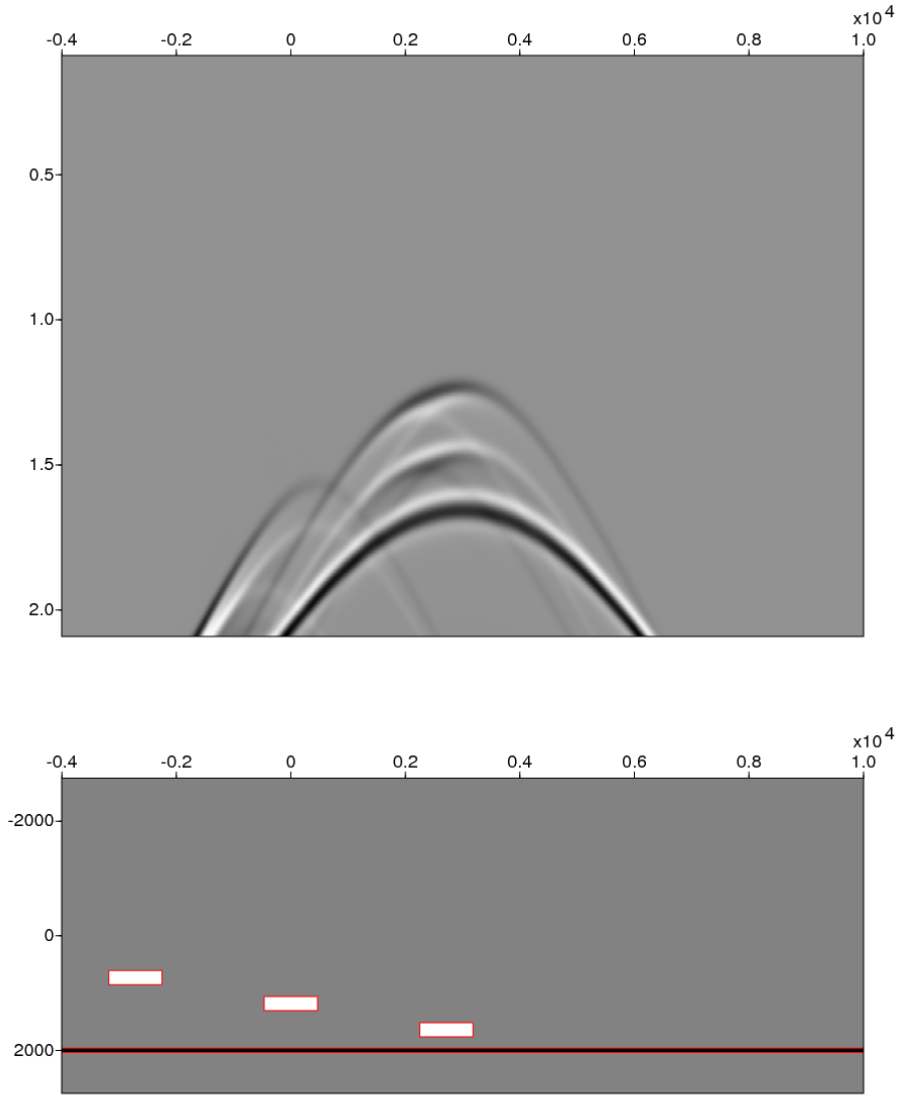

Figure 32: Reflection data (top) and the corresponding geological model (bottom) with $x_s = 3000(\mathtt{m})$.

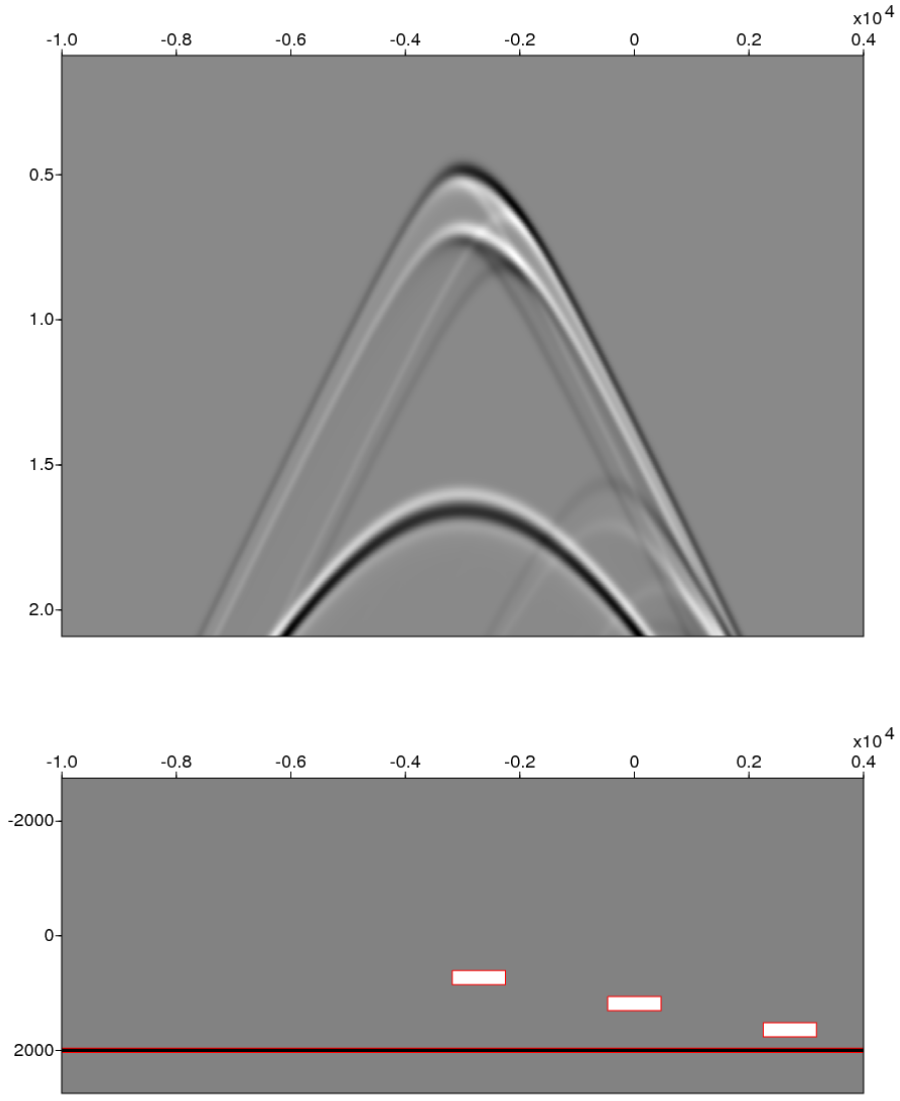

Figure 33: Reflection data (top) and the corresponding geological model (bottom) with $x_s = -3000(\mathtt{m})$.

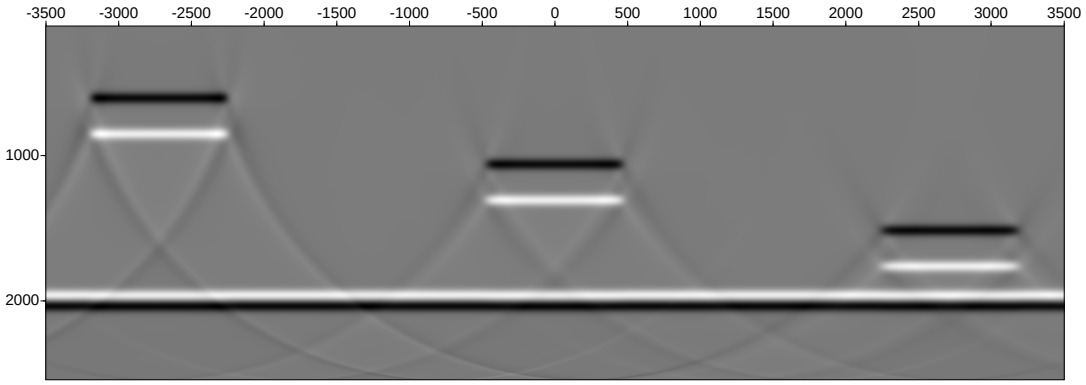

Figure 34: $\frac{\partial \alpha_1}{\partial z}$. The vertical axis is depth (m), the horizontal axis is lateral coordinate x (m).

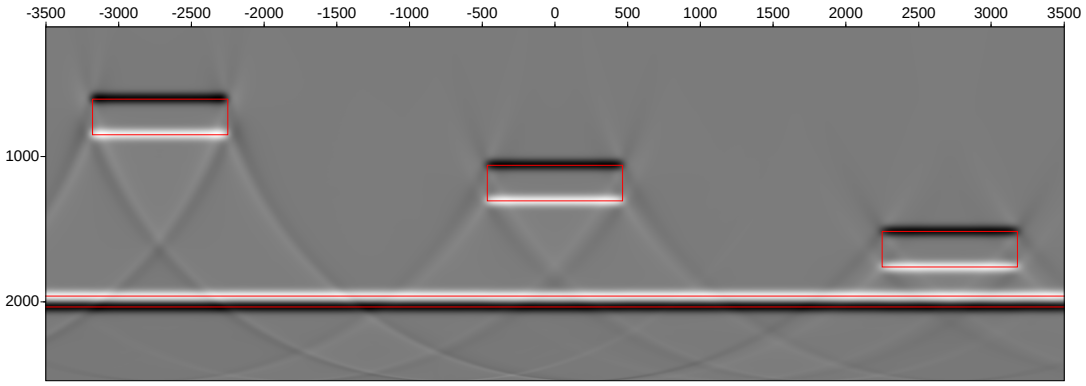

Figure 35: $\frac{\partial \alpha_1}{\partial z}$ with geological benchmarks (red lines). The vertical axis is depth (m), the horizontal axis is lateral coordinate x (m).

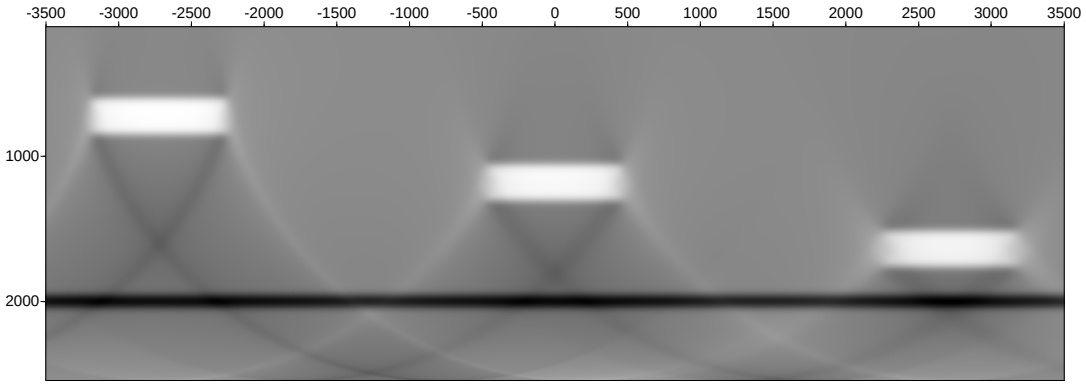

Figure 36: α_1. The vertical axis is depth (m), the horizontal axis is lateral coordinate x (m).

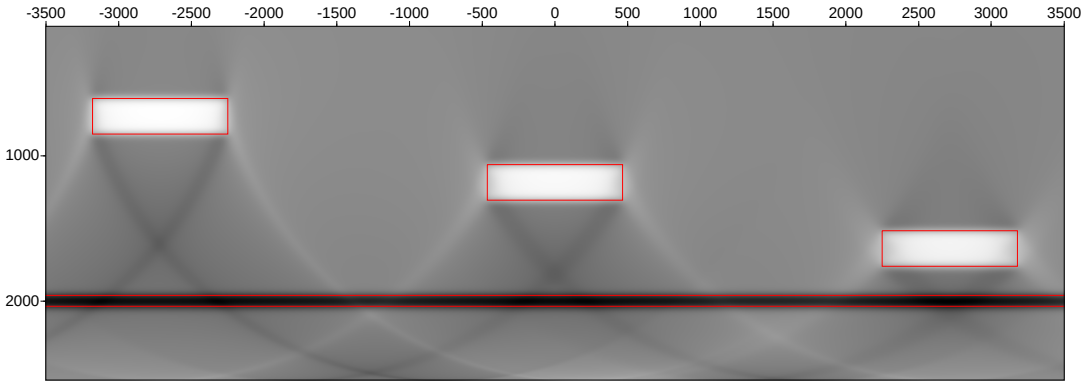

Figure 37: α_1 with geological benchmarks (red lines). The vertical axis is depth (m), the horizontal axis is lateral coordinate x (m).

bandlimited seismic data from different angles. This is a crucial step towards the goal of excluding the density contribution to the reflection coefficient.

Future work involves extending this logic to the elastic model and to earth with lateral variations, and incorporating the observations in future spike-moving logic. The computational framework for elastic imaging that incorporates the understanding gained from M-OSRP's previous research based on the analytic data in the pseudodepth (or τ-p) domain and the divergence ($\bigtriangledown\cdot$) and curl ($\bigtriangledown\times$) necessary for the vectorized displacement measurement in the x-t domain is one of the necessary and imminent steps.

11 Acknowledgments

Jim Mayhan measured the model from Ross (1994) to test the issue of velocity ambiguity. Zhiqiang Wang and Di Chang provided the proofreading of the manuscript. The authors would like to thank all M-OSRP members and sponsors. This work has been partially funded by NSFCMG award DMS-0327778 and DOE Basic Energy Sciences Award DE-FG02-05ER15697.

12 Appendix A: Some basic notations and conventions of Radon transform

The Radon transform, or slant stacking, is commonly called the $\tau - p$ transform in seismic exploration where τ is the vertical time and p is the slope. The Radon transform of a function $f(x,t)$ into the (τ, p) domain, denoted as $F(\tau, p)$, is:

$$F(\tau,p) = \int_{-\infty}^{\infty} f(x, \tau + px)dx. \tag{12.1}$$

Note that for $p \neq 0$, $\tau + px$ may occur somewhere in between the original sampling grids. In other words, interpolation between two grids may become necessary. This interpolation can be done via a Fast Fourier transform:

$$f(x,\tau+px) = \frac{1}{2\pi}\int_{-\infty}^{\infty} \widetilde{f}(x,\omega)e^{-i\omega(\tau+px)}d\omega \qquad \texttt{where} \qquad \widetilde{f}(x,\omega) = \int_{-\infty}^{\infty} f(x,t)e^{i\omega t}. \tag{12.2}$$

Consequently, the Radon transform in equation 12.1 can be written as:

$$F(\tau,p) = \int_{-\infty}^{\infty} f(x,\tau+px)dx = \frac{1}{2\pi}\int_{-\infty}^{\infty} e^{-i\omega\tau}\int_{-\infty}^{\infty} dx\widetilde{f}(x,\omega)e^{-i\omega px}. \tag{12.3}$$

Note that the last term in equation 12.3 is actually a Fourier transform over x: $\int_{-\infty}^{\infty} dx\widetilde{f}(x,\omega)e^{-ikx}$ in the frequency domain, where the wavenumber k is set to be proportional to the frequency, $k = \omega p$.

If in equation 12.3 the last integral is denoted as $\widetilde{\widetilde{f}}(p,\omega) = \int\limits_{-\infty}^{\infty} dx \widetilde{f}(x,\omega) e^{-i\omega px}$, the Radon transform can be implemented as:

$$\begin{aligned} F(\tau,p) &= \int\limits_{-\infty}^{\infty} f(x,\tau+px)dx = \frac{1}{2\pi}\int\limits_{-\infty}^{\infty} e^{-i\omega\tau}\int\limits_{-\infty}^{\infty} dx\widetilde{f}(x,\omega)e^{-i\omega px} \\ &= \int\limits_{-\infty}^{\infty} f(x,\tau+px)dx = \frac{1}{2\pi}\int\limits_{-\infty}^{\infty} e^{-i\omega\tau}\widetilde{\widetilde{f}}(p,\omega). \end{aligned} \tag{12.4}$$

Note that in equation 12.4, if p is fixed, the last integral is an inverse Fourier transform from ω to the vertical time τ domain.

13 Appendix B: The seismic data in the pseudodepth domain

In this appendix, we present our best understanding of the seismic data in inverse scattering series parameter inversion, i.e., the data described by Zhang (2006), Jiang et al. (2008), Li et al. (2008); Li and Weglein (2010), Wang et al. (2009), and Liang et al. (2009).

For simplicity, let's consider a 1D case where the recorded data are a function of time $d(t)$[14]. However, the data used in Zhang (2006); Jiang et al. (2008); Li et al. (2008); Li and Weglein (2010); Wang et al. (2009); Liang et al. (2009) are all a function of depth $D(z)$[15]. How are they connected?

First of all, an event in the time domain, its arrival time; for example, t is converted to pseudo depth $z = \frac{c_0}{t}$ where c_0 is the reference velocity. This can be achieved by letting them be equal in the Fourier domain $\widetilde{D}(k_z) = \widetilde{D}(2\omega/c_0) = \widetilde{d}(\omega)$, where their definitions in the Fourier domain are:

$$\widetilde{d}(\omega) = \int_{-\infty}^{\infty} dt e^{i\omega t} d(t), \tag{13.1}$$

and

$$\widetilde{D}(k_z) = \int_{-\infty}^{\infty} dz e^{ik_z z} D(z). \tag{13.2}$$

Consequently, $D(z)$ can be linked to $d(t)$ as follows: $z = c_0 t/2$, $t = 2z/c_0$:

$$\begin{aligned} D(z) &= \frac{1}{2\pi}\int_{-\infty}^{\infty} dk_z e^{-ik_z z}\widetilde{D}(k_z) = \frac{1}{2\pi}\int_{-\infty}^{\infty} e^{-i(2\omega/c_0)z}\widetilde{D}(2\omega/c_0)d(2\omega/c_0) \\ &= \frac{2}{c_0}\frac{1}{2\pi}\int_{-\infty}^{\infty} e^{-i\omega(2z/c_0)}\widetilde{D}(2\omega/c_0)d\omega = \frac{2}{c_0}\frac{1}{2\pi}\int_{-\infty}^{\infty} e^{-i\omega(2z/c_0)}\widetilde{d}(\omega)d\omega \\ &= \frac{2}{c_0}d(2z/c_0) \end{aligned} \tag{13.3}$$

From equation 13.3, the data in the depth domain can be obtained from data in the time domain by stretching the argument by a factor $\frac{c_0}{2}$ and squeezing it by its reciprocal $\frac{2}{c_0}$. Consequently, the total areas remain the same: $\int_{-\infty}^{\infty} d(t)dt = \int_{-\infty}^{\infty} D(z)dz$.

[14] We used the lowercase d to denote data in the time domain.

[15] We used the uppercase D to denote data in depth.

References

Alford, R M, K R Kelly, and D M Boore. "ACCURACY OF FINITE-DIFFERENCE ACOUSTIC MODELING OF THE ACOUSTIC WAVE EQUATION." *Geophysics* 39 (1974): 834–842.

Bickel, Samuel H. "Velocity-depth ambiguity of reflection traveltimes." *Geophysics* 55 (1990): 266–276.

Chang, D., A. B. Weglein, and F. Liu. "Developing multidimensional depth imaging for a velocity and density varying earth: an initial imaging study and 2D 2-parameter modeling to generate data in the (x,t) domain needed to test ISS imaging algorithms." *2010 M-OSRP Annual Report* (2010): 115–128.

Clayton, R. W. and R. H. Stolt. "A Born-WKBJ inversion method for acoustic reflection data." *Geophysics* 46 (1981): 1559–1567.

Innanen, Kristopher. A. *Reflector location using high-order inverse scattering series terms.* PhD thesis, 2004.

Jiang, S. and A. B. Weglein. "Deriving an imaging algorithm for a laterally invariant multi-parameter acoustic medium from the inverse scattering series." *M-OSRP Annual Report* (2007).

Jiang, S., A. B. Weglein, and S. A. Shaw. "Progressing multiparameter imaging using the inverse scattering series: An initial analytic test of the leading order imaging subseries (LOIS) closed form and its extended higher order imaging subseries (HOIS) closed form for a laterally invariant two-parameter acoustic medium." *M-OSRP Annual Report* (2008).

Kelly, K R, R W Ward, Sven Treitel, and R M Alford. "SYNTHETIC SEISMOGRAMS: A FINITE-DIFFERENCE APPROACH." *Geophysics* 41 (1976): 2–27.

Li, X., F. Liu, S. Jiang, and A. B. Weglein. "Depth imaging without the velocity cares about the phase and amplitude information of events: Focusing on the use of the angle dependent amplitude information of events." *M-OSRP Annual Report* (2008).

Li, X. and A. B. Weglein. "ISS imaging for type 1 and type 2 AVO targets: analysis of forward and inverse series for target identification, part I." *2009 M-OSRP Annual Report* (2010).

Liang, H., A. B. Weglein, , and X. Li. "Discussion of the impact of shear waves on the model type assumption for ISS depth imaging: how far below the water bottom might we expect value for a velocity and density varying acoustic ISS imaging algorithm." *M-OSRP 2009 Annual meeting* (2011): 90–104.

Liang, H., A. B. Weglein, and X. Li. "Initial tests for the impact of matching and mismatching between the earth model and the processing model for ISS imaging and parameter estimation." *2009 M-OSRP Annual Report* (2009).

Liu, F. and A. B. Weglein. "Conservation of cumulative reflection coefficients." *2007 M-OSRP Annual Report* (2008): 159–168.

Liu, F. and A. B. Weglein. "Addressing the bandlimited nature of seismic source and rapid lateral variations of the Earth: source regularization and cascaded imaging operator." *2009 M-OSRP Annual Report* (2010): 72–117.

Liu, F., A. B. Weglein, B. G. Nita, and K. A. Innanen. "Inverse scattering series for vertically and laterally varying media: application to velocity independent depth imaging." *M-OSRP Annual Report* 4 (2005).

Liu, Fang. *Multi-dimensional depth imaging without an adequate velocity model.* PhD thesis, University of Houston, 2006.

Morse, Philip M. and Herman Feshbach. *Methods of theoretical physics.* McGraw-Hill Book Co., 1953.

Ross, Warren S. "The velocity-depth ambiguity in seismic traveltime data." *Geophysics* 59 (1994): 830–843.

Shaw, S. A., A. B. Weglein, D. J. Foster, K. H. Matson, and R. G. Keys. "Isolation of a leading order depth imaging series and analysis of its convergence properties." *M-OSRP Annual Report* 2 (2003): 157–195.

Shaw, Simon. A. *An inverse scattering series algorithm for depth imaging of reflection data from a layered acoustic medium with an unknown velocity model.* PhD thesis, University of Houston, 2005.

Stork, Christof and Robert W. Clayton. "Using constraints to address the instabilities of automated prestack velocity analysis." *Geophysics* 57 (1992): 404–419.

Swan, Herbert W. "Removal of offset-dependent tuning in AVO analysis." *67th Annual Internat. Mtg., Soc. Expl. Geophys., Expanded Abstracts.* . Soc. Expl. Geophys., 1997. 175–178.

Wang, Z., A. B. Weglein, and X. Li. "New capture of direct velocity independent depth imaging in a one-dimensional two-parameter acoustic earth." *2009 M-OSRP Annual Report* (2009).

Weglein, A. B. "M-OSRP 2008 Introduction and Preface." *2008 M-OSRP Annual Report* (2009): 114–128.

Weglein, A. B., F. V. Araújo, P. M. Carvalho, R. H. Stolt, K. H. Matson, R. T. Coates, D. Corrigan, D. J. Foster, S. A. Shaw, and H. Zhang. "Inverse scattering series and seismic exploration." *Inverse Problems* 19 (2003): R27–R83.

Weglein, A. B., D. J. Foster, K. H. Matson, S. A. Shaw, P. M. Carvalho, and D. Corrigan. "Predicting the correct spatial location of reflectors without knowing or determining the precise medium and wave velocity: initial concept, algorithm and analytic and numerical example." *Journal of Seismic Exploration* 10 (2002): 367–382.

Weglein, A. B., K. H. Matson, D. J. Foster, P. M. Carvalho, D. Corrigan, and S. A. Shaw. "Imaging and inversion at depth without a velocity model: Theory, concepts and initial evaluation." *70th Annual Internat. Mtg., Soc. Expl. Geophys., Expanded Abstracts.* . Soc. Expl. Geophys., 2000. 1016–1019.

Weglein, Arther B. and Bruce G. Secrest. "Wavelet estimation for a multidimensional acoustic or elastic earth." *Geophysics* 55 (1990): 902–913.

Zhang, H. *Direct non-linear acoustic and elastic inversion: Towards fundamentally new comprehensive and realistic target identification.* PhD thesis, University of Houston, 2006.

Zhang, H. and A. B. Weglein. "Target identification using the inverse scattering series: inversion of large-contrast, variable velocity and density acoustic media." *M-OSRP Annual Report* 2 (2003).

Progress of ISS depth imaging without velocity for more complex cases -Overview of Zhiqiang Wang's thesis

Z. Wang

May 25, 2012

Abstract

This report is a brief overview of the author's dissertation on the progress of ISS depth imaging without velocity. The key points include: derivation of the HOIS closed form; the HHOIS closed form for the medium with large contrast; "HOIS plus laterally exclusive" (HOIS that is extended to a medium with lateral variations); "beyond conjecture," an imaging algorithm that is an extension of "the imaging conjecture" algorithm and that can accommodate large contrasts for velocity- and density-varying media; and a combined algorithm of FK migration and the asymptotic method for processing data with a limited crossline aperture for a 3D medium.

1 Introduction

Current migration algorithms have the assumption that the velocity is known, having been obtained from a procedure called "velocity analysis." For complex media, in which the velocity analysis has difficulties, the assumption is not satisfied and the performances of the algorithms are affected. One way to avoid these problems is to improve the performance of the velocity analysis; another is to develop algorithms that do not require the actual velocity. The inverse scattering series (ISS) has been used to derive candidate direct nonlinear imaging algorithms following the latter route (Weglein et al., 2002).

The ISS is a form of the perturbation theory: one sets up a reference media, and considers the difference between the actual medium and the reference medium as a perturbation. It expands the perturbation into a series in different orders of the scattered wavefield. Each term in the series can be solved using the reference Green's function and the scattered wavefield. No actual velocity is required during this process.

There are still many challenges needing to be addressed in ISS direct depth imaging. Among them, the author is most interested in and has been working on the following:

1. The size of the difference between the actual velocity and the reference velocity, and the duration of the difference,

2. The incident angles where the reflection events occur,

3. The number of parameters that describe the medium, and

4. The number of dimensions of the medium.

Each of these challenges has its own requirements for the imaging algorithms, and many times they are coupled together. That means even if one imaging algorithm can solve several challenges seperately, it may fail when these challenges happen together.

In this report, Sections 2, 3, 4, and 5 are discussions corresponding to the challenges listed above, and Section 6 is a brief summary.

2 ISS for a large contrast medium

Applying the inverse scattering theory to a 1D normal-incidence case, Shaw et al. (2004) identified the leading-order imaging subseries (LOIS) and compacted it into a closed form. It includes the leading-order imaging terms in each V_i (in the one-parameter case, α_i) and makes the series truncation unnecessary. Thus, instead of adding terms one by one, one reference velocity FK migration and one LOIS adjustment accomplish the task. This saves a large amount of time in both programming and computation. LOIS works well for small-contrast media and requires improvements for large-contrast media, because of the imaging terms that are not included in LOIS.

By studying the terms not included in LOIS, the shifted LOIS (SLOIS, see Zhang et al., 2006) and the higher-order imaging subseries (HOIS, Liu, 2006) were proposed. Numerical tests indicate that they can accommodate a larger contrast than LOIS can. But no clear derivations are provided for both algorithms. This limits a better understanding of the closed forms and inhibits progress beyond them.

Wang et al. (2009a) first showed the derivation of the HOIS closed form, and Wang et al. (2009b) proposed HHOIS for a larger contrast medium, which HOIS could not accommodate.

In this section, we will use analytic and numerical examples to show the accuracy of different closed forms.

2.1 Derivation of HOIS

Wang et al. (2009a) expands α_i in a new form which is different from Shaw et al. (2004). The second and third order terms in the new form are illustrated in Figures 1 and 2, where (i) represents α_i, α_{ij} represents the jth term in α_i, (i) besides n dashed arrows represents $(\int_{-\infty}^{z} \alpha_i)^n$, and (i) pointed to by n dashed arrows means $d^n\alpha_i/dz^n$. We have omitted the coefficients in the schematic diagrams.

LOIS captures the leading-order imaging terms in each α_i, e.g., α_{22} within α_2 and α_{32} within α_3. It can be illuminated in a schematic diagram (Figure 3). After expanding in the new form, I can also prove that SLOIS captures α_{33}, α_{43}, etc. and HOIS captures α_{34}, α_{44}, etc. Their schematic diagrams are shown in Figures 4 and 5.

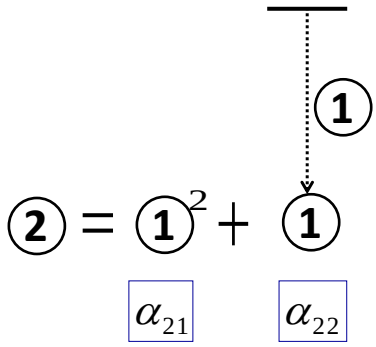

Figure 1: A schematic diagram of α_2.

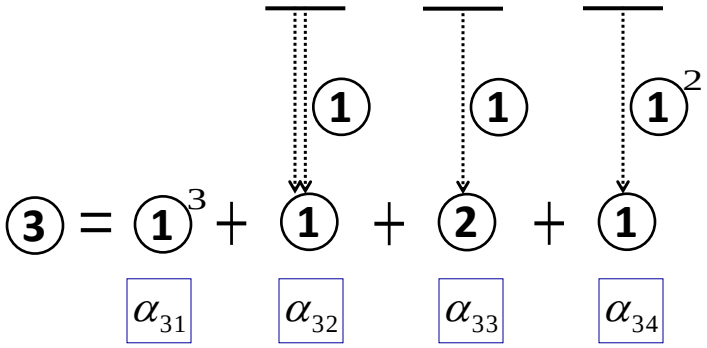

Figure 2: A schematic diagram of α_3.

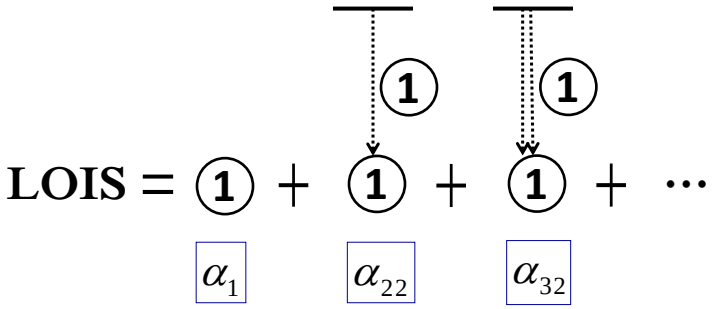

Figure 3: A schematic diagram of LOIS

2.2 Analytic analysis

An analytic analysis provides a clear and transparent way to see how accurate the linear approximation α_1 and different closed forms are.

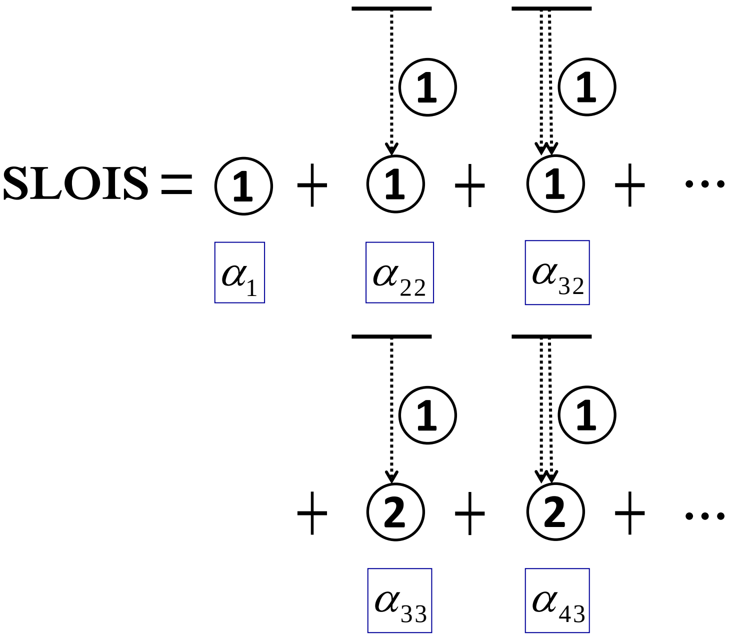

Figure 4: A schematic diagram of SLOIS

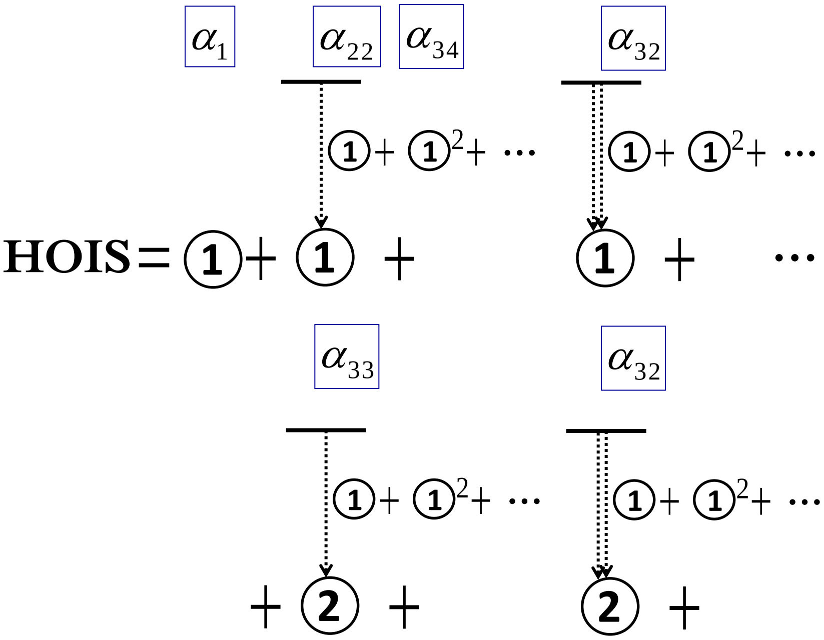

Figure 5: A schematic diagram of HOIS

We use a 1D four-layer constant-density acoustic model, which is simple but sufficient to indicate the accuracies of these algorithms. In this model, the layers have velocities c_0, c_1, c_2, c_3 and thicknesses d_0, d_1, d_2, ∞. The reflection coefficients at each interface are as follows:

$$R_1 = \frac{c_1 - c_0}{c_1 + c_0}, \quad R_2 = \frac{c_2 - c_1}{c_2 + c_1}, \quad R_3 = \frac{c_3 - c_2}{c_3 + c_2}.$$

Table 1 puts together the differences between the actual depths and predicted depths of the interfaces, Δz_i, for α_1 and different closed forms, where i means for the ith interface, with higher orders omitted. Details about how the results are obtained can be found in Wang (2012). From the Table, there are some interesting conclusions that can be drawn:

Table 1: Comparison of the accuracy of different algorithms

Closed forms	Δz_1	Δz_2	Δz_3
α_1	0	$-2R_1d_1$	$-2R_1d_1 - 2(R_1 + R_2)d_2$
LOIS	0	$-2R_1(R_1 - 2R_2)d_1$	$-2R_1(R_1 - 2R_2)d_1 - 2R_1d_2$
SLOIS	0	$-2R_1^2d_1$	$-2R_1^2d_1 - 2R_1d_2$
HOIS	0	0	$-2R_1R_2^2d_2$
HHOIS	0	0	$-2R_1^3R_2^2d_2$

1. All of the algorithms locate the first interface at the right depth, because the velocity in the first layer is the same as the reference velocity. HOIS and HHOIS also image the second interface at the right depth.

2. Δz_3 is getting smaller, in the order of α_1, SLOIS, HOIS, HHOIS. The same is true for the accuracy of the closed forms. Usually, HOIS is accurate enough. For example, if $R_1 = R_2 = 0.1$ and $d_2 = 500m$, $\Delta d_2^{HOIS} \approx 1m$. This can be ignored. But when the differences between the actual and the reference media are big and/or the durations of these differences are large, for example $R_1 = R_2 = 0.5$ and $d_2 = 1000m$, the deviation would be $\Delta d_2^{HOIS} \approx 250m$ and can not be neglected. In such cases, HHOIS can provide much better results. The deviation Δd_2^{HHOIS} is about 62.5m for the same example.

3. For LOIS, Δz_2 is related to R_2, and Δz_3 is related to R_3, meaning that it uses properties at deeper depths to image for a shallower depth (Zhang et al., 2006). When R_i is small, LOIS usually generates better results than α_1 does, but when R_i is big, it has a large impact on the imaging and sometimes LOIS generates even worse results than α_1 does.

2.3 Numerical tests

The synthetic data used for the numerical tests are generated from a 1D model (model parameters change only in the vertical direction) in a 2D experiment (the wave is propagating in 2D space). The model parameters, just velocity in this model, are shown in Table 2. The model has a large

Table 2: The model parameters

	Velocity (m/s)	Thickness(m)
First layer	1500	300
Second layer	2000	1200
Third layer	5000	1500
Fourth layer	3000	∞

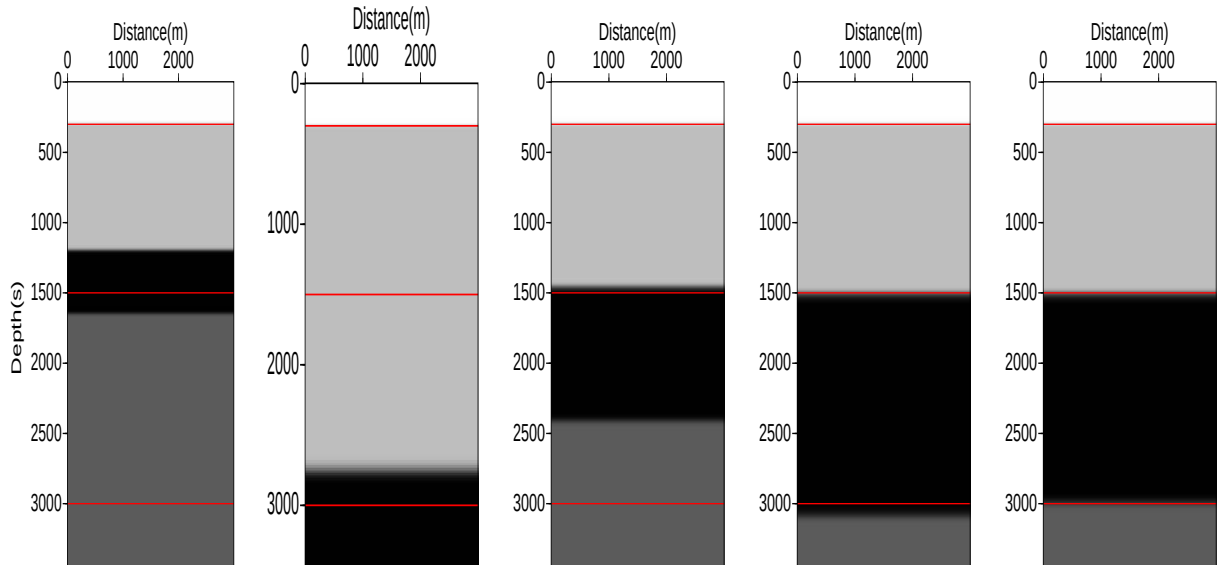

(a) α_1 (b) LOIS (c) SLOIS (d) HOIS (e) HHOIS

Figure 6: Comparing the imaging results of α_1 and different closed forms

contrast, so the differences among the results of α_1 and the various closed forms can be seen clearly.

Figure 6 shows the imaging results. α_1 locates the first interface correctly but not the second and third ones. LOIS performs the same on the first interface as α_1 does, but performs poorly on the second and third interfaces. This is because the model has a large contrast, and using energy scattered from greater depths to image for a shallower depth generates a large deviation. SLOIS captures additional terms, which keeps the pros and amends the cons. HOIS and HHOIS both locate the first and second interfaces at the right depths, and HHOIS performs better on the third interface than HOIS does.

3 The "HOIS plus laterally exclusive" algorithm (HOISPLE)

ISS is wave-equation based and has the potential capability to image a reflector with any dipping angle, while a 1D earth is assumed in the derivations of the LOIS and HOIS closed forms, HOIS

performs well when this assumption is satisfied. Liu (2006) studied ISS depth imaging for the medium with lateral variations and showed that HOIS is just a part of the whole series. Many new terms related to lateral variations arise and are not captured by the HOIS closed form, which is the reason why only a certain degree of lateral variations can be accommodated.

In this section, the same technique, which is used for derivation of the HOIS closed form in the previous section, is applied to recognize and capture the terms for a medium with lateral variations ("laterally exclusive" terms) and thereby to extend the work of Liu (2006) to accommodate large lateral variations in the medium.

3.1 HOIS for a medium with lateral variations

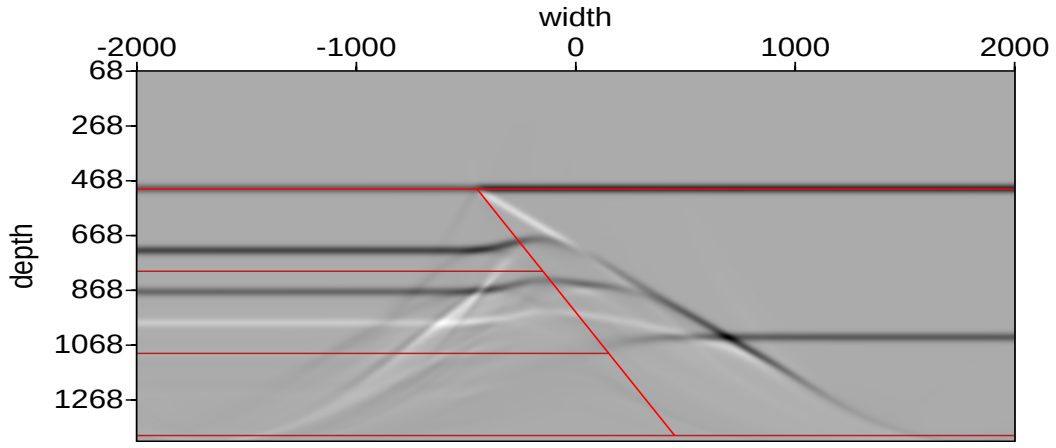

Figure 7: Water-speed Stolt migration for the fault model.

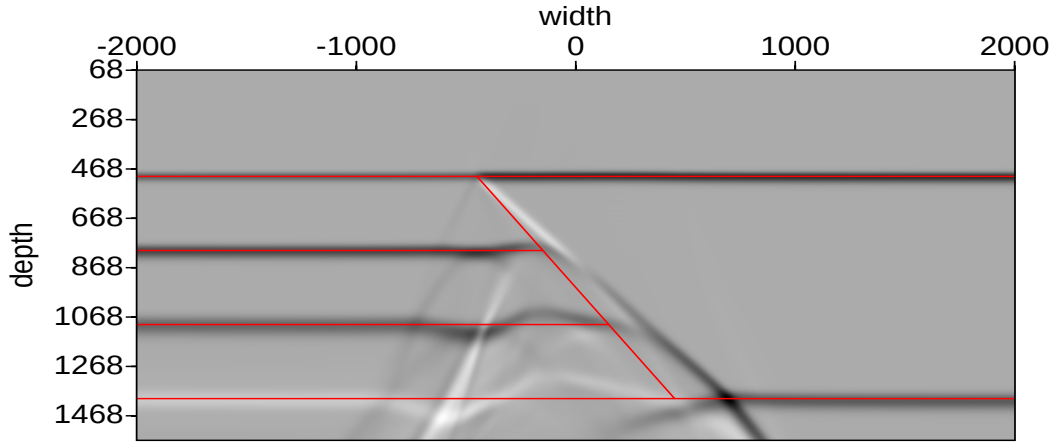

Figure 8: HOIS for the fault model.

Figure 7 shows the water-speed Stolt migration for the fault model (Liu and Weglein, 2009), and Figure 8 shows the imaging result after applying the HOIS closed form. For the flat reflectors, the HOIS imaging result shows improved accuracy, and for the dipping reflectors the accuracy is good but there is still room for improvement. This issue will be addressed by those terms that are not captured by HOIS.

3.2 Lateral terms

Applying ISS for a 2D medium, with lateral variations, the second-order term of $\alpha(x,z)$ can be expressed as follows (Liu, 2006, and Wang, 2012):

$$\begin{aligned}\alpha_2(x,z) =& \frac{1}{16\pi^3}\int_{-\infty}^{\infty} dk_2\, e^{ik_2x}\int_{-\infty}^{\infty} dk_3\, e^{ik_3x}\int_{-\infty}^{\infty} dz_1\, \widetilde{\alpha}_1(k_2,z_1)\\ &\times\int_{-\infty}^{z_1} dz_2\, \widetilde{\alpha}_1(k_3,z_2)\int_{-\infty}^{\infty} dk_z\, e^{i(z_1-z)k_z}\, i\frac{k_z^2+(k_2+k_3)^2}{u_1}e^{i\frac{z_1-z_2}{2}(u_1-k_z)},\end{aligned} \tag{3.1}$$

where

$$u_1 = sgn(k_z)\sqrt{k_z^2+4k_2k_3}.$$

1. If the medium is 1D, i.e., if it just has changes in the z direction, then

$$\alpha(x,z)=\alpha(z) \Longrightarrow \widetilde{\alpha}(k,z)=\int_{-\infty}^{\infty} dk\, e^{-ikx}\alpha(z)dx = \alpha(z)\delta(k).$$

Thus,

$$\begin{aligned}\alpha_2(x,z) &= \frac{1}{16\pi^3}\int_{-\infty}^{\infty} dz_1\, \widetilde{\alpha}_1(z_1)\int_{-\infty}^{z_1} dz_2\, \widetilde{\alpha}_1(z_2)\int_{-\infty}^{\infty} dk_z\, e^{i(\varepsilon_0+\varepsilon_1)k_z}\, i\frac{k_z^2+0}{k_z}e^{i\varepsilon_1(k_z-k_z)}\\ &= -\frac{1}{2}\left(\alpha_1^2(z)+\left[\frac{d\alpha_1(z)}{dz}\right]\int_{-\infty}^{z}\alpha_1(u)du\right),\end{aligned} \tag{3.2}$$

which is exactly the same as α_2 for the 1D case in Shaw et al. (2004) and Zhang (2006).

2. If $k_2 \ll k_z$ and $k_3 \ll k_z$, which means that the medium has a small lateral variation, Wang (2012) shows that the first- and second-order approximations will give us the following terms:

$$\alpha_{21}(x,z) \;=\; -\frac{1}{2}\alpha_1^2(x,z)-\frac{1}{2}\frac{\partial\alpha_1(x,z)}{\partial z}\frac{\partial F(x,z)}{\partial z} \tag{3.3}$$

and

$$\alpha_{22}(x,z)=\frac{1}{2}\frac{\partial\alpha_1(x,z)}{\partial x}\frac{\partial F(x,z)}{\partial x}, \tag{3.4}$$

where

$$F(x,z)=\int_{-\infty}^{z} du\int_{-\infty}^{u}\alpha_1(x,v)dv\,. \tag{3.5}$$

These are the α_{21} and α_{22} terms in Liu (2006). The assumption is violated when the dipping angle of the reflector is large, making α_{21} and α_{22} inadequate.

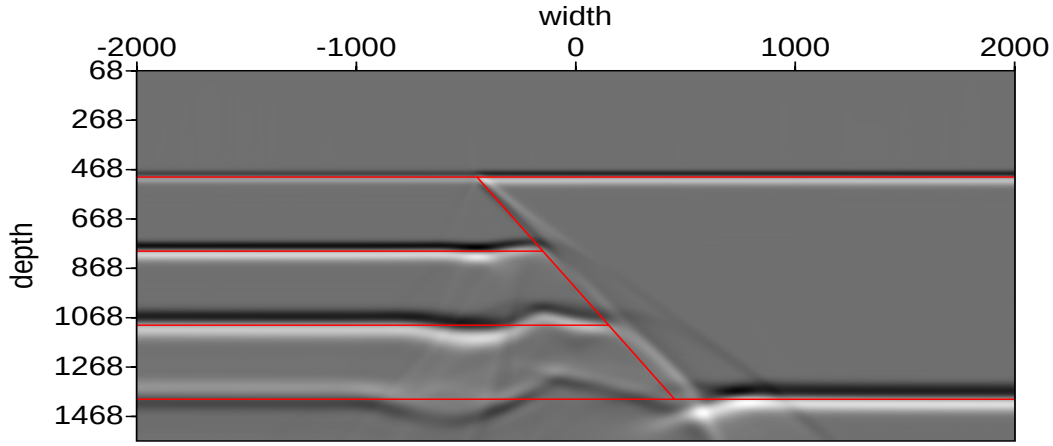

Figure 9: HOISPLE image for the fault model.

3.3 The "HOIS plus laterally exclusive" (HOISPLE) algorithm

No rigid laterally exclusive algorithm has been developed yet. Below is just one method that has been tried and showed good capability. The idea is that the migration shouldn't not be done just in the z direction. Instead, similarly to Kirchhoff migration, migration should be carried out in every direction and the interference over different angles will construct the desired part and destruct the undesired part.

The algorithm will be referred to as HOISPLE in the following text, and mathematically it has the form,

$$\alpha^{HOIS}\left(\vec{r}+\hat{u}*\frac{1}{2}\int_{-\infty}^{z}du\frac{\alpha_1(x,u)}{1-0.25\alpha_1(x,u)}\right)=\alpha_1(\vec{r}), \tag{3.6}$$

where

$$\hat{u}=\sin\psi\hat{x}+\cos\psi\hat{z}, \qquad \psi\in[\pi/2,\pi/2] \tag{3.7}$$

and the final imaging $I(x,z)$ equals the interference of α over different angles,

$$I(x,z)=\sum_{\psi}\alpha^{''}(x,z,\psi)\,. \tag{3.8}$$

Here I use α'' instead of α to cancel the non-wavefront parts by destructive interference. The term ψ represents the migration angle with respect to the z direction, which could range in $[\pi/2,\pi/2]$. But for most cases, a subset is chosen to save computational time.

Figure 9 is the HOISPLE imaging result for the fault model. An amplitude gain has been used to make the deeper parts in Figure 9 more apparent. The fault location is closer to the actual location than it was in the result of the original HOIS in Figure 8. Also, the diffraction effect is attenuated after HOISPLE imaging.

Figures 10 and 11 are the HOIS and HOISLE imaging results for the salt model (Liu, 2006). An amplitude gain has been used in Figure 11. As in the fault model, the bottom of the salt body after

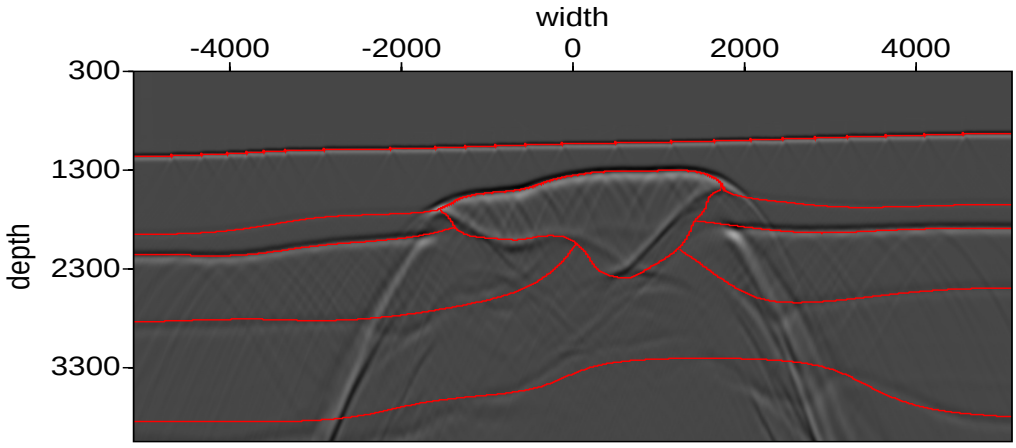

Figure 10: HOIS image for the salt model.

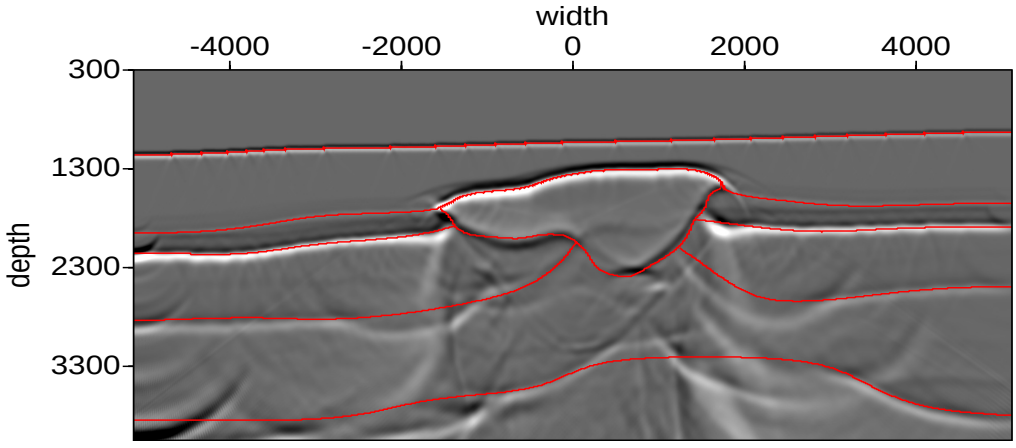

Figure 11: HOISPLE image for the salt model.

HOISPLE migration is located much closer to the actual location than it was in the HOIS result, and the diffractions are largely reduced.

4 ISS depth imaging with both velocity and density changes

In ISS depth imaging, α_1, LOIS, HOIS and HHOIS can accommodate increasingly larger contrasts within the medium and HOISPLE improves the processing of lateral variations, but all of these algorithms work for a one-parameter medium. When we are going from a one-parameter medium to a two-parameter medium (one with variations in both velocity and density), however, an extension is required and has been proposed in what is called the "imaging conjecture" algorithm (Weglein, 2008, Pages 1-8). The imaging conjecture algorithm has a multi-parameter front-end (sitting on top of a Fang Liu type of HOIS imaging algorithm engine) that excludes density-only reflections and outputs reflectivity. It can deal with a very-large-contrast one-parameter medium (for the constant-density case, it will be the same as HOIS) and also deals with a small-contrast two-parameter medium (Jiang et al., 2008, and Li et al., 2008).

Chapter 4 in Wang (2012) shows the detailed derivation of the "imaging conjecture" algorithm. Furthermore, a new capture, including additional imaging terms, is provided that extends the previous capability of the ISS imaging for a multi-parameter earth to accommodate larger differences between actual and reference velocities. It will be referred to as the "beyond conjecture" algorithm in the following.

4.1 The imaging conjecture algorithm for a two-parameter medium

For a two-parameter earth model (e.g., a model with bulk modulus and density or velocity and density), the wave equations in the actual and reference media (Clayton and Stolt, 1981; Weglein et al., 1997) have the following forms,

$$\left[\frac{\omega^2}{K(\mathbf{r})} + \nabla \cdot \frac{1}{\rho(\mathbf{r})} \nabla \right] G(\mathbf{r}, \mathbf{r}_s; \omega) = \delta(\mathbf{r} - \mathbf{r}_s), \tag{4.1}$$

$$\left[\frac{\omega^2}{K_0(\mathbf{r})} + \nabla \cdot \frac{1}{\rho_0(\mathbf{r})} \nabla \right] G_0(\mathbf{r}, \mathbf{r}_s; \omega) = \delta(\mathbf{r} - \mathbf{r}_s), \tag{4.2}$$

where $G(\mathbf{r}, \mathbf{r}_s; \omega)$ and $G_0(\mathbf{r}, \mathbf{r}_s; \omega)$ are respectively the free-space causal Green's functions that describe the wave propagation in the actual and reference media, $K = c^2\rho$ is P-wave bulk modulus, and c is P-wave velocity and ρ is density. The quantities with subscript '0' are the corresponding quantities in the reference medium.

The perturbation is

$$V = L_0 - L = \frac{\omega^2 \alpha}{k_0} + \nabla \cdot \frac{\beta}{\rho_0} \nabla \tag{4.3}$$

where $\alpha = 1 - K/K_0$ and $\beta = 1 - \rho_0/\rho$.

As in the one-parameter case, V, α, and β can be expanded as different orders of the scattered wave field,

$$V = V_1 + V_2 + \cdots \tag{4.4}$$

$$\alpha = \alpha_1 + \alpha_2 + \cdots \tag{4.5}$$

$$\beta = \beta_1 + \beta_2 + \cdots \tag{4.6}$$

For a 1D acoustic two-parameter earth model, the relationship for α_1, β_1 and the scattered wave field can be derived using the equation in ISS for the first order (Zhang, 2006; Jiang and Weglein, 2007):

$$\begin{aligned} D(z,\theta) &= -\frac{\rho_0}{4}\left[\frac{1}{\cos^2\theta}\alpha_1(z) + (1-\tan^2\theta)\beta_1(z)\right] \\ &= -\frac{\rho_0}{4}\left[\frac{1}{\cos^2\theta}\left(\alpha_1(z)-\beta_1(z)\right) - 2\beta_1(z)\right]. \end{aligned} \tag{4.7}$$

and a new "imaging composite" $\mathscr{D}(z,\theta)$ is defined as follows:

$$\mathscr{D}(z,\theta) = \frac{1}{\cos^2\theta}\left[\alpha_1(z)-\beta_1(z)\right] - 2\beta_1(z) = -\frac{4}{\rho_0}D(z,\theta). \tag{4.8}$$

It is a quantity related to the reflectivity.

Weglein (2008) proposed the imaging conjecture algorithm after studying the similarity between the two-parameter case and the one-parameter case:

$$\mathscr{D}^{HOIS}\left(z + \frac{1}{2}\int_{-\infty}^{z} dz' \frac{\alpha_1(z')-\beta_1(z')}{\cos^2\theta - 0.25[\alpha_1(z')-\beta_1(z')]}, \theta\right) = \mathscr{D}(z,\theta). \tag{4.9}$$

This closed form has been proved by Wang et al. (2009) using a clear derivation by applying the same method as for the derivation of HOIS.

The middle panels of Figure 12 and Figure 13 show the results of the imaging conjecture algorithm for a small- and large-contrast media, respectively. The model used in Figure 12 has a smaller velocity contrast (about 6.7%), and the one used in Figure 13 has a bigger velocity contrast (about 23.3%). We see that for the small-contrast medium the imaging conjecture corrects locations of the mislocated reflectors in FK constant-velocity migration, while for the large-contrast medium the second interface is still mislocated, especially at large angles. This indicates that there are more challenges to address for large-contrast media.

4.2 The beyond conjecture algorithm

The derivation of the imaging conjecture algorithm also indicates that there are still imaging terms in the third order that are not included in the imaging conjecture algorithm. Wang et al. (2009) is able to capture parts of them, and has proposed the beyond conjecture algorithm:

$$\mathscr{D}^{HOIS}\left(z + \frac{1}{2}[1-\beta_1(z)]\int_{-\infty}^{z} dz' \frac{\alpha_1(z')-\beta_1(z')}{\cos^2\theta - 0.25[\alpha_1(z')-\beta_1(z')]}, \theta\right) = \mathscr{D}(z,\theta). \tag{4.10}$$

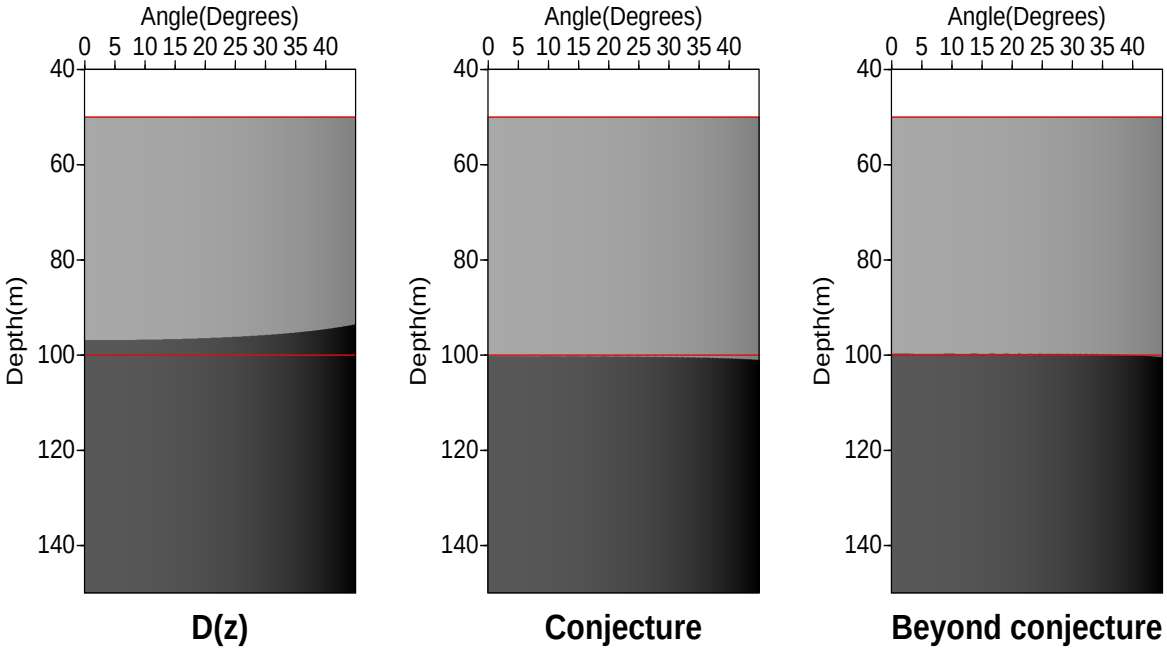

Figure 12: The comparison of the imaging conjecture and beyond conjecture algorithms using a three-layer model with small contrasts in properties: $v_0 = 1500m/s$, $\rho_0 = 1.0g/cm^3$; $v_1 = 1600m/s$, $\rho_1 = 1.1g/cm^3$; $v_2 = 1700m/s$, $\rho_2 = 1.2g/cm^3$. The left panel is the imaging result of $D(z, \theta)$ using FK constant-velocity migration, the middle panel is the result of the conjecture capture, and the right panel is the result of the beyond conjecture imaging capture.

This algorithm captures more terms than the imaging conjecture algorithm does and has a better capability. The testing results for the two models stated above are shown in the right panels of Figure 12 and Figure 13. Note that compared with the imaging conjecture algorithm, the beyond conjecture algorithm improves the location of the second reflector and the range of angles within which the image is reliable.

5 Preparing data with a finite crossline aperture for input into 3D ISS nonlinear imaging algorithms

For a 3D medium, if complete data are collected, the inline and crossline directions will be equal. There are not many changes needed in the theory (Liu et al., 2007, and Wang, 2012) when going from 2D to 3D. The challenges arise from processing the large amount of data in programming and from the incompleteness of the data.

Seismic imaging methods input measurements that are made on the earth's surface to make infer-

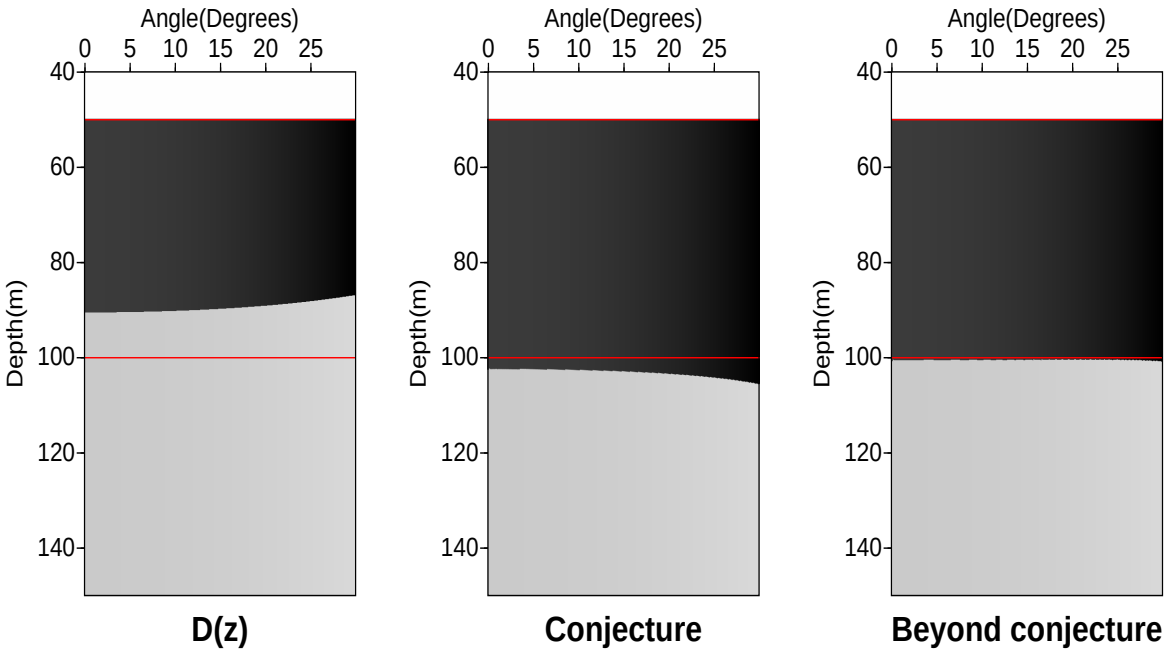

Figure 13: The comparison of the imaging conjecture and beyond conjecture algorithms using a three-layer model with large contrasts in properties: $v_0 = 1500m/s$, $\rho_0 = 1.0g/cm^3$; $v_1 = 1850m/s$, $\rho_1 = 1.1g/cm^3$; $v_2 = 1350m/s$, $\rho_2 = 1.2g/cm^3$. The left panel is the imaging result of $D(z, \theta)$ using FK constant-velocity migration, the middle panel is the result of the imaging conjecture capture, and the right panel is the result of the beyond conjecture imaging capture.

ences about subsurface reflectors' locations. When a source generates a wave into a medium, the wave is ubiquitous, traveling to all points on the measurement surface. Wave propagation and imaging methods require that measurements be made on the measurement surface where wave theory predicts the wave will arrive, i.e., everywhere on the measurement surface. When data collection is limited by economic and/or practical considerations, a modification to wave theory can be made by using asymptotic analysis to image limited data with a compromised theory.

In this section, we assume that the data are adequately sampled in the inline direction but have a serious aperture limitation in the crossline direction. Our objective is to provide a wave-theory imaging in the direction that has adequate collection and an asymptotic migration in the crossline limited-aperture direction. This objective is deriving an imaging algorithm that will allow the near-future anticipated less-than-full crossline coverage and the adequate inline acquisition to be input into the velocity-independent inverse scattering imaging algorithm pioneered by Liu et al. (2007).

5.1 The algorithm

Currently, data collection is often adequate in the inline direction but has a serious aperture limitation in the crossline direction, because of economic and/or practical considerations. Thus the wave-theoretic algorithm stated in Liu et al. (2007), which requires full data collection in both directions, does not suit this case well. In Stolt and Benson (1986), Chapter 3, the authors developed an asymptotic method to do 2.5D finite-aperture migration. Their method is extended to 3D by applying the asymptotic method in the crossline direction and keeping the inline direction wave theoretic (Wang et al., 2007, and Wang, 2012):

$$\alpha_1(x,y,z) = \frac{2z}{c}\int_{-\infty}^{+\infty} e^{ik_{mx}x}dk_{mx}\int_{-\infty}^{+\infty} dy_s \int_{y_s+h_1}^{y_s+h_2} dy_g \frac{r}{(r_g r_s)^{\frac{3}{2}}}\frac{1-\beta^2\gamma^2}{(1+\beta^2)(1+\gamma^2)}\frac{1}{\gamma_2-\gamma_1}P_F, \tag{5.1}$$

where

$$\begin{aligned} P_F &= \frac{1}{2\pi}\int_{-\infty}^{+\infty} d\omega\ e^{-ik'(r_g+r_s)}\frac{i\omega}{c_0}F(k_{mx},\omega)D(0.5k_{mx},y_g,-0.5k_{mx},y_s,\omega) \\ &= -\frac{1}{2\pi}\int_{-\infty}^{+\infty} d\omega e^{-ik'(r_g+r_s)}\frac{4\pi ik'}{\omega/c_0}D(0.5k_{mx},y_g,-0.5k_{mx},y_s,\omega). \end{aligned} \tag{5.2}$$

Equation 5.1 represents a wave propagation in the inline direction and a finite-aperture integration in the crossline direction. All of the collected data are used.

The imaging results is generated by substituting the result into the leading-order or higher-order closed forms in Liu et al. (2007):

$$\alpha^{LOIS}(\vec{x},z) = \alpha_1\left(\vec{x}, z-\frac{1}{2}\int_{-\infty}^{z}\alpha_1(\vec{x},u)du\right), \tag{5.3}$$

$$\alpha^{HOIS}\left(\vec{x}, z+\frac{1}{2}\int_{-\infty}^{z} du\frac{\alpha_1(\vec{x},u)}{\cos^2\theta_x+\cos^2\theta_x-\frac{1}{4}\alpha_1(\vec{x},u)}\right) = \alpha_1(\vec{x},z), \tag{5.4}$$

Note that, in equation 5.4, $\theta_x = 0$, because the assumption that $k_{hx} = 0$ has been made.

5.2 Numberical tests

Although the algorithm is derived in 3D, only the aymptotic part, i.e., the y direction in Equation 5.1, will be tested and compared with the wave-theoretic method using aperture-limited data.

A two-interface model, shown in Figure 14, where the location for each interface and the velocity for each layer are labeled, is used for testing. Here we will not be able to migrate the second interface correctly, and we would use the nonlinear imaging algorithms (which only depend on α_1,) to improve the result.

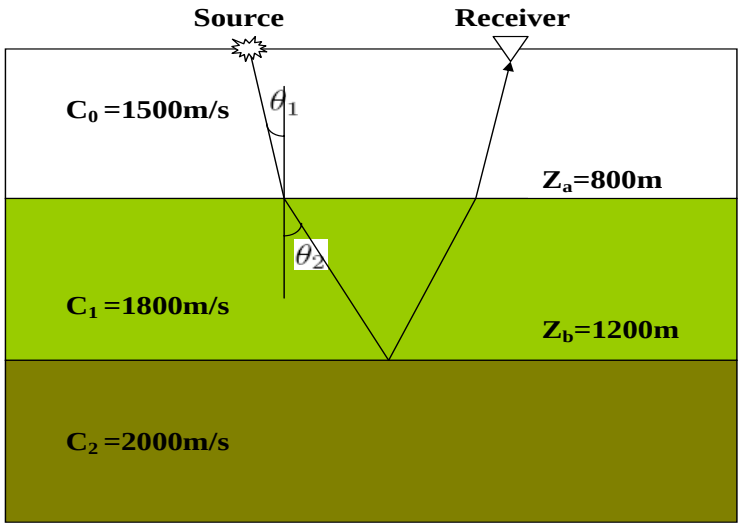

Figure 14: Two-interface model

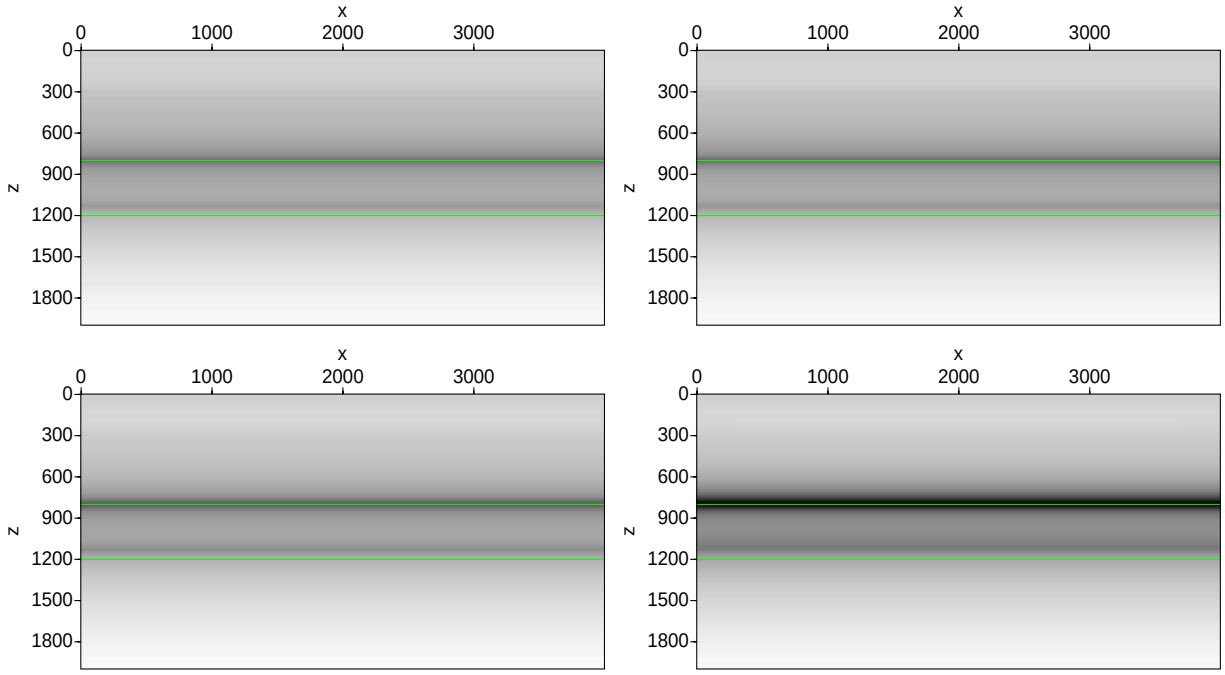

Figure 15: The imaging results of α_1 for Model 2, with apertures of $50m$ (upper left), $250m$ (upper right), $1000m$ (lower left), and $4000m$ (lower right).

The linear imaging result, α_1, is shown in Figure 15 for four different aperture cases. Figure 16 is picking the line at $x = 2000m$ in Figure 15 and drawing the amplitudes of those cases. We see that the first interface is correctly located but the second interface is not, which is expected. The amplitude of α_1 is different from its analytic calculation (Figure 17). Also, the second interface is

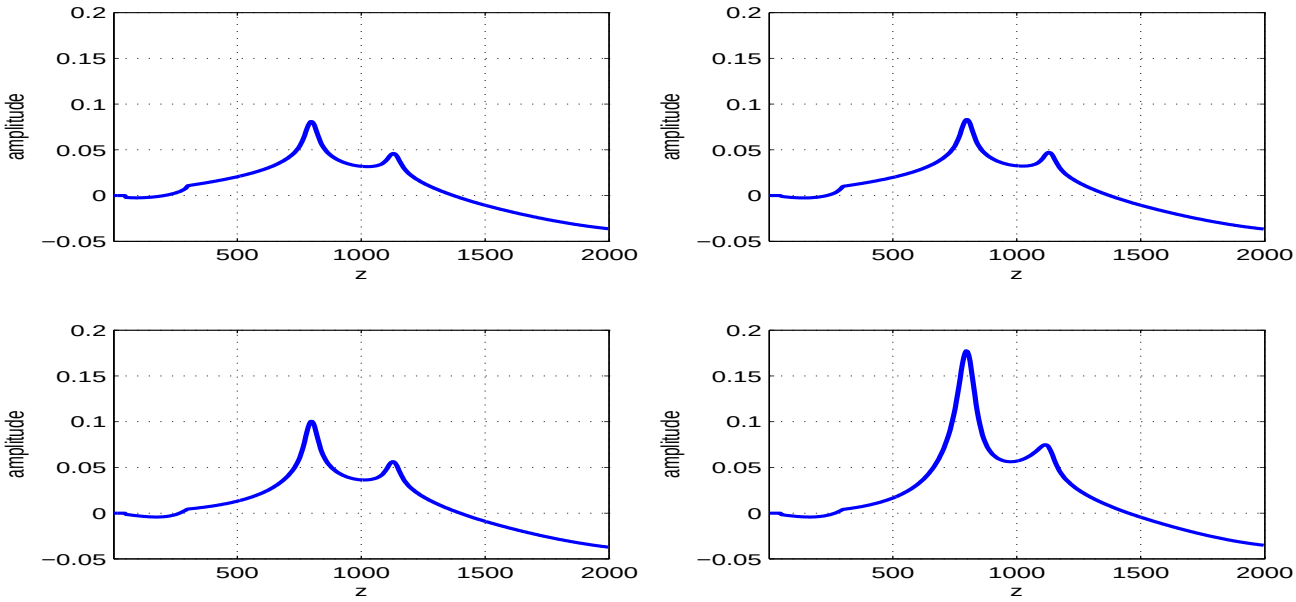

Figure 16: Amplitudes of α_1 at the line $x = 2000m$ with apertures of $50m$ (upper left), $250m$ (upper right), $1000m$ (lower left), and $4000m$ (lower right).

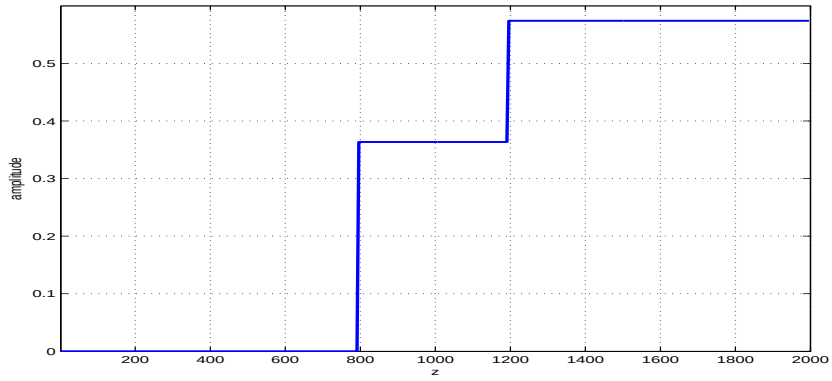

Figure 17: α_1 from analytical calculation.

dimmed by the tail of the first interface. Figure 18 is the result of using the HOIS algorithm. We can see that it moves the second interface towards the desired location but not significantly. It also moves the first interface, an undesired result.

Figure 19 is the result of α_1 using wave-theoretic method and Figure 20 is its amplitudes at the line $x = 2000m$ for different apertures. We can see that when the aperture increases, the amplitudes of α_1 become more box-like, the way the true values should look like. Figure 21 shows the result after

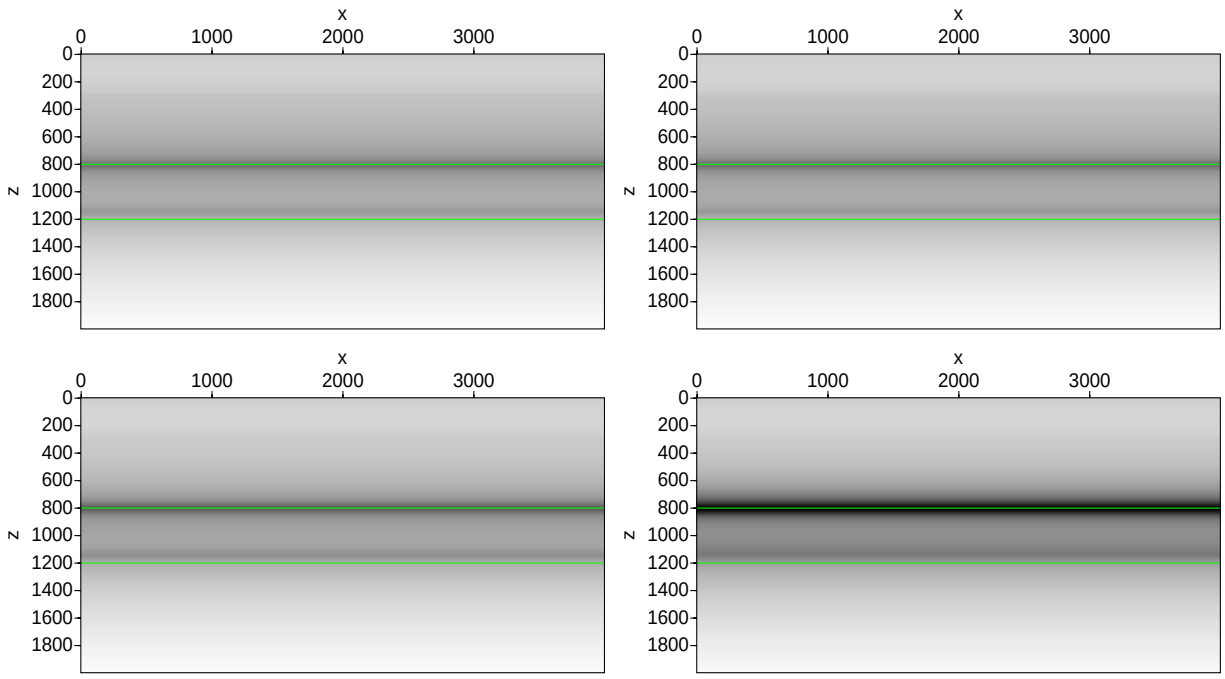

Figure 18: The imaging results of α_{HOIS} for Model 2, with apertures of $50m$ (upper left), $250m$ (upper right), $1000m$ (lower left), and $4000m$ (lower right).

applying α_1 into the HOIS closed form. The results largely depend on the size of the aperture. The larger the aperture, the better the result. This is consistent with the amplitude of α_1.

Comparing the results of the aperture-limited and wave-theoretic algorithms, we report the following conclusions:

1. For the location of interfaces provided by α_1, the wave-theoretic algorithm and the aperture-compensated algorithm give the same result, independently of the size of the aperture.

2. However, when we are using the entire α_1 to get α_{HOIS}, the results are different:

   (a) When the aperture is large, the wave-theoretic algorithm's requirement for complete data is satisfied and provides a perfect result, while the aperture-compensated asymptotic algorithm doesn't equally respect/treat low frequency compared with high frequency.

   (b) When the aperture is small, the wave-theoretic algorithm performs a Fourier Transform to the data with zeros beyond the aperture and generates artifacts that will affect α_{HOIS}. The aperture-compensated asymptotic algorithm is expecting the aperture problem and adjusting with it. Although still somewhat abusing the low frequency, the aperture-

compensated asymptotic algorithm can provide better results for HOIS than the wave-theoretic α_1 can for limited-aperture data.

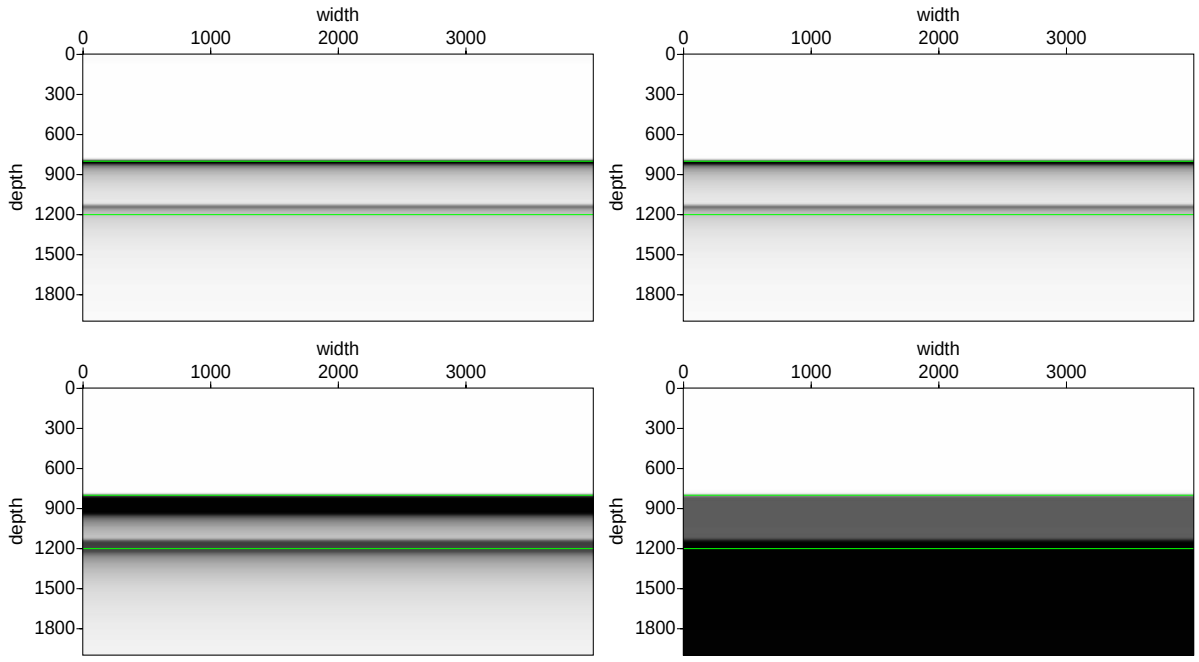

Figure 19: The imaging results of α_1 using the wave-theoretic method, with apertures of $50m$ (upper left), $250m$ (upper right), $1000m$ (lower left), and $4000m$ (lower right).

6 Discussion and conclusions

In this report, we give a brief overview of my PHD dissertation on the progress of ISS depth imaging without velocity: The derivation of HOIS helps us have a better understanding of the ISS; α_1, LOIS, SLOIS, HOIS, and HHOIS include increasingly more imaging terms and can generate increasingly better imaging results. The HOIS-plus-laterally-exclusive algorithm is a progression of ISS depth imaging for the medium with large lateral variations. The beyond conjecture algorithm includes terms in addition to those in the imaging conjecture algorithm, for a medium with varying velocity and density, and can accommodate larger contrasts. For 3D data with a limited crossline aperture, the algorithm proposed in section 5, which uses FK migration in the inline direction and asymptotic migration in the crossline direction, is not consistent with ISS nonlinear imaging algorithms in treating the low-freeuency information. However, it provides a way of dealing with the inadequate information and may be valuable in other imaging algorithms and other seismic processing tools.

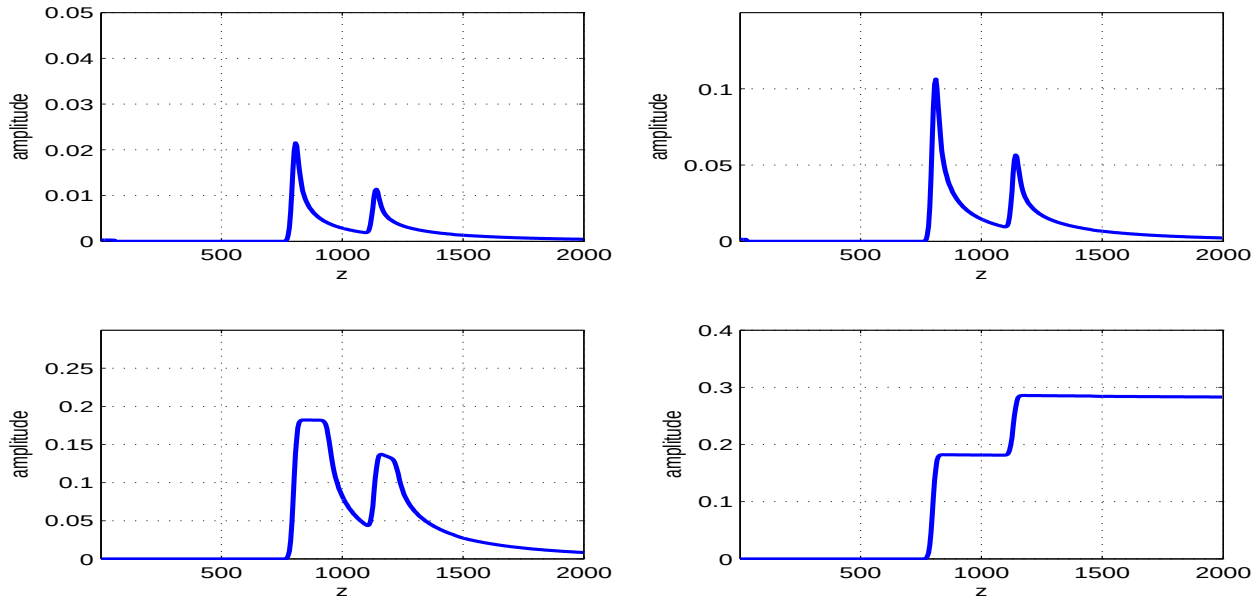

Figure 20: Amplitudes of α_1 at the line $x = 2000m$, with apertures of $50m$ (upper left), $250m$ (upper right), $1000m$ (lower left), and $4000m$ (lower right).

7 Acknowledgements

All M-OSRP sponsors are gratefully appreciated for their support in the research. This work has been partially funded by NSF-CMG (award DMS-0327778) and U.S. DOE-BES (Grant No. DOE-De-FG02-05ER15697). I would like to thank Dr. Arthur B. Weglein for his mentoring, and Dr. Fang Liu and Di Chang for suggestions.

References

Clayton, R. W. and R. H. Stolt. "A Born-WKBJ inversion method for acoustic reflection data." *Geophysics* 46 (1981): 1559–1567.

Jiang, S. and A. B. Weglein. "Deriving an imaging algorithm for a laterally invariant multi-parameter acoustic medium from the inverse scattering series." *Mission-Oriented Seismic Research Program (M-OSRP) Annual Report*. Houston: M-OSRP, 2007.

Jiang, S., A. B. Weglein, and S. Shaw. "Progressing multiparameter imaging using the inverse scattering series." *Mission-Oriented Seismic Research Program (M-OSRP) Annual Report*. Houston: M-OSRP, 2008.

Li, X., F. Liu, S. Jiang, and A. B. Weglein. "Deriving an imaging algorithm for a laterally invariant multi-parameter acoustic medium from the inverse scattering series." *Mission-Oriented Seismic Research Program (M-OSRP) Annual Report*. Houston: M-OSRP, 2008.

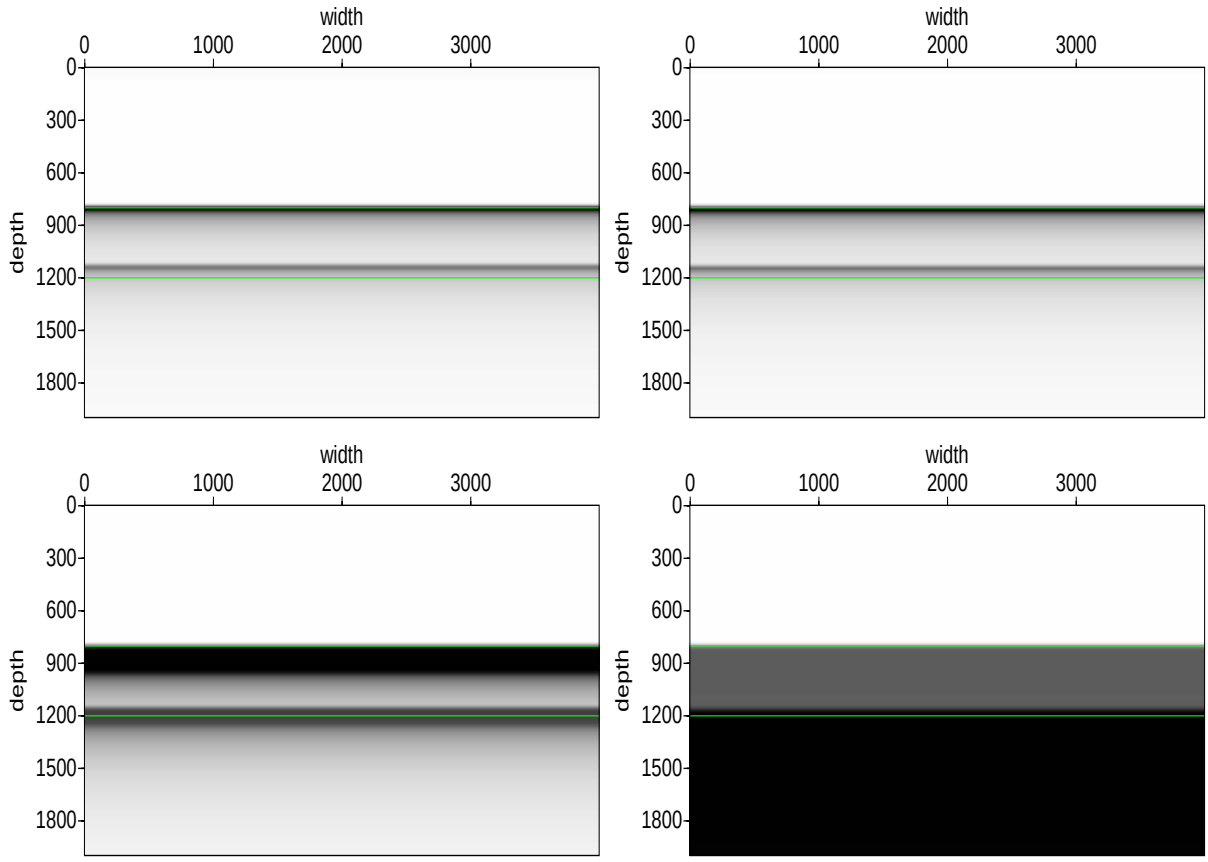

Figure 21: The imaging result of α_{HOIS} using the wave-theoretic method, with apertures of $50m$ (upper left), $250m$ (upper right), $1000m$ (lower left), and $4000m$ (lower right).

Liu, F. *Multi-dimensional depth imaging without an adequate velocity model.* PhD thesis, University of Houston, 2006.

Liu, F., A. B. Weglein, and K. A. Innanen. "Inverse scattering series with lateral variations in 3D." *Mission-Oriented Seismic Research Program (M-OSRP) Annual Report.* Houston: M-OSRP, 2007.

Liu, Fang and Arthur B. Weglein. "Addressing the bandlimited nature of seismic source and rapid lateral variations of the Earth: source regularization and cascaded imaging operator." *M-OSRP Annual Report.* Houston: M-OSRP, 2009.

Shaw, S. A., A. B. Weglein, D. J. Foster, K. H. Matson, and R. G. Keys. "Isolation of a leading order depth imaging series and analysis of its convergence properties." *Journal of Seismic Exploration* 2 (November 2004): 157–195.

Stolt, Robert H. and Alvin K. Benson. *Seismic Migration: Theory and Practice.* Volume 5 of Handbook of Geophysical Exploration Series. London and Amsterdam: Geophysical Press, 1986.

Wang, Z. *Progress of ISS depth imaging without velocity, for more complex media or input data with limited aperture in the crossline direction.* PhD thesis, University of Houston, 2012.

Wang, Z., A. Weglein, and F. Liu. "Preparing data with finite cross-line aperture for input to 3D non-linear imaging algorithms." *Mission-Oriented Seismic Research Program (M-OSRP) Annual Report.* 2007.

Wang, Z., A. B. Weglein, and X. Li. "New capture of direct velocity independent depth imaging in a one-dimension two-parameter acoustic earth." *Mission-Oriented Seismic Research Program (M-OSRP) Annual Report.* Houston: M-OSRP, 2009.

Wang, Z., A. B. Weglein, and F. Liu. "Note: A derivation of the HOIS closed form." *Mission-Oriented Seismic Research Program (M-OSRP) Annual Report.* Houston: M-OSRP, 2009.

Wang, Z., A. B. Weglein, and F. Liu. "Note: Evaluations of the HOIS closed form and its two variations." *Mission-Oriented Seismic Research Program (M-OSRP) Annual Report.* Houston: M-OSRP, 2009.

Weglein, A. B. "Introduction and preface." *Mission-Oriented Seismic Research Program (M-OSRP) Annual Report.* Houston: University of Houston, 2008.

Weglein, A. B., D. J. Foster, K. H. Matson, S. A. Shaw, P. M. Carvalho, and D. Corrigan. "Predicting the correct spatial location of reflectors without knowing or determining the precise medium and wave velocity: initial concept, algorithm and analytic and numerical example." *Journal of Seismic Exploration* 10 (2002): 367–382.

Weglein, A. B., F. A. Gasparotto, P. M. Carvalho, and R. H. Stolt. "An Inverse-Scattering Series Method for Attenuating Multiples in Seismic Reflection Data." *Geophysics* 62 (November-December 1997): 1975–1989.

Zhang, H. *Direct non-linear acoustic and elastic inversion: Towards fundamentally new comprehensive and realistic target identification.* PhD thesis, University of Houston, 2006.

Zhang, J., F. Liu, Kristopher Innanen, and Arthur B. Weglein. "Comprehending and analyzing the leading order and higher order imaging closed forms derived from inverse scattering series." *Mission-Oriented Seismic Research Program Annual Report* 1 (2006): 149–159.

Finite-difference modeling, accuracy, and boundary conditions

D. Chang, F. Liu and A. B. Weglein, M-OSRP, University of Houston

May 25, 2012

Abstract

This short report gives a brief review on the finite difference modeling method used in M-OSRP and its boundary conditions as a preparation for the Green's theorem RTM. The first part gives the finite difference formulae we used and the second part describes the implemented boundary conditions. The last part, using two examples, points out some impacts of the accuracy of source fields on the results of modeling.

1 Finite difference method review

The finite difference scheme implemented in M-OSRP has a second order in time difference and a fourth order in space difference. Taking the homogeneous 2D acoustic wave equation as an example,

$$\rho(x,z) \bigtriangledown \cdot [\frac{1}{\rho(x,z)} \bigtriangledown P(x,z,t)] - \frac{1}{c^2(x,z)} \frac{\partial^2}{\partial t^2} P(x,z,t) = 0 \tag{1.1}$$

where $\rho(x,z)$ is the medium density, $c(x,z)$ is the wave propagation velocity in the medium and $P(x,z,t)$ is the scalar pressure wave field.

Using the 2nd order central finite difference scheme for time, the wave fields $P_{t\pm1}$ are expanded in Taylor series in terms of P_t and its derivatives to the 2nd order of $\triangle t$, i.e.,

$$\begin{aligned} P_{t-1} &= P_t - P'_t \cdot \triangle t + P''_t \cdot (\triangle t)^2/2! \\ P_{t+1} &= P_t + P'_t \cdot \triangle t + P''_t \cdot (\triangle t)^2/2! \end{aligned} \tag{1.2}$$

from which we can express the 2nd derivative of the pressure wave field with regard to t as,

$$P''_t = [P_{t-1} + P_{t+1} - 2P_t]/(\triangle t)^2 + O((\triangle t)^2). \tag{1.3}$$

Similarly, using the 4th order central finite difference scheme for space, the wave fields $P_{x\pm1}$ and $P_{x\pm2}$ are expanded in Taylor series in terms of P_x and its derivatives to the 4th order of $\triangle x$, i.e.,

$$\begin{aligned}
P_{x-2} &= P_x - P_x' \cdot (2 \triangle x) + P_x'' \cdot (2 \triangle x)^2/2! - P_x''' \cdot (2 \triangle x)^3/3! + P_x'''' \cdot (2 \triangle x)^4/4! \\
P_{x-1} &= P_x - P_x' \cdot \triangle x + P_x'' \cdot (\triangle x)^2/2! - P_x''' \cdot (\triangle x)^3/3! + P_x'''' \cdot (\triangle x)^4/4! \\
P_{x+1} &= P_x + P_x' \cdot \triangle x + P_x'' \cdot (\triangle x)^2/2! + P_x''' \cdot (\triangle x)^3/3! + P_x'''' \cdot (\triangle x)^4/4! \\
P_{x-2} &= P_x + P_x' \cdot (2 \triangle x) + P_x'' \cdot (2 \triangle x)^2/2! + P_x''' \cdot (2 \triangle x)^3/3! + P_x'''' \cdot (2 \triangle x)^4/4! \quad (1.4)
\end{aligned}$$

from which we can express the 1st and 2nd derivatives of the pressure wave field with regard to x as,

$$\begin{aligned}
P_x' &= (-P_{x+2}/12 + 2P_{x+1}/3 - 2P_{x-1}/3 + P_{x-2}/12)/ \triangle x + O((\triangle x)^4) \\
P_x'' &= (-P_{x+2} + 16P_{x+1} - 30P_x + 16P_{x-1} - P_{x-2})/12(\triangle x)^2 + O((\triangle x)^4). \quad (1.5)
\end{aligned}$$

Discretizing the domain of interest with meshes ($x = m \triangle x$, $z = n \triangle z$ and $t = l \triangle t$), writing the pressure wave field with discontinuous labels $P_{m,n,l}$ and using equation (3) gives the iteration relationship to calculate the wavefield at time step $l+1$ in terms of its values at l and $l-1$,

$$P_{m,n,l+1} = \triangle t^2 c_{m,n}^2 \rho_{m,n} \bigtriangledown \cdot (\frac{1}{\rho_{m,n}} \bigtriangledown P_{m,n,l}) + 2P_{m,n,l} - P_{m,n,l-1}. \quad (1.6)$$

Now, all that remains is to consider the space term, i.e., the first term in expression (6). Substituting expression (5) into (6) results in the finite difference formula for equation (1),

$$\begin{aligned}
P_{m,n,l+1} = [2 - 5D^2]P_{m,n,l} - P_{m,n,l-1} + \frac{4}{3}D^2(1 + A\rho_{m,n})P_{m+1,n,l} + \\
\frac{4}{3}D^2(1 - A\rho_{m,n})P_{m-1,n,l} - \frac{1}{12}D^2(1 + 2A\rho_{m,n})P_{m+2,n,l} - \\
\frac{1}{12}D^2(1 - 2A\rho_{m,n})P_{m-2,n,l} + \frac{4}{3}D^2(1 + B\rho_{m,n})P_{m,n+1,l} + \\
\frac{4}{3}D^2(1 - B\rho_{m,n})P_{m,n-1,l} - \frac{1}{12}D^2(1 + 2B\rho_{m,n})P_{m,n+2,l} - \\
\frac{1}{12}D^2(1 - 2B\rho_{m,n})P_{m,n-2,l} + \\
0(h^4 + \triangle t^2), \quad (1.7)
\end{aligned}$$

where

$$\begin{aligned}
D &= \triangle t \cdot c_{m,n}/h \\
A &= -\frac{1}{24}\frac{1}{\rho_{m+2,n}} + \frac{1}{3}\frac{1}{\rho_{m+1,n}} - \frac{1}{3}\frac{1}{\rho_{m-1,n}} + \frac{1}{24}\frac{1}{\rho_{m-2,n}}
\end{aligned}$$

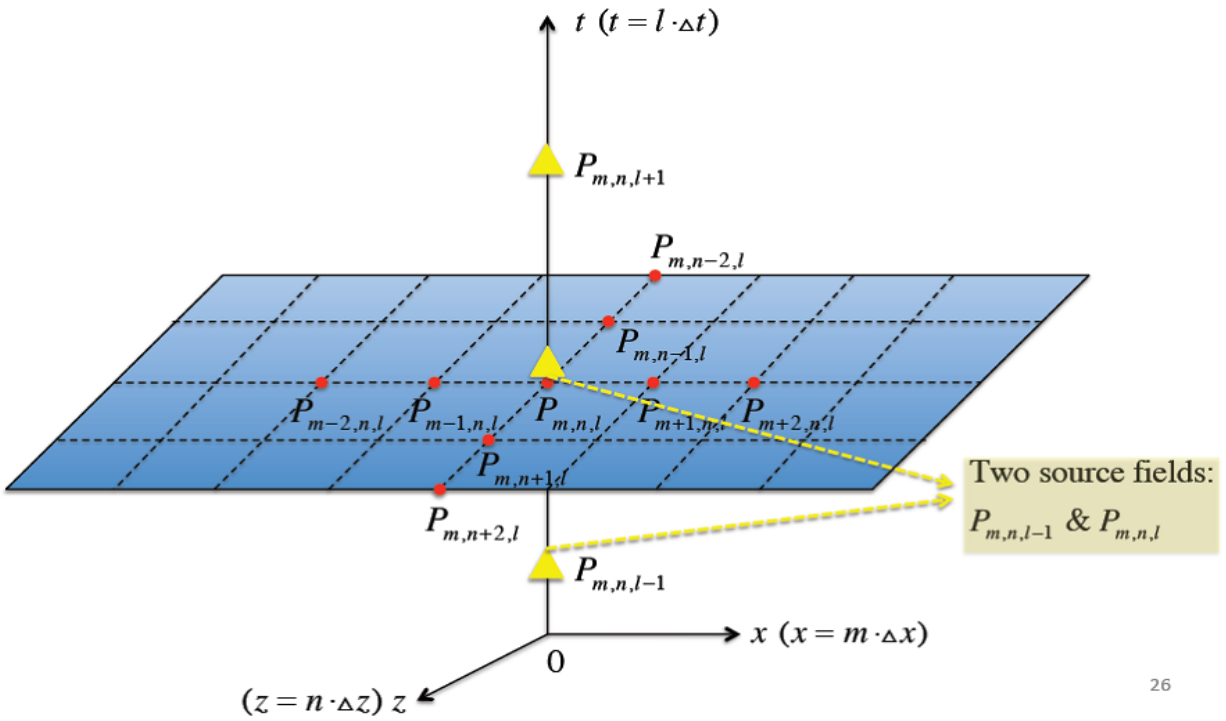

Figure 1: Grid approximation of finite difference method

$$B = -\frac{1}{24}\frac{1}{\rho_{m,n+2}} + \frac{1}{3}\frac{1}{\rho_{m,n+1}} - \frac{1}{3}\frac{1}{\rho_{m,n-1}} + \frac{1}{24}\frac{1}{\rho_{m,n-2}}. \tag{1.8}$$

Expression (7) shows that the calculation of $P_{m,n,l+1}$ requires the values of the wave field at ten neighboring points (Figure 1). The blue area represents the calculation at time step l; The yellow points represent time iteration at three points. The red points are the "neighbors" needed to construct the wave field at the center. In a recursive way, the forward modeling can be realized by giving a forward order to the source fields and data can be constructed. Figure 2 gives an example of a snapshot as wave propagates for 1s with a central source.

The finite difference approach is based on the acoustic/elastic wave equation without any physical approximations (complete numerical wave theory), so the method automatically accounts for the proper relative amplitudes of the various arrivals and includes the contributions of different kinds of waves (K. R. Kelly and Alford, 1976). In the next section, on the basis of the scheme given here, we further analyze the boundary conditions in finite difference method to illustrate how reflections happen as wave propagates to a boundary or interface.

2 Boundary and boundary conditions

In finite difference method, the model is bounded laterally and at depth by artificial interfaces as a result of the finite memory capacity of the computer. Large models allow no reflections from

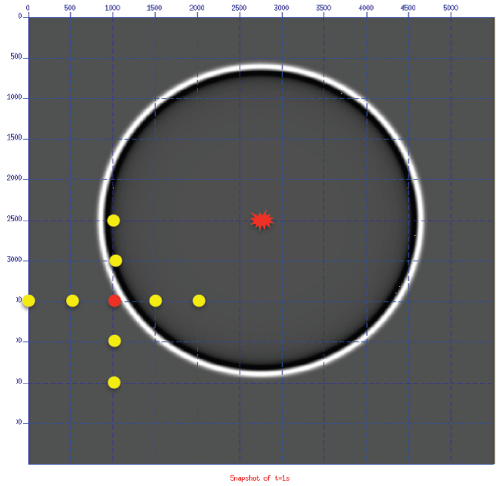

Figure 2: Snapshot at $t = 1s$

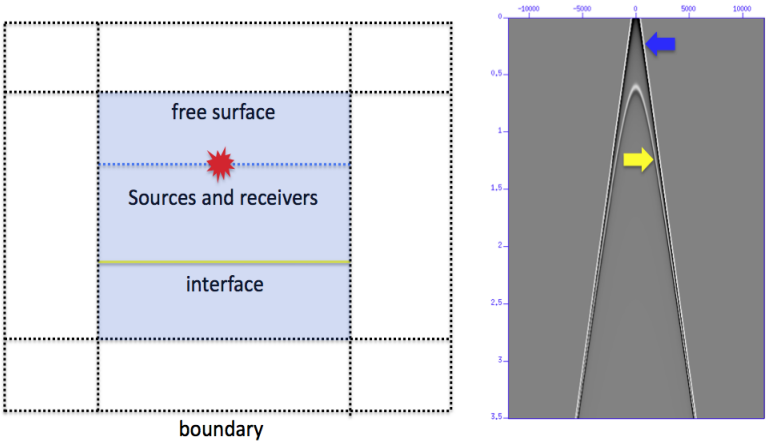

Figure 3: A large model allows no boundary reflections to be recorded: model (left) and a shotgather (right).

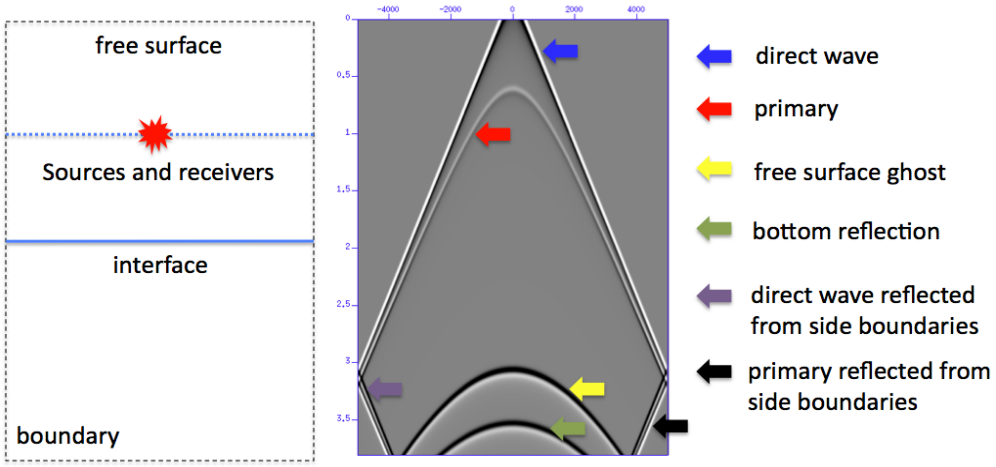

Figure 4: A small model generates all kinds of reflections: model (left) and a shotgather (right).

the artificial boundaries. Figure 3 gives an example in which the area of interest is smaller enough compared with the whole area so that reflections have no time to reach the receivers. However, this kind of model also costs more computer memory. If we reduce this model to the area of interest to save memory, as shown in Figure 4, all reflections including those from artificial boundaries and the interface come into data, which might mask the true and meaningful events.

It is useful for us to take a close look at what happens when the wave hits the boundary. Figure 5(a) demonstrates that when the value of the wave field at the left boundary (red point) is calculated, the fourth order difference scheme requires two extra points to the left to make the code well-defined. Usually Dirichlet or Neumann (D/N) condition is imposed on the outer boundaries. A simple 1D example is shown in Figure 5(b) where a plane wave is propagating to the right and hitting the boundary, so the total wave is

$$\phi_{total} = e^{i(\omega t - kx)} + Re^{i(\omega t + kx)} \tag{2.1}$$

with a Dirichlet or Neumann condition at the boundaries $x = \pm a$

$$\phi(\pm a, t) = 0 \text{ and } \frac{\partial \phi}{\partial x}(\pm a, t) = 0. \tag{2.2}$$

Substituting ϕ_{total} into (10) gives the reflection coefficient $|R| = 1$ where $R = -1$ for Dirichlet condition and $R = 1$ for Neumann condition. Thus imposing D/N conditions generates strong spurious reflections, as shown by Figure 5(c). Reflections from corners happen in the same way. If the boundaries are set to be homogeneous, i.e., the earth properties at the outer boundaries are set to be equal to those inside, the contributions from the yellow points would construct a zero value at the red point and reflections would not occur. Otherwise, they will contribute a non-zero value to the reflected wave at the red point. Similar analysis is applicable to the primary from an interface in the medium, as shown in Figure 5(d). The Perfectly Matched Layer (PML) method was proposed to reduce reflections from artificial boundaries through imposing absorbing boundary conditions.

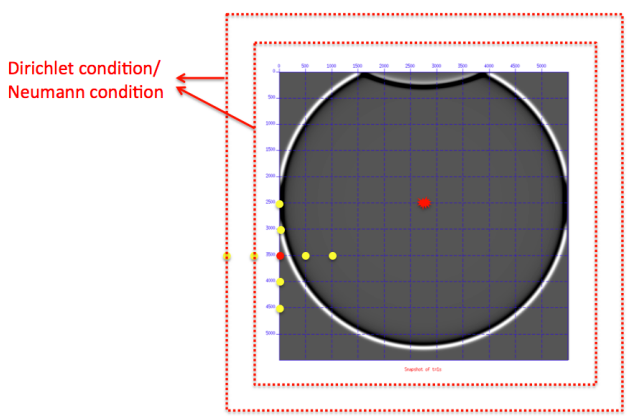

(a)

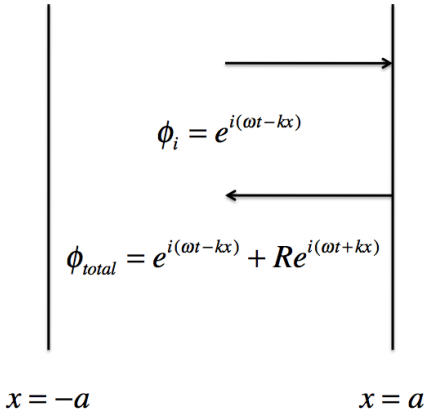

(b)

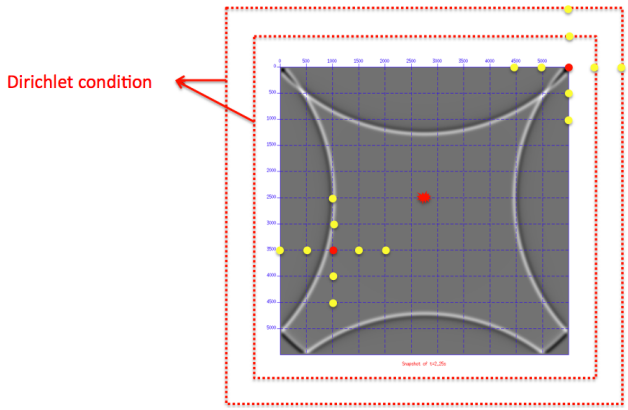

(c)

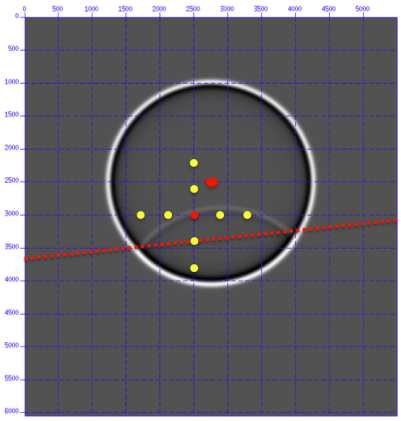

(d)

Figure 5: Wave hits boundaries and an interface: (a) wave at the boundaries; (b) 1D plane wave example; (c) wave reflected from boundaries and (d) wave reflected from an interface.

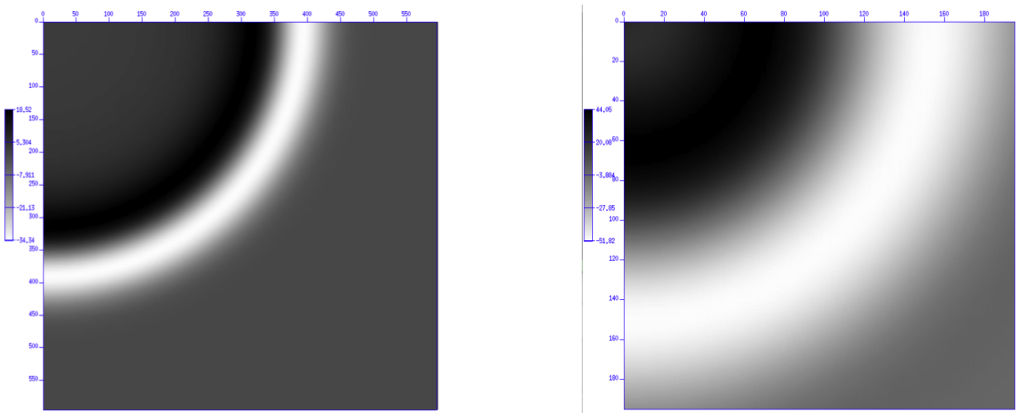

(a) (b)

Figure 6: Example of two source fields: (a) is considered to be a better source field than (b).

3 Impact of the accuracy of the source fields on modeling

In this section, we emphasize the impact of the accuracy of the source fields on the results of finite difference modeling using two examples. The fourth order spacial difference scheme should satisfy the stability condition $D = c_0 \triangle t/h \leq \sqrt{3/8}$. Under this restriction, the grid size should be as small as possible to reduce the grid dispersions. The direct source contribution is calculated analytically from the known solution for a source in an infinite region,

$$P_0(r, r', t_1) = \frac{1}{2\pi} \int_{-\infty}^{\infty} [i\pi H_0^{(1)}(k|r - r'|) \cdot F(\omega)] e^{-i\omega t_1} d\omega$$
$$P_0(r, r', t_2) = \frac{1}{2\pi} \int_{-\infty}^{\infty} [i\pi H_0^{(1)}(k|r - r'|) \cdot F(\omega)] e^{-i\omega t_2} d\omega, \tag{3.1}$$

which are corresponding to the two yellow points $P_{m,n,l-1}$ and $P_{m,n,l}$ in Figure 1. The source and its inclusion are treated as in the homogeneous case, so it requires the source to be located in the interior of a homogeneous zone of dimensions at least as large as the source square. First, the medium is assumed to be homogeneous within a certain distance from the source; Second, the energy of the wave can be neglected outside the source circular region (Liu and Weglein, 2005). Figure 6 shows two source fields where 6(a) obeys these rules better than 6(b).

We use two examples to demonstrate the impact of these two different source fields on the accuracy of modeling: One is a linear inversion result based on a 1D model; The other is designed to observe zero-crossing phenomena using finite difference data.

3.1 An inversion example

The linear estimation of the perturbation for a 1D earth model can be analytically calculated (Zhang, 2006). Take a simple 1D model shown on the left of Figure 4 as an example and assume

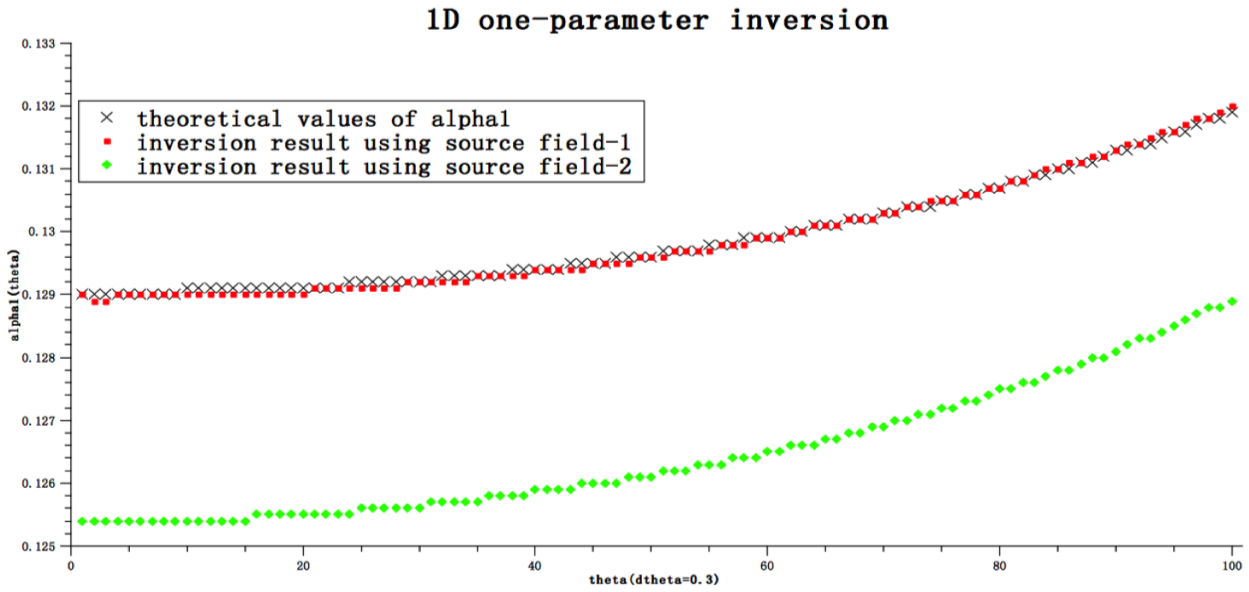

Figure 7: An inversion example showing the better source field resulting in more accurate linear estimation

that only velocity varies across the interface ($c_0 = 1500m/s, c_1 = 1600m/s$), we first use the two different source fields to generate data and then calculate their linear evaluations of the perturbation α (defined to be $1 - c_0^2/c_1^2$) using a 1D 1-parameter algorithm (Zhang, 2006) and compare them with the theoretical prediction.

The results are shown in Figure 7: The black line is the theoretical value of α_1; The red line is the linear estimation result calculated using the source field in Figure 6(a) and the green line is the result using 6(b). The data processing flows for these two cases are same and the better source field leads to a more accurate linear estimation.

3.2 A zero-crossing example

Although verifying the accuracy of the traveltime produced by a seismic modeling program is fairly easy, checking the accuracy of the amplitude response of a synthetic seismogram is limited to comparisons with the few known exact solutions of the wave equation. However, it is a simple matter to design an acoustic or elastic model that causes polarity reversals at any desired offset, which provides a quick check on the accuracy of the program's amplitude information (Keys, 1989).

Last year, we reported some difficulties in observing zero-crossing using finite difference data compared with using reflectivity data. This year, using finite difference data with the better source field, we give an example in which the zero-crossing phenomena can be seen clearly. Figure 8(a) is the tested model. The second interface is designed for polarity reversal occurring. Using the better source field, polarity reversal can be seen clearly both in the shot gather and $\tau - p$ domain.

The angle where zero-crossing happens can be calculated analytically by setting the reflection coefficient (Jiang and Weglein, 2009) to zero

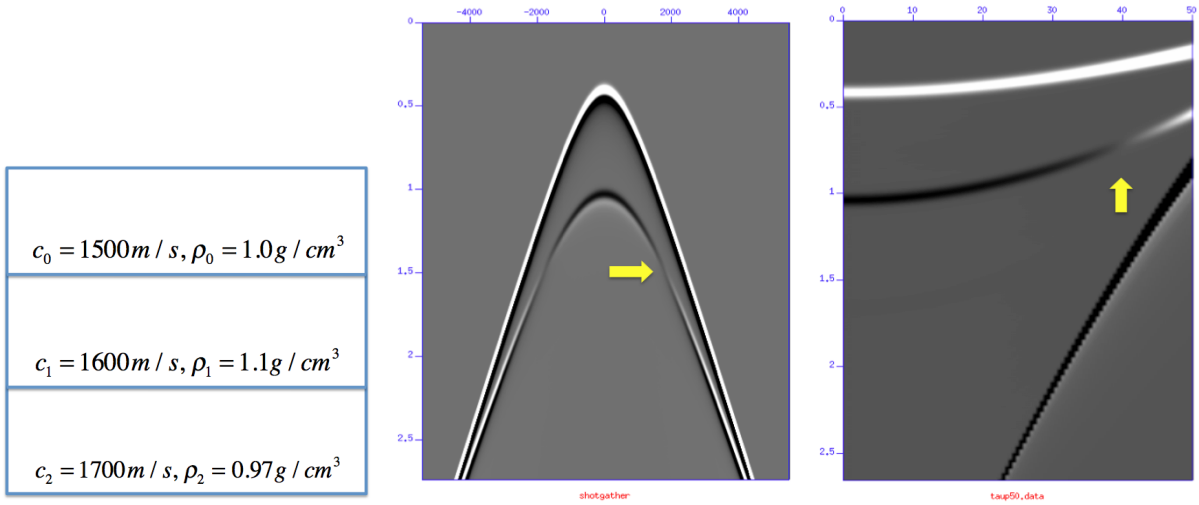

(a) (b)

Figure 8: Observing polarity reversal using finite difference data with the better source field: (a) model; (b) data in $x-t$ domain and $\tau-p$ domain

$$\begin{aligned} R(\theta) &= \frac{I_2 - I_1}{I_2 + I_1} \\ &= \frac{c_2\rho_2/\sqrt{1-c_2^2p^2} - c_1\rho_1/\sqrt{1-c_1^2p^2}}{c_2\rho_2/\sqrt{1-c_2^2p^2} + c_1\rho_1/\sqrt{1-c_1^2p^2}} \\ &= 0, \end{aligned} \tag{3.2}$$

where $p = \frac{sin\theta}{c_0}$. Substituting the model parameters into (12) and solving for θ leads to $\theta = 44.23°$. Figure 8(b) shows that the test result is consistent with the theoretical prediction.

4 Conclusion

We reviewed in this report the application of finite difference method in seismic modeling and analyzed how reflections occur at boundaries/interfaces. We emphasized the importance of the accuracy of source fields in modeling, first put forward in Liu and Weglein (2005), by giving two examples. The "quality control method" proposed in Liu and Weglein (2005) is also recommended in checking the accuracy of finite difference data.

5 Acknowledgements

We are grateful to all M-OSRP sponsors for long-term encouragement and support in this research. The author especially thanks F. Liu for his education in finite difference modeling and W. Herrera and L. Tang for reading this report and giving suggestions.

References

Jiang, S. and Arthur B. Weglein. "Progressing multi-parameter imaging using the inverse scattering series: an initial analytic test on the Leading Order Imaging Subseries (LOIS) closed form and its extended Higher Order Imaging Subseries (HOIS) closed form for a laterally invariant two-parameter acoustic medium." (2009): 91–113.

K. R. Kelly, Sven Treitel,R. W. Ward and R. M. Alford. "Synthetic seismograms: a finite-difference approach." *Geophysics* 41 (1976): 2–27.

Keys, R. G. "Polarity reversals in reflections from layered media." *Geophysics* 54 (1989): 900–905.

Liu, Fang and Arthur Weglein. "Accurate implementation of the wavelet in finite-difference modeling." (2005): 111–125.

Zhang, H. *Direct non-linear acoustic and elastic inversion: Towards fundamentally new comprehensive and realistic target identification.* PhD thesis, University of Houston, 2006.

Short note: A formalism for (1) modeling the amplitude and phase of pressure waves from a heterogeneous elastic medium and (2) selecting and predicting P-wave events that have only experienced pressure-wave episodes in their history

Arthur B. Weglein, M-OSRP/Department of Physics/University of Houston

May 25, 2012

Abstract

The coupled pressure- (P-) and shear- (S-) wave equations for 2D and 3D inhomogeneous elastic media are recast as an uncoupled single-channel P-wave equation. That P-wave equation allows for all histories and intermediate episodes of P- and S-wave propagation that contribute to a P-wave at an observation point. This in turn leads to a formalism for selectively modeling and predicting P-waves (and P-wave events in recorded data) that have source-observation point histories with only P-wave-propagating experiences. In this note, we provide a wave-theory method that can model the amplitude and phase of waves that spend their entire histories as P-waves. This brings a P-wave-only-history selection algorithm to wave-theory modeling.

1 Introduction

Techniques for modeling wave propagation in multidimensional heterogeneous elastic media can be roughly categorized as either wave or ray theories. Ray-theory methods, valid in the high-frequency regime, are approximate but allow a selection of ray paths, including a selection chosen according to a wave type of interest. Wave-theory methods, such as finite-difference modeling, are, in principle, more accurate and inclusive of wave-propagation phenomena. However, these methods do not lend themselves to the type of path selectivity that ray-theory methods allow. In the following sections, we present a wave-theory method that provides a capability for path selectivity based on wave types of interest. In particular, our formalism allows for the selective modeling of waves that spend their entire histories as P-waves in a completely heterogeneous isotropic elastic medium. As a result, we bring a P-wave-only-history selection algorithm to wave-theory modeling.

2 2D Isotropic Heterogeneous Elastic Media

We choose (here for convenience, although it is unnecessary) to describe the medium as a homogeneous background plus a perturbation in background material properties that results in actual medium properties. For this specific case, the coupled equations for P- and S-waves, ϕ_P and ϕ_S respectively, can be written as

$$\begin{aligned}\left[\nabla^2 + \frac{\omega^2}{{\alpha_0}^2}\right]\phi_P &= V_{PP}\phi_P + V_{PS}\phi_S + f_P \text{ and} \\ \left[\nabla^2 + \frac{\omega^2}{{\beta_0}^2}\right]\phi_S &= V_{SS}\phi_S + V_{SP}\phi_P + f_S\end{aligned} \tag{2.1}$$

where α_0 is the reference P-wave velocity, β_0 is the reference S-wave velocity, $(V_{PP}, V_{PS}, V_{SP}, V_{SS})$ are the matrix elements of the perturbation operator in the P-S representation, and (f_P, f_S) are the components of the source function in the P-S representation.
We rewrite the second equation presented above as

$$\left[\nabla^2 + \frac{\omega^2}{{\beta_0}^2} - V_{SS}\right]\phi_S = V_{SP}\phi_P + f_S \tag{2.2}$$

and introduce a Green's function G_S to satisfy

$$\left[\nabla^2 + \frac{\omega^2}{{\beta_0}^2} - V_{SS}\right]G_S = \delta. \tag{2.3}$$

This Green's function can be expressed, using the Lippmann-Schwinger equation, as a sequence of reference shear-wave propagations, G_S^0, and a scattering from the self-coupling shear perturbation operator, V_{SS}, given by

$$G_S = G_S^o + G_S^o V_{SS} G_S = \sum_{k=0}^{\infty} G_S^o (V_{SS} G_S^o)^k, \tag{2.4}$$

where G_S^o satisfies the relation:

$$\left[\nabla^2 + \frac{\omega^2}{{\beta_0}^2}\right]G_S^o = \delta. \tag{2.5}$$

The causal solution to equation 2.2 is

$$\phi_S = \int G_S \left(V_{SP}\phi_P + f_S\right). \tag{2.6}$$

where G_S in equation 2.6 is chosen to be the causal whole space solution to equation 2.3. Substituting this result back into the first equation of equation 2.1, we obtain

$$\begin{aligned}\left[\nabla^2 + \frac{\omega^2}{{\alpha_0}^2}\right]\phi_P &= V_{PP}\phi_P + V_{PS}\int G_S V_{SP}\phi_P \\ V_{PS}\int G_S f_S + f_P.\end{aligned} \tag{2.7}$$

For the case where

$$\vec{f} = \begin{pmatrix} f_P \\ 0 \end{pmatrix} \tag{2.8}$$

and the source generates only P-waves, $f_S = 0$, and the solution of equation 2.5 can be written as

$$\phi_P = G_P^o V_{PP}\phi_P + G_P^o V_{PS}\int G_S V_{SP}\phi_P + G_P^o f_P, \tag{2.9}$$

where G_P^o is the causal solution to

$$\left[\nabla^2 + \frac{\omega^2}{{\alpha_0}^2}\right] G_P^o = \delta. \tag{2.10}$$

If we define a new form of the perturbation, responsible for self-coupling and inter-channel coupling of the propagating P-wave, as

$$\mathbf{V} = V_{PP} + V_{PS}\int G_S V_{SP}, \tag{2.11}$$

and make the identification that the reference wave field results from propagating the source with the reference P-wave Green's function, i.e., $\phi_P^0 = G_P^0 f_P$, equation 2.9 can be rewritten as

$$\phi_P = \phi_P^0 + G_P^0 \mathbf{V}\phi_P. \tag{2.12}$$

This is a single-channel equation for the total pressure wave field, ϕ_P, and it builds in all of the S-channel interactions that influence the P-channel, without solving for ϕ_S. The equation for ϕ_P is an integral equation for which the solution can be expanded, using the Born series:

$$\phi_P = \phi_P^0 + G_P^0 \mathbf{V}\phi_P^0 + G_P^0 \mathbf{V} G_P^0 \mathbf{V}\phi_P^0 + \dots\ . \tag{2.13}$$

Equation 2.13 is a direct modeling equation for a P-wave in an inhomogeneous elastic medium.

3 3D Isotropic Heterogeneous Elastic Media

For a 3D inhomogeneous elastic medium, the (P, S_H, S_V) representation of the perturbation matrix is (Stolt and Weglein, 2012, page 165):

$$\hat{V} = \begin{pmatrix} V_{PP} & V_{PS_H} & V_{PS_V} \\ V_{S_HP} & V_{S_HS_H} & V_{S_HS_V} \\ V_{S_VP} & V_{S_VS_H} & V_{S_VS_V} \end{pmatrix}, \tag{3.1}$$

where S_H is the shear-horizontal channel and S_V is the shear-vertical channel. The three-dimensional elastic wave equation in this representation becomes

$$\begin{aligned} &\hat{L}\vec{\phi} = (\hat{L}_0 - \hat{V})\vec{\phi} = \\ &\begin{pmatrix} {L_0}^P - V_{PP} & -V_{PS_H} & -V_{PS_V} \\ -V_{S_HP} & {L_0}^{S_H} - V_{S_HS_H} & -V_{S_HS_V} \\ -V_{S_VP} & -V_{S_VS_H} & {L_0}^{S_V} - V_{S_VS_V} \end{pmatrix} \begin{pmatrix} \phi_P \\ \phi_{S_H} \\ \phi_{S_V} \end{pmatrix} \\ &= \begin{pmatrix} f_P \\ f_{S_H} \\ f_{S_V} \end{pmatrix} = \vec{f}. \end{aligned} \tag{3.2}$$

From the matrix equation above, if we assume that our source generates only P-waves, i.e., that

$$\vec{f} = \begin{pmatrix} f_P \\ 0 \\ 0 \end{pmatrix}, \tag{3.3}$$

we obtain a system of three coupled equations for the components of the wave field:

$$\left[\nabla^2 + \frac{\omega^2}{{\alpha_0}^2} - V_{PP}\right]\phi_P = V_{PS_H}\phi_{S_H} + V_{PS_V}\phi_{S_V} + f_P \tag{3.4}$$

$$\left[\nabla^2 + \frac{\omega^2}{{\beta_0}^2} - V_{S_HS_H}\right]\phi_{S_H} = V_{S_HP}\phi_P + V_{S_HS_V}\phi_{S_V} \text{ and} \tag{3.5}$$

$$\left[\nabla^2 + \frac{\omega^2}{{\beta_0}^2} - V_{S_VS_V}\right]\phi_{S_V} = V_{S_VP}\phi_P + V_{S_VS_H}\phi_{S_H}, \tag{3.6}$$

where α_0 is the reference P-wave velocity and β_0 is the reference S-wave velocity.

To construct an effective, single-channel equation for the P component of the wave field, we first solve our equation by introducing the Green's function:

$$\left[\nabla^2 + \frac{\omega^2}{{\beta_0}^2} - V_{S_VS_V}\right]G_{S_V} = \delta. \tag{3.7}$$

Therefore, the SV component of the wave field is

$$\phi_{S_V} = G_{S_V} \left(V_{S_V P} \phi_P + V_{S_V S_H} \phi_{S_H} \right) \tag{3.8}$$

where G_{S_V} in equation 3.8 is the whole-space causal solution to equation 3.7. All Green's functions in the Lippmann-Schwinger forms in this paper are the whole-space causal solutions of their respective equations. Similarly, introducing the Green's function defined by

$$\left[\nabla^2 + \frac{\omega^2}{{\beta_0}^2} - V_{S_H S_H} \right] G_{S_H} = \delta, \tag{3.9}$$

and substituting the right-hand side of equation 2.7 into equation 2.5, we obtain

$$\begin{aligned} \phi_{S_H} = & G_{S_H} \left(V_{S_H P} + V_{S_H S_V} G_{S_V} V_{S_V P} \right) \phi_P \\ & + G_{S_H} V_{S_H S_V} G_{S_V} V_{S_V S_H} \phi_{S_H}, \end{aligned} \tag{3.10}$$

which becomes

$$\begin{aligned} & \left(1 - G_{S_H} V_{S_H S_V} G_{S_V} V_{S_V S_H} \right) \phi_{S_H} = \\ & G_{S_H} \left(V_{S_H P} + V_{S_H S_V} G_{S_V} V_{S_V P} \right) \phi_P. \end{aligned} \tag{3.11}$$

Inverting the operator acting on ϕ_{S_H} in the equation above gives us:

$$\left(1 - G_{S_H} V_{S_H S_V} G_{S_V} V_{S_V S_H} \right)^{-1} = \sum_{k=0}^{+\infty} \left(G_{S_H} V_{S_H S_V} G_{S_V} V_{S_V S_H} \right)^k. \tag{3.12}$$

Thus, we now have an expression for ϕ_{S_H} in terms of ϕ_P

$$\begin{aligned} \phi_{S_H} = & \left[\sum_{k=0}^{+\infty} \left(G_{S_H} V_{S_H S_V} G_{S_V} V_{S_V S_H} \right)^k \right] \\ & G_{S_H} \left(V_{S_H P} + V_{S_H S_V} G_{S_V} V_{S_V P} \right) \phi_P. \end{aligned} \tag{3.13}$$

Substituting this expression into equation 2.4, we find that the P component of the wave field, as it propagates through a 3D heterogeneous elastic medium, is governed by the scalar equation:

$$\begin{aligned} \phi_P = \phi_P^0 + G_P^0 V_{PP} \phi_P + G_P^0 V_{PS_H} \left[\sum_{k=0}^{+\infty} \left(G_{S_H} V_{S_H S_V} G_{S_V} V_{S_V S_H} \right)^k \right] G_{S_H} \left(V_{S_H P} + V_{S_H S_V} G_{S_V} V_{S_V P} \right) \phi_P \\ + G_P^0 V_{PS_V} G_{S_V} \left(V_{S_V P} + V_{S_V S_H} \left[\sum_{k=0}^{+\infty} \left(G_{S_H} V_{S_H S_V} G_{S_V} V_{S_V S_H} \right)^k \right] G_{S_H} \left(V_{S_H P} + V_{S_H S_V} G_{S_V} V_{S_V P} \right) \right) \phi_P. \end{aligned} \tag{3.14}$$

Rewriting equation 3.14 gives the form:

$$\phi_P = \phi_P^0 + G_P^0 \mathcal{V}_{PP} \phi_P. \tag{3.15}$$

A Born or Neumann series form of equation 3.15 provides a modeling equation for ϕ_P:

$$\phi_P = \phi_P^0 + G_P^0 \mathcal{V}_{PP} \phi_P^0 + G_P^0 \mathcal{V}_{PP} G_P^0 \mathcal{V}_{PP} \phi_P^0 + \dots \tag{3.16}$$

Equation 3.16 models P-waves directly in a heterogeneous elastic medium with all intermediate P, SH, and SV episodes in the predicted P-wave's experience and history included.

$$\phi_P = \phi_P^0 + G_P^0 V_{PP} \phi_P^0 + G_P^0 V_{PP} G_P^0 V_{PP} \phi_P^0 + \dots \tag{3.17}$$

Equation 3.17, with $\mathcal{V}_{PP}$ replaced by V_{PP} (from equation 3.1), will predict a P-wave and P-wave events in measured data, when those P-waves and events only have intermediate P-wave episodes in their history.

4 Conclusions

1. In this paper, we provided: (a) a formalism for modeling the amplitude and phase of P-waves in a heterogeneous elastic medium, and (b) a procedure for selecting and modeling the amplitude and phase of P-waves (and P-wave events in measured data) that have only intermediate P-wave episodes in their experiences and history. The latter could be a useful compromise and timely interim practical response to the daunting full 3D elastic modeling problem.

2. Analytic forward-series calculations of equation 2.13 in 2D and equation 3.17 in 3D, for example, with an oblique incident plane wave reflecting off a single reflector (and then two reflectors) where elastic properties change, will allow us to examine the way different actual converted and un-converted wave events are constructed from reference P and S properties and contributions within the series. The implications and impact of the ideas and formalism put forth in this paper for: (a) large-scale modeling, such as SEAM, (b) RTM, (c) so-called "FWI", and (d) moving the inverse scattering series imaging without the velocity from viable (Weglein et al., 2012) to delivering differential added value — will be examined and reported in future correspondence.

3. The Born series form described for P-wave-only-history P-waves in a heterogeneous isotropic elastic medium could be well-suited for a modeling project (such as SEAM modeling) with a smooth background with small, rapid perturbations generating reflections and where events with converted wave episodes are often treated as noise. Also, methods to directly solve the Fredholm integral equation of the second kind, equations 2.12 and 3.16, will be investigated.

5 Acknowledgements

I would like to thank the M-OSRP sponsors for their encouragement and support. I am particularly grateful to Lasse Amundsen, Nicola Bienati, Nizar Chemingui, Fred Hoffman, Jacques Leveille,

Eugenio Loinger, Yi Luo, Scott Morton, Bob Stolt, Denes Vigh, Haiyan Zhang, and Jingfeng Zhang for their interest and encouraging this specific project. I would like to thank Mason Biamonte and Jim Mayhan for useful and worthwhile discussions and for their help in preparing this manuscript.

References

Stolt, Robert H. and Arthur B. Weglein. *Seismic Imaging and Inversion, Volume 1.* Cambridge University Press, 2012.

Weglein, Arthur B., Fang Liu, Xu Li, Paolo Terenghi, Ed Kragh, James D. Mayhan, Zhiqiang Wang, Joachim Mispel, Lasse Amundsen, Hong Liang, Lin Tang, and Shih-Ying Hsu. "Inverse scattering series direct depth imaging without the velocity model: First field data examples." *Journal of Seismic Exploration* 21 (2012): 1–28.

Antidote to P-wave "FWI"

Arthur B. Weglein

May 25, 2012

Abstract

A frank and forthright commentary on direct and indirect methods and the so-called "FWI" phenomena and movement — and a suggestion for what a method that would actually warrant and deserve that title would look like, if you found it. An actual FWI is proposed, and a plan to test and evaluate it is described, for both shallow-hazard location and top-salt-velocity analysis.

We advocate and develop direct methods for solving processing problems and providing prerequisites. Direct methods offer many conceptual and practical benefits over indirect methods. Advantages of direct methods begin with actually knowing that you are solving the problem that you are interested in solving. How can you recognize a direct versus an indirect method? Consider the quadratic equation $ax^2+bx+c=0$, and the solution $x=(-b\pm\sqrt{b^2-4ac})/2a$; the latter is a direct solution for the roots of the former. On the other hand, if you see a cost function involved in a solution, the solution is indirect. Also, if you see a modeling equation being solved in an inverse sense, that's a hint and an indirect indicator of an indirect solution and a model-matching approach, which too often can start with an incorrect or insufficient modeling equation and a matching of fundamentally inadequate data. By "inadequate data," we mean something much more basic and fundamental than limitations due to sampling, aperture, and bandwidth. That is, indirect solutions can (and often do) input data that are fundamentally inadequate from a basic and direct inverse perspective and understanding. The indirect methods then search locally and globally around error surfaces with Frechet derivatives and conjugate gradients, and they keep hordes of math, physics, geophysics, and computer scientists busy using giant and super-fast computers looking at outputs and 3D color displays, and being convinced that with all the brainpower and resources that are invested, they are on track and are on their way to solving the problem.

Indirect methods such as flat Common Image Gathers (CIGs) were developed as a response to the inability to directly solve for and adequately provide a velocity model for depth imaging, and those CIGs represent a necessary condition at the image that an accurate velocity would satisfy. Many wrong velocity models can and do also satisfy a flat-common-image-gather criterion, especially under complex imaging circumstances. Indeed, unquestioned faith in the power of satisfying the flat-common-image-gather criterion can and does contribute to dry-hole drilling. Mathematicians who work on the latter types of problems would better spend their time describing the underlying lack of a necessary and sufficient condition and the consequences rather than dressing up and obfuscating the necessary but insufficient condition in fancy, rigorous, and abstract new clothes.

Today, we basically remain fixed and without significant progress (at a one-in-ten success rate) in drilling successful exploration wells in the deep-water Gulf of Mexico.

Indirect methods should only be considered when direct methods are not available or are inadequate, or when you cannot figure out how to solve a problem directly. Indirect methods are often and reasonably employed to allow a channel and an adjustment (a dial) for phenomena and components of reality that are outside and external to the physics of the system you have chosen and defined. Of course there always are, and always will be, phenomena outside your assumed and adopted physics and system that need to be accommodated and that are ignored at your peril. That's the proper realm and role for indirect methods. Even then, though, they need to be applied judiciously and always with scrutiny of what resides behind cost-function-criteria assumptions. We discuss that specific issue in a report on seeking adaptive criteria, beyond and as a replacement for energy minimization. However, using indirect methods for phenomena and processing goals within the system, and for providing prerequisites within the system, is in general a conceptual and practical mistake. There has been a dangerous and growing trend to solve everything inside and outside the system by using indirect methods and cost functions. We recognize, support, and require ever faster computers. However, the growth in computational physics at the expense of mathematical physics, and the availability of ever-faster computers, encourages the rush to "cost functions" and searching without thinking, and represents a misguided and unfortunate trend.

A direct method provides a framework of precise data needs, and it delivers a straight-ahead formula that takes in your data and actually solves and explicitly and directly outputs the solution that you seek. Indirect methods can never provide that clarity or confidence, and model matching and iterative updating by any fancy name, such as a new "Frechet derivative," and the so-called "Full Wave Inversion," are model matching and are never, ever equivalent to a direct inversion for the earth's elastic mechanical property changes. The distinction is significant and has both conceptual and mercantile consequences.

Let me present an example of the difference. Let's suppose someone said that you could take a single seismic trace that is, a single function of time, and invert simultaneously for velocity and density, each as a function of depth in a 1D earth.

Today, you might reasonably be cautious and concerned because the dimension of the data is less than the overall dimension of the quantities you seek to determine. We have learned as an industry to be dubious in the latter single-trace, solve-for-two-functions-of-depth case. We look skeptically at those who would model match and pull all kinds of arcane cost functions and generalized inverses together, using different norms and constraints and full-wave predictions of that single trace that can be model matched with amplitude and phase so that we can call that model-matching scheme "full wave inversion." Why can't we solve for density and velocity uniquely from a single trace, since we can certainly model the single trace from knowing the velocity and density as a function of depth? What came along in that earlier time, as a response to this question, were direct acoustic inversion methods that said that inverting for velocity and density as a function of depth from a single trace is impossible, or at least that it is impossible to provide the unique and actual velocity and density as a function of depth. That direct inversion framework convinced many (hopefully most) people that the one-trace-in, two-functions-out approach is not a question or an issue of which indirect algorithm you are using. It is more basic and stands above algorithm; it's an inadequate-data issue. No algorithm with those single-trace data should call itself "inversion," even if that single trace was

model matched and computed with amplitude and phase and markets itself as "full wave inversion." We learned to stop running that single trace through search algorithms for velocity and density — and that lesson was absorbed within our collective psyches in our industry — for whatever the cost function and local or global minimum you employed. Using the wrong and fundamentally inadequate data closes the book and constitutes the end of the story. Thus, we learned to look for and respect dimension between the data and the sought-after parameters we want to identify. That is a good thing, but it turns out that it's not a good-enough thing. In fact, direct acoustic wave inversion for a 1D earth requires all the traces for a given shot record in order to determine one or more than one parameters (e.g., V_p and density) as a function of depth.

When it comes to directly inverting for changes in elastic properties and density, there are direct and explicit formulas for the linear and non-linear estimates. Further, those direct and explicit non linear formulas are only derivable from the direct inverse machinery of the inverse scattering series (please see the references below.) Those direct non linear formulas are like the direct solution for the quadratic equation mentioned above and solve directly and non linearly for changes in V_p, V_s, and density in a 1D elastic earth. Those formulas prescribe precisely what data you need as input, and they dictate how to compute those sought-after mechanical properties. There is no search or cost function, and the unambiguous and unequivocal data needed are full multi component data, PP, PS, SP, and SS, for all traces in each of the P and S shot records. The direct algorithm determines first the data needed and then the appropriate algorithms to use those data to directly compute the sought-after changes in the earth's mechanical properties. Hence, any method that calls itself inversion (let alone full-wave inversion) for determining changes in elastic properties, and in particular V_p, and that inputs only P data, is more off base, misguided, and lost than the methods that sought two or more functions of depth from a single trace. You can model match P data until the cows come home, and that takes a lot of computational effort and people with math and physics advanced degrees from the most elite and prestigious universities computing Frechet derivatives, and requires sophisticated cost-function search engines, so it must be scientific and worthwhile. Why can't we use just PP data to invert for changes in V_p, V_s, and density, since Zoeppritz says that I can model PP from those quantities, and since I have, using PP data with angle variation, enough dimension? As I said above, data dimension is good, but not good enough for a direct inversion of those elastic properties. The frameworks, data needs, and algorithms provided by direct inversion all matter. The framework of a direct method helps you understand what will allow things to work in principle, and, equally important, it helps you identify the issue or problem when things don't work. Indirect methods, on the other hand, never can match that definiteness, clarity, and value. When we use just P-wave data with an acoustic or elastic model matching "FWI" for shallow-hazard detection or velocity estimation at top salt, and then issues arise, perhaps the framework and requirements described in this note might be items behind a lack of predictive stability and usefulness.

Using P-waves with amplitude and phase for an acoustic earth model flies in the face of 40 years of AVO experience, which says that the elastic earth is the minimum realistic earth model for any amplitude issue or processing method. Using P-wave data for an elastic earth model, with algorithms that utilize amplitude and phase, violates the necessary multi component data needs prescribed by direct inversion of V_p, V_s, and density. Having the adequate data (defined by a direct inversion framework) is better than not having the necessary and sufficient data and is a good place to start. However, even when one is starting with the indicated multi-component data, the train can still be taken off the track by indirect search and iterative linear updating algorithms, when

direct inverse algorithms are available.

Some might say in response that P-wave "FWI" with either an acoustic or elastic medium and then using some search algorithm represents "an approximation," and what's wrong with approximations. The answer is precisely that, "what IS wrong with the approximation?" If you purposely or inadvertently ignore (or wish away) the framework and algorithms that a direct solution to the elastic parameter estimation provides, you will never know what you are ignoring and dropping and what your approximation is approximating and what your method actually means.

In summary, so-called P-wave "FWI" is in general the wrong (acoustic) earth model, the wrong data, and the wrong method — besides that, it has a lot going for it.

M-OSRP plans to progress direct elastic inversion for shallow-hazard-identification and top-salt-velocity updates. We intend to compare with current approaches for those serious and significant velocity-analysis challenges.

References

Weglein, Arthur B., Haiyan Zhang, Adriana C. Ramírez, Fang Liu, and Jose Eduardo M. Lira. "Clarifying the underlying and fundamental meaning of the approximate linear inversion of seismic data." *Geophysics* 74 (November-December 2009): WCD1–WCD13.

Zhang, Haiyan. *Direct non-linear acoustic and elastic inversion: towards fundamentally new comprehensive and realistic target identification.* PhD thesis, University of Houston, 2006.

Short note: An alternative adaptive subtraction criteria (to energy minimization) for free surface multiple removal

A. B. Weglein

May 25, 2012

An idea: The idea starts by considering the following perturbation forms in 2D.

$$\text{1 parameter acoustic} \quad V_p = \omega^2 \left(\frac{1}{K_0} a_1(\vec{k}-\vec{p}) \right) = V_p(\vec{k},\vec{p},\omega)$$

$$\text{2 parameter acoustic} \quad V_{pp} = \omega^2 \left(\frac{1}{K_0} a_1(\vec{k}-\vec{p}) + \frac{1}{\omega^2} \frac{\vec{k}\cdot\vec{p}}{\rho_0} a_2(\vec{k}-\vec{p}) \right)$$

$$\text{elastic} \quad V_{pp} = \omega^2 \left(\frac{1}{K_0} a_1(\vec{k}-\vec{p}) + \frac{1}{\omega^2} \frac{\vec{k}\cdot\vec{p}}{\rho_0} a_2(\vec{k}-\vec{p}) - 2\frac{\beta_0^2}{\omega^4} |\vec{k}\times\vec{p}|^2 a_3(\vec{k}-\vec{p}) \right)$$

where $\vec{k}$ and $\vec{p}$ are arbitrary 2D vectors, K_0, ρ_0, and β_0 are the bulk modulus, density, and shear velocity of the reference medium, a_1 is the relative change in the bulk modulus, a_2 is the relative change in density, and a_3 is the relative change in shear modulus. On the measurement surface, $\vec{k} = \vec{k}_g$, $\vec{p} = \vec{k}_s$, and $|\vec{k}_g| = |\vec{k}_s| = \omega/c_0$. The input to the inverse scattering series free surface multiple algorithm is $V_1(\vec{k}_g, \vec{k}_s, \omega)$, which for the three forms listed above has an overall ω^2/c^2 factor.

$$D^{WOFS} = \underbrace{G_0^d V_1 G_0^d}_{\omega^2} + \underbrace{G_0^d V_1 G_0^{FS} V_1 G_0^d}_{\omega^4} + \underbrace{G_0^d V_1 G_0^{FS} V_1 G_0^{FS} V_1 G_0^d}_{\omega^6} + \ldots$$

where D^{WOFS} is deghosted data without free surface multiples and the first term on the right hand side is D^{WFS}, deghosted data with free surface multiples.

The new adaptive criteria is

$$\lim_{\omega\to 0} \left[\frac{D^{WFS} - D^{WOFS}}{\omega^2} \right] = 0$$

or minimize $(D^{WFS} - D^{WOFS})/\omega^2$ with respect to a "wavelet" factor.

Determination of reflection coefficients by comparison of direct and reflected VSP events

J. E. Lira, Petrobras E&P-EXP,
A. B. Weglein, University of Houston, M-OSRP,
C. W. Bird and K. A. Innanen, University of Calgary, CREWES Project

May 25, 2012

Abstract

VSP experiments provide a much greater opportunity to estimate local reflectivity information than do surface-constrained experiments. In this paper we describe a simple, data driven means by which the reflection coefficient associated with an interface at depth, uncontaminated by transmission losses, may be determined, regardless of the origins of these losses or of the overburden parameters associated with them. An amplitude correction operator is formed through a comparison of the direct and reflected waves just above a generating interface. Error grows as the distance above the generating interface at which the two events are compared grows. The formulation of the problem is in the plane-wave domain, but with a slight additional error the approach can be applied to data associated with fixed zero or nonzero offset. The method can be applied to generate scalar reflectivity values in acoustic/elastic environments, or phase and amplitude spectra of reflectivities in anacoustic/attenuative environments. A field data example from the Ross Lake heavy oil field in Saskatchewan, Canada illustrates the method. Our sense is that these results indicate applicability to more complex geometries, walkway or 3-D VSP surveys, assisting with the construction of AVO/AVA panels.

1 Introduction

The VSP has become an increasingly important tool for oil exploration during the last two decades. In that time, the development of computational and instrument technology, along with an increased need to understand and monitor production of existing reservoirs, has led to an evolution of the VSP method from 1D time-only measurements to far more complex multi-D geometries. The first 3D VSP, for instance, was acquired by AGIP in 1986 (Chopra et al., 2004), and since then 3D has become an affordable and viable option for monitoring production (Kuzmiski et al., 2009). For a historical review see Hardage (1985). VSPs are used for anisotropic parameter estimation (Grechka and Mateeva, 2007), attenuation studies (Omnes and Heprenschmidt, 1992), anisotropic AVO analysis (Leaney et al., 1999), stiffness tensor calculation (Dewangan and Grechka, 2002), mapping of fluid pathways Owusu and Mubarak (2009), etc.

As in surface seismic exploration, the need for *a priori* Earth property information is characteristic of conventional VSP processing. In the surface case, the attempt to reduce this need has met with remarkable success, in, e.g., free-surface multiple elimination (Carvalho, 1992; Verschuur et al., 1992), internal multiple attenuation (Araujo et al., 1994; Ramirez, 2007), and is the subject of more recent advances in imaging (Weglein et al., 2010). The literature contains a shorter record of this kind of progress for the VSP problem, yet the interest exists there too: Xiao et al. (2006) and He et al. (2009), for instance, present VSP imaging approaches that avoid the requirement for prior knowledge of medium properties. In this paper we consider a related problem: determining the reflection coefficients associated with structures in a VSP experiment directly from the amplitudes of the VSP data, which contain the reflectivity but are also influenced by overburden transmission of various kinds.

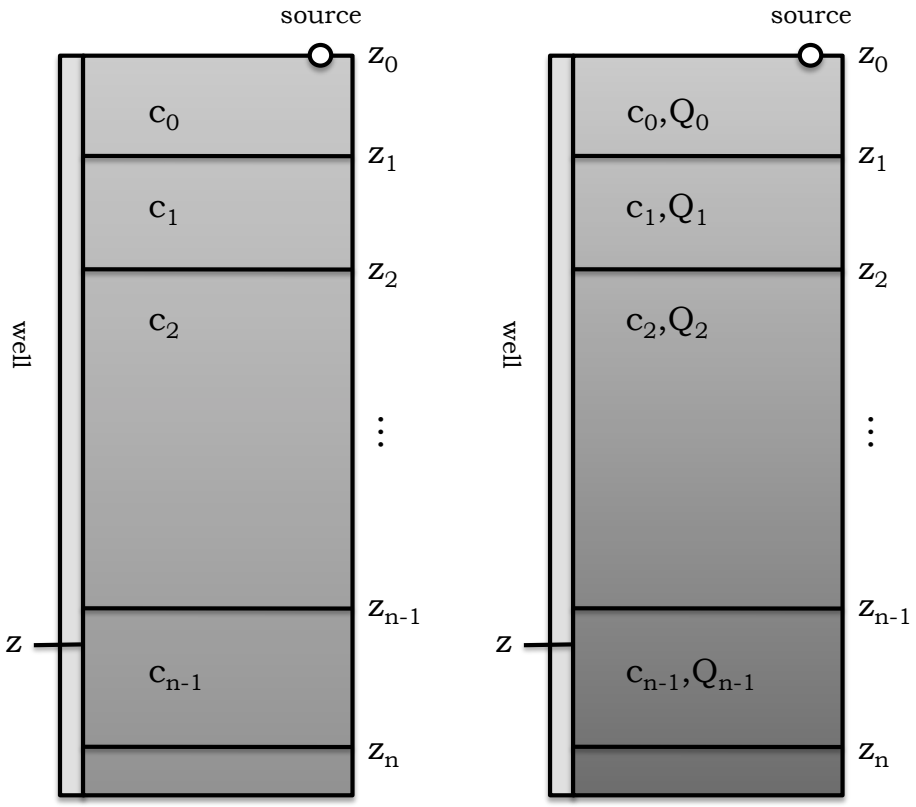

Figure 1: 1D zero-offset VSP geometry and parameters. Left: one-parameter acoustic model. Right: two-parameter anacoustic (i.e., attenuative and dispersive) model.

The approach we take is based on a simple picture of the origins of the amplitude of a reflected primary. This amplitude, say P, is represented as involving the influence of propagation down through the overburden, P_D, reflection at an interface, R, followed by propagation back up through

some or all of the overburden, P_U. The amplitude is thus the cumulative effect of three influences:

$$P = P_D \, R \, P_U. \tag{1.1}$$

The success of most VSP data processing and/or imaging problems is connected to the ability to identify and remove the influence of P_D and P_U, recovering the reflectivity information R.

Our approach involves a compensation procedure, in which we correct P for its transmission losses, by designing an operator (a "primary correction operator", or PCO for short) directly from the raw VSP data (i.e., directly from the shot records), absent medium property information. The operator, which is effectively of the form $PCO = \frac{1}{[P_D][P_U]}$, is constructed through a combination of the amplitude spectra of the primary and its direct wave counterpart, each recorded at the same receiver. A related combination of direct and transmitted waves is discussed by Hardage (1985). Its precise form is deduced, in this paper, from a study of the direct and reflected amplitude spectra for Earths of two distinct types, acoustic and anelastic.

We illustrate its use with simple numerical examples for a zero-offset VSP. We emphasize, however, that the approach with which data from one or more non-zero offsets is processed is unchanged. We discuss the gradual increase in correction error with increase in offset in an upcoming section.

2 VSP models and configuration

We consider a VSP experiment with a fixed offset (Figure 1). We assume, first, layered acoustic media, and second, layered anacoustic media (i.e., involving attenuation and dispersion). The nth layer lies between the nth and $n+1$th interface. These choices are made to exemplify the procedure, which is not constrained to media of these types, but is essentially independent of model-type.

2.1 Case I: R beneath an acoustic overburden

We begin by deducing the form of the primary amplitude correction operator PCO for an acoustic, one-parameter overburden, pictured in the the left-hand panel of Figure 1. Suppose the direct wave and the primary reflecting from interface n are both measured by a geophone at depth z (Figure 2). In one spatial dimension, the phase and amplitude of the primary are constructed as follows:

$$\begin{aligned} P = & e^{ik_0(z_1-z_0)} T_{01} e^{ik_1(z_2-z_1)} T_{12} e^{ik_2(z_3-z_2)} \dots \\ & \times R_n \exp\left[ik_{n-1}(2z_n - z_{n-1} - z)\right], \end{aligned} \tag{2.1}$$

such that

$$|P| = [T_{01} T_{12} T_{23} \dots T_{(n-1)n}] \times R_n, \tag{2.2}$$

where z_n is the depth of the nth interface, $k_n = \frac{\omega}{c_n}$, c_n is the wave velocity in the nth layer, ω is the frequency, and T_{ij} is the transmission coefficient at the interface between layers i and j.

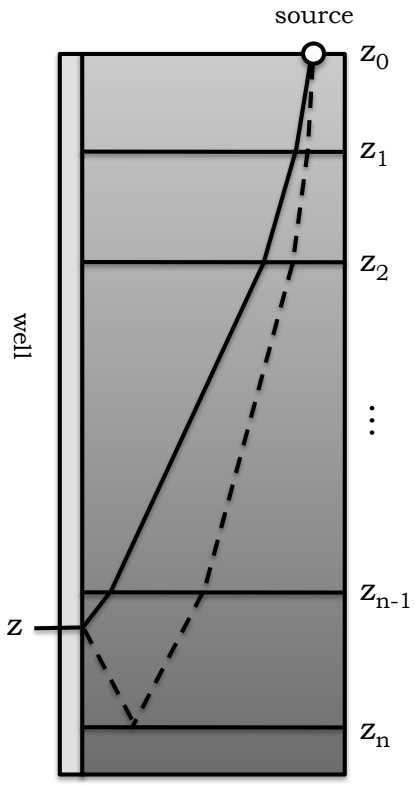

Figure 2: 1D zero-offset VSP survey. The direct wave (solid) and the primary P_n, generated at interface n (dashed), are depicted. The two paths are identical except for (1) small differences in path length ddue to offset, and (2) a small additional path segment experienced by the primary below z.

The phase and amplitude of the direct wave are likewise constructed via

$$\begin{aligned} D =& e^{ik_0(z_1-z_0)}T_{01}e^{ik_1(z_2-z_1)}T_{12}e^{ik_2(z_3-z_2)}\dots \\ & \times \exp\left[ik_{n-1}(z-z_{n-1})\right], \end{aligned} \tag{2.3}$$

such that

$$|D| = [T_{01}T_{12}T_{23}\dots T_{(n-1)n}]. \tag{2.4}$$

Evidently, the reciprocal of the direct wave spectrum in equation 2.4 must be the desired operator (PCO) described above, which, when applied to the primary spectrum, corrects for the transmission

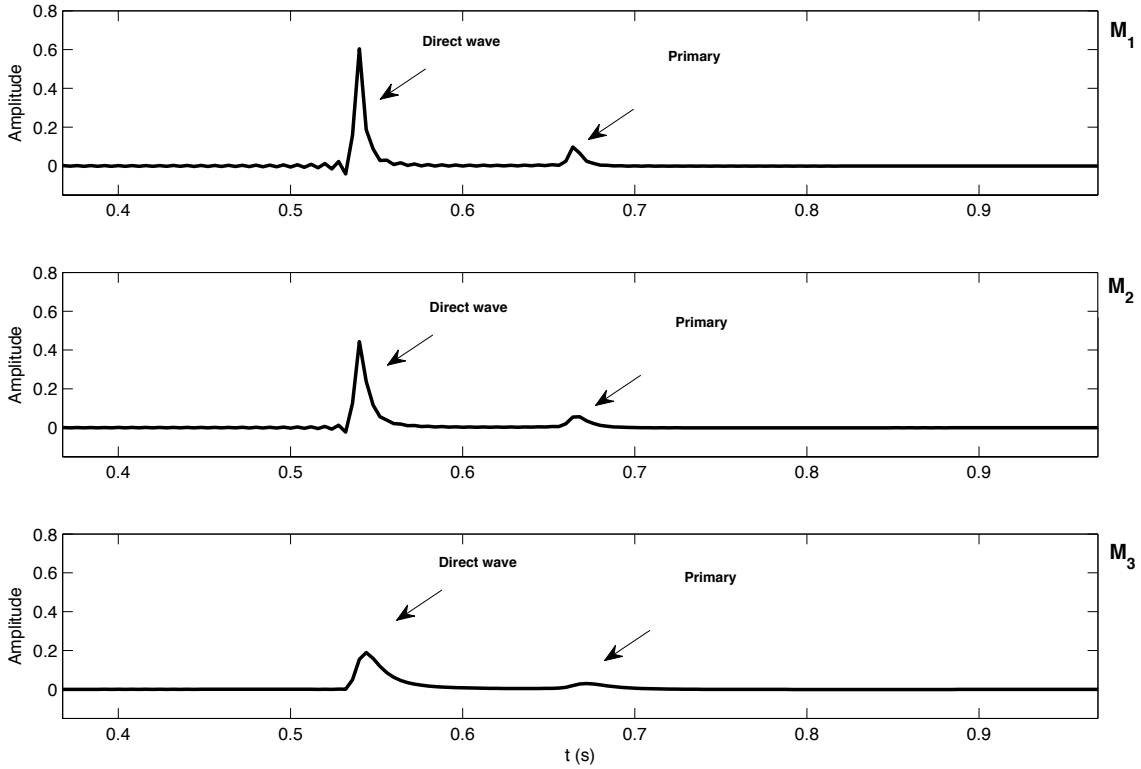

Figure 3: Three zero-offset traces generated with the survey geometry depicted in (a), using parameters in Table 1. Two events are shown: the direct wave and the primary.

losses:

$$\begin{aligned} P_{\text{cor}} =& |P| \times PCO \\ =& |P| \times \frac{1}{|D|} \\ =& [T_{01}T_{12}T_{23}\ldots T_{(n-1)n}] \times R_n \\ & \times \frac{1}{[T_{01}T_{12}T_{23}\ldots T_{(n-1)n}]} \\ =& R_n. \end{aligned} \tag{2.5}$$

This 1D model of amplitudes is correctly understood as applying to a plane wave, in which domain equation (2.5) can be applied at normal or oblique incidence. However, since in a VSP experiment we rarely have sufficient spatial source coverage to permit Fourier transformation to the plane-wave domain, we will analyze this formula as applied in the spatial domain, that is, involving data from fixed zero or non-zero offsets.

In the fixed offset case several aspects of the model in equations (2.1)–(2.5) are inaccurate – for instance no account of spherical spreading has been taken. We point out, however, that since two events with nearly identical paths of propagation are being compared, and all amplitude influences

shared by the two events are "divided out", the additional error introduced by applying a correction based on this model to fixed offset VSP data should be relatively small.

2.2 Case II: $R(\omega)$ beneath an attenuating overburden

To study the attenuative case, in which transmission losses are magnified considerably, we adopt the model reviewed by Aki and Richards (2002) wherein the acoustic propagation constants k_j in equation (2.1) is replaced by the complex k_j^*, such that for the jth layer

$$k_j^* = \frac{\omega}{c_j}\left[1 + \frac{1}{Q_j}F(\omega)\right], \tag{2.6}$$

where

$$F(\omega) = \frac{i}{2} - \frac{1}{\pi}\log\left(\frac{\omega}{\omega_0}\right), \tag{2.7}$$

and ω_0 is a reference frequency. Substituting k_j^* for k_j in equation (2.1) and re-grouping the terms, we express the anelastic primary as:

$$\begin{aligned} P_{\text{an}} =& e^{ik_0^*(z_1-z_0)}\mathcal{T}_{01}e^{ik_1^*(z_2-z_1)}\mathcal{T}_{12}e^{ik_2^*(z_3-z_2)}\dots \\ &\times R_n(\omega)\exp\left[ik_{n-1}^*(2z_n - z_{n-1} - z)\right], \end{aligned} \tag{2.8}$$

where the absorptive transmission coefficients $\mathcal{T}_{ij}$ are defined as follows:

$$\begin{aligned} \mathcal{T}_{ij} =& \left[\frac{2c_j\left(1+\frac{F(\omega)}{Q_j}\right)^{-1}}{c_i\left(1+\frac{F(\omega)}{Q_i}\right)^{-1} + c_j\left(1+\frac{F(\omega)}{Q_j}\right)^{-1}}\right] \\ &\times \underbrace{e^{-\frac{\omega}{2Q_ic_i}(z_i - z_{(i-1)})}}_{\text{attenuation component}}\ e^{\frac{i\omega}{\pi Q_ic_i}\log(\frac{\omega}{\omega_0})(z_i - z_{(i-1)})}, \end{aligned} \tag{2.9}$$

as discussed by Lira et al. (2010). We re-write the direct wave in analogy to equation (2.3):

$$\begin{aligned} D_{\text{an}} =& e^{ik_0^*(z_1-z_0)}\mathcal{T}_{01}e^{ik_1^*(z_2-z_1)}\mathcal{T}_{12}e^{ik_2^*(z_3-z_2)}\dots \\ &\times \exp\left[ik_{n-1}^*(z - z_{n-1})\right]. \end{aligned} \tag{2.10}$$

Equations (2.8) and (2.10) are to the anelastic case what equations (2.1) and (2.3) are to the acoustic case, hence we repeat the procedure and define an absorptive operator PCO_{an}, which, when applied to the spectrum of the primary produces:

$$PCO_{\text{an}} \times P_{\text{an}} = \frac{1}{D_{\text{an}}} \times P_{\text{an}} = R_n(\omega) \times e^{ik_{n-1}^* 2(z_n - z)}. \tag{2.11}$$

Neglecting the (small) term $e^{ik_{n-1}^* 2(z_n-z)}$ in equation (2.11), we again have generated the correction operator. In comparing the acoustic and attenuative cases, the only difference is that we have retained the phase content of the reflections in the latter. In spite of this slight implementation difference, the operator is designed the same way independent of the mechanism of transmission loss in the overburden: no matter what type of medium is assumed, the correction is carried out the same way.

3 Sources of error

There are two main sources of error in the operator design as we have presented it. One source of error is visible in the construction of the operators. Consider again equation (2.11). The extra factor,

$$\exp\left[ik_{n-1}^{*}2(z_n - z)\right], \tag{3.1}$$

being extraneous, throws the calculation off slightly. The origin of this term lies in the fact that we must compare the direct wave and primary some small but finite distance above the generating reflector. This adds a short component to the primary's path not shared by the direct wave (see Figure 2). The error is kept small provided the distance from the generating interface to the receiver is relatively small. In this case

$$|k_{n-1}^{*}2(z_n - z)| \ll 1, \tag{3.2}$$

and

$$OP_{\text{an}} \times P_{\text{an}} \rightarrow R_n(\omega). \tag{3.3}$$

Beyond this source of error, the diagram in Figure 2 also illustrates the influence of offset on the accuracy of the operator construction. Briefly, the greater the offset, the longer the path of the primary *not* shared by the direct wave must be. This effectively increases the importance of the extra term (equation 3.1).

4 Synthetic Examples

Here we illustrate with synthetic examples the transmission loss compensation in action on a $1D$ zero-offset VSP experiment in an absorptive medium as mathematically modeled in the previous section. We generate three zero-offset traces from plane-waves incident normally upon the model depicted in the right-hand panel of Figure 1. We use parameter values given in Table 1.

Layer	Depth (m)	c (m/s)	M_1	M_2	M_3
0	000-100	1500	∞	∞	∞
1	100-350	1700	400	300	100
2	350-600	1800	200	150	50
3	600-850	1950	100	75	25
4	850-1100	2000	50	25	15
5	1100-∞	2100	25	15	10

Table 1. Attenuative Earth models. The columns labelled M_1, M_2, and M_3 contain the layer Q values for models 1, 2 and 3 respectively.

In Figure 3 the three input traces are illustrated. The Q values used for each trace range from low to high attenuation. Our goal is to correct the amplitude of the primary using the direct wave. The

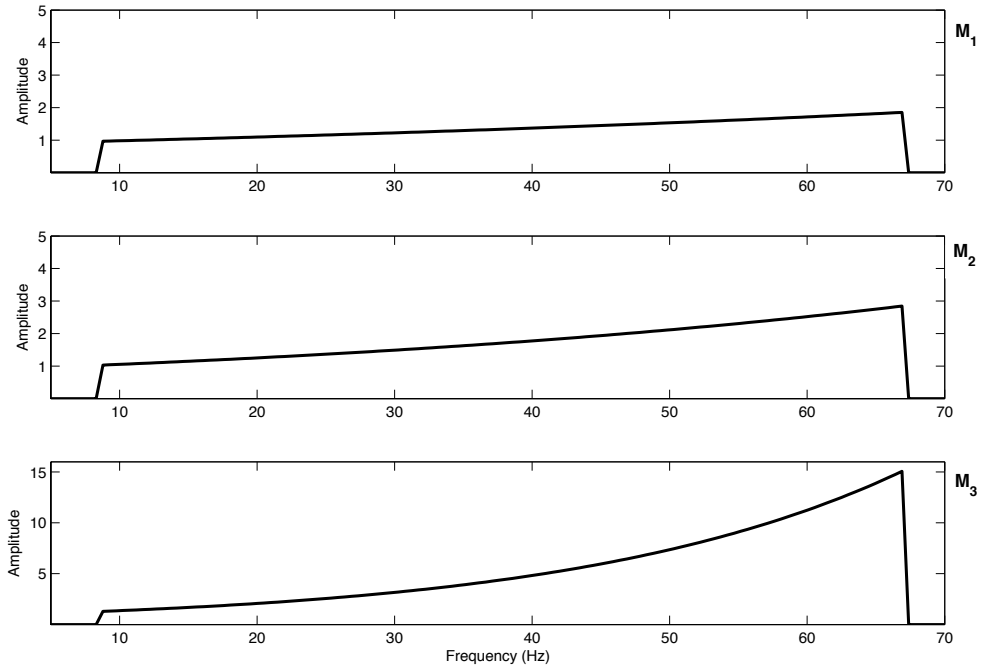

Figure 4: Illustration of the three PCO spectra calculated from the direct waves illusrated in Figure 2.

procedure is: (1) the primary and its direct counterpart, at the same receiver, are isolated and their spectra calculated, (2) the reciprocal of the spectrum of the direct wave, which is identified as the operator PCO, is taken, and (3) the spectrum of the primary is multiplied by the operator. The reciprocal spectra, i.e, the PCOs, are displayed in Figure 4. Figure 5 compares the original primary with the corrected primary and both vs. the idealized case (modeled with no transmission losses) which serves as a benchmark.

Comparing the latter two traces, we observe that the overburden transmission losses are largely compensated for, with some small visible error attributable to the distance above the reflector at which the analysis is conducted.

5 Field Data Example: Ross Lake

The Ross Lake heavy oil field is located in the southwest of Saskatchewan (see Figure 6), and is owned and operated by Husky Energy Inc. (Zhang, 2010). In a collaboration between CREWES/University of Calgary, Husky Energy, and Schlumberger Canada, a number of VSP experiments were performed using the well $11-25-13-17W3$, including a zero-offset VSP.

The zero-offset VSP will be the focus of this paper. The data were acquired using 3-component receivers and both horizontal and vertical vibrators (Zhang, 2010). The receiver spacing in the

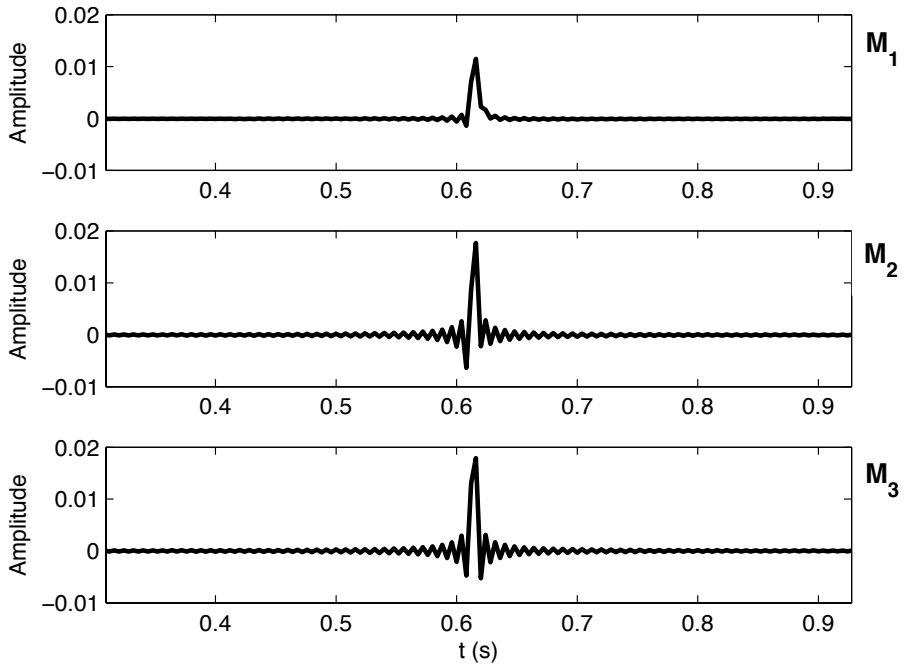

Figure 5: Result of correction of primary M_2. Top panel: input; middle panel: corrected with the PCO. Bottom panel: benchmark: primary modeled in the absence of transmission influences.

borehole was 7.5m. There is a reflector at roughly 600m depth which is likely associated with the Lea Park/Milk river unconformity. In Figure 7 for the stratigraphic column is illustrated.

In Figures 9 and 10 the vertical component of the downgoing and upgoing wave fields are plotted respectively. Wave field separation was performed using a median filtering technique (Kommedal and Tjostheim, 1989; Hinds et al., 1996). Figure 10 shows the aforementioned reflection at $600m$ which has been interpreted and is highlighted in orange.

A Q_P profile was obtained by Zhang (2010) using the spectral shift method (e.g., Hauge, 1981) on the VSP data to obtain a profile of Q_P in the vicinity of the wellbore. This Q_P profile is on the far left panel of Figure 8. Importantly for our current purposes, there is a negligible attenuation contrast at the Lea Park/Milk River interface. Therefore, we expect that there should be little frequency dependence of the reflection coefficient and we may use the ratio of the peak amplitudes to provide the estimate of the reflection coefficient.

We extract the amplitudes of the interpreted direct arrival on the downgoing wavefield dataset, then we extract the amplitude of the interpreted Lea Park/Milk River horizon on the upgoing wavefield dataset.

We then divide the reflected amplitudes by the direct arrival amplitudes for each receiver to obtain an estimate of the reflection coefficient. For receivers just above the reflector the result of dividing the reflected amplitude from the direct amplitude should be a close approximation to the reflection coefficient. However, as we move up the borehole the extracted amplitudes of the primary will

Figure 6: Ross Lake oil field in Saskatchewan. From Zhang (2010).

decay due to the propagation effect of the attenuative medium and so the estimate of the reflection coefficient obtained by dividing the reflected amplitude by the direct amplitude should be less than the correct reflection coefficient.

Figure 11 shows a plot of the estimated reflection coefficient versus the distance of the receiver above the reflector from which the estimate was obtained. The blue curve shows the actual values of the reflection coefficient and the red curve is a line of best fit. Notice that the reflection coefficient drops as the distance above the reflector increases, as expected. The best estimate of the reflection coefficient in Figure 11 will be where the receiver is closest to the reflector which is about 0.08. This seems to be a reasonable value for a reflection coefficient but comparing this result with well log values is a topic of future work.

6 Conclusions

We discuss a strategy for correcting the transmission losses of a primary using an operator built from data only. The operator is calculated with no *a priori* Earth property information, and the procedure is identical no matter what type of medium, or mechanism of transmission loss, is present, and the correction is achieved in principle directly from shot records.

We illustrate three zero-offset synthetic examples involving low and high levels of overburden attenuation. The results of the numerical study have been sufficiently encouraging to warrant field data testing.

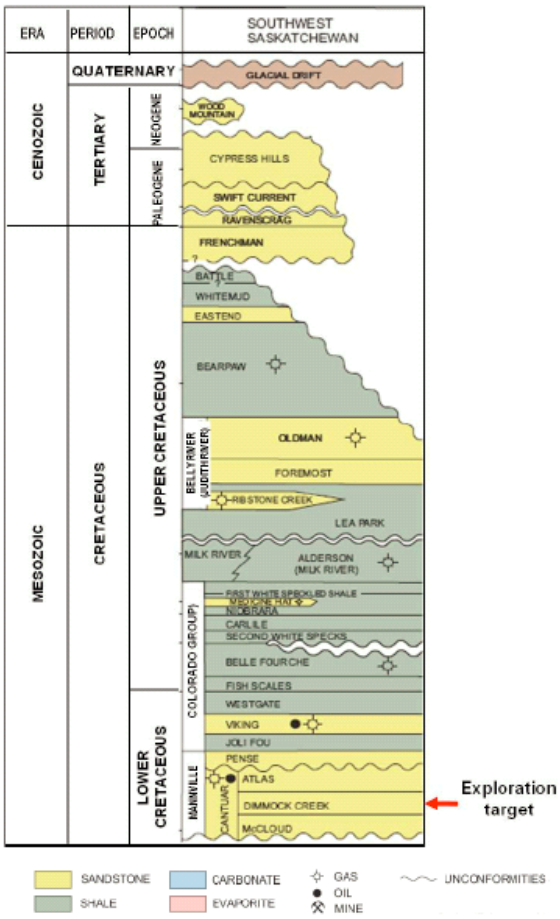

Figure 7: Stratigraphic column of study area. From Saskatchewan Industry and Resources, 2006; adapted from Zhang (2010).

We apply the approach to field data from the Ross Lake oil field in southwest Saskatchewan, obtaining a reasonable result for a reflection coefficient for the Lea Park/Milk River reflector. This result will need to be verified with well log data.

Our sense is that these results indicate applicability to more complex geometries, walkway or 3-D VSP surveys, assisting with the construction of AVO/AVA panels. These panels could be produced, in principle, as the shots are being recorded at the time of acquisition.

7 Acknowledgments

J. Lira thanks Petrobras. A. B. Weglein thanks the sponsors of M-OSRP. C. Bird and K. Innanen thank the CREWES Project, and are additionally supported by an NSERC Discovery grant.

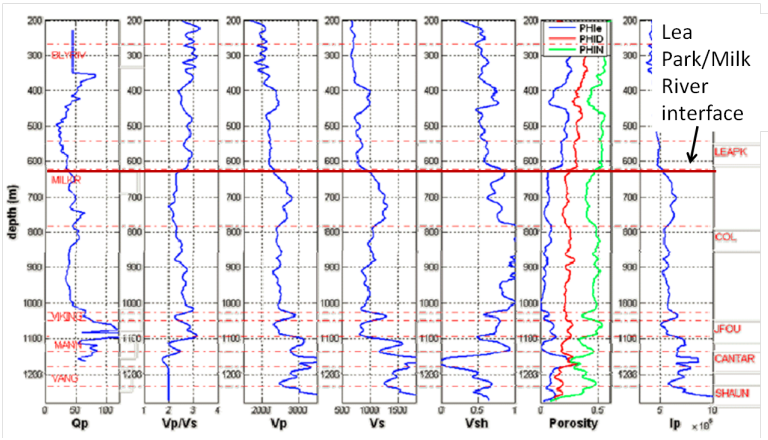

Figure 8: Left column: Q_P profile using spectral shift method. From Zhang (2010).

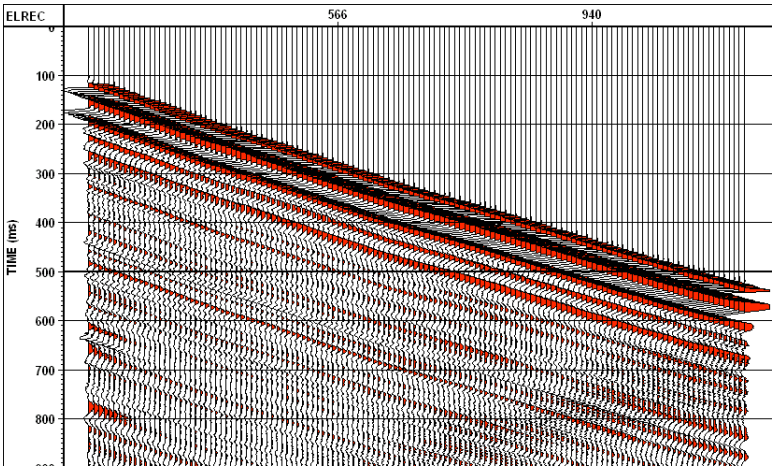

Figure 9: The downgoing wavefield, separated using median filtering.

References

Aki, K. and P. G. Richards. *Quantitative Seismology.* 2nd edition. University Science Books, 2002.

Araujo, F. V., A. B. Weglein, P. M. Carvalho, and R. H. Stolt. "Inverse scattering series for multiple attenuation: An example with surface and internal multiples." *64th Ann. Internat. Mtg.* Soc. of Expl. Geophys., 1994, 1039–1041.

Carvalho, P. M. *Free-surface multiple reflection elimination method based on non-linear inversion of seismic data.* PhD thesis, Universidade Federal da Bahia, Bahia, Brazil, 1992. *in portuguese.*

Chopra, S[], V[] Alexeev, A[] Manerikar, and A[] Kryzan. "Acquisitions/Process-

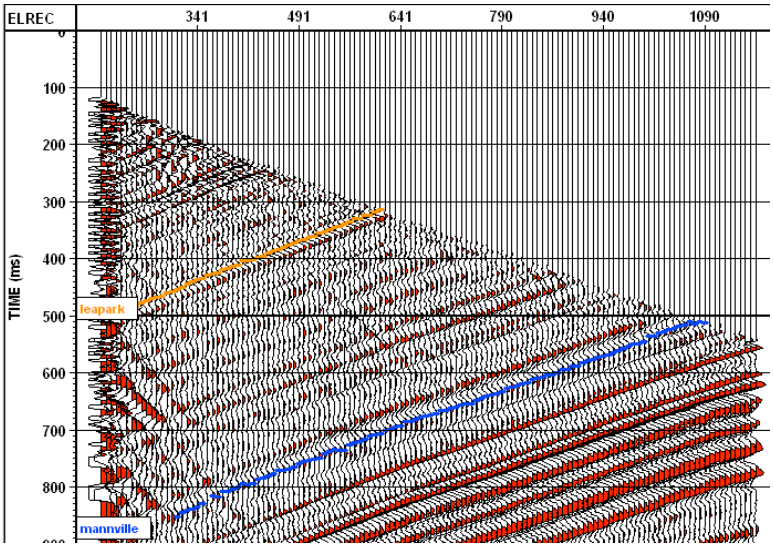

Figure 10: The upgoing wavefield, separated using median filtering, with the Lea Park and Mannville horizons interpreted.

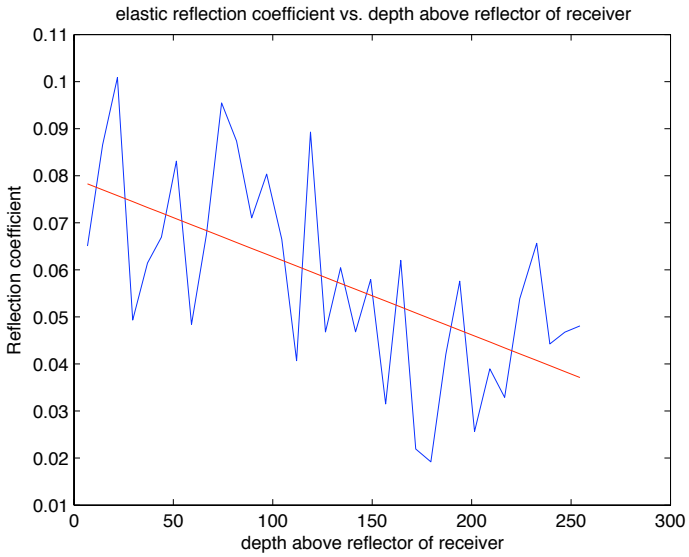

Figure 11: estimate of the reflection coefficient as a function of receiver distance above the reflector.

ingï£¡Processing/integration of simultaneously acquired 3D surface seismic and 3D VSP data." *The Leading Edge* 23 (2004): 422–430.

Dewangan, P[] and V[] Grechka. "Inversion of multicomponent, multiazimuth, walkaway VSP data for the stiffness tensor." *72nd Ann. Internat. Mtg.* Soc. of Expl. Geophys., 2002, 161–164.

Grechka, V. and A. Mateeva. "Inversion of P-wave VSP data for local anisotropy: Theory and case study." *Geophysics* 72 (2007): D69–D79.

Hardage, B. A. *Vertical seismic profiling, Part A: Principles, 2nd Ed.,* in Handbook of geophysical exploration*, K. Helbig, S. Treitel, eds.* Volume 14A . Geophysical Press, 1985.

Hauge, Paul S. "Measurements of attenuation from vertical seismic profiles." *Geophysics* 46 (1981): 1548–1558.

He, R., M. Karrenbach, B. Paulsson, and V. Soutryne. "Near-wellbore VSP imaging without overburden." *Geophysics* 74 (2009): SI9–SI14.

Hinds, R. C., N. L. Anderson, and R. D. Kuzmiski. *VSP Interpretive Processing: Theory and Practice.* Society of Exploration Geophysicists, 1996.

Kommedal, J. H. and B. A. Tjostheim. "A study of different methods of wavefield separation for application to VSP data." *Geophysical Prospecting* 37 (1989): 117–142.

Kuzmiski, R., B. Charters, and M. Galbraith. "Processing considerations for 3D VSP." *Recorder* 34 (2009): 30–40.

Leaney, W[] S[], C[] M[] Sayers, and D[] E[] Miller. "Analysis of multiazimuthal VSP data for anisotropy and AVO." *Geophysics* 64 (1999): 1172–1180.

Lira, J. E. M., K. A. Innanen, A. B. Weglein, and A. C. Ramirez. "Correction of primary amplitudes for plane-wave transmission loss through an acoustic or absorptive overburden with the inverse scattering series internal multiple attenuation algorithm: an initial study and 1D numerical examples." *Journal of Seismic Exploration* 19 (2010): SI9–SI14.

Omnes, G[] and A[] Heprenschmidt. "Use of VSP data for P and S wave attenuation studies in a fractured reservoir." *62nd Ann. Internat. Mtg.* Soc. of Expl. Geophys., 1992, 148–150.

Owusu, J. C. and M. Mubarak. "High-fidelity walkaround VSP anisotropy analysis." *The Leading Edge* 28 (2009): 966–972.

Ramirez, A. C. *I - Inverse scattering subseries for 1: Removal of internal multiples and 2: Depth imaging primaries; II - Green's theorem as the foundation of interferometry and guiding new practical methods and applications.* PhD thesis, University of Houston, 2007.

Verschuur, D. J., A. J. Berkhout, and C. P. A. Wapenaar. "Adaptive surface-related multiple elimination." *Geophysics* 57 (1992): 1166–1177.

Weglein, A. B., F. Liu, Z. Wang, X. Li, and H. Liang. "The inverse scattering series depth imaging algorithms: development, tests and progress towards field data application." *Proc. of the SEG Annual Meeting* (2010).

Xiao, X., M. Zhou, and G. T. Schuster. "Salt-flank delineation by interferometric imaging of transmitted P- to S-waves." *Geophysics* 71 (2006): SI197–SI207.

Zhang, Z. *Assessing attenuation, fractures, and anisotropy using logs, vertical seismic profile, and three-component seismic data: heavy oilfield and potash mining examples.* University of Calgary, 2010.